UNIVERSITÉ SORBONNE PARIS NORD MEMBRE :

Thèse de doctorat

Bottom-up strategy for the development of optically transparent and nanostructured $MgAl_2O_4$ spinel ceramics

Université Sorbonne Paris Nord

École doctorale N°146 (Galilée) - Sciences, Technologies et Santé

Laboratoire des Sciences des Procédés et des Matériaux UPR3407 - CNRS

Spécialité de doctorat : Sciences des Matériaux

Thèse présentée et soutenue à Villetaneuse, le 12 juillet 2023

Par **Hugo SPIRIDIGLIOZZI**

Composition du Jury

M. Salvatore GRASSO Associate professor, Queen Mary University of London	Rapporteur
M. Anatoli POPOV Senior researcher, University of Latvia	Rapporteur
M. Claude ESTOURNES Directeur de recherche CNRS, Université Paul Sabatier	Président
Mme Souad AMMAR Professeur des Universités, Université Paris Cité	Examinatrice
Mme Gaëlle DELAIZIR Maître de conférences-HDR, Université de Limoges	Examinateur
M. Christophe COUREAU Responsable R&D, Société SOLCERA	Examinateur
M. Dominique VREL Directeur de recherche CNRS, Université Sorbonne Paris Nord	Invité
M. Frédéric SCHOENSTEIN Professeur des Universités, Université Sorbonne Paris Nord	Directeur de thèse
M. ANDREI KANAEV Directeur de recherche CNRS, Université Sorbonne Paris Nord	Co-directeur de thèse

Thèse de doctorat

NNT :

Le Rêve d'un curieux

« J'étais comme l'enfant avide du spectacle,

Haïssant le rideau comme on hait un obstacle…

Enfin la vérité froide se révéla :

[…]

— Eh quoi ! n'est-ce donc que cela ?

La toile était levée et j'attendais encore. »

Charles Baudelaire, ***Les Fleurs du mal****, 1857*

This page intentionally left blank.

This thesis is dedicated to the memory of

Belaid BEN BAHA,

Angela LIBERATORE

and Anna-Maria LIBERATORE

This page intentionally left blank.

Disclaimer

This work has been carried out within the framework of the EUROfusion Consortium, funded by the European Union via the Euratom Research and Training Programme (Grant Agreement No 101052200-EUROfusion). Views and opinions expressed are however those of the author(s) only and do not necessarily reflect those of the European Union or the European Commission. Neither the European Union nor the European Commission can be held responsible for them.

This page intentionally left blank.

Ackowledgements

This page intentionally left blank.

This page intentionally left blank.

Abbreviations

a.u.: arbitrary unit

BG: bang gap

BP: boiling point

BPR: grinding ball to powder mass ratio

BSE: backscattered electrons

BUT: butanediol

CB: conduction band

cfc: cubic face-centered

CL: cathodoluminescence

CS: crystallite size

CSP: cold sintering process

CSPS: cool spark plasma sintering

DEG: diethylene glycol

DLS: dynamic light scattering

dpa: displacement per atom

DPSPS: deformable punch spark plasma sintering

DSC: differential scanning calorimetry

DT(A): differential thermal (analysis)

DTG: derivative of TG

EBSD: electron backscattering diffraction

ED: electron diffraction

EDX: energy-dispersive X-ray spectroscopy

EG: ethylene glycol

EPR: electron paramagnetic resonance

FAST: field assisted sintering technique

(I)FFT: (inversed) fast Fourier transform

FS: flash sintering

FTIR: Fourier-transformed infrared

GB: grain boundary

GF: grain growth factor

GS: grain size (mode)

GSD: grain size distribution

HFS: hyperfine structure

HIP: hot isostatic pressing

HP: hot pressing

HPSPS: high pressure spark plasma sintering

IPF: inverse pole figure

IQ: image quality

IR: infrared

LDH: layered double hydroxide

LDO: layered double oxide

LSH: layered single hydroxide

MAS: magnesium aluminate spinel

MT_2: $MgTa_2O_6$ phase

M_4T_2: $Mg_4Ta_2O_6$ phase

MW: average molecular weight

MWS: microwave sintering

NIR: near infrared

n.u.: normalized (arbitrary) unit

PAMWS: pressure-assisted microwave sintering

PEG: polyethylene glycol

PEN: pentanediol

PL: photoluminescence

PLE: photoluminescence excitation

PLS: pressureless sintering

PP: primary particle

PRO: propanediol

PS(D): particle size (distribution)

PVP: polyvinylpyrrolidone

RE: rare-earth

RT: room temperature

RIT: real in-line transmittance

SAED: selected area electron diffraction

SE: secondary electrons

SEM: scanning electronic microscopy

SP: secondary particle

SPS: Spark plasma sintering

(I)T/T_{il}: (in-line) transmittance

TEG: tetraethylene glycol

(S)TEM: (scanning) transmission electronic microscopy

TFT: total forward transmittance

TG(A): thermogravimetric (analysis)

TJ: triple junction

TL: thermoluminescence

TMES: trimethylethoxysilane

TR: total reflectance
TrEG: triethylene glycol
UPA: ultraporous alumina
UV: ultraviolet
VB: valence band
VDF: virtual dark field
XPS: X-ray photoelectron spectrometry
XRD: X-ray diffraction
ZFS: zero field splitting

Symbols

α: heating rate
ΔH: linewidth of a signal in electron paramagnetic resonance
γ: particle surface energy
θ: X-ray diffraction Bragg angle
λ: wavelength
μ: chemical potential
μ_B: Bohr magneton
v: microwave frequency
v_{GB}, v_p: velocity of grain boundary and pore, resp.
ρ: density
ϕ: solid loading in suspension
a, c (crystallography): lattice parameters
a (UPA microstructure): UPA fibers length
$\mathrm{a_i}$ (electron paramagnetic resonance): $\mathrm{i^{th}}$ allowed line of hyperfine structure
A: interface area
$\mathrm{A_0}$: hyperfine splitting constant of a signal in electron paramagnetic resonance
B: mass transport parameter during densification
B (electron paramagnetic resonance): external magnetic field
c: the speed of light in vacuum
$\mathrm{C_T}$: total concentration of $\mathrm{Al^{3+}}$ and $\mathrm{Mg^{2+}}$ in solvent
$\mathrm{d_{hkl}}$: interplanar spacing
d (UPA microstructure): UPA fibers diameter
d (microstructure): density/relative density
d_p: pores diameter
D: diffusion coefficient
E: energy of a particles beam
$\mathrm{f_i}$ (electron paramagnetic resonance): $\mathrm{i^{th}}$ forbidden line of hyperfine structure

F_{GB}, F_p: driving force for grain boundary and pore mobility, resp.

ΔG: Gibbs free energy

g: the Landé g-factor

h (physics): Planck constant

h (synthesis): hydrolysis ratio

H_0: mean resonance field of a signal in electron paramagnetic resonance

I: cationic inversion in spinel material

K_0: Arrhenius constant for grain growth

M: molar mass

M_{GB}, M_p: mobility of grain boundary and pore, resp.

n (spinel composition): atomic ratio Al:Mg within spinel phase

n_i (spinel synthesis): set n in MgO-Al_2O_3 synthesis

n (optic): refractive index

n, m (sintering mechanism): grain growth exponents

N_p: number of pores per unit grain boundary area

oh: hydroxide ratio

p: vapor pressure

P: mechanical applied pressure

P_E: effective applied pressure

P_G: gas pressure within the pores

Q: grain growth activation energy

r (powder): particle radius

r (synthesis): additive ratio, specifically acetate ratio

R: gas constant

s (sintering mechanism): stress exponent

t: time

t: thickness

t_d: sintering dwell time

T: temperature

T_c: critical temperature of two-step spark plasma sintering

T_d: sintering dwell temperature

V_M: molar volume

w: grain boundary thickness

W: spectral weight of a signal in electron paramagnetic resonance

x (LDH composition): substitution (insertion) rate in LDH-type1 (LDH-type2)

x (MgO-Al_2O_3 composition): Al_2O_3 mole fraction

x_i (spinel synthesis): set x in MgO-Al_2O_3 synthesis

x_t (MgO-Al_2O_3 composition): total Al_2O_3 mole fraction in polyphasic samples

Table of content

Introduction

The work presented in this thesis has been carried out within the framework of the EUROfusion Consortium, with the task specification MAT-4.1.2-T016 aiming for the development of reproducible radiation resistant polycrystalline optical materials. Indeed, among a great deal of possible applications (medicine, space engineering, optoelectronics…), their application as optical windows for use in extreme environments is foreseen, including in future nuclear fusion facilities. Specifically, development of ceramics with high optical transparency and ultrafine microstructures are anticipated as one of the major priorities of the EUROfusion Consortium research program, for applications in the field of ionizing radiations tolerant detectors.

Optical materials are valuable in diagnostic systems in nuclear powerplant, and have to withstand neutron irradiation in the order of megaelectronvolts. When a material is subjected to ionizing radiation, radiation damage occurs by continuous displacement of each atom away from its crystal site measured in *displacement per atom* (dpa), which then quickly moves to the surfaces, leading to the swelling of the material while vacancies are left behind [1]. Hence, the capacity of a material to resist irradiation on a microstructural level depends on its ability to limit the formation of pairs of interstitial defects / vacancies, and avoid the subsequent movement toward surfaces of these interstitials. Fortunately, nanostructured materials have shown promising radiation resistance by a "self-healing" mechanism [2]: grain boundaries are able to capture the formed interstitials, which are later recombined with nearby vacancies for the defects pairs to be annihilated, as illustrated in *Figure 1*. However, critical grain size under which radio-resistance is effective is unknown at the moment, even if grain size at the nanoscale (< 100 nm) makes consensus [1, 2]. For this reason, our objective as members of the EUROfusion Consortium is to develop optically transparent ceramics with grain size at the nanoscale for their radiation tolerance to be tested.

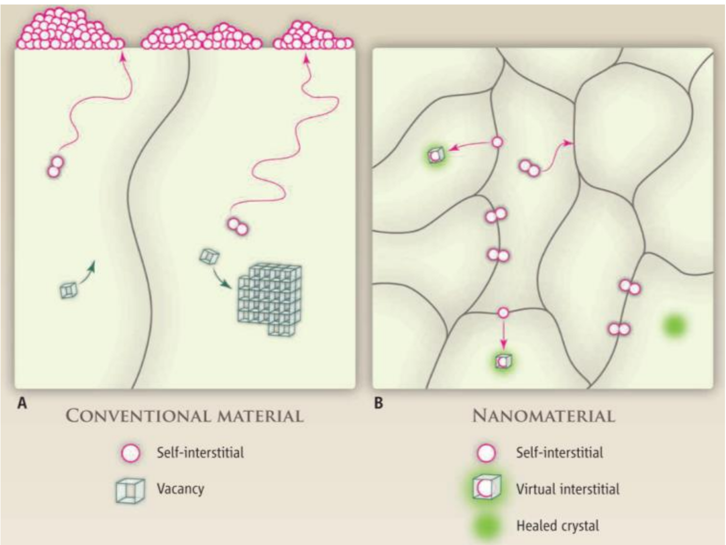

Figure 1: Interstitial defects caused by irradiation in (A) conventional material and (B) nanostructured material [1]

In addition to the microstructural features of the material, several research groups have been focused on the radiation tolerance arising from their specific structural properties [3–10]. Between the different crystallographic structures envisaged, complex oxides and particularly spinel structure has been reported to exhibits very high tolerance to radiations due to its peculiar lattice [3, 4], which allows atomic displacements in the material without degradation of the properties. Hence, damage induced by ionizing radiation is reduced. Among the variety of compounds with spinel structure, $MgAl_2O_4$ is of the highest interest because of its general properties: it exhibits very good optical properties, with a theoretical transmittance of 87% between 160 nm and 6000 nm wavelength [11], as well as a high hardness of 16 GPa [12, 13], and up to 28 GPa when strengthened by nanostructuration (Hall-Petch relationship) [14]. Thus it is a very good candidate for the desired application of transparent window for optical detectors in fusion reactors.

By consequences of the above-mentioned features, the objective of this work is to develop a reproducible method of fabrication for optically transparent $MgAl_2O_4$ spinel ceramics, with the finest possible microstructure at the nanoscale, for their resistance to ionizing radiations to be tested subsequently by our EUROfusion collaborators. This work should lead to a better understanding of the influence of nanostructuring on the irradiation resistance properties and to the determination of the optimal size of the nanograins.

However, production of a transparent ceramic demands a high relative density, normally requiring high processing temperature, while minimizing the grain size demands a reduced temperature of processing, hence the challenge of this work. Unconventional methods have to be used in order to reach the objectives.

In this study, a bottom-up approach will be considered, from the synthesis of the spinel nanopowder to its subsequent sintering.

The preparation of the finest possible $MgAl_2O_4$ nanopowder precursor will be carried out following two original synthesis routes well-known in our research group. The first method used is the soft chemistry polyol-mediated synthesis, known for the wide variety of nanoscaled compounds easily achievable [15, 16]. The second method consists on the liquid impregnation of an nanofibrous alumina, prepared beforehand, by a solution containing the stoichiometric amount of Mg^{2+} cation [17].

The synthesized powders will then be consolidated by Spark Plasma Sintering (SPS), together with commercially available powders for comparison purpose. The SPS is an innovative technique allowing very fast processing and enhanced densification rate, which provide better control over the final microstructure of the sample, and is especially useful to obtain nanograined ceramics with high relative density [18, 19].

Following this introduction, the body of this thesis is formed by five chapters and a conclusion.

Chapter 1 – State of the art – is an overview on the general knowledge and state of the art relative to the topic of this thesis. The MgO-Al_2O_3 system is first described, before focusing on the $MgAl_2O_4$ structure and properties. Then, the physic of transparent medium and required conditions in achieving high transparency is reviewed. Afterward, the different methods for synthesizing spinel nanopowders and for their sintering into transparent ceramics are overviewed, and a focus on the techniques specifically used in this work is carried out.

Chapter 2 – Materials and methods – details the materials and protocols used for the synthesis, the sintering, the sample preparation for characterization and the characterization techniques used in this work.

Chapter 3 – Synthesis of $MgAl_2O_4$ nanopowders – presents the experimental results obtained for the synthesis of the nanocrystalline $MgAl_2O_4$ powders by the polyol-mediated route and the liquid impregnation of nanofibrous alumina. For the polyol route, reference synthesis conditions are first defined, and the resulting material and reaction mechanism is thoroughly investigated, then a study on the influence of the synthesis parameters is carried out. The possibility of doping the spinel phase during the synthesis is also assessed. For the impregnation route, the influence of the crystallographic state of the alumina precursor on the mechanism of formation of the magnesium aluminate spinel phase is thoroughly investigated, as well as the resulting features of the powders. The possibility to extent the applicability of UPA and impregnation process for the synthesis of numerous alumina based compounds is also investigated.

Chapter 4 – Consolidation of $MgAl_2O_4$ ceramics - presents the experimental results obtained for the sintering of different powders by spark plasma sintering processing. The densification is mostly carried out on commercially available powders. First, the influence of comminution on the sintering of the powders is carried out, and a thorough parametric study on two different commercial powders is performed. Afterward, the sintering of the in-lab synthesized nanocrystalline powders is studied, and then the effects of post-sintering treatments are presented. Finally, we investigated the phenomenology during SPS of ionic conductors with the cases of Ta_2O_5 and Ta_2O_5 added $MgAl_2O_4$ powders.

Chapter 5 – Physical investigation of the defects in $MgAl_2O_4$ and irradiation behavior – presents the results of luminescence and electron spin resonance spectroscopies, in order to assess the intrinsic and extrinsic defects introduced through the processing of our materials. In particular, the evolution of the defects during sintering and after irradiation has been studied.

This page intentionally left blank.

Chapter 1

State of the art

In this chapter, an overview is given on the general knowledge and the state of the art relative to the current work. First, the MgO-Al_2O_3 system is presented, and a focus is made on the magnesium aluminate spinel (MAS) structure and on its properties. Then, the next part focuses on the theoretical aspects of optical transparency and the transparency of polycrystalline ceramics. The different methods for synthesizing spinel nanopowders, with a focus on the synthesis routes used in this work (polyol-mediated route and liquid impregnation of nanofibrous alumina) are presented in the third sub-chapter. Finally, in the last section, the general aspects and the phenomenology of sintering are overviewed, prior to presenting the state of the art of the sintering techniques used for processing MAS, and especially the spark plasma sintering technique, as well as the methods of improvement of the sinterability of MAS.

I. The MgO-Al_2O_3 system

1. MgO-Al_2O_3 phase diagram and magnesium aluminate spinel MgO·$n$$Al_2O_3$

Before presenting $MgAl_2O_4$ and the complex spinel structure and properties, it is worthy rapidly introducing the binary oxides composing it, since they will have an interest in the work presented here.

i. MgO structure

The magnesium oxide MgO knows only one crystal structure in normal P-T conditions: as two-thirds of the monoxide minerals, it crystallizes in the **cubic face centered (*cfc*) halite** (or rocksalt) structure space group $Fm\bar{3}m$, illustrated in *Figure 1.1*, with a lattice parameter a = 4.212 Å. However, in contrast with the halite representative compound NaCl, the ions in MgO are divalent, hence the bonds are 25% covalent, increasing the structure's thermal and chemical stability [20]. The crystalline magnesia is generally referred to as its mineral form, **periclase**.

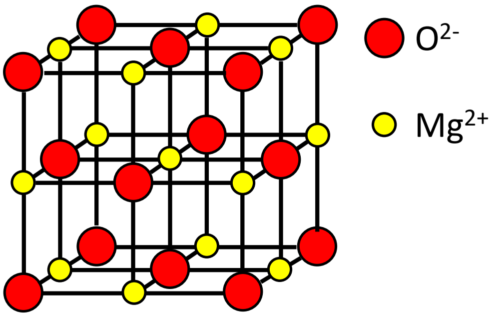

Figure 1.1: MgO halite crystal structure - periclase

ii. Al_2O_3 structure

In contrast with MgO, alumina exists in various crystalline stable and metastable forms at ambient conditions. Here, we will summarize the structural data on the most common Al_2O_3 polymorphs (*Table 1.1*). It is to be mentioned that there is no consensus on the structure for metastable aluminas due to their generally low crystallinity, and the most relevant reported structures have been chosen to be presented here.

Table 1.1: Structural data on most reported alumina polymorphs [21–23]; in bold are the the most common forms

Polymorph	Space group	Z	a (Å) b (Å)	c (Å)	Structure type	Density
a-Al_2O_3					**Amorphous**	
γ- Al_2O_3	**$Fd\bar{3}m$**	**10.66**	**7.90**	**7.90**	**Cubic defective spinel**	**3.67**
δ- Al_2O_3	$P\bar{4}m2$	16	7.93	23.50	Tetragonal spinel superstructure	3.6 - 3.7
θ- Al_2O_3	$A2/m$	4	5.62 2.91	11.79 β 103.8°	Monoclinic spinel-related	3.6 - 3.7
η- Al_2O_3	$Fd\bar{3}m$	10.66	7.91	7.91	Cubic defective spinel	3.6 - 3.7
κ- Al_2O_3	$Pna2_1$	8	4.844 8.330	8.955	Orthorhombic	3.98
χ- Al_2O_3	$Fd\bar{3}m$	10.66	~7.91	~7.91	Cubic defective spinel	3.67
α- Al_2O_3	**$R\bar{3}c$**	**6**	**4.76**	**12.99**	**Hexagonal, corundum structure**	**3.99**

The **amorphous alumina**, often denoted ***a*-Al_2O_3**, is indeed of complex nature and cannot be structurally described as a polymorph in general, since it is depending on the preparation conditions [21]. However, it has been reported that *a*-Al_2O_3 has only moderate thermal stability (increasing with decreasing particle size) for $T < 700°C$, above which crystallization is observed. It presents interest though, since this moderate stability often provides better reactivity.

The only **thermodynamically stable alumina** on the whole temperature range from ambient to melting point is the **corundum structure**, denoted as **α-Al_2O_3**. It has a trigonal symmetry with rhombohedral Bravais centering, and its lattice is often considered as a hexagonal closed packed (*hcp*) arrangement of O^{2-}, with Al^{3+} occupying 2/3 of the octahedral sites (*Figure 1.2*). Corundum ceramics are very relevant materials with high stability, high hardness, high melting point (2053°C) and high thermal and electrical resistance. α-Al_2O_3 is obtained by irreversible transformation of metastable alumina generally at $T \geq 1100°C$.

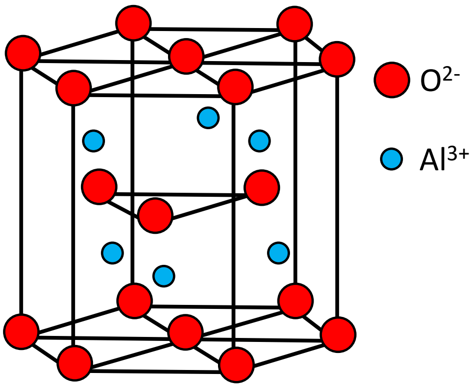

Figure 1.2: Al_2O_3 corundum crystal structure

Numerous metastable alumina structures have been reported, and can be divided into two broad categories: **the low temperature** (γ, η, χ) and **the high temperature polymorphs** (δ, θ, κ). It is often considered that the low temperature phases exhibit close structures, conventionally described as **defective spinels** [23]. The cubic normal $MgAl_2O_4$ and defective spinel structures will be described later on (*Figure 1.5*). Of all the low temperature polymorphs, **γ-Al_2O_3** is by far the most studied and the most documented. γ-Al_2O_3 is often described by the formula $\mathbf{(Al_{2/3}\square_{1/3})^T(Al_2)^OO_4}$, where $(.)^T$, $(.)^O$ and $\square$ denotes a tetrahedral site, an octahedral site and a cation vacancy, respectively. This formula implies that the *cfc* O^{2-} sublattice is fully occupied and the octahedral sites are normally occupied by Al^{3+}, whereas the divalent cations are replaced by 2/3 trivalent Al^{3+} and 1/3 vacancies to achieve charge balance, resulting in a cation deficiency with respect to spinel stoichiometry. A mobility of the Al^{3+} in the lattice has been reported, leading to octahedral vacant sites instead [21]. The XRD patterns of the low temperature polymorphs are presented in *Figure 1.3.a*; it can clearly be seen that the patterns are similar, due to their spinel structure. The high temperature polymorphs have different structures, and are generally not-well known. Since it is obtained from its calcination, θ-Al_2O_3 has a monoclinic structure derived from the γ-Al_2O_3 spinel, through deformation and ordering distribution of Al^{3+} with 50% in octahedral and 50% in tetrahedral sites [21]. Consequently, its XRD pattern is not from spinel, but it can be seen that its reflections are formed from γ-Al_2O_3 reflections (*Figure 1.3.b*). The metastable Al_2O_3 structures have shown great catalytic properties [21].

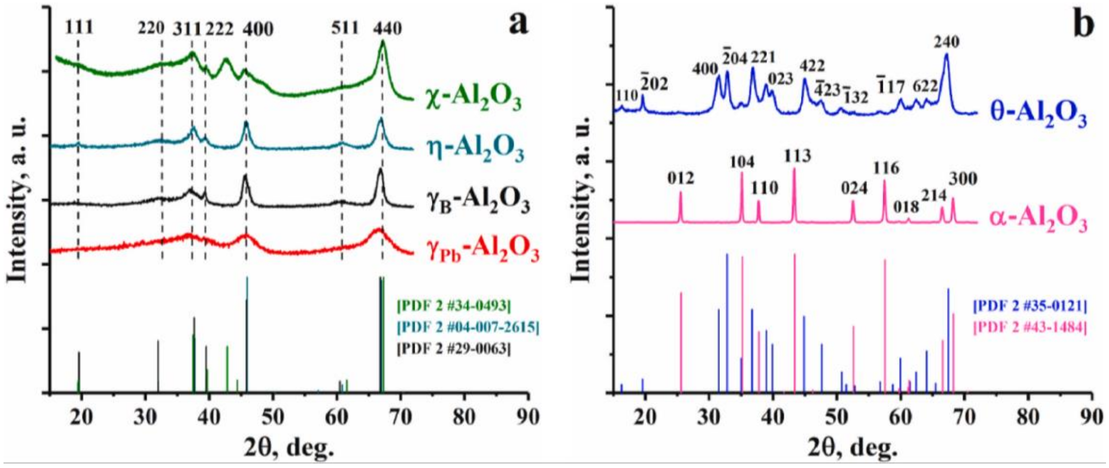

Figure 1.3: XRD of Al_2O_3 polymorphs with a) metastable defective spinel structures and b) θ-Al_2O_3 and α-Al_2O_3 [23]

iii. MgO-Al_2O_3 phase diagram

The system MgO-Al_2O_3 has been thoroughly and extensively studied for over a century, as the need for highly refractory ceramics in industrial applications increased. The first phase diagram for the system was reported by Rankin and Mervin in 1916 [24], and despite being largely erroneous, it remained unchanged until the more accurate work of Alper *et al.* in 1962 [25], on the MgO-$MgAl_2O_4$ part of the diagram. Finally, Hallstedt made reassessment on the whole system based on thermodynamic model correlating experimental data [26], calculating a new diagram still used nowadays with minor adjustments (*Figure 1.4*).

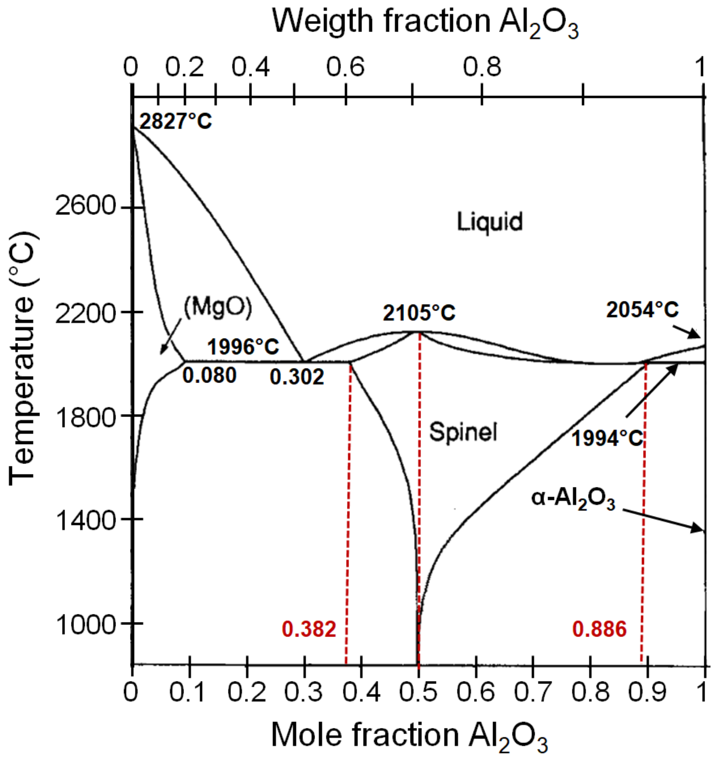

Figure 1.4: MgO-Al_2O_3 phase diagram; red dashed lines indicates the maximum thermodynamical limits of the pure spinel phase compositions and the stoichiometric composition. Adapted from [26] with modifications from [11, 13]

The system MgO-Al_2O_3 presents only one stable intermediate compound, the **magnesium aluminate spinel (MAS)**, which is stoichiometric for the composition MgO:Al_2O_3 of 1:1, or $x = 0.5$, where x is the mole fraction of Al_2O_3. Additionally, two eutectic reactions are observed for $x = 0.302$ and $x \approx 0.886$; the Al-rich one has been argued to rather undergo a peritectic transformation [27], but the small debated discrepancies are difficult to evidence experimentally. The MgO-rich eutectic microstructure consists on exsolved MgO precipitates surrounding MAS grains and exsolved MAS precipitates within MgO grains [28], while the Al_2O_3-rich one exhibits a “divorced eutectic microstructure”, with the phases in massive form, as sharp and dendritic alumina grains in a MAS matrix [27]. The stable α-Al_2O_3 does not admit any range of solid solution with MAS, while MgO admits a fair content of Al_2O_3 in solid solution up to $x = 0.080$ for $T \geq 1600°C$.

2. Magnesium aluminate spinel $MgO{\cdot}nAl_2O_3$

i. The spinel structure

As mentioned above, magnesium aluminate spinel (MAS) is the **only stable intermediate compound** in the system MgO-Al_2O_3. From the phase diagram (*Figure 1.4*), it is clear that the thermodynamically stable spinel range below ~1000°C consists on the sole $x = 0.5$ composition. However, the solubility of both MgO and Al_2O_3 increases with temperature, with the maximum range $0.382 \leq x \leq 0.886$ at 1995°C [26]. In practice, **non-stoichiometric spinel** in a reduced range is metastable at ambient conditions, hence MAS is often described as **$MgO{\cdot}nAl_2O_3$**, where **$n = Al_2O_3/MgO$** and $0.618 \leq n \leq 7.8$ [25, 27]. It is remarkable that Al_2O_3-rich MAS stability range is far greater than MgO-rich MAS range. Stoichiometric MAS melts congruently at approximately 2105°C, and excess of either constituting oxides leads to a lowering of the melting point.

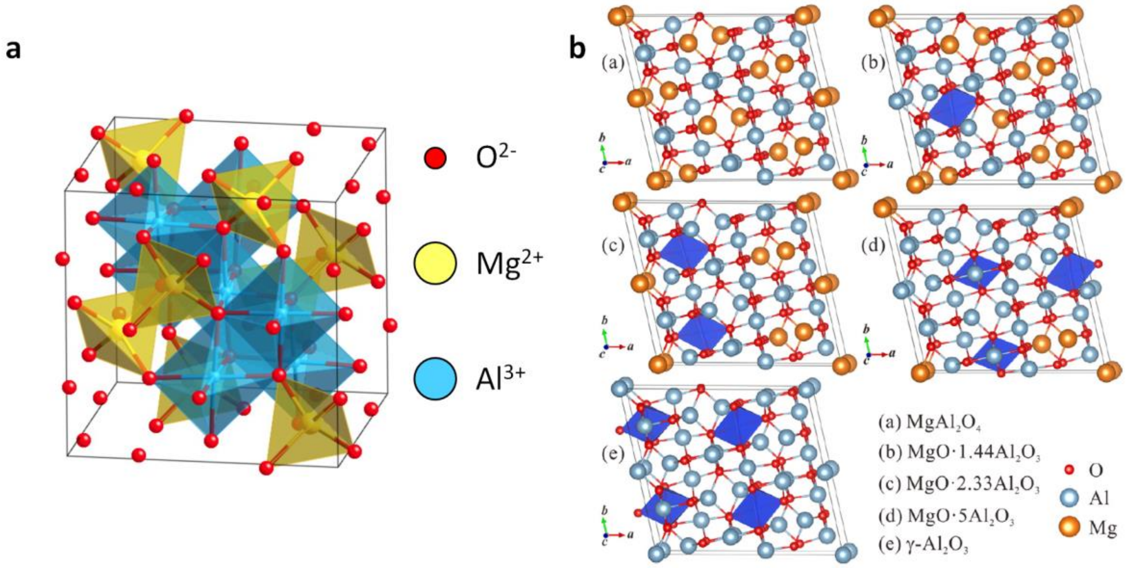

Figure 1.5: a) $MgAl_2O_4$ spinel crystal structure depicting the octahedral (blue), tetrahedral (yellow) and naturally vacant interstices. b) Supercell evolution with composition from $MgAl_2O_4$ to γ-Al_2O_3; blue octahedrons indicate supplementary cationic vacancies [29]

$MgAl_2O_4$ is the representative candidate of the spinel family, which exhibits a **complex lattice structure** represented in *Figure 1.5.a*. A symmetric spinel unit cell contains eight $MgAl_2O_4$ formula units, where the 32 O^{2-} anions form a *cfc* lattice with $Fd\bar{3}m$ space group and cell constant $a = 8.0826$ Å [30]. The unit cell has 96 interstices, among which 64 tetrahedral ones and 32 octahedral ones. However, only 1/8 of the tetrahedral positions are occupied by Mg^{2+}, and ½ of the octahedral positions are occupied by Al^{3+}.

The $MgO{\cdot}nAl_2O_3$ composition has indeed a great influence over the material properties, but also on the crystal structure. In non-stoichiometric spinel, the stability of the structure is ensured by clusters of intrinsic defects which preserve overall and local charge neutrality [31]. The lattice is impacted by the composition, as the cell constant follows a Vegard's law [29]. Viertel and Seifert, pioneers of the fabrication of synthetic spinel, developed an empirical equation to estimate n (*Equation 1.1*), still used nowadays [32]:

$$\boldsymbol{n = \frac{8.6109 - a}{3a - 23.7295}} \qquad \textit{Equation 1.1}$$

where a is the spinel lattice parameter, such as for stoichiometric MAS, $n = 1$ and $a_0 = 8.0826$ Å.

The MgO-rich composition is relatively unknown to date: since early works of Alper *et al.* [25] and Shirasuka *et al.* [33] seeking for precise measurements of the crystal data for $n < 1$, only a few publications addressed the matter. Sarkat *et al.* [34] unsuccessfully tried to formed magnesia-rich spinel by solid oxides mixture reaction at high temperature, and concluded that no solid solution range of spinel with $n < 1$ existed. Authors in [35] found instead that monophasic spinel could be obtained for $n \geq 0.957$, which is still far from the limit of 0.618. More recently, Li *et al.* [36] prepared monophasic $MgO{\cdot}0.667Al_2O_3$ spinel, still through solid state reaction but with prior comminution and a modern furnace. These strong discrepancies with phase diagram data are explained by the high energy required for incorporation of Mg^{2+}, from 2 to 5 times the one required for Al^{3+} [31]. In addition, the phase diagram and particularly the domains frontiers were determined through melting of oxides mixtures, then rapidly brought to the desired temperature, and finally air-quenched to room temperature [25]. The variation in the methodology used indeed explains the differing results.

On the other hand, the Al_2O_3-rich part of the MAS composition range has been thoroughly studied since it is easily obtained. Theoretical [29], thermodynamic [27, 37], physical [38] and sintering [39–41] studies have been carried out on $MgO{\cdot}nAl_2O_3$ with $n > 1$. Alumina-rich MAS can be seen as a stoichiometric spinel in which some Mg^{2+} have been substituted by Al^{3+}. Indeed, to preserve the electrical neutrality, for two inserted Al^{3+}, three Mg^{2+} have to be pulled out of the lattice. Thus, cationic vacancies are induced, in addition to the "naturally" vacant interstices [29]. The greatest is n, the higher is the density of vacancies, until all Mg^{2+} has been replaced by Al^{3+}, leading to the defective γ-Al_2O_3 structure already discussed in *Chapter 1.I.1.ii*. The supercell models for MAS with n = 1, 1.44, 2.33, 5 and ∞ (γ-Al_2O_3) are presented in *Figure 1.5.b*. It is interesting to note that while this model explains well the observed Vegard's law for lattice constant, it implies an uninterrupted solid solution range between $MgAl_2O_4$ and γ-Al_2O_3, which is not in agreement with thermodynamic reports [26]. In fact, Mg^{2+} substitution by Al^{3+} is not the only mechanism for Al-rich MAS formation, as Schottky defects may be formed (Mg^{2+} and O^{2-} vacancies pairs) to maintain the local charge. The decrease in MgO content during thermally activated spinelization is favored by its vapor pressure 1000 times higher than Al_2O_3 one at high temperature, and even more in reducing atmospheres [42].

ii. The intrinsic defects

The "natural vacancies" in the structure offer a high flexibility for the displacement of the cations within the spinel lattice; hence several types of **intrinsic (or structural) defects** exist and are stabilized in spinel, which is one of the main factor making the structure radio-resistant [43]. The more frequent types [11] are schematized in *Figure 1.6.a*. The simplest are the **Mg^{2+} vacancy V_{Mg}^{2-}**, the **Al^{3+} vacancy V_{Al}^{3-}** and the **O^{2-}**

vacancy V_o^{2+}, all exhibiting the inverse charge of the missing ion. The **“Schottky defect**” consists on cationic and anionic vacancies counteracting the charge. The **antisite defects** are either Al^{3+} on Mg^{2+} interstice (Al_{Mg}^{+}) or Mg^{2+} on Al^{3+} site (Mg_{Al}^{-}), which present electrical charge due to valence difference of both cations, and are only counteracted when both types of antisites are simultaneously present in the structure. Lastly, the **cationic auto-interstitials defects** Al_i^{3+} and Mg_i^{2+} are observed when Al^{3+} or Mg^{2+}, respectively, are in a normally vacant site *i*. If the interstitial cation left its normal site and created a vacancy while migrating to *i*, the counteracting pair Al_i^{3+}-V_{Al}^{3-} is called **“Frenkel defect”**. The increasing interest surrounding these defects arises from their important role in the resistance to ionizing radiation [44].

Among these defects, the vacancies types are of primary interest. We can divide them into two classes: the cationic vacancies which are called **“V-type centers”** and the anionic vacancies called **“F-type centers”**. The V centers are negatively charged (V^{2-} or V^{3-}, depending on missing cation), but the nearby O^{2-} ions can trap electronic holes as a stabilizing mechanism, becoming O^-, hence the charge is reduced to V^- or V^{2-}, respectively [45]. Some specimen of V-type centers are represented in *Figure 1.6.b*. The F-type centers are initially positively charged (F^{2+} center), but the oxygen vacancies are known to be able to trap one or two free electrons, thus forming F^+ and F^0 centers, respectively [8]. In addition to these elementary defects, numerous complex defects can be formed by association or clustering of the “simple” defects: F_2 center (2 nearby F centers interacting, with 0 to 4 e^- trapped in the system), F_3 …

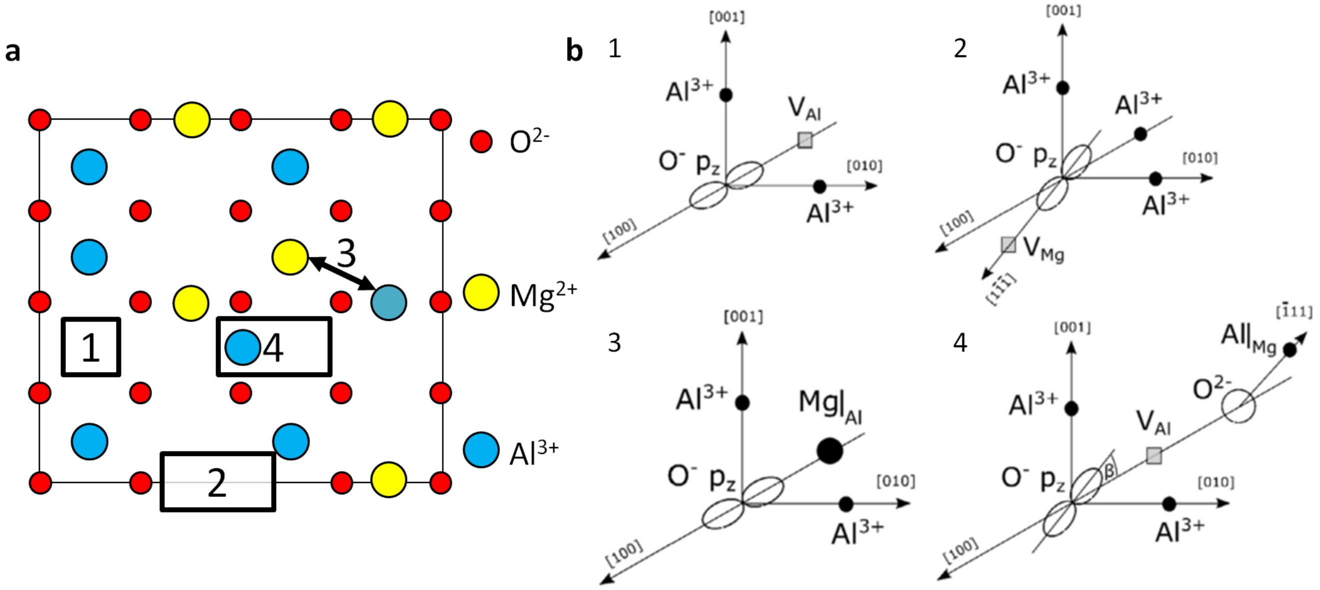

Figure 1.6: a) Schematic of intrinsic defects in spinel: (1) is a Al^{3+} vacancy, (2) is a Schottky defect formed by combined Mg^{2+} and O^{2-} vacancies, (3) is an antisite defect and (4) is a Frenkel defect; b) models of some V-centers: (1) $V_1 \equiv O^-$-V_{Al}^{3-}, (2) $V_2 \equiv O^-$-V_{Mg}^{2-}, (3) $V_{22} \equiv O^-$-$Mg|_{Al}^-$ and (4) $V_3 \equiv O^-$-V_{Al}-$Al|_{Mg}^+$ [45]

The exchange of positions between Al^{3+} and Mg^{2+}, *i.e.* double antisite defects (or **cation inversion**) is one of the most stable defects in spinel, therefore it is often encountered. The **degree of disorder** arising from it can be expressed as the inversion parameter *I*, defined as the fraction of bivalent Mg^{2+} in octahedral sites. Therefore, *I* can range from 0 for the so-called **normal spinel $(Mg)^T(Al_2)^OO_4$** to 1 for the **inverse spinel $(Al)^T(MgAl)^OO_4$**, where $(X)^T$ and $(X)^O$ indicate a cation occupying a tetrahedral and an octahedral interstice respectively, and assuming values $0 < I < 1$ for a **mixed (or partially inversed) spinel** [43]. It should be noted that *I* is sometimes defined as the fraction of trivalent Al^{3+} in tetrahedral sites, only modifying its range to $0 < I < 0.5$ [43]. Ball *et al.* showed by calculation [46] that increasing I parameter leads to a decreasing lattice constant, and recent experiments found an empirical linear dependence as $a = a_0 - 0.0416*I$ [47]. However, both experiments and predictions have been made only up to I = ~0.4.

iii. The properties of $MgO·nAl_2O_3$

Table 1.2: Physical and chemical properties of $MgAl_2O_4$ ceramics, summarized from reviews [11, 13, 30]

Property		Values
Structural / Phase diagram	Melting point (°C)	2105 - 2135
	Stoichiometry max. range (at% Al_2O_3) at 1995°C	0.382 - 0.886
	Stoichiometry practical range (at% Al_2O_3)	~0.49 - 0.75
	Density (g/cm^3)	~3.58
Mechanical	Young's modulus (GPa)	~300
	Shear modulus (GPa)	192
	Poisson's ratio	0.26
	Hardness knoop 200g (GPa)	10.2 - 13.98
	Hardness Vickers H_V10 (GPa)	12 - 16.8
	Flexure strength (MPa)	250 - 470
	Fracture toughness (MPa√m)	1.4 - 2.0
Dielectric	Dielectric constant, ε at 1 kHz, 1 MHz	8.2, 9.19
	Loss tangent, δ (10^{-4}) at 1 kHz, 1 MHz, 9.3 GHz	2.5, 2, 1
Electric	Resistivity (Ω/cm) at 25°C, 500°C	$> 10^4$, 2×10^4
Thermal	Thermal expansion (K^{-1}) at 25°C–1000°C	7.9×10^{-6}
	Thermal conductivity (W/m.K) at 25°C, 100°C	24.7, 14.8
	Thermal Shock resistance (kW/m)	1.1 - 2.1
Optical	Band gap (eV)	7.7
	Refractive index, n at 530 nm, 1000 nm	1.718, 1.704
	Transmission window (nm)	~190 - 6000
	Theoretical transmittance at 530 nm	87%
	Theoretical reflectance at 530 nm	6.8%
	Absorption coeff. (cm^{-1}) at 193 nm, 532 nm, 3.39 µm	2.7, 0.4, 0.018
Chemical	Erosion by rain (756 km/h, 20 min, 2 mm drop size)	No damage, high resistance
	Erosion by sand (75 m/s, 3 mg/cm^2 loading, 38-44 µm)	No damage, high resistance
	Chemical resistance	HF, H_2SO_4, HNO_3, NaOH

The physical and chemical properties of MAS ceramics are summarized in *Table 1.2*. $MgAl_2O_4$ material is mostly considered for applications in the fields of defense, jewelry and laser, requiring combination of thermal, optical and mechanical properties. MAS is a refractory with relatively low density compared to other ceramics also considered for the same applications, which would make future devices lighter, especially for military ballistic applications (light-weight transparent armor [48]). Its mechanical properties are quite high, even if Al_2O_3 shows better hardness (~20 GPa). However, $MgAl_2O_4$ has a greater machinability, and can be prepared with various shapes (*e.g.* transparent domes [30]). Overall, $MgAl_2O_4$ has very good optical properties with **theoretical transparency of 87%** in the wavelength range 190 – 6000 nm, the IR-cut-off being at higher wavelength than α-Al_2O_3 and γ-AlON [11]. Together with its high chemical inertness, thermal and electric refractoriness and dielectric properties, the above mentioned properties have attracted a lot of interest since the 2000's. In addition, MAS flexible structure allows doping with a large range of elements, providing further tunable properties, in particular of optical luminescence.

iv. Investigation of the defects by physical methods

This paragraph is dedicated to the investigation of intrinsic and extrinsic defects in MAS by physical methods. In particular, we will discuss physical characterizations not usually used for polycrystalline ceramics, but that we believe could help understand better both the defects formation and evolution, and the sintering mechanism.

Indeed, many characterization techniques exist and are (almost) systematically employed for investigating $MgAl_2O_4$ nanopowders and ceramics developed for transparent polycrystalline material application, such as X-Ray Diffraction (XRD), Scanning/Transmission Electronic Microscopy (SEM/TEM) and UV-Vis-NIR transmittance/FTIR spectroscopies, mostly. However, MAS has also been studied for decades by physicists, in order to understand the defects environment and stability, generally working on single crystals of high purity to facilitate the analysis of specific defects in specific orientations. They have used powerful tools, such as luminescence spectroscopies, precise optical absorption spectroscopy and Electron Paramagnetic Resonance (EPR) spectroscopy. Unfortunately, the two fields investigating MAS, *i.e.* fabrication vs investigation, have barely considered each other yet, as if the advances made by each field had few consequences on the work of the other field. Hopefully, the situation is currently changing, as few teams have started to adopt an intermediary approach. In the ceramic development research field, Morita *et al.* have used Raman and EPR spectroscopies since 2014 to attribute loss of transparency to specific defects [49, 50], while since 2018 physicist Kiryakov *et al.* used EPR on nanocrystalline transparent MAS to investigate the role of grain boundaries on the defects environment [51].

Raman spectroscopy is a more conventional method for ceramics characterization, as it is often used mostly as an identification tool, allowing rapid and easy detection of the spinel fingerprints [52]. However, the technique offers non-negligible advantages compared to XRD: **local investigation** and easier **detection/quantification of intrinsic defects**. As mentioned above, Morita has used the technique to link the transparency loss of his ceramics to carbon contamination [53]. He was then able to show inhomogeneous volume distribution through the material. Moreover, it has been known for over 30 years that in the well-known Raman signature of MAS, some vibrational modes arise from cation disorder, specifically the peak at 727 cm^{-1} and the shouldering in the peak at 409 cm^{-1}, as observed in *Figure 1.7* [54]. These defects, not present in natural spinel minerals formed in Earth mantle which has been able to equilibrate over geological timescales, are always observed in synthetic specimens. Hence, the inversion parameter I could be easily estimated from the relative intensities of the normal and inverse modes [43].

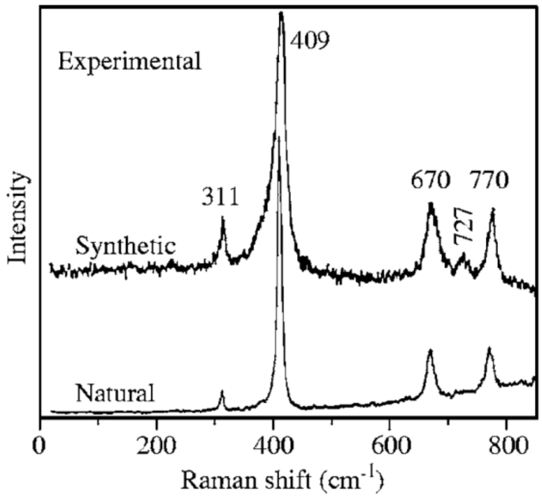

Figure 1.7: Raman spectra for natural (normal) and synthetic (partly inverse) $MgAl_2O_4$ spinels [54]

The **EPR spectroscopy** is a powerful method to investigate **magnetic center** in a material. Since in pure and non-defective MAS, no intrinsic paramagnet exists, no EPR signal should be observed. However, some of the intrinsic defects described in *Chapter 1.I.2.ii* are paramagnetic, typically the F^+ center (one unpaired electron trapped in the O^{2-} vacancy) and the V-centers associated with trapped holes on nearby O^{2-}. Hence, specific EPR signals arise from these defects (*Figure 1.8*): a single sharp and isotropic band at g = 2.005 arising from F^+ center, while a multiband hyperfine structure (HFS) on a wide structureless band around g = 2.00 – 2.05 arise from V-centers. As the F-centers are isotropic, so are their signals which do not present angular-dependency, while V-centers are directional and their signals depend on their orientation.

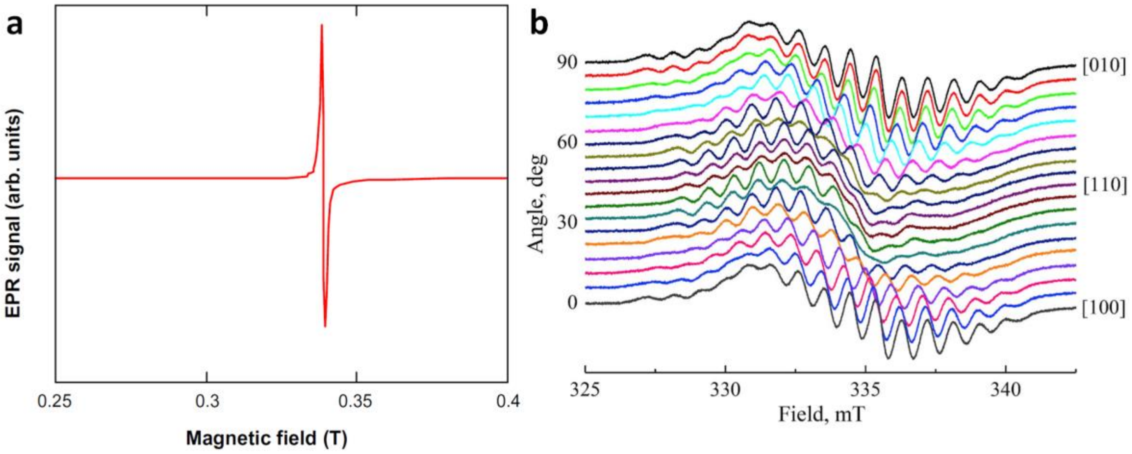

Figure 1.8: EPR spectra of MAS single crystal: a) F^+ centers [8] and b) V_1 center with rotation around [001] direction [38]

Advanced optical spectroscopic techniques are amongst the most promising methods for thorough characterization of MAS defects. Accurate **absorption spectra** can be obtained with a UV-Vis spectrometer setup working under vacuum and equipped with integrating sphere (*Figure 1.9.a* and *c*), every defect having a specific energy of absorption, generally in the UV: 5.04 eV and 4.67 eV for F and F^+ centers, respectively [55], and in the range 2.67 - 4.60 eV for V centers [56]. Defects closely related often present convoluted signals, and **luminescence spectra** can bring additional information allowing the speciation. Numerous luminescence techniques exist, *e.g.* **cathodoluminescence** (CL), **photoluminescence** (PL), thermoluminescence… depending on the excitation source; the first two are by far the most used. A simpler set-up is used for CL, the excitation source being an electron beam which can be integrated within a SEM to carry on mapping on the defects distribution [57]. Precise PL requires a more complex installation with photon excitation, often carried out on a synchrotron beamline, and presents the advantage of allowing monochromatic excitation. Spectra on PL excitation (PLE) give supplementary informations on the nature and number of defects. Generally, multiple physical techniques have to be used and compared, in order to fully understand the defects and their environment. *Figure 1.9.b* and *d* illustrate the importance of PL spectroscopy to distinguish the F-type and V-type centers, respectively, in complement to absorption (*Figure 1.9.a* and *c*). Indeed, F and F$^+$ centers signals are far better differentiated in PL spectrum.

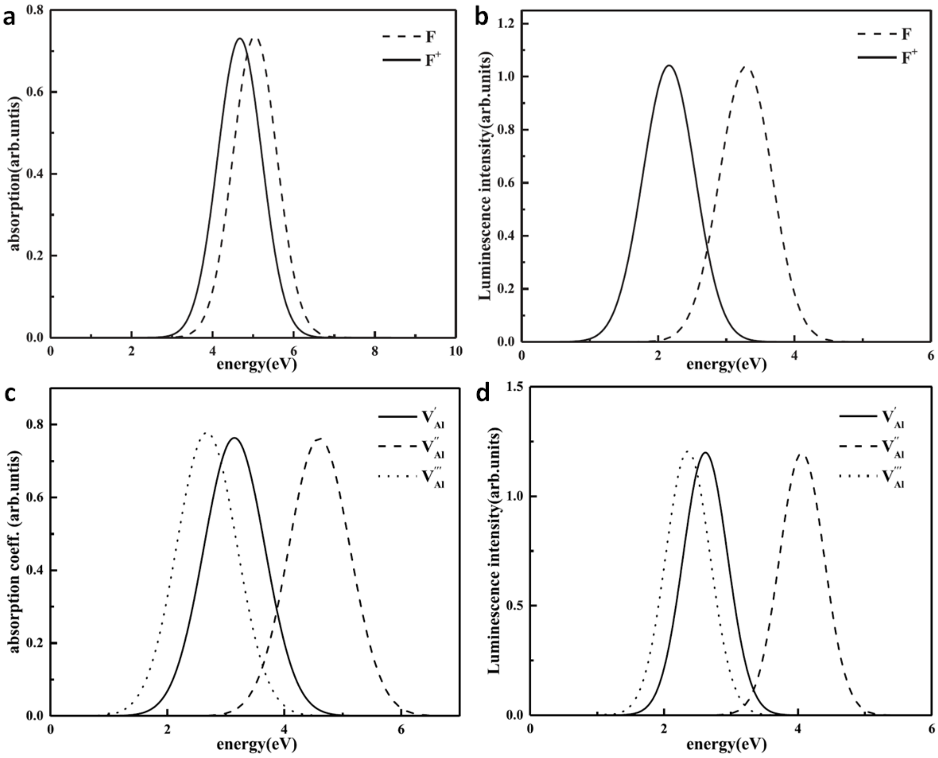

Figure 1.9: a), c) Absorption and b), d) luminescence spectra of a), b) F-type [55] and c), d) V-type centers [56] in MAS crystals

While the present paragraph is focused on the investigation of intrinsic defects, the physical techniques are widely used to characterize and quantify **extrinsic defects** as well. Typically, ESR and luminescence are can detect impurities down to the ppb [57]. For instance, Mn^{2+} and Cr^{3+} are usual contamination in MAS, and both have been extensively studied by EPR [58–61] and luminescence [59, 62–64]. Other impurities implanted as doping agents for luminescent properties include rare earth (RE) cations for applications as elements of both “active” and “passive” optical materials [65–67] and atoms exhibiting multiple charge state for phosphor application. MAS doped with Ti [68, 69] and Mn [70, 71] are both considered for the latter application, as they show different optical properties in the A^{+3} and A^{+4} states, and can undergo the A^{+3} → A^{+4} conversion within the host under oxidative conditions, and reversely under reductive conditions. The stoichiometry of MAS also affects the doping agent state, as investigated in [70] by correlated EPR of Mn^{2+} characteristic HFS signal and Mn^{2+}/Mn^{4+} luminescence bands. It was found that in Mg-deficient MAS, Mn^{2+} solely substitutes lacking Mg^{2+} in tetrahedral sites and induces green luminescence (520 nm), while in Mg-rich MAS, Mn^{4+} formation is favored by substitution of Al^{3+} and provokes a strong red luminescence (660 nm); stoichiometric MAS exhibits both Mn^{2+} and Mn^{4+} luminescence bands. This property has received a lot of interest recently, and has not been extensively studied yet.

II. Optical transparency in solid media

1. Definitions and characterizations of a medium transparency

The transparency of a medium is measured and characterized by a physical quantity that is the **transmittance**. This quantity is a function of the studied wavelength, in the range ~100 nm - 10 µm in general when speaking of optical media, and is measured by a spectrophotometer which will determine the percentage of the incident light beam I_0 transmitted through the medium (I_T).

However, for a given medium sample, the measured transmittance is greatly impacted by the spectrophotometer apparatus, specifically by the distance between the sample and the transmitted light detector and overall by the angle of opening of the apparatus. Hence, several types of transmittance can be defined, depending on the measurement setup, and are illustrated in *Figure 1.10* [72]:

- The **total forward transmittance** (TFT), measured with a spectrophotometer setup equipped with an integrating sphere. All the light passing through the sample, both unscattered and scattered (diffuse), is counted. The TFT has mainly an interest when added together with the total reflectance (TR, measure of all the reflected light with the same setup) to reveal the absorbed part of the light due to defects, and compared with the RIT (see below) to quantify the scattering of the medium.
- The **real in-line transmittance** (RIT) is measured with an apparatus where the detector is placed at ~1 m from the sample with opening ≤ 0.5°. In this case, only the unscattered light is taken into account. A high RIT allows clear observation through the medium to long distance, hence this is the characterization required for window applications. Nonetheless, commercial apparatus generally do not fit the conditions cited above, and homemade set-up are designed, using laser diode as a source for simplification [72].
- The **in-line transmittance** (IT or T_{il}) measured with an apparatus where the detector is placed generally at 10 - 20 cm of the sample (3-5° opening). Mostly the unscattered light is measured, and some of the scattered one. This corresponds to a typical commercial setup.

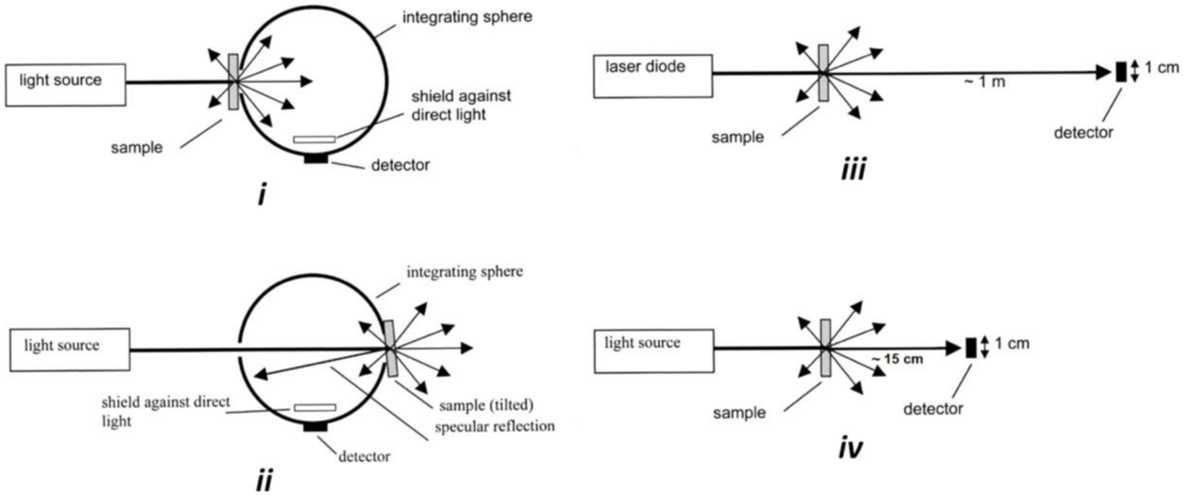

Figure 1.10: Measurement setup principle for i) total forward transmittance (TFT), ii) total reflectance (TR), iii) real in-line transmittance (RIT) and iv) in-line transmittance (IT or T) in classic commercial apparatus. Adapted from [72]

The understanding of these different definitions of the transmittance is essential before going further in the study of transparent media. From the difference between diffuse and in-line transmissions arises the distinction between translucency, transparency and opacity:

- An **opaque material** is characterized by both **low TFT and RIT**, as most of the light is either reflected or absorbed by the medium.
- A **translucent material** exhibits a **high TFT but a low RIT**, as most of the transmitted light is diffused; hence images observed through are indistinct, as illustrated in *Figure 1.11.i*.
- A **transparent material** exhibits both **high TFT and RIT**, and images can be clearly observed through even at high distances, as illustrated in *Figure 1.11.ii.*

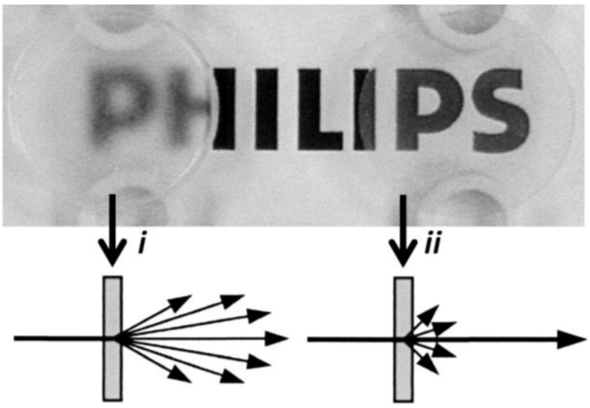

Figure 1.11: i) Translucent and ii) transparent polycrystalline alumina [72]

2. Theoretical aspects

i. *Concepts of linear optics: light-matter interactions*

The wave-matter duality as introduced by Einstein allows defining the light either as an electromagnetic wave of frequency v or as a beam of photons, particles transporting the quantum of energy E according to:

$$\boldsymbol{E = \frac{hc}{\lambda}}$$

Equation 1.2

where h = 6.626x10^{-34} m^2.kg.s^{-1} is the Planck constant, c = 2.998x10^8 m.s^{-1} is the speed of light in vacuum and λ is the wavelength associated to the photon.

When light goes through a medium of **refractive index *n***, they interact together. Several phenomena can occur: the light can be **reflected or refracted** (redirection of the wave) at the different interfaces (R), **absorbed** (A), **transmitted** (T) or **scattered** (S), as illustrated in *Figure 1.12*.

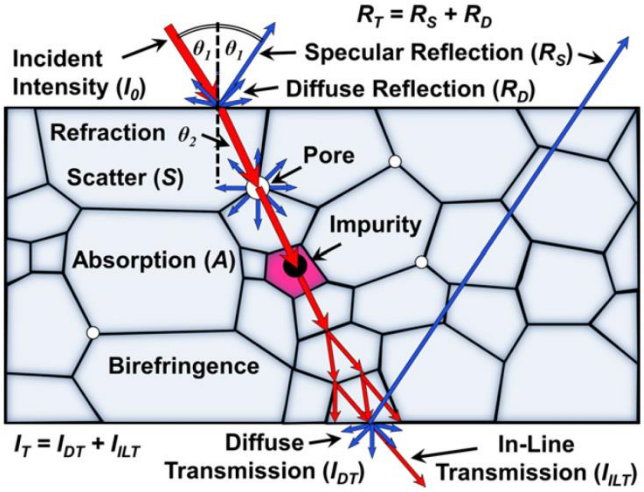

Figure 1.12: Light transmission through a ceramic with the most important light-scattering mechanisms [11]

Since the energy transported by the photons must be conserved, and considering an incident light with a zero angle of incidence (no refraction) and smooth and planar surfaces (negligible diffuse reflection), the relationship between the intensity I_0 of the incident monochromatic radiation and the radiations resulting from interactions is given by the following equation:

$$\boldsymbol{I_0 = I_R + I_S + I_A + I_T} \qquad \textit{Equation 1.3}$$

The former relation can then be normalized to I_0 for the resulting radiation fractions to appear:

$$\boldsymbol{1 = R + S + A + T} \qquad \textit{Equation 1.4}$$

where R, S, A, T are the reflectance, the scattering, the absorptance and the transmittance, respectively.

The reflection considers the specular reflectance from the two interfaces “external medium”/“considered medium”, due to their different refractive indexes. Indeed, without modification of the medium or its surface (*e.g.* antireflective coating), the most “ideal” material is to be subject to reflectance. It is only dependent on the smoothness and planarity of the surfaces, hence it is not affected by thickness.

The scatter, which is thickness dependent, is caused by change of the refractive index within the medium. Scattering can originate from different sources: 2D or 3D impurities (grain boundaries, pores, precipitates and minor phases), local variation of the medium refractive index (variation in stoichiometry and stress) and change of the crystallographic direction (birefringence). Impurities are the major source of scatter. Mie theory permits modelling the light scattering, and several scattering ranges can be distinguished depending on the size of the scattering center d relative to the wavelength λ [11]: Rayleigh–Gans–Debye scatter for $d > \lambda$, Mie scatter for $d \approx \lambda$, and Rayleigh scatter for $d < \lambda/10$. In UV-Vis-NIR range, Mie scatter has the greatest impact.

Absorption arises from mainly two sources: transition of electronic, atomic or molecular states from the host, leading to a band of absorption, or from absorbing centers which can lead to bands of absorption or absorption over the whole wavelength range. In practice, a band of absorption gives a monochromatic coloration to the medium, while absorption over the whole wavelength leads to opacity. Since absorption obeys a Beer-Lambert relationship and increases exponentially with thickness, even small fractions (ppm) of absorbing centers can lead to total opacity in thick medium (~1 cm) [11].

The RIT is the fraction of incident light which has not been subjected to any of the above phenomena.

ii. Optical transparent window: from band gap to multiphonon cut-off

Considering the different phenomena possibly occurring during light-matter interactions and linked to incident radiation by *Equation 1.4,* and their dependency on λ, the transmittance T(λ) can be expressed as:

$$\boldsymbol{T(\lambda) = 1 - R(\lambda) - S(\lambda) - A(\lambda)} \qquad \textit{Equation 1.5}$$

On a typical **transmittance spectrum** of transparent material, such as the ones presented in *Figure 1.13* for $MgAl_2O_4$, sapphire (monocrystalline α-Al_2O_3) and AlON, the transmission behavior can be distinguished into three areas of wavelength indicated in the graph: (A) the **band gap**, (B) the **optical transparency window** and (C) the **multiphonon cut-off** [11].

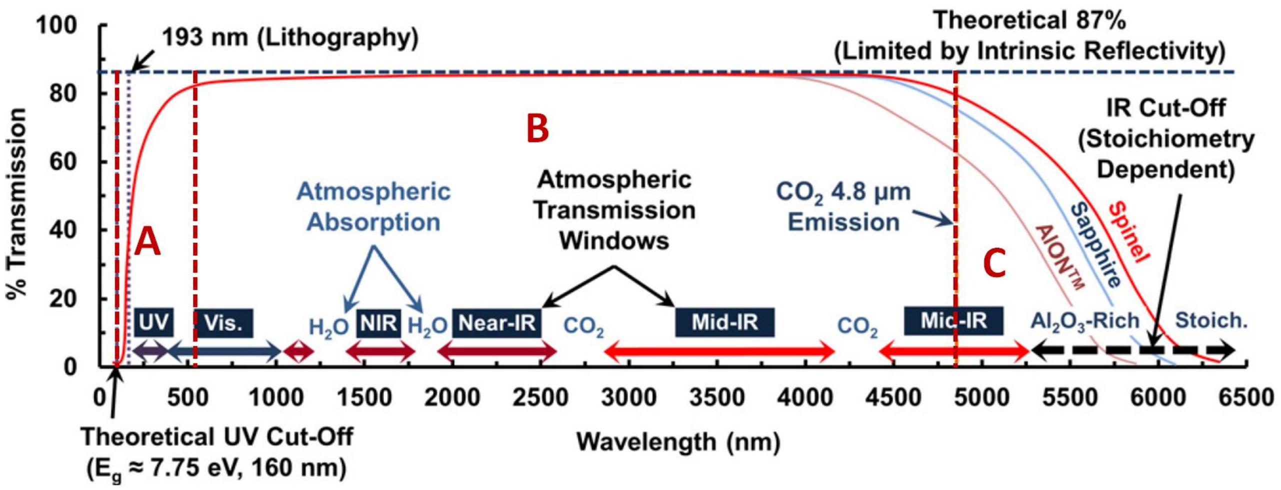

Figure 1.13: Typical transmission spectrum for MAS, along with other transparent materials; (A) the UV cut-off or band gap, (B) the optical transparency window and (C) the multiphonon or IR cut-off [11]

At low enough wavelength, a full absorption area is observed: the incident photons have an energy E (*Equation 1.2*) high enough to make an electron go from the valence band VB to the conduction band CB through the band gap BG ($E_{BG} = E_{CB} - E_{VB}$). Hence, all photons are absorbed until λ reaches the value corresponding to E_{BG} ($\sim\lambda_{(A)}$). Indeed, $\lambda_{(A)}$ depends on the material composition, and for MAS, $E_{BG} \approx 7.75$ eV and $\lambda_{BG} = 160$ nm. Defects and crystalline state have also an influence on the UV cut-off.

Above the λ_{BG} threshold, photons are not absorbed by the medium anymore; the light is then transmitted, reflected and scattered: it is the optical transparency window (B).

Finally, when λ increases such as the energy of the incident photons decreases to the magnitude of the vibrational energy of the lattice, the radiation is absorbed by the chemical bonding between the atoms of the medium: it is the high wavelength edge multiphonon MP absorption (C). It is more progressive than the band gap, and its wavelength can be approximated by a Hooke's law, considering the chemical bond as a spring:

$$\lambda_{MP} = 2\pi c \sqrt{\frac{\frac{m_1 m_2}{m_1+m_2}}{k}} \qquad \textit{Equation 1.6}$$

where c is the light speed, m_1 and m_2 the masses of the bonding atoms and k the spring constant.

This absorption is, again, intrinsic to the material and consequently depends on its composition: considering a same k value, λ_{MP} is only impacted by the masses of the atoms. The heavier the medium elements are, the higher will be its MP cut-off. For $MgAl_2O_4$, $\lambda_{MP} \approx 6000$ nm but the stoichiometry $MgO \cdot nAl_2O_3$ has an influence over the k value (*Figure 1.13*) [11].

For $\lambda_{EG} < \lambda < \lambda_{MP}$, the transparency depends on the reflection, the scattering and the absorbing centers mechanisms, as stated before. Considering a planar material with surfaces mirror-polished and the "external medium" to be the air of refractive index $n = 1$, the minimal total reflectance is only linked to the refractive index of the material by the following relationship:

$$R_{min}(\lambda) = \frac{(1-n(\lambda))^2}{1+n^2(\lambda)} \qquad \textit{Equation 1.7}$$

Since n is almost constant in the optical transparency window, R_{min} can be considered independent of the wavelength in first approximation, thus a constant. In a non-scattering and non-absorbent material, R_{min} is limiting the transmittance to a **theoretical value T_{th}** also independent of the wavelength:

$$\boldsymbol{T_{th} = 1 - R_{min} = \frac{2n(\lambda)}{1+n(\lambda)^2}} \qquad \textit{Equation 1.8}$$

$n(\lambda)$ can be calculated from the empirical Sellmeier equation [73]:

$$\boldsymbol{n^2 = 1 + \frac{1.8938\lambda^2}{\lambda^2 - 0.09942^2} + \frac{3.0755\lambda^2}{\lambda^2 - 15.826^2}} \qquad \textit{Equation 1.9}$$

For $MgAl_2O_4$, $n(\lambda) \approx 1.718$ for $\lambda > 500$ nm, hence the limit values can be calculated to be $R_{min} \approx 13\%$ and $T_{th} \approx 87\%$; T_{th} only sensibly decreases for $\lambda < 300$ nm. For comparison, amorphous silica (typical glass) transparency can reach 93%.

The in-line transmittance expression should include the thickness-dependent contributions from scatter and absorption [72], such as:

$$\boldsymbol{RIT(\lambda) = T_{th}.\, e^{\left(-\left(\gamma_T(\lambda)+\alpha_T(\lambda)\right).t\right)} = T_{th}.\, e^{(-\alpha.t)}} \qquad \textit{Equation 1.10}$$

where γ_T and α_T are the total scattering and total absorption coefficient, respectively, and α an apparent coefficient for all “non-transmitting” phenomena summed up in the first two coefficients. As mentioned above, scattering and absorption have multiple sources, all included in these coefficients, which can be assigned by decorrelation [74].

TFT measurement allows suppressing the scattering contribution:

$$\boldsymbol{TFT(\lambda) = T_{th}.\, e^{(-\alpha_T(\lambda).t)}} \qquad \textit{Equation 1.11}$$

Hence, α_T can be known precisely, and γ_T can be deduced by differentiation between *RIT* and *TFT*.

Experimental transmittance is expected to follow *Equation 1.10*, hence careful attention should be brought to the samples thickness when comparing transmittance spectra. However, during surface preparation, it is hard to reach the exact same thickness every time, and normalization to a standard t value is necessary for proper comparison. From *Equation 1.10*, the following can be established:

$$\boldsymbol{T(t_1) = (1-R).\, e^{-\alpha.\frac{t_1}{t_2}t_2}} \qquad \textit{Equation 1.12}$$

$$\boldsymbol{\Rightarrow T(t_2) = (1-R).\left(\frac{T(t_1)}{(1-R)}\right)^{\frac{t_2}{t_1}}} \qquad \textit{Equation 1.13}$$

where $T(t_1)$ and $T(t_2)$ refer to the *RIT* for a thickness t_1 and t_2, respectively, of the same sample.

The wavelength dependency, which is not displayed in *Equation 1.12* and *Equation 1*.13 for simplicity, is implied by the dependency of α on λ while R is considered constant in the UV-Vis-NIR range as stated before. Kim *et al.* found the same relation of normalization [75], and used a total reflection loss $R = 0.1314$, which will thus be used in this thesis. Anyway, *Equation 1.13* is useful but should be limited to small deviations from standard thickness (or to very homogeneous materials), as α does not take into account the eventual inhomogeneities of transparency through sample thickness due to volumetric distribution of defects.

3. Transparency of polycrystalline ceramics

Numerous materials are studied for transparent ceramic application, such as alumina, YAG and spinel ($MgAl_2O_4$, $ZnAl_2O_4$, $ZnGa_2O_4$, γ-Si_3N_4), and their transparency depends on several factors, mostly extrinsic. These factors are the same for every material, but their impacts vary with composition.

The intrinsic factors have been detailed above, and depend on the material chemical composition and structural arrangement. The chemical formula fixes the refractive index through the mass of the composing elements, hence impacts T_{th} and the optical transparency range; MAS is affected through non-stoichiometry. The second intrinsic factor is birefringence of the medium due to differences of n along the crystallographic directions, which causes scattering. In $MgAl_2O_4$, this phenomenon is marked between the more densely packed <111> unit cell cube diagonals versus the <001> cube edges, while still much lower than for trigonal alumina [11]. Anyway, in polycrystalline material with randomly oriented grains, no birefringence exists.

Among the transparent materials, MAS has already shown very good results in thick samples with high transparency, as illustrated in *Figure 1.14.a*. However, extrinsic factors of transparency loss are still a matter of study [76]. Large opaque flaws can be observed in the bottom photography (circled), as they are caused by microstructural defects distributed within the volume of the material (*Figure 1.14.b*). These defects are not only altering the optical properties, but the mechanical and radio-resistance ones as well, since they act as fragile points for initial damaging then propagated to the whole material. Hence, extrinsic defects, mostly due to the elaboration conditions (precursor synthesis and sintering), should be avoided as much as possible.

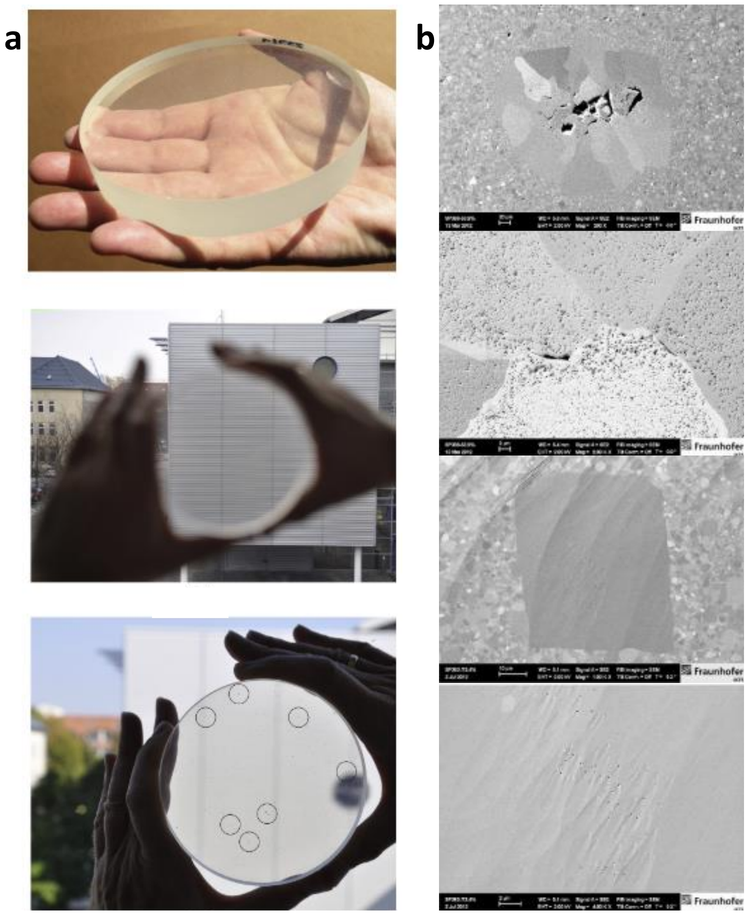

Figure 1.14: a) 17.4 mm thick MAS ceramic with $T(t = 4\ mm) = 81.7\%$; from top to bottom: general view, focus on distant objects and focus on ceramic (circles mark large defects) [76]. b) SEM of local microstructural defects; from top to bottom: exaggerated grain growth associated with large pores, small pores within large grains and nanoscale pores cluster in large grain [76]

Extrinsic defects include both the absorption and the diffusion phenomena. In spinel, the absorption occurs through vacancies (F- and V-type centers, *Figure 1.9.a* and *c*) and inclusions (minor phases, precipitates). The latter can be more deleterious, as very small concentration of impurities into the host material can lead to very strong coloration or even complete opacity [77]. High caution should be particularly taken during the sintering process, since contamination is favored at high temperature [49].

The **scattering sources** are by far the first cause of transparency loss in ceramics, and are all of microstructural nature; the influences of the most common scattering sources are illustrated in *Figure 1.15*. Grain size (GS) can be a critical parameter in some case, like alumina (*Figure 1.15.a*): if GS ≥ ~10 µm, the scattering profile (transmitted intensity in function of the angle of transmission) indicates translucency, while fine-grained alumina profile exhibits a sharp peak at small scattering angles, hence transparency [72]. GS has no influence by itself, but it induces scattering of the light at the grain boundaries because of variation of n, which annuls itself when light goes through enough grains. Anyway, in spinel, grain boundaries contribute minimally to scatter in Vis/IR wavelengths due to their small thickness (< 5 nm) and small n deviation [11].

Stress-induced microstructural defects (deformation of the lattice, dislocations, and microcracks) have an effect on transparency as well. Grain boundary microcracking has indeed shown a logarithmic relationship with the specular transmission, as illustrated in *Figure 1.15.b* [78]. Extensive scattering is induced by these defects once again locally modifying n. Stress-induced defects are generally observed when ceramics are processed under applied charge and cooled down too quickly, and they can be avoided with a thermal dwell at T << sintering T, while progressively releasing pressure to anneal stress [79].

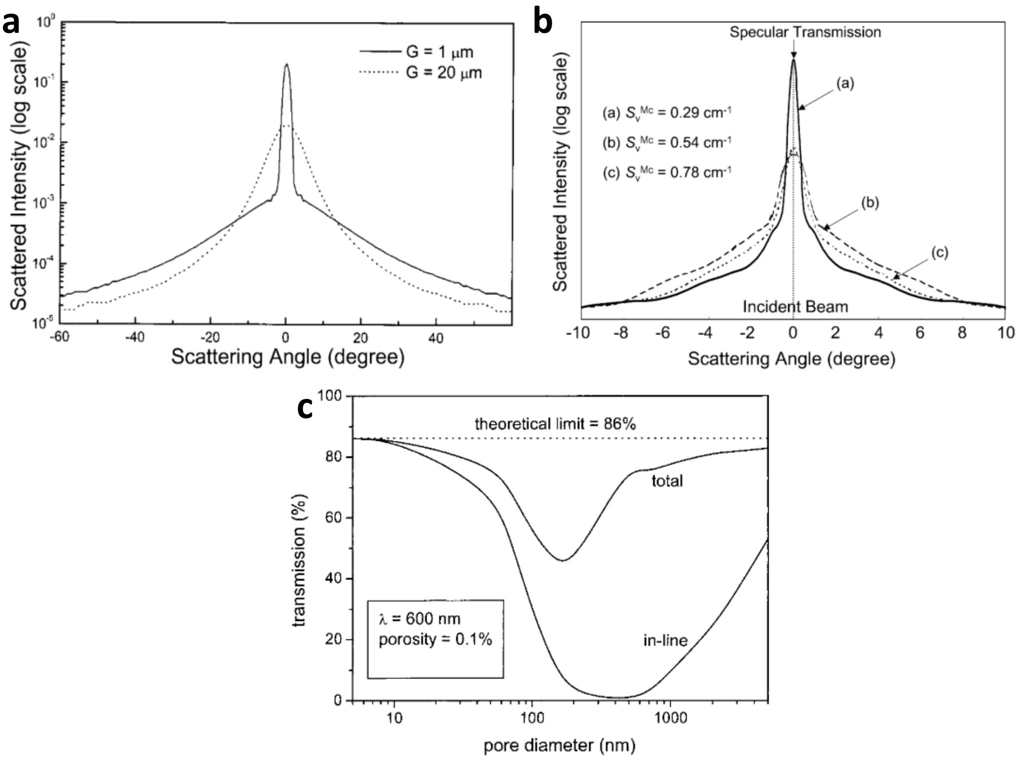

Figure 1.15: Influence of some microstructural features on the loss of transparency on ceramics. Scattering profiles of a) polycrystalline alumina with grain size G [72] and b) MgAl2O4 ceramics with different amounts of microcracking S_V^{MC} *[78]; c) TFT and RIT at λ = 600 nm of polycrystalline alumina in function of the pores diameter, assuming constant porosity of 0.1% [72]*

The main source of scattering in ceramics is **porosity** due to the low index $n \approx 1$ in pores. Residual porosity as low as 0.01% can lead to translucency [72] depending on the pores diameter d_p (*Figure 1.15.c*), while higher remaining porosity (> 0.1% - 1%) generally leads to opacity. Three areas can be distinguished on the curves in *Figure 1.15.c*: for $\lambda \leq 10\ d_p$ no transmission loss is observed (Rayleigh regime), for $\lambda \approx d_p$ the transmission loss is maximum (Mie regime), and for $\lambda \geq 10\ d_p$ the transmittance is not affected anymore (Rayleigh–Gans–Debye regime) [72]. *Figure 1.15.c* shows that not only *RIT* is affected by porosity, but *TFT* as well, since part of the scattered light will be backscattered/reflected in the surface of the pores.

To summarize the paragraphs above, the **ceramic transparency conditions** in spinel are mainly of **microstructural nature** (except for impurity contamination), and following criteria should be respected:

- surfaces should be **mirror-polished** in order to limit any surface scattering
- **no second-phase or precipitates** should be present, and grain boundaries should be clean
- stress-induced defects should be limited by an annealing at T < sintering T while releasing the load
- **very low porosity** should be reached (< 0.1%) with pore size ≤ 50 nm
- to avoid optical inhomogeneity, microstructure (grain size and pores distribution) should be uniform.

III. Synthesis of $MgAl_2O_4$ nanopowders

In the present section, we will first present the most important powder features and the techniques for their characterization, after what we will briefly review the synthesis routes which have been used in literature for the preparation of $MgAl_2O_4$ powder and the resulting properties of the material. Then a focus will be made on the thermal decomposition of hydroxide precursors into magnesium aluminate spinel, and finally we will present the synthesis routes used in our research team, which will be adapted for MAS synthesis in the experimental part of this work.

1. The features of the powder and their characterization

The potential of applicability of a material powder for a specific set of desired properties does not solely depend on the material itself, but on all the powder features. Hence, assessing the relative "quality" of the powder requires high knowledge of its features, compositional and physical, through proper characterization.

The **compositional features** include **chemical** and **crystalline purity** as well as **chemical homogeneity**, in particular in the case of polyphasic or doped powders. Chemical purity is generally characterized by chemical analyses, spectroscopy and DT-TG analysis, while crystalline purity is assessed by XRD and homogeneity by microscopic techniques including energy-dispersive X-ray (EDX) spectroscopy. Most of the common compositional features relevant to spinel have already been discussed in *Chapter 1.I.2*.

Within the **physical features**, two groups should be distinguished: the microscopic and the macroscopic characteristics. The **microscopic features** consist on the characteristics of individual particles and their interactions together: their size and size distribution (dynamic light scattering DLS), shape, shape yield and agglomeration (microscopy) and the specific surface and internal porosity (N_2 adsorption, He adsorption-desorption). The **macroscopic characteristics** are called the pulverulence, sometimes referred to as powderiness, and concern the property of the precursor powder as a whole: apparent volumic mass and relative density of loose/compacted bed, internal friction and compactability. Indeed, the macroscopic features arise from the microscopic (and compositional) features.

These characteristics are indeed directly responsible for the powder properties, and in particular high knowledge of the microscopic features can provide very valuable informations about how well the powder will sinter. However, accurate characterization is often an issue due to confusion in terminology, insufficient characterization or misunderstanding of the characterized object/property. The major issue is the misinterpretation of the microscopic features terminology, from which arises the improper understanding and in term treatment of agglomeration.

Therefore and prior to all, it is necessary to define the terminology allowing full description of a powder microstructure [80]. When described in literature, powder constituents are frequently referred to as particles, a generic term used by default, as a ***particle*** is a collection of crystalline or amorphous solid matter as an independent unit in the powder that can be of several types illustrated in *Figure 1.16.a*. The particle can be a ***primary particle*** (PP) if it is bulk, in which case it can be either amorphous, crystalline or polycrystalline, or a ***secondary particle*** (SP) if it is the collection of primary particles.

In the latter case, depending on the interactions between PP within the SP, and on the strength required to deform the SP or separate the constituting PP by appliance of a mechanical force, SP can be of two types. An ***agglomerate*** (*Figure 1.16.b*) is a particle consisting of primary particles held together by **weak Van der Waals forces** or hydrogen bonding, both favored by humidity even at low level. In the other hand, in ***aggregates*** (*Figure 1.16.c*) **strong forces** (*i.e.* primary bonding) hold the primary particles together. Unfortunately, the two types of SP are rarely differentiated in literature, and are both assimilated to agglomerates [80]. While it can be beneficial for some properties, agglomeration is generally deleterious for the sinterability.

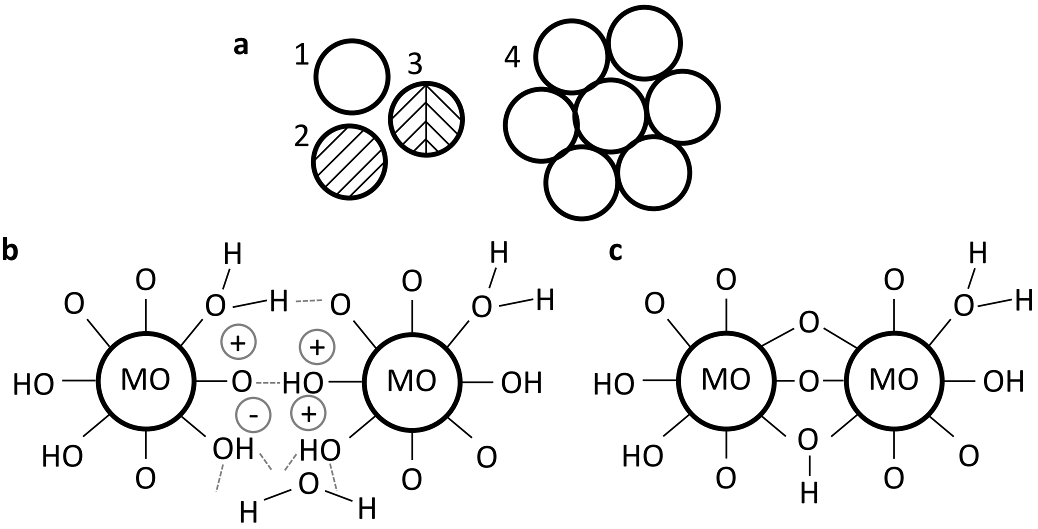

Figure 1.16: a) Schemes of the different types of particles with 1) – 3) primary particles with different crystallinity as 1) amorphous, 2) monocrystalline and 3) polycrystalline, and 4) a secondary particle. Schemes of the different types of secondary particles as b) the “soft” agglomerate and c) the “hard” aggregate

For coarse primary particles with characteristic length ≥ 10 μm, high volume interactions allow neglecting the surface interactions, and secondary particles are most of the times not observed. However, as PP size is reduced toward the nanoscale, the surface effects and interactions eventually overcome the volumic ones, and agglomeration/aggregation becomes inevitable in a dry powder, even if particles were perfectly dispersed in a liquid phase during synthesis prior to its removal and exposure to the vapor phase.

Hence, it is pointless to try to suppress the formation of SP, and often hard to even reduce it for little (when not opposite) effect on properties like sinterability, as it generally leads to higher SP size distribution and heterogeneous properties. Instead, recent studies are rather aimed to **control the formation of SP** by appropriate processing to obtain weakly bonded PP into SP of regular shapes and narrow size distribution, providing more homogeneous results than smaller PP with uncontrolled formation of SP [12].

Aggregation can only occur after agglomerates have been formed, for example from a dehydration reaction between surface hydroxyl groups of two different hydroxylated PP within the same agglomerate. A water molecule is then freed and a strong bridging oxygen bond between the two particles is created, as illustrated by the transition from *Figure 1.16.b* to *c*. In most cases, oxide powders are aggregated *via* this mechanism, as a number of synthesis processes relies on calcination of as-synthesized hydroxide powders, while high temperature favors the dehydration. However, metal and oxide powders can also aggregate due to surface-hydroxylated particles, and more often due to adsorbed water molecules during drying process. At particles contact, the capillary force can retain water at temperatures above its vaporization point, allowing it to retain and concentrate small amounts of solutes (even from atmospheric contamination) as the water is eliminated everywhere but the capillaries. Eventually the solutes concentration can exceed their solubility limit, leading to their precipitation into solid bridges between the particles [80].

2. Review of the different synthesis routes

Numerous varieties of precursors and methods have been used for synthesizing magnesium aluminum spinel (MAS) powders, while the resulting materials are not always suitable for densification into transparent ceramics. The different techniques can be roughly divided into two groups: the **solid state reaction** (high temperature syntheses), and the **soft solution chemistry routes** (low temperature syntheses) [13].

Indeed, techniques also exists for the preparation of thick/thin $MgAl_2O_4$ films (chemical or physical vapor deposition methods [81]) and fibers/single crystals by fusion methods (Verneuil process [82] and Czochralski method [83]). Synthetic monocrystals have numerous applications in addition to allow deep understanding of the spinel structure and behavior under various solicitations. For instance, doped crystals can replace the rare natural occurrences for jewelry applications as corundum-like gemstones, *i.e.* sapphires and rubies [84] (MAS with red appearance, called spinel-rubies or balas rubies, are highly appreciated, *Figure 1.17*), and visible or IR laser applications [83, 85] . However, these MAS forms are not appropriate for the desired application requiring fine microstructure and high transparency, hence will not be addressed.

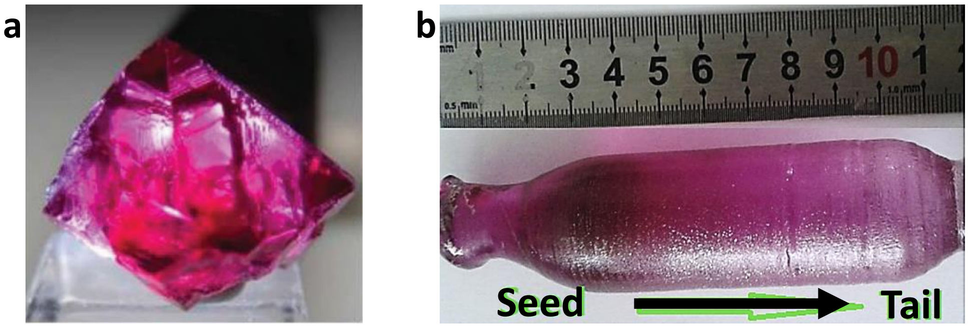

Figure 1.17: a) Natural spinel-rubies [43] and as-grown synthetic Czochralski Cr:MgAl2O4 crystal Ø3 cm x 7 cm [83]

i. Solid state reaction routes

Solid state reaction routes are mainly used for MAS powders production in bulk quantity for refractory applications. In the conventional solid state route, MAS is formed by a **two-stage firing at high temperature** (~1600°C) of a $MgO/\alpha\text{-}Al_2O_3$ mixture, with an intermediary grinding step essential for faster reaction [13]. The underlying mechanism is the Mg^{2+} and Al^{3+} counter diffusion through the oxides interface, while O^{2-} remain at initial position [86]. If this mechanism is strictly followed and for the electroneutrality to be maintained, Mg^{2+} diffusion within Al_2O_3 should be 3 times greater than Al^{3+} diffusion within MgO; however, experimentally a factor of 6 can be reached depending on conditions. Due to this unequal counter diffusion in each reactant and their different densities (MgO: 3.58 g/cm^3; $\alpha\text{-}Al_2O_3$: 3.99 g/cm^3; $MgAl_2O_4$:3.58 g/cm^3), the initial MgO and Al_2O_3 portions shrink and expand, respectively, for a global volume expansion of ~8.0%, resulting in inhomogeneous particles size and shape [13]. Replacing $\alpha\text{-}Al_2O_3$ by $\gamma\text{-}Al_2O_3$ limits the expansion ($\gamma\text{-}Al_2O_3$: 3.67 g/cm^3) and favors MAS formation, due to their similar crystal structures [87].

Additives can be used to reduce the temperature of MAS formation (AlF_3, V_2O_3, $MgCl_2$) [13], however except for Mg^{2+} and Al^{3+} based ones, contamination is induced and limits the application range. It is also possible to vary the $MgO\cdot nAl_2O_3$ stoichiometry, as Al_2O_3-rich mixtures favor MAS formation [88]. The raw materials have a strong impact as well, especially through their microstructure and purity [89]. High energy milling has been considered to reduce the particle size and improve the reactant homogeneity. Although it greatly decreases the reaction temperature, thus the MAS grain size to ~100 nm [90], contamination occurs due to abrasion of the grinding media; hence, use of fine precursors gently mixed should be favored instead.

Alternatives to the conventional solid state reaction have been proposed. Single stage short firing at the mixture melting point allows volatilizing the impurities, and MAS of very high purity can be obtained [13]. Microwave assisted reaction has also been investigated with graphite addition as susceptor [91], and greatly reduces the synthesis duration. Another alternative relies on metal/oxide reactants mixture (MgO + Al or Mg + Al_2O_3) under oxidant atmosphere [13, 92], where the metal is melted (~650°C) and oxidized *in situ*. Kinetic of the previous reaction can be enhanced following a self-propagating high temperature synthesis (SHS) combustion route, initiated by a small amount of thermite mixture (85%Fe_3O_4 and 15%Al) [13].

Nevertheless, such solid state reaction synthesis routes are not suitable for the fabrication of transparent ceramics with grain size at the nanoscale due to several drawbacks: uncomplete MAS formation (residual precursors grains), volume expansion and agglomeration of the particles during the reaction induce a minimum porosity of ~2% after sintering, and globally large grain size > 1 µm [13].

ii. Soft-solution chemistry routes

For applications requiring powder with finer grains in narrow distribution, higher purity and homogeneity and controlled shape, soft-solution chemistry routes are preferred. Indeed, the low temperature processes involved can provide the desired features, while synthesized quantities per batch are smaller and generally costlier, limiting their use for advanced ceramic products. These relatively low-temperature prepared MAS nanopowders have been synthesized from a wide variety of precursors and methods.

The earliest, simplest and most used *chimie douce* technique for MAS synthesis is the **coprecipitation route** [93–98], involving the precipitation of metallic cation hydroxides from a precursor salt within a basic solution generally aqueous, followed by a calcination to reach the oxide form. The nucleation and growth are controlled by the precipitating agent, the pH, the temperature and the controlled release of anions/cations, allowing the synthesis of monodispersed particles. However for mixed oxides, complex hydroxides mixtures are synthesized and the control of chemical and microstructural homogeneity is difficult [94].

In most experimental procedures for mixed Mg^{2+}/Al^{3+} coprecipitation, water solvated nitrate salts are used as cation source [93, 95–98] and then slowly dropped into a precipitating agent solution (generally NH_4OH) to keep a constant pH ~10 at 20 - 80°C, to favor an homogeneous composition [93–96]. The obtained hydroxides mixtures generally contain Mg-Al hydrotalcite and $Al(OH)_3$, thermally decomposed at ~800°C into MAS with crystallite size as small as 7 nm in loosely bonded agglomerates [96], depending on the former hydroxides microstructure.

The **pH of coprecipitation** (*i.e.* precipitating agent concentration) is one of the most determining parameter for compositional as well as microstructural features. While a low pH reduces the agglomeration state, *Figure 1.18* shows a drastic impact on composition for pH < 9, leading to alumina-rich MAS [95]. Constant pH ~10 is required for stoichiometric MAS synthesis. Mg and Al chlorides as cationic source [94] and NaOH as precipitating agent [97] have been used as well, and gave similar results. Nam *et al.* [98] used a NH_4OH/NH_4HCO_3 mixture to obtain hydrotalcite along with dawsonite $NH_4AlCO_3(OH)_2$ instead of $Al(OH)_3$, which allowed modifying the microstructure. As shown in *Figure 1.19*, slightly modifying the pH has great impact on the particles shape: 150 nm spheroidal aggregates at pH = 9.35, 300 nm short bundles at pH = 9.5 and 300 nm rods are obtained at pH = 9.8. After calcination, the particles morphology is kept while the primary particle size of ~25 nm is invariant.

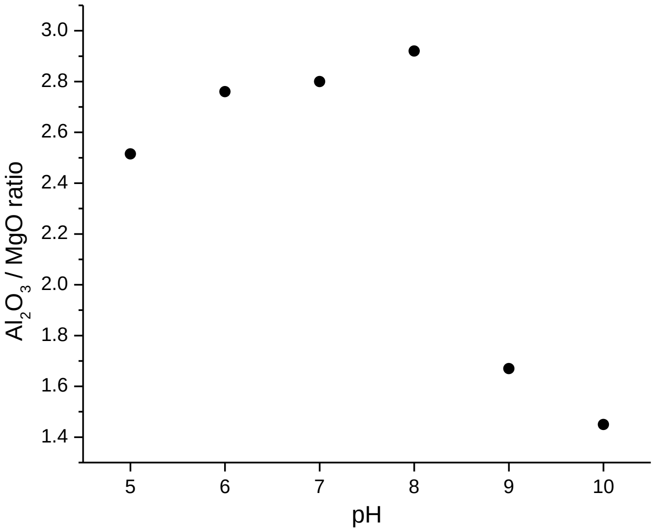

Figure 1.18: Effect of the pH during coprecipitation synthesis over the spinel stoichiometry; plotted from data in [95]

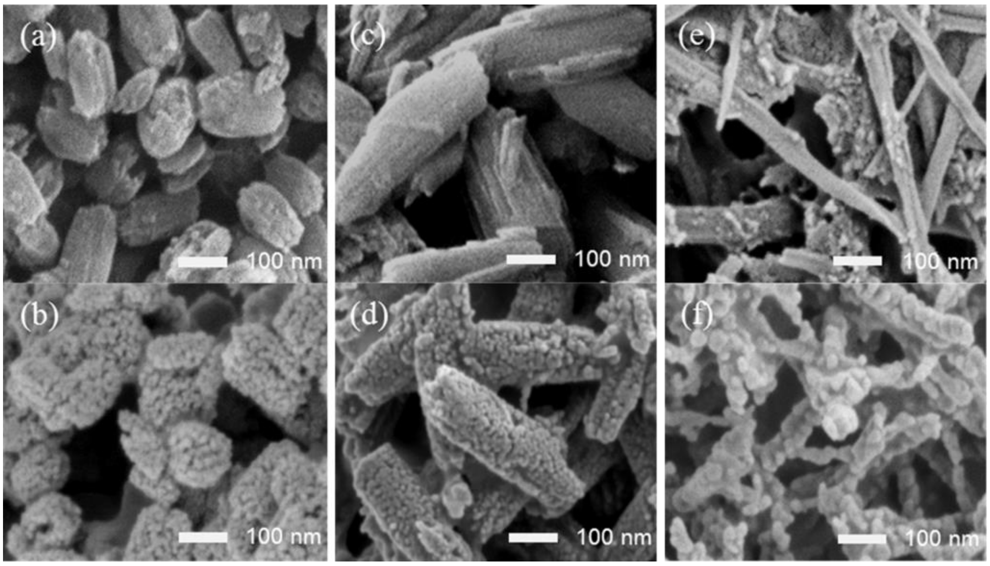

Figure 1.19: SEM of a), c), e) as precipitated precursors and b), d), f) MAS powders after calcination at 1100°C, with a), b) pH = 9.35 c), d) pH = 9.5 and e), f) pH = 9.8 [98]

Another popular technique for $MgAl_2O_4$ powder synthesis is the **combustion route** [60, 99–102], which is very **simple** to set-up and the **quickest method** possible, since the whole combustion process is completed in less than 5 min. It is based on the redox reaction between the nitrate salts as oxidant reactants and an adequate fuel as reductive reactant, mixed together into a paste. Initially the fuel acts as a chelating agent and an intermediary compound is formed, then the mixture is ignited at 300 - 500°C. Within minutes the paste foams and flames to high temperature, the combustion lasting only few seconds. The controlling parameters are the used fuel and the reducer-to-oxidizer ratio. The most common fuel is urea [60, 99, 101], allowing very high combustion temperature (> 1000°C [60]) hence an *in situ* calcination, as the spinel phase is readily obtained with crystallite size from ~5 to ~30 nm. However, the uncontrolled temperature leads to large crystallite size distribution, and most of all to highly aggregated, micronic, angular and irregular particles, with high internal porosity [60, 101]. Other fuels such as glycine [100, 102] and β-alanine [99] lead to less exothermic combustions, hence more controlled microstructures. Nevertheless, these less energetic reactions do not allow *in situ* formation of spinel, and amorphous compounds with high carbon content are obtained, requiring a subsequent heat treatment at $T \geq 700°C$ for crystallization of pure MAS. Narrow PP size distributions around ~10 - 14 nm are observed, while still highly aggregated into sharp and porous SP.

Several techniques are not widespread, but deserve to be mentioned here, as they are very promising. Abdi *et al.* [103] prepared spherical spinel particles of 12 nm through a short **energetic mechanical activation** of Mg and Al chlorides salts mixed with NaOH in a planetary mill at 300 rpm for 10 min. After milling, a hydroxides mixture was obtained together with NaCl removed by washing. A heat treatment at 800°C led to the pure spinel particles. Naeini *et al.* [104] used a **melting salt route**, simply heating at 850°C for 1-5 h a mixture of AlOOH, MgO and NaCl as a melting medium. Non agglomerated $MgAl_2O_4$ crystallites were obtained, with average size ~10 nm. Several attempts were made for synthesizing MAS through **hydrothermal synthesis**. Chen *et al.* [105] heated in autoclave a suspension of AlOOH in $Mg(NO_3)_2$ aqueous solution at 400°C for 12 h. After washing and drying, they obtained a unique $MgAl_2O_4$ microstructure consisting in triangular platelets of ~200 nm width and ~25 nm thickness. In [106, 107], MAS was synthesized by hydrothermal microwave synthesis from suspensions of AlOOH and MgO in NH_4HCO_3. After synthesis at 180°C and 165 psi, they obtained mixed hydroxides and could not convert them into pure spinel with calcination up to 1000°C, hinting for an insufficient temperature of hydrothermal treatment.

In addition to the classic coprecipitation method, numerous *chimie douce* synthesis routes are developed, as these techniques are by far the most promising and studied nowadays. They allow numerous modifications of experimental conditions, hence better control over the intermediary compounds, the size and shapes of the PP and SP and the stoichiometry of the final product. The principle of the techniques varies, but in each of them, complexation of Mg^{2+} and/or Al^{3+} by an organic anion as chelating agent occurs in the first step.

A first group of techniques relies solely on **complexation principle**. In the so-called evaporation route [108], Mg and Al nitrates are dissolved in 2M HNO_3, then oxalic acid is added to the solution and magnesium aluminooxalate $Mg[Al(C_2O_4)_3]$ is formed. The solution is then evaporated at boiling point, while HNO_3 is concentrated until it can oxidize the oxalate. The dried powder is then calcined at 700°C to provide spinel phase with ~30 nm crystallites. A similar technique is presented in [99], where the nitrate salts and some ethylene glycol (EG) are mixed in water and heated at 100°C. The nitrates induce formation of HNO_3, then EG is subsequently oxidized into glyoxal and glyoxylate $Al_2Mg(OH)2(C_2H_2O_4)_3{\cdot}xH_2O$ [99]. Calcination at 700°C leads to ~10 nm crystallites, with micronic and sharp stone-like aggregates.

Indeed, the **sol-gel method** has been extensively studied for the synthesis of spinel nanopowders since the last ten years, along with processes derived from the sol-gel technique. A **metal alkoxide precursor** $M(OR)_z$ is generally used, and may be formed *in situ* using another metal precursor. It is first dissolved or finely dispersed in a medium, aqueous or not, to be **hydrolyzed**:

$$\boldsymbol{M(OR)_z + H_2O \leftrightarrow M(OR)_{z-1}(OH) + ROH} \qquad \textit{Equation 1.14}$$

Depending on the kinetic and hydrolysis rate, the process can be divided in two types based on the nature of the sol: colloidal and polymeric sol-gel [109]. The dispersed particles/molecules should be in the range of 1 nm to 1 μm to respect the definition of a sol. In the **colloidal route**, the hydrolysis is fast and uncontrolled, generally *Equation 1.14* is complete and $\mathbf{M(OH)_z}$ is formed and precipitates. The mechanical stirring helps break down the precipitates clusters into a dispersed state, after what pH effect creates surface charges provoking electrostatic repulsion which further breaks down the agglomerates and homogenizes the suspension. This process of colloidal sol preparation is called the peptization [109]. In the **polymeric route**, the hydrolysis is controlled and only partial, leading to $\mathbf{M(OH)_{z-1}(OH)}$ which does not precipitate. Once the hydrolysis starts, two partially hydrolyzed molecules can react by condensation, leading to M-O-M bonding (*Equation 1.15*). By extent of the condensation, polymerized molecules are formed, with solvent and byproducts trapped in this network. This process of polymeric sol preparation is called the **polycondensation** [109]. Through aging and/or heating, sols are converted into **gels** by destabilization of the particles (via double layer reduction or removal of steric barriers) or cross-linking between polymeric clusters providing a 3D network. The gelation is accompanied by a drastic increase of viscosity [109]. Finally, the gel is dried and converted to powder, which can be readily in the oxide form, or necessitate a further calcination.

$$M(OR)_{z-1}(OH) + M(OR)_{z-1}(OH) \leftrightarrow (OR)_{z-1}M - O - M(OR)_{z-1} + H_2O \qquad \text{Equation 1.15}$$

For synthesizing MAS powders through sol-gel process, the usual starting salts are nitrates. The simplest colloidal sol-gel process is an inorganic route derived from coprecipitation [93], using water as a solvent and a strong base to form mixed hydroxides particles. However with appropriate synthesis conditions (low temperature, vigorous stirring, slow addition of precipitating agent and small amount of peptizing agent afterward) a nanoparticulate sol is prepared. Spinel nanoparticles are obtained by calcination of the dried gel, but the method results in quite large secondary particles (*Figure 1.20.a*) [110]. Polymeric sol-gel routes generally give less agglomerated powders. Using a non-aqueous solvent to control the hydrolysis step, typically an alcohol (diethylene glycol monoethyl ether [111], absolute ethanol [112]), and a complexing agent (citric acid [111], propylene oxide [112]) to first form the Mg^{2+}/Al^{3+} organic salt *in situ*, which is then turned to sol and gel through polycondensation. Non-agglomerated crystallites are as small as 10 nm after calcination at 700 - 800°C [111, 112] (*Figure 1.20.b*). Modified non-hydrolytic sol-gel routes have been proposed, using anhydrous reactant in non-aqueous medium (*e.g.* chlorides and ethanol in CH_2Cl_2 solvent), where organic intermediary is formed by alcoholysis. The gel still needs to be calcined at 900°C [113].

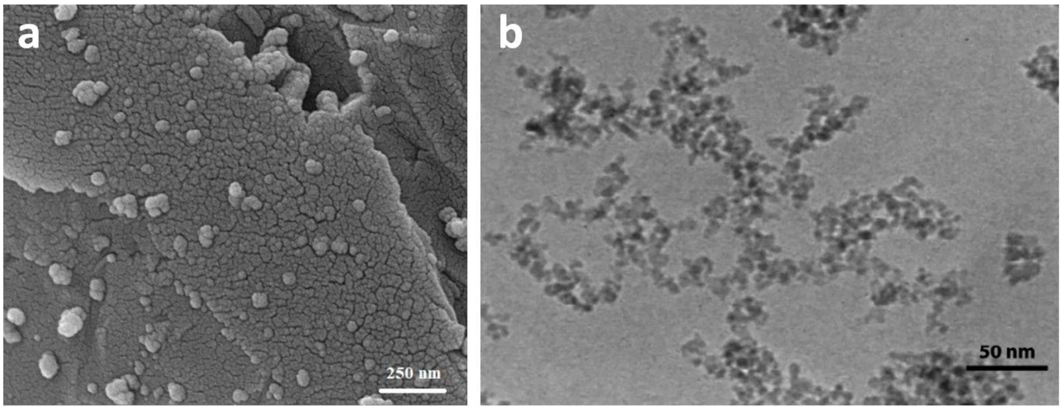

Figure 1.20: MAS powders synthesized through a) inorganic colloidal [110] and b) polymeric sol-gel routes [111]

To synthesize complex oxide nanoparticles with high homogeneity, the **complexation/polymerization method** sol-gel related called **Pechini process** is well adapted. Unlike the classical sol–gel route in which the metal alkoxides participate in the gel-forming reactions, this process is based on a gelation reaction between acid and alcohol reagents. A polymeric organic resin is obtained and contains a good distribution of the metal cations/particles, which yields the oxide upon calcination. In practice, a modified Pechini process is often used for $MgAl_2O_4$ preparation, where gelation occurs through reactions between acid/alcohol and alkoxides/alcohol. The typical reactants are nitrate salts, citric acid (CA) and ethylene glycol (EG) solvated in either H_2O, EG or another alcohol. First, the metal cations are chelated at low temperature by CA to form metal complexes, as in the citrate route [114], then the solution is heated for the chelates to polymerize with EG. As excess water is removed at high temperature, the solid polymeric resin is formed. In [115], the complexation is carried out in EG at 80°C, then the temperature is raised to 180°C for the polymerization, after what a calcination at 700°C provides spherical 10 nm MAS crystallites loosely agglomerated. When the same process is carried out in H_2O, the calcination leads to strong aggregation with large distribution of crystallite size [96], showing the importance of the solvent. Hao *et al.* [63] also showed the effect of solvent, adding mixed hydrophobic toluene and hydrophilic propylene oxide in ethanol. After thermal treatment at 900°C, the resulting MAS powder morphology was modified to uncommon 10 nm thick imbricated foils.

Finally, sol-gel closely related polyol-mediated synthesis has been used by Feldmann to synthesize numerous mixed oxides, including MAS [116, 117]. This method will be developed in *Chapter 1.III.4*.

3. From hydroxides mixture to oxide compounds

As it has been shown above, the synthesis of MAS particles through soft-solution chemistry always goes through the formation of intermediary compounds, and in most cases the precursor prior to calcination is a **mixture of hydroxides**. Hence, this section is aimed to understand the relation between the hydroxides mixture and the oxide features, in order to better control the latter. We will briefly present the most usual Al and Mg simple and mixed hydroxides obtained as MAS precursors, then we will focus on their thermal decomposition to oxide forms and the MAS formation from hydroxide mixtures calcination.

i. $Mg(OH)_2$, $Al(OH)_3$ and AlOOH

Magnesium has only one common hydroxide compound, which is the **brucite $Mg(OH)_2$** of the larger brucite crystallographic group. Its trioctahedral structure is composed by regularly layered hexagonal sheets in which edge-sharing $Mg(OH)_6$ occupy octahedral sites, with the OH^- groups oriented perpendicularly to the sheets [118] (*Figure 1.21.a*). Within the non-charged layers, the cohesion is ensured by strong ionocovalent bonding, while the interlayer cohesion is solely ensured by weak Van der Waals and hydrogen bonding.

In comparison, aluminum has several known hydroxide phases, including four $Al(OH)_3$ polymorphs: the extensively investigated monoclinic **bayerite α-$Al(OH)_3$** and **gibbsite γ-$Al(OH)_3$**, and the less common triclinic doyleite and nordstrandite, the latters mainly encountered as natural minerals [21]. The structures of all polymorphs are based on an identical single layer as building block (*Figure 1.21.b*) [119]. The $Al(OH)_3$ sheets are brucite-like with $Al(OH)_6$ octahedra arrangement similar than in the $Mg(OH)_2$ sheets. However, the Al^{3+} charge is not compensated by its six bonded OH^-, thus to keep the charge neutrality only two-third of the octahedra sites are occupied, with bridging hydroxyl groups connecting two octahedra. To emphasize the brucite nature of this dioctahedral structure, it can be described as **$(Al^{3+}_{2/3}\square_{1/3})(OH)_2$**, with $\square$ the 1/3 vacant sites. On the opposite faces of a single layer, the octahedra point in different directions, allowing differentiating them as A and B sides. The bayerite and the gibbsite are solely differentiated by their AB-AB and AB-BA stacking sequence, respectively [119] (*Figure 1.21.c* and *d*).

In addition to the $Al(OH)_3$ polymorphs, two common **oxohydroxide AlOOH** structures are known, the hexagonal close packed diaspore α-AlOOH and the orthorhombic **boehmite γ-AlOOH** [21]. Diaspore is rarely encountered in powder synthesis, and will not be detailed. The structure of boehmite is characterized by double layers of O/OH octahedra partially filled with Al^{3+} ions (*Figure 1.21.e*), with the tetracoordinated O^{2-} groups bonding the two layers together while the external OH^- groups are bridging two Al^{3+}. The stacking of the layers is such that the OH^- groups of one bilayer are located over the depression between the OH^- groups in the adjacent bilayer, inducing zig-zag chains of hydrogen bonds holding the sheets together. Poorly crystallized boehmite is often obtained by synthetic routes, and referred to as “pseudoboehmite”.

The brucite and brucite-like structure of these compounds explains their common hexagonal flake-like particles and the easy cleavage on the basal plane (001). However, synthesized powders of these hydroxides can present several types of morphology, such as needle- and rod-like particles [120–122].

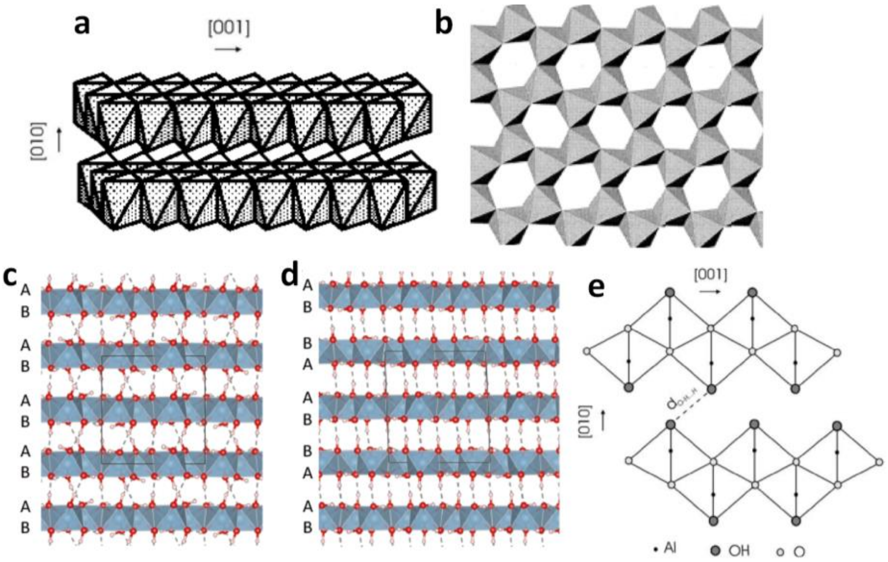

Figure 1.21: Structures of a) brucite $Mg(OH)_2$ [118] and of b) the layer common to every $Al(OH)_3$ polymorphs [21], and c), d) layer stacking and hydrogen bonds for bayerite and gibbsite, respectively [119]; e) layering structure of AlOOH boehmite [21]

ii. Layered double hydroxide LDH and layered single hydroxide LSH

In addition to the simple forms of Al^{3+} and Mg^{2+} hydroxides present above, several structures based on them have been reported and are more or less known and investigated.

The mixed hydroxides are certainly the most famous structure based on simple hydroxide, especially the **layered double hydroxides (LDH)** which are a particular kind of anionic clay mineral. Two types should be differentiated, which will be called LDH-type1 and LDH-type2 (no official speciation in the denomination for now) depending on the relative content M^{2+}/M^{3+} in the compound and the structure on which it is based.

The most studied **LDH-type1** is a compound with general formula **$[M^{2+}_{1-x}M^{3+}_{x}(OH)_2][(A^{n-})_{x/n}\cdot mH_2O]$** in a **brucite-based structure**, with M^{2+} a divalent metallic cation (Mg^{2+}, Mn^{2+}, Fe^{2+}, Co^{2+}, Ni^{2+}, Cu^{2+}, Zn^{2+}), M^{3+} a trivalent metallic cation (Al^{3+}, Mn^{3+}, Fe^{3+}, Co^{3+}, Ni^{3+}, Cr^{3+}, Ga^{3+}), x the substitution rate of M^{2+} by M^{3+} in the brucite sheets and A^{n-} the interlayer anion of charge n [123]. Since it occurs naturally as hydrotalcite mineral of particular formula $Mg_6Al_2(OH)_{16}(CO_3)\cdot 4H_2O$, LDH-type1 is referred to as hydrotalcite-like. Its structure consists of brucite layers in which **an amount x of Mg^{2+} is substituted by Al^{3+}**, inducing a charge x+ in the layers. H_2O-coordinated anions A^{n-} are located in the interlayers to compensate the charge, ensuring the integrity of the layered structure [124] (*Figure 1.22.a*). LDH-type1 can typically be synthesized with a M^{2+}/M^{3+} ratio of 2 - 4 ($0.20 \leq x \leq 0.33$) [125], even if some studies reported successful preparation with Mg/Al ratio of 1 - 20 [126]. However, for Mg/Al ratio outside of classical range, LDH was of very poor crystallinity. In fact, for $x < 0.2$ there is a loss of cohesion between the layers due to their too small positive charge and $Mg(OH)_2$ tends to form, while for $x \geq 0.33$ the increase of electrostatic repulsion between the cations in the sheets, and between the anions in the interlayer spaces, provokes the structure to collapse.

The **LDH-type2** is based on the **gibbsite "defective brucite" structure**, and it can be formulated as **$[M^{3+}_{2/3}\square_{(1/3)-x}M^{2+}_{x}(OH)_2][(A^{n-})_{x/(2n)}\cdot mH_2O]$** with **$x$ the insertion rate of M^{2+}** in the vacancies of the gibbsite layers, while the interlayered A^{n-} are aligned with the M^{2+}/vacancies for a better stabilization (*Figure 1.22.b*). The doping cation can also be monovalent, as $LiAl_2$-LDH was synthesized [127], however we are solely interested by M^{2+} insertion. LDH-type2 has been synthesized only a few times to the best of our knowledge, systematically through hydrothermal synthesis starting from $Al(OH)_3$ particulate suspensions, for a sheet composition of $[M^{2+}Al^{3+}_4(OH)_{12}]$ [128–130]. Interestingly, no study considers a LDH-type2 synthesis with M^{3+} other than Al^{3+}, nor the possibility to vary the rate *x*. Indeed, the only reported value $x = 0.167$ corresponds to half the gibbsite vacancies filled, while from a steric approach a complete filling ($x = 0.333$) could be considered, which conveniently corresponds to the cationic ratio in stoichiometric spinel.

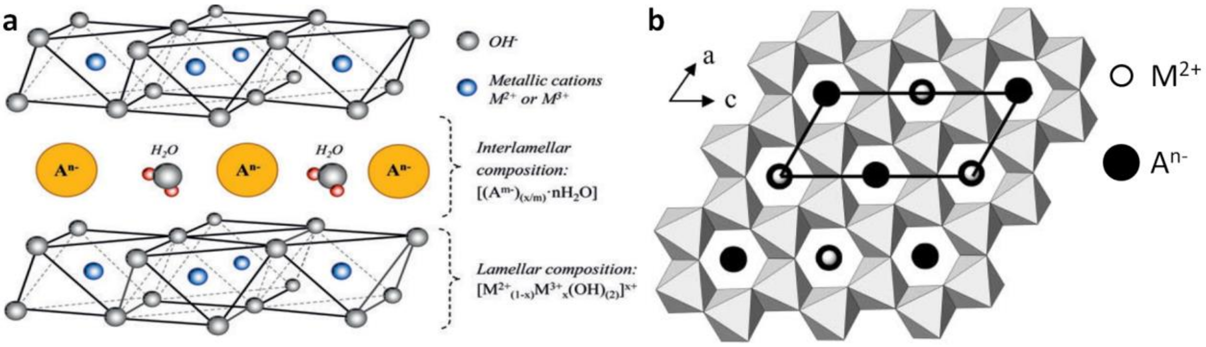

Figure 1.22: Structures of layered double hydroxides a) brucite-based (LDH-type1) [124] and b) gibbsite-based (LDH-type2) [128]

LDH materials have two specific properties which have been widely studied. First, they possess a **high anion exchangeability**, as the intercalated anion can be replaced by another one depending on their affinity with LDH and the conditions (pH, temperature…) [123]. Any kind of anions can be intercalated; however, the A^{n-} affinity order in the interlayer is established as $CO_3^{2-} > SO_4^{2-} > OH^- > F^- > Cl^- > Br^- > NO_3^- > I^-$ [131], hence LDH in water has a tendency to capture the CO_3^{2-} formed through CO_2 dissolution. In the other hand, the so-called "**memory effect**" property consists in the recovery of the LDH structure after its collapse. Indeed, LDH are decomposed through calcination into mixed oxides, which keep a layered structure as layered double oxide (LDO) as long as LDH is treated below 700°C [132]. Afterward, LDO can be rehydrated to LDH by contact with water, with the anion of highest affinity in solution intercalated [133].

LDH are generally platelets particles [134], but they can be synthesized with different morphology, like non-agglomerated 22 nm thick micronic sheets [135], agglomerated spheres ~20 nm or cauliflower-like particles [134] depending on the nucleation/growth mechanisms and kinetics.

The LDH-type1 lattice is hexagonal ($R\bar{3}m$ rhombohedral symmetry) and greatly impacted by its composition. The influence of the nature of A^{n-} and the M^{2+}/M^{3+} ratio is easily noticeable on XRD patterns (*Figure 1.23*). A **typical LDH diffractogram** includes **low angles basal planes (00*l*)** such as sharp and intense (003) and (006), and **higher angles planar lines (*hk*0)** like (110). The basal planes are associated to the layers stacking, and it is accepted that d_{003} corresponds to the interlayer plus the brucite sheet heights [136], hence mostly depends on A^{n-} [137]: d_{003} goes from ~0.77 nm for CO_3^{2-} to ~2.56 nm for dodecyl sulfate (*Figure 1.23.a*). Non-basal planes are related to cations arrangement within the layers and are impacted by M^{2+}/M^{3+} nature and ratio (*Figure 1.23.b*) [138]. The cell constants $c = 3d_{003}$ and $a = 2d_{110}$ [138] decrease when M^{3+} content increases, due to the bigger M^{2+} ionic radius (*e.g.* Mg^{2+}: 0.065 nm *vs* Al^{3+}: 0.050 nm)

[139]. The lattice of LDH-type2 is generally indexed on a monoclinic cell *$P2_1/c$* [128] or *$P2_1/n$* [130], although it appears to depends on the inserted cations.

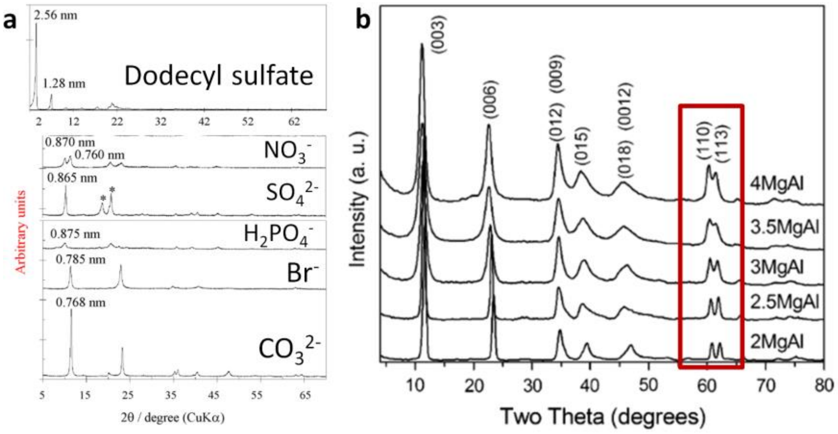

Figure 1.23: Influence of the a) intercalated anion [129] and b) of the M^{2+}/Al^{3+} ratio [125] on the LDH-type1 XRD patterns

It is worth mentioning that **layered single hydroxide LSH** compounds of formula $M(OH)_2$ (M = Ni, Co) have been synthesized. The stable β-$M(OH)_2$ phase is isostructural to brucite but the metastable α-$M(OH)_2$ is hydrotalcite-like, due to Van der Waals interactions and hydrogen bonding (water in the interlayer region) strong enough to ensure cohesion, without need for charge in the layers (though it stabilizes the phase) [140]. Variations of α-$M(OH)_2$ have been reported as hydroxyethylenglycolate [141, 142] and hydroxyacetate LSH structures, with glycolate/acetate groups partially replacing up to 1/4 of the OH^- groups for an increased LSH stability [143]. However, no LSH structure has been reported for $Mg(OH)_2$ for now.

iii. Thermal decomposition

The **oxide forms** of the as-synthesized precursors are obtained through **thermal decomposition**; hence in this paragraph we will present the literature on the oxides preparation upon calcination of the above mentioned hydroxides, and of the common hydroxides mixtures leading to pure MAS.

$Mg(OH)_2$ is decomposed into periclase in a single step at ~400°C [93]. $Al(OH)_3$ (gibbsite) is also decomposed in a single step between 208°C and 370°C, with complete transformation to alumina around 500°C [122]. In [144], authors proposed a mechanism in two stages: first the slow formation of AlOOH at ~250°C, then the formation of oxide at 310°C while the first one is not complete yet. The phase transition toward Al_2O_3 is complex and includes numerous possible paths depending on conditions [21]. XRD evolution upon calcination (*Figure 1.24.a*) [122] confirms the partial dehydroxylation to boehmite at 300°C, and total dehydroxylation at 500°C into metastable spinel Al_2O_3, up to high temperature of ~900°C.

LDH-type1 is decomposed in three endothermic steps. First, at low T < 200°C, a broad and progressive mass loss corresponds to the loss of physisorbed H_2O, followed at ~250°C by **dehydration** of the interlayer, while the LDH undergoes a loss of crystallinity up to ~310°C, with the decrease of XRD basal reflections as the layered structure collapse [93]. At 400°C, a second mass loss corresponds to the loss of OH^- groups in the sheets (**dehydroxylation**), and then the decomposition of interlayered CO_3^{2-} (decarboxylation) occurring as the former is still ongoing [145]. At this point, LDO is badly crystallized in a periclase-like structure [93]. For T ~900°C, a mixture of MAS and MgO is obtained, as spinel is exsoluted from the periclase phase [145].

LDH-type2 decomposition goes through the same mechanisms, except for the dehydroxylation and decarboxylation occurring at the lower temperatures of 300°C and 330°C, respectively [129], but no information about LDH-type2 crystallography after calcination is available.

Pure MAS is generally obtained after decomposition of **LDH-type1/gibbsite mixtures** at 700 - 800°C [93]. The XRD patterns evolution upon calcination and the mechanism of thermal decomposition into spinel are presented in *Figure 1.24.b* and *c*, respectively [94, 97]. At low temperature, the LDH layers collapse, then at 250°C the gibbsite is decomposed into η-Al_2O_3. At 400°C, LDH is progressively decomposed and integrates the metastable alumina [93, 94, 145]. Finally, at 800°C, all the MgO has integrated the spinel-like phase and stoichiometric spinel $MgAl_2O_4$ is crystallized [97].

Upon decomposition, the morphology of the particles are rarely kept, and the platelets or rose-shaped particles are often turned into spherical MAS crystallites in formless agglomerates [97]. However, if the initial secondary particles of hydroxides are big enough (> ~1 µm), their shape and size can be maintained through the phase transition until the temperature of effective atomic diffusion activation is reached, then the particles sinter and becomes spherical [122].

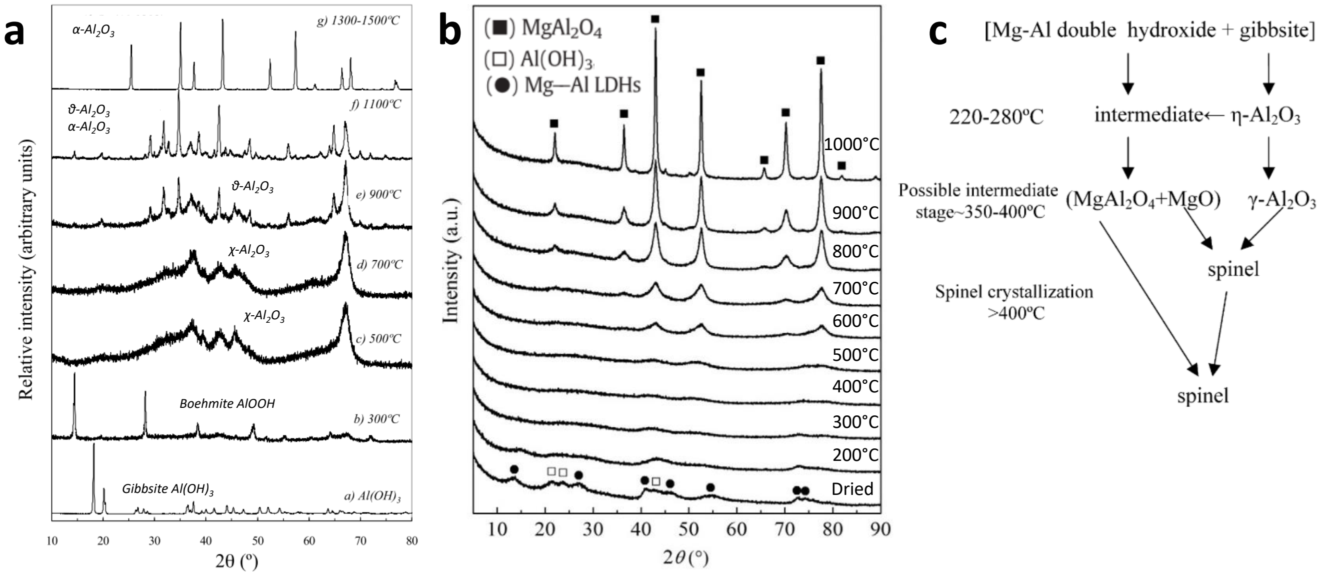

Figure 1.24: XRD patterns evolution of a) gibbsite [122] and b) a LDH-type1 and gibbsite mixture [97] upon heat treatment; c) mechanism of thermal decomposition into $MgAl_2O_4$ of the latter mixture [94]

4. Synthesis techniques developed in our research team

Our research operation MNM (Matériaux Nanostructurés Multifonctionnels, *i.e.* Multi-functional Nanostructured Materials) has acquired expertise in two synthesis methods that can be used for the preparation of $MgAl_2O_4$ nanopowders. These processes are presented here.

i. Nanofibrous ultraporous alumina (UPA) monoliths and liquid impregnation

An original process for the **synthesis of nanofibrous ultraporous alumina** (UPA) monoliths and **alumina-based compounds** has been developed and patented in our research team in the past decades by J-L. Vignes [17, 146–151]. The process relies on the catalyzed oxidation of an aluminum plate of high purity (99.999%) through a liquid layer containing Ag^+ - Hg^{2+}, where Ag^+ plays a reaction-stabilizing role and Hg^{2+} is the catalyst. The reaction is carried out into a climate chamber with a controlled atmosphere fixed at 25°C and 80% humidity, to regulate the highly exothermic oxidation of Al. The catalyzed reaction results in a UPA monolith growing perpendicularly to the surface of the plate, at a rate of 1 cm/h (which equals to ~1 g/h for a 50 cm^2 plate), as shown in *Figure 1.25*. The reaction can be carried on for up to 16 h with the monolith remaining stable and integer, using an Al plate of solely 1 mm thickness [17]. The as-prepared monoliths are very brittle and easy to dissolve by permeation in an aqueous solution.

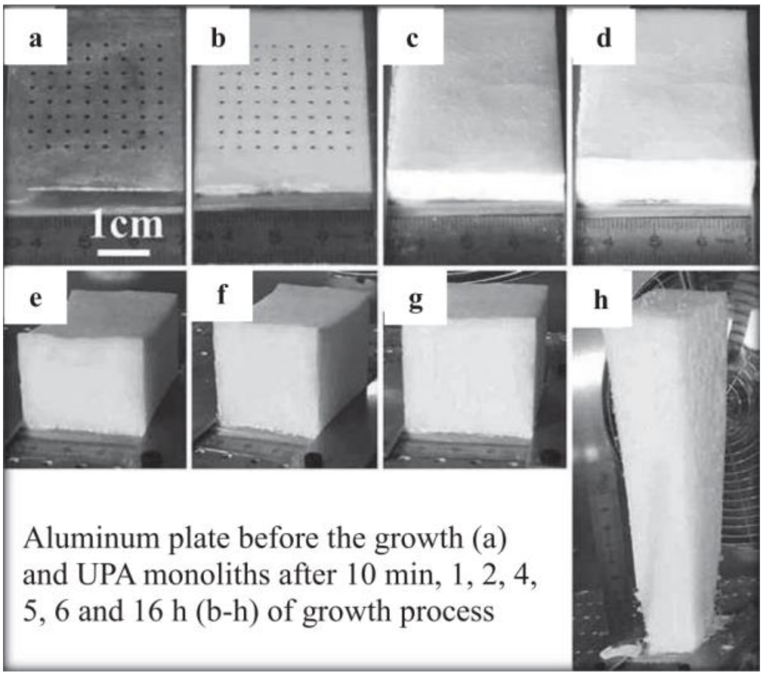

Figure 1.25: Evolution of the UPA monolith through the growth process [17]

The as-grown monoliths are highly porous (> 99 vol%) with extreme purity as they are not contaminated by the Hg^{2+}/Ag^{+} liquid layer, and contain 40 to 43 wt% of H_2O (adsorbed and structural). The microstructure consists in a **network of tangled alumina fibers** of diameter d_0 ~5 nm and length a_0 ~150 nm [148], forming pores of ~10 nm, together with micrometric pore channels parallel to the growth direction (*Figure 1.26*).

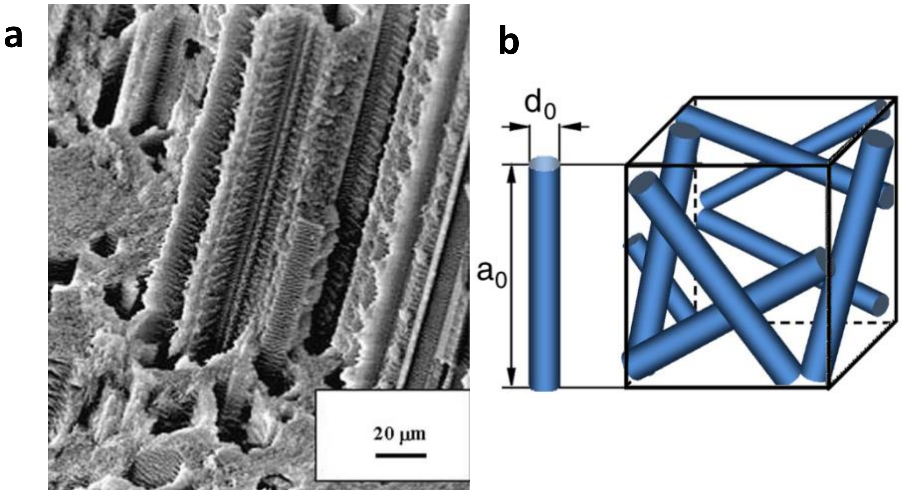

Figure 1.26: a) SEM of the pore channels in UPA monolith [17] and b) 3D schematic structure of the UPA [148]

The amorphous hydrated alumina can be **dehydrated and crystallized** through thermal treatment at appropriate temperature for generally 4 hours, depending on the desired final state. It has been shown that as-grown UPA has an approximate composition of $Al_2O_3{\cdot}3.6H_2O$, and can be dehydrated to amorphous Al_2O_3

by an annealing at 300 - 500°C [148]. Thermal treatment at higher temperature leads to crystallization, as demonstrated in *Figure 1.27*: from ~870°C to 1050°C the **spinel-like γ-Al_2O_3** is obtained, from 1050°C to 1180°C pure **θ-Al_2O_3** is obtained and above 1250°C the stable **α-Al_2O_3** is obtained [17].

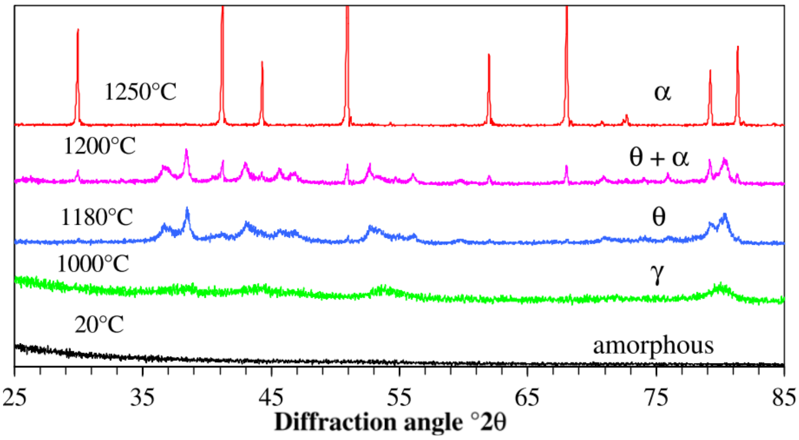

Figure 1.27: XRD of UPA treated at different temperatures during 4 hours [17]

The highly porous UPA morphology with high specific surface is maintained until the crystallization of θ-Al_2O_3. The fibrils aspect ratio a/d (*Figure 1.28.a*) is almost conserved upon dehydration (*Figure 1.28.b*), then it slightly decreases up to 1050°C because of fibrils fragmentation (d ~d_0, a < a_0) [148]. Once high temperature allotropes are formed, a/d rapidly decreases to ~2 due to significant coarsening of the particles, and they become ellipsoidal (*Figure 1.28.c*) [148]. When kept in monolithic form, UPA drastically shrinks after treatment at T ≥ 1050°C; it is then stabilized and no longer collapse when in contact with water [17].

One big advantage of UPA is that it can be easily doped through a **liquid or vapor impregnation**, as the very high porosity of raw monoliths allows a rapid and homogeneous fluid circulation. In particular, when UPA is placed in an atmosphere saturated by trimethylethoxysilane (TMES) vapor, the silicon alkoxide is hydrolyzed by the hydrated alumina surface [151]. Then through thermal decomposition, a Si-O-Al monolayer (~6 wt% of SiO_2) covers the fibrils, providing an increased stabilization of the structure and microstructure. Indeed, the silica layer has both coarsening and phase transition inhibition effects, and the γ-Al_2O_3 phase is conserved with fibrils diameter < 10 nm up to 1250°C [151].

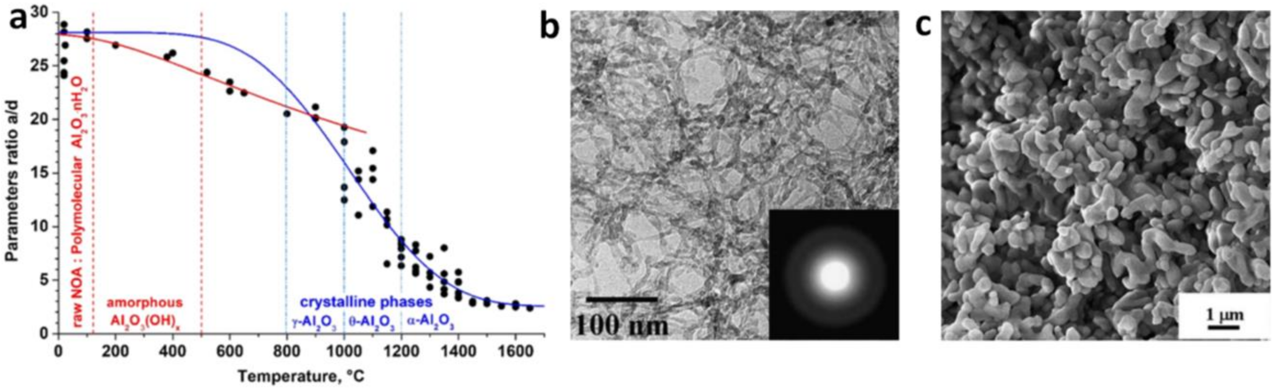

Figure 1.28: a) UPA fibrils aspect ratio evolution with T [148] and micrographs of b) 350°C and c) 1250°C treated UPA [17]

Another interesting possibility is to synthesize **nanostructured materials derived from alumina**. For instance, pure mullite $3Al_2O_3{\cdot}2SiO_2$ nanocrystallites have been synthesized using tetraethoxysilane which has four hydrolysable functions, allowing higher silica addition than TMES [152]. The synthesis of nanocrystalline aluminate spinel MAl_2O_4 (M: Mg, Ni, Co) through liquid impregnation (*Figure 1.29*) has also been reported [146, 149–151]. However, no thorough study of the process has been made, as previous works focused on keeping the monolithic form through reaction.

The interest of this method lies in the high variety of compounds that can be easily obtained, and on the relatively high producible amount per synthesis. Until now, UPA and derivatives had been considered for applications mostly relying on their high specific surfaces: immobilization and treatment of acid vapor and nuclear waste products [151, 153] and removal of pollutant from industrial wastewater [154, 155]. UPA is also a good candidate for waterproof self-cleaning photonic devices due to superhydrophobic properties and intense luminescence when it is functionalized [156].

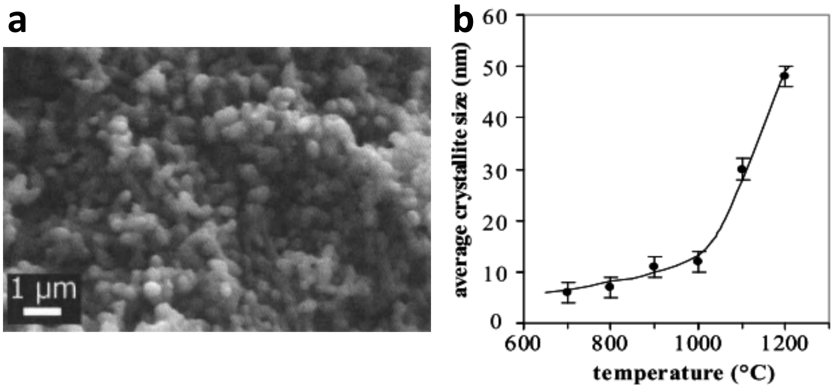

Figure 1.29: a) SEM of $MgAl_2O_4$ particles obtained from UPA impregnation [149] and b) crystallite size with temperature [151]

ii. Synthesis via the polyol process

Polyols (or polyalcohols, also referred to as glycols) have emerged as a very useful class of solvents for the preparation of **metal, oxide and hydroxide nanoparticles**, depending on the synthesis conditions, in the sol-gel related polyol route. Synthesis of numerous chalcogens and metal chalcogenide (Se^0, Te^0, FeS_2, SnS, $NiCo_2S_4$, $CuInSe_2$, Bi_2Te_3…) and non-metal (C-dots) nanoparticles has also been carried out *via* polyol route [157], but will not be considered here, as only metal oxides/hydroxides are of matter for our work.

Polyol media offer several advantages for synthesis [157, 158]. First, they can **dissolve most common metal salts** used as precursors, due to their high dipole moment compensating their dielectric constant lower than H_2O. Moreover, polyol molecules have **coordinating properties** as their multiple OH^- groups provide a chelating effect, which allows **complexation** of the metal precursors into intermediary alkoxides *in situ*, and **complexation** of the particles surface as surfactant, hindering their coalescence. Polyols are also **reducing agents**, allowing easy synthesis of metal nanoparticles without additional reductant, thus they have been intensively used to produce noble metals (Au, Ag, Pd, Pt, Rh, Ru) and ferromagnetic metals (Fe, Co, Ni) particles. Furthermore, the **high boiling point** of glycols (*Table 1*.3) permits better dissolution of poorly soluble precursors, enhanced reactivity/kinetic and high crystallinity without subsequent heat treatment (for some materials). Finally, polyol solvents exhibit **high viscosity**, which favors a diffusion-controlled regime, thus the nucleation and growth steps can be separated, resulting in controlled morphologies and size [158].

The polyol family is composed by **aliphatic diols** and starts with the 1,2-ethanediol, commonly called **ethylene glycol** EG. Based on EG, diols are divided into *i)* **etherglycols** (EG-oligomers) HO-$(CH_2CH_2O)_n$-H and *ii)* **alkanediols** $C_mH_{2+2m}O_2$; polyols with more than two OH groups (*e.g.* glycerol) are more rarely used in the polyol process [158]. The most widely used polyols are presented along with their boiling point (BP) in *Table 1.3*. Their BP, polarity and viscosity increase with increasing chain length. Etherglycols include diethylene glycol (DEG), triethylene glycol (TrEG), tetraethylene glycol (TEG) and polyethylene glycol (PEG) for n > 4, with the average molecular weight (MW) indicated in the name. For MW ≤ 600, PEG are highly viscous liquids at room temperature, readily usable as solvent [159, 160], but for MW ≥ 800, PEG are waxy solids with low melting point (PEG1000: ~35°C, PEG8000: ~60°C) used as cosolvent in water [159]. Alkanediols used as polyol solvents include EG, propanediol (PRO), butanediol (BUT) and pentanediol (PEN), with alcohol groups at any positions (except geminal diols).

Table 1.3: Selected etherglycols $HO(CH_2CH_2O)_nH$*, alkanediols* $HO(CH_2)_mOH$ *and their boiling point (BP) [157, 158]*

Etherglycol - n	2	3	4	~9	~181
Name	Diethylene glycol	Triethylene glycol	Tetraethylene glycol	Polyethylene glycol MW400	Polyethylene glycol MW8000
Acronym[a]	DEG	TrEG	TEG	PEG400	PEG8000
BP (°C)	244	291	314	> 350	> 350

Alkanediol - m	2	3	4	5
Name	1,2-ethanediol	1,3-propanediol	1,4-butanediol	1,5-pentanediol
Acronym[a]	EG	1,3PRO	1,4BUT	PEN
BP (°C)	197	213	235	242

[a] Several acronyms can be found for some polyols in literature; the selected ones have been chosen arbitrarily

In a typical polyol synthesis, different steps have been identified in the reaction mechanism: *i)* the **dissolution of the precursors**, *ii)* the eventual **formation of a solid intermediary** phase serving as cation reservoir, *iii)* the **nucleation** from monomer species and iv) the **growth of nuclei** into particles.

The overall redox process, through which the metal precursor is reduced by the polyol while the polyol is oxidized successively in different products, is an important aspect for the formation of metal particles and intermediate compounds. For the most popular polyol EG, the two-electron oxidation products are first glycolaldehyde HO-CH_2-CH=O, then glycolic acid HO-CH_2-COOH (or glyoxal O=CH-CH=O in basic conditions), followed by glyoxylic acid O=CH-COOH and oxalic acid HOOC-COOH, to finally lead to CO_2 [158]. However, all metallic cations cannot be reduced in sole presence of the polyol medium, as the most electropositive ones cannot be brought to the zero-valent state. Fe is considered difficult to reduce in polyol and may correspond to the limit of the process [158].

The **dissolution of the precursors** is facilitated by the coordinating ability of polyols, through the formation of metal-polyol or metal-polyolate complexes, while the initial salt counter-anion is kept in the coordinating sphere. The complexes obtained are highly important in the process, since they influence the reaction thermodynamic and kinetic. The ethylether groups O–CH_2–CH_2–O in etherglycols strongly favor chelation, because it leads to the formation of the very stable metallacyclopentadienes [158].

Upon heating of the solubilized precursors/formed complexes, an **intermediary phase can precipitate**, depending on the cation, its initial oxidation state, the species in the coordination sphere and the basicity of the medium. For instance, no intermediate precipitation occurs for noble metals, whereas Cu^{2+} has been reported to form Cu(II) glycolate, then transformed to CuO_2 prior to its final reduction to Cu^0 [158]. For Fe, Co and Ni, alkoxides and hydroxycarboxylates can be formed before reduction. These intermediary phases act as cation reservoirs, and their progressive dissolution controls the concentration of dissolved metal species; hence, this step is determining for the kinetic of the following ones. With appropriate synthesis conditions, it is possible to control which intermediary phase is formed and how it will react [16]. It should be noted that "intermediary solid phase" is a notion relative to the final/desired compound (for instance an oxide or hydroxide if a metal powder is aimed), and it can often be isolated as pure solid product as well.

The **nucleation and growth** steps generally follow the model of LaMer and Dinegar [161] in which they are assumed to be successive. It is often verified for the polyol route, because very narrow nuclei size distributions are typically observed, preventing simultaneous nucleation/growth. The nucleation is the formation of the first clusters (nuclei) of desired material, and its mechanism depends on the material: reduction for metals, hydrolysis or hydroxylation-olation for hydroxides, forced hydrolysis or hydroxylation-oxolation for oxides [158]. The growth of the nuclei occurs afterward, and the resulting crystallites are often monodispersed with low aggregation, as the surface-bonded polyol molecules hinder their coalescence.

If the polyol route was initially studied for metallic nanoparticles synthesis, the water-comparable and chelating properties of glycols are ideal for oxide nanoparticles preparation as well. The polyol solvent can coordinate to the as-formed particle nuclei, allowing high control over the crystallite size, size distribution and agglomeration. Typically, polyol syntheses lead to colloidally stable suspensions of almost non-agglomerated oxide nanoparticles with solid content up to 20 wt% [116]. However, direct oxide synthesis is not always possible, and some systems require subsequent calcination for decomposition/crystallization.

Members of our team have studied the polyol-mediated synthesis for the past twenty five years. In the last decades, our group has synthesized numerous compounds through the polyol route, including metals (Ni [162]) and intermetallic (Ag_3Sn [163], Ag_4Sn), layered hydroxides (acetate intercalated Zn-, Co- and Ni-LSH [143], NiFe-LDH [164]) and oxides among which spinel structures ($NiFe_2O_4$ [165] and $CoFe_2O_4$ [166]).

The synthesis parameters have a great influence over the synthesized particles (nature, shape, size, size distribution and agglomeration state). The most important parameters are the temperature and duration of reaction, the type of precursor salts and their concentration, the used polyol solvent, the uses of additives and their concentration and the concentration of water in solution.

One of the most crucial parameter over the nature of the synthesized compound is the **hydrolysis ratio *h***, defined as the ratio of H_2O molecules over the M^{z+} cations in solution (*Equation 1.16*). An appropriate ratio h can favor the preparation of either metals in anhydrous condition ($h = 0$), oxides for moderate amount of H_2O allowing forced hydrolysis and inorganic polymerization ($0 < h < {\sim}20$) or hydroxides for low temperature synthesis with high water content ($h > {\sim}20$), as illustrated in *Figure 1.30* for Co^{2+} [16]. However, the reducing strength of polyol is sometimes insufficient to form metals of electropositive cations [16], and an adequate polyol solvent should be used depending on the compound aimed. In [165], $NiFe_2O_4$

was synthesized in DEG, while the stronger reducing agents EG and 1,2PRO led to Ni and Fe oxide mixtures.

$$\boldsymbol{h} = \frac{\boldsymbol{n}(\boldsymbol{H_2O})}{\sum \boldsymbol{n}(\boldsymbol{M^{z+}})}$$ *Equation 1.16*

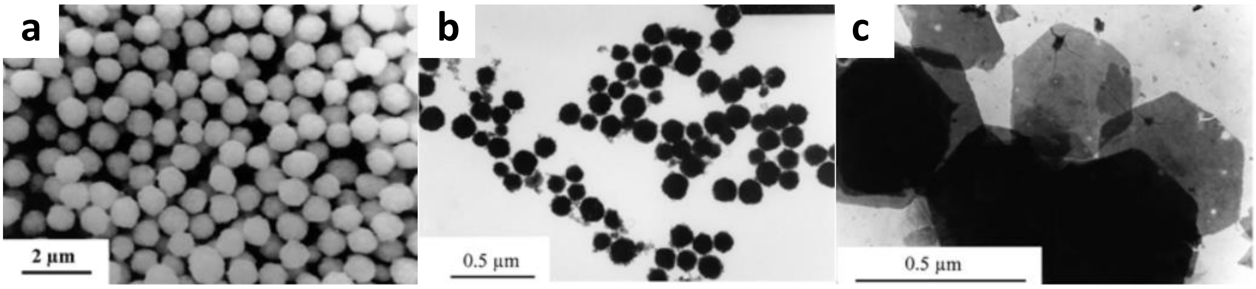

Figure 1.30: TEM of different Co^{2+}-based compounds illustrating the influence of the hydrolysis ratio: a) Co^0 for h = 0, b) CoO for h = 4 and c) $Co(OH)_2$ for h = 26 [16]

Temperature T and **duration *t*** of the synthesis are the basic parameters governing the reactivity, as T controls the kinetics and thermodynamics of possible reactions, and *t* dictates how close to the equilibrium stands the synthesis state from solubilized precursors to the (meta)stable compound [167]. Indeed, these aspects cannot be discussed in general, as they depend on the system studied. T and *t* also influence the particles shape, size and agglomeration. Increase of T has been reported to either increase or decrease the crystallites size (CS) and particles size (PS). For Al_2O_3 synthesis in EG, the increase of T from 140°C to 180°C led to diminution of both CS from 5.5 nm to 3.3 nm, resp., and PS from ~1 µm to 142 nm, resp. [168]. This result was explained by a slow nucleation with low nucleation rate at low T inducing a high cation concentration available for the subsequent growth, while high T allowed high and fast nucleation, hence reduced available cations for the growth. A two-steps synthesis can further separate the nucleation and growth, as reported for $Mg(OH)_2$ synthesis in DEG [169]: while PS of 20 nm was obtained for a single stage at 100°C for 30 min, PS of 100 nm was reached by a two-step process with nucleation at 50°C for 30 min and growth at 240°C for 10 min. The nucleation/growth kinetic can also be controlled *via* hot injection (introduction of the reagents at high T), which allows the synthesis of nonequilibrium nanostructures with complex morphologies [160]. The synthesis duration is indeed a key parameter in the control of the morphology, as longer syntheses favor the growth and coalescence of nuclei and particles [160].

The **nature of the precursor salts** has been reported to determine the crystallites shape. The effect of the precursor-solvent combination was investigated in a thorough study on the nucleation and growth of rhodium nanoparticles [160, 170]. As Rh salts are dissolved, the counter-anions stay in Rh^{3+} coordinating sphere and become surface-coordinating ligands of the nuclei. In the early stages, 1 - 2 nm spherical Rh clusters are formed independently of the ligand environment, and later serve as a stock of embryonic species for the formation of crystallites with predictable morphology [170]. Indeed, during the growth step, the ligand affects the favored crystallographic planes as well as the type of crystallinity through the growth pathway as illustrated in *Figure 1.31.a-c* [170]. Weakly bound ligands ($COOCF_3^-$) result in twinned particles *via* clusters coalescence, ultimately forming polycrystalline icosahedra [160]. Strongly bound ligands (Br^-) promote epitaxial growth through Ostwald ripening and monomer addition, resulting in monocrystalline cubes [160]. Moderately bound ligands (Cl^-) favor the formation of monocrystalline triangular plates by combination of both mechanisms [170]. A linear dependence between concentration and CS allows controlling the latter [160]. These insights were demonstrated to be general to all noble metal synthesis *via* polyol route (Pt and Pd [170], Ag nanospheres with $(NO_3)^{2-}$ and nanowires with Cl^- addition [171]), but no extrapolation can be made *a priori* for another system, *a fortiori* as different as a complex spinel oxide.

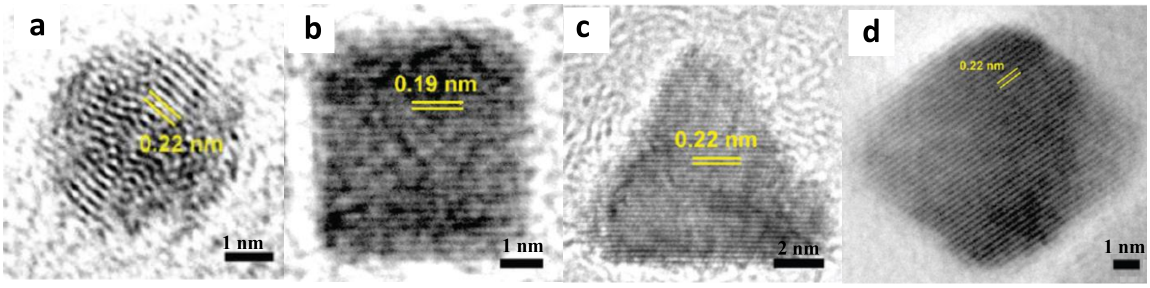

Figure 1.31: TEM of Rh nanoparticles synthesized from a) Rh2(COOCF3)4 in EG, b) RhBr3 in DEG, c) RhCl3 in TrEG and d) RhCl3 hot injected in 240°C TEG [160]

At the heart of the polyol process, the **solvent** is to be considered the primary lever for manipulating the growth rate, hence determining whether particles form in a kinetic or thermodynamic growth regime. As stated before, the ligand environment largely defines the crystallites shape and the concentration helps control their size, but the polyol used appears to improve the monodispersity and shape yield. The different oxidation potential of each polyol solvent leads to specific temperature of particle formation, and through judicious polyol selection and tuning of nucleation/growth temperature, it is possible to further tailor the particle morphology. Returning to the example of Rh synthesis, in addition to the surface-coordinating ligands, change of the polyol solvent was necessary (*Figure 1.31*) to reach very high shape yields [160]. Combining this approach with the hot injection method, Rh nanooctahedra were obtained in TEG instead of triangular plates in TrEG (*Figure 1.31.d*). Similar observations were made for other metal systems. Synthesizing Ag colloids in either EG or PEG, from PEG200 to PEG600, nanospheres were obtained with CS increasing proportionally to the solvent MW [171].

However, the role of the solvent has been reported to be more important for oxides synthesis. In [159], ZnO nanoparticles were synthesized from $Zn(CH_3COO)_2$, and the morphology of the powders was highly dependent on the solvent. While micrometric hexagonal particles were synthesized in H_2O, reaction in EG led to highly agglomerated nanoclusters, reaction in DEG led to ~50 nm long nanorods and PEG400 resulted in well-dispersed ~10 nm ZnO nanospheres. This effect of the solvent is in fact due to its complexation properties, as it enters the cation coordination sphere prior to the nucleation step, then favors the growth of some crystallographic planes. The solvent also acts as a surfactant during the growth step, and longer glycol chains induce higher steric/electrostatic repulsion between nuclei and/or particles, limiting their coalescence.

Finally, it is also possible to control the nature of the compounds or the morphology of the particles with the use of **additives**, which can be of various natures. In a general way, the effect of the additives depends on the additive ratio, *i.e.* number of additive groups over M^{z+} cations (*Equation 1.17*). This ratio can take numerous notations depending on the additive, and will be called *r* for general definition.

$$\boldsymbol{r = \frac{n(additive)}{\sum n(M^{z+})}} \qquad \textit{Equation 1.17}$$

Reducing agent (*e.g.* citrate, hydrazine, sodium hypophosphite [162], sodium borohydride [163, 171]) can be added for the synthesis of metals, if the reducing strength of polyol is not enough. **Basicity agents** (typically NaOH [162, 163, 169]) favor hydroxides/oxides precipitation and prevent metals nanoparticles dissolution in acidic polyol. For metal particles, **oxidants** addition (*e.g.* Cl^-, Br^- or Fe^{3+} combined with O_2 from air) may allow oxidative etching mechanisms, which can provide control over crystallinity, particle size, growth mode for anisotropic particles and morphology (truncation of edges, facet selectivity, etching and regrowth, fabrication of hollow nanostructures and galvanic replacement for bimetallic structures) [172]. However, the most used additives are **surfactants** (*e.g.* carboxylates such as acetate, polymers like polyvinylpyrrolidone PVP or PEG) for additional complexing effects, and tailoring of the particles shape and size; in particular, PVP has been widely used for all type of compounds from metals to oxides. For MgO nanoparticles synthesis in EG from acetate salt, the ratio r of PVP58000 drastically impacted the morphology (*Figure 1.32*): with $r = 0.3$, 3 nm spheres were obtained, while with $r = 5$, 10 nm x 30 µm nanowires were obtained [173]. Nonetheless, in [174], still for MgO synthesis in EG but from chloride salt instead, no sensible effect was observed for PVP10000 and PEG10000 on the particles morphology. It was concluded that with Cl^- in the ligand environment of Mg^{2+}, EG already serves as a strong enough chelating agent, and spherical MgO particles uniformly distributed were obtained without need for additional capping agent.

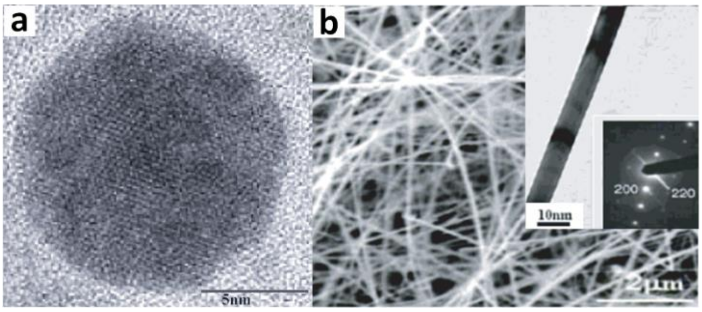

Figure 1.32: MgO nanoparticles synthesized by thermolysis at 500°C of as-synthesized product in EG from Mg.(ac)$_2$, with addition of PVP as capping agent: a) Mg^{2+}: 0.1 M and r = 0.3, b) Mg^{2+}: 0.025 M and r =5 [173]

As mentioned above, numerous (hydr)oxides have been synthesized *via* the polyol route. In particular, reports on the synthesis of layered hydroxides (LSH and LDH), MgO, Al_2O_3 and spinel compounds are of interest for our study. However, for electropositive metals, the formation of oxide form generally requires a subsequent thermal treatment. Regrettably, the as-synthesized intermediary compounds are rarely thoroughly studied, as the authors are often only interested in the final product they are trying to synthesize. Hence, little information is available on the synthesis mechanisms, useful to help set appropriate synthesis conditions.

Layered hydroxides synthesis in polyol has been reported several times, systematically from acetate precursors, and hydrolysis of alkoxyacetate intermediates has been invoked as reaction mechanism, with the hydrolysis ratio as a key parameter. Early studies on these compounds highlighted the impact of both M^{2+} and M^{3+} cations on the necessary H_2O amount of water. For M^{2+}-LSH synthesis, depending on M^{2+} different morphologies are obtained and different hydrolysis ratios are required: $h > 2$ for Zn-LSH, $h > 26$ for Co-LSH and $h \geq 4$ for Ni-LSH [143]. For lower h, the acetate salts are forced to react with EG, to successively form alkoxyacetates and alkoxides [175]. Similarly, for (Ni,Co)Al-LDH [167], $h \geq 150$ is required for full hydrolysis, while $h = 40$ is sufficient for NiFe-LDH [164]. Prévot *et al.* [167, 176] explained the formation of

M^{2+}Al-LDH by M^{2+} adsorption on the normally insoluble nor hydrolysable dibasic Al^{3+} acetate, allowing its progressive forced dissolution. Then, the solubilized Al^{3+}-CH_3COO^- complex forms an alkoxyacetate and the M^{2+} ions-Al^{3+} complexes interactions prevent the simple M^{2+} salt hydrolysis in LSH. Finally, precipitation occurs through concomitant mass transfers from the Al-based solid to the polyol solution and from the polyol solution to the LDH, as the progressively solubilized precursor serves as cation reservoir.

MgO synthesis in polyol medium has been reported numerous times, with various synthesis conditions (chloride or nitrate salts, EG or DEG, …) [169, 173, 174, 177]. In practice, colloidal $Mg(OH)_2$ nanoparticles are synthesized, later calcined around 300°C to form MgO [169]. In contrast, **Al_2O_3 synthesis** in polyol has only been reported once, from nitrates in EG at 140 - 180°C [168]. The authors claimed to have readily synthesized amorphous Al_2O_3, then crystallized to γ-Al_2O_3 at 800°C with CS down to 2.5 nm. However, no TG-DT analysis was performed, and by analogy with other soft chemistry syntheses, it is to be assumed that an intermediary was obtained and thermally decomposed to alumina.

Numerous **spinel compounds** have been obtained in polyol medium. Interestingly, ferrites ($CoFe_2O_4$ [166], $NiFe_2O_4$ [165], $Ni_{1-x}Zn_xFe_2O_4$ [178], $MnFe_2O_4$ [179]) are readily obtained and crystallized, without subsequent thermal treatment, with hydrolysis and acetate ratios fixed by the precursor salts. Although hydrolysis is believed to be the reaction mechanism, for the synthesis of $MnFe_2O_4$ from acetylacetonate in PEG8000, PRO or TEG, no H_2O was introduced in solution ($h = 0$) and the spinel oxide was obtained anyway [179]. Among searchers using the polyol-mediated synthesis, Feldmann and his team have specialized in the synthesis of oxide nanoparticles [116, 117, 157, 169, 180, 181], including several aluminate spinel ($CoAl_2O_4$ and $MgAl_2O_4$ [116, 180, 181]). Unfortunately, in most of their communications, informations on experimental conditions are scarce. Thereby, **$MgAl_2O_4$ synthesis** is not detailed, and it is only mentioned that the synthesis was carried on by “mixing a suitable metal precursor (*e.g.* acetate, oxalate, alkoxide) and a defined amount of water with diethylene glycol”, followed by heating at 180°C for 2 h, and finally $MgAl_2O_4$ was obtained after calcination “at relatively low temperature” [116]. However, synthesis protocols have been detailed for $CoAl_2O_4$ [180] and $Mg(OH)_2$/MgO [169], and the preparation conditions for $MgAl_2O_4$ nanopowders can be assumed from these. Since MgO and $CoAl_2O_4$ were obtained after the calcination of the as-synthesized products using $MgCl_2 \cdot 6H_2O$ and acetates, respectively, with $h = 1$-10 at high reflux in DEG, $MgAl_2O_4$ has probably been synthesized from $MgCl_2 \cdot 6H_2O$ and Al^{3+} acetate in DEG at high reflux, with $h = 1$-10. In a more recent study, $CoAl_2O_4$ synthesis from chlorides and acetates were compared, and no sensible differences on the particles features were observed [15].

The different synthesis conditions used for LDH, MgO/Al_2O_3, and spinels in literature will serve as basis for polyol synthesis of MAS in this thesis.

IV. Sintering

As stated in *Chapter 1.II.3*, the fabrication of transparent ceramics requires densification close to ~100% to avoid light diffusion at pores surface, with the smallest possible structural defects concentration. The fabrication of polycrystalline materials meeting these requirements is carried on through a sintering step involving mechanisms that should be fully understood in order to be controlled as well as possible.

1. Definition

The **sintering** is the thermal consolidation of a powder into a massive polycrystalline material. It is a crucial step dictating the final microstructure state on which rely most of the material properties. However, the term “sintering” should be clarified, since it does not systematically designates the same process principles depending on the usage and points of view. Numerous definitions exist, and the following, proposed by Olevsky [182] were selected:

- from a mechanical angle, sintering is a “thermally activated transition of a powder or porous system to a thermodynamically more stable state through a decrease of the surface energy”;
- from a physical angle, sintering is a “thermal treatment for bonding particles into a coherent, predominantly solid structure *via* mass transport events that often occur on the atomic scale, leading to improved strength and lower system energy”.

Thus, sintering is the process of **densification/consolidation** of a powder by thermal effect, employing temperature below the melting point. Based on the mechanisms involved, sintering types are distinguished:

- the **solid phase sintering**, if every constituents stay in solid state during the process;
- the **transient liquid phase assisted sintering**, if a small fraction of liquid is formed during the process, favoring particles rearrangement and dissolution–precipitation mechanisms enhancing the densification;
- the **viscous flow sintering**, mostly for amorphous powders undergoing densification due to high viscosity under thermal effect (partially molten surface, glass transition, pressure gradients). Its primary use is for the fabrication of amorphous massive materials (*e.g.* silica) [183];
- the **reactive sintering**, if the heat treatment is used for simultaneously reacting the powder constituents and densifying the novel phase, both mechanisms benefitting from the other one. Reactive sintering includes the densification of compounds undergoing phase transition.

2. General aspects

The consolidation of materials with controlled microstructure and relying properties requires two main conditions: a **complete understanding** and **mastering** of the consolidation process, and an **appropriate precursor powder**. For this thesis, we will focus solely on aspects relative to the solid phase sintering.

i. *Driving forces of the sintering*

The driving force of the sintering is the **diminution of the system Gibbs free energy ΔG**. Several mechanisms intervene in the process, but from a thermodynamic aspect the so-called global driving force is the **reduction of the interface area** in the powder compact following *Equation 1.18*.

$$\boldsymbol{\Delta G = \gamma_{ss}\Delta A_{ss} + \gamma_{sg}\Delta A_{sg}} \quad \textit{Equation 1.18}$$

During the consolidation, the solid-gas interfaces area A_{sg} (surfaces of the particles) of surface energy γ_{sg} progressively decreases and the solid-solid interfaces area A_{ss} (sinter necks, grain boundaries GB) of surface energy γ_{ss} increases. Hence, $\Delta A_{ss} > 0$ and $\Delta A_{sg} < 0$, while respecting the **thermodynamic criterion $\Delta G < 0$** [80]. The driving force can be enhanced to favor the densification through increase of the ratio γ_{sg}/γ_{ss}, by activation of the particle surface (increase of γ_{sg}) or stabilization of the GB (decrease of γ_{ss}).

During the early stages of sintering, strong bounds are formed at the contact points between particles (sinter necks), resulting in local curvatures extrema: convex particles surfaces and concave sintering necks. Compared to a stable plane surface, the convex surface of particles exhibits an excess of atoms while the neck exhibits a vacancy concentration, inducing the latter to act as a sink, dragging matter from the former to the neck area (*Figure 1.33*) under thermal activation. Hence, these curvature differences are the **local driving forces** governing the kinetic of surface reduction, as indicated by the Gibbs-Thomson equation:

$$\Delta\boldsymbol{\mu}(\boldsymbol{r}) = \boldsymbol{RT}\,\Delta\boldsymbol{ln\,p} = \frac{\boldsymbol{2\gamma V_M}}{\boldsymbol{r}}$$

Equation 1.19

with $\Delta\mu(r)$ and $\Delta ln(p)$ the differences of chemical potentials and ln vapor pressure, respectively, between a surface of curvature *r* and a flat surface, *R* the gas constant, T the temperature, and V_M the molar volume.

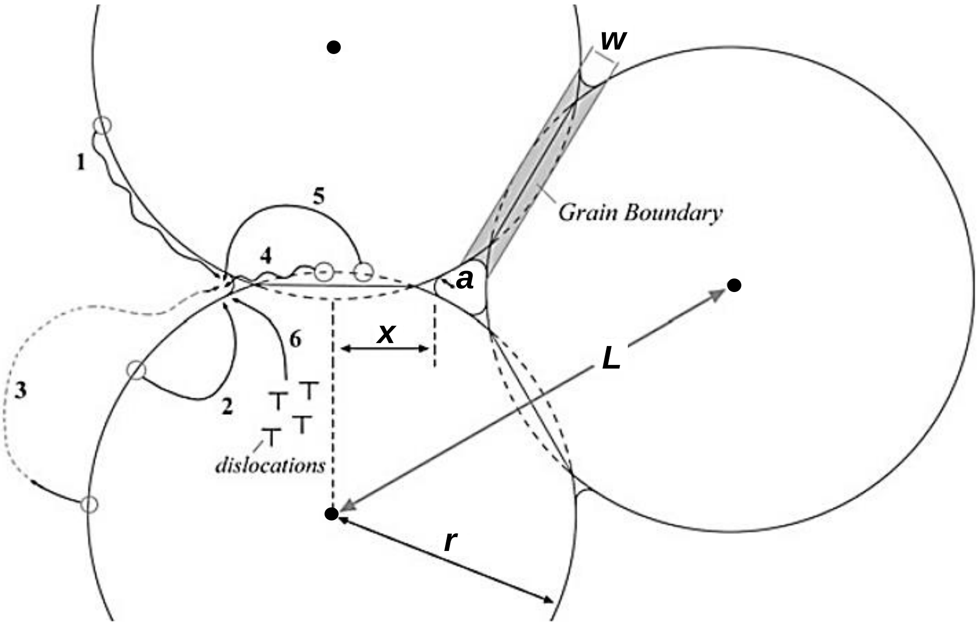

Figure 1.33: Illustration of the sintering mechanisms represented by numbers explained in Table 1.4 [80]. x, a and r are the radii of the neck section, its curvature and the particle, resp.; L is the distance between particles mass centers, and w is the boundary thickness

Equation 1.19 implies that the chemical potential and vapor pressure/solubility strongly depend on the particle size, as smaller ones are more reactive and more subjected to dissolution/evaporation from their surface and reprecipitation in the neck area [184]. As the sintering goes on, the sintering necks grow and the particles are deformed (displacement of their center of mass) resulting in greatly reduced local curvatures differences, hence the sintering potential decreases and the kinetic of the process is slowed down.

The previously described curvature gradients are generating **material flux** through several **diffusional mechanisms**, distinguished by the material source and the atomic path (*Figure 1.33* and *Table 1.4*). The mechanisms can be classed depending on the effect they have on the particles edifice:

- the **consolidating mechanisms** (from 1 to 3) for which the matter is provided by the particles' surface. They allow the neck formation and enlargement, hence to have a coherent structure, but solely by particles elongation without getting their mass centers closer, resulting in low densification;
- the **densification mechanisms** (from 4 to 6), for which the matter comes from either the neck/GB itself or the particles' bulk (migration of defects). Hence the neck area grows through mass centers approach.

During the sintering, once the atomic diffusion is sufficient, the diminution of the system ΔG occurs *via* concomitant and competing phenomena thermally activated: **densification** and **grain growth**, distinguished by how the driving forces are acting and by the contribution of each diffusion mechanism [80].

Table 1.4: The different mechanisms intervening in solid phase sintering for densification and consolidation effects

Mechanism	Nature of transport	Source of material	Effect
1	Surface diffusion	Grain surface	Consolidation
2	Bulk diffusion	Grain surface	Consolidation
3	Evaporation/condensation	Grain surface	Consolidation
4	Boundary diffusion	Grain boundary	Densification
5	Bulk diffusion	Grain boundary	Densification
6	Bulk diffusion/plastic deformation	Bulk (defects)	Densification

The **densification** occurs *via* replacement of solid-gas by solid-solid interfaces ($A\Delta\gamma$), the neck dragging material from all over the bonded particles to the detriment of porosity. Instead, the **grain growth** induces a global interface area reduction ($\gamma\Delta A$) through coalescence or boundary diffusion. Generally, the sintering occurs by a combination of both phenomena, following an intermediate path such as $\Delta(A\gamma)$ [184].

The general grain growth kinetic, dependent on temperature, follows an Arrhenius law:

$$\Delta(r^n) = K_0 exp(-Q/RT).t \qquad \text{Equation 1.20}$$

In this equation, r is the particle radius (replaced by grain size GS once GB are formed), n is a growth exponent relative to the growth mechanism (*i.e.* n = 1: viscous flow; n = 2: evaporation/condensation; n = 3: volume diffusion; n = 4: surface or GB diffusion), K_0 is Arrhenius constant and Q is the grain growth activation energy. These parameters can be determined from experiments through GS evolution: isothermal sintering of different durations allow to determine K_0, Q and n(T), while isochronous sintering at different T reveal the different grain growth domains [185]. For ceramics, n is typically in the range 2 - 4 [186].

If the particles size distribution is too large to be considered monodisperse, their **coalescence** is observed from the very early sintering stages. It is a growth process by which the smaller particles of high curvature are dragged by the larger ones, and which occurs through evaporation/condensation to reduce A_{sg} (or dissolution/precipitation to reduce A_{ss}), following an Ostwald ripening model [80]:

$$\Delta(r^3) = \frac{D\, p_0\, \gamma\, M}{\rho^2 RT}.t \qquad \text{Equation 1.21}$$

where D is the diffusion coefficient, ρ is the density and M is the molar mass. This equation shows that for a given system, the temperature T and the processing time at T are the critical parameters controlling the **coalescence growth**, which **evolves in r^3**.

As soon as sinter necks are formed, and even more when density is high (*i.e.* $A_{ss} > A_{sg}$) and the atomic diffusion is activated enough, the grain growth occurs through **boundary diffusion**, as the GB is enabled to migrate through the bulk. While GB energy is the driving force, the boundaries displacement is due to their curvature, pushing them toward the curvature center to reach the stable state of plane GB with 120° angles triple junctions (joining point of three GB). The growth of grain through GB migration is described by [80] :

$$\Delta(r^2) = k.\frac{4D_{GB}\,\gamma_{GB}\,V_M}{w\,RT}.t$$ *Equation 1.22*

where D_{GB}, γ_{GB} and w are the GB diffusion, energy and thickness, resp., and k is a constant. This equation is similar to the one describing coalescence (*Equation 1.21*), however, **this process evolves in r^2**.

In order to **enhance the sintering**, it can be carried out **under applied pressure**, to increase the contact pressure between particles and bring additional localized energy to the system. To introduce the beneficial contribution of pressure-assisted sintering, the densification rate can be expressed as follow [187]:

$$\frac{d(d)}{d(t)} = \frac{(1-d)}{(1-d_0)}B\left[\frac{g.\gamma}{2r} + P_E - P_G\right]$$ *Equation 1.23*

where d and d_0 are the relative density at t and t_0, resp., B is a thermally activated mass transport parameter, and P_E and P_G are the effective external pressure and the gas pressure in pores, resp.

Since contact areas are small until significant densification, in early stages the **effective applied pressure P_E** is several times the applied pressure P, and its contribution to densification is often highly superior than the one from surface energy [187]. Hence, the applied pressure effects dominate the densification rate, first through powder compaction, then through combined pressure-temperature effects (*Chapter 1.IV.3.iii.c*). From *Equation 1.23*, the gas pressure during sintering appears to be important as well, as it may lead to pores filled with gas, which retards densification and precludes total suppression of the porosity. Hence, primary vacuum is often applied to limit this problem, while mechanical pressure will helps preventing gas entrapment.

ii. Phenomenology of the sintering

a. The sintering stages

The sintering process of a powder can be decomposed into **several stages**, differentiated by the microstructure of the material and the phenomena involved. These stages can be distinguished on the dilatometric curve of the powder, which is a plot of the shrinkage versus the temperature (*Figure 1.34*).

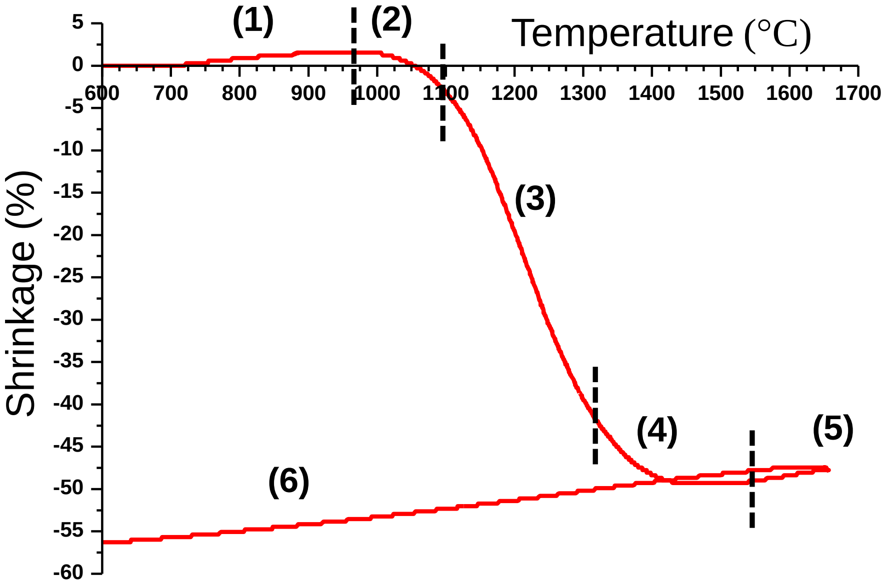

Figure 1.34: Dilatometric analysis of a $MgAl_2O_4$ powder during sintering; the process is divided in numbered stages

It is important to note that these stages are only a didactic division, and the sintering process involves the same driving forces from the beginning to the end. However, the microstructure evolution impacts the contribution of each mechanism, hence modify the system behavior under thermal stimulation, giving rise to the division. Five steps can be observed (*Figure 1.34*), including three sintering stages from (2) to (4) [188]:

(1) *Thermal expansion of the green body prior to the consolidation*. In this stage, the temperature is too low to activate the diffusion mechanisms, and the expansion of the grains leads to their partial rearrangement. It is accompanied by water, gas and organic impurities desorption.

(2) *Early stage:* ***sintering necks formation and enlargement***. This stage is initiated at the particles contact points bonded by weak interactions, when the atomic mobility is activated enough to enable strong bonds formation (necks, *Figure 1.35.a*). The consolidating mechanisms are mostly involved, hence from surface source, and the necks enlargement induces a surface energy reduction by 50%. Densification is very limited in this stage, and at the end of (2) the relative density reaches 60 - 66% [187].

(3) *Intermediate stage: the* ***densification***. In the intermediate stage, the densification mechanisms have a higher contribution due to the increased temperature. The particles are deformed as their mass centers are getting closer, and their area of contact enlarges further, hence porosity decreases. During this stage, the system is not a compacted pulverulent medium anymore, but a coherent solid: the particles become grains and the sinter necks become GB. At the end of (3), the microstructure consists in stacked polyhedral grains (truncated cuboctahedron) bonded by their faces, with a network of open porosity channels alongside their edges (*Figure 1.35.b*). The density reaches 88-92%, and the grains start to grow.

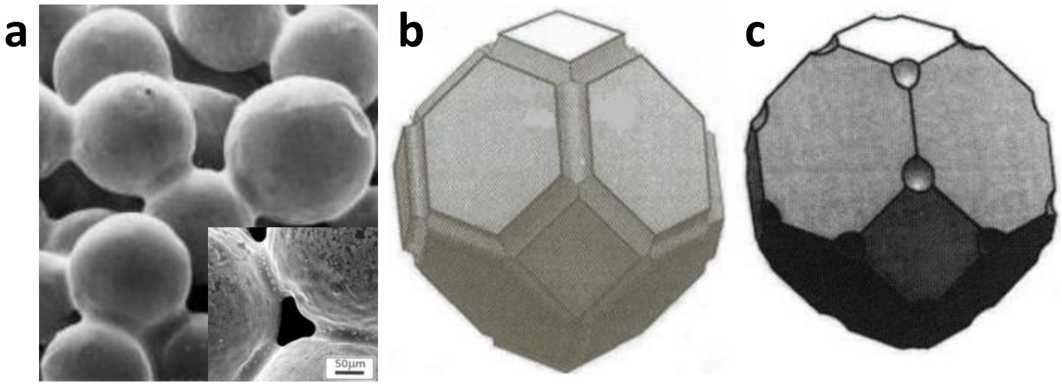

Figure 1.35: Evolution of the morphology during sintering: a) initial stage, spherical particles bonded by sinter necks [187], b) intermediate stage, grains assimilated to truncated cuboctahedra bonded by their faces with interconnected pore channels along the edges [184], c) final stage, isolated spherical pores at the vertices [184]

(4) *Final stage:* ***porosity elimination and grain growth***. In the final stage, the grain growth rate eventually overcomes the densification rate, and the porosity network becomes instable because of the decrease of the channels curvature. As a consequence, the channels are divided into closed spherical pores isolated at GB and GB junctions (*Figure 1.35.c*), which continue to shrink *via* bulk and GB diffusion mechanisms. The full densification (~99.9%) is reached on the shrinkage *plateau*.

(5) *Oversintering: further grain growth and secondary porosity*. When the full densification *plateau* is exceeded, the grains continue to grow and the pores coalesce, and eventually the material expands back from thermal dilatation. Depending on their crystallographic orientation, all grains do not expand equally, and cracks or new pores can be formed.

(6) *Cooling to RT*. The cooling part of the curve can be used to control the contraction rate. Especially in the case of ceramic densification, the cooling and applied pressure release rates are important, as uncontrolled contraction can lead to cracking of the speciment due to stress gradients.

b. *The densification: evolution of the porosity*

As mentioned above, the densification (*i.e.* the suppression of the porosity) and the grain growth both involve diffusion from the bulk and the solid-solid interfaces by grain boundary migration. However, **the pores** can have great effect on the grain growth depending on their location, considering that pores also diffuse within the material, analogically to vacancy clusters diffusion. Except for the case of gas atmosphere trapped within the specimen, easily avoided under slight vacuum, pores basically contain vapor phase from the material and form solid–vapor interfaces with the grains. Initially, the pores are located at GB and hinder their migration by a pinning effect, which has for main effect to inhibit grain growth [80].

For pores located at GB junctions, several cases can be distinguished. Under specific conditions, *i.e.* six grains surrounding the pore (in 2D projection), all angles will be 120° with flat pore-grains interfaces, ensuring stability. Otherwise, curved interfaces will be formed, providing local driving force for their displacement. From the pore referential, less surrounding grains induces concave interfaces promoting their migration toward the pore, leading to its shrinkage, while more surrounding grains conducts to convex interfaces, and the pore will have a tendency to grow, and to coalesce with other pores [184].

In the case of a pore located on a GB, the pore stability will depend on the GB stability. When the GB is plane, the pore shape is oval, elongated along the GB, and both their mobilities are weak, but when the GB becomes curved, the pore is deformed and presents distinct curvatures in each direction of the GB. In the latter case, the pore is dragged by the GB and exerts a pinning effect on its movement as mentioned before, decreasing the velocity of GB mobility v_{GB} [184] which is expressed as:

$$\boldsymbol{v_{GB} = M_{GB}(F_{GB} - N_p . F_p)} \qquad \text{Equation 1.24}$$

where M_{GB} is the GB mobility, F_{GB} and F_p are the driving forces for GB and pores mobility, respectively, and N_p is the number of pores per unit grain boundary area. For a combined migration of pores and GB, *i.e.* pores velocity equivalent to GB velocity, *Equation 1.24* can be rewritten:

$$\boldsymbol{v_{GB} = \frac{M_{GB}}{1+N_p(M_{GB}/M_p)} . F_{GB}} \qquad \text{Equation 1.25}$$

From *Equation 1.25*, two extreme cases can be considered [184]: *i)* $NpM_{GB} >> M_p$ and *ii)* $NpM_{GB} << M_p$. Condition *i)* applies to systems containing **numerous pores with low mobility**, thus with GB migration (and coarsening) controlled by **the pore migration**, while condition *ii)* is satisfied for boundaries with **few pores of high mobility**, and GB migration is controlled by its **intrinsic mobility** as it is not affected by pores.

Separation of the pores from the GB occurs when the velocity of GB migration is higher than the pore’s one (generally in final sintering stage), and results in **intragranular porosity** (pores entrapped within monocrystalline grains), which is in term almost impossible to suppress. As pores are detached from them, no pinning effect hinders the GB mobility anymore, and grain growth rate increases.

c. The grain growth

Based on the influence of porosity on the grain boundaries migration, it is clear that **coarsening** of the grains occurs mostly in the late stage of the sintering when the density of pores is too low for a pinning effect to be effective, as in dense material the grain growth is mainly controlled by the GB velocity.

Figure 1.36.a illustrates the most common **grain growth mechanisms**. At the left is the **classical growth** mechanism, occurring through **GB migration** due to curvature of the interface (dependence on the GB energy) and boundary junction deviating from stable 120° tri-angles (geometrical dependency: number of 2D neighboring grains $\neq 6$ and large grain size distribution) [80]. The GB progressively moves toward its center of curvature while the bigger grains grow further to the detriment of the smaller ones, and ultimately the GB merge together. In nanomaterials, grain growth also proceeds through the **rotation of the grains/coherently scattering domains** within the grains, for the crystallographic planes of neighboring grains to be aligned, followed by the GB crystallization, as shown at the right of *Figure 1.36.a* [189]. Indeed, when the grains are small enough, the migration of GB all the way through the grain can require more energy than the combined movement of the reduced number of bulk atoms in the rotation mechanism [187, 190].

Starting from a unimodal grain/crystallite size distribution, coarsening can be divided in two types, normal and abnormal (or exaggerated), depending on the final grain size distribution, as illustrated in *Figure 1.36.b*. For **normal grain growth**, the grain size has increased, but the distribution is still **unimodal**, while **abnormal grain growth** leads to **bimodal distribution** with microstructure consisting on few large grains grown unusually quickly in a matrix of fine grains with slow growth rate [184]. Abnormal grain growth is considered to be effective when the second grain size mode is higher than 2 times the median diameter GS_{50}. It is an undesired phenomenon leading to heterogeneous properties, and often associated with intragranular pores in the large grains due to the high local velocity of GB migration that cannot be reached by the pores. The factors leading to abnormal growth are *i)* impurities/second-phases in high content, *ii)* high anisotropy in interfacial energy, *iii)* high material inequilibrium [184].

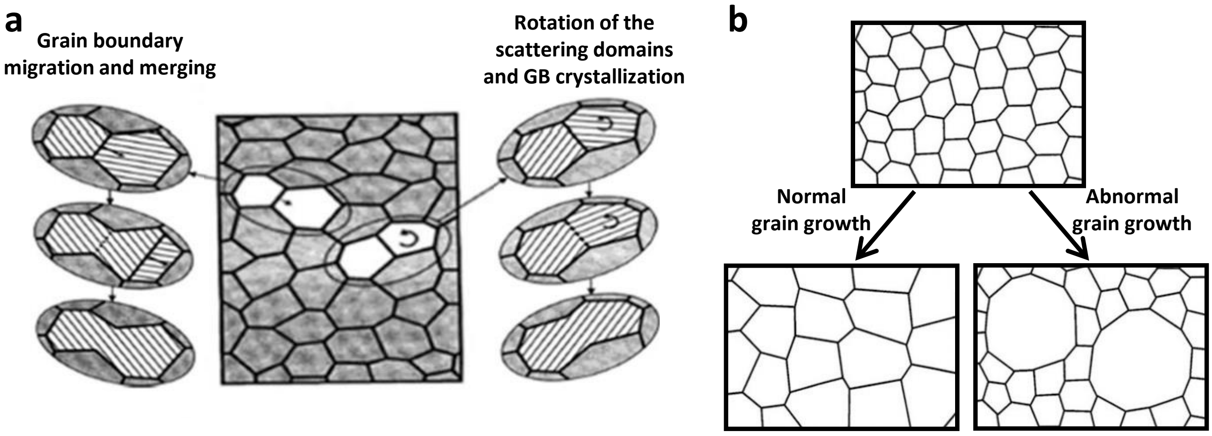

Figure 1.36: Schemes of a) grain growth mechanisms through (left) boundary migration and merging and (right) rotation of the coherently scattering domain, and of b) normal and abnormal grain growth [189]

iii. Precursor powder and green body features effect on the sintering behavior

The **first determining parameter** on the sintering and overall on the properties of the sintered material is the **precursor powder** which is used, and the green body formed prior to the thermal sintering. The ability of a powder to be sintered, comparatively to other powders of the same compound, is called the sinterability. However important, the development of an optimized sintering approach is not the key to reach desired properties, and even the most advanced techniques cannot provide state-of-the-art materials without selection of the appropriate raw powder and subsequent processing. Hence, fabrication of a dense material through sintering requires high knowledge of the powder characteristics.

The **physical features** are the most impacting on the **powder sinterability**, and *Figure 1.37* illustrates the difference of "quality" in the packing pattern of primary particles PP in secondary particles SP; the underlying logic is also valid for green body packing. An ideal packing state consists in a regular and dense organization of PP to maximize surface-surface contacts, and regularly shaped SP with surface state enabling similar level of contact between neighboring SP and neighboring PP. However, it is only possible to approach such a packing state in practice, and a good processing leads to low intraparticular porosity whereas poor processing will provide high intraparticular porosity and complex PP shapes. In any case, aggregation ("hard agglomeration") must be avoided due to its highly deleterious effect on densification, while agglomeration is more easily accommodated during the green body processing or the sintering.

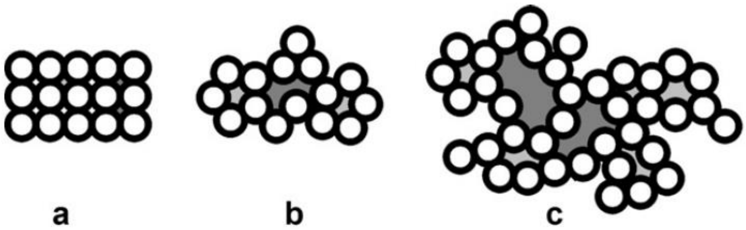

Figure 1.37: Schematic representation of the primary particles packing pattern in a secondary particle/green body. a) Ideal state, b) low intraparticular porosity state (optimized processing), c) high intraparticular porosity state (poor processing) [12]

The PP and SP size of the powder has a high influence on the kinetic of the sintering, which is well explained by **Herring's similarity/scaling law** (*Equation 1.26*). This law considers the sintering of two powders with particles of similar shapes but different sizes r_1 and r_2, under the same experimental conditions and through the same mechanism, to reach the same degree of sintering (ratio of the neck radius over the particle radius) [191]. The respective required sintering times t_1 and t_2 are related as:

$$\frac{t_1}{t_2} = \left(\frac{r_1}{r_2}\right)^m \qquad \text{Equation 1.26}$$

where m is the scaling law exponent, similar to the grain growth exponent n in *Equation 1.20*.

The significant consequence of this law is that **reducing the particle size** allows sintering at either **lower temperature** ineffective for coarse powders, or for **reduced processing time** at similar temperatures. From *Equation 1.26*, it can be calculated that if $r_1 \geq 10.r_2$ and the sintering occurs by diffusive transport predominantly from the grain boundaries ($m = 4$), the processing time drastically decreases as $t_1 \geq 10000\ t_2$. Experimentally, it was shown by Andrievski [192] that decreasing nickel particles size from the macroscale (50 µm) to the microscale (5 µm) and further to the nanoscale (50 nm) allows reducing the onset temperature of sintering and the full densification temperature by several hundreds of degrees (*Figure 1.38*).

Indeed, the interest of using nanopowders increases exponentially with m, which depends on the particle size and the sintering stage. For Al_2O_3 powders, the scaling law exponent evolves through the sintering such as in the early stage, $m > 4$ due to interface reactions helping the sintering process, then the exponent drops to $m < 3.5$ at the beginning of the intermediate stage and is expected to reach 3 before the final stage [193].

The particle shape and size distribution are important too: to reach high density with limited coarsening, ideal powders exhibit spherical, fine and monodisperse particles [80]. Interestingly, flat surfaces (platelets, cubes) may allow better packing, but reduce the sintering driving forces due to their lack of curvature [187].

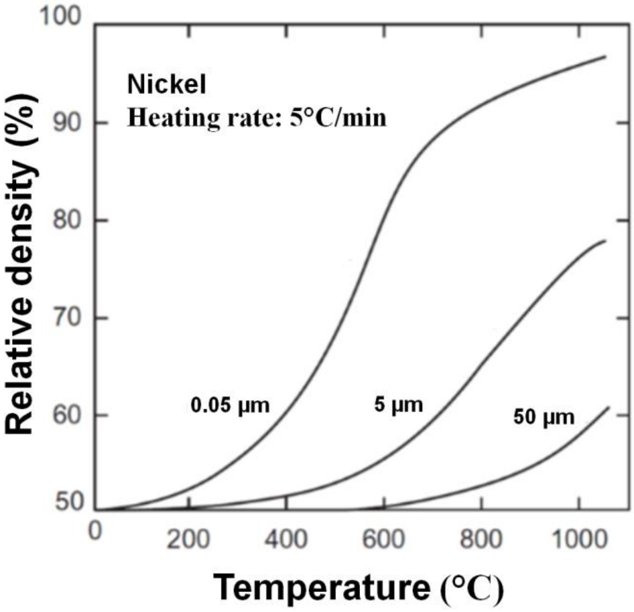

Figure 1.38: Influence of the particle size, from nanoscale to macroscale, on the sinterability for a Nickel powder [192]

Finally, the **green body formation** and its microstructure are crucial as well, and depend on both the powder features and the formation technique. Briefly, regardless of the technique used, reaching a high green density helps with the sintering but achieving high uniformity in the green body microstructure is more important in order to get homogeneous sintering behavior and sintered microstructure. One of the major causes for non-uniform green microstructure is the result of inter- versus intraparticular porosity, because SP have an internal porosity depending on the PP packing (*Figure 1.37*), while a second level of porosity between SP is introduced by their packing during the green body formation. If the two level of porosity are too different (size, shape and distribution), so will be the local sinterability. For instance, higher packing density within SP results in faster local sintering, and the original PP tend to coalesce together leading to the initial SP becoming the new effective PP prior to sensible densification. Hence, the practical sintering occurs between the initial SP, and the benefit of having small initial PP is lost. The key to efficient green body processing is to obtain **microstructural uniformity**, in which inter- and intraparticular porosities are similar.

3. The sintering of transparent $MgAl_2O_4$

In recent years, transparent polycrystalline ceramics have engendered increasing interest and efforts into their fabrication owing to the synergy of their optical properties and high physical strength, making them ideal for protective window applications in harsh environments. $MgAl_2O_4$ is certainly one of the most representative candidates in the literature, along with the related α-Al_2O_3. Therefore, in the past decades the sintering technology has been extensively and systematically studied for the preparation of MAS ceramics.

i. The different sintering approaches

As a hard-to-sinter ceramic, MAS sintering has been extensively studied using various technologies. Densification of transparent $MgAl_2O_4$ ceramics by simple thermal pressureless sintering (PLS) with heating rate of 1-10°C/min was of course attempted from early studies, but neither long firing at high temperatures above 1800°C nor atmosphere/vacuum were sufficient to reach transparency [194]. Recently, the microwave sintering (MWS) has emerged as a promising technique, but the unconventional heating relies on suitable electrical properties not possessed by MAS, which is in practice heated *via* thermal radiation from susceptor, and specimens densities do not exceed 95% [195]. Such densification states are far below the requirements for transparent ceramics, and they can only be considered as such for refractories/catalytic applications at the moment.

The basic principle for **fabricating polycrystalline MAS** is to **associate thermal and pressure effects** during the sintering. Thus, the existing techniques are differentiated by the means and ways applied to heat and to compress the powders. The most popular methods to produce MAS ceramics dense enough to be transparent, or promising enough to expect very good results in the next years are briefly presented hereafter. Since in most of these techniques the powder is contained in a mold for pressure to be applied, a casting step prior to the sintering is rarely required, as the raw powder can be used directly. However, depending on the method, green bodies are more or less frequently performed anyway to ensure microstructural uniformity.

The **hot pressing (HP)** is a process allowing the sintering at high temperature up to 2200°C in a furnace under vacuum or inert atmosphere with an hydraulic ram actuator system providing moderate uniaxial applied load up to 10 tons (250 tons for industrial apparatuses), leading to the compaction of the powder/green body placed in a mold, generally in graphite. HP has been used for MAS sintering since the 1970s, when Hamano *et al.*[196] first fabricated fully-dense spinel ceramics through reactive HP of a stoichiometric $MgO\text{-}Al_2O_3$ mixture at 1300-1400°C for 1 h under 32 MPa. The produced samples exhibited fine microstructures with GS $\approx$ 1-2 µm and promising translucency of ~40% at 500 nm (1.2 mm thick). The apparatuses have been improved in the following decades and the sintering conditions have been optimized, and $MgAl_2O_4$ ceramics with similar GS and better transparency (RIT > 60% at 500 nm, 1 mm thick) have been prepared from commercial MAS nanopowders since then [197].

The **hot isostatic pressing (HIP)** process is based on the same principle as the HP sintering, and relies on the same heating method. However, HP and HIP are distinguished by the pressure patterns: in the latter case, the load (maximum 400 MPa) is applied on the sample by an inert pressurizing gas (Ar or He) to be isostatic, *i.e.* homogeneous in every direction. Although the technique allows direct processing of the powder (encapsulated in a flexible/ductile canister sealed under vacuum), for the fabrication of MAS ceramics, HIP has only been carried out as a second step on pre-sintered samples. The **pre-sintering** can be carried out *via* any method, as long as the state of close porosity is reached. The simplest pre-sintering technique is conventional PLS under air; Liu *et al.* [198] obtained high transparency > 80% in the range 400–1100 nm for 1.8 mm thick samples by PLS at 1500°C for 3 h followed by HIP at 1600°C for 1 h under 150 MPa. It is possible to obtain similar results with vacuum PLS which prevents gas entrapment in the pores [199], or

MWS to reach high density with shorter processing at lower temperature [200]. Pre-sintering by HP has been long studied and is probably the most used procedure [78]. Recently, a new approach based on a combination of spark plasma sintering (SPS, developed below) and HIP has been used by Cohen *et al.* to increase the sample thickness up to 8 mm [201]; nonetheless, the processing is long and expensive, limiting its appeal.

At the present time, HP and HIP approaches are the most reliable in fabricating large size MAS ceramics with demanded optical transparency, and they have been used for military and industrial applications since the 1990s (transparent armor, IR-transparent windows for missile launchers and transparent domes for IR-seeking missiles, watch windows…) [11]. However, these processes are slow (usually one day per batch, more for two-step processing) and require rather high temperatures; hence they are not ideal for the fabrication of nanostructured ceramics, as optimized sintering generally leads to GS ≥ ~1 µm.

In order to perform fast sintering and have better control over the microstructure, some processes using electric current to provide rapid heating have been developed and are known as **field assisted sintering techniques** (FAST). Among them, **spark plasma sintering (SPS)** is certainly the most used and promising. This method is used in the experimental sintering chapter of this work, and it is further described in *Chapter 1.IV.3.ii*. Briefly, as in HP processing, a uniaxial pressure (up to 1GPa) is applied on the powder in a conductive die, but in SPS a pulsed direct current flows through the die/sample to generate the heat by Joules effect, thus high heating rates ≥ 100°C/min can be achieved. The electric field may also have an influence on the sintering mechanisms.

New sintering processes are constantly under development, and even if they are not used/able to produce transparent MAS yet, some of the most innovative ones must be considered as promising alternatives. Translucent MAS were fabricated *via* a **moldless pressure-assisted microwave sintering** (PAMWS) with load of 30 MPa at 1150°C for 8 min, after a prior low temperature PLS consolidation [202]. This adaptation of MWS allows very fast sintering in a simple and low-cost set-up, with no risk of sample contamination, and adaptations for using a mold could allow higher pressure, whereupon state of the art results would be reachable. One of the most important recent sintering advances is the **cold sintering process** (CSP), in which the powder is sintered with a minority liquid phase in a non-hermetic die, for the liquid to act as a metastable transient phase which evaporation enhances the sintering [203]. For the liquid not to evaporate before the actual sintering, high pressure (≥ 100 MPa) is applied for a temperature never exceeding ~500°C. The full densification of ceramics through the process is enabled at lower temperature, hence the name of the process. The technique has been extended to the use of any compound decomposed and at least partially evacuated as a gas during the sintering. In this manner, ferrite spinels were sintered in water at 300°C with addition of chelate complexes [204]. Very recently, $Al(OH)_3 \cdot xH_2O$ was sinter at 400°C through decomposition into translucent nanograined γ-AlOOH, then annealed into dense γ-Al_2O_3 for the first time [205].

ii. The Spark Plasma Sintering (SPS) technique: an overview

As mentioned above, **spark plasma sintering (SPS)** is a process involving the fast consolidation of a powder *via* **combined effects of uniaxial pressing and high electric current**, the latter providing Joule heating. The process has been investigated since the 1900s, but it has mostly been developed from the late

1980s to improve the then-existing sintering techniques (HP and HIP), hence it is relatively new. *Figure 1.39* presents a schematic representation of the SPS apparatus principle. In a typical experiment, the raw powder is loaded into a graphite die lined with graphite foils to ensure good mechanical and electrical contacts. The mold is then placed inside the water-cooled SPS chamber in controlled atmosphere (vacuum, argon, air). Upper and lower punches allow pressure application, and also serve as electrodes to force the current through the die and/or sample. The punches position, temperature and pressure are recorded and regulated. The apparatus uses low voltage (< 10 V) to produce high pulsed direct current (up to 1-10 kA), enabling high heating rates > 100°C/min, with a maximum load of 50-250 kN. It is then possible to sinter at relatively low temperature within very short durations, providing high control over the microstructure [206].

The sintering results from three effects: **thermal, mechanical and electrical** [206]. As for every sintering technique, the diffusion mechanisms are thermally activated. In SPS processing, the **fast heating rates** often enhance the densification, while the **short duration** limit the coarsening, allowing producing nanostructured materials. The **applied pressure** permits first to increase the green density by rearranging the particles (T below activation of the diffusion), then to enhance the sintering through creep (high T, surface softening).

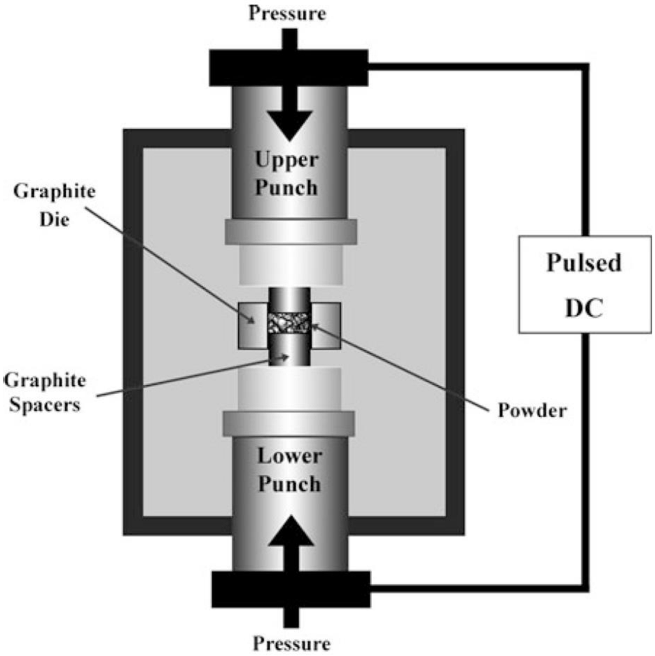

Figure 1.39: Schematic representation of the SPS apparatus principle [80]

On the other hand, the **electrical effects**, differentiated into **current and field effects**, highly depend on the powder’s conductivity relatively to the die’s one, as illustrated in *Figure 1.40* [207, 208]. For SPS of a conductive powder (*e.g.* Cu), the current flows through the compact and Joule heating occurs *in situ*. Because of the high initial porosity, it is assessed that a network of percolating current paths is formed, inducing hot-spots (higher current densities and temperatures up to ΔT > 1000°C) at contact points [209], then the heat is transmitted to the rest of the powder by thermal conduction. Once the porosity decreases, the percolation effect fades off for a more homogeneous heating mode. For insulating materials (*e.g.* Al_2O_3, MAS), the current (mostly) flows through the mold, with highest temperatures at the sample radial surface (*Figure 1.40.b*) [208]. Hence, the sample is radially heated *ex situ* through the mold/graphite foils. However, field effects, still not well understood, may occur in the process, affecting GB migration and matter transport [210]. The formation of sparks or plasma discharges between the particles induced by the current have been suggested by the inventors of the process, hence its misleading name. These phenomena would clean the particles surface of adsorbed substance and activate the sintering in the same time [211]. However, so far neither spark nor plasma could be indubitably detected, and the phenomenology of SPS is still under debate.

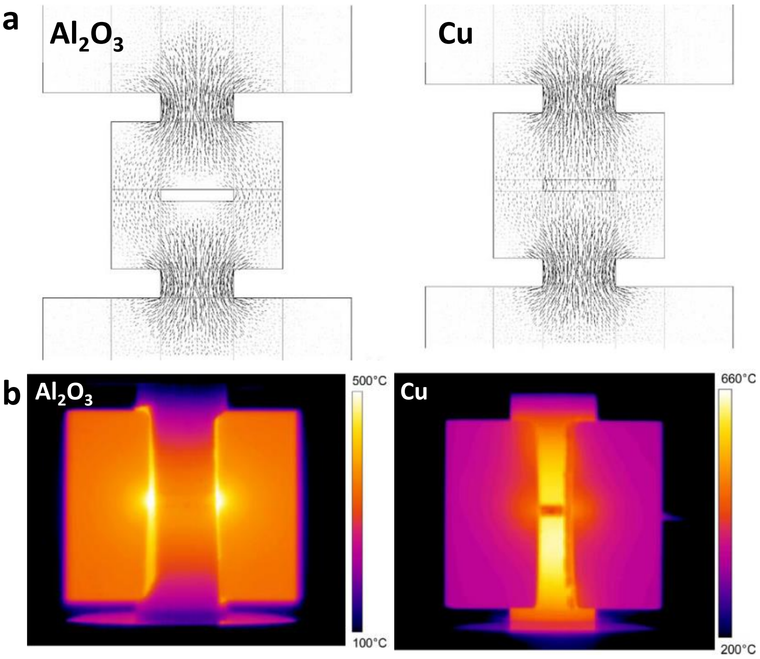

Figure 1.40: a) Modeling of SPS current distributions for Al_2O_3 and Cu [207] and b) experimental temperature distributions [208]

SPS allows obtaining unique microstructures with reduced processing costs and increased fabrication rates, but is mostly used to produce small discs at lab scale. However, complex shaping and up-scaling are investigated [212], making it even more appealing for industrial applications.

iii. Controlling the material properties: influence of the sintering conditions

With highly innovative and unconventional sintering techniques such as SPS, numerous parameters can be studied to better control the sintering mechanisms and final microstructure. SPS processing of transparent MAS has been popular since the mid-2000s, and the sintering conditions include the temperature, the heating rate, the applied pressure and loading schedule, the dwell time, the current percolation and the atmosphere.

a. The dwell temperature T_d

The **temperature T_d** hold during the sintering dwell is the most directly impacting parameter on sintering, and as such one of the first criterions for evaluating the efficiency of a sintering process. Hence, the range of T_d for which transparent MAS can be sintered was investigated since early studies; in that goal Morita *et al.* sintered a fine powder at 1275-1500°C, with applied pressure P = 80 MPa, heating rate α = 10°C/min, dwell time *t* = 20 min (*Figure 1.41*) [213]. Indeed, the grain size (GS) increased exponentially with T_d, exceeding 1 µm at 1400°C, while the porosity decreased linearly down to ~0.05%. However, the highest $T_{il\text{-}500\ nm}$ ~60% was reached for 1300-1325°C: T_d < 1300°C resulted in translucency due to low density (ρ ~99.5%), while T_d > 1300°C led to darkening of the materials and opacity at 1500°C (cf. *Chapter 1.IV.3.iv*).

More recently, the sinterability of MAS nanopowders has been investigated [214, 215] and the same coarsening tendency was noted, yet more pronounced due to higher reactivity. However, full densification and highest transparency was reached for the slightly lower T_d = 1275°C, while higher T_d led to a new porosity forming, likely due to abnormal grain growth, resulting in loss of optical properties [215].

Thus, MAS should be SPSed at **~1300°C** in order to reach high transparency while maintaining fine microstructure. In comparison, HIP processing is often performed at $T_d \geq 1600°C$ to reach high transparency.

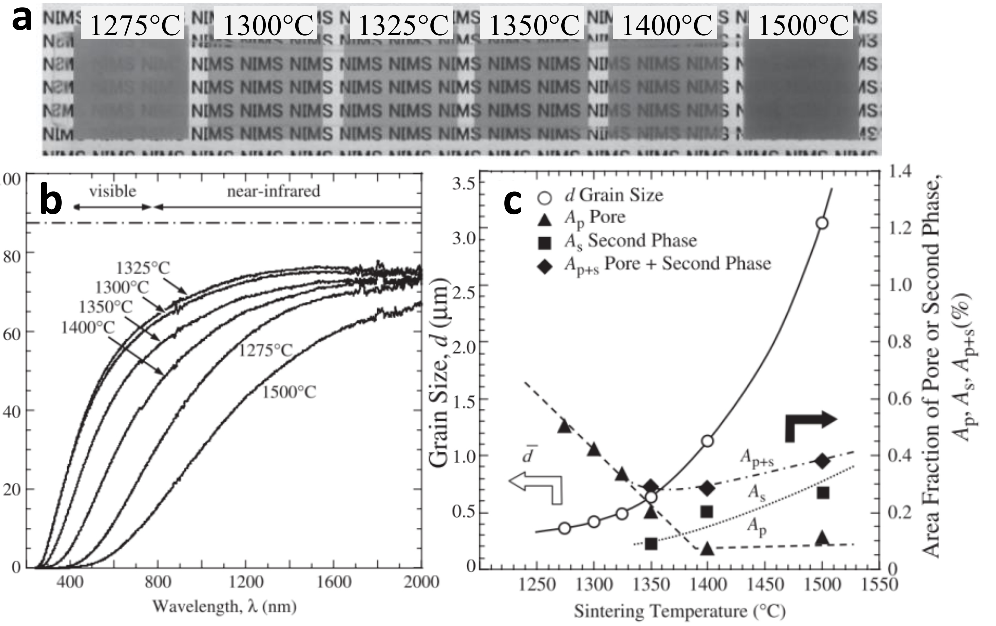

Figure 1.41: Effect of the sintering temperature T_d on MAS samples SPSed (20 min soak, 10°C/min heating rate): a) photographs, b) transmittance spectra and c) grain size and fractions of pores/second phase. Adapted from [213]

b. The heating rate α

One of the most promising features of SPS is the unrivalled **high heating rates** > 100°C/min operable. Indeed, high α can be used to bypass the early sintering stage, which provides the specimen with a neck-consolidated skeleton resistant to densification, due to insufficient time for the necks to form/enlarge, and directly reach higher T at which densification mechanisms are efficiently activated [213]. In this manner, the classic sintering kinetic and dynamic are overcame, and the latter mechanisms benefit from increased driving forces (high curvatures) to be more impactful, and finer microstructure can be obtained [11].

Unfortunately, it was shown that fast heating is **detrimental for the transparency** of ceramics SPSed at high T_d > 1000°C (Al_2O_3 [216, 217], $Y_3Al_2O_5$ and $Y_3Al_5O_{12}$ [218], $MgAl_2O_4$ [213, 219]). Excessive α lead to insufficient time for volatile species removal, and enhance the contrast of local differential sintering, increasing the importance of uniformity in the compacted powder to a critical point [11]. In terms of effect on the microstructure, high α hinder the grain growth for very short dwell [213]. However, large porosity may remain if the dwell is not long enough for a complete densification, while the pinning effect of pores on grain growth is less effective at high T, so substantial and abnormal growth would occur after a critical duration [216]. For SPS of MAS at 1300°C (20 min, 80 MPa), Morita *et al.* [219] observed no α-dependence for GS, while the porosity increased almost linearly from ~0% at 2°C/min to 1.4% at 100°C/min, resulting in a progressive transparency loss for α > 10°C/min (*Figure 1.42*). Moreover, the darkening effect was drastically more pronounced at high rates, and even translucency was not reached (cf. *Chapter 1.IV.3.iv*).

In order to benefit from fast heating anyway, SPS processing in several stages has been investigated. In [220], multiple oxides were sintered by **multi-stage SPS**, consisting in a 200°C/min heating with three 5 min dwells at 900°C, 1100°C and T_d, so the diffusion mechanisms could be separated. Higher densities and lower GS were reached than with single-stage SPS. A **two-step heating processing** has also been developed [79, 221, 222] and consists on a rapid heating (~100°C/min) until a **critical temperature T_c** in the early/intermediate sintering stage, at which α is decreased to ≤ 10°C/min. T_c has a high influence on the densification kinetic, and ultimately controls the darkening of the material (cf. *Chapter 1.IV.3.iv*) [222]. Finally, another approach has been investigated to process a single high heating rate stage, and rely on a two-step loading schedule [223, 224], which will be discussed in the paragraph examining the pressure effect.

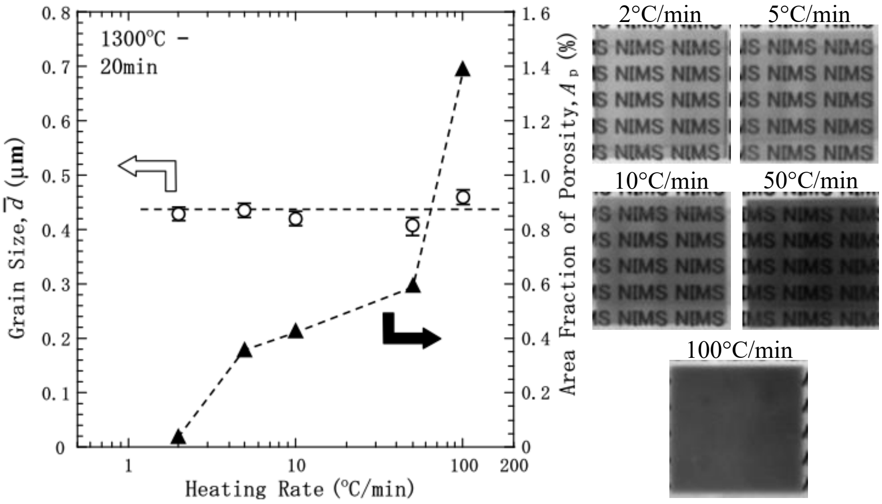

Figure 1.42: Influence of the heating rate on the grain size, porosity and appearance of MAS SPSed (1300°C, 20 min, 80 MPa) [219]

The effect of the **cooling rate** must be addressed as well, as fast cooling can cause residual stress and cracking, especially for ceramics [11]. Typically, the cooling rate is set at 100°C/min, while the pressure is progressively released simultaneously. A secondary dwell at $T \leq T_d - 150°C$ may also be applied for *in situ* stress-relief annealing, while the relatively low temperature does not affect the microstructure [221].

c. The dwell time t_d

In SPS, the **duration of the dwell at T_d** required for a full densification is drastically reduced compared to HP and HIP processing, due to the enhanced sintering mechanisms. Indeed, longer dwell time increases ρ and GS following a root dependence [225, 226], while the duration required to reach full density depends on T_d since higher temperatures increase the mass transport kinetic [225]. However, for high P > 100 MPa, a de-sintering phenomenon resulting in local opacity has been reported upon extended dwell time, initially from the sample's center and expanding toward the edges [227]. It was attributed to abnormal grain growth forming new pores subsequently to coarsening, through a creep process due to high temperature plasticity.

No proper study of the influence of t_d has been carried out for MAS; however, the widely used MAS nanopowder from Baikowski has been SPSed to transparency with t_d of 3 min (1300°C, 100 MPa) [224], 15 min (1200°C, 250 MPa) [228] or 30 min (1200°C, 63 MPa) [229]. Hence, depending on T_d and P, the dwell time should be optimized to reach high density while avoiding unnecessary grain growth and de-sintering.

d. The pressure P

Several advantages arise from **pressure application** in SPS processing. The first interest lies in the ***in situ* green body formation**, as the secondary particles not too strongly bonded are deformed or even broke, for a more efficient and uniform packing, so the importance of the agglomeration state in the powder is restrained. Then, once the diffusion is thermally activated, the applied pressure **modifies/enhances the densification mechanisms**. Even with low P, the small fraction of contact areas significantly amplifies P at the contact points, and the induced stress promotes rapid diffusion and GB formation. Combined with thermal softening of the particles surface, the stress concentration may result in early densification or grain rearrangement through **GB diffusion creep** (sliding/rotation of the grains) or **volume diffusion creep** (plastic deformation) [187]. For hard and crystalline ceramics such as MAS and with conventional SPS conditions ($P \leq 100$ MPa and $T \leq 1400$°C), Chaim *et al.* [230] advocated that plastic deformation is unlikely to occur, hence grain rearrangement and GB sliding are the principal mechanisms explaining the rapid densification kinetic.

In classic range of $P \leq 100$ MPa, increasing pressure allows full densification at greatly reduced T_d (for Al_2O_3: 1250°C at 50 MPa, 1150°C at 100 MPa) resulting in decreased GS [225]. Optimization of the loading schedule adds benefits to P. A **two-step pressure profile**, with the lowest possible $P_1 \leq 20$ MPa applied during the heating up and high P_2 applied at T_d ~1250°C has shown great profit: *i)* high $\alpha = 100$°C/min can be used without strong darkening effect, *ii)* finer microstructures are maintained [223, 224]. It was suggested that the high temperature loading enhances densification due to better sliding of the soften particles [231].

In order to enhance the pressure effects, several SPS devices allowing $P \geq 100$ MPa have been developed. The main interest for **high pressure sintering** is the greatly reduced T_d required to reach high density, particularly useful to consolidate hard-to-sinter materials (nitride [232], carbide [233], tungsten [234]…). In addition, lower T_d results in smaller GS, thus increased properties (hardness [19, 235, 236], radio-resistance [1]), and suppressed darkening effect [235, 237]. High P/low T also allow sintering dense metastable materials: unstable composites (Ta-WO_3 thermite mixture [238], Al-Cr-Fe reinforcements in Ti matrix [239]), metastable phases (transparent hydroxyapatite [18, 240], boehmite γ-Al_2O_3 [205]) low T allotropes [241, 242], amorphous material [243]), highly doped materials without segregation [244].

High pressure devices for SPS include cool SPS (CSPS), **high pressure SPS (HPSPS)** and deformable punch SPS (DPSPS). In CSPS, the graphite mold and punches are replaced by WC-Co ones holding up to ~600 MPa, but T is limited since WC-Co creeps for $T \geq$ ~400°C [245]. The first **HPSPS** device was based on a multi-die principle allowing P up to ~1GPa with $T > 1000$°C. Developed in 2006 by Anselmi-Tamburini *et al.* [246] and modified by several teams through the years [228, 247], the latest version consists on **graphite outer die/punches** enabling electrical conduction and Joule heating, and **SiC inner die/punches** for increased mechanical properties [228]. Later, Grasso *et al.* [248] proposed a simple and cheap configuration based on a carbon fiber composite mono-die, reducing the operating pressure to 400 MPa. More recently, Muche *et al.* developed the DPSPS ($P \leq 2$ GPa) [14, 249] based on a HPSPS device equipped with WC punches, and relying on their plastic deformation under combined P and T effects. The creep of the punches provides transversal forces promoting grain sliding, and transparent MAS was sintered under 2 GPa at 720°C for 4 min [14]. While promising, DPSPS appears as an expensive alternative due to the one-use WC punches.

HPSPS has been deeply investigated for the sintering of Al_2O_3 and MAS ceramics, especially by the research team of the Department of Materials Engineering from Ben-Gurion University of the Negev (Israel) [19, 228, 250, 251]. They showed that densification depends on the coupled **P-T_d conditions**, which can be plotted as in *Figure 1.43.a*: dense MAS is obtained for 250 MPa-1250°C and 1 GPa-1000°C [19]. With increasing P, the lower T_d reduces the diffusion mechanisms: the pores are smaller due to their hindered coalescence, so T_{il} increases in the low visible and UV for $\lambda \leq \sim 500$ nm (*Figure 1.43.b*), and GS decreases from 170 nm at 1200°C to 50 nm at 1000°C (*Figure 1.43.c*).

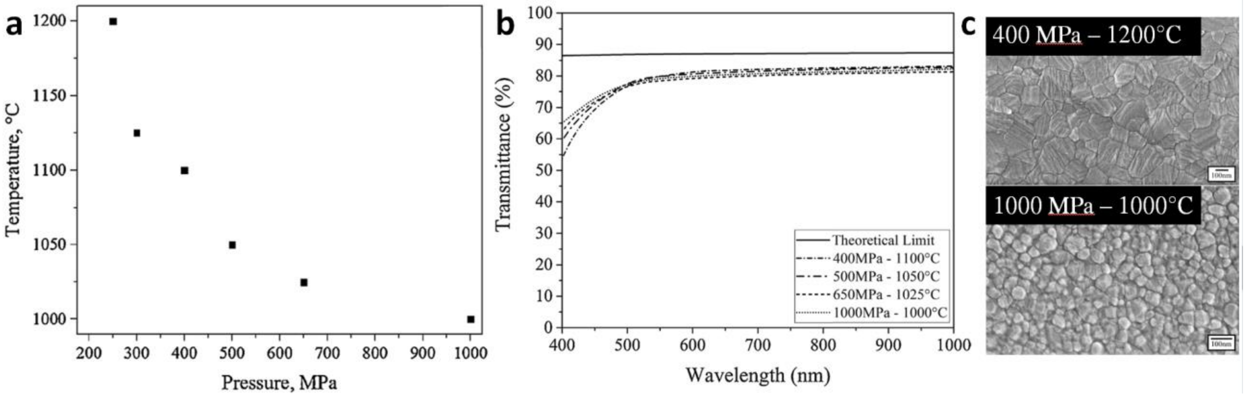

Figure 1.43: MAS ceramics densified by HPSPS: a) P-T_d conditions for full densification, b) transmittance spectra for different P-T_d conditions and c) SEM for 400 MPa-1200°C and 1000 MPa-1000°C samples. Adapted from [19]

e. The atmosphere

Different **sintering atmospheres** can be applied in the SPS chamber including air, vacuum, or various gas (Ar, N_2, O_2, He) static or in flux. However, vacuum (~10 Pa) is generally applied, as it provides a greater removal of volatile species [11]. Other atmospheres have no sensible benefits for MAS.

Reducing atmosphere such as vacuum, and more generally reducing environment, are particularly impactful for transparent oxide materials. Since $MgAl_2O_4$ is easily reduced, the oxygen partial pressure may play a role on its densification. It was indeed shown for ZnO that O^{2-} vacancies are preferentially formed in vacuum, and even more with increasing T_d [252]. In addition, the graphite from the die can slightly sublimate at low gas pressure, or reduce the oxide in the material (graphite reacts at $T > 600°C$ in presence of oxygen). This would result in the formation of C/CO gas *in situ*, hence a local reducing atmosphere, while intensive gas transport can take place between the die and the sample as long as open porosity exists [209]. Then, reduction of oxides or even precipitation of carbides/carbon in the sample can occur. The contamination by carbon (even in small amounts) and the formation of O^{2-} vacancies, both light-absorbing defects, greatly degrade the optical transmission though darkening (cf. *Chapter 1.IV.3.iv*).

f. The electrical effects

The use of an **electrical field/current** is certainly the most particular feature in the FAST processing family, including SPS. However, for insulating materials, the electric current has been shown to flow mostly through the graphite mold and papyex resulting in an *ex situ* heating (*Figure 1.40*), and the low E-field (voltage < 10 V) applied in SPS may be insufficient for significant field effects to occur. In this case, no difference between SPS and HP processing of insulating ceramics should be observed. However, little attention has been paid to this matter in the FAST literature, except for a few investigations showing no or little influence of the DC current pulse-sequence on alumina microstructure [225, 231].

Nevertheless, for **ionic materials**, **E-field** (contacting or not contacting) might modify the sintering kinetic and mechanisms anyway *via* several mechanisms, such as polarization or electrotransport [80]. Indeed, if low fields are applied in SPS, the field strength can be locally dramatically amplified at contact points for dielectric materials exhibiting high polarization [80]. In ionic and mixed (ionic/electronic) conductors such as $MgAl_2O_4$ for T > 400°C [253], an **ionic current**, *i.e.* a flux of charged particles (ions, electrons or holes), can be developed through the material under E-field. The applied field can also enhance the GB mobility, or modify the solid state reactivity as it was demonstrated that an external field can hinder or enhance spinel formation depending on its direction [80].

The electrical effects have been especially exploited in **flash sintering (FS)** which is a technique relying on the application of high E-fields directly to the green body to force the current to flow through it, for the ceramic to experience a sudden densification within seconds/minutes during a flash event [245]. FS of MAS has been performed with onset temperature of 1408°C at 1000 V/cm, while lower field could not trigger the flash [254]. Preceding the flash, a **field-activated regime** was identified with an increase of conductivity due to Mg^{2+} and V_{Mg}^{2-} migration to the negative and positive electrodes, respectively, resulting in a gradual microstructure coarsening. The electric neutrality was maintained by V_O^{2+} formation. Same observations were made for FS of CeO_2 [255], but conduction occurred *via* O^{2-} migration from the cathode to the electrode through GB, resulting in graduated oxygen depletion toward the relatively porous cathode (*Figure 1.44.a*).

In polyphasic materials, it was reported that the current preferentially flows through the most conductive phase, thus **percolation paths of the current** can form [256]. These preferential paths may induce the formation of hot-spots, resulting in local melting and microstructural inhomogeneities (*Figure 1.44.b*) [257].

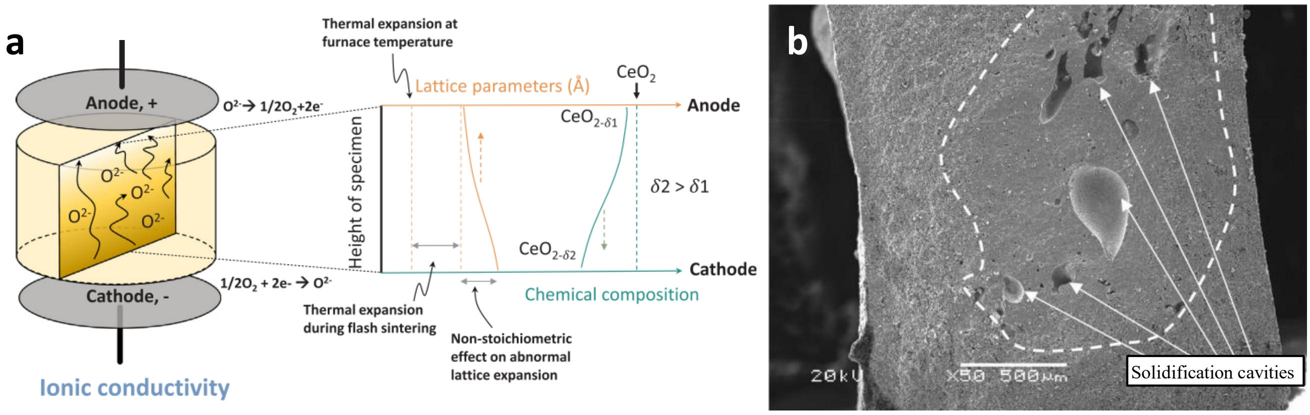

Figure 1.44: a) O^{2-} migration in CeO_2 from cathode to anode during FS inducing gradients of composition and cell constant [255]. *Hot-spot generated in celsian subjected to FS, with some shrinkage cavities due to local melting* [257]

As SPS processing relies in much smaller E-field and higher current, phenomena occurring in FS cannot be expected to occur at the same scale/importance. Nevertheless, several studies hinted that electric effects are impactful as well in SPS. A recent work demonstrated a non-negligible role of current/field effect during SPS of oxides, as ZnO was sintered to the same density but with GS divided by two when the powder was insulated from the die by Al_2O_3 layers [252]. Moreover, it was calculated that under specific T/P conditions, a fraction of the total DC current could percolate through the sample even for insulating material [258].

Then, it was assessed that **dielectric discharge** and **plasma** may occur locally until close-packed state is reached for specific chemical composition (LiF [259] and YAG [260]). Such claims have been made for conductive materials as well, resulting in hot-spots and local melting [261]. However, other works concluded that SPS voltage < 10 V is about one order of magnitude below required conditions to generate plasma [262].

iv. The darkening phenomenon issue

One of the main drawbacks of SPS especially for the fabrication of transparent materials is the **darkening effect** already mentioned, occurring for sintering at T_d > ~1000°C. In early works, the discoloration was thought to be mostly dependent on the heating rate, and transparent materials were SPSed with $\alpha \leq 10$°C/min. However, it was soon shown that α up to 100°C/min could lead to limited darkening with loading at T ~1250°C [231]. The darkening effect has been attributed to **carbon contamination** from the die (absorption from visible to IR) and **intrinsic defects** (absorption at low wavelength, mainly UV) [50].

Recently, the effect of a **critical temperature T_c** on the darkening of MAS was studied through a two-step heating schedule, with α = 100°C/min up to T_c then α = 2.5°C/min up to T_d (*Figure 1.45.a*) [222]. For T_c > 1150°C, a discoloration caused by carbon contamination was observed, stronger as T_c increased. During the heating stage, the graphite vaporizes into carbonaceous gas which penetrates into the open porosity, and is entrapped within the pores when they close [50]. It is favored by high α, as the pores stay open at higher T (*Figure 1.45.b*), but independent of T_d since only the pore-closure temperature matters [49]. In the latter sintering stage, the pores shrink and the gas within is pressurized from SPS vacuum (~10 Pa) to hydrostatic pressure equaling P, provoking the volatile species to precipitate as glassy carbon or graphite [222]. Interestingly, the discoloration occurs only in the center of the samples while their edges are pristine, which is attributed to a locally higher temperature allowing the precipitation. The contamination can be avoided by isolating the powder from the mold using Pt [263] or Mo foil [264] instead of the standard graphite foil.

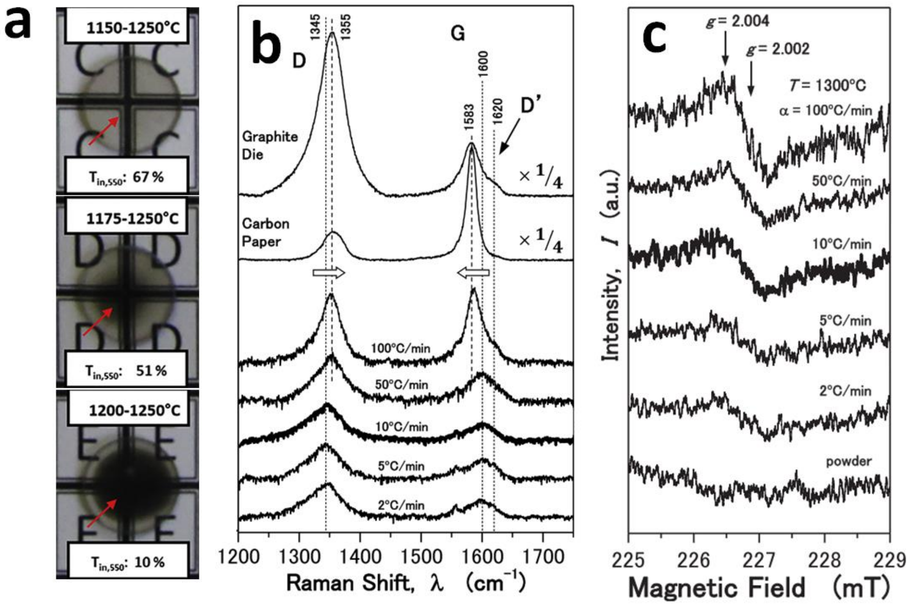

Figure 1.45: a) Photographs of MAS produced with 100°C/min up to T_c then 2.5°C/min up to 1250°C [222]. *Heating rate dependent b) Raman spectra of graphite signature [49] and c) ESR spectra in the F^+/V centers range for MAS SPSed at 1300°C, 20 min [49].*

The other cause reported for darkening is the **formation of intrinsic defects**, and especially **oxygen vacancies**. Their formation is favored during the intermediate sintering stage for T ~1150°C due to plastic deformations in the material, and further enhanced for high heating rate due to higher densification rate (*Figure 1.45.c*) [49]. In the latter sintering stage, the diffusion mechanisms are activated and the defects are partially annealed. Since the SPS atmosphere is reductive, the formation of oxygen vacancies in high concentration is favored. Indeed, severe reduction of $(Ni,Zn)Fe_2O_4$ during SPS resulted in precipitation of metallic Ni [265]. In addition, the formation of intrinsic defects in oxides including MAS has been shown to be provoked due to electrical effects during flash sintering [254, 257], as a partial reduction mechanism in O^{2-} conductors induces an oxygen vacancy V_O^{2+} (F^{2+}-center) current toward the cathode. There, they trap electrons from the electric current to get to the discharged state V_O (F-center), and an associated darkening referred to as "electrochemical blackening" is observed [257]. The lower DC current used in SPS processing may lead to a similar phenomenon, for which no evidence has been provided yet. As a consequence, strong darkening may result in MAS [254]. The intrinsic defects introduced during the sintering can be annealed with subsequent heat treatment in air. However, the radio-resistance of MAS may benefit from these [4].

v. Improvement of the sinterability and ceramic properties

The optimization of the sintering conditions in SPS is not sufficient to consolidate a material with controlled microstructure and properties, and several other parameters have to be considered.

a. Choice of the powder

As mentioned before, the **raw powder** to be sintered is the **first determining factor** for the properties of the final ceramic. Comparing the sinterability and ceramic properties of different powders helps understanding the optimal powder features for the fabrication of transparent and nanostructured MAS ceramics. Both commercially available and in-lab synthesized powders have been used in this effort, with different features arising from their synthesis route and conditions.

Commercial powders are often used for the fabrication of transparent fine-grained MAS ceramics. The most widely sintered ones in literature are produced by **Baikowski** (S25CR and S30CR, France) [195, 197, 228, 266] and **Taimei** (TSP-15 and TSP-20, Japan) [213, 267–269]. The Baikowski powders are processed by thermal decomposition of sulfates, and exhibit high residual sulfur content (300 ppm for S25CR and 600 ppm for S30CR) as main impurity. The crystallite size is ~70 nm, and the particle size is ~200 nm for both powders. A comparative SPS study showed that S30CR fully densify at slightly lower T_d, but its higher sulfur content results in a yellow tint [266]. The Taimei products are synthesized from thermal decomposition of ammonium carbonates, which induces less impurities with a slightly smaller particle size, but a doubled crystallite size [76]. Due to the peculiar features of both powders, Taimei precursors result in green bodies with fewer and smaller pores, but the smaller CS of Baikowski provides much higher sinterability [269]. Hence, while both powders have been used to produce transparent materials, Baikowski-based ceramics are reported to exhibit higher RIT with fewer opacifying macroscopic flaws [76].

Reactive sintering from Al_2O_3-MgO mixtures has also been investigated, to beneficiate from enhanced driving forces. As a general rule, reactive sintering of $MgAl_2O_4$ can provide translucent/transparent ceramics with dense, fine and homogeneous microstructures, but the results do not compete with non-reactive sintering. In this manner, translucent ceramics with homogeneous microstructures (GS ~1-2 µm) were made by HP of a pre-reacted mixture at 1300°C-1400°C for 1 h under 32 MPa [196], and transparent Al-rich MAS with marked abnormal coarsening were fabricated by reactive pre-PLS and HIP, both steps at 1500°C for 3 h [40, 270]. However, short processing as for SPS leads to fully opaque coarse-grained specimens [271, 272].

Finally, only few studies investigated **in-lab synthesized powders** sintering. Sokol *et al.* [250] synthesized MAS crystallites of 12 nm through a nitrate combustion route, which after HPSPS resulted in highly transparent ceramics with GS as low as 17 nm. Muche *et al*. synthesized 3.6 nm MAS crystallites *via* a simple reverse strike coprecipitation route, and subsequently consolidated the powder through DPSPS into ceramics with GS of 8.0 nm with very good optical properties [249]. In [272], an amorphous $MgAl_2O_4$-based powder was partially crystallized to MAS at low temperature calcination and further crystallized during SPS, resulting in quite promising relatively transparent specimen with GS ~500 nm.

Hence, the powder features providing highest sinterability/ceramic properties are *i)* a crystallite size as small as possible, even with low crystallinity, *ii)* a low agglomeration state and *iii)* a low impurity level.

b. Pre-processing: deagglomeration, comminution, granulation, shaping and annealing

Raw powders do not always have ideal microstructural features for good sinterability, thus it can be improved *via* several techniques leading to enhanced ceramics properties. The **pre-processing** of the powder can include one or several steps among deagglomeration, comminution, granulation, shaping and annealing, performed on either dry or wet powder. In the latter case, depending on the solvent, the solid loading ϕ and the resulting viscosity, a differentiation can be made between suspensions, slurries, pastes or moistened powders, for viscosity behavior increasing toward the dry state. The optimal state depends on the raw powder and pre-processing, but **slurries** are often used, with eventual addition of dispersant (*e.g.* carboxylic acid-based Dolapix CE64 [273], ammonium polyacrylate-based Darvan 821A [269]) to optimize the viscosity.

The **deagglomeration** consists on the "gentle" dispersion of the particles, and has solely an effect on weakly bonded agglomerates. It can be carried out by stirring [201] or ultrasonication [222] in a liquid medium. In [274], Yang *et al.* investigated the preparation of Cu pastes with different media on the agglomeration state. Due to the high surface tension of ethylene glycol, it was found less likely to fill the gaps between primary particles, resulting in a reduced tendency to agglomerate, hence a better sinterability.

The **comminution** is a mechanical treatment aimed to break the agglomerates/aggregates in powders, and it can deeply impact densification through their refinement, while the morphology of the primary particles remains unchanged for hard materials (*Figure 1.46.a*). Classical techniques consist in **ball milling**, and the effectiveness depends on the grinding media (material and ball size), the ball-to-powder mass ratio (BPR), the milling speed, the duration and the powder wetness state. For MAS, ZrO_2 is typically used as grinding media, with small ball size down to 1 mm for better powder refinement [275], and dry powders have been found less effective [276] than highly loaded slurries for the increase of sinterability (*Figure 1.46.b*) [273].

The comminution can be **low-** or **high-energy processing**, the latter being more efficient to break aggregates [277] and activate reactivity/sinterability due to high degree of structural disorder [276, 278], but also favoring contamination from the grinding media abrasion [279]. In typical **low-energy treatments**, powders are mixed in a tumbler [279] or 3D mixer [277] at low speed (< 100 rpm) over extended time (≥ 24 h), with low BPR. **High-energy treatments** (attrition milling [269], tumbling ball milling [279], planetary ball milling [276]) relies instead on high BPR (up to 40 [278]) and high speed (up to 400 rpm [278]). The processing duration should be optimized depending on the other parameters: too short comminution only affects the large bundles and too long treatment provokes severe re-agglomeration, while appropriate duration produces greatly reduced and unimodal particle size (*Figure 1.46.c*) [273].

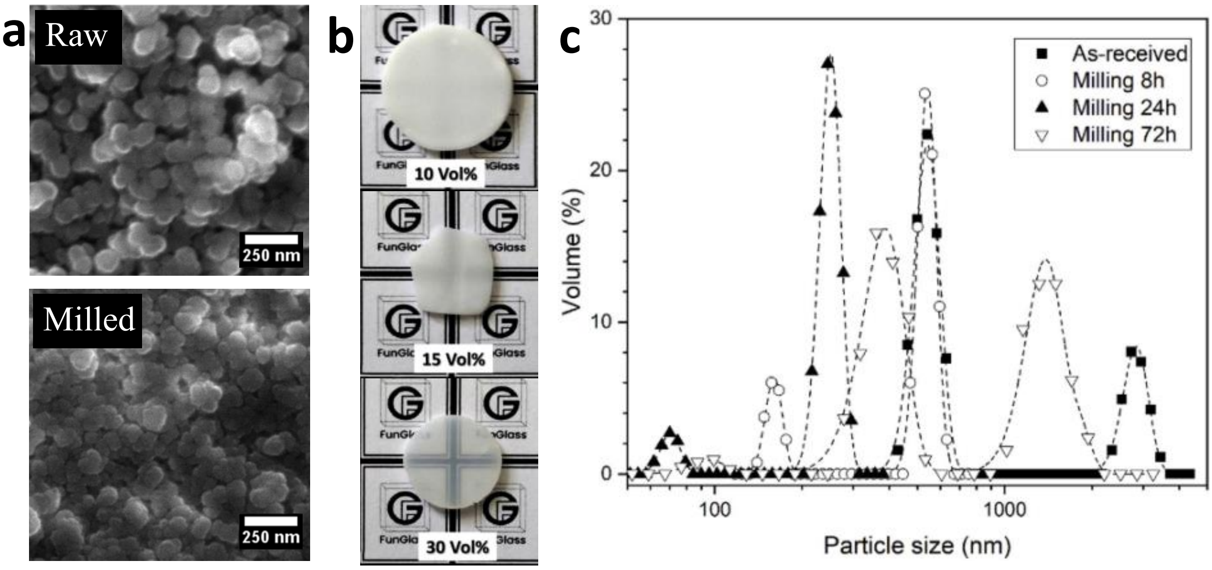

Figure 1.46: a) SEM of raw and milled powders [276], *b) photographs of air sintered (1550°C, 2 h) MAS from suspensions with different solid loading* [273] *and c) particle size distribution of MAS powders after ball milling for 8, 24 and 72 h* [273]

Unconventional comminution by microfluidization has shown excellent results for MAS compared to ball milling [280]. The process relies on Venturi effect: the pressurized slurry passes from a mm-wide tube through a micronic channel, resulting in uniform disintegration of agglomerates and unimodal nanoparticles.

When a nanopowder is pre-processed, especially in wet conditions, it is at least very hard to prevent its deleterious ulterior spontaneous re-agglomeration, hence a **granulation step** can be carried out by intended re-agglomeration into uniformed and controlled particle morphology. The granulation is often carried out during the drying process, in a rotary evaporator [276], a freeze dry apparatus [201, 281] or a spray dryer [282]. A binder can be added in low content (~0.1 wt%) for strengthening of the granulated particles [282].

The **forming/shaping step** consists in the preparation of a green body. Since the powder is in a mold and constantly pressed in SPS, a compact is formed *in situ* and forming is not required. However, it can be performed anyway to ensure green uniformity. The forming processes can be separated in two groups: the wet forming and the dry forming. In **wet forming** (slip casting [202, 280], its derivative gel casting [268, 283], pressure filtration forming [269]), the slurry is casted into a porous mold which dries the powder by capillarity, with the remaining moisture removed in furnace. Instead, **dry forming** consists in compacting the powder by uniaxial pressing [197] or cold isostatic pressing CIP (compaction in an elastomeric mold pressurized by a liquid/gas) [280]. Comparative studies showed that wet forming provides denser and more uniform green bodies, while dry pressing can annihilate all benefits from prior deagglomeration [280].

Finally, several studies have shown that an **annealing pre-sintering** at high $T < T_d$ is beneficial for transparency and microstructure homogeneity. Long treatments (≥ 50 h) homogenize the particles/crystallites size distribution *via* coalescence of the smallest ones, and thereafter prevent abnormal growth and residual porosity during sintering [284]. For SPS of MAS, powders annealed at 1100°C for 1 h [285] or at 1000°C for 2 h [286] also greatly improved the transparency by reducing the volatile species content. However, in [286] it is observed that best results are obtained for annealing at 900°C, higher temperature inducing pre-sintering.

c. Additives

Mixing **additives** with the powder prior to the sintering is a common way to modify the sinterability/ceramic properties. Depending on its concentration and solubility in the host material, the additive can integrate the host lattice within the grain (doping) or at grain boundary (segregating), remain as a second phase (precipitating) or react with the host (reacting) [287, 288]. Segregating and precipitating agents provide a layer surrounding the grains which hinders the GB mobility by pinning effect, and finer GS is maintained [288–290]. However, second-phase inclusions are often unsuitable for transparency [287, 291].

For MAS, many additives have been studied to impact the sinterability. **LiF** is the most popular sintering aid and forms a transient liquid phase around 850°C, facilitating the contact between MAS particles through lubrication and pore filling. Around 1200°C, it is then vaporized and removed from the material before pore closure [292]. In addition, the carbon contamination is suppressed by LiF addition, allegedly by cleansing effect *via* formation of volatile $(CF)_n$ [293]. However, it also favors rapid and abnormal grain growth [281, 294] and decomposition of MAS by formation of opaque $LiAlO_2$ precipitates [293]. MgF_2 has been used in the same idea without decomposition of the host [292]. SiO_2, $CaCO_3$ and TiO_2 also greatly promote the densification, allowing reduction of T_d by more than 200°C [295]. On the contrary, other additives act as **grain coarsening inhibitor**, and hinder densification as well. This is typically observed when adding trivalent elements, segregating at GB [287, 288, 291, 296, 297]. For FAST processes like SPS, the addition of an ionic conductor can induce electrical effect and drastic change on sintering mechanisms [298, 299].

Numerous additives are also used to **functionalize the properties of MAS**. Some dopants are well known for affecting the optical absorption/luminescence. For example, Co^{2+} and Ni^{2+} are considered for passive Q-switching saturable absorber application [12, 77, 85]. Optically active MAS ceramics doped with rare-earths are also investigated for photonic applications [291, 297, 300].

Regardless of the additive, the precursor microstructure and preparation prior to sintering are very important. A highly homogeneous distribution in the starting powder should be ensured by an appropriate mixing procedure, in order to obtain uniform densification and microstructure in bulk [289, 290, 293]. The amount of additive is also of primary importance, since generally the limit of solubility in MAS is very low (10^{-3}-10^{-1} at%) and higher concentration leads to heterogeneous microstructure [77, 85, 291, 293, 296, 300]. Fortunately SPS processing has been proven efficient to increase doping level higher than thermodynamic equilibrium solubility because of its very short duration [291, 297].

d. Post-sintering treatments

Few **post-SPS treatments** have been investigated to improve the properties, most often the transparency. The most used are annealing in air and HIP for further densification.

Post-annealing in air at temperature at least 100°C below T_d, to avoid further grain growth, is a popular method to reduce/suppress the sample discoloration by removing residual stress, lattice defects (oxygen vacancies and antisite defects) and carbon contamination. However, for the last point, annealing has been found particularly ineffective and even deleterious for the transparency in the case of MAS. While dark discoloration is removed after long treatment ≥ 20 h allowing diffusion of O^{2-} through the whole specimen thickness [301], the MAS samples become fully opaque [302] because the carbon phases in the volume of the sample transform into pressurized CO_2 gas due to the reaction with oxygen, then forming pores [53]. Ultimately, CO_2 can react with the oxide phase and form carbonate phases [301].

When the state of closed porosity has been reached by SPS, **further densification** can be attained by subsequent **HIP**. Cohen *et al.* [201] fabricated 4-8 mm thick samples by SPS at 1400°C, which exhibited cloudiness due to remaining pores. They were totally eliminated after a 10 h HIP treatment at 1800°C, and the samples appeared homogeneous and highly transparent (*Figure 1.47*). However, a coarse microstructure was obtained. In [226], translucent alumina with GS < 500 nm was obtained through SPS at 1150°C, 6 min (closed porosity with finest possible microstructure) followed by HIP at the same temperature.

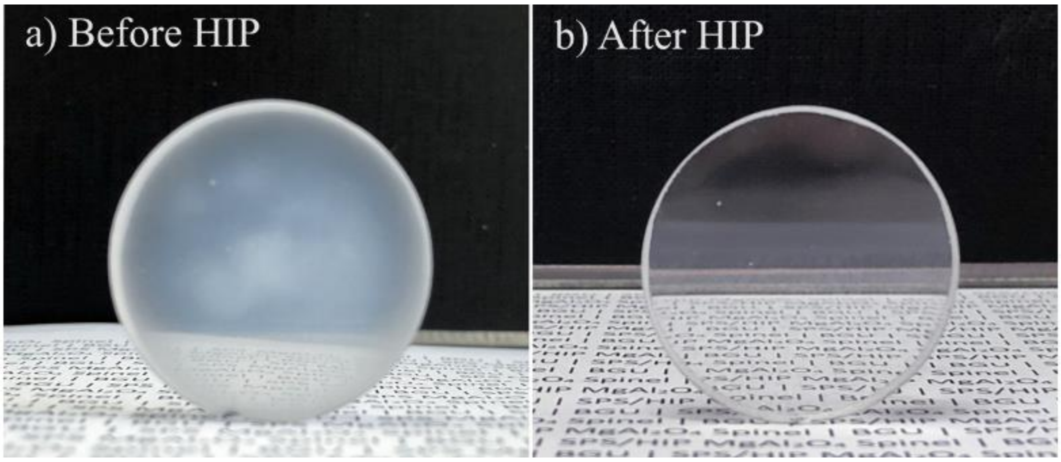

Figure 1.47: MAS ceramics (4 mm thick) after a) SPS at 1400°C and b) subsequent HIP at 1800°C for 10 h [201]

Chapter 2

Experimental techniques and materials

In this chapter, the different characterization techniques used in the experimental parts of this work will be briefly overviewed in a first part, then the experimental set-ups and materials used for the preparation of the samples will be presented together with the commercially available powders used in this thesis.

I. Characterization techniques

1. Powder specific characterizations

i. Thermal analysis

The thermal analysis of a material allows following its evolution through thermal treatment by precise measurement of the sample's mass, temperature or amount of heat required to increase its temperature, while comparing with a reference. It reveals the decomposition mechanism of the material, with temperature and kinetics of reactions, crystallizations, phase transitions and change of physical states.

Thermal differential and thermogravimetric (DT-TG) analysis has been carried out using a Labsys apparatus from SETARAM equipped with a S-type thermocouple (ambient-1600°C), under N_2 flow with a 10°C.min^{-1} heat-up. The analyzed mass of sample was in the range 25-100 mg, using alumina crucibles.

For the study of solid state reaction between commercial powders requiring more precise measurements, **differential scanning calorimetry** (DSC) analyses were carried out by Loïc PERRIERE (MAM, ICMPE, UPEC, France) on a Pegasus F1 apparatus from Netzsch. The measurements were carried out in the range ambient-1650°C, with a heat-up of 10°C.min^{-1} under Ar flow with samples' mass of about 40 mg in alumina crucibles.

ii. Size distribution of secondary particles

In order to investigate the influence of the comminution process on the commercial powders' size distribution of secondary particles, we carried out **dynamic light scattering** (DLS) measurements. The technique uses monochromatic light source, which goes through a highly diluted suspension of the powder sample in a solvent (water in our case) in a polystyrene cell. The scattered light is collected by a photomultiplier to measure the diffusion coefficient of the Brownian motion, and through data treatment of the auto-correlation function the hydrodynamic radius distribution is obtained.

We used a Zetasizer Nano-ZS equipment from Malvern Panalytical for classical 90° DLS measurements with the laser wavelength of 532 nm, and the standard data analysis method of cumulant (Z_{ave}). The apparatus allows the size analysis of materials from 0.6 nm to 6 µm. Prior to characterization, the powder suspensions were subjected to indirect probe sonication at 40 W for 5 min to break up the weakly bonded particle agglomerates and create stable dispersion with more uniform particles sizes.

iii. Infrared spectroscopy

The **infrared spectroscopy** in the mid-infrared region 4000-400 cm^{-1} is a technique used to obtain the infrared spectrum of absorption of a sample, allowing the study of the fundamental vibrations of its molecules bonds.

The mid-IR spectra were measured using a Nicolet iS10 Fourier-transform infrared (FTIR) spectrometer (ThermoFisher Scientific) with KBr as a carrier. The measurements were carried out by Zhengjie LIU (School of Chemistry and Chemical Engineering, Anhui University, China).

iv. X-ray photoelectron spectroscopy (XPS)

The **X-ray photoelectron spectroscopy** (XPS) is a surface-sensitive quantitative spectroscopic technique, based on the photoelectric effect (emission of electrons when a material is submitted to electromagnetic radiation, X-ray in this case). It allows identification and quantification of the elements at the surface of the material, as well as their biding states. The technique is generally probing to a depth of 10 nm within the material, as the signals detected deeper below the surface decrease exponentially.

XPS analyses were carried out by Zhengjie LIU (Anhui University, China), using the ESCALAB 250Xi system (ThermoFisher Scientific) equipped with monochromatic Al Kα source (1486.6 eV) for the excitation of photoelectrons, under a base pressure of 2.1 $\times 10^{-9}$ Torr, with hemispherical analyzer and source power of 150 W (15 kV × 10 mA). Survey scans with pass energy of 50 eV were performed twice, and narrow scans with a step of 0.05 eV and pass energy of 20 eV were performed for 20 times for precise analysis of the binding energy of specific elements. The C 1s line with a binding energy of 284.8 eV was used as reference to eliminate the charging effect with flood guns. The software XPSPEAK Version 4.1 was used for spectral fitting, with Smart background subtraction using the Gaussian and Lorentzian curve, with peaks shape assumed to be 80% Gaussian and 20% Lorentzian.

2. X-ray diffraction (XRD)

X-ray diffraction provides crystallographic information on the material, following Bragg's law:

$$\boldsymbol{2d\,sin\,\theta = n\,\lambda} \qquad \textit{Equation 2.1}$$

with d the inter-plane distance, θ the scattering angle, n the integer representing the order of diffraction peak and λ the X-ray wavelength. The XRD patterns of crystalline materials allow identification and quantification of the phases, and determination of the structural parameters (lattice parameters, crystallite sizes, residual stresses…).

In this work, XRD characterizations were carried out on several equipments, depending on availability. Most generally, the measurements were carried out on a diffractometer EQUINOX 1000 (INEL) with Co $K\alpha_1$ radiation source (λ = 1.7890 Å), in the range 5-110° 2θ (omega kept at 6°) for a minimal collection duration of 2 hours, in order to improve the signal-to-noise ratio. Alternatively, XRD patterns have been collected on a diffractometer EQUINOX 1000 (INEL) with Cu $K\alpha_1$ radiation source (λ = 1.5406 Å), all other measurement conditions being unchanged. Conversion from 2θ(Cu $K\alpha_1$) to 2θ(Co $K\alpha_1$) ranges has been performed using Bragg's law presented above, for comparison purpose. Lastly, the XRD analyses presented in the experimental part on synthesis *via* the liquid impregnation of nanofibrous alumina (*Chapter 3.III*) were carried out by Olivier ROULEAU (MAM, ICMPE, UPEC, France) on a D8 ADVANCE diffractometer (Bruker) with Cu-$K\alpha_1$ radiation source. All measurements in this study were collected with the same scanning time of 1 h. Sample preparation was the following: ceramic pellets were fixed on the sample holder, and powders were set into a small cuvette.

The phase identification from XRD patterns was carried out with the software Match! (Crystal Impact) using the Crystallography Open Database (COD).

For precise determination of the phase parameters from the XRD patterns, the data treatment was performed using the **Rietveld refinement** method which uses least squares approach to refine a theoretical line's properties (setup details, background, crystalline phase percentages, structural parameters, etc) until it matches the experimental pattern. Refinements were performed using the software MAUD (Materials Analysis Using Diffraction) developed by Luca Lutterotti *et al.* [303]. The most used COD phase files for Rietveld refinements were the following: spinel (#9007116, MgAl2O4); α-alumina corundum (#1010914, Al2O3); γ-alumina spinel (#1200015, Al2O3); periclase (#1000053, MgO).

3. Electronic microscopy

Scanning electron and **transmission electron microscopies** have been used to characterize the materials synthesized and used in this work. The micrographs were treated with software ImageJ for determination of crystallite/grain size (at least 100 grains measured) and inter-plane distance d.

i. Scanning electronic microscopy (SEM)

Scanning electron microscopy (SEM) produces images of a material by scanning the surface with a focused beam of electrons. The interactions of the primary electron beam with atoms in the specimen, producing various signals providing different informations about the sample's topography and composition, which can be analyzed separately.

In this work, two different SEM apparatuses were used depending on the signal analyzed. The FEG-SEM SUPRA 40VP (ZEISS) was used to obtain **secondary electron (SE)** and **backscattered electron (BSE)** micrographs, as well as to collect **electron backscattering diffraction (EBSD)** data, while **energy-dispersive X-ray spectroscopy (EDX)** analyses were carried out on Leica S440 (LEO) SEM:

- **SE imaging mode** was used to characterize powders, because it gives the best topographical and morphological information. The imaging was carried out at acceleration voltages of 3-5 kV in high vacuum, with a 30 µm diaphragm.
- **BSE imaging mode** was used to characterize the consolidated ceramics due to the best compositional contrast provided. Heavier elements backscatter more electrons than lighter elements because of their higher atomic number, and thus appear brighter. In addition, contrast of local crystalline directions in polycrystalline material is observed, so this detection provides information on the atomic weight as well as morphology. To achieve high enough contrast to differentiate crystalline grains, measurements were carried out at 15 kV, in low vacuum ~15 Pa, with a 60-120 µm diaphragm.
- **EBSD measurements** were carried out on relatively large area of ceramic samples for producing grain size and crystal orientation mapping, in order to investigate texture effect as well as locally inhomogeneous microstructure. Measurement conditions were identical to BSE's ones, except for a 70° tilted sample to allow the diffracted electrons to create a pattern, following Bragg's law. The general analysis of the EBSD data was conducted by using the commercial TSL OIM Analysis software.
- **EDX measurements** are based on ionizing the atoms of the specimen by the primary electron beam, generating holes in the core shells followed by electrons from outer shells filling these holes, thus emitting X-ray fluorescence lines. This mode allows elemental mapping and quantification.

ii. Transmission electronic microscopy (TEM)

Transmission electron microscopy (TEM) is a microscopy technique in which the image is formed from the primary electrons which are transmitted through a thin specimen, in comparison with SEM imaging.

In this work, two different TEM apparatuses have been used, depending on the analysis carried out. The JEM-2011 TEM (JEOL) was used for general characterizations of powders in bright-field mode with selected area electron diffraction (SAED) pattern. Imaging on Themis Z G3 TEM (ThermoFisher Scientific) were acquired at 80 kV by Eric GAUTRON (IMN, Nantes University, France) for powder analysis in EDX mode as well as for sintered ceramic analysis in scanning transmission electron microscopy in high-angular annular dark-field (STEM-HAADF) and four-dimensional STEM (4D-STEM) modes:

- in **bright-field mode**, the electrons directly transmitted through the sample form an image with dark particles on a bright background. **SAED** is used to determine the local crystalline nature of particles.
- **EDX measurements** allow elemental mapping and quantification, as indicated above for EDX in SEM; maps were acquired with 4 windowless silicon drift detectors (Super-X system).
- **STEM-HAADF mode** principle relies on the study of scattered electrons at high angles during interaction with atoms, for a very high image resolution with contrast on inclusions and defects; images were acquired with 20.7 mrad convergence angle and 33-197 mrad collection angles.
- in **4D-STEM mode**, a converged electron probe is rastered over sample in a 2D array, and a 2D diffraction pattern is imaged at each position, thus generating a 4D data cube. The 2D electron diffraction patterns were imaged with a OneView CMOS camera, and in order to avoid superimposition of the diffracted disks, convergence angle was lowered to 0.65 mrad; pixel size (1 nm) is almost the same as the probe size.

The analyzed powders where put in dilute suspension in ethanol prior to deposition on carbon film grids. For sintered ceramic sample analysis, a thin TEM lamella was prepared with a focalized ion beam (FIB Crossbeam 550L, Zeiss), then ion polished by Ar beam (PIPS 691, Gatan).

4. Gas pycnometry

Micromeritics AccuPyc II 1340 pycnometer equipped with a 3.5 cm^3 cell was used for all **density measurements**. The challenge in measuring density lies in accurate determination of the sample volume, the pycnometer uses inert gas displacement (in our set-up He) to do so.

A sample with known weight is enclosed into the instrument cell of known volume, then a known volume of gas is guided to the sample chamber and expanded into a second precision chamber as equilibrium is reached. Equilibrium will also be reached in comparison to the second chamber. The pressures measured while filling the sample chamber and later emptying it into the second chamber are then used to calculate the volume of the sample's solid phase, which is then divided by the sample mass to reach volumic mass ρ. For relative density d calculation, ρ is divided by theoretical volumic mass ρ_0 of the material phase. For $MgAl_2O_4$ spinel, theoretical volumic mass was taken to be 3.578 $g.cm^{-3}$ [280].

In order to increase the reliability of the characterization, each density was measured 40 times and the values were averaged.

5. Spectroscopic characterizations

i. *UV-visible optical transparency measurements*

The **UV-Vis spectroscopy** is the most important characterization techniques for the assessment of the quality of a material's optical transparency, and allows investigation of defects centers in the structure and microstructure.

The **in-line transmittances T** of the sintered ceramic samples were measured in the wavelength range 190-1100 nm, with a 1 nm step and an average scanning time of 0.1 s.nm^{-1}, using a UVmc1 spectrophotometer (SAFAS, Monaco). The sample was positioned at about 10 cm from the light source, and 1 cm from the detector. A 5 mm pinhole was placed between the light source and sample to narrow down the measurement area and suppress most of the scattered light, in order to get closer to real in-line transmittance. The **transmittance data were systematically normalized for a thickness of sample of 1 mm** using *Equation 1.13*.

ii. *Raman spectroscopy*

The **Raman spectroscopy** is a spectroscopic technique providing information about vibrational modes of the molecules in the sample. It is commonly used to provide a structural fingerprint for identification of crystallographic phases, as well as to investigate defects in the structure.

Raman spectra were obtained with a HR800 (HORIBA Jobin-Yvon) apparatus operating at 473 nm excitation wavelength, with an aperture confocal slit of 100 µm. Each measurement was carried out at room temperature, with recording time of 30 s and 10 accumulations.

iii. *Cathodoluminescence (CL) measurements*

Cathodoluminescence (CL) measurements were carried in collaboration with Eduard FELDBACH (Institute of Physics, University of Tartu, Estonia). The CL setup is equipped with a vacuum cryostat and two monochromators covering spectral range from NIR (~1700 nm) to VUV (~110 nm). Detailed description of the set-up can be found in [304]. Measurements were carried out at 5 K, after the deposition of a 3 nm platinum coating onto the sample to avoid surface charging. Alternatively, some CL imaging was performed at ambient temperature with a CLUE system (HORIBA Jobin-Yvon) using a 10 kV electron beam produced in a JEOL7001F FEG-SEM [305]. The samples were coated with a gold layer to avoid surface charging.

CL spectra of samples obtained with the same precursor powders were normalized with respect to the intensity of the Cr^{3+} peak expected to be constant through the process.

iv. *Photoluminescence (PL) measurements*

The **photoluminescence (PL) measurements** presented in this work have been carried out on two different setups, in collaboration with Eduard FELDBACH (University of Tartu, Estonia).

The PL and **PL excitation (PLE)** experiments carried out for the investigation of Ta^{5+} doping and He^{+} irradiation on MAS structure were carried out at the BL3B beamline [306] of UVSOR facility with synchrotron radiation excitation in the UV–Vis spectral range. The samples were mounted on the cold finger of a LHe flow type cryostat, which permitted stabilizing the sample temperature in the range between 300 and 8 K. The vacuum in the samples chamber was ~3 $\times 10^{-7}$ Pa. The measured PLE spectra were corrected on the detector sensitivity and optical line transmission.

The PL and PLE spectroscopy carried out for the investigation of the grain size on MAS ceramics were measured at the new P66 beamline at PETRA III synchrotron source. This beamline was relocated and refurbished from the old Supelumi beamline at DORIS synchrotron [307]. The PL analysis range was limited to 300 nm $\leq \lambda \leq$ 900 nm for this study.

v. Electron Paramagnetic Resonance (EPR) spectroscopy

The microscopic detectection and characterization of paramagnetic sites was performed using **electron paramagnetic resonance (EPR)** spectroscopy, carried out in collaboration with Guillaume LANG (LPEM, ESPCI Paris, PSL University, France) and Silvana MERCONE (GREMAN, Tours University, France).

The principle of the technique relies on the Zeeman effect described by the fundamental equation of EPR [308]:

$$\boldsymbol{\Delta E = h\nu = g\mu_B B} \qquad \textit{Equation 2.2}$$

with h = 6.626 $\times 10^{-34}$ $m^2.kg.s^{-1}$ the Planck constant, ν the microwave frequency, g the Landé g-factor characterizing the magnetic moment and angular momentum of magnetic centers, μ_B = 9.274 $\times 10^{-24}$ $J.T^{-1}$ the Bohr magneton and B the external magnetic field.

The EPR analyses were performed at room temperature using a conventional X-band (9.47 GHz) operating at 1.97 mW on a EMX spectrometer (Bruker) with a TE102 resonant cavity. Measurements were carried out with a modulation frequency of 90 kHz, a modulation of 3 G and an attenuation of 20 dB. Powder samples (~0.0050g) were inserted in glass tubes, while solid samples (~2 × 3 × 1 mm, ~0.0100g) were glued to PTFE rods with precise positioning, allowing study with angular dependency using a goniometer.

6. He^+ irradiation

In order to evaluate structural damage induced by ionized irradiation, **He^+ bombarding** was performed on selected samples. The irradiation was performed on the KIIA 500 kV ion implanter in the Accelerator Lab of Helsinki University in collaboration with Eduard FELDBACH (University of Tartu, Estonia) and Hugo MANDAR (University of Tartu, Estonia). The spinel samples were irradiated with a 150 keV He^+ ions beam for the total dose of 10^{17} $ions.cm^{-2}$, corresponding to about 0.5 dpa.

II. Experimental setups and materials for the preparation of the samples

1. Synthesis processes

i. Polyol-mediated synthesis setup

The reference conditions for the synthesis *via* polyol-mediated route were based on previous studies reporting the synthesis of spinel oxide compounds other than magnesium aluminate spinel [165, 166, 181]. The setup is shown in *Figure 2.1*.

The conditions (precursor salts, temperature of synthesis, concentration, temperature of addition of the precursors, solvent) will be investigated in *Chapter 3.I*. Briefly, in **reference conditions**, 0.0333 M of $MgCl_2 \cdot 6H_2O$, 0.0667 M of $AlCl_3 \cdot 6H_2O$ and 0.267 M of $NaCH_3COO$ were dissolved in 200 ml of EG, then the blend was heated under constant mechanical stirring (500 rpm) at 185°C for 2 h. After cooling to room temperature, the received mixture was centrifuged and washed several times with deionized water to remove physisorbed EG, then once by acetone and left to dry in air at temperature $\leq$ 100°C.

Afterward, spinel oxide materials were obtained through thermal treatment in a muffle furnace at temperature of 800°C and above.

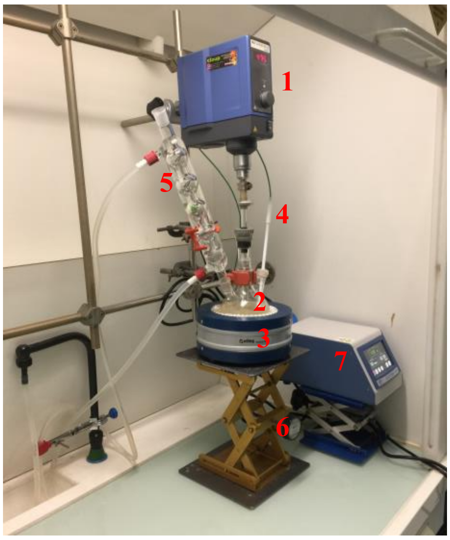

1: mechanical stirrer

2: 500 ml round-bottom flask

3: flask heater

4: thermocoulpe type K

5: condenser (with water)

6: platform

7: thermostat

Figure 2.1: Experimental setup of the synthesis by polyol route within a fume hood

ii. Growth of the alumina monolith and impregnation synthesis route setup

The **growth of alumina monoliths** in this work was carried out according to the patent [146] and article [17] published by CEA-CNRS and LSPM-CNRS. However, there is a new, more stable climate chamber (Weiss GmbH environmental engineering simulation systems, WK3-180) in use for the process.

Firstly, the climate chamber is set up with the **controlled atmosphere of 25°C and 80% humidity**, and the cryostat and water flow for the cooling system is set at 23°C. The cooling radiator is kept 2°C lower than the set chamber temperature to further aid the cooling of aluminum plates oxidizing *via* exothermic reaction.

Afterward, we proceed to the preparation of the aluminum plates for controlled oxidation. Firstly, 1 mm thick 99.999% purity laminated aluminum plates (5 x 5 cm, Goodfellow) are cleaned with acetone to remove any organic contamination from the surface. Then, the aluminum plate is fixed to a glass tube by adhesive putty Patafix®, helping for positioning of the plate in parallel with the level of treatment solutions. Indeed, it is important to treat only a single side of the plate in order to effectively remove heat by the other, as the oxidation reaction of aluminum is highly exothermic. The adhesive exhibits good adhesion with the aluminum and glass, and can be easily peeled off without leaving adhesive on the plate.

The surface to be treated is firstly put into contact with a **10% NaOH solution** for 2 minutes to dissolve the thin Al_2O_3 layer protecting the metal (**depassivation**). Gas bubbles are observed on the plate as hydrogen gas is released through the oxidation reaction of Al by $(OH)^-$. After rinsing the treated surface with distilled water (without drying), it is put in contact with the **catalytic solution** formed by mixture of equal volumes of a **silver nitrate** (2 ×10^{-2} M in 2 M HNO_3) and **mercury nitrate solutions** (10^{-1} M in 2 M HNO_3). The acidic medium prevents the precipitation of mercury oxide. The duration of treatment is 3 minutes, during which a Ag^+-Hg^{2+} liquid layer is adsorbed on the plate and diffuse within the outer Al surface in shallow depth.

The plate is rinsed with deionized water and gently dried. Rinsing the depassivated and amalgamated surface activates the Al oxidation in developing a non-passivating Al_2O_3 layer. Then the plate is quickly attached to the radiator in the climate chamber, as the oxidation reaction starts immediately after drying with rapid kinetic. The monolith begins to grow perpendicularly to the surface of the plate, and the process is carried out for at least 8 h. Finally, the monolith is collected by carefully detaching it from the plate.

The **dehydration and crystallization** of amorphous UPA is carried out in a muffle furnace, with thermal treatment conditions depending on the desired alumina state. Then, the monolith is crushed to fine powder in an agate mortar.

The **synthesis of $MgAl_2O_4$ *via* nanofibrous alumina impregnation route** is based on previous preliminary studies [149, 151]. The process consists in the liquid impregnation of the UPA powder with a Mg^{2+} containing solution. The impregnation solution was prepared by addition of stoichiometric amount of $Mg(NO_3)_2{\cdot}6H_2O$ salts to the crushed UPA and then small amount of deionized water was added in order to dissolve the salts and obtain a slurry. This paste-like state was chosen to avoid the loss of Mg-precursor due to excess liquid while having a homogeneous distribution of the precursor.

The slurry mixture was homogenized for two hours in 3D-mixer (Turbula®, WAB) at 32 rpm with 2 mm ZrO_2 balls (ball to powder weight ratio of 3). The mixture was retrieved and dried to powder at 100°C overnight, then heat treated at temperature between 500 and 1000°C for 1 h in a muffle furnace to obtain MAS, with a heating rate of 300°C/min. The powder was grinded in a mortar afterward for deagglomeration.

2. Commercial powders and mechanical treatments

i. $MgAl_2O_4$ commercial powders

Two **commercial $MgAl_2O_4$ powders** are used in this work: the **Puralox Mg28 powder** provided by Sasol GmbH (Germany) referred to as the **Sasol powder**, and the **S25CR powder** from **Baikowski** (France).

The **Sasol powder** is produced through the synthesis of mixed Mg-Al hydroxides, including the hydrotalcite LDH-type1, by a refined sol-gel method *via* hydrolysis of heterometallic alcoholate with the ratio Mg/(Mg + Al) = 28 wt% with consideration for $MgAl_2O_4$ cationic composition. After slurry processing and calcination at 1100°C, the oxide form is obtained, followed by a sieving step. The analysis report provided by the company indicates typical **impurity content of 258 ppm** (Na: 30 ppm, Si: 70 ppm, Fe: 100 ppm, Ca: 5 ppm, Ti: 10 ppm, Cr: 10 ppm, Ni: 5 ppm, Zn: 25 ppm, Zr: 3 ppm, no information on S and C) and a **median size particle d_{50} ~30 µm**, for a specific surface area of ~7 $m^2.g^{-1}$. Powders from the lots M7225, M10125 and M10590 have been used in this work, the properties of each being arguably the same.

The most commonly used commercial powder **S25CR** from Baikowski is synthesized through the ALUM process, which consists in the coprecipitation of a crystallized and purified sulfate-based compound from Al, Mg and NH_4 sulfate salts. The spinel phase is then formed by thermal decomposition at high temperature (unspecified) prior to further calcination and desulphurization, and finally jet milling to adjust the particle size and surface area. The analysis report provided by the company for the powder used in this work (lot number 200259) indicates **low impurity content** (Na: 13 ppm, Si: 20 ppm, Fe: 13 ppm, Ca: 17 ppm, K: 21 ppm) except for **549 ppm of C and 209 ppm of S**, due to the synthesis route. The particle size distribution is such as **d_{50} = 0.18 µm**, d_{90} = 0.8 µm and **d_{100} = 2 µm**, for a specific surface area of 21.5 m^2.g^{-1}.

Both powders have been **calcined at 900°C for 4 h prior to sintering**, in order to homogenize the particles/crystallites size distribution and reducing the volatile species content [286]. The loss on ignition was 0.4 wt% for Sasol and 0.6 wt% for S25CR.

The XRD patterns and micrographs of Sasol and S25CR powders are presented in *Figure 2.2*. The XRD analysis reveals that both powders are mostly composed by $MgAl_2O_4$ spinel phase, with however **free MgO** remaining in content such as ~3 wt% for Sasol and only traces < 1 wt% for S25CR. The Rietveld refinement of Sasol's XRD pattern indicates a crystallite size of **139(5) nm** and a cell parameter **a = 8.1039(2) Å** superior to a_0 reported in literature for stoichiometric spinel, due to **MgO-rich spinel**, in agreement with excess free MgO observed, while the S25CR powder presents crystallite size of **75(1) nm** and cell parameter **a = 8.0733 Å** close to **stoichiometric spinel** value. The micrographs of Sasol powder (*Figure 2.2.b*) show **~30 µm spherical particles** composed by **aggregated ~2 µm platelets**; high magnifications reveals that they are constituted of sintered round crystallites of 100-150 nm diameter. The micrographs of S25CR powder (*Figure 2.2.c*) reveal **loosely bonded agglomerates** of size in the range **10 – 500 µm**; the primary particles are directly the rounded crystallites of ~70 nm size.

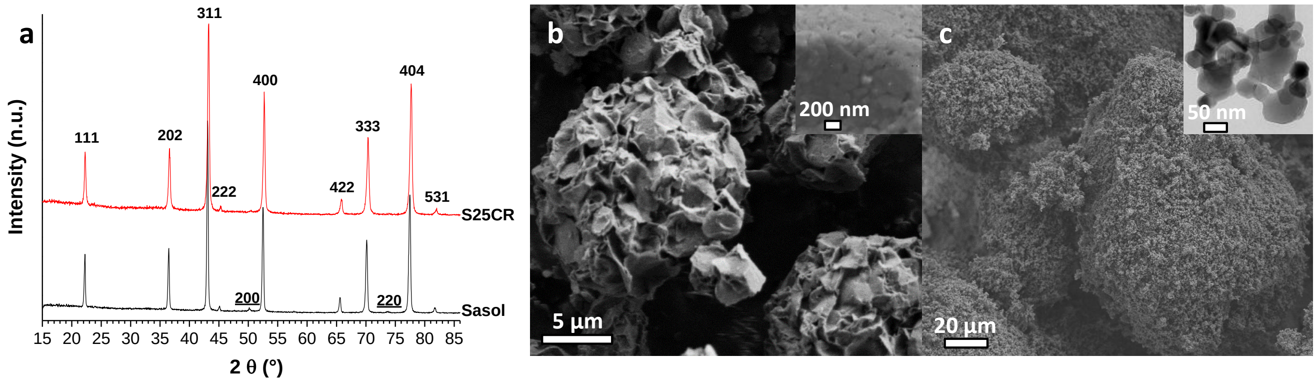

Figure 2.2: a) XRD patterns with indexation for spinel $MgAl_2O_4$, except underlined indexation for periclase MgO; micrographs of the b) Sasol and c) S25CR commercial powders

Figure 2.3 shows the FTIR and Raman spectra for both spinel powders. While the main feature in FTIR spectrum of S25CR is the O-M absorption bands in the region < 700 cm^{-1} [111], with presence of H_2O (3200-3400 cm^{-1}, 2976 cm^{-1}, 1630 cm^{-1} [110, 111]) and CO_3^{2-} (1380 cm^{-1} [309]) from adsorbed atmospheric gas, the spectrum obtained for Sasol contains several additional bands, especially in the region 1350-2800 cm^{-1}, which cannot be attributed and indicate contamination and/or structural disorder within the spinel phase. This is confirmed by Raman spectra with typical fingerprint of $MgAl_2O_4$ in both cases [52, 54, 310]. However, several Raman modes marked by * have been ascribed to **cationic inversion** between Al^{3+} and Mg^{2+} previously [52, 310]; it is clear that the relative intensities of "disorder" modes are greater for the Sasol precursor, indicating that S25CR powder has a more ordered spinel lattice possibly due to its stoichiometric composition.

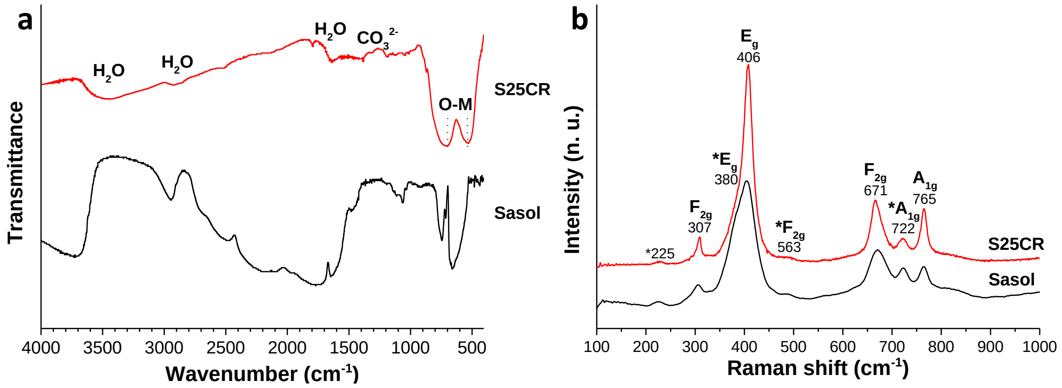

*Figure 2.3: a) FTIR and b) Raman spectra of Sasol and S25CR powders; Raman modes marked by * arise from cationic inversion*

The **XPS spectra of the powders** are presented in *Figure 2.4* for surface chemical analysis, and the surface compositions determined by the analysis are in *Table 2.1*. The survey spectra reveal the presence of magnesium, aluminum, oxygen and carbon, in agreement with literature [311]. Al2p, Mg1s and O1s spectra show unique peaks similar for the two powders, although slightly broader for Sasol because of the cationic inversion inducing larger distribution of bonding energy. The C1s spectra are split into characteristic signals C_A (284.8 eV) and C_B (289.1 eV), corresponding to C-C and C-O bonding, respectively [312, 313], and which are often observed as adventitious carbon. The **surface Al/Mg ratios** determined by XPS are **2.32 and 2.69 for Sasol and S25CR**, respectively, confirming the higher Mg content in Sasol powder. These ratios are higher than expected from XRD, which is due to the shallow analysis of XPS technique (penetration depth of ~5 nm) and indicates that $MgAl_2O_4$ particles' surface is richer in Al than the bulk.

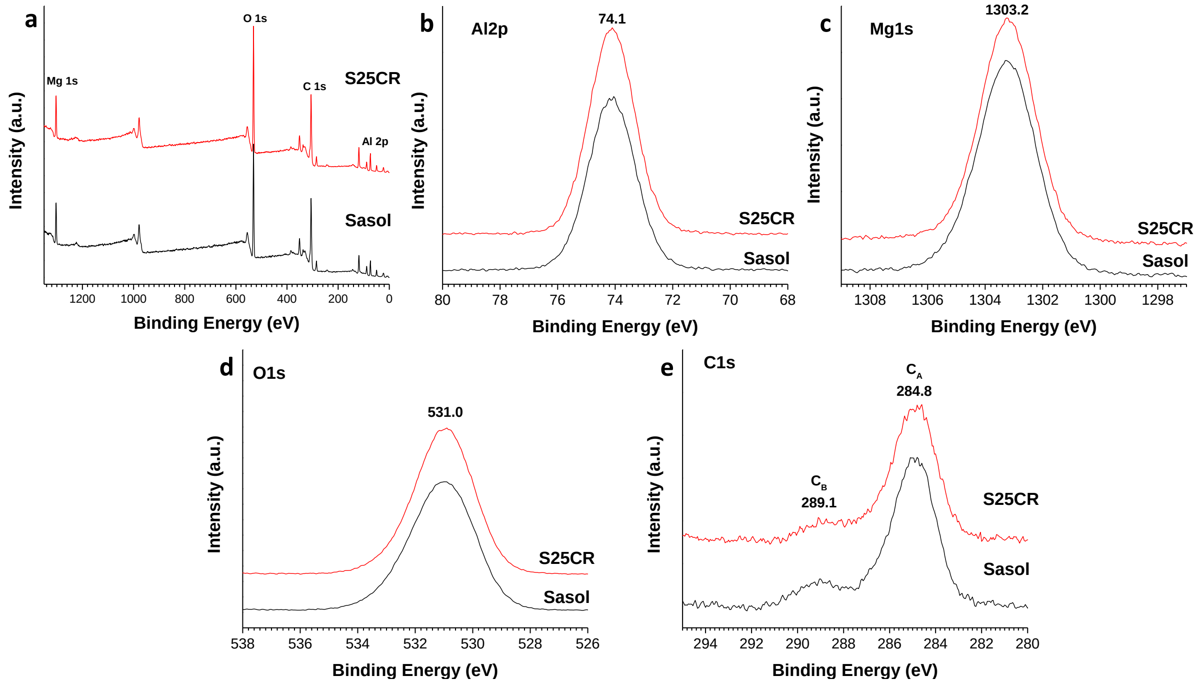

Figure 2.4: XPS spectra of Sasol and S25CR commercial powders: a) survey, b) Al2p, c) Mg1s, d) O1s and e) C1s

Table 2.1: Surface composition of Sasol and S25CR commercial spinel powders determined by XPS

Composition	Mg (%)	Al (%)	**Al/Mg**	O (%)	C_A (%)	C_B (%)	C (%)
Sasol	10.23	23.74	**2.32**	53.97	9.87	2.19	12.06
S25CR	9.72	26.17	**2.69**	54.07	7.79	2.26	10.05

ii. *Ta_2O_5 commercial powders*

In order to investigate **the influence of Ta_2O_5 as an additive** on $MgAl_2O_4$ sintering, two commercial powders have been used: a **L-Ta_2O_5 powder** with 99.9% purity from ChemPur GmbH (Germany) and a ***a*-Ta_2O_5** ~325 mesh powder with 99.85% purity (metals basis) from Alfa Aesar (USA).

The XRD patterns and Raman spectra of Ta_2O_5 powders are presented in *Figure 2.5*. The XRD pattern of L-Ta_2O_5 powder reveals pure orthorhombic β-Ta_2O_5 phase [314, 315], stable at temperature < ~1370°C, with crystallite size of **~310(20) nm** and lattice constants a = 6.1894(1) Å, b = 40.2566(1) Å and c = 3.8839(1) Å calculated by Rietveld refinement. Raman spectroscopy confirms this results, with spectrum of L-Ta_2O_5 powder consistent with the fingerprint of the orthorhombic phase [314–316]. In comparison, the XRD pattern and Raman spectrum of *a*-Ta_2O_5 powder are characteristic of **amorphous Ta_2O_5** [315, 317].

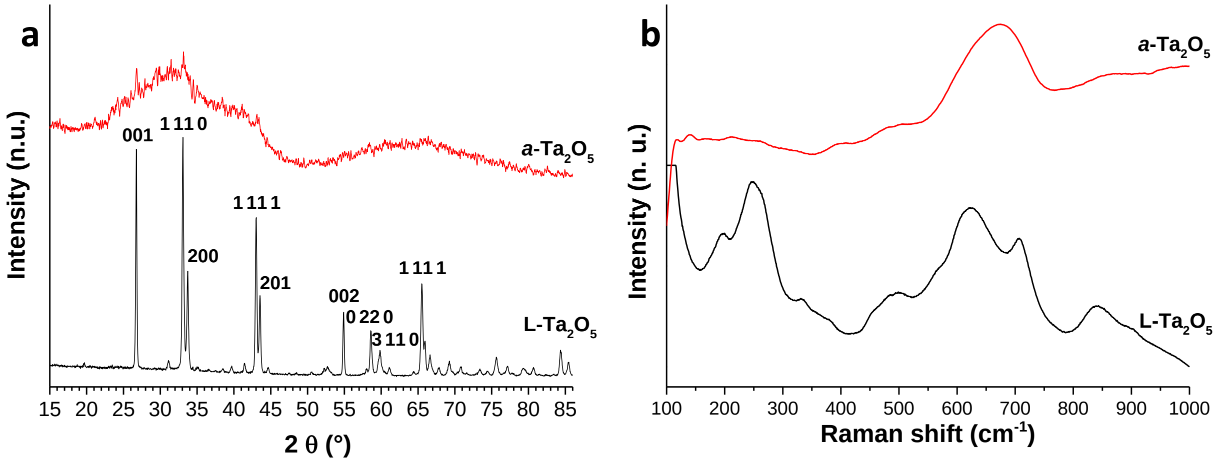

Figure 2.5: a) XRD patterns and b) Raman spectra of Ta_2O_5 commercial powders

The SEM micrographs of these powders are presented in *Figure 2.6*. The L-Ta_2O_5 powder is constituted by **large soft agglomerates** of hundreds µm, with average size of faceted primary particles about **300-500 nm**. The *a*-Ta_2O_5 powder morphology consists of 10-50 µm **hard agglomerates**, with sintered rounded primary particles of large distribution size between 100 nm and over 1 µm.

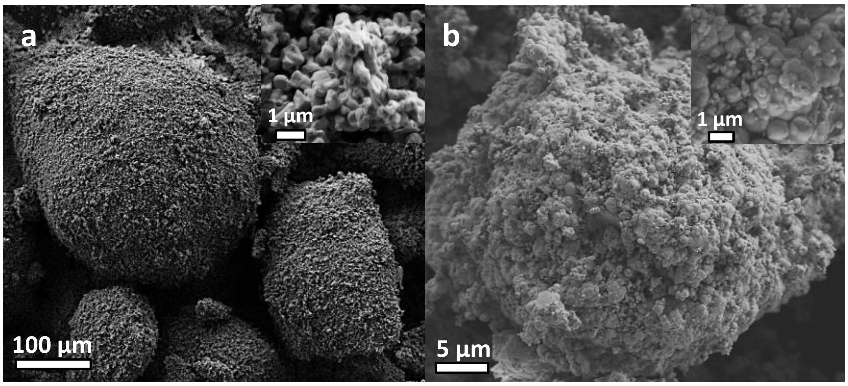

Figure 2.6: Micrographs of a) L-Ta_2O_5 and b) a-Ta_2O_5 commercial powders

Generally and unless otherwise indicated, the addition and mixture of Ta_2O_5 and spinel powders was carefully carried out in an agate mortar, in small quantity of 0.500 g to minimize inhomogeneous distribution of Ta_2O_5. The mixture was grinded for several minutes until homogeneous resulting powder was obtained.

iii. Mechanical processing of the powders

The influence of a **mechanical pre-processing** on the commercial powders has been investigated in this work (*Chapter 4.I*). Two comminution processes have been used in this purpose: a **high-energy** and a **low-energy ball milling**. The processing has been carried out in dry and wet (deionized water) conditions in both cases. After treatment, the powders are retrieved, and heat treated at 900°C for 4 h to eliminate traces of organic contamination from the mechanical processing.

The **high-energy process** has been carried out on a planetary ball mill PULVERISETTE 7 classic line (Fritsch GmbH, Germany), equipped with two steel grinding vials with a maximum loading capacity of 20 ml each. The powder to be treated is loaded into these jars, together with 10 mm steel balls with specific ball to powder BPR ratio, and the milling is then carried out by means of a double rotation effect of the vials and support disc in opposite directions. It results in a friction effect from the balls along the vials' inner walls, as well as an impact effect of the balls on the opposite wall and between each other. The milling is operated by 15 min milling cycle at rotary speed of 100/200 rpm with BPR of 10/20, separated by 5 min breaks in order to let the system cool and avoid damage to the grinding media. When processing was performed in wet conditions, a powder loading of ~35 vol% was used in order to reach an oily viscosity of slurry.

The **low-energy treatment** was carried out in a 3D mixer TURBULA® (WAB-GROUP, Switzerland). The powder to be treated (10 g) is first introduced into 30 ml PE centrifugation tubes with 2 mm ZrO_2 balls (30 g, BPR = 3), with or without solvent. In case of wet processing, 30 ml of solvent is added to reach viscous slurry state with solid loading of ~35 vol%. Four PE tubes are prepared in parallel, and then introduced into a hermetically sealed PE mixing vessel. The container is attached within the milling apparatus, and subjected to 3D rotating movements with a rotating speed of 32 rpm for 24 h, promoting excellent and gentle contact between particles and balls for a homogeneous mixing.

3. Sintering and polishing of ceramic samples

i. Spark Plasma Sintering (SPS)

The sintering method used in this work is the **spark plasma sintering (SPS)**, with a Dr. Sinter LAB Series SPS-515S (Fuji Electronic Industrial, Japan) system located in CNRS-ICMPE (Thiais, France), benefitting from the technical expertise of Benjamin VILLEROY (CNRS-ICMPE, France). This apparatus allows using sintering temperatures up to 2000°C with heating rate up to 600°C/min and pressing force up to 50 kN. During sintering experiments, the different experimental parameters (temperature, pressure, displacement of the punches, vacuum pressure, current and voltage) are measured *in situ* and recorder, for a self-regulation depending on the programmed conditions.

The system is composed by three main modules (*Figure 2.7*): I – the sintering module which includes the sintering chamber, pyrometer/thermocouple and gas valves; II – the temperature programming module, together with temperature displacement, current, voltage and vacuum controllers; III – the pressure programming module, together with a computer for data visualization and recording.

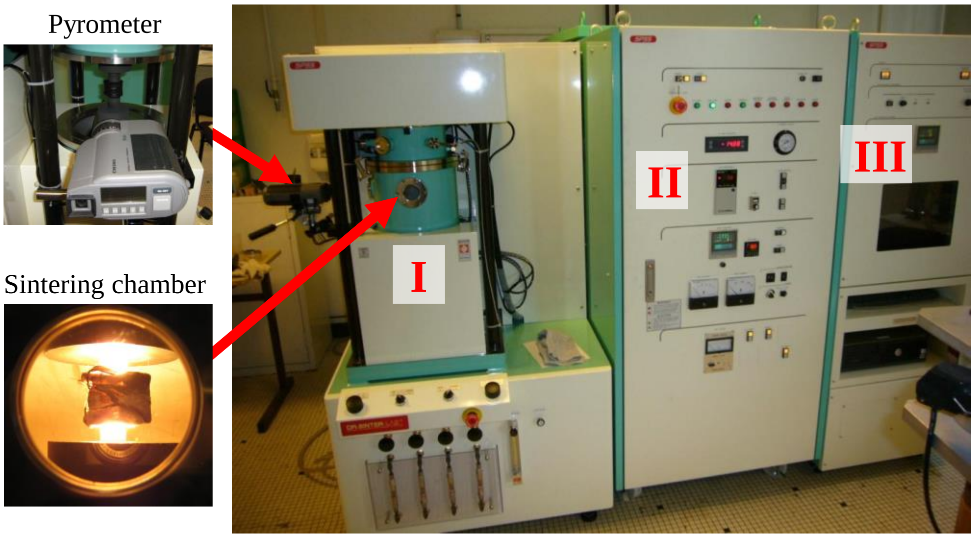

Figure 2.7: SPS system with I - sintering module, II – temperature programming module and III – pressure programming module

Samples were prepared by pouring the powder into a graphite paper (Papyex®) insulated die. Two types of dies have been used depending on the applied pressure. For sintering with **applied pressure up to 100 MPa**, 1.15-1.25 g of spinel powder was introduced in a **15 mm diameter standard graphite molds** (quality 2334 Mersen, *Figure 2.8.a*). The **HPSPS experiments (P ≤ 1 GPa)** were carried out by pouring 0.25-0.30 g of $MgAl_2O_4$ powder into a **pressure-tolerant 8 mm inner diameter silicon carbide die**, within a **42 mm outer graphite die** allowing electrical current to heat the system (Mersen, *Figure 2.8.b*). This die was designed based on scheme in Ref. [228]. After sintering, the received pellets had a thickness of about 2 mm. Since used sintering temperatures were ≥ 1000°C, the sample die was wrapped in carbon felt to suppress heat radiation from the sample.

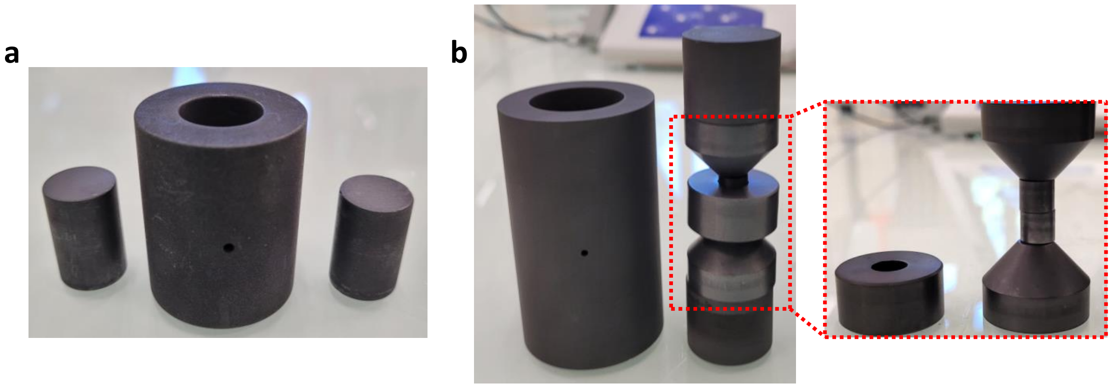

Figure 2.8: a) Graphite die used for standard SPS (P ≤ 100 MPa) and b) SiC inner die within graphite die for HPSPS (P ≤ 1 GPa)

In our experiments, the pulse pattern of the SPS system was kept at the recommended standard 12:2 (on-off, pulse duration 3.4 ms). Sintering was carried out in slight vacuum of ~20 Pa. Temperature was measured by an optical pyrometer (CHINO IR-AH) focused on an area of the sample die not covered by carbon felt (see dies in *Figure 2.8*).

For this study, a two-step SPS scheme that we established in a preliminary work [318] has been used, with few modifications based on literature. The **general sintering schedule** is schematized in *Figure 2.9*. At first and for all sintering experimentations, a 10 min dwell at 600°C is applied to remove the water adsorbed on our powder while allowing the pyrometer to detect the temperature on surface of the die (minimum threshold at 573°C). In parallel, the pressure is progressively applied in 4 min, in a way that P is reached at the end of the 600°C dwell; the pressure is then maintained until the cooling step. Once P is applied, the temperature is raised to the critical temperature of two-step SPS T_c with a rate of 100°C/min, then further heating to the sintering temperature T_d is achieved with the rate α. T_d is held for the duration t_d. Afterward, the pressure is progressively released while the temperature is cooled to 900°C (100°C/min) and maintained for 5 min ($P \leq 100$ MPa), 10 min ($100 \text{ MPa} < P \leq 300$ MPa) or 15 min ($300 \text{ MPa} < P \leq 1000$ MPa) to diminish internal stresses in the material and avoid cracking during the pressure release. Finally, the system is cooled to room temperature. The critical temperature is set as $T_c = T_d - 150°C$, with a maximum value of 1150°C based on the work of Talimian *et al.* [222].

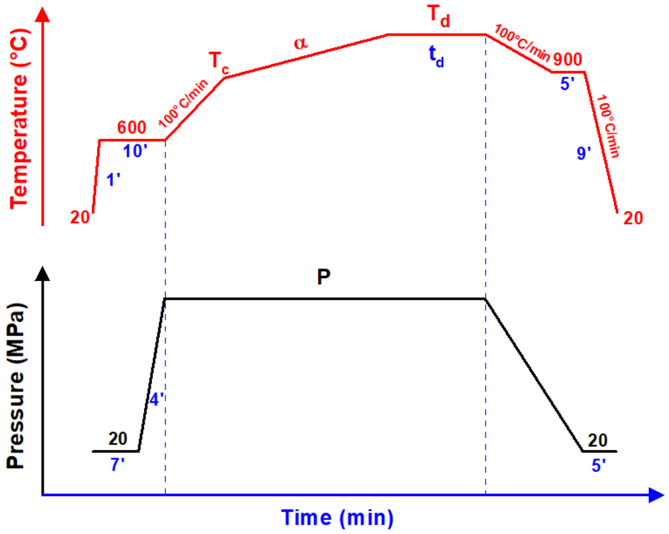

Figure 2.9: General two-step spark plasma sintering scheme for the investigation of the effect of the sintering parameters

ii. Hot isostatic pressing (HIP)

Hot isostatic pressing (HIP) was investigated in this work as a post-densification technique. The benefit of using HIP in addition to SPS is its isostatic pressure application *via* gas, allowing further densification of the samples in directions other than uniaxial SPS, in order to close small intergranular pores.

The HIP apparatus (Nova Swiss) used in this work allows applying pressure up to 400 MPa with argon as pressurizing gas at maximal temperature of 1450°C, with a maximum heating rate 15°C/min, cooling rate of 50°C/min and dwell time of 5 hours.

iii. Polishing of sintered ceramics

The **polishing** of the ceramics to **mirror surface quality** is carried out prior to any characterization. Polishing hard ceramic materials demands proper equipment and good procedure, in what can arguably be considered as the most daunting yet tedious and monotonous step of this work.

Prior to polishing, the samples are cold mounted by embedding them within KM-BACK acrylic resin (PRESI, France), which can be dissolved in acetone after processing.

The polishing is carried out on semi-automatic machine MECATECH 300 SPC (PRESI, France), using Reflex lubricant and diamond suspensions, and polishing discs from PRESI with the following protocol:

1. grinding disc IMAX-R yellow 54 µm; disc rotation 250 rpm; samples rotation 150 rpm; 2.5 kN pressure; water; 900s
2. grinding disc IMAX-R gray 18 µm; disc rotation 150 rpm; samples rotation 125 rpm; 2 kN pressure; water; 600s
3. grinding disc MED-R 9 µm; disc rotation 150 rpm; samples rotation 125 rpm; 1.5 kN pressure; 0.10 ml/30 s of lubricant and 0.15 ml/30 s of 9 µm diamond suspension; 600s
4. polishing cloth Reflex PAD-MAG TOP; disc rotation 125 rpm; samples rotation 100 rpm; 1.5 kN pressure; 0.10 ml/30 s of lubricant and 0.15 ml/30 s of 9 µm diamond suspension; 300s
5. polishing cloth Reflex PAD-MAG RAM; disc rotation 125 rpm; samples rotation 100 rpm; 1 kN pressure; 0.10 ml/30 s of lubricant and 0.15 ml/30 s of 3 µm diamond suspension; 300s
6. polishing cloth Reflex PAD-MAG NT; disc rotation 125 rpm; samples rotation 100 rpm; 1 kN pressure; 0.10 ml/30 s of lubricant and 0.15 ml/30 s of 1 µm diamond suspension; 300s
7. polishing cloth Reflex PAD-MAG SUPRA; disc rotation 100 rpm; samples rotation 85 rpm; 1 kN pressure; 0.10 ml/30 s of lubricant and 1 spraying of 1/4 µm diamond suspension every 30 s; 300s

It should be noted that the duration of grinding steps 1-3 depends heavily on the desired final thickness of the sample and rate of thickness decrease, hence can be prolonged in consequence.

After the polishing step, thermal post-treatments in air have been carried out on some samples, at temperature at least 150°C below sintering temperature, in order to better reveal the microstructure.

Chapter 3

Synthesis of $MgAl_2O_4$ nanopowders

The goal of this first experimental part of the PhD project is to synthesize magnesium aluminate spinel precursor powders with adequate features for subsequent sintering into transparent fine-grained ceramics, specifically nanosized crystallites, controlled and limited agglomeration state, narrow size distribution and high chemical/phase purity. For this purpose, we are using and adapting two synthesis routes well established in our research team, the polyol-mediated synthesis and the impregnation of nanofibrous alumina.

In this chapter, the synthesis methods are studied independently, and focus is put on the investigation of the specific synthesis conditions offered by each ones to better control the powder features. In order to identify more properly what would be the ideal compositional and physical features for a MAS precursor sinterable into transparent ultrafine-grained ceramics, our purpose is to synthesize different $MgAl_2O_4$ precursors with a large range of features. Investigations on their sinterability will be carried out in the next chapter, and conclusions or perspectives on the "quality" of the precursors will be made at this moment.

I. Synthesis *via* a polyol-mediated route

In this sub-chapter, we are presenting our work on the synthesis of nanocrystalline spinel particles *via* a **polyol-mediated route**. After defining reference synthesis conditions based on literature, and subsequent inquiry of the thermal decomposition of the as-synthesized compound into spinel phase, we investigated the main impacting factors on the reaction mechanism and the chemical, structural and microstructural properties. The **investigated conditions** are the temperature of synthesis, the relative quantities of Mg^{2+} and Al^{3+} in solution, the nature of the used precursors, additives and polyol solvent, the temperature of addition of the precursors, the synthesis duration, the hydrolysis ratio and the concentration of precursor salts. In order to demonstrate the interest of a polyol medium for the synthesis, comparative reactions in aqueous medium are also carried out. Since the polyol route does not lead directly to the formation of spinel, particular attention is given to the as-synthesized compounds before thermal decomposition, for a better emphasizing of correlation between precursor and oxide structures. Finally, as a perspective and desire to extend the potential of the developed route, the **doping** of the synthesized spinel with various elements during the synthesis is addressed, together with the versatility of the method to produce **other aluminate spinel materials**.

Since a focus on the as-synthesized compounds is put, the lector is advised to refer himself to the bibliographical paragraph describing the different precursors for $MgAl_2O_4$ synthesis (*Chapter 1.III.3*) for a better apprehension of this work.

1. Reference synthesis

As mentioned in *Chapter 1*, a research group has previously reported the synthesis of $MgAl_2O_4$ nanoparticles *via* a polyol-mediated route [116, 117], unfortunately no synthesis conditions were reported with enough indications to be reproduced. Consequently, we decided to fix our reference synthesis conditions from studies reporting the synthesis of spinel oxides $CoFe_2O_4$ [166], $NiFe_2O_4$ [165] and $CoAl_2O_4$ [181] in polyol media.

Table 3.1: Reference conditions for the polyol-mediated synthesis of $MgAl_2O_4$ precursor

	Solvent	Mg^{2+} salt	Al^{3+} salt	Additive
Chemical	Ethylene Glycol	$MgCl_2·6H_2O$	$AlCl_3·6H_2O$	$NaCH_3COO$
Volume (ml)	200	-	-	-
Mass (g)	-	1.355	3.219	4.375
Concentration (M)	-	0.0333	0.0667	0.267
Quantity (mmol)	3632	6.666	13.34	53.34
$C_T = [Mg^{2+}+Al^{3+}]$ (M)	$h = \frac{H_2O}{Mg^{2+}+Al^{3+}}$	$r = \frac{CH_3COO^-}{Mg^{2+}+Al^{3+}}$	T(°C) = BP	Duration (h)
0.100	6	2.67	185	2

The **reference synthesis conditions** are presented in *Table 3.1* and the **experimental protocol** is described herein. In a typical preparation, 1.355 g (6.66 mmol, 1 eq) of $MgCl_2·6H_2O$ and 3.219 g (13.33 mmol, 2 eq) of $AlCl_3·6H_2O$ are dispersed in 200 ml of ethylene glycol (EG), corresponding to a total concentration $C_T = [Mg^{2+} + Al^{3+}] = 0.100$ M and a ratio Al/Mg = 2, with respect to $MgAl_2O_4$ composition; as a counter-ion for Cl^- and a source of acetate, 4.375 g (53.33 mmol, 8 eq) of anhydrous $NaCH_3COO$ are added to the mixture before mechanical stirring is set to 500 rpm. The hydrolysis ratio $h = 6$ is fixed by the amount of water in the precursor salts, and the sodium acetate ratio r is set at 2.67. The solution is then heated with a rate of 5°C/min to **60°C** and the temperature is maintained **20 min** in order to dissolve all salts and ensure high chemical homogeneity of reactants in the polyol medium prior to reaction. Then, temperature is raised to **165°C** for another **20 min** to stabilize the reaction. Indeed, the solution becomes opaque white around 120°C, indicating that particles start to nucleate, and at 165°C a foam appears on top of the solution due to reaction. Without this stabilization step at 165°C, the amount of foam becomes uncontrollable and overflows from the flask. After this *plateau*, the foam disappears and the mixture is **brought to a boil** (~185°C) **for 2 h**. After cooling to room temperature, the synthesized white gel is separated from the solution by centrifugation and washed three times with water, once with acetone and dried in air at $T \leq 100$°C. The synthesized precursor powder is then thermally decomposed to MAS through calcination.

The XRD pattern of the as-synthesized powder is presented in *Figure 3.1.a.* Two phases can be identified, with a molar ratio of ~1: the **magnesium-rich layered double hydroxides structure (LDH-type1) $[Mg_{(1-x)}Al_x(OH)_2][(A^{n-})_{x/n}\cdot mH_2O]$** and the **aluminum hydroxide α-$Al(OH)_3$ gibbsite** (*c.f. Chapter 1.III.3*). The phase composition is the same that what was obtained in [93] by coprecipitation of Mg and Al nitrates by NH_4OH at pH = 10; however, synthesis mechanism cannot be similar here since no strong base is added, hence a rather acid solution is expected (polyols are slightly acid [167]). Several pure LDH-type1 have been synthesized *via* polyol route, and the exact composition obtained here is discussed below. The crystallite size from peaks broadening have been estimated to be **~10 nm for LDH** and **~15 nm for $Al(OH)_3$**. Nevertheless, it should be remarked that LDH reflections are asymmetrical on the low angles side, due to stacking disorder for basal reflections (non-parallel and equidistant layers) and turbostratic disorder for non-basal reflections (twisted and/or translated against each other sheets) [140]; it is to be assumed that the LDH structure is **highly disordered**. The d-spacings of the (003) and (110) reflections of the LDH phase are indicated on *Figure 3.1.a*, as they are related to the interlayer distance and the cation-cation distance in brucite sheets, respectively (*c.f. Chapter 1.III.3*). The $d_{003} = 7.60$ Å is quite common, and generally associated with intercalated CO_3^{2-}, presenting the highest affinity for the brucite-like layers [131]. However, it is unlikely that carbonates are found in our compound, since their introduction through the synthesis process is not expected, due to the slight acidic pH conditions neutralizing CO_3^{2-} [167]. The simpler anions to be intercalated here are Cl^- and CH_3COO^-, for which reported values of d_{003} are 8.04 Å for Cl^- and 8.54 Å [319], 9.77 Å [320] and 12.5 Å [167] for CH_3COO^-, depending on its orientation arrangement. The smaller observed d_{003} value in our case indicates either a smaller intercalated anion or a divalent one (stronger attraction). Thus, the intercalated anion may have been formed *in situ*, through decomposition/reaction of EG and/or acetate, hence composed solely by C, H and/or O atoms and entirely decomposable through calcination, including CO_3^{2-}. Intercalation of EG/EG^- could be considered as well, but d_{003} value should be even higher up to 12.83 Å for monodentate $(HOCH_2CH_2O)^-$ [136]. However, in the case of a double deprotonation of EG to the divalent ethanediolate $(OCH_2CH_2O)^{2-}$ of much stronger ionic strength, the LDH layers could be maintained closer together, but no mention in literature has been found. The d_{110} = 1.52 Å corresponds to a ratio Mg^{2+}/Al^{3+} of ~2, hence a Al^{3+} content of $x = 0.333$ [125].

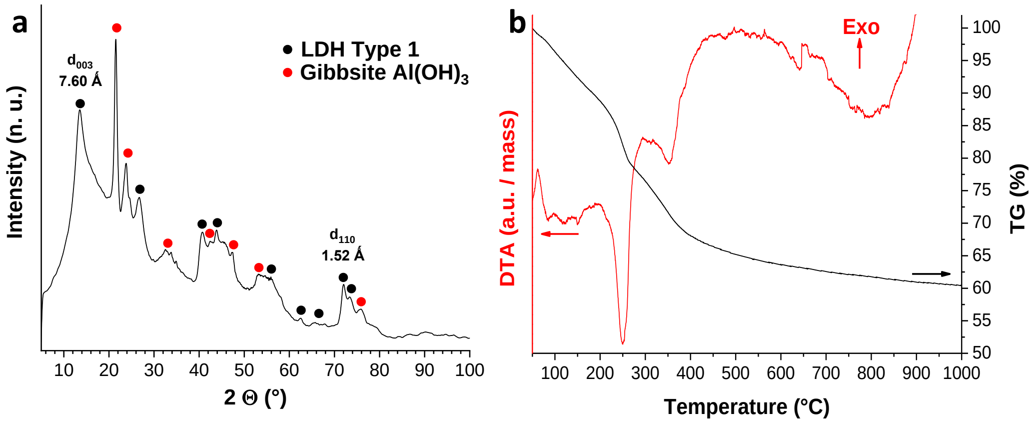

Figure 3.1: a) XRD patterns of polyol-synthesized material with reference conditions and b) its DTA-TG analysis

The DT-TG analysis of the synthesized powder presented in *Figure 3.1.b* shows a decomposition of the hydroxides through several steps. First, for < ~120°C the powder is dehydrated of its physisorbed water, then it undergoes endothermic **dehydration** of the **interlayer H_2O at 150°C**, with a mass loss of ~15%. A second endothermic mass loss (~15%) occurs at **250°C**, from the **dehydroxylation of $Al(OH)_3$**, and finally a third and progressive mass loss (~11%) **from 350 to 600°C**, accompanied by a small endothermic effect centered at 350°C, attributed to **dehydroxylation of LDH** and **decarboxylation of interlayer anions**. No further DT or TG phenomenon is observed at higher temperature. This is in good agreement with the thermal decomposition of similar coprecipitated hydroxides in [93]. However, identification of the interlayer specie is difficult through DT-TG analysis, since several organic anions have almost the same molecular mass and are decomposed in the same range of 250-400°C [319], overlapping with LDH dehydroxylation.

Figure 3.2.a presents the evolution of the XRD pattern of the powder through 1 h heat treatment up to 1600°C. At 150°C, no structural change is observed, confirming that the endothermic loss of mass at this temperature is just dehydration of the powder. **At 250°C**, the gibbsite reflections are not present anymore but metastable **η-Al_2O_3** pattern appears, proving the decomposition of $Al(OH)_3$, while LDH reflections are still observed. The formed alumina crystallites seem very small from their broad reflections, but no quantitative analysis is possible. The **layered structure starts to decompose at 400°C**, its basal reflections being extinguished while the in-plane reflections are not impacted indicating the **collapse of the layering** while the brucite-like sheets are not degraded yet. Thus, the decomposition of the interlayer anion occurs before the hydroxyl groups' one. It should be noted that at this point the LDH structure could be fully recovered thanks to its memory effect (*c.f. Chapter 1.III.3*). The LDH in-plane reflections progressively decrease in intensity and shifts toward higher angles due to slow dehydroxylation up to 600°C, to eventually merge with the η-Al_2O_3 reflections. An **intermediate phase** arises from the **incorporation of Mg^{2+} in the cfc alumina** lattice based on its XRD pattern with asymmetric reflections, but relative intensities evolve and positions shift toward spinel peaks. These observations are in agreement with DT-TG analysis of the mixed hydroxide decomposition into oxide form (*Figure 3.1.b*), and a similar decomposition mechanism through η-Al_2O_3 formation had been proposed in [93, 94] but no clear proof was brought by these works. With the

temperature increasing to **800°C**, this intermediate structure evolves into **well-crystallized spinel**, with lattice constant ***a* = 8.082 Å**. Higher temperatures lead to sharper reflections, indicating the coarsening of the crystallites. At 1200°C, some minor MgO precipitates, probably due to a slight deviation from stoichiometry.

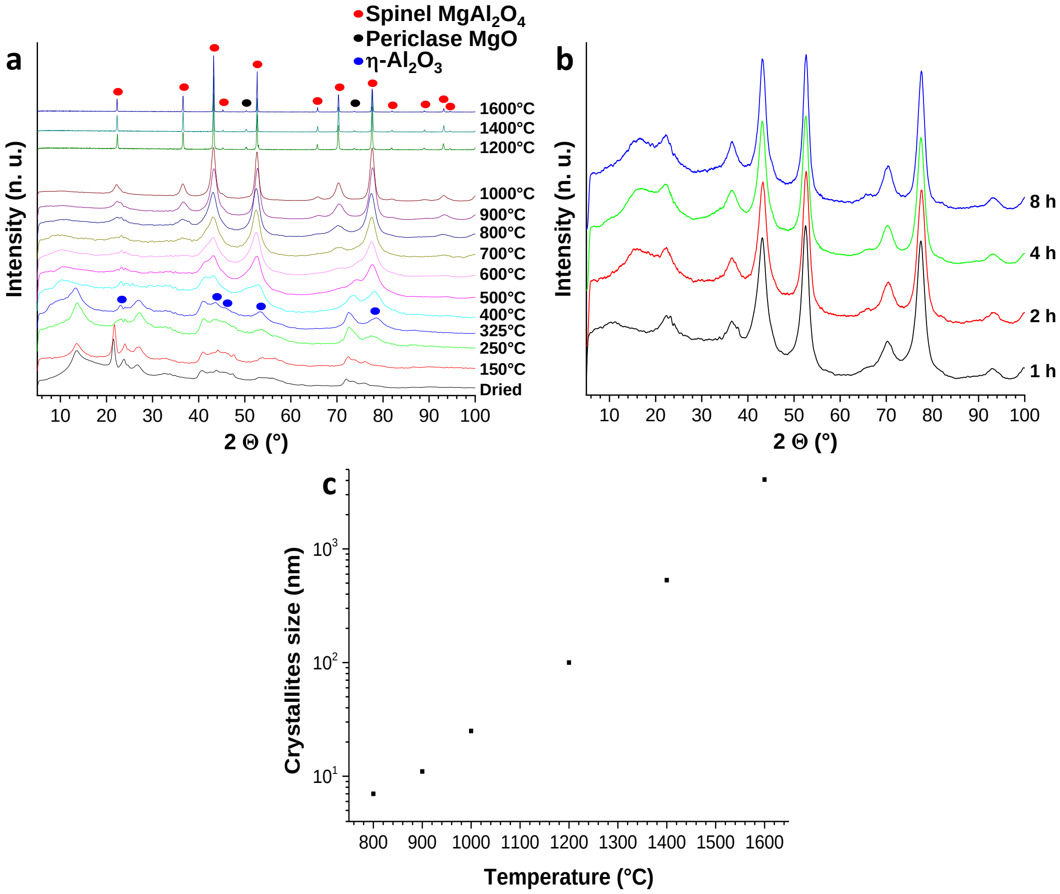

Figure 3.2: XRD pattern evolution of polyol as-synthesized material with reference synthesis conditions through heat treatment a) at different temperature for 1 h and b) at 800°C for different durations; c) spinel crystallite size versus temperature of heat treatment

Figure 3.2.b shows the effect of the duration of heat treatment at 800°C on the structure, from 1 h to 8 h. No changes are noted, except for the apparition of an amorphous bump at 2θ = 15°, which is attributed to the sample holder. Better crystallization of the phase does not occur through longer thermal treatment.

The measured spinel crystallite size from XRD refinement and micrographs for T ≥ 1400°C (*Figure 3.3*) in function of the calcination temperature is presented in *Figure 3.2.c*. The **crystallite size** (CS) evolution follows a **quasi-exponential law**, from **7.0(1) nm** at **800°C** through 11.0(1) nm at 900°C, 24.9(2) nm at 1000°C, 101(1) nm at 1200°C, 530 nm at 1400°C, to over 4 µm at 1600°C. The prepared MAS powder exhibiting small CS < 10 nm with high crystallinity is quite uncommon, only reported in [99] where authors obtained highly agglomerated particles *via* complexation, combustion and sol-gel routes.

Microstructures of the sample before and after the different thermal treatments are presented in *Figure 3.3*. It can be seen that the **as-synthesized powder** (*Figure 3.3.a*) is composed by **dense agglomerates** of crystallites with **sheet-like** shape **randomly oriented**, in agreement with the stacking disorder of LDH-type1 observed in the XRD pattern (*Figure 3.1.a*). Since extended TEM analysis did not lead to the observation of several shapes of crystallites or agglomerates, we assume that LDH-type1 and gibbsite phases exhibit similar crystallites shape and size which cannot be differentiated from micrographs, and that they are intimately mixed together resulting in a **high chemical homogeneity**. The secondary particles have a **"stone-like" morphology**, common for LDH [321] and even more when they are synthesized in polyol medium [167]. They seem to be aggregates, *i.e.* with strong bonding between the crystallites, and with size ranging from few µm to hundreds of µm and very low surface area as they are non-porous at the mesoscale.

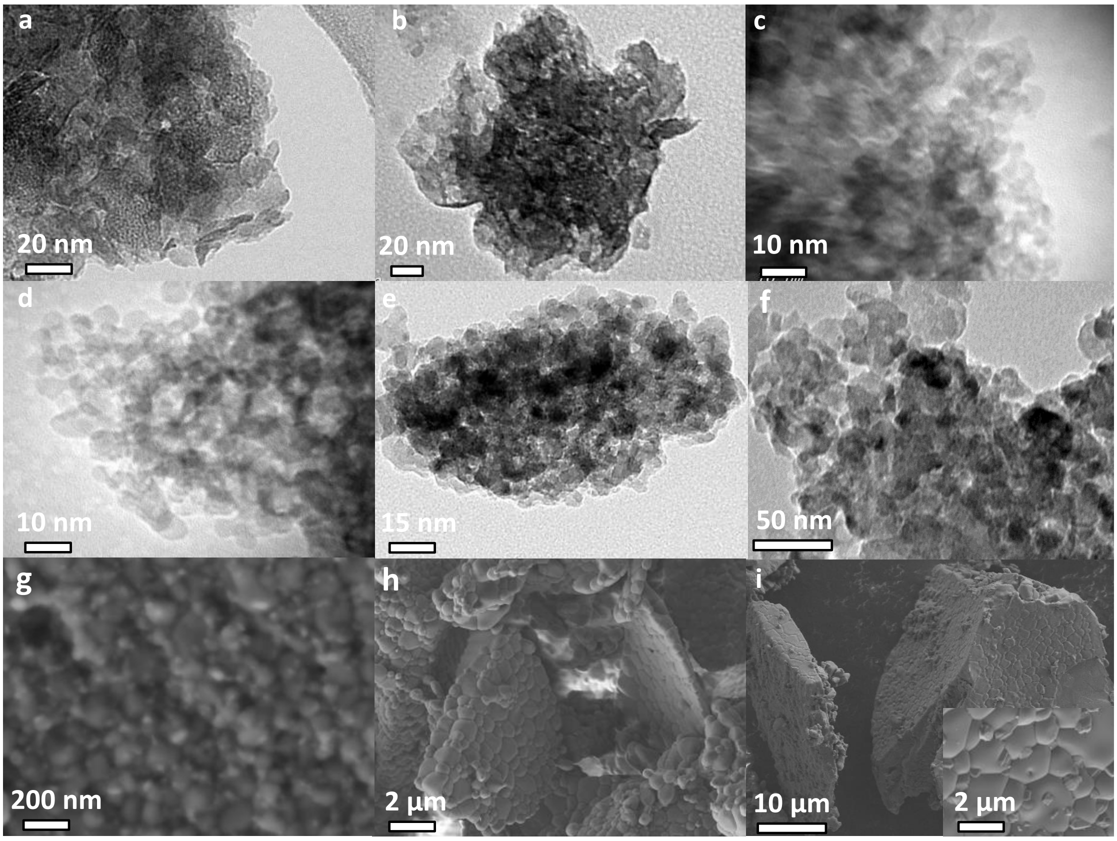

Figure 3.3: Micrographs of polyol synthesized sample with reference synthesis conditions a) before calcination, and after calcination for 1 h at b) 250°C, c) 500°C, d) 800°C, e) 900°C, f) 1000°C, g) 1200°C, h) 1400°C and i) 1600°C

After calcination at **250°C** (*Figure 3.3.b*) the secondary particles are still **dense agglomerates** of hundreds of nm, but constituent crystallites are much harder to distinguish, as $Al(OH)_3$ has decomposed into very small **η-Al_2O_3 rather spherical crystallites** (*Figure 3.2.a*). However, sheet-like LDH crystallites can still be distinguished. The **intermediate phase** obtained with calcination at **500°C** (*Figure 3.3.c*) consists of very **homogeneous ~5 nm spherical crystallites**, which confirms that when the LDH is decomposed, the freed Mg^{2+} and Al^{3+} cations incorporate the pre-existing η-Al_2O_3 crystallites which keep their shape. When the spinel is well-crystallized at **800°C** (*Figure 3.3.d*), the **spherical crystallites** have now a homogeneous size of ~7 nm. As the calcination temperature increases (*Figure 3.3.e-i*), CS increases as well, and the measured values are in good agreement with XRD refinements analysis, confirming that the apparent grains in micrographs are monocrystalline. For calcination at 1400°C and 1600°C (*Figure 3.3.h-i*), coarsening of the primary particles occurs resulting in faceted large grains. Furthermore, the stone-shaped morphology of the secondary particles remains through thermal treatment, with some few-µm-thick sheets of aggregated MAS crystallites remaining from the layered hydroxides structure. This persistent morphology may prevent full densification during sintering, thus a milling step prior to the calcination may enhance the sinterability of the powder. On *Figure 3.3.i* smaller grains can be observed at triple junctions of the main grains, and are believed to be MgO phase from recrystallization, as observed in XRD pattern (*Figure 3.2.a*).

Spectroscopic techniques have been used to further characterize the synthesized material, in order to clearly identify its composition prior to calcination and detect undesired contamination. FTIR and Raman spectra are presented in *Figure 3.4*.

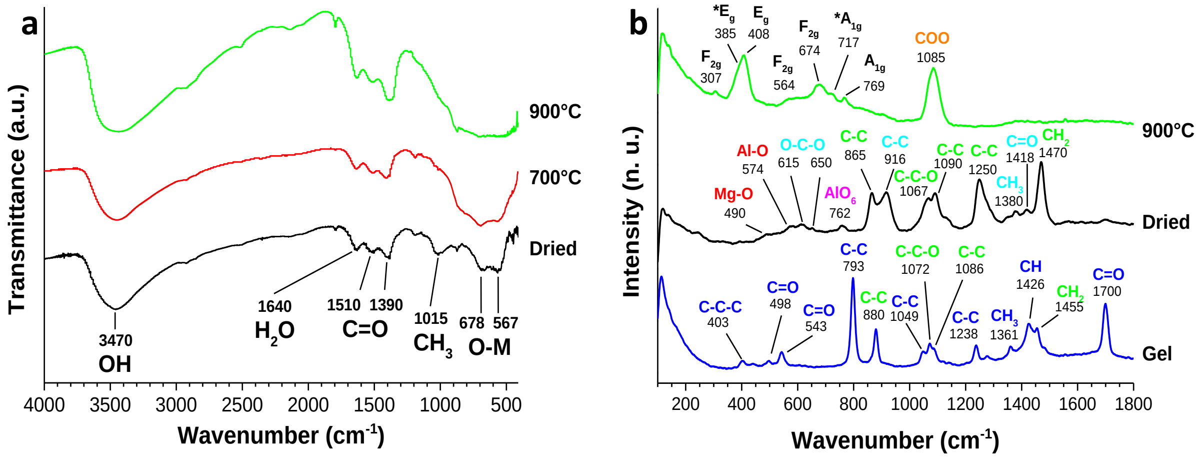

*Figure 3.4: a) FTIR and b) Raman spectra of polyol synthesized material with reference synthesis conditions before and after calcination. Raman modes are assigned in dark blue for acetone, green for ethylene glycol, light blue for acetate, red for LDH, pink for Al(OH)$_3$, black for spinel and orange for carbonates; spinel modes marked with * arises from antisites*

Infra-red analysis (*Figure 3.4.a*) of uncalcined powder reveals the presence of a broad and asymmetrical absorbance band centered at 3470 cm^{-1} from the stretching vibrations of OH^- and H_2O groups, always observed in hydroxides [320], and the band at 1640 cm^{-1} is attributed to the bending mode of the water molecule [322]. The bands at < 900 cm^{-1} are assigned to the stretching modes of **Mg-O** and **Al-O**, in agreement with literature on LDH [322]. The absorption at 1510 cm^{-1} and 1390 cm^{-1} belongs to the antisymmetric and symmetric stretching of **COO group** [319], and the one at 1015 cm^{-1} is characteristic of **CH_3** [167], indicating the intercalation of species containing COO and CH_3 groups. Solely the acetate anion possesses both attributes, thus FTIR analysis tends to indicate the **intercalation of CH_3COO^-** in the LDH gallery. However, the intercalation of both acetate and EG species cannot be excluded by this spectrum. According to Nakamoto rules, $\Delta\nu = \nu_{asym} - \nu_{sym} = 120\ cm^{-1}$ indicates a **bidentate chelating carboxylate** structure with delocalization of the π-bond such as $O\overset{\cdots}{-}C\overset{\cdots}{-}O$, since the value is significantly less than prior reported ones for monodentate carboxylate (~220 cm^{-1}) [320] or ionic carboxylate (~164 cm^{-1}) [323]. This stronger bonding could explain the d_{003} lower than previously observed for monodentate acetate [143].

After formation of the intermediate structure (700°C) or spinel phase (900°C), the FTIR spectra are not greatly impacted. Absorption bands at 3470 cm^{-1} and 1640 cm^{-1} are still observed, hinting of a high quantity of physisorbed H_2O in the powder, and COO^- signature is also still present. However, the peak at 1390 cm^{-1} is more intense after decomposition of the hydroxides, and the CH_3 signature (1015 cm^{-1}) is not observed anymore. It can be inferred that the intercalated bidentate specie has been decomposed to **bidentate carbonate**, explaining the absence of methyl group and the remaining of COO in the material, with a marked 1390 cm^{-1} absorption, very often sole observed band for CO_3^{2-} [321]. The remaining of carbonates (and water) in such proportion after calcination is peculiar, as it should normally be evacuated when vaporized. It can be suggested that the dense and large aggregates (stone-like morphology) do not allow the full evacuation of the species vaporized within their volume. Therefore, the **volatile impurities are entrapped into the aggregates**. Similar results were obtained in [94] after thermal decomposition of coprecipitated hydroxide mixture, and the same conclusion was made. It is to be noted that O-M vibrations < 900 cm^{-1} become less defined after heat treatment, which is to be attributed to structural disorder in the oxide, most probably from antisite defects.

Raman spectrum (*Figure 3.4.b*) carried out on the gel obtained after the washing step mostly exhibits the signature of acetone (modes assigned in dark blue) [324], rendering the characterization of the material difficult. The other visible peaks are to be attributed to **ethylene glycol** [325] (assigned in green), indicating the remaining presence of the polyol medium despite thorough washing. After drying, acetone modes were not observed, while EG modes were still present and somehow shifted from initial position in the gel, together with other Raman modes. The main new modes detected belong to the **acetate signature** [176, 320] (assigned in light blue). Some bands of very small intensity are observed for Raman shifts < 800 cm^{-1}, that we assign to **Al-O** and **Mg-O** vibrations in LDH sheets [326] (490 cm^{-1} and 574 cm^{-1}, respectively; indicated in red) and to **AlO_6 groups** in $Al(OH)_3$ structure (762 cm^{-1}; indicated in pink). These results confirm the intercalation of acetate anions in the interlayer space of the LDH. The remaining presence of EG after drying could indicate either its adsorption on the particles (high temperature of evaporation) or the insertion of a glycol specie, for a **mixed intercalation of CH_3COO^- and EG/EG$^{-/2-}$**. Both hypotheses would be in agreement with FTIR. After heat treatment at 900°C, the spinel fingerprint is well identified [52] (Raman modes assigned in black), with modes arising from **antisite defects** (*E_g at 385 cm^{-1} and *A_{1g} at 717 cm^{-1}). At 1085 cm^{-1}, a very intense peak is observed (assigned in orange), and is attributed to **CO_3^{2-}** vibrations [326], coming from decomposition of the intercalated species, in agreement with FTIR (*Figure 3.4.a*).

Lastly, X-ray photoelectron spectrometry (XPS) has been carried out on the powders (*Figure 3.5*) for surface chemical analysis. The survey spectrum reveals the presence of magnesium, aluminum, oxygen and carbon, which is very consistent with the analysis of commercial powders (see *Figure 2.4*) and literature on analysis of LDH and $MgAl_2O_4$ [123, 139, 311]. Since FTIR and Raman spectroscopies could not provide information on this point, it can be noted that **no chloride has been introduced** in synthesized powder as interlayered anions in particular, even if $AlCl_3 \cdot 6H_2O$ and $MgCl_2 \cdot 6H_2O$ were used as precursors. As intended, Cl^- probably reacted with Na^+ and precipitated as NaCl, thereafter washed prior to the calcination.

Al2p and Mg1s spectra show unique peaks with no strong modification after calcination, only a small spreading is noted especially for Mg1s (*Figure 3.5.c*), which could be due to larger distribution of bonding energy because of the cationic inversion revealed by Raman spectroscopy. It is interesting to observe that the O1s peak (*Figure 3.5.d*) before calcination is the convolution of at least two signals O_A (531.2 eV) and O_B (531.7 eV), respectively attributed to **O bonded to Al/Mg** and **O within OH^- and CO^-/COO^- groups** [312, 322]. After spinelization, only O_A is still observed, confirming the decomposition of hydroxides and intercalated species. The spectra from C1s (*Figure 3.5.e*) are split into characteristic signals C_A (284.8 eV), C_B (286.1 eV) and C_C (289.1 eV), corresponding to **C-C**, **CH_3**, and **C-O bonding**, respectively [312, 313]. C_A and C_C are often observed as adventitious carbon contamination, hence they should be considered with cautiousness. However, it is remarkable that the uncalcined sample has greater intensities for C_A and Cc, and even more for C_B than after treatment, hinting that the content in CO/COO bearing species is decreased. It is indeed in good agreement with the decomposition of the intercalated anions. It should be underlined that by contrast with FTIR and Raman spectroscopies, XPS analysis **does not indicate the remaining of carbonates** after heat treatment, suggesting once again that the calcination only allows removal of volatile species located at the surface of particles, while the ones located in bulk remain entrapped.

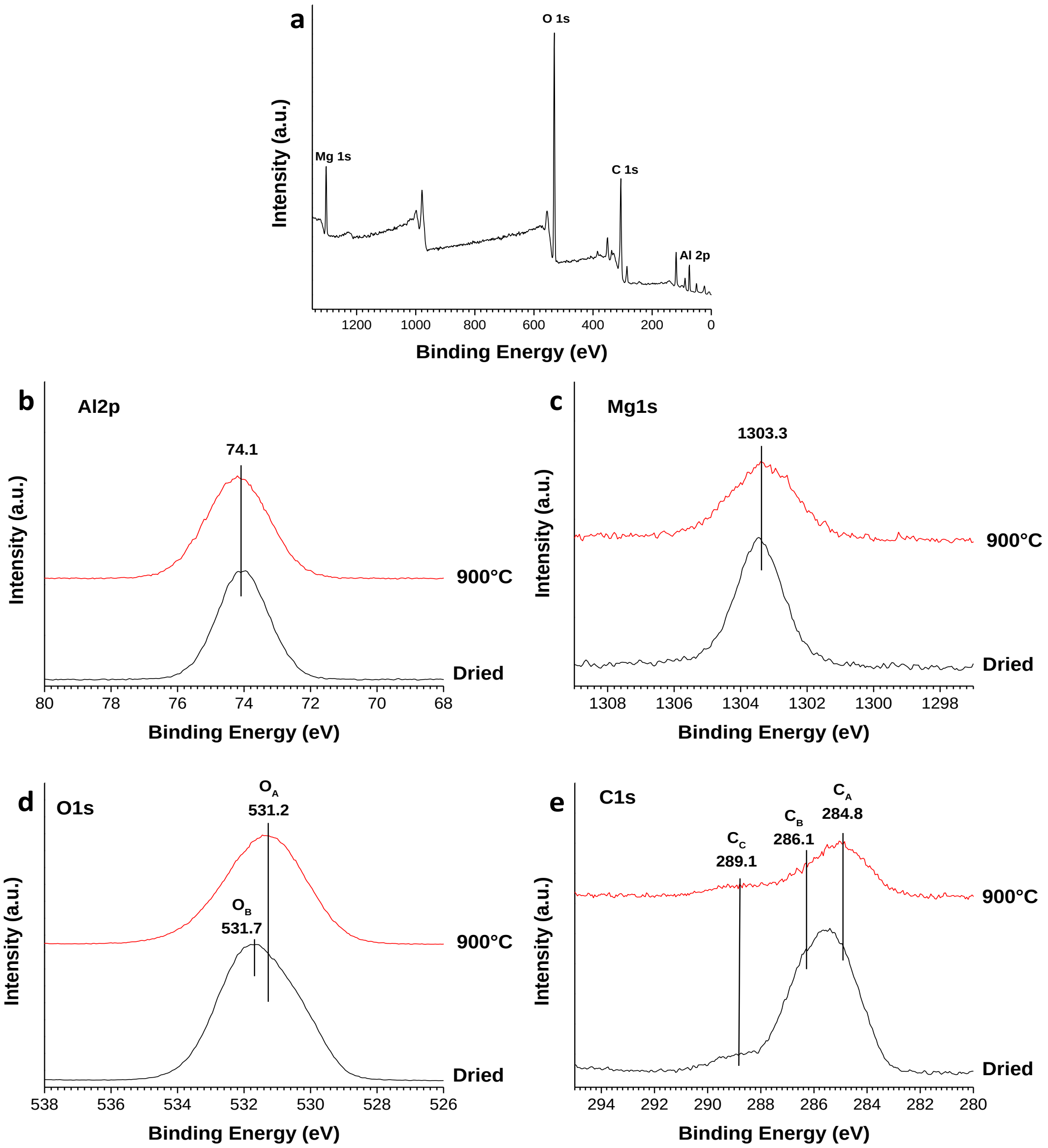

Figure 3.5: a) XPS survey spectrum of polyol as-synthesized material with reference synthesis conditions, and XPS spectra for the samples as-synthesized and calcined at 900°C in the range of b) Al2p, c) Mg1s, d) O1s, and e) C1s

From these characterizations and since no clear speciation could be made between acetate and glycolate intercalated anions, **mixed intercalation** was assumed, and the composition of the synthesized hydroxides mixture is assessed to be:

$$0.5\ [Mg_{0.667}Al_{0.333}(OH)_2][(CH_3COO^-/HOCH_2CH_2O^-)_{0.333}\cdot 0.75H_2O] + 0.5\ \alpha\text{-}Al(OH)_3$$

The low interlayer spacing of ~7.60 Å is small for such anions to be intercalated, but it is doubdtfull that CO_3^{2-} has integrated the interlayer galleries due to its neutralization by the acidic polyol [167]. We suggest that the organic anion intercalated may be integrated in an almost **flat position parallel to the layers**, which would greatly decrease the interlayer spacing, as was previously reported for dies-intercalated LDH [327–329]. In [329] in particular, the interlayer spacing drastically decreased from 23.7 Å (dye molecule perpendicularly oriented to the brucite sheets) to 8.28 Å (dye molecule parallelly oriented to the sheets).

2. Comparison with synthesis in water

The synthesis in polyol medium of both $M^{II}M^{III}_2O_4$ spinel and LDH-type1 material have been reported to present great interest in comparison with sol-gel synthesis in water [117, 164, 167]. However, the reference polyol synthesis conditions (*Section I.1*) could not provide $MgAl_2O_4$ phase directly and required a subsequent thermal treatment, decreasing the interest of the polyol route. Moreover, it was found that the as-synthesized mixed hydroxides phases composition was rigorously identical to the ones produced by coprecipitation in water from Mg and Al nitrates mixture by NH_4OH [93]. Then, it is legitimate to ask ourselves: is there any added interest in synthesizing our precursor hydroxides in polyol rather than in water? In this section, we will try to bring response to this interrogation, first by comparison with a classic **basic coprecipitation in water**, and later using the **reference polyol synthesis conditions with deionized water** replacing the polyol medium in order to go through a similar reaction mechanism involving acetate.

i. Reaction with NaOH (coprecipitation)

For the synthesis of a hydroxides mixture in deionized water, we changed as little as possible the synthesis conditions from the reference ones described in *Table 3.1*. Indeed, the solvent is deionized water, the precipitating agent is NaOH and the synthesis temperature is either 20°C or 100°C (reflux), as indicated.

As a preliminary study, we carried out pH assays of $AlCl_3$ and $MgCl_2$ solutions by 0.250 M NaOH (*Figure 3.6*). For **sole $AlCl_3$** (*Figure 3.6.a*), the initial solution is very acid (pH = 2.5) and **two pH jumps** are observed at pH = 7.4 and 11.5, indicating three areas of predominance: for **pH < 4**, only the **ionic form Al^{3+}** is present, for **4 ≤ pH ≤ 10.4**, **$Al(OH)_3$ precipitates** and the solution turns opaque white, then at **pH ~11**, it progressively becomes clear again until pH = 12.5 as $Al(OH)_3$ is further hydroxylated into **$Al(OH)_4^-$**. For **sole $MgCl_2$** (*Figure 3.6.b*), the solution is slightly acid (pH = 4.8) and becomes basic (pH ≈ 10.5) after the first drops of NaOH, due to the weak acid properties of Mg^{2+}. Only **one pH jump at pH = 11.7** occurs as Mg^{2+} precipitates into **$Mg(OH)_2$**. Since its precipitation occurs at the same pH than $Al(OH)_3$ dissolution, their simultaneous coprecipitation is difficult. The pH assay of **mixed Mg^{2+}-Al^{3+}** (*Figure 3.6.c*) shows a similar trend than sole $AlCl_3$: initial pH = 2.5 fixed by Al^{3+}, and two pH jumps at pH = 6.2 and 11.4. The second pH jump at pH = 11.4 does not seem to be impacted by the simultaneous presence of Al^{3+} and Mg^{2+}, but the first jump occurs at lower pH than for pure Al^{3+}. In fact, $Al(OH)_3$ starts to precipitate at pH = 4 while magnesium is still in ionic form, but is fully precipitated at pH = 9 instead of 10.4. The pH increases slowly in the area of the synthesis conditions (hydroxyl ratio *oh* = 2.67, analogous to the acetate ratio *r*), then for pH > 9.5 it increases rapidly to pH = 13 as $Al(OH)_3$ is dissolved into $Al(OH)_4^-$. Between the pH jumps, in the area of synthesis conditions, we assume the difference in pH evolution compared to sole Al^{3+} pH assay is caused by the **coprecipitation of the LDH**, either from the already formed $Al(OH)_3$ or from the non-yet hydroxylated Al^{3+} fraction. When $Al(OH)_3$ is later dissolved, the LDH phase is notaffected and the solution remains white. Finally, we carried out a pH assay of the precedent solution (LDH and $Al(OH)_4^-$) by a citric acid solution at 0.250 M, in order to assess the LDH resistance to acid (*Figure 3.6.d*). Only one slow pH drop is observed for pH ≈ 7.8 from the progressive LDH dissolution, as it does not tolerate acid conditions, and $Al(OH)_3$ did not precipitate back possibly due to a different kinetic of precipitation from $Al(OH)_4^-$.

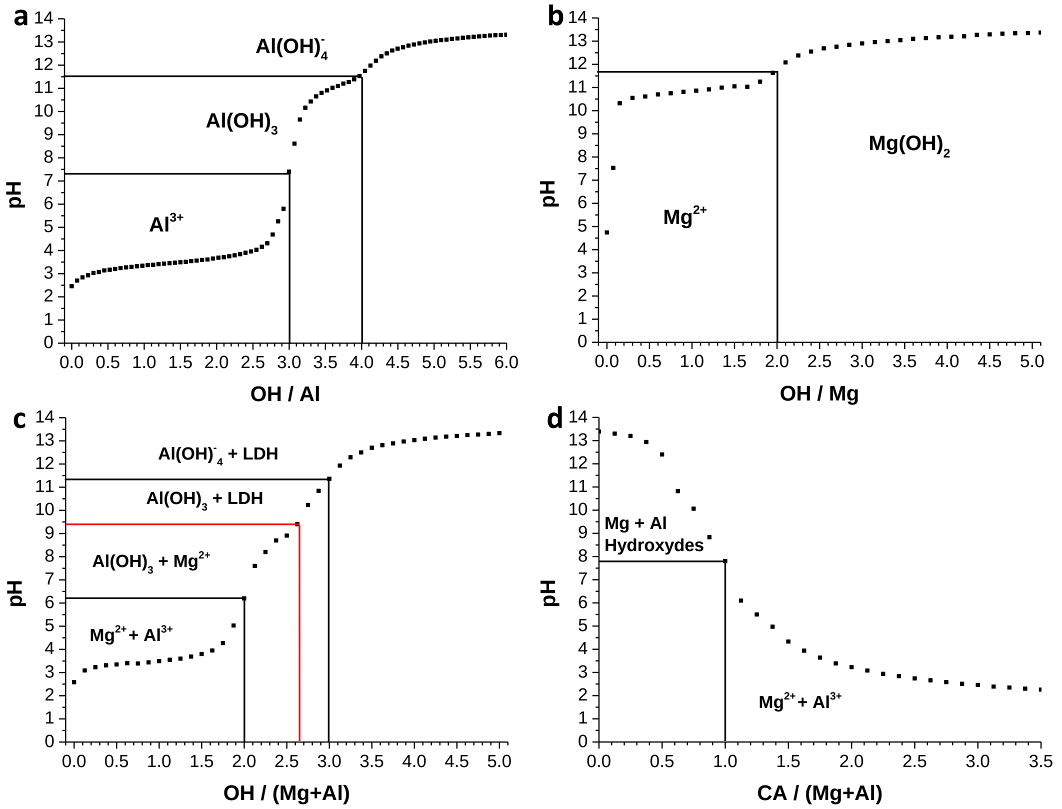

Figure 3.6: pH assays of a) $AlCl_3$ (0.0667 M), b) $MgCl_2$ (0.0333 M) and c) (Al+Mg) chloride mixture in water by a 0.250 M NaOH solution; d) pH assay of the dissolution of (Mg + Al) hydroxides obtained in c) by a 0.250 M citric acid CA solution. Black lines delimitate predominance areas and red lines indicate synthesis conditions

The *Figure 3.7* presents the XRD patterns of the samples synthesized by coprecipitation in water. As shown in *Figure 3.7.a*, after precipitation at **room temperature**, the powder is composed by **LDH and gibbsite** $Al(OH)_3$, as for synthesis with reference conditions in polyol (*Figure 3.1.a*). When the solution is heated to 100°C after the hydroxides formation, the LDH exhibits no change of lattice thus composition (same peaks positions) but a better crystallinity (sharper peaks). The intercalated anion is most probably CO_3^{2-} from atmospheric CO_2 dissolution, as it is common in basic aqueous solution. More importantly, $Al(OH)_3$ has been converted to **oxyhydroxide boehmite AlOOH**, which normally occurs in hydrothermal conditions, but can be assumed to be due to the same dissolution-precipitation mechanism [330]. However, after calcination at 800°C for 1 h, similar spinel structures (cell parameter, stoichiometry and crystallite size) are obtained, and do not differ from the results obtained for synthesis *via* polyol route (*Figure 3.2.a*).

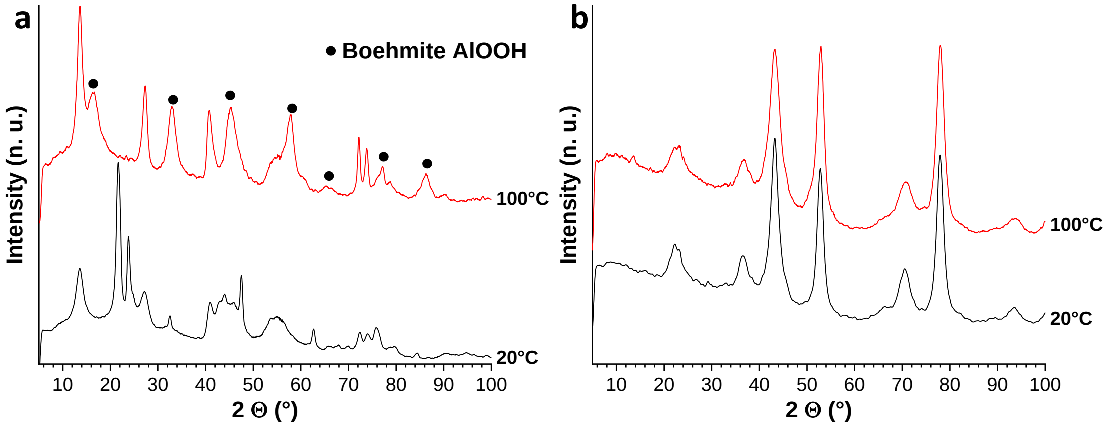

Figure 3.7: XRD of the samples synthesized in H_2O with NaOH at 20°C and 100°C: a) before and b) after calcination at 800°C

The DT-DTG analysis of the coprecipitated powders is presented in *Figure 3.8*. No sensible variation of the thermal decomposition is observed compared to the reference sample synthesized in polyol, except for a slight shift toward high temperature of the first phenomenon (270°C vs 250°C) for the sample synthesized at 100°C, since it consists in the decomposition of AlOOH instead of $Al(OH)_3$. This emphasizes that the **chemical/phase composition dictates the decomposition mechanisms**, regardless of the synthesis route.

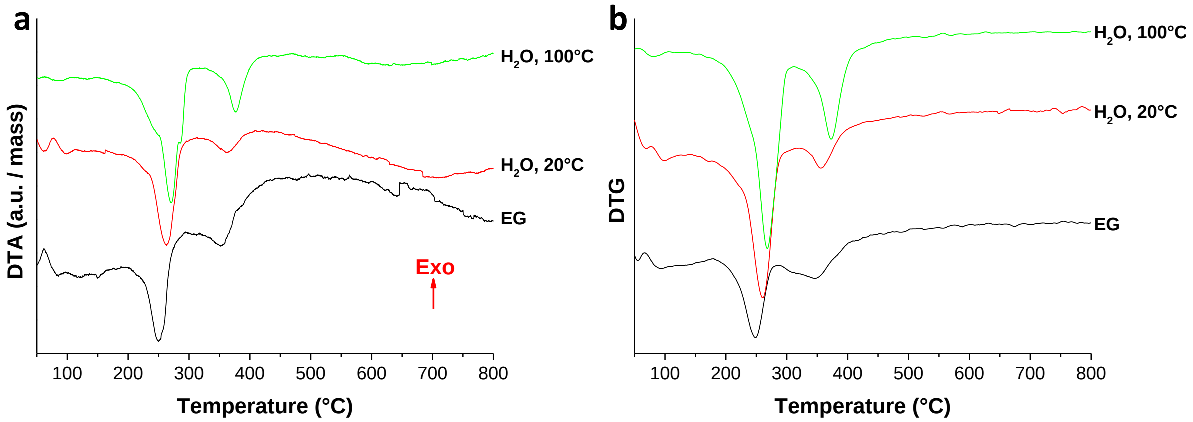

Figure 3.8: a) DT and b) DTG analysis of materials synthesized by coprecipitation in water at different synthesis temperature

The microstructure of the samples obtained by coprecipitation in water after calcination at 800°C for 1 h is shown in *Figure 3.9*. The spinel obtained from sample synthesized at **20°C** (*Figure 3.9.a*) shows particles with **large distribution of size and shape**, namely spherical crystallites aggregated in particles of hundreds of nanometers, short rod-like particles (10 nm x 50 nm) and thinner needle-like/platelets particles (clear distinction could not be made). On the other hand, the sample synthesized at **100°C** (*Figure 3.9.b*) is composed mostly by **highly agglomerated thin platelets/needles**. The anisotropic morphology of these particles is to be attributed to remaining morphology of the initial hydroxides. Such microstructures are non-ideal for sintering as poor packing and local differentiate densification should be expected.

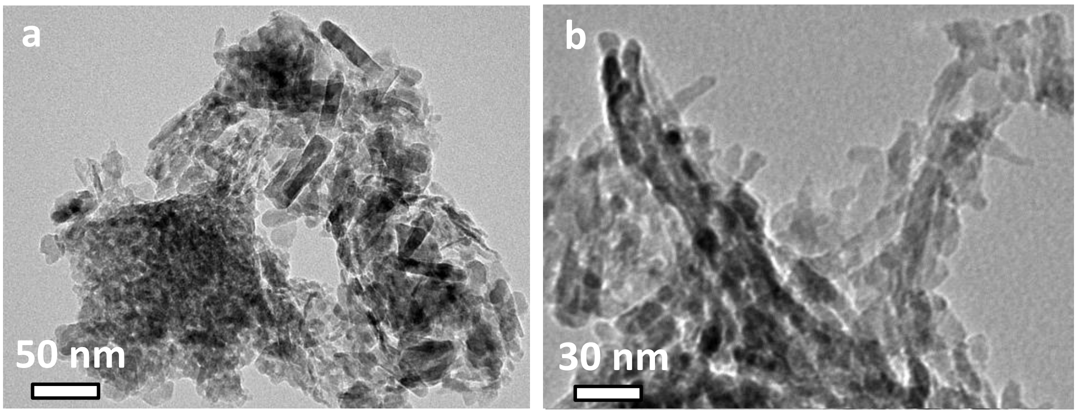

Figure 3.9: TEM of the 800°C heat treated samples coprecipitated in water at temperature of a) 20°C and b) 100°C

ii. Reaction with $NaCH_3COO$

In this paragraph, the synthesis has been carried out with the reference conditions, except for deionized water replacing EG as the solvent. No precipitation was observed until boiling point at 100°C was reached.

The XRD patterns of the sample as-synthesized and calcined at 800°C for 1 h are presented in *Figure 3.10.a*. The as-synthesized powder is highly crystalline and consists mostly of basic aluminum acetate $Al(OH)(CH_3COO)_2$ [331], with the very sharp reflections indicating large crystallites of several hundreds of nanometers in agreement with SEM (not shown) revealing non-aglomerated spherical particles of 100 – 200 nm. However, some XRD reflections do not arise from $Al(OH)(CH_3COO)_2$, and it is inferred that they may belong to the XRD pattern of the dibasic aluminum acetate $Al(OH)_2(CH_3COO)$ since the rather low acetate concentration is favorable for its formation [332]; unfortunately, no reference XRD pattern for this compound could be found in literature. After calcination at **800°C**, the as-synthesized compound decomposed to the **defective spinel phase γ-Al_2O_3**, with no or negligible magnesium content. Hence, the **as-synthesized compound contains only Al^{3+} cation**, hinting that only Al^{3+} is able to react directly through the acetate-related mechanism, and confirming that both as-synthesized phases are aluminum-based.

The pH assay of the Mg-Al cationic mixture by CH_3COO^- was carried out (*Figure 3.10.b*) in order to assess the mechanism of reation, and in particular to verify that it is not merely a coprecipitation in slightly acid solution. As expected, no amount of added CH_3COO^- could lead to $pH > 5$, and **no pH jump or precipitation** at room temperature was observed. It appears that in the aqueous medium, the synthesis of $Al(OH)(CH_3COO)_2$ occurred *via* reaction of the solubilized aluminum chloride and sodium acetate, with the exchange of the anions within the respective cations' coordinating spheres, such as detailed in *Equation 3.1*. Meanwhile, the solubilized Mg^{2+} did not react and staid in solution.

$$\boldsymbol{AlCl_3}_{\,(aq)} + \boldsymbol{NaCH_3COO}_{\,(aq)} \rightarrow \boldsymbol{Al(OH)(CH_3COO)_2}_{\,(s)} + \boldsymbol{NaCl}_{\,(aq)} \qquad \textit{Equation 3.1}$$

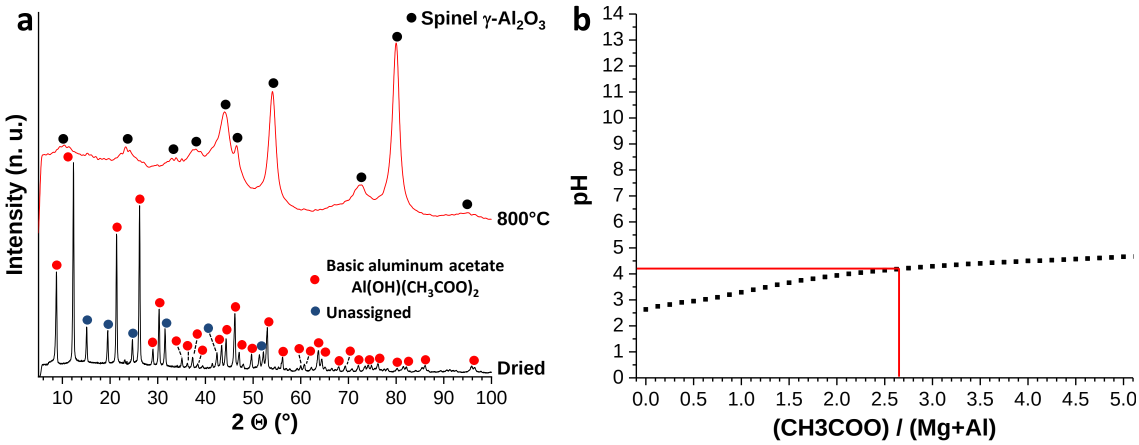

Figure 3.10: a) XRD patterns of the sample synthesized in water with $NaCH_3COO$ before and after calcination at 800°C and b) pH assay of the Al^{3+} and Mg^{2+} mixture by $NaCH_3COO$ (0.250M); red lines indicate synthesis conditions

In comparison with the results presented in this section, we can discuss the synthesis mechanism for the reference synthesis conditions in polyol medium. In a **first step**, similarly to what is observed for the synthesis in water (*Equation 3.1*), it is believed that the solubilized Al^{3+} reacts with both acetate and polyol species to form an **alkoxyacetate intermediate**. In a **second step**, the solubilized Mg^{2+} reacts with the intermediate, possibly **catalyzing the lysis of the CH_3COO^- group**, in agreement with the mechanism proposed by Prévot *et al.* for LDH synthesis in polyol [167]. Therefore, the polyol medium is essential in this synthesis mechanism for the reaction of both Al^{3+} and Mg^{2+}, allowing the elaboration of a precursor for $MgAl_2O_4$ nanopowder.

In comparison, the basic coprecipitation in water provided small MAS crystallites, but with particles of various shapes and sizes inadequate for subsequent sintering. For the sake of comparison, coprecipitation in EG will be carried out and presented in *section I.4.iii*.

3. Influence of the temperature of synthesis

During the synthesis with reference conditions in EG, several distinctive phenomena are observed: the **solution turns white at 120°C** and **foam is formed at 165°C**. In order to understand the structural and compositional evolution of the powder with the temperature, and correlate them to the mechanism of reaction, syntheses were carried out at 120°C and 165°C for 2 h. It should be noted that the sample synthesized at 120°C was soluble in water prior to thermal treatment.

The *Figure 3.11* presents the XRD patterns of the samples synthesized in EG at different temperatures. Before calcination (*Figure 3.11.a*), the sample synthesized at **120°C** (**first stage of reaction**) is **amorphous**, as indicated by the broad peaks (intensity is not relevant since patterns were normalized). When synthesis temperature is raised to the stage of **foaming at 165°C**, the diffractogram only reveals the presence of **gibbsite $Al(OH)_3$** with broader reflections than for the 185°C synthesis indicating smaller crystallites, and no LDH is observed. After calcination at 800°C for 1 h (*Figure 3.11.b*), the **120°C-compound** decomposes to **γ-Al_2O_3 with no or negligible Mg^{2+} insertion**, while the **165°C-product** decomposes to **MAS with slight MgO deficiency**, noticeable by a smaller cell parameter (peaks shift toward higher angles, *cf. Chapter 1.I.2*). It is remarkable that while no phase containing magnesium is observed before calcination, MAS with composition close to stoichiometry is obtained afterward. It can be deduced that an **amorphous phase containing a Mg^{2+} moiety exists along $Al(OH)_3$ at 165°C**. Based on the evolution of the composition, we assume that the **Al^{3+}-containing amorphous compound** formed at 120°C **progressively reacts with the Mg^{2+} solute** with increasing temperature, the latter being integrated within the amorphous material, until **$Al(OH)_3$ is crystallized out of it at 165°C** in a foaming process. The remaining amorphous structure then continues to react with and to incorporate the Mg^{2+} solute left, until it **crystallizes as LDH-type1 at 185°C**.

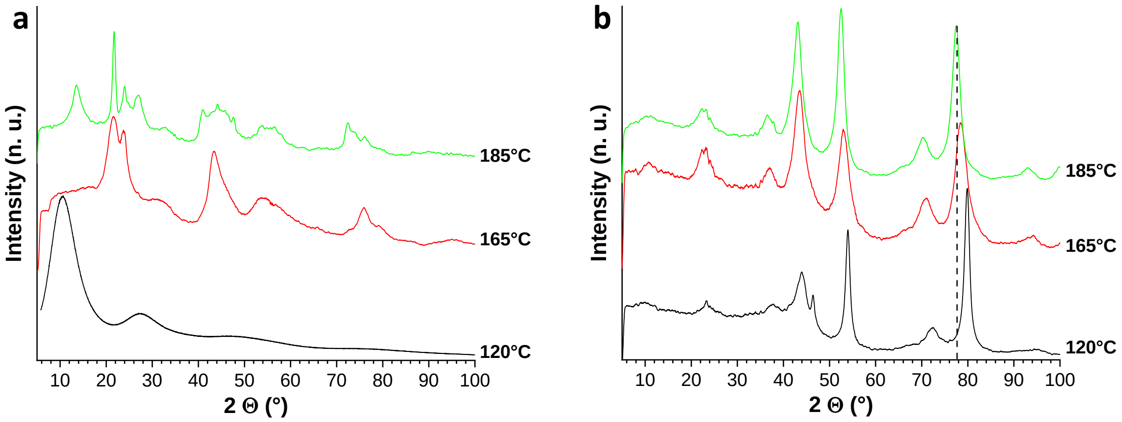

Figure 3.11: XRD patterns of the samples synthesized at different synthesis temperature a) before and b) after calcination at 800°C

The DT-DTG analysis of the sample synthesized at 120°C is presented in *Figure 3.12*. Its decomposition occurs in **two successive steps at 320°C and 380°C** for a total mass loss of 65%, the former being slightly endothermic. This high mass loss at T > 300°C excludes the possibility of $Al(OH)_3$ decomposition, which would have led to a loss of ~35%. Instead, we can assume that the synthesized material is **an aluminum hydroxyacetate**, first **losing its hydroxyl groups between 200°C and 270°C**, causing shouldering in the low temperature range of the 320°C-DTG peak. Then, the **acetate groups decompose to carbonate at 320°C**, then to **CO_2 at 380°C**. Such a thermal decomposition mechanism was proposed by Sato [333], who noted the almost athermic decomposition of CO_3^{2-} under inert gas. Based on the 65% mass loss, the OH^- moiety should be ~1.4, hence the compound obtained at 120°C would exhibit the intermediate composition $Al(CH_3COO)_{1.6}(OH)_{1.4}$. Nevertheless, neither basic nor dibasic aluminum acetates are soluble in water contrarily to the prepared compound, and implication of the polyol medium within the reaction mechanism and composition has to be considered. Hence, the formation of an **aluminum alkoxide Al-EG** or an **aluminum alkoxyacetate Al-EgAc** is assumed, based on previous report on Co-EG [175]. Further characterizations are required to thoroughly elucidate the intermediate amorphous structure.

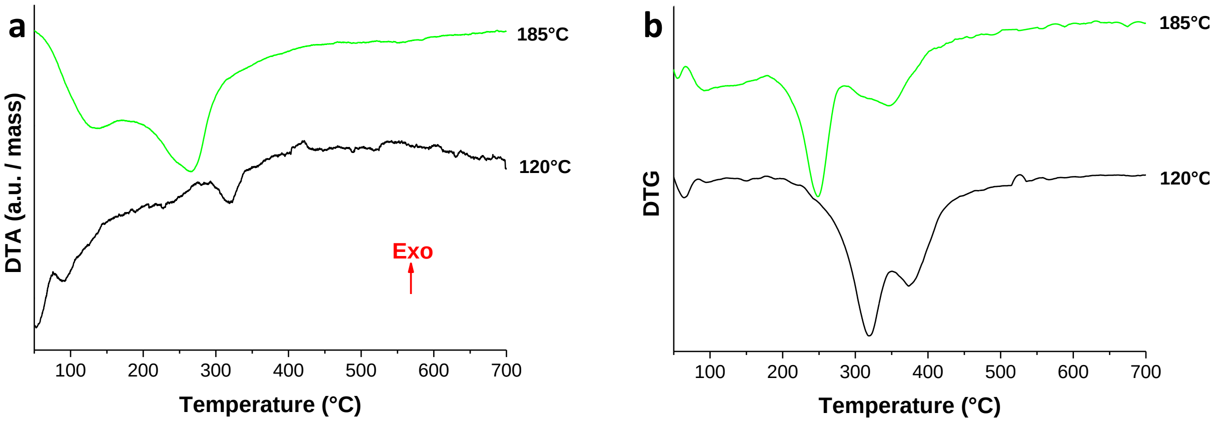

Figure 3.12: a) DTA and b) DTG analysis of materials synthesized in polyol at different synthesis temperature

The SEM of the samples obtained at 120°C and 165°C after calcination at 800°C are presented in *Figure 3.13*. The powder obtained with 120°C synthesis is composed by dense and agglomerated particles of size > 100 nm (*Figure 3.13.a*), while the one synthesized at 165°C consists of homogeneous crystallites with very small size < 10 nm agglomerated in large particles of hundreds of nm (*Figure 3.13.b*).

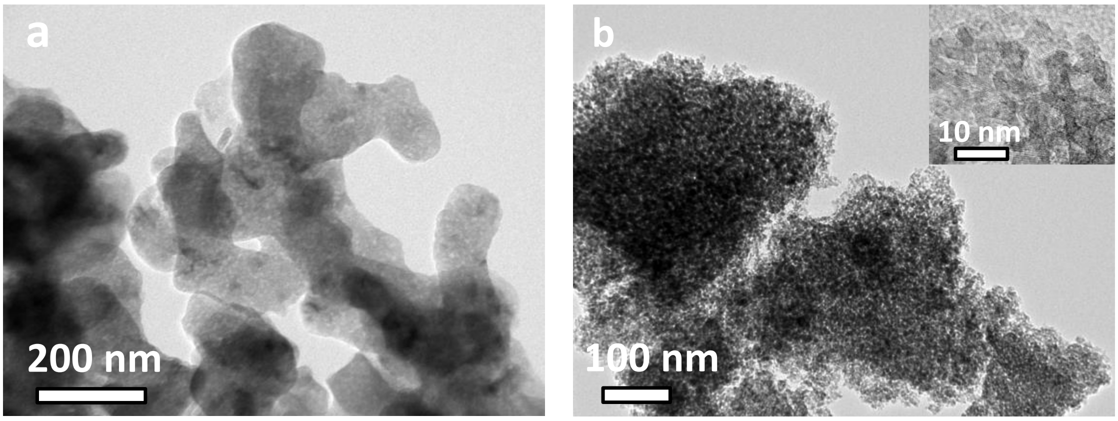

Figure 3.13: SEM of the calcined powder synthesized in polyol with synthesis temperature of a) 120°C and b) 165°C

From the results presented in this section, it can be concluded that the solute Al^{3+} and CH_3COO^-/EG react around 120°C to form an amorphous aluminum alkoxyacetate as a first reaction stage, similarly to what was previously observed for Co^{2+} reaction mechanism [175]. At higher temperature, the Al-EgAc compound reacts with Mg^{2+} which is progressively integrated in the amorphous compound in a second stage of reaction. This stage possibly occurs through the lysis of the CH_3COO^- group catalyzed by Mg^{2+}, in agreement with the mechanism previously proposed by Prévot *et al.* for NiAl and CoAl LDH synthesis in EG and DEG [167]. Then, when the lysis rate is high enough at ~165°C, gibbsite $Al(OH)_3$ is precipitated out of the amorphous material (third stage), with intense foaming possibly due to highly exothermic reaction. Meanwhile, the amorphous Mg-Al mixed hydroxide/acetate continues to react with Mg^{2+} through the second stage mechanism, until its crystallization into LDH-type1 at 185°C, and the freed CH_3COO^- as intercalated anion.

4. Influence of the chemicals precursors and additives

The nature of the metallic cations salt precursors as well as the nature and amount of additives have been reported to be determinant in the synthesis mechanism in polyol medium, which controls the intermediate complexes and solid compounds nature, the oxidation state of the metals and the shape and size of the synthesized particles (*cf. Chapter 1.III.4.ii*). In this section, we investigate the nature of the cation salts and additive on the reaction mechanisms, and on the chemical and structural properties of the product.

i. Nature of the Mg^{2+} and Al^{3+} precursor salts

Three different types of Mg^{2+} and Al^{3+} salts were compared, namely chlorides, acetates and nitrates. Hydroxide precursors are sometimes used as insoluble cation reservoirs, but since the synthesized product with reference conditions is already a hydroxides mixture, it was found of low interest to use hydroxide salts.

The precursors used for the different synthesis performed in this study are detailed in *Table 3.2*, all other synthesis conditions being identical to reference conditions presented in *Table 3.1*. In the synthesis with acetate salts, we used basic aluminum acetate in order to bypass the first step of the reaction mechanism with reference conditions, and react directly from the insoluble acetate (magnesium acetate is soluble). No additive was used since CH_3COO^- is already introduced with cations in this case. Comparison with reference synthesis will help understand further the reaction mechanism. Nitrates precursors have been considered for oxide synthesis *in situ*, since NO_3^- anion is an oxidant, avoiding subsequent thermal treatment leading to crystallite growth and aggregation. $NaCH_3COO$ was not added for the nitrate synthesis to avoid competing mechanism with acetates oxidation by NO_3^-; sole reaction of EG with cations, then nitrates, was expected.

Table 3.2: Precursor salts used for the study of the influence of the chemical precursors nature in polyol medium

Nature of the chemical precursors	Mg^{2+} salt	Al^{3+} salt	Additive
Chloride salts - reference	$MgCl_2 \cdot 6H_2O$	$AlCl_3 \cdot 6H_2O$	$NaCH_3COO$
Acetate salts	$Mg(CH_3COO)_2 \cdot 4H_2O$	$Al(CH_3COO)_2OH \cdot 0.5H_2O$	-
Nitrate salts	$Mg(NO_3)_2 \cdot 6H_2O$	$Al(NO_3)_3 \cdot 9H_2O$	-

The XRD patterns of the compounds obtained with the different precursors are presented in *Figure 3.14*. Starting from **acetate salts** led to the formation of the same compounds than using chloride salts, as **gibbsite $Al(OH)_3$ and LDH-type1** reflections can be observed (*Figure 3.14.a*). However, for acetate salts, reflections are very broad and do not allow thorough analysis. Still, it is remarkable that the basal reflections of LDH phase corresponding to (003) at 13° and (006) at 26° are extinguished, revealing very high disorder in the layering. Using **nitrate salts** led to the formation of a compound of very low crystallinity, seemingly a $Al(OH)_3$-based layered structure **LDH-type2** [130]; pattern could not be further analyzed. After calcination at 800°C for 1 h, the compound synthesized with **acetate salts** was decomposed to **spinel** with identical structural feature than the synthesis with chloride salts, while the **nitrate salts** synthesis led to mostly **amorphous material**, with few distinguishable reflections from defective spinel γ-Al_2O_3 (*Figure 3.14.b*).

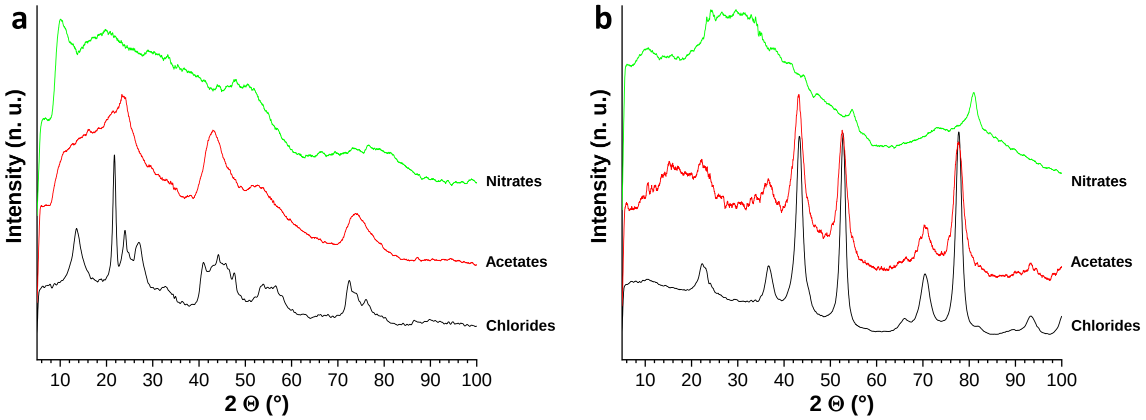

Figure 3.14: XRD patterns of the samples synthesized with different precursor's types a) before and b) after calcination at 800°C

The microstructure of the calcined powder synthesized with acetate salts is presented in *Figure 3.15*. It is composed by **~6 nm crystallites** (similar to reference synthesis), within few hundreds of nm to few µm spherical aggregates, hence less agglomerated with no stone-like particles, by contrast with reference.

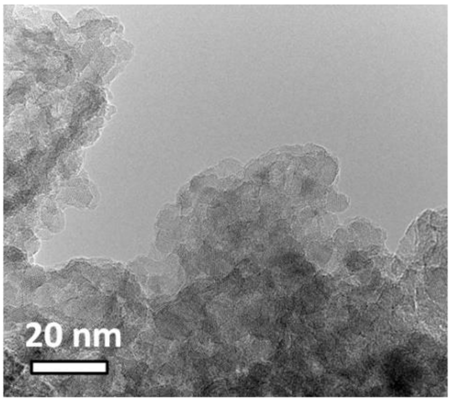

Figure 3.15: TEM of the calcined powder synthesized in polyol with acetate salts

From the presented results, it appears that acetate salts as precursors provides similar compounds than chloride salts with addition of acetate, which confirms the reaction mechanism proposed for reference synthesis conditions. It is believed that the noted discrepancies arise from the insolubility of the basic aluminum acetate. Indeed, it was observed in [167] that the **aluminum salt servs as a reservoir for Al^{3+}** for LDH synthesis, through **forced progressive dissolution** due to M^{2+} cations adsorption on the solid acetate, limiting the Al^{3+} concentration in polyol and the kinetic/reactivity. In contrast, when chlorides are used, a much more soluble **amorphous aluminum alkoxyacetate** is formed as intermediate, believed to be more reactive, thus causing a difference of kinetic and in term a different nucleation/growth mechanism. It could be interesting to further investigate the reaction mechanism using aluminum acetate and magnesium chloride salts, in order to observe the influence of the chloride specie on the reaction. It is also remarkable that nitrate salts could not lead to the synthesis of spinel, as it appears that **NO_3^{2-} interfers with the property of the polyol medium**, possibly by its oxidation into ketone or carboxylic acid.

ii. Use of $NaCH_3COO$ as additive - acetate ratio r

Starting from the chloride salts chemical precursors with the addition of $NaCH_3COO$, as for reference synthesis conditions, we investigated the role and the influence of the acetate addition through **variation of the acetate ratio *r*** from 0 to 5.34. All the other parameters remained unchanged for proper comparison.

Syntheses carried out with an acetate ratio ***r* < 1.85**, specifically *r* = 0, 0.94 and 1.34, led to **no reaction** in the polyol medium, *i.e.* a solution remaining transparent, no foam for T ≥ 165°C, and no powder after centrifugation. This demonstrates the **key role of CH_3COO^-** in the reaction mechanism *via* polyol route.

The XRD patterns of the compounds obtained with different acetate ratio are presented in *Figure 3.16*. For **1.85 < *r* < 2.67**, **poorly crystallized LDH-type2** is formed. After calcination, a **Al_2O_3-rich spinel** is obtained (shift toward high angles), confirming the $Al(OH)_3$-based nature of the prior LDH. For ***r* ≥ 2.67**, *i.e.* reference conditions, up to at least ***r* = 5.34**, **LDH-type1 and $Al(OH)_3$ gibbsite** are obtained. Hence, the **critical ratio r_c = 2.67** is required for precipitation of a mixture with a ratio **Al^{3+}/Mg^{2+}:2**. However, for the higher ratio ***r* = 5.34**, the reflections are much broader, especially for the LDH phase, and the basal reflections corresponding to (003) at 13° and (006) at 26° are almost extinguished, revealing **very high disorder in the layering**, as for the synthesis starting from acetate precursor salts. After thermal treatment at 900°C for 1 h, both *r* = 2.67 and 5.34 provided **stoichiometric $MgAl_2O_4$** with comparable crystallite size.

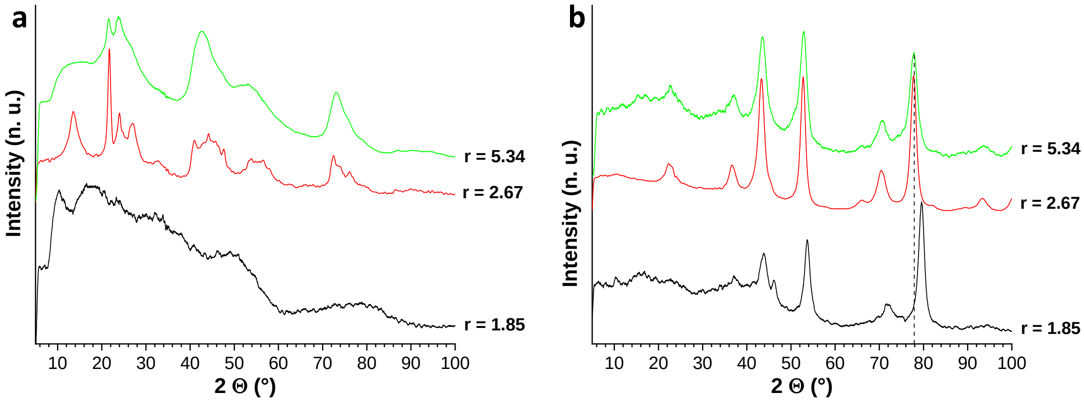

Figure 3.16: XRD patterns of the samples synthesized with different acetate ratio a) before and b) after calcination at 900°C

The microstructure of the calcined ***r* = 5.34** powder is presented in *Figure 3.17*. **Three types of primary particles** are observed: mainly **spherical crystallites** (*Figure 3.17.b*) similar to those obtained for *r* = 2.67, **~5 nm-nanorods** with length of tens of nm (*Figure 3.17.b*), and larger **~40 nm-rods** with length of hundreds of nm (*Figure 3.17.c*). High magnifications in *Figure 3.17.c* reveal that the rods are **single crystal with a (100) orientation**. However, the planes are strained, somehow bended locally, which may explains the small interplanar spacing d_{100} = ~6.80 Å instead of the expected ~8.08 Å. $MgAl_2O_4$ rod-shaped single crystals with (100) orientation have been produced before by single crystal growth techniques involving melting [334], and it was indeed mentioned that most often high strain and shift from stoichiometry are observed.

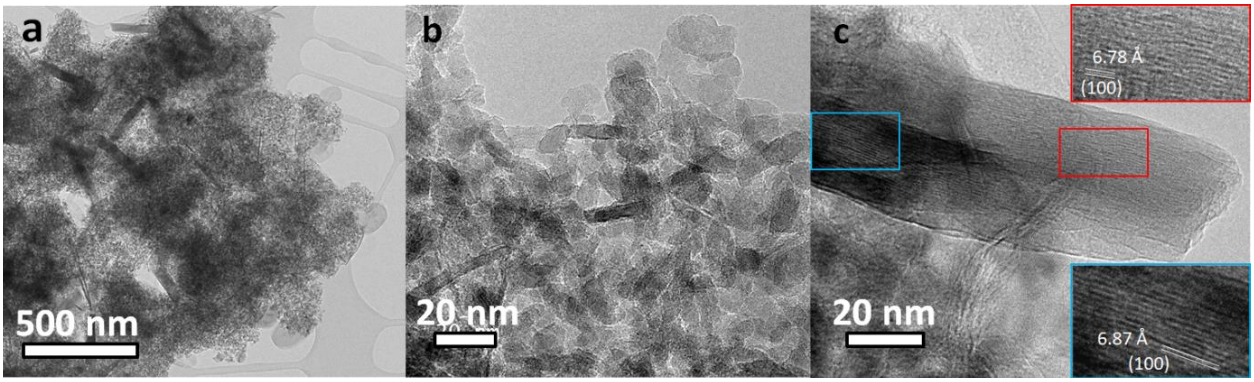

Figure 3.17: TEM of the calcined powder synthesized in polyol with acetate ratio r = 5.34, with a) general view, b) focus on small spherical crystallites and nanorods, and c) focus on a rod. Insets in c) show high magnifications of indicated areas.

From these results, CH_3COO^- ratio appears to **control the reactivity** and **crystallinity**. For $1.85 < r < r_c$, the formed compound is seemingly based on **$Al(OH)_3$ with $Al^{3+}/Mg^{2+} > 2$**, indicating the favored reaction of Al^{3+} with acetate/EG followed by the reaction of Mg^{2+} with the former intermediate, in agreement with the results from synthesis at 120°C (*Chapter 4.I.3*). We assume CH_3COO^- integrate the cations coordination spheres, with a **required threshold $1.34 < r < 1.85$** for the reaction to occur. **With increased acetate concentration**, Mg^{2+} reaction rates progressively increases and LDH-type2 converts to **LDH-type1 and gibbsite**. We explain it by a recrystallization, due to the **Mg^{2+} insertion rate exceeding the limit** in LDH-type2 at some point in the reaction, leading to the **exsolution of Al^{3+}** to form $Al(OH)_3$ and LDH-type1 with common and stable $x = 0.333$. Moreover, for **$r > r_c$** the additional CH_3COO^- may act as a surfactant, **refining and tailoring the crystallites**, as already observed in polyol [158]. It could be the cause for both the smaller LDH crystalites and the formation of rods. Further experiments will provide better understanding of the acetate role and assess the possibility to obtain pure rods/nanorods (*e.g.* with $r > 5.34$).

iii. Use of NaOH as additive - hydroxyl ratio oh

For the sake of comparison between the synthesis mechanisms, in this section we study the **synthesis of $MgAl_2O_4$ precursors *via* coprecipitation in polyol**, replacing $NaCH_3COO$ by NaOH as an additive. We also investigate the influence of the hydroxyl ratio **$oh = [OH^-]/[Mg^{2+} + Al^{3+}]$**, analogical to the acetate ratio *r*. Results obtained by coprecipitation in aqueous medium (*Chapter 4.I.2.i*) will serve as a second reference standard, to discuss the reaction mechanism. Lowest investigated ratio **$oh = 0.94$ led to precipitation**.

The influence of *oh* on the XRD patterns is presented in *Figure 3.18*. Interestingly, for **$oh = 0.94$**, *i.e.* insufficient OH^- to fully complex Al^{3+} and precipitate as $Al(OH)_3$, a compound with high crystallinity is formed while similar conditions in aqueous medium did not lead to precipitation. This pattern corresponds to the **ε-Al_{13} Keggin structure** compensated by Cl^- (ε-Al_{13} chloride). Such a material with a glycol-coordinated polyhydroxyoxoaluminum cluster $[AlO_4Al_{12}(OH)_{12}(O\text{-}CH_2\text{-}CH_2\text{-}OH)_{12}]^{7+}$ was synthesized for the first time in 2018 [335]. It is formed through **partial hydrolysis** of the aluminum salts, as the initial H_2O coordinating Al^{3+} lose a H^+ due to pH increase and the OH groups condensate, while glycolate chelates the 12 surrounding Al^{3+}. A thorough study of this material will be carried out in *Chapter 4.I.6.ii*. After calcination at 900°C, **ε-Al_{13} decomposes to pure γ-Al_2O_3**, confirming that no Mg^{2+} had reacted and integrated its structure.

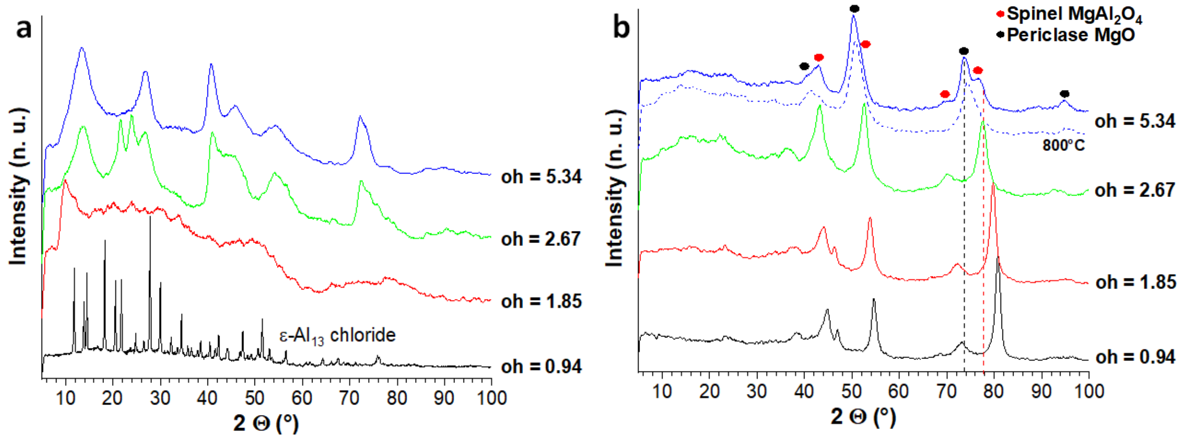

Figure 3.18: Evolution of the XRD patterns with hydroxyl ratio a) before and b) after calcination at 900°C unless stated otherwise. Red and black dotted lines are guide for the eyes to emphasize peaks shifts from $MgAl_2O_4$ spinel and MgO periclase, respectively.

For ***oh* = 1.84**, the material exhibits a **LDH-type2**'s XRD pattern similar to the one obtained for *r* = 1.84 (*Figure 3.16.a*). Indeed, this condition is close to $Al(OH)_3$ precipitation in water (*oh* ≈ 2, pH ≈ 4) and it is assumable that it occurs in EG as well with partial insertion of Mg^{2+} in the $Al(OH)_3$ layers. In agreement, **Al_2O_3-rich spinel** is obtained after calcination. For ***oh* = 2.67**, corresponding to pH ≈ 9.5 in water, **mixed LDH-type1 and gibbsite $Al(OH)_3$** are formed, as for coprecipitation in H_2O and reaction *via* acetate route in EG. However, the reflections of both phases and particularly LDH are much broader in this case, similarly to XRD patterns of *r* = 5.34 synthesis. After thermal treatment, **stoichiometric MAS** is obtained with crystallite size ~11 nm comparable to reference synthesis. Finally, for ***oh* = 5.34**, a **pure LDH-type1** is obtained, as these conditions correspond to *oh* ≥ 3 (pH = 13) in water with **$Al(OH)_3$ converting to $Al(OH)_4^-$**. In agreement, **Mg-rich oxide** compositions are obtained after calcination. A treatment at **800°C** leads to pure **periclase-like phase** with reflections shifted toward high angles due to Al^{3+} insertion, seemingly corresponding to layered double oxide (LDO) rehydratable to LDH due to "memory effect" [123]. Treatment at **900°C** leads the former **LDO to decompose** with its reflections split into pure MgO and MgO-rich spinel.

The microstructure of the calcined powder prepared with *oh* = 2.67 is presented in *Figure 3.19*. It is highly similar to what was observed for *r* = 5.34, with the same types of primary particles: **spherical crystallites**, **nanorods** (*Figure 3.19.b*) and highly strained **single crystal rods (100)-oriented** (*Figure 3.19.c*). Since rod-like and nanorods/needles particles were obtained for coprecipitation in water (*Figure 3.9*), the microstructure obtained for coprecipitation in polyol is coherent with the synthesis mechanism.

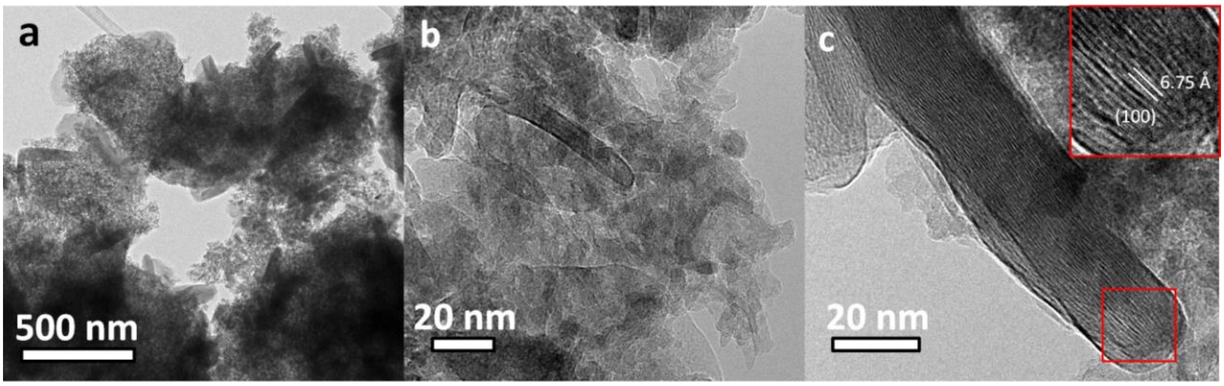

Figure 3.19: TEM of the calcined powder synthesized in polyol with hydroxyl ratio oh = 2.67, with a) general view, b) focus on small spherical crystallites and nanorods, and c) focus on a rod. Inset in c) shows high magnification of indicated area.

It can be remarked that syntheses with *oh* = 1.85 and *r* = 1.85, and *oh* = 2.67 and *r* = 5.34, respectively, lead to materials with similar structures and microstructures, even so the synthesis mechanisms are different for acetate or hydroxyl addition. Indeed, for *r*/*oh* = 1.85, the additive content is insufficient to allow total reaction of the solubilized Mg^{2+} and Al^{3+}, and Al^{3+} reaction is favored in both case, as it is mainly a matter of additive concentration, independently of the mechanism. In contrast, for the formation of a compound with $Al^{3+}/ Mg^{2+} = 2$, it appears that hydroxyl addition has a stronger effect on the respective reactions since *r* = 5.34 and *oh* = 2.67 lead to similar results. Hence, for the sole purpose of subsequent sintering of the synthesized MAS, basic coprecipitation in polyol is less adequate than the acetate route as it offers less or no range for optimization, and could not produce a spinel powder with spherical crystallites.

5. Influence of the polyol solvent

The polyol solvent is indeed at the heart of the polyol route, as the primary lever for controlling the growth rate. Due to their chelating properties, the polyol species can enter the coordination sphere of the solubilized cations to control the particle morphology and size, as well as integrate the composition, *e.g.* in the LDH interlayer [176] or as alkoxide [175]. In this section, we investigate **the influence of the polyol** serving as medium for the synthesis, all other parameters being identical to the ones in *Table 3.1*. The selected polyols with acronyms and boiling points are presented in *Table 1.3*. Three types of solvents have been investigated: etherglycols HO-$(CH_2CH_2O)_n$-H with different length n, alkane-1,m-diol HO-$(CH_2)_m$-OH with different length m, and butane-1,x-diol $C_4H_{10}O_2$ with different position x of the second alcohol group.

i. Synthesis in etherglycol HO-$(CH_2CH_2O)_n$-H

Seven different etherglycol media were compared, with increasing chain length n and ether groups (n-1): diethylene glycol (DEG, n = 2), triethylene glycol (TrEG, n = 3), tetraethylene glycol (TEG, n = 4), polyethylene glycol of average MW400 (PEG400, n ≈ 9), PEG600 (n ≈ 13), PEG1000 (n ≈ 22) and PEG8400 (n ≈ 190). At ambient temperature, all of the above were viscous liquids except for PEG1000 and PEG8400, which were waxy solids requiring melting at 35°C and 65°C, respectively, prior to the addition of the precursor salts. In every case, temperature was brought to the boiling point and interestingly, no foaming phenomenon was observed at intermediate temperature, in comparison with synthesis in EG.

The XRD patterns of the compounds synthesized in the different etherglycols are presented in *Figure 3.20*. For as-synthesized powders (*Figure 3.20.a*) and in comparison with the reference synthesis in EG, **two groups** of XRD patterns can be defined from **DEG to PEG400** ($2 \leq n \leq 9$) and from **PEG600 to PEG8400** ($n \geq 13$). In all experiments, it can be seen that no gibbsite $Al(OH)_3$ was formed, but **boehmite AlOOH** was obtained instead, as for coprecipitation in water at boiling point (*Figure 3.7.a*). The formation of the oxyhydroxide seems to be favored or provoked by the presence of ether groups in the medium. In the first group from DEG to PEG400, the powders are composed by **boehmite and LDH-type1**, which can be undoubtfully identified by the non-basal reflections (012) at 2θ ~41° and (110) at 2θ ~72°. However, the basal (003) peak is shifted toward low angles compared to d_{003} = 7.60 Å in EG, as 10.00 Å, 10.77 Å, 11.65 Å and 10.79 Å are found for increasing n. Except for PEG400, d_{003} increases proportionally to the etherglycol length n, which seems to confirm the intercalation of polyol species in the LDH interlayer, at least partially, and excludes the sole intercalation of acetate as hinted from characterizations of the compound synthesized in EG (*Chapter 4.I.1*). PEG400 is much bigger than TEG, and may exceed the critical size to be intercalated in LDH. However, in practice PEG are mixtures of etherglycols with different chain length for an average indicated MW, hence molecules with $n \leq 4$ constitute an important moiety of PEG400 that may have been intercalated, resulting in the broad (003) reflection at intermediate position. These compounds all thermally decomposed to **stoichiometric $MgAl_2O_4$** after calcination at 900°C, with no sensible differences from the XRD pattern from the reference synthesis in EG except for slightly sharper reflections (*Figure 3.20.b*).

The second group of XRD patterns for **PEG600-8400** exhibits solely reflections from **boehmite**, hence no crystalline phase containing magnesium, with no noticeable differences between the different patterns. In agreement, calcination led to **spinel phases with very low or no Mg^{2+}** content in every case, with very broad reflections indicating small crystallites. In addition, some unidentified reflections are observed for calcined powder synthesized in PEG8400, and are believed to arise from impurities contained in raw PEG.

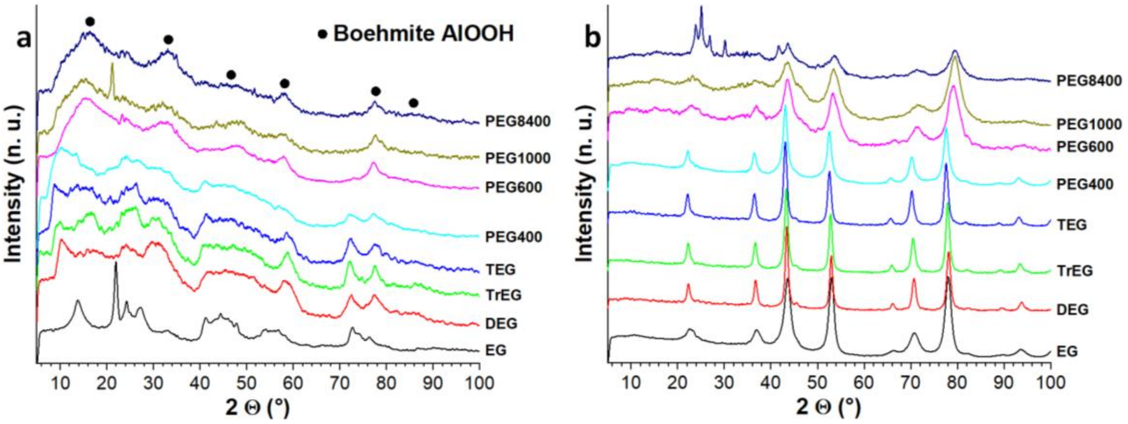

Figure 3.20: XRD patterns of compounds synthesized in different etherglycol media a) before and b) after calcination at 900°C

The microstructure of the calcined powder prepared with DEG, TrEG, TEG, PEG400 and PEG600 are presented in *Figure 3.19*. Low magnification (not shown) reveals **highly agglomerated particles**, with stone-like morphology and sharp edges often associated with poor sinterability, as for reference synthesis in EG, while the crystallites are also quite spherical. However, in agreement with XRD, bigger crystallites with **size ~20 nm** are observable for DEG, TrEG and TEG, while MAS synthesized *via* reaction in PEG400 has CS comparable to the one from EG, and γ -Al_2O_3 crystallites from PEG600 synthesis are very small (~5 nm).

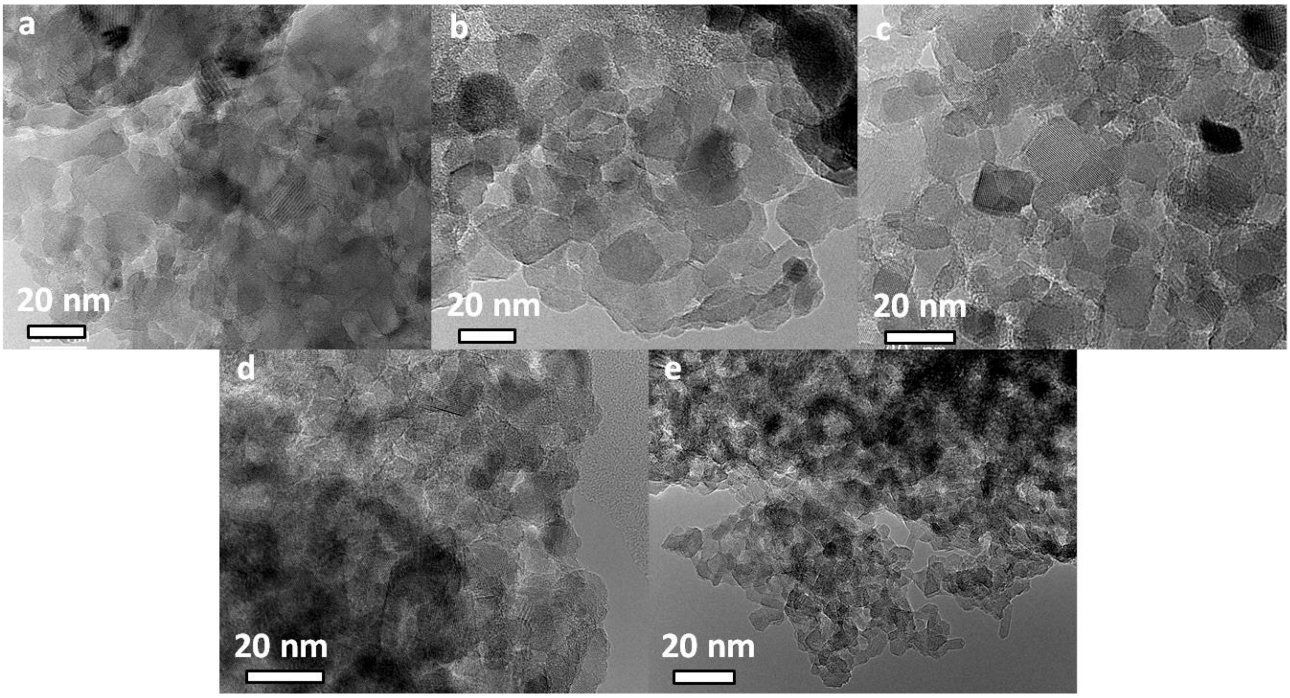

Figure 3.21: TEM of the calcined powders synthesized in etherglycol media: a) DEG, b) TrEG, c) TEG, d) PEG400 and e) PEG600

In summary, while etherglycols have a clear effect on the as-synthesized compounds, no benefits are obtained on MAS particles, since for n > 9 poor magnesium content is obtained, and for n < 9 the CS is bigger than from reference synthesis in EG and similarly agglomerated. The thermal decomposition behavior has not been studied, and could reveal more interest if MAS is obtained for lower calcination temperature.

ii. Synthesis in alkane-1,m-diol HO-(CH$_2$)$_m$-OH

In addition to the ethane-1,2-diol (EG, m = 2), three other alkane-1,m-diol solvents have been used for comparison, differing by the length m of their carbon chain. They are the propane-1,3-diol (1,3PRO, m = 3), the butane-1,4-diol (1,4BUT, m = 4) and the pentane-1,5-diol (1,5PEN, m = 5). In this study as well, synthesis temperature was brought to the boiling point and foaming phenomenon was not observed either.

The XRD patterns of the compounds synthesized in the alkane-1,m-diol media are presented in *Figure 3.22*. For as-synthesized powders (*Figure 3.22.a*), it is interesting to observe that the **LDH-type1** phase is observed for synthesis in all the alkane-1,m-diol media studied, with increasing crystallinity, especially for the basal planes, hinting for a better stacking order of the layers. For **1,4BUT and 1,5PEN**, the gibbsite Al(OH)$_3$ is not observed anymore, and **boehmite AlOOH** crystallizes instead. In addition, a new reflection of high intensity is observable at low angle around 10°, and is believed to arise from a basal plane of a layered phase. Such phenomenon can be observed in LDH's XRD patterns due to **interstratification** *via* a segregation scheme, which consists in the coexistence of interlayers with different thicknesses due to the presence of different anions clustered into completely discrete domains [118, 336, 337]. It was for instance observed during intercalation of direct red 2 dye in MgAl LDH-type1 with different orientations, giving rise to the formation of two LDH phases with same brucite-like layers and two different interlamellar distances [329]. However, it is unlikely that the observed basal reflection around 10° arises from interstratification of the LDH-type1 intercalated by two anions, *e.g.* CH$_3$COO$^-$ and a glycolate, as the (003) reflection at ~10.25 Å would yield at least a (006) higher harmonic at ~5.13 Å (20°), which is absent of the pattern. Instead, we assume that this reflection is from a **LDH-type2** phase, as we identified this phase before mostly by this basal reflection, the other being poorly resolved (*Figure 3.16.a*). For 1,5PEN, compared to 1,4BUT, LDH-type2 and boehmite phases seem to be more important. It has to be noted that the d$_{003}$ of LDH-type1 is similar around ~7.60 Å for EG, 1,4BUT and 1,5PEN, while it is sensibly higher at 8.11 Å for 1,3PRO. Additionally, whenever LDH-type2 is formed, excess Al^{3+} is systematically in boehmite AlOOH form. Hence, it could be argued that LDH-type2 is based on AlOOH bilayer structure, instead of the "defective brucite" Al(OH)$_3$ as mentioned in literature [128–130]. Further analyses should clarify this point. After calcination (*Figure 3.22.b*), all alkane-1,m-diol media decompose to MgAl$_2$O$_4$, with somehow sharper reflections for 1,4BUT and 1,5PEN synthesized compound.

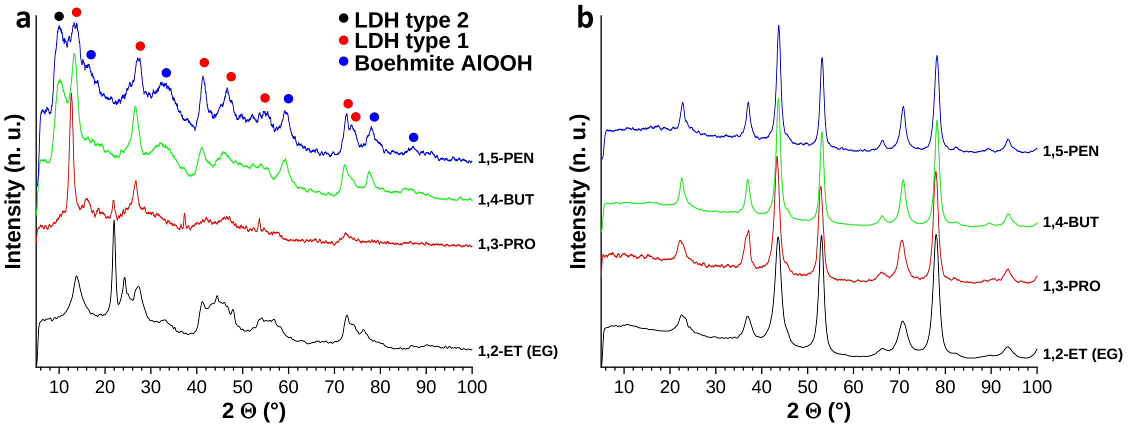

Figure 3.22: XRD patterns of the compounds synthesized in alkane-1,m-diol media a) before and b) after calcination at 900°C

The microstructures of the calcined powders prepared with 1,3PRO, 1,4BUT and 1,5PEN are presented in *Figure 3.23*. It can be seen that for **1,3PRO**, the primary particles are **strongly aggregated** with a stone-like morphology as for the reference synthesis. Interestingly, the particles prepared in **1,4BUT and 1,5PEN** consist in severely agglomerated **micronic sheets**, which is highly uncommon for MAS powders, and is possibly linked to the LDH-type2/boehmite composition. However, these sheet-like particles should most likely exhibit poor sinterability, so this peculiar feature and the potential properties arising from it will not be further studied. For all the spinel particles showed in *Figure 3.23*, the crystallites shape is quite spherical, as for the synthesis in EG, with similar crystallites size of ~15 nm.

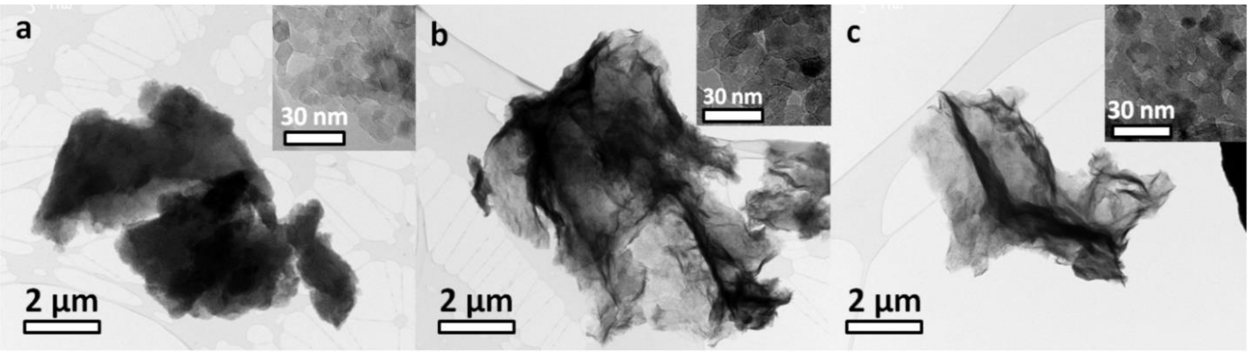

Figure 3.23: TEM of the calcined powder synthesized in alkane-1,m-diol media: a) 1,3-PRO, b) 1,4-BUT and c) 1,5-PEN

iii. Synthesis in butane-1,x-diol $C_4H_{10}O_2$ regioisomers

Finally, we investigated **the influence of regioisomerism** on alkanediol media for the synthesis of MAS precursors, in particular with the comparison of the reaction in different butane-1,x-diol $C_4H_{10}O_2$ solvents with different position x of the second alcohol group: 1,2BUT, 1,3BUT and 1,4BUT. Indeed, since the chelating properties of the polyol media arise from their two alcohol groups, the length of alkane chain separating them should affect the reactivity, in a similar way than for alkane-1,m-diol solvents. No great differences of BP (~183°C) or particular observation were noted during syntheses.

The XRD patterns of the compounds synthesized in the butane-1,x-diol media are presented in *Figure 3.24*. A great effect of the regioisomerism is observed on the as-synthesized compounds (*Figure 3.24.a*). While the already discussed **1,4BUT** led to **mixed boehmite AlOOH, LDH-type1 and LDH-type2**, **1,2BUT** provided **AlOOH** (mostly identifiable by the reflections at 58.8°, 77.2° and 85.5°) and **LDH-type1** and **1,3BUT** led to **gibbsite $Al(OH)_3$ and LDH-type1**. Interestingly, the 1,3BUT pattern is highly similar to the 1,3PRO, with especially the same high crystallinity of LDH-type1 and very intense (003) reflection at d_{003} = 8.33 Å close to the 8.11 Å measured for 1,3PRO. Indeed, 1,3BUT can be seen as 1,3PRO with a branched methyl group in C3, and the two (OH) groups positioned on C1 and C3 in both cases may hint for the **influence of the length of the chain separating the (OH) on the chelating properties**. The 1,2BUT presents the peculiarities of high LDH-type1 interlayer spacings d_{003} = 11.63 Å (8.82°), d_{006} = 6.22 Å ≈ $d_{003}/2$ (16.55°) and d_{009} = 4.20 Å ≈ $d_{003}/3$ (24.60°), with abnormally broad and intense (009) reflection. Due to their particularly low angles, these bands could be indexed as LDH-type2 basal planes, however all the non-basal LDH-type1 reflections are clearly observable with high relative intensities. In this case, 1,2BUT does not provide similar results with 1,2ET (EG), even if in both species the two $(OH)^-$ are on C1 and C2 positions. This could be due to the fact that 1,2BUT can be seen as EG with a branched ethyl group in C2, thus a branched function as long as the chain between the (OH), which may induce too much of a steric hindrance for the same reaction mechanism to occur. It has to be considered that the bigger interlayer spacing may be provoked by **intercalated glycolate species of 1,2BUT**. Additional experiments are required to verify that other alkanediols lead to similar trends and assess the nature of the intercalated anions.

After calcination (*Figure 3.24.b*), all 1,xBUT provided pure $MgAl_2O_4$ spinel phase, with no variation of cell parameter or crystallite size, confirming the good reactivity of both Mg^{2+} and Al^{3+} in the different media.

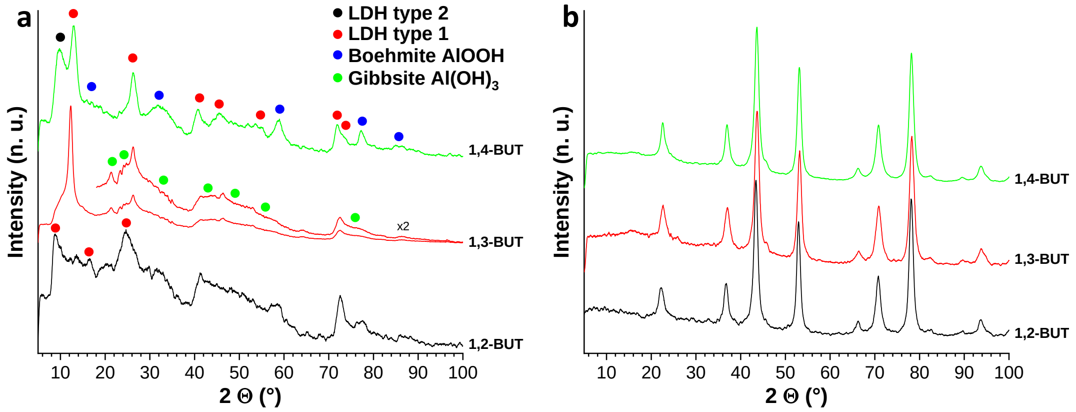

Figure 3.24: XRD patterns of compounds synthesized in regioisomers of butanediol a) before and b) after calcination at 900°C

The microstructures of the calcined powders prepared with the different 1,xBUT are presented in *Figure 3.25*. The sheet-like particles obtained with 1,4BUT are not observed for 1,2BUT and 1,3BUT, which led to more **aggregated primary MAS particles** with stone-like morphology, as for EG and 1,3PRO. In addition, it seems that 1,2BUT secondary particles are bigger, more agglomerated and with sharper edges than the 1,3BUT ones. However, the primary particles are quite similar in shape (spherical) and size (~15 nm) for all 1,xBUT media. These observations tend to confirm the strong influence of the alkane chain's length between both alcohol groups of polyol. Moreover, it indicates indeed that the powder structural composition prior to calcination (*i.e.* LDH-type1/LDH-type2, intercalated specie in LDH and $Al(OH)_3$/AlOOH formation) is highly determining for the secondary particles microstructure after calcination, even if the influence on structural composition and primary particles microstructure is rather marginal.

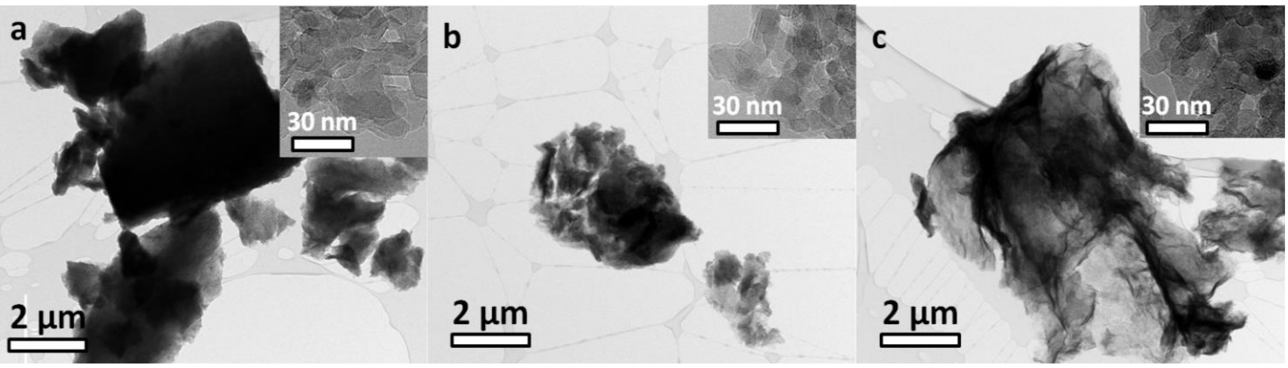

Figure 3.25: TEM of the calcined powder synthesized in butane-1,x-diol media: a) 1,2-BUT, b) 1,3-BUT and c) 1,4-BUT

6. Al and Mg relative quantities

As discussed in *Chapter 1.I.2*, the spinel structure indulges a large range of composition: described as $MgO \cdot nAl_2O_4$, with $n = 1$ corresponding to $MgAl_2O_4$ and a maximum solid solution range as $0.618 \leq n \leq 7.8$ [25, 27]. Though nonstoichiometric spinels may have interesting properties, they are hard to synthesize, especially magnesia-rich compounds (n < 1), due to their domain of stability existing only at high temperature > 1200°C. Since MgO·nAl$_2$O$_3$ oxides preparation *via* the polyol route goes through the thermal decomposition of hydroxides mixtures and progressive conversion to spinel lattice, as shown in *Figure 3.2.a*, it can be expected to be a good method to obtain nonstoichiometric spinel with grain size at the nanoscale. Moreover, the synthesis of a monophasic precursor with cationic composition already corresponding to the desired ratio n would be preferable for chemical homogeneity and high purity. As LDH phases can also accommodate a large range of composition, their calcination could lead to single-phase spinels formation with stoichiometry controlled by the chemical composition of the as-synthesized hydroxides.

In order to verify these assumptions, we performed syntheses with **non stoichiometric Al^{3+} and Mg^{2+} salts quantities**, *i.e.* Al^{3+}/Mg^{2+} $\neq 2$, together with experiments with pure Al^{3+} and Mg^{2+} compositions for better understanding of the synthesis mechanisms, all other parameters kept identical from reference synthesis conditions (*Table 3.1*). The studied set compositions x_i and n_i are presented in *Table 3.3*, together with the synthesis temperature (at boiling temperature BT) and the mass yield of resulting oxide after calcination, while the results of the structural characterizations are summarized in *Table 3.4*.

Table 3.3: MgO-Al$_2$O$_3$ synthesis compositions and corresponding boiling temperature BT and mass yield after heat treatment

x_i [a]	0	0.167	0.286	0.375	0.444	0.5	0.556	0.625	0.714	0.833	1
n_i [b]	0	0.2	0.4	0.6	0.8	1	1.25	1.67	2.5	5	∞
BT (°C)	192	190	187	184	182	182	181	179	178	174	173
Mass yield (%)	73	83	75	72	54	44	6	16	33	10	69

[a] x is the Al$_2$O$_3$ molar fraction used for general study of the MgO-Al$_2$O$_3$ system
[b] n is the Al$_2$O$_3$:MgO ratio preferred for study of stoichiometry in spinel compound

Table 3.4: Summary of the structural results obtained for the synthesis with different Al and Mg relative quantities

Composition		As-synthesized			After heat treatment at 900°C, 1 h	
x_i	n_i	Phases	Cell constants (Å) [a]		Phases	Cell constant a (Å) [b]
			a	c		
0	0	LSH	3.073	25.05	Periclase	4.2078
0.167	0.2	LDH-type1	3.066	26.57	Periclase Spinel	~4.208 8.089
0.286	0.4	LDH-type1	3.022	27.35	Periclase Spinel	~4.208 8.078
0.375	0.6	LDH-type1	2.998	26.04	Periclase Spinel	~4.208 8.076
0.444	0.8	LDH-type1 Boehmite	3.000 -	26.49 -	Periclase Spinel	~4.208 8.075
0.5	1	LDH-type1 Gibbsite	3.044 -	22.96 -	Spinel	8.0638
0.556	1.25	LDH-type1/2	2.957	25.77	Spinel	7.964
0.625	1.67	LDH-type2	~2.78	33.07	Spinel	7.923
0.714	2.5	LDH-type2	~2.78	34.63	Spinel	7.901
0.833	5	LDH-type2	~2.78	30.85	Spinel	7.871
1	∞	ε-Al$_{13}$ chloride	-	-	Spinel	7.823

[a] Only for layered phases, assuming hexagonal lattice with $R\bar{3}m$ rhombohedral symmetry for all LDH/LSH
[b] Calculated only from (440) and (220) reflections positions for spinel and periclase, respectively

It can be noted from *Table 3.3* that the boiling temperature at which synthesis was set is almost that of pure EG (~196°C) for pure Mg^{2+} salt, and linearly decreases with the increase of Al^{3+} content down to 173°C for pure Al^{3+} salt. In addition, the foaming phenomenon during the heat up stage was only observed for $0.375 \leq x_i < 1$, which may indicate a change in reaction mechanisms with composition, and potentially explains the very high variations of mass yield depending on composition x_i.

i. Synthesis of pure Mg2+ compound, x = 0

The evolution of the XRD pattern of the powder synthesized for $x_i = 0$ through calcination is presented in *Figure 3.26.a*. The as-synthesized material is conserved upon calcination up to 250°C, and has a pattern typical of **layered hydroxides**, with a basal plane (003) at 12.32° (8.34 Å) and a planar reflection (110) at 71.21° (1.54 Å), assuming a $R\bar{3}m$ hexagonal lattice as for LDH-type1. The asymmetry of the (*hk*0) lines indicates a **turbostratic disorder**, arising from the loss of registry in the stacking of the hydroxide layers. Such **Mg-LSH** structure has not been reported before, to our best knowledge. For calcination at **T ≥ 400°C**, **MgO** is formed (a = 4.2386(2) Å at 400°C, a = 4.2078(1) Å at 800°C, a = 4.2002(1) Å at 1200°C) with sharpening of the reflections with increasing temperature due to the coalescence of the crystallites.

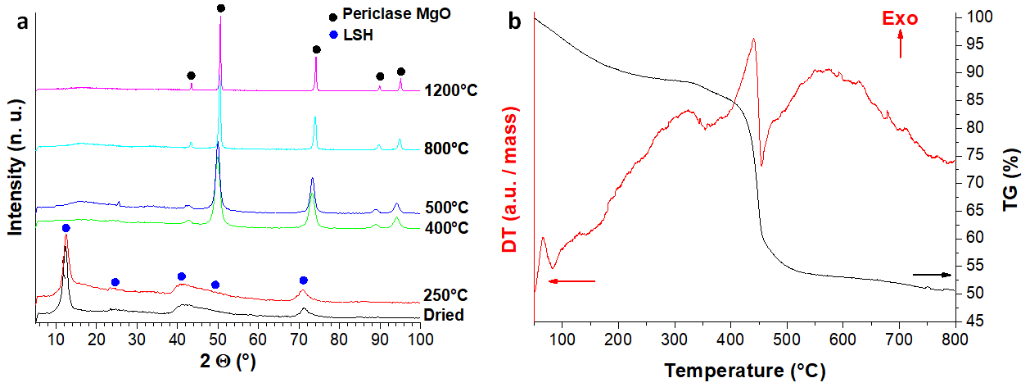

Figure 3.26: a) XRD patterns of the compound synthesized for $x_i = 0$ (pure Mg^{2+} compound) prior and after heat treatment at different temperatures for 1 h and b) DT-TG analysis of the as-synthesized compound

The thermal analysis (DT-TG) of the as-synthesized powder is presented in *Figure 3.26.b*, and indicates a weight loss of as-prepared material in three steps. In a first step, a weight loss of ~12% accompanied by a wide endothermic peak is observed in the range **50-250°C** from **evaporation of the physisorbed water** (dehydration of the material), in agreement with the conservation of the layered hydroxide phase up to the upper range limit. A second small endothermic weight loss (3.4% of dry mass) peaks at **375°C**, and is attributed to the **loss of interlamellar species and delayering of the hydroxide sheets**. Assuming a brucite composition of the sheets, as layered hydroxide phases are generally based on stacked brucite-like layers, it is expected that during the delayering of the second step (375°C), brucite $Mg(OH)_2$ is formed; however, additional characterizations are necessary to confirm this hypothesis. Finally, a third endothermic mass loss (25% of dry mass) is observed at **450°C** and is attributed to the **dehydroxylation** of the hydroxide into MgO, in agreement with XRD. The decomposition occurs at particularly high temperature, typical value for brucite nanoparticles being in the range of 350-400°C, depending on the size of hydroxide particles [169, 338].

The microstructure analyses of the $x_i = 0$ synthesized compound before and after calcination at 400, 800 and 1200°C are presented in *Figure 3.27*. The microstructure of the **as-synthesized material** (*Figure 3.27.a*) consists in ~5 nm thick **nanoflakes-assembled microspheres** (~1 µm) typical of turbostratic layered structures [142], and the EDX analysis reveals an **elemental composition of Mg:O = 1:2.33** with no residual Cl^- or Na^+. This composition shifts from the 1:2 expected for $Mg(OH)_2$, and indicates indeed the intercalation of an oxygen-bearing specie in the galleries. After calcination at **400°C** and decomposition of the hydroxide to MgO (*Figure 3.27.b*), the microspheric assembles are maintained with an average size shrunk to **~500 nm**, while the original flake crystallites are decomposed to **~15 nm spherical primary particles** (confirmed by XRD). For higher temperatures of treatment up to 1200°C, the spherical aggregates are still observed with roughly the same size, and the crystallite size increases to ~50 nm at 800°C and 100-200 nm at 1200°C.

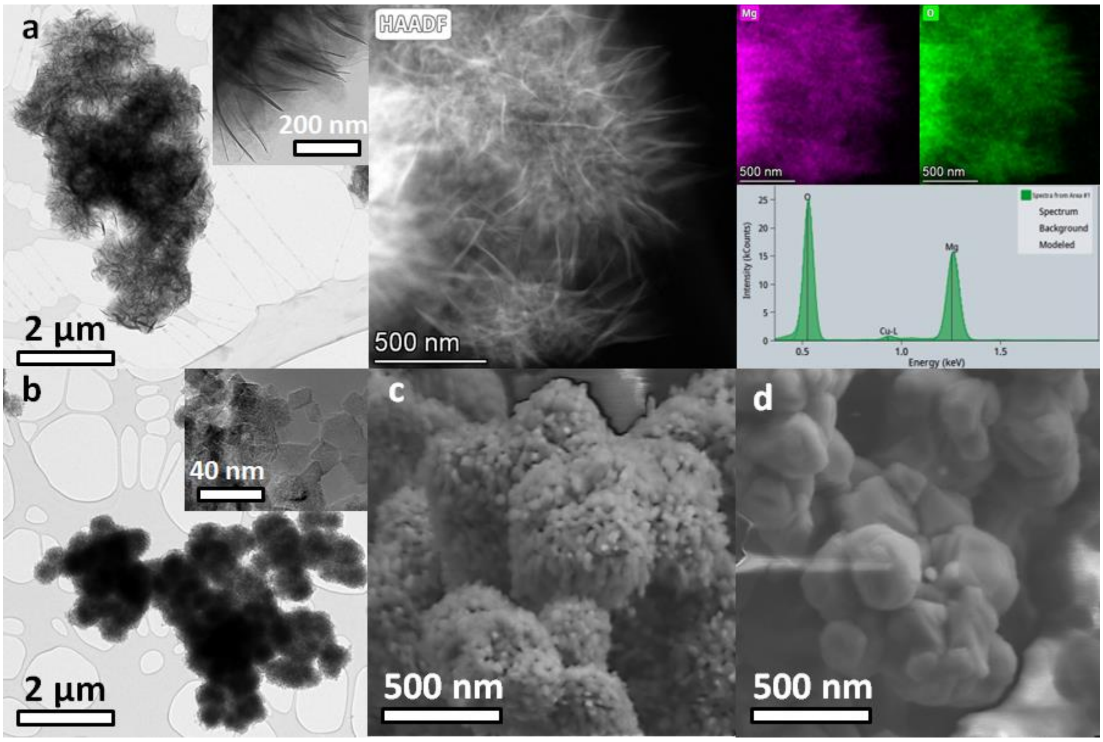

Figure 3.27: Micrographs of the powder synthesized with composition x_i = 0: a) as-synthesized, with HAADF and EDX analyses, and calcined at b) 400°C, c) 800°C and d) 1200°C

Based on these characterizations and previously reported LSH structures, the nature of the synthesized LSH material can be discussed. It is clear from XRD, DT-TG and TEM that the synthesized compound is a layered single hydroxide based on brucite-type sheets, such as hydrotalcite-like α-$Mg(OH)_2$ [339, 340], hydroxyacetate [143] or hydroxyethyleneglycolate [141]. Hydroxychloride or ethyleneglycolate alkoxide $Mg(OCH_2CH_2O)$/MgEG, which should exhibit similar XRD pattern based on CoEG and NiEG [142, 175], are excluded since the EDX analysis did not reveal any sensible Cl nor C in the material. Hydroxyacetates, with CH_3COO^- ions partially replacing up to 1/4 of the OH^- groups in the brucite-like sheets, have been reported to exhibit much higher d_{003} than the here observed 8.34 Å (14.75 Å for Zn, 12.84 Å for Co, 10.64 Å for Ni) [143]. Although the interlayer spacing (and generally the structure of the layered hydroxysalt) depends on M^{2+}, the value obtained for Ni-LSH was considered close to the smallest possible [143], therefore the formation of a Mg hydroxyacetate can be ruled out. Due to its possible bivalence and chelating properties which could bring closer the sheets, or even "bridge" them, and reduce the interlayer distance, a hydroxyethyleneglycolate structure cannot be excluded based on the performed characterizations. It is also important to note that the obtained LSH structure thermally treated at 250°C did not undergo any contraction of its lattice along the *c* axis during dehydration, contrarily to α-$Ni(OH)_2$ intercalated with water under similar treatment [341]. It can be concluded that the interlayer of the synthesized Mg-LSH does not contain sensible amount of water. It is instead assumed that EG molecules are located in the galleries in vertical monolayer, which would induce a ~4.2 Å interlamellar distance [136]. The lower experimental 3.54 Å (calculated from d_{003} deduced of the 4.8 Å thickness of brucite sheet) can be explained by partial replacing of hydroxyl groups by ethyleneglycolate, as mentioned before. In that case, the layering in Mg-LSH is ensured solely by hydrogen bonds between hydroxyls/ethyleneglycolate and interlayered EG. The d_{110} = 1.54 Å is in good agreement with previously reported values for α-$Co(OH)_2$ [140, 339], which supports the hypothesis of a **α-$Mg(OH)_2$ structure**.

Further characterizations (FTIR, Raman spectroscopy, ion chromatography) are required for a complete description of the synthesized LSH, and especially better understanding the interlayer composition.

ii. Synthesis of pure Al^{3+} compound, x = 1

The compound synthesized for $x_i = 1$, *i.e.* pure aluminum, is extremely soluble in water, and has to be washed by ethanol instead of water.

The evolution of the XRD pattern of the powder through calcination is presented in *Figure 3.28.a*. The initial compound is a **ε-Al_{13} Keggin structure** based on a glycol-coordinated polyhydroxyoxoaluminum cluster compensated by Cl^-, **ε-Al_{13} chloride**, which was already encountered for the coprecipitation in EG with *oh* = 0.94 (*Figure 3.18.a*). Such a material was prepared for the first time in 2018 by solvothermal synthesis in EG, with the Keggin structure $[AlO_4Al_{12}(OH)_{12}(O\text{-}CH_2\text{-}CH_2\text{-}OH)_{12}]^{7+}$ [335]. Its formation was explained by **partial hydrolysis of the aluminum salts**: the initial H_2O molecules coordinating Al^{3+} lose a H^+ due to pH increase and the OH^- groups condensate, while glycolate chelates the 12 surrounding Al^{3+}. The ε-Al_{13} chloride structure belongs to the cubic space group $Fd\bar{3}m$. The ε-Al_{13} cluster consists in a central AlO_4 tetrahedron surrounded by twelve AlO_6 octahedra assembled in four planar trimeric $Al_3(OH)_6$ units. Each AlO_6 unit inner-coordination sphere includes one O-oxo shared within its trimeric $Al_3(OH)_6$, and linking it to the central AlO_4, two OH-hydroxy, two O-glycols and one OH-glycol, as the glycolates are part of a bidentate chelate. The structure of the Keggin cluster is more thoroughly described and represented in reference [335].

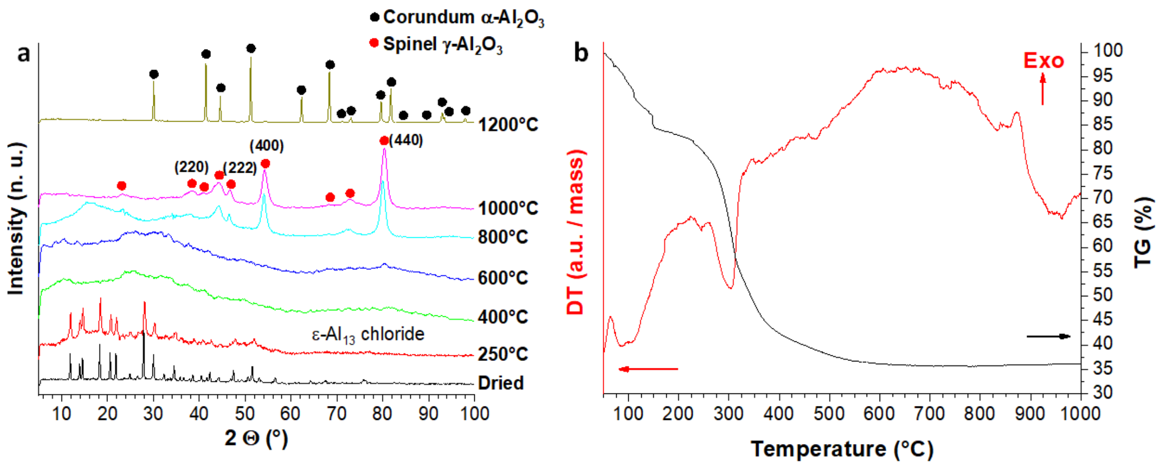

Figure 3.28: a) XRD patterns of the compound synthesized for $x_i = 1$ (pure Al^{3+} compound) prior and after heat treatment at different temperatures for 1 h and b) DT-TG analysis of as-synthesized compound

The sharp XRD reflections indicate **large crystallite size**. From Rietveld refinement of the XRD pattern using the crystal structure CCDC 1813736 from [335], all the observed reflections for the as-synthesized material in *Figure 3.28.a* are indeed belonging to the ε-Al_{13} chloride phase, with a very good correspondence of positions for a lattice constant ***a* = 24.677(2) Å**, in very good agreement with the *a* = 24.6762(11) Å found in [335]. However, discrepancies in the relative intensities of the reflections are observed, and in particular the first and main reflection (111) at d = 14.25 Å (2θ ~7.2°) is normally ~20 times more intense than the second main reflection (222) while it is totally extinguished in our case. These differences could arise from texturing or compositional variation, in particular in the Keggin cluster, since the synthesis protocol differs.

The ε-Al_{13} chloride material is **conserved upon calcination up to 250°C**, with somehow broader reflections and apparition of a broad background, which seems to indicate a partial degradation and amorphization of the compound. For calcination at **400°C ≤ T ≤ 600°C**, the material is totally **amorphous**.

For calcination at **800°C ≤ T ≤ 1000°C**, **pure γ-Al_2O_3** spinel is cristallized. From structure refinement, the crystallite size **CS = 14(1) nm** has been calculated for both 800 and 1000°C, indicating that no coalescence of the particles occurs in this range of temperature. The cell parameters are *a* = 7.874(1) Å at 800°C and *a* = 7.849(1) Å at 1000°C, in agreement with the value of 7.94(5) Å previously reported as well as its evolution with temperature of calcination [335]. Since the γ-Al_2O_3 lattice is defective by nature, inducing a Al^{3+} distribution in both normal octahedral sites Al_O and inverse tetrahedral sites Al_T, with respect to the spinel lattice, the variation of the lattice constant can be explained by the rearrangement of Al^{3+} sites distribution with increasing temperature. Based on the dependence between *a* and the inversion parameter *I* in spinel structure defined by $(M^{II}_{1-I}M^{III}_{I})(M^{II}_{I}M^{III}_{2-I})O_4$ [46, 47], we can extrapolate the reasoning to γ-Al_2O_3 spinel cationic distribution. Indeed, it was shown in [46, 47] that increasing *I*, *i.e.* the fraction of Al^{3+} in Al_T sites, leads to a decreasing *a*. In the case of γ-Al_2O_3, since an occupied Al_T site is not somehow compensated by a M^{II}_O site but let vacant as V_O, the influence of Al_T/Al_O occupancy is expected to be even greater on the *a* value. Therefore, the smaller *a* = 7.874(1) Å at 800°C indicates a lower Al_T occupancy, while the greater *a* = 7.849(1) Å at 1000°C implies that the Al_T sites are more populated due to higher Al^{3+} diffusion. This is in agreement with previous studies reporting that a disordered γ-Al_2O_3 structure is more stable, with a most stable spinel formula of $(Al_T)(Al_O)_{5/3}(V_O)_{1/3}(O)_4$ [342]. In addition, it can be observed that all the reflections on the XRD patterns do not have the same width. In particular, the **(222) reflection**, dominated by scattering from the **O^{2-} sublattice**, is sharp, indicating that this sublattice is **fairly well ordered** [342]. The **(220) reflection** arising from scattering from the **Al_T sublattice** has greater intensity and resolution after calcination at 1000°C, confirming the higher population of Al_T sites [342]. It is noticeable that both ε-Al_{13} chloride and γ-Al_2O_3 spinel crystallizes in the cubic space group $Fd\bar{3}m$, with a ratio ***a*(ε-Al_{13})/ *a*(γ-Al_2O_3) ~3**; this may hint for a **topotactic transition** during thermal treatment.

Finally, after calcination at **1200°C**, stable **corundum α-Al_2O_3** is crystallized. The reflections are sharp, indicating that the crystallites have coalesced upon recrystallization and are not nanosized anymore.

The DT-TG analysis is presented in *Figure 3.28.b*, and several thermal phenomena are observed. In a first step, an endothermic **mass loss of 20 % occurs below 200°C**, corresponding to the **evaporation** of the remaining physisorbed water and ethylene glycol, in agreement with the conservation of the ε-Al_{13} chloride material up to 250°C. Then a second endothermic **loss of mass of 33%** of the dried compound occurs in **two successive steps** during the decomposition of the ε-Al_{13} chloride, *i)* mainly from **260°C to 375°C**, due to the **loss of the structural glycolates and hydroxides**, and *ii)* from **375°C up to 525°C**, with a broad and weak endothermic peak accompanying the slow and gradual mass loss, probably due to the departure of the remaining hydroxides to **complete the transformation to oxide form Al_2O_3**. Finally, an exothermic peak is observed from **830°C to 900°C**, with no mass loss, which corresponds to the **crystallization of γ-Al_2O_3**.

The microstructure analysis of the x_i = 1 compound before and after calcination at 400°C, 800°C and 1200°C is presented in *Figure 3.29*. The synthesized **ε-Al_{13} chloride** microstructure (*Figure 3.29.a*) consists in non-agglomerated **octahedral single crystals of 1-3 µm** with very smooth surfaces, already observed in the first report of EG-coordinated ε-Al_{13} chloride with ~15 µm octahedra [335]. The EDX analysis reveals a composition of Al: 23(4) at%, O: 47(5) at%, C: 20(2) at% and Cl: 10(2) at% corresponding to the Keggin structure of empirical formula **$Al_{13}O_{30}C_{12}Cl_7H_{72}$**, with addition of the hydrogen not quantified by EDX in order to reach neutral charge. Therefore, the molecular structure of the synthesized EG-coordinated ε-Al_{13} chloride is assessed to be **$[AlO_4Al_{12}(OH)_{18}(OCH_2CH_2OH)_6]Cl_7$**, which is sensibly different than the formula $[AlO_4Al_{12}(OH)_{12}(OCH_2CH_2OH)_{12}]Cl_7$ obtained in [335], with especially a smaller moiety of EG^- within the Keggin ion. The different compositions are assumed to arise from the differing synthesis protocols and could explain the discrepancies between the XRD patterns (*Figure 3.28.a*). After decomposition of the ε-Al_{13} chloride upon calcination at **400°C** and loss of crystallographic structure (*Figure 3.29.b*), the initial microstructure seems to have been kept intact, as the **octahedra are conserved** with their surface apparently remaining smooth. The EDX analysis indicates a composition of **Al_2O_3**, hence a **full transition to oxide form**, with remaining traces of C and Cl elements, in agreement with DT-TG analysis (*Figure 3.28.b*).

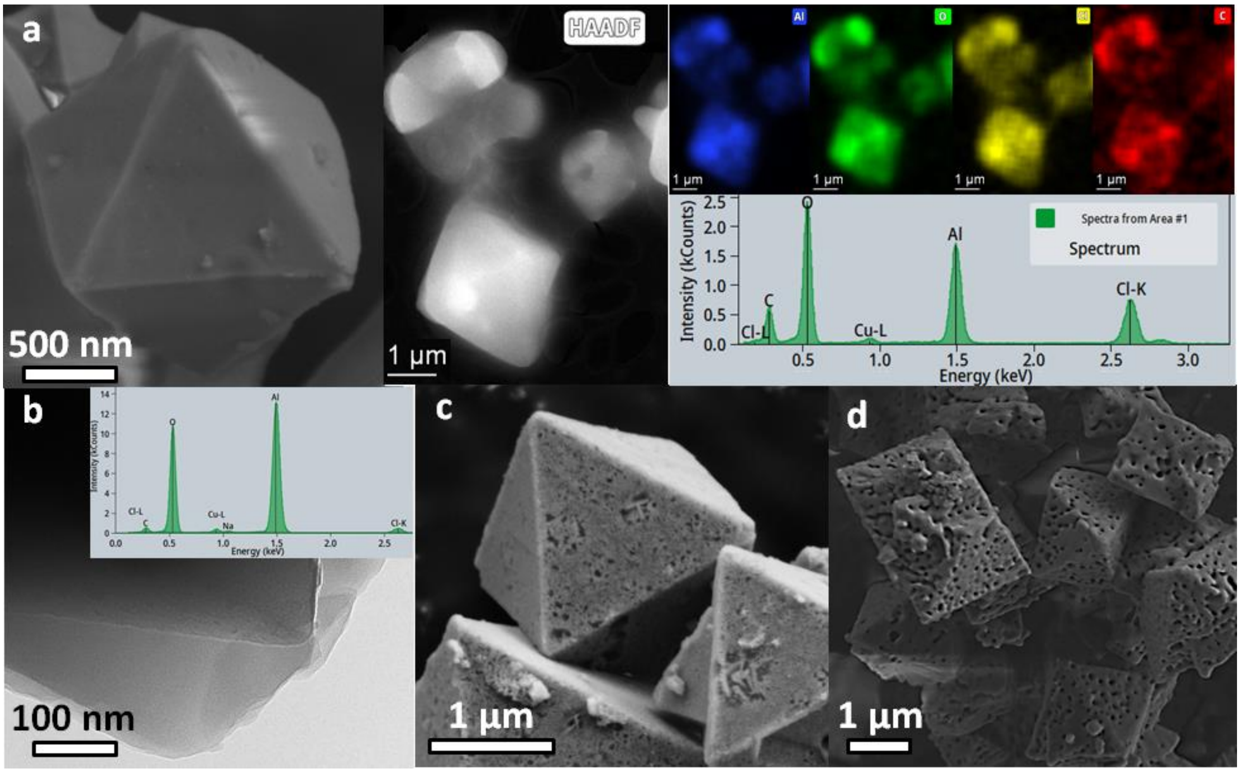

Figure 3.29: Micrographs of the synthesized powder with composition x_i = 1: a) as-synthesized, with HAADF and EDX analyses, and calcined at b) 400°C, c) 800°C and d) 1200°C

Upon calcination up to 1200°C, the **octahedral morphology remains while porosity** is progressively formed as the alumina phases crystallize. After thermal treatment at **800°C** and formation of γ-Al_2O_3 (*Figure 3.29.c*), the octahedra still possess net and sharp edges but are now **mesoporous**, with pores of size from **~10 to ~70 nm**, while after treatment at **1200°C** and transition to α-Al_2O_3 (*Figure 3.29.d*) the particles have rounded edges and are **macroporous** with pore sizes of **300-500 nm**. The formation of pores and their increasing size with temperature appears to be due to the **increase of volumic mass** during recrystallization as $\rho(\varepsilon\text{-}Al_{13}$ chloride$) = 1.43\ g.cm^{-3}$ [335], $\rho(\gamma\text{-}Al_2O_3) = 3.56\ g.cm^{-3}$ and $\rho(\alpha\text{-}Al_2O_3) = 3.98\ g.cm^{-3}$, together with **coalescence of the pores**. It seems less probable that the pores are formed during decomposition of ε-Al_{13} chloride by a cratering mechanism as vent holes in the crystals to evacuate the volatile species, since no pores could be observed by TEM after decomposition at 400°C (*Figure 3.28.b*). However, it is possible that micropores ($\leq$ 2 nm) are in fact already formed but could not be seen because of the high thickness of the particles, the pores then coalescing at higher temperature. Measurement of the surface area's evolution is required to assess the mechanism of formation of the pores, and indicate the evolution of specific surface area with temperature of treatment and nature of the pores, *i.e.* surface pores or network of channels.

It should be noted that the square bipyramidal morphology of alumina particles has never been reported before to the best of our knowledge, and deserves further investigation as well as the initial ε-Al_{13} chloride material. It is believed that through the optimization of the synthesis parameters, the composition of the Keggin ion could be tuned (different EG^- moieties for instance), and that the octahedral particles size could be controlled from the nanoscale to hundreds of µm.

iii. Synthesis of mixed Mg^{2+}/Al^{3+} compound, $0 < x < 1$

This paragraph is dedicated to the study of the compounds synthesized with **mixed Mg^{2+}/Al^{3+} compositions $0 < x_i < 1$** (*Table 3.3*). It should be noted that for $x_i \geq 0.714$, the as-synthesized products are extremely soluble in water, and therefore have been washed with ethanol instead of water.

The *Figure 3.30.a* shows the XRD evolution of as-synthesized compounds with x_i. **All as-synthesized materials** (except for $x_i = 1$) exhibit **layered hydroxide phases**, and the evolution of their cell constants is plotted in function of x_i in *Figure 3.30.c*, assuming a common $R\bar{3}m$ hexagonal lattice (LDH-type2 generally indexed on a monoclinic cell $P2_1/c$ [128] or $P2_1/n$ [130]), and the values are reported in *Table 3.4*. **Five domains of cell constants** are observed. In ①, for **$0 \leq x_i \leq 0.286$**, **pure layered phases** are formed: Mg-LSH for $x_i = 0$ (*Chapter 4.I.6.0*) and **LDH-type1** for $x_i > 0$; $x \approx 0.33$ is reported to be the limit of substitution in MgAl LDH-type1 [132] and constitutes an expected threshold. The constant a decreases linearly with increasing x_i indicating effective **Al^{3+} insertion** in the brucite-like layers, while c increases linearly hinting for the **interlayer enlargement**. Higher Al^{3+} insertion rates are reported to decrease c due to stronger layers-intercalates interactions [139], so this increase is attributed to a **modification of the interlayer composition**, *i.e.* bigger intercalates, higher concentration of intercalates or different interlayer arrangements (bilayering [136], solvent swelling [319], horizontal/tilted intercalation [343]). In **domain ② with $0.286 < x_i \leq 0.5$**, **Al^{3+} content exceeds the insertion threshold** in brucite layers, so weak boehmite reflections can be seen for x_i = 0.444 and intense gibbsite ones for x_i = 0.5. The constant a reaches its minimum value at **$x_i = 0.375$** while c

stagnates until $x_i = 0.444$ due to **Al^{3+} saturation** in LDH, then at **$x_i = 0.5$**, *a* increases back and *c* drops as excess Al^{3+} crystallizes as **$Al(OH)_3$**. A clear distinction can be made for the XRD patterns separated by **$x_i = 0.5$**, as it marks a **frontier between LDH-type1 and type2 formation domains**. In **③ with $0.5 < x_i < 0.625$**, a pure and poorly crystallized layered phase is observed. The in-plane constant *a* decreases strongly toward 2.78 Å due to **increased Al^{3+} insertion** in the phase, while the **basal constant *c* increases greatly** toward > 30 Å. This domain seems to be **transitory**, resulting in the poor crystallinity and intermediary cell constants between LDH-type1 and type2. The **domain ④ with $0.625 \leq x_i < 0.833$** corresponds to the range of **pure LDH-type2**. The poor crystallinity, especially leading to the extinction of in-plane reflections, does not allow observing variation of *a*. However, the constant *c* seems to increase with Al^{3+} content until **$x_i = 0.714$** before decreasing back, although additional experiments are required to confirm these trends. The maximum value of *c* could correspond to **$x = 0.800$**, *i.e.* the very stable sheet composition $[M^{2+}Al^{3+}{}_4(OH)_{12}]$ with half the $Al(OH)_3$ gibbsite vacancies filled by Mg^{2+} [128–130]. Shift from this particular composition could decrease the layering strength and stability, thus alter the interlamellar spacing. It should be noted that LDH-type2 diffractograms reported in literature exhibit a first basal reflection at ~7.5-9.0 Å [128, 130, 344], while we observe the sensibly higher *d* ~11 Å; generally speaking, the XRD patterns reported in this work are somehow different, which may hint for a different structuration of the layered phases. Lack of experimental points prevents the proper analysis of **domain ⑤**, but a **x_i-threshold** is expected, **separating domains of LDH-type2 and ε-Al_{13} based** materials. By default, we place this threshold at $x_i = 0.833$, as the synthesized material was soluble in water as the one synthesized with $x_i = 1$.

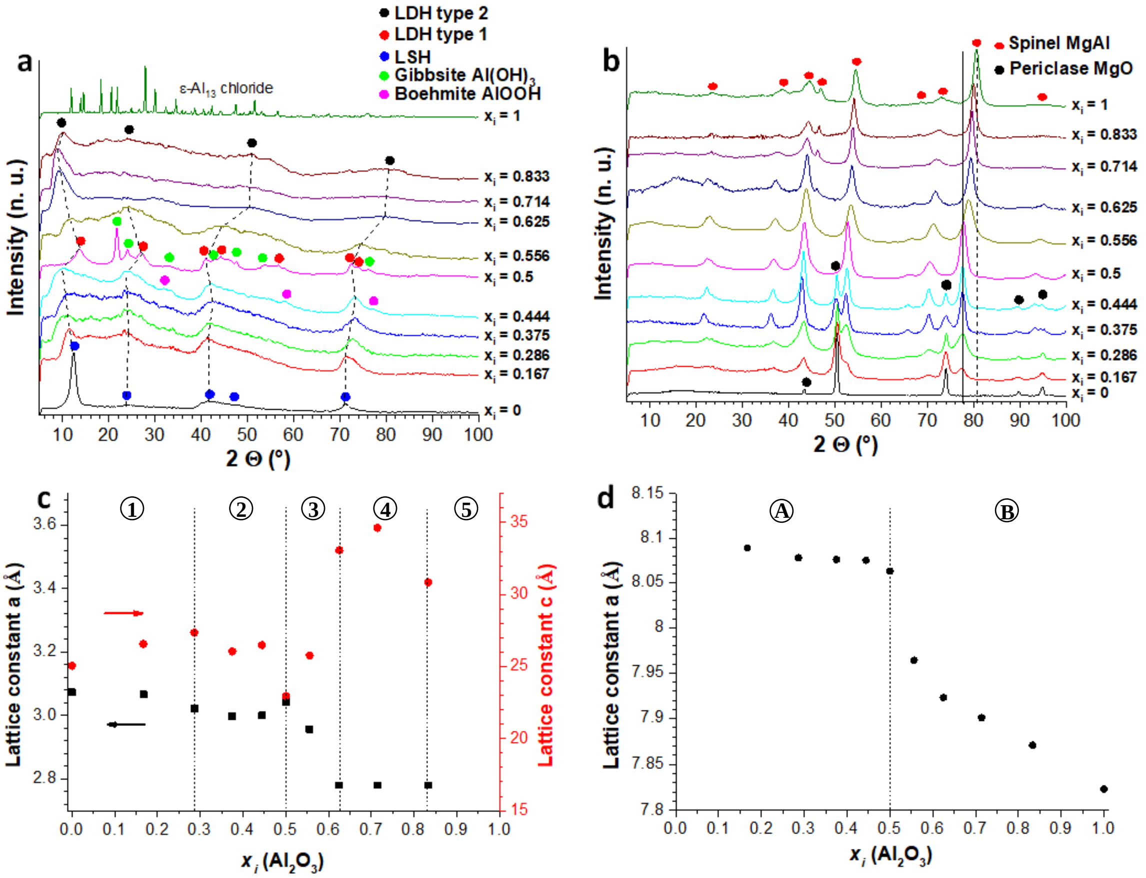

Figure 3.30: XRD patterns of the compounds synthesized with different x_i a) as-synthesized and b) after heat treatment at 900°C, 1 h; c) and d) show the evolution of the cell constants of layered hydroxide phases in as-synthesized powders and spinel phase in calcined samples in function of x_i, respectively. Dotted and straight lines in a) and b) are a guide for the eyes to emphasize peaks shifts

The *Figure 3.30.b* shows the XRD evolution of the compounds after heat treatment at 900°C for 1 h; the evolution of the lattice parameter of the spinel phase is plotted in function of x_i in *Figure 3.30.d* and the values are reported in *Table 3.4*. **Two domains Ⓐ and Ⓑ of cell constants** are observed. In **Ⓐ with $0 < x_i < 0.5$**, two phases are observed as **MgO periclase** and **$MgAl_2O_4$ spinel**, with spinel proportion increasing with x_i. The cell constant *a* of the spinel phase only slightly decreases with increasing x_i, from 8.089 Å at x_i = 0.167 to 8.063 Å at x_i = 0.5 for stoichiometric spinel, while the periclase lattice parameter is constant at ~4.208 Å. This indicates only **low shift from spinel stoichiometry**, as excess Mg^{2+} mostly crystallizes as MgO. Indeed, MgO-rich MAS has often been reported to be a hard-to-synthesize material [32, 34, 88, 345]. In **domain Ⓑ with $0.5 \leq x_i \leq 1$**, only **single-phase spinel** is obtained, with *a* rapidly dropping with increasing x_i, due to **incorporation of all Al^{3+} excess** in the structure. While Al_2O_3-rich MAS is known to be easily synthesized, successful syntheses without any second phase precipitation are rarely reported for composition exceeding x = 0.667 [41]. Thus, it should be noted that through thermal decomposition of a single-phase LDH-type2 synthesized in polyol medium, we were able to synthesize **alumina-rich MAS with composition up to x_i = 0.833, *i.e.* n_i = 5**, highly superior to what was previously reported.

The DT-DTG analysis of the as-synthesized materials with different x_i is presented in *Figure 3.31*. The endothermic mass loss at T < 150°C common to all compounds corresponds to dehydration and residual solvent evaporation. As the Al^{3+} content increases in the domain of existence of **Mg-LSH and LDH-type1** for **$x_i \leq 0.5$**, the **temperature of decomposition** of the layered phases **progressively decreases from 450°C at x_i = 0 to 350°C at x_i = 0.5**, while the endothermic phenomenon is progressively spread over a larger range of temperature. As mentioned in *Chapter 4.I.1*, the first mass loss at 250°C for x_i = 0.5 corresponds to the decomposition of $Al(OH)_3$ into η-Al_2O_3, and therefore is not observed for the single-phased powders. In the domain of existence of **LDH-type2 for $x_i > 0.5$**, the decomposition occurs at **365-370°C**, with little influence of the Al^{3+} content. This temperature of decomposition being slightly higher than that of the LDH-type1 at x_i = 0.5, in spite of the higher Al^{3+} insertion rate, confirms that LDH-type2 is most likely not based on brucite-like sheets but rather $Al(OH)_3$/AlOOH layers. By comparison, the ε-Al_{13} chloride compound synthesized for x_i = 1 undergoes decomposition through a different path in multiple steps, showing that this material and LDH-type2 products do not share a similar structure indeed.

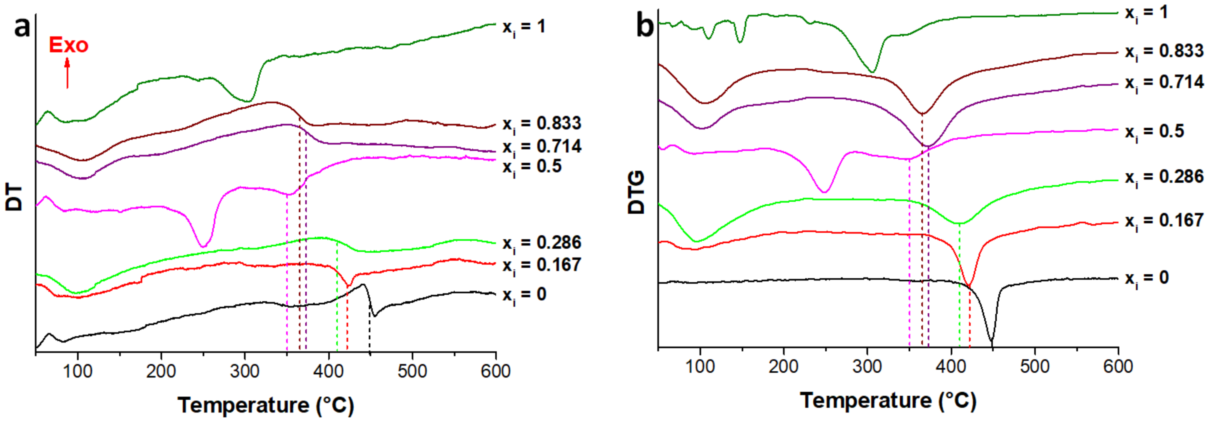

Figure 3.31: a) DT and b) DTG study of the as-synthesized precursors with different Al and Mg relative quantities

The microstructural analysis of the compound synthesized with $0 < x_i < 1$ before and after calcination at 900°C is presented in *Figure 3.32*. The as-synthesized material with $\boldsymbol{x_i}$ **= 0.167** (*Figure 3.32.a*) is composed by **highly agglomerated formless particles** of hundreds of nanometers, within which the crystallites are hardly distinguished. The typical "sand rose" morphology of LDH is not observed, in contrast with the microstructure of Mg-LSH (*Figure 3.27.a*). Prévot *et al.* [167] previously noted as well that a polyol medium greatly influences the LDH morphology, modifying the crystal growth and leading to highly compact particle aggregation, so individual hexagonal particles cannot be distinguished. However, the SEM micrograph in inset reveals that the particles consist in fact in a **porous network of thin nanometric sheets**. The LDH-type1 synthesized with $\boldsymbol{x_i}$ **= 0.375** (*Figure 3.32.c*) is composed by **two types of particles**, the first one similar to what is observed for $x_i = 0.167$ and the second one **acicular-like**. This peculiar morphology seems to occur due to the oversaturation in Al^{3+} in this particular condition. The microstructure of the **LDH-type2** materials synthesized with $\boldsymbol{x_i}$ **= 0.625 and 0.833** (*Figure 3.32.e* and *g*, resp.) consists in **massive irregular and aggregated particles**. As for the LDH-type1 synthesized with $x_i = 0.167$, the inset in *Figure 3.32.e* shows that the aggregates are composed by a **porous network of ultrathin sheets**, though the sheets and the pores seem much smaller in this case. **After thermal treatment**, the LDH-type1 materials decomposed into mixed spinel and periclase with homogeneous, weakly agglomerated rounded particles (*Figure 3.32.b* and *d*). In comparison, the microstructure of the **Al-rich MAS** obtained from decomposition of LDH-type2 is composed by very small **spherical crystallites with size < 5 nm** (*Figure 3.32.f* and *h*), while the morphology of the massive, irregular aggregated particles with sharp edges has remained.

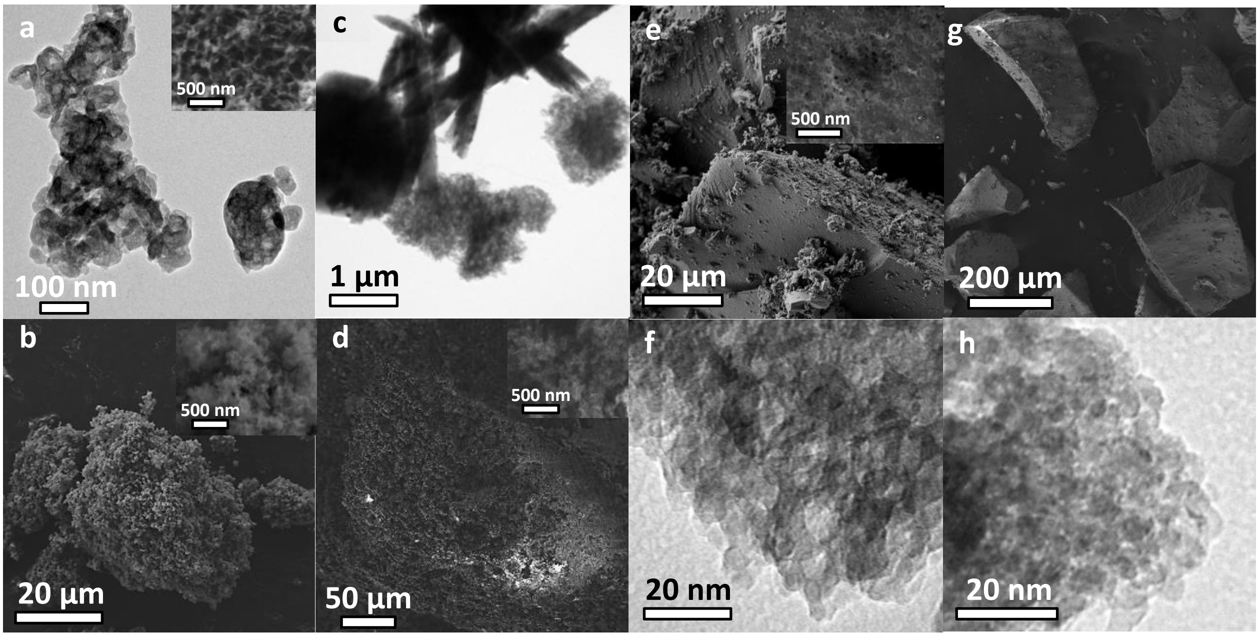

Figure 3.32: Micrographs of the powders synthesized for a)-b) $x_i = 0.167$, c)-d) $x_i = 0.375$, e)-f) $x_i = 0.625$ and g)-h) $x_i = 0.833$, with a),c),e),g) the as-synthesized materials and b),d),f),h) the materials after calcination at 900°C, 1 h

According to the results presented in this section, it appears that the synthesis of monophasic precursors with $x_i \leq 0.444$ does not lead to monophasic MgO-rich MAS after subsequent calcination with the set-up and conditions that we have used. However, further experiments should be carried out in order to assess the possibility of synthesizing MgO-rich spinel with $0.444 < x_i < 0.5$, which would have more chances of success since these conditions are within the range of metastable solid solution on the phase diagram (*Figure 1.4*).

Therefore, we attempted to **modify the reference set-up** presented and used otherwise in this work, in order to synthesize magnesia-rich spinel, with unchanged synthesis conditions. The modified set-up is based on the reference one, but **the gas outlet of the condenser is closed to prevent any loss of evaporated species**, especially water molecules. The XRD and TEM of the material after calcination at 900°C are presented in *Figure 3.33*. The reflections of the spinel phase obtained with the modified set-up are shifted toward low angles in comparison with reference set-up, for a cell parameter $\boldsymbol{a}$ **= 8.1326 Å** and a crystallite size of **17 nm** (Rietveld refinement). The lattice constant is quite high compared to the one of stoichiometric spinel $a_0 = 8.0826$, and following Viertel and Seifert's law (*Equation 1.1*) the composition can be estimated to be $\mathbf{MgO{\cdot}0.716Al_2O_3}$, corresponding to $\boldsymbol{x}$ **= 0.412**. Therefore, we **successfully synthesized MgO-rich spinel** *via* polyol route with a modified "no-evaporation" set-up. The microstructure of the material consists in **spherical crystallites of size about 15 nm**, in agreement with XRD analysis.

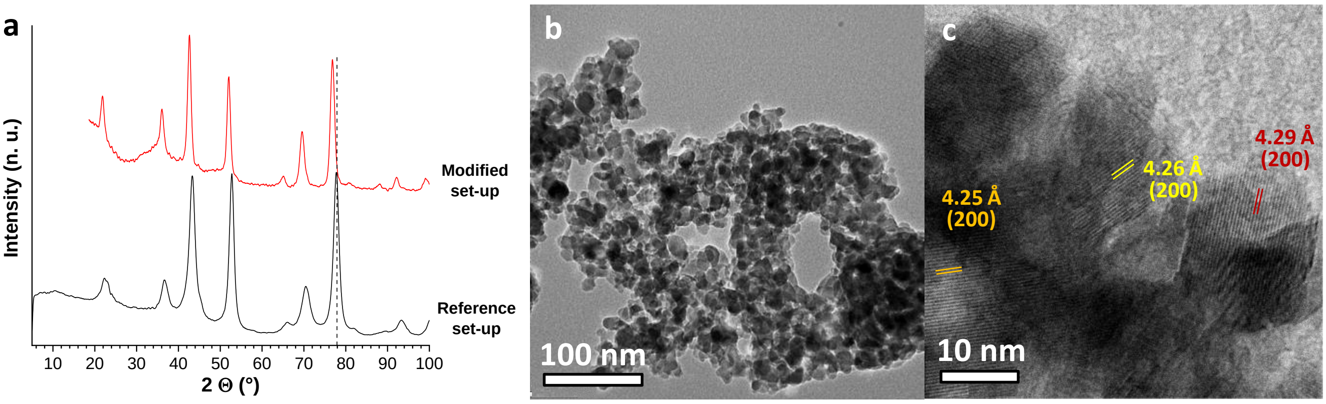

Figure 3.33: a) XRD patterns and b),c) TEM of the MgO-rich spinel synthesized with a modified "no-evaporation" set-up

From the results presented in this paragraph, it appears that **single phase LDH** can be obtained in two separated range of composition: **pure LDH-type1 for** $\mathbf{0 < x_i \leq 0.375}$ seemingly based on Mg-LSH material with Mg^{2+} substituted by Al^{3+}, and **pure LDH-type2 for** $\mathbf{0.675 \leq x_i < 1}$ based on $Al(OH)_3$/AlOOH with Mg^{2+} filling vacancies. Between these domains, the charge of the layers is too great, leading to their collapse and the formation of a second phase. The synthesis of LDH-type2 is not widely reported, systematically through long hydrothermal reaction of $Al(OH)_3$ dispersed in M^{2+} solution at 150-200°C, and seems to require higher temperature than for LDH-type1. Therefore, the polyol route is adequate for this purpose, as *i)* $Al(OH)_3$ is formed at 165°C prior to LDH (*Figure 3.11*), and *ii)* high temperatures above 200°C are allowed.

In contrast, **pure spinel phase** could only be obtained for $\mathbf{x_i \geq 0.5}$ after calcination, independently of the number of phases as-synthesized. **Modification of the set-up** to prevent any loss of evaporated species has provided interesting preliminary results for the synthesis of **MgO-rich spinel nanopowders**.

Finally, some general observations can be made, for better understanding of the reaction mechanism. It is remarkable that the boiling temperature decreases linearly from 192 to 173°C with the aluminum content (*Table 3.3*), indicating that $\mathbf{Al^{3+}}$ **interacts with EG**, as evidenced by the formation of EG-coordinated ε-Al_{13}. In fact, the temperature of particles formation is 185°C for $x_i = 0$, 120°C for $x_i = 0.5$ and 165°C for $x_i = 1$. Hence, it appears that **simultaneous presences of** $\mathbf{Mg^{2+}}$ **and** $\mathbf{Al^{3+}}$ **in polyol activate a reaction mechanism**, as confirmed by the foaming phenomenon only observed for mixed compositions. It can also be noted that the mass yield is particularly low for LDH-type2, possibly due to short synthesis duration.

iv. Spectroscopic study of the single-phased spinel in the range $0.5 \leq x_i < 1$

All the studied compositions in the range $0.5 \leq x_i < 1$ led to the formation of pure magnesium aluminate spinel phase, as shown in the previous paragraph. In order to verify that the spinel cation composition x corresponds to the initial x_i composition set by synthesis conditions, EDX and XPS spectroscopies were carried out on MAS materials synthesized with different x_i *via* polyol route, as well as on the commercial $MgAl_2O_4$ powders Sasol, S25CR and S30CR used in this thesis and presented in *Chapter 2.II.2.i*.

EDX spectra in the range of Mg $K\alpha_1$ and Al $K\alpha_1$ emitted X-ray energies are presented in *Figure 3.34.a* for the Sasol and S25CR commercial powders and for $x_i = 0.5$ and $x_i = 0.85$ polyol synthesized MAS. It can be seen that the relative intensity of Mg $K\alpha_1$/Al $K\alpha_1$ is somehow higher for Sasol than for S25CR, which is slightly higher than for $x_i = 0.5$, and finally it is very low for $x_i = 0.85$. The measured spinel compositions were very close to the ones set by synthesis conditions, *i.e.* $\boldsymbol{x \sim x_i}$, while commercial powders presented higher shift from expected stoichiometry than the $x_i = 0.5$ spinel powder. The Sasol powder has a higher MgO content corresponding to $x = 0.467$, in agreement with the highest cell parameter above 8.1000 Å. The S25CR and S30CR powders both have composition close to $x = 0.5$ and lattice constants around $a \approx 8.07$ Å, while the stoichiometric spinel synthesized by polyol route ($x = 0.506$) has a constant $a = 8.0820$ Å.

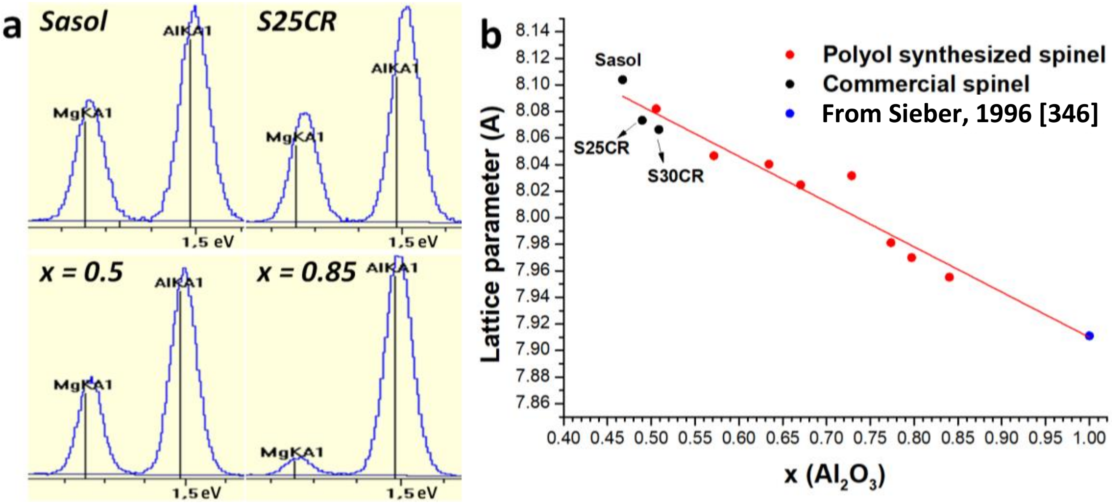

Figure 3.34: a) EDX spectra in the range of Mg $K\alpha_1$ and Al $K\alpha_1$ for Sasol and S25CR commercial powders and $x_i = 0.5$ and $x_i = 0.85$ polyol synthesized spinel, and b) spinel lattice parameter evolution with x measured from EDX

The EDX compositions were used to correlate the lattice parameter a measured by XRD to the aluminum content x, and the resulting curve is presented in *Figure 3.34.b*. A **linear correlation** is observed from stoichiometric spinel to γ-Al_2O_3, the lattice constant of the latter taken as $a(x = 1) = 7.911$ Å from bulk measurement [346], since the values obtained in this study were depending on the temperature of calcination, thus could not be considered as references. In good agreement with literature, the composition dependence of a follows a **Vegard's law** [29, 35] described by *Equation 3.2*, valid at least in the range $0.5 \leq x \leq 1$. From this law, the theoretical lattice constants for stoichiometric spinel and γ-Al_2O_3 can be calculated as $\boldsymbol{a(x = 0.5) = 8.081}$ **Å** and $\boldsymbol{a(x = 1) = 7.910}$ **Å**, respectively. Additional investigations in the composition ranges $0.85 < x_i < 1$ and $0.45 \leq x_i < 0.5$, if successful for synthesizing single-phased MAS, would allow to make this law more accurate near γ-Al_2O_3 and eventually extend its validity domain to MgO-rich spinel, respectively.

$$\boldsymbol{a = 8.251 - 0.341 * x(Al_2O_3)} \qquad \text{Equation 3.2}$$

The synthesized spinel powders with compositions $x_i = 0.5$ and $x_i = 0.85$ were further analyzed by XPS to compare their surface composition and chemical state. The spectra for Al2p, Mg1s, O1s and C1s are presented in *Figure 3.35*, and the surface compositions determined by the analysis can be found in *Table 3.5*. It is remarkable that XPS spectra of Al2p, O1s and C1s (*Figure 3.35.a*, *c* and *d*, resp.) are **highly similar** for both compositions, in binding energy distribution as in intensity. It is barely noticeable that Al2p and O1s peaks are slightly spread for $x_i = 0.85$, most likely because of larger distribution of environments in the partially inversed non-stoichiometric spinel. The C1s peaks are slightly less intense, but since they are mostly adventitious, it is not inherent to the sample. However, the **Mg1s** spectra (*Figure 3.35.b*) reveal a **strong decrease of intensity for $x_i = 0.85$**, with the same binding energy of 1303.3 eV, leading to an **Al/Mg ratio of 14.62** (*Table 3.5*) expected for $MgO.nAl_2O_3$ spinel with $n > 7$. The surface Al/Mg ratio determined by XPS are higher than the ones determined by EDX, which is due to the extremely shallow analysis of XPS technique, with an average penetration depth of ~5 nm, while EDX technique allows interactions of the electron beam within dozens of micrometers in the material, hence indicates bulk composition. Thus, the sample $x_i = 0.5$ presents the same Al/Mg surface ratio of 2.67 than the commercial S25CR spinel powder (*Figure 2.4*). Comparison between bulk and surface compositions hints that surface is richer in aluminum.

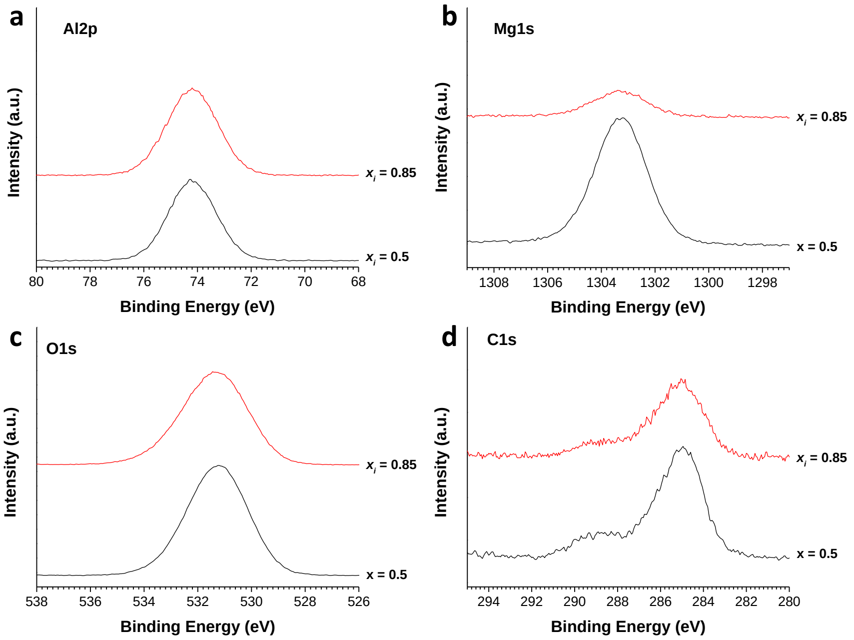

Figure 3.35: XPS of polyol synthesized spinel with $x_i = 0.5$ and $x_i = 0.85$ in the range of a) Al2p, b) Mg1s, c) O1s, and d) C1s

Table 3.5: Surface composition of polyol synthesized spinel with compositions $x_i = 0.5$ and $x_i = 0.85$ determined by XPS

Composition	Mg (%)	Al (%)	**Al/Mg**	O (%)	C_A (%)	C_B (%)	C_C (%)	C (%)
$x_i = 0$	8.99	23.97	**2.67**	55.64	6.76	2.52	2.11	11.39
$x_i = 0.85$	2.14	31.28	**14.62**	57.62	4.72	3.09	1.15	8.96

7. Temperature of addition of the precursor salts

In the previous section, it was shown that Mg and Al relative quantities have a big impact on the structures and microstructures that could be obtained, both before and after calcination, especially for the monocationic compounds. In order to assess the possibility to modify these properties of the material by multi-step synthesis, we investigated **the effect of the solvent temperature when introducing the precursor salts** into the reaction medium. For this purpose, we used the reference synthesis conditions ($[Mg^{2+}]$ = 0.033 M, $[Al^{3+}]$ = 0.067 M, EG = 200 ml, h = 6, r = 2.67, T = boiling temperature) but the precursor salts were added to the medium at different temperatures. In the reference conditions, all the precursors are introduced to the solution at room temperature (RT), while in this section they are added either at RT or boiling temperature (BT), in the last case after dissolution in the minimal required amount of water. Several interests could be seen in such protocol: *i)* modifications of the reaction mechanism could be expected, bypassing the reactions occurring at lower temperatures and forcing specific ones by delayed precursors introduction, *ii)* structures and microstructures could be greatly impacted by the first point, notably if starting from pure magnesium or aluminum (x = 0 and x = 1), as shown in the previous section.

Along with reference synthesis RT, four conditions were investigated and are reported in *Table 3.6*, along with the structural characterizations before and after calcination at 900°C, and the mass yields. For BT:Na sample, only $NaCH_3COO$ was added at BT, for BT:MgAl sample both Mg and Al precursors were added at BT, and for BT:Al and BT:Mg, magnesium or aluminum salts were introduced at BT, respectively. The solutions were let to boiling temperature for 10 minutes before addition, for the reaction to have been initiated. Synthesis with all precursors added at BT has not been performed, since $NaCH_3COO$ is harder to dissolve in EG, hence results should be similar to BT:Na.

Table 3.6: Conditions, structural characterizations and mass yield for syntheses with precursors' addition at different temperatures

Sample name	RT	BT:Na	BT:MgAl	BT:Al	BT:Mg
Precursor salt	Temperature of addition [a]				
$MgCl_2.6H_2O$	RT	RT	**BT**	**BT**	RT
$AlCl_3.6H_2O$	RT	RT	**BT**	RT	**BT**
$NaCH_3COO$	RT	**BT**	RT	RT	RT
Composition as-synthesized	$Al(OH)_3$ LDH-type1	LDH-type2	LDH-type1 LDH-type2	LDH-type1 LDH-type2	LDH-type2
Composition after calcination	Spinel	Al-rich spinel	Spinel	Spinel	Al-rich spinel
Mass Yield (%)	43.5	38.9	52.2	62.7	49.3

[a] RT and BT indicate respectively an addition at room temperature and at boiling temperature

The XRD patterns of the synthesized powders before and after heat treatment at 900°C for 1 h are presented in *Figure 3.36*. *Figure 3.36.a* clearly shows that the temperature and order of addition of the precursor salts have a **crucial impact on the structural composition** of the as-synthesized product. For **BT:Na**, Mg^{2+} and Al^{3+} salts are already dissolved and homogeneously mixed prior to the solubilized $NaCH_3COO$ introduction, without having reacted yet as shown in *Chapter 4.I.iii* for the synthesis with r = 0. As soon as the acetate salt is added, the solution immediately turns white (formation of particles) with **instant foaming** like we previously observed for reference synthesis conditions, emphasizing the role of acetate in the reaction. The XRD pattern shows the formation of an apparently **pure LDH** structure with very broad reflections, thus not well defined. Based on the position of all reflections for $2\theta > 15°$, and especially (110) around 73.8°, it is to be assumed that the layered phase in presence is **LDH-type1** based on brucite layers, though the low crystallinity precludes certainty. However, the (003) reflection is observed under 2θ = 7°, and cannot be seen in its whole because of our limitation in low angles at 5°, for an estimated $d_{003} \approx 16$ Å indicating that the hot-injection of the acetate reactant led to a **modified interlayer composition**, greatly increasing its thickness. After calcination, an **Al_2O_3-rich spinel** is obtained (*Figure 3.36.b*), indicating that **part of the reacted Al^{3+} has not integrated the LDH-type1** sheets since the Al/Mg ratio in this phase cannot exceed ~1/2. It is to be assessed that the Al^{3+} moiety not observed in the XRD pattern is most probably presents in an amorphous part of the material, or intercalated as a complex anion in the LDH galleries, the latter hypothesis which might explain the large d-spacing.

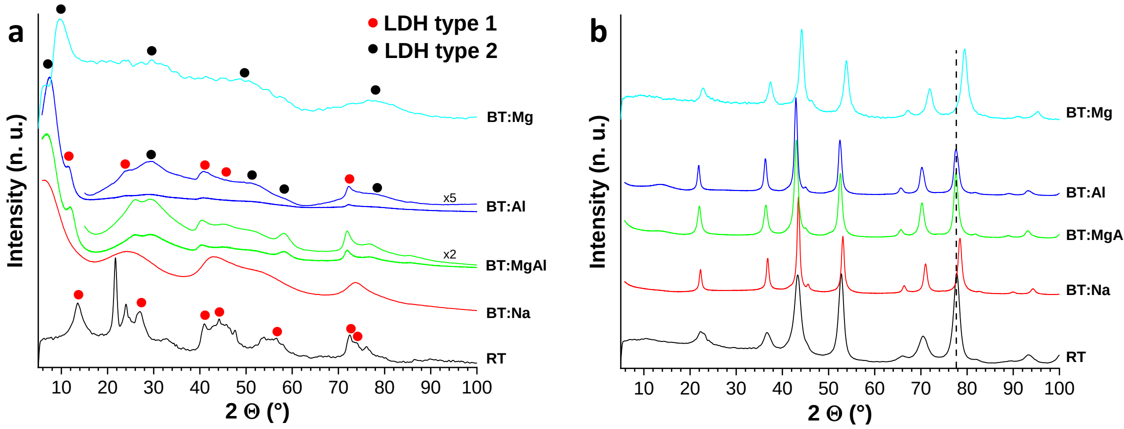

Figure 3.36: XRD of samples synthesized with different temperature of addition of the precursor salts a) before and b) after calcination at 900°C

When the acetate salt is introduced at RT instead for **BT:MgAl**, the solution once again instantly turns white with foam formation as the Mg and Al salts are hot-injected. The XRD measurement reveals a more complex pattern (*Figure 3.36.a*), that we explain by the presence of **both Mg-rich LDH-type1 and Al-rich LDH-type2**. In comparison with the XRD patterns of LDH phases obtained with different Mg/Al relative quantities (*Figure 3.30.a*), the LDH-type1 phase has peaks positions very close to the pattern of as-synthesized $x_i = 0.167$, indicating a **Mg/Al ratio of ~ 2.5**, while the peaks positions of the LDH-type2 phase are consistent with the ones obtained for Al-rich compositions $0.625 \leq x_i \leq 0.833$. However, the non-basal reflections for LDH-type2 are better resolved in the present case, thus can be better observed and analyzed. As hypothesized before in this work, rather than based on $Al(OH)_3$ gibbsite or bayerite sheets as stated in other studies [128, 130], the **LDH-type2 seems to be derived from the AlOOH boehmite structure**, given the similarity of the in-plane reflections at 58° and 77°. After calcination, a well-crystallized **stoichiometric spinel** is obtained. The differences observed between BT:Na and BT:MgAl experiments can be explained by the reaction kinetic of each cations and the instantaneous concentration of CH_3COO^- surrounding them. In BT:Na, Mg and Al cations are well distributed in the medium when the acetate solution is progressively added by rapid drop by drop, thus the CH_3COO^- concentration remains low during reaction. Since Al^{3+} has a greater reactivity, as shown in *Chapter 4.I.3* and *4*, it most likely reacts prior to Mg^{2+}, which then only reacts with the intermediary product when most of Al^{3+} has reacted, explaining the Mg-deficit in the composition. In BT:MgAl, the opposite situation is observed: CH_3COO^- is well distributed in EG when the MgAl solution is injected, so its high relative concentration allows for **both cations to react at the same time in competitive mechanisms** leading to the two types of LDH as products, respectively rich in Mg^{2+} and in Al^{3+}.

For **BT:Al**, the experiment started in similar conditions than for $x = 0$ synthesis, hence no foaming occurred and **Mg-LSH** was formed at first. Following the introduction of Al^{3+}, the white solution **turned back to transparent**, due to either the dissolution of the Mg-LSH particles or the dispersion of the layers into delaminated nanometric sheets. After a few minutes, the solution turned white again **without any foaming**. The XRD pattern shows the same reflections than for BT:MgAl, indicating the **formation of both types of LDH**, with somehow different peaks intensities and slightly shifted positions. The similarity between both patterns suggests that the **Mg-LSH particles were dissolved** prior to the LDHs formation, hence leading to close compositions. Indeed, stoichiometric spinel is obtained after calcination. Interestingly, the mass yield is greater in the case of BT:Al (*Table 3.6*), possibly because of the different reaction path. It is to be deduced that the **reaction with Al^{3+} is favored** in such a way that even pre-existing magnesium hydroxide phases will be decomposed for it to be formed.

Finally for **BT:Mg**, initial conditions are similar than for $x = 1$ synthesis, so **ε-Al_{13} chloride** is formed in a foamingless mechanism as a first step. When Mg^{2+} is introduced, **no visible alteration** of the ε-Al_{13} material was observed. The XRD pattern indicates that the crystallographic structure obtained is **pure LDH-type2**, with same peaks positions than for the $x_i = 0.625$ synthesis, which was determined to be the composition with maximum Mg^{2+} content in the LDH-type2 phase in *Chapter 4.I.6.iii*. Consequently, an **Al-rich spinel** is formed after calcination. It can be inferred that the ε-Al_{13} chloride is progressively dissolved by the injected Mg^{2+}, while the LDH-type2 forms instantly as Al^{3+} is available and excess Mg^{2+} not incorporated remains in solution and is removed during the washing process.

The microstructure for calcined BT:Na, BT:MgAl and BT:Al are presented in *Figure 3.37*. It appears to be very close for all samples, and highly similar to reference synthesis conditions. Micrographs of BT:Mg are not shown because they are very similar to BT:Na's. TEM analysis reveals that the **particles are agglomerated**, and even highly aggregated in the case of BT:MgAl. The crystallites seem to be spherical or rounded with average size of about **10 nm**. More interestingly, neither the BT:Al nor BT:Mg samples present the original microstructure obtained for $x = 0$ and $x = 1$ synthesis, *i.e.* nanoflake assembled microspheres (*Figure 3.26*) and porous octahedra (*Figure 3.27*), respectively. It could be inferred that the reaction following the hot-injection is not topotactic and occurs by decomposition of the prior particles, in agreement with observations during syntheses and XRD. However, since the initial solutions were only let at BT for 10 minutes before hot-injection, there is no certainty that these morphologies were obtained in the first place.

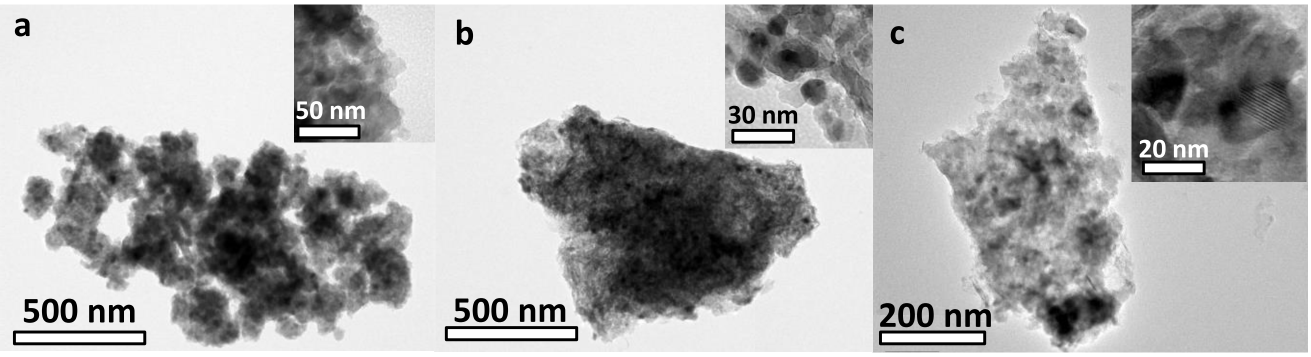

Figure 3.37: TEM micrographs of the powders calcined at 900°C, 1 h synthesized with a) BT:Na, b) BT:MgAl and c) BT:Al

This study shows the **strong impact** of the **order and temperature of addition of the precursor salts on the synthesis mechanism**, and several reflections can be made. Firstly, it is interesting to observe that the **foaming phenomenon** during the synthesis **is not directly linked to the formation of specific phases**. Indeed, BT:MgAl and BT:Al led to the same phases, but no foam was observed in the latter. Instead, the foaming seems to depend on **the reaction path**, and especially occurs when either of the LDH types is formed directly without pre-existing phase, otherwise the reaction happens to the detriment of the already-formed intermediary compound. It can be supposed that the foaming phenomenon is in fact the sign of a **strong exothermic reaction**, producing a gas (or vaporizing some of the solvent) which is trapped within the viscous EG, creating bubbles and ultimately turning to foam. It is consistent with the fact that if a solid is already formed and need to be decomposed for the reaction to occur, it will consume a part of the released energy, resulting in a less exothermic overall mechanism. Hence it is possible to synthesize a given compound without the inconvenient foaming by hot-injection. Secondly, Al^{3+} should not be introduced in a way that favors its prior reaction, otherwise the desired stoichiometry will not be reached. Thirdly, when Al^{3+} is introduced at high temperature, LDH are better crystallized, and it is possible to synthesize both LDH-type1 and LDH-type2 together, which could be very interesting for homogeneity through thermal decomposition. A more thorough investigation should be carried out to understand the spatial distribution of the different LDH relatively to each other, and eventually assess the possibility to form an interstratified LDH, with alternating LDH-type1 and -type2 layers. Lastly, the solution were let boiling for only 10 minutes before hot-injection, which may have been too short for first-stage reactions to be complete and the expected phases and microstructures to be formed. This issue should be investigated further, to assess the possibility of modifying the morphology and size of the particles, as well as optimizing their stoichiometry.

8. Effect of the synthesis duration

The duration of the synthesis dwell at boiling temperature is indeed an important parameter, because it can affect the phase, composition and crystallinity through reaction kinetics, as well as the microstructure through nucleation/growth mechanisms. Therefore, we carried out a set of syntheses with **dwell duration between 10 min and 24 h**, all other parameters corresponding to reference synthesis conditions.

The XRD patterns obtained for the different synthesis duration are shown in *Figure 3.38*. The diffraction data of the as-synthesized materials (*Figure 3.38.a*) indicate that for synthesis shorter than 2 h, the typical patterns of mixed LDH-type1 and gibbsite are not observed, while after 2 h and up to 24 h the characteristic signature of these two phases is observed without noticeable change whatever the duration of reaction. The material prepared through **10 min synthesis is amorphous**, as the few broad reflections observed are typical of the sample holder and should not been mistaken for poorly crystalized LDH. It indicates that such a short synthesis allows the particles to nucleate but not to crystallize. For a **1 h synthesis**, the diffraction pattern clearly shows some broad non-basal reflections from **LDH phase**, with very low crystallinity judging from the very ill-resolved reflections. It is possible than an amorphous moiety of material remains in these conditions. After **calcination at 800°C** for 1 h, spinel structure is obtained independently of the synthesis duration (*Figure 3.38.b*). However, for synthesis duration **below 2 h**, **Al-rich compositions** are obtained, with more important deviation from stoichiometry as the synthesis is shorter, as indicated by the peaks shift toward high angles. Moreover, it can be noted that spinel reflections are much sharper for duration ≤ 2 h, which indicates better crystallisation and bigger crystallites after calcination of low-crystalline precursors.

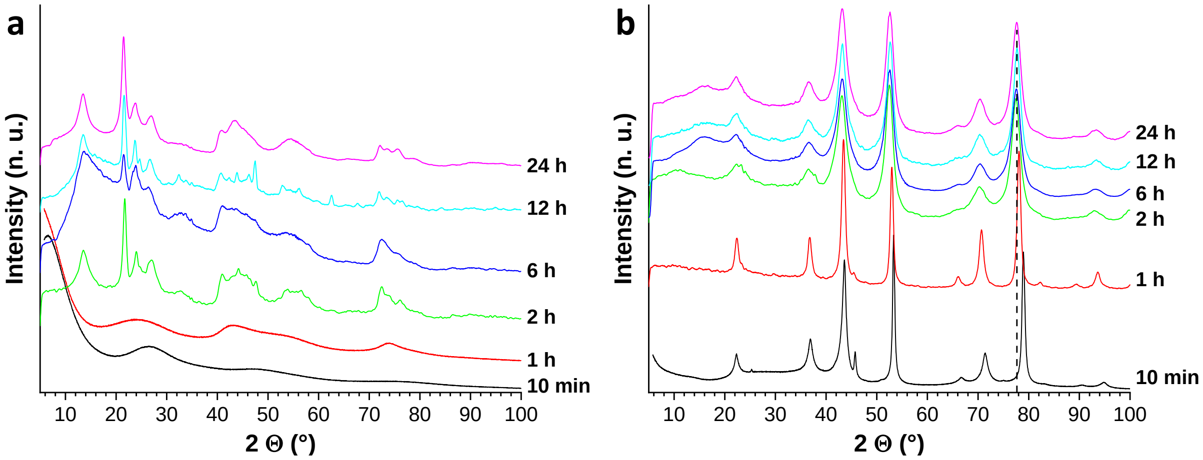

Figure 3.38: XRD of polyol synthesized materials for different synthesis duration a) before and b) after calcination at 800°C, 1 h

The thermal analysis (*Figure 3.39*) performed on the samples obtained for synthesis duration between 10 min and 2 h indicates a difference of composition for the materials prepared with short syntheses. The 10 min-sample decomposition occurs through an endothermic **dehydration below 200°C** with 35% mass loss, followed by a **second mass loss of 30% at 375°C**, attributed to **dehydroxylation**. The 1 h-material follows the same mechanism of decomposition, with a 25% mass loss below 200°C and a 30% mass loss at 400°C. The dehydroxylation may be slightly exothermic, but the data do not allow certainty. Both samples lose 30% of their mass during dehydroxylation, which shows their similar nature though their crystallization states are different. From comparison with the 2 h-sample and the thermal analysis of the materials synthesized with different x_i compositions (*Figure 3.31*), it appears that these materials are Al-rich **LDH-type2** and do not contain $Al(OH)_3$ (decomposition at 250°C), in agreement with the Al-rich spinel obtained after calcination. The higher temperature of dehydroxylation for the 1 h-sample seems to arise from its higher Mg^{2+} content, as demonstrated in *Figure 3.31*. The high mass losses during dehydration indicate that these materials are very hygroscopic compared to the 2 h-sample, which shows only 15% of mass loss under 200°C.

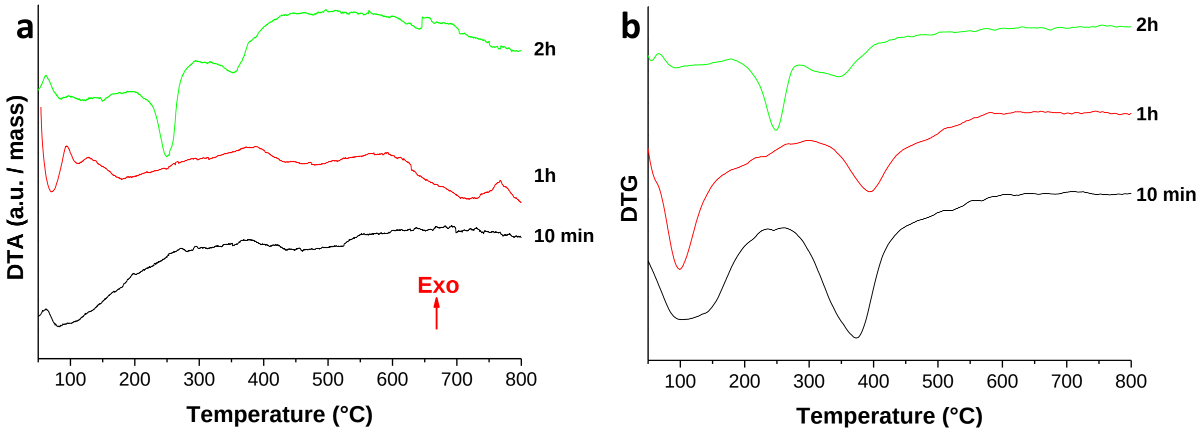

Figure 3.39: a) DT and b) DTG analysis of polyol synthesized materials with different synthesis duration

The microstructures of the spinel samples obtained with a 1, 6 and 24 h syntheses are presented in *Figure 3.40*. The morphologies show no major differences from the spinel obtained with reference synthesis (*Figure 3.3*), as the powders are **highly agglomerated** and the primary particles are hardly distinguishable.

However, the primary particles seem to be sensibly bigger for the 1 h synthesis sample in *Figure 3.40.a*, which is consistent with the sharper reflections observed on its XRD pattern (*Figure 3.38.b*). Nevertheless, this feature will not be further investigated, since the desired stoichiometry is not reached in this sample.

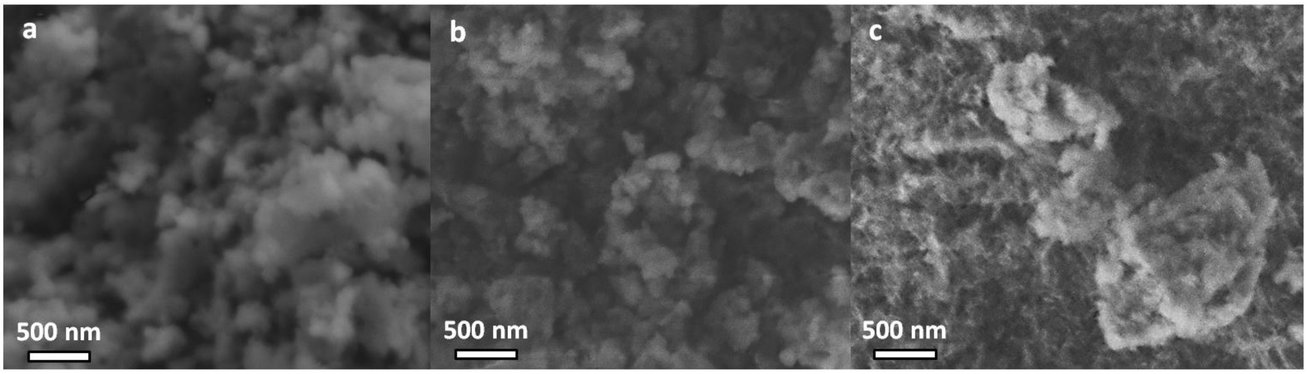

Figure 3.40: SEM micrographs of heat treated polyol synthesized materials with duration of a) 1 h, b) 6 h and c) 24 h

Figure 3.41 shows the evolution of oxide material mass obtained after calcination and the corresponding yield in function of the synthesis duration. From **10 min to 2 h**, the **yield remains around 45%** as the reaction is in the **nucleation/crystallization phase** toward the final composition and stoichiometry, then it progressively **increases to 80% for 12 h during the growth phase**. Longer synthesis of 24 h only allows small increase, possibly because of the low Mg^{2+} and Al^{3+} concentrations remaining in the polyol medium.

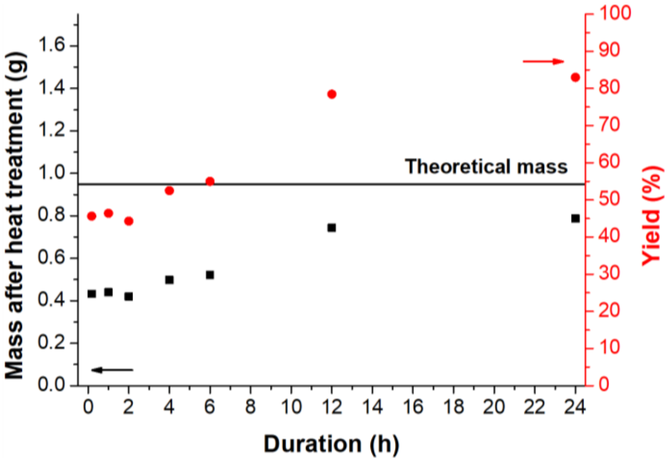

Figure 3.41: Mass of oxide material obtained after heat treatment and mass yield in function of the synthesis duration

From these results, we can deduce that the $\mathbf{Al^{3+}}$ **reacts first** in the medium, possibly due to reaction onset at lower temperature (*Chapter 4.I.3*), then $\mathbf{Mg^{2+}}$ **progressively integrates the structure** leading to the formation of **LDH-type2** within 1 h. When the $\mathbf{Mg^{2+}}$ **content becomes too high** to be fully accommodated within the layered structure, it is **demixed into the most stable phases LDH-type1 and** $\mathbf{Al(OH)_3}$ **gibbsite**. Mg^{2+} seems to substitute Al^{3+} in the structure, since the mass yield does not increase until demixtion. Once the stable composition is obtained, the yield increases progressively to 80% over time, indicating that the nucleation mechanism is over and the growth mechanism is ongoing, activated by the self-seeding effect of already formed particles. After 24 h, the remaining Mg^{2+} and Al^{3+} concentrations in solution are too low for the reaction to further progress. In order to obtain a spinel compound with the desired stoichiometry, synthesis should last at least 2 h, and to maximize the mass obtained, it should last 12 h.

9. Effect of the hydrolysis ratio *h*

It has been previously reported that the synthesis of layered hydroxides in polyol medium involved several steps, including the dissolution of the metal salts, followed by the formation of intermediary complexes which are finally hydrolyzed [143]. The work and analysis presented hereabove seem to be in agreement with such reaction mechanism. The kinetic and extent of the hydrolysis step are highly dependent on the **hydrolysis ratio *h***, *i.e.* the quantity of water per metallic cations (*Equation 1.16*). Depending on the cations, it is possible to obtain either metal, oxide or hydroxide with the appropriate hydrolysis rate [16]. Therefore, it could be possible to synthesize directly the MAS phase in polyol, without subsequent calcination. **The effect of *h* in the range 0-20** on the synthesis achievement is investigated in this section. For synthesis conditions with $h < 6$, anhydrous magnesium and aluminum chlorides were used, while for $h = 14$, $NaCH_3COO\cdot 3H_2O$ was used and for $h = 20$, 5 ml of deionized H_2O was added to synthesis.

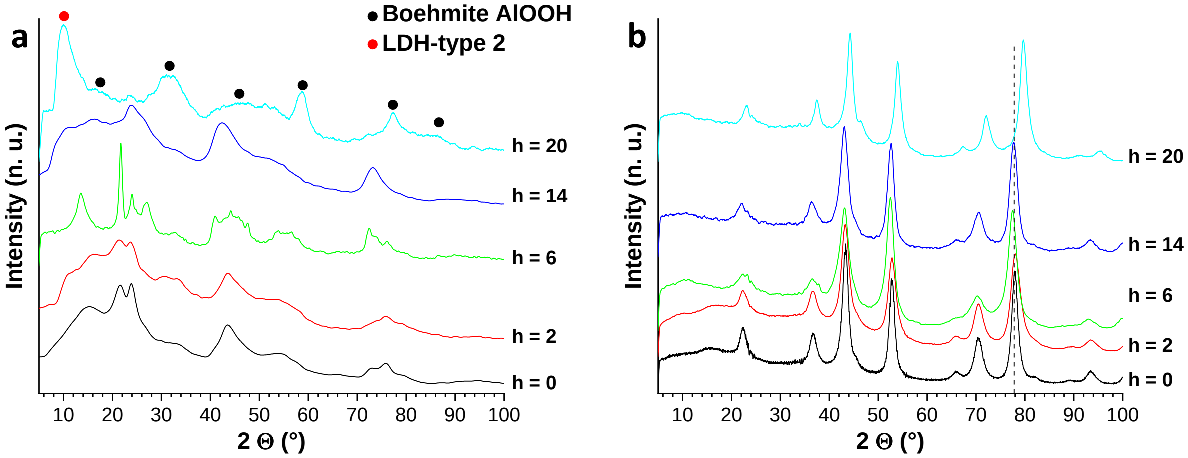

Figure 3.42: XRD of polyol synthesized materials with effect of hydrolysis ratio a) before and b) after calcination at 900°C, 1 h

The XRD patterns of the samples obtained with different *h* are presented in *Figure 3.42*. The diffraction data before calcination (*Figure 3.42.a*) indicate that for ***h* < 6**, **no clear difference in composition** occurs in the materials, though their poor crystallization state prevents careful comparison. Reflections from gibbsite $Al(OH)_3$ are predominant, but LDH-type1 one's are distinguishable, with a broad and weak (003) reflection around 2θ = 15° and more importantly the (110) reflection at 2θ = 72° evidencing the presence of brucite-like sheets. After heat treatment at 900°C for 1 h, the XRD pattern of **stoichiometric spinel** phase is observed (*Figure 3.42.b*), confirming the presence of both hydroxides phases in the as-synthesized materials. For ***h* = 14**, the **formation of gibbsite cannot be deduced** from the diffraction pattern, but **LDH-type1** reflections are observed. However, after calcination a stoichiometric spinel is obtained, inducing that **amorphous $Al(OH)_3$** may be present. For ***h* = 20**, **LDH-type2 and boehmite AlOOH** are obtained, hinting for the close relation between the two structures, and subsequent calcination forms an **Al-rich spinel** as some of the Mg^{2+} must have remained in solution.

In contrast with conclusions in [143, 167], our work tends to indicate that **no or low amount of water is required for the synthesis of LDH and gibbsite** since we were able to synthesize them with *h* = 0, so the **reaction mechanism cannot include a hydrolysis step**. Instead, it can be supposed that an **alcoholysis or alcoxolation** step intervenes. However, hydrolysis may occur for intermediary hydrolysis ratio, as

crystallization is enhanced at *h* = 6. With further increase of *h* to 14, $Al(OH)_3$ does not crystallize anymore, and AlOOH and LDH-type2 are formed instead for *h* = 20, possibly through hydrolysis, and part of the dissolved Mg^{2+} does no react. Therefore, **excessive amounts of water (*h* > 6) are detrimental to reach the desired structure and stoichiometry**. Indeed, the increased presence of H_2O in the medium at high temperature favors the transformation of $Al(OH)_3$ to AlOOH, as our experiments in pure aqueous medium demonstrated in *Chapter 4.I.2.i*. It can be deduced that the preferential formation of boehmite favors in turn the formation of LDH-type2 instead of LDH-type1, with a required temperature for reaction to occur reached in EG with *h* = 20 for which BT ~168°C while it could not be achieved in sole deionized water solvent with BT ~100°C. Then, the Al-rich LDH structure was not able to integrate all dissolved Mg^{2+}, possibly because of a greater dissolution constant in H_2O than the LDH-type2 formation constant.

Figure 3.43 shows the microstructures of the spinel samples obtained with *h* = 0 and 2. The microstructures of samples obtained with *h* > 6 were not investigated, since these conditions do not allow preparation of stoichiometric spinel, *h* = 14 being considered as the threshold as $Al(OH)_3$ is amorphous. From comparison with reference sample with *h* = 6 (*Figure 3.3*), **the morphology of the particles does not seem to be impacted by the hydrolysis ratio**, since similar agglomerated rounded crystallites with size of ~10 nm are obtained.

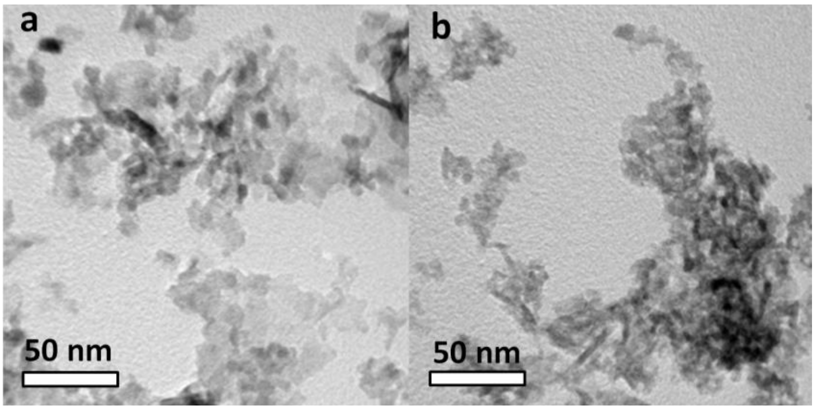

Figure 3.43: TEM micrographs of heat treated polyol synthesized materials with hydrolysis ratio a) h = 0 and b) h = 2

In conclusion, in order to reach the desired MAS stoichiometry and favor the reaction with the studied synthesis conditions: *i)* the **hydrolysis rate *h* is not a key parameter** for the mechanism of formation of the hydroxides, *ii)* an **hydrolysis ratio *h* ~6**, set by the hydrated Mg and Al precursor salts is required for **good crystallization of the LDH-type1 and gibbsite phases**, *iii)* an **hydrolysis ratio *h* > 14 favors** the formation of **AlOOH and LDH-type2**, detrimental for stoichiometry and *iv)* **direct synthesis of the magnesium aluminate spinel phase cannot be achieved** in ethylene glycol. Surprisingly, the reaction mechanism occurring for our cationic system appears to be different than the one observed in previous studies for the synthesis of LDH and spinel in polyol medium. Nevertheless, this may be explained by the fact that these studies focused on the preparation of LDH or spinel containing at least one easily reducible metal cations (typically 3d metals like Ni, Co or Fe), whereas Mg^{2+} and Al^{3+} are too electropositive to be reduced by the mild reducing power of polyols [16].

10. Effect of the concentration of the precursor salts

Since the synthesized powders are aimed to be used for sintering which requires a certain mass of material, scale-up must be considered, and therefore it is important to determine **the effect of concentration of precursors** on the material, as well as to determine the threshold concentration to obtain the desired product. All parameters but concentration $C_T = [Mg^{2+} + Al^{3+}]$ were kept identical to reference conditions.

The X-Ray diffractograms of the materials synthesized with concentration C_T in the range **0.050 M to 0.300 M** are presented in *Figure 3.44*. In *Figure 3.44.a*, it can be seen that the **as-synthesized materials** with **0.025 M ≤ C_T ≤ ~0.125 M** exhibit similar XRD patterns, and are all composed of **LDH-type1 and $Al(OH)_3$ gibbsite**, the reflections of layered phase being particularly poorly crystallized for C_T = 0.125 M which appears to be a critical concentration. For **C_T = 0.150 M**, three phases are observed: **gibbsite $Al(OH)_3$, LDH-type1 and -type2**, the latter being identified by its basal reflection (003) below $2\theta = 10°$. **For C_T > 0.150 M**, **LDH-type2 has entirely replaced LDH-type1**, and **$Al(OH)_3$ converted to boehmite AlOOH**. Considering our previous observations hinting that LDH-type2 is based on AlOOH layers, it may be supposed that $Al(OH)_3$ started to convert to AlOOH for C_T ~0.125 M, the latter forming LDH-type2 in turn. After **calcination at 900°C** for 1 h (*Figure 3.44.b*), **$MgAl_2O_4$** is obtained for **C_T ≤ 0.150 M**, while higher concentrations lead to Al_2O_3-rich MAS. These results indicate that when LDH-type2 is formed, the full incorporation of Mg^{2+} in the phase is not possible, and part of the cations remains in solution.

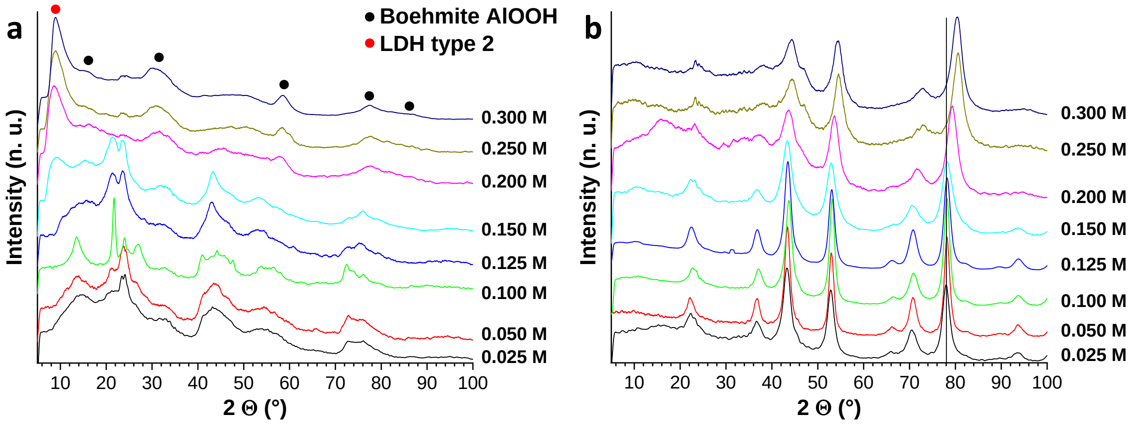

Figure 3.44: XRD of polyol synthesized materials with effect of the concentration a) before and b) after calcination at 900°C, 1 h

TEM micrographs of the spinel powders obtained with C_T = 0.050 and 0.300 M are presented in *Figure 3.45*. The microstructure issimilar to the one obtained with reference conditions C_T = 0.100 M (*Figure 3.3*) independently of the concentration, with **~7 nm spherical crystallites** quite agglomerated.

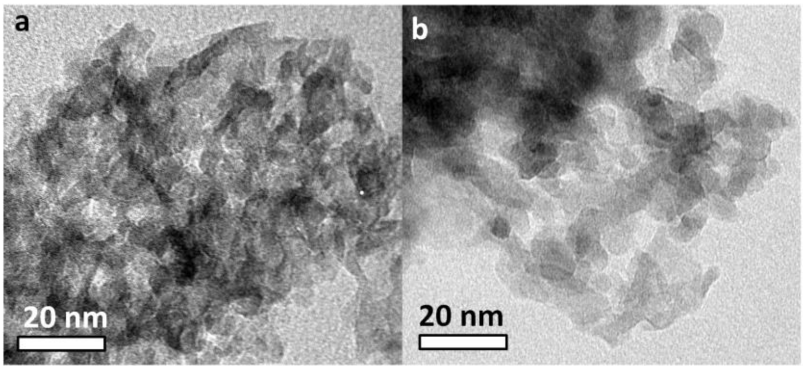

Figure 3.45: TEM of the polyol synthesized MAS powders calcined at 900°C, 1 h for concentration of a) 0.050 and b) 0.300 M

In order to explain the evolution of the composition with the increase of concentration, it is interesting to analyze the evolution of the **water content $w = H_2O/(H_2O + EG)$** with C_T. Indeed, the hydrolysis ratio $h = H_2O/C_T$ is fixed at 6, so **w increases linearly with C_T**: $w \approx 3$, 5 and over 9% for $C_T = 0.100$, 0.150 and 0.300 M, respectively. It can be deduced that **Al^{3+} reactivity is impacted by w**, favoring the formation of AlOOH and LDH-type2 for high relative content of water, as for high hydrolysis rate $h \geq 14$ (*Chapter 4.I.9*). The H_2O molecules may occupy a larger part of the Mg^{2+} and Al^{3+} coordinating sphere, and **prevent EG and CH_3COO^- species to become ligands and initiate the reaction mechanism** occurring in reference synthesis conditions. In addition, increasing w leads to *i)* a rapid **decrease of the boiling temperature** from 196°C for 0.025 M to 175°C for the threshold concentration 0.150 M, then followed by *ii)* a slow decrease to 170°C up to 0.300 M. Considering that low synthesis temperature of 165°C was demonstrated to decrease Mg^{2+} integration in LDH (*Chapter 4.I.3*), the progressive decrease of BT with increasing C_T may be at cause for the progressive Mg^{2+} deficiency in the synthesized material with $C_T > 0.150$ M.

Based on these results, the **Mg + Al concentration should be set at 0.100 M** in order to avoid any risk of deviation from desired stoichiometry while maximizing the mass of product per synthesis.

11. Synthesis of Co^{2+}, Cr^{3+}, Fe^{2+} and Ti^{4+} doped $MgAl_2O_4$ and $ZnAl_2O_4$

As a perspective and with the desire to extend the potential of the developed route, in this section we address **the synthesis of Co^{2+}, Cr^{3+}, Fe^{2+} and Ti^{4+} doped $MgAl_2O_4$ as well as the synthesis of zinc aluminate spinel $ZnAl_2O_4$**, following the same protocol as for the reference synthesis. Such materials find many interests in the literature for technologic applications: Co^{2+}:$MgAl_2O_4$ as passive laser Q-switching in the 1.3-1.7 µm range for saturable absorbers [347], Cr^{3+}:$MgAl_2O_4$ as low-cost red-emitting phosphor [64], Fe^{2+}:$MgAl_2O_4$ for saturable absorbers of 2-3 µm lasers [348], Ti^{4+}:$MgAl_2O_4$ as blue-emitting diode in laser material at 490 nm [68], and $ZnAl_2O_4$ as an alternative for $MgAl_2O_4$ in numerous applications [349]. The **doping amount was set at 1 at%**, with Co^{2+}/Fe^{2+} substituting Mg^{2+} and Cr^{3+}/Ti^{4+} substituting Al^{3+}. In addition, we carried out a 1 at%Fe^{2+} and 1 at%Ti^{4+} co-doping experiment. The precursor salts were $CoCl_2 \cdot 6H_2O$, $Cr(NO_3)_3 \cdot 9H_2O$, $FeCl_2 \cdot 4H_2O$, $TiCl_4$ and $ZnCl_2$, depending on the desired doped $MgAl_2O_4$.

The XRD and photographs of the doped materials are presented in *Figure 3.46*. The *Figure 3.46.a* shows the evolution of the XRD for the **1 at%Co^{2+} sample** with calcination up to 1000°C for 1 h. The **as-synthesized** material contains poorly crystallized **LDH-type1**. After calcination at **700°C**, the **intermediate phase between η-Al_2O_3 and spinel** is formed, and **pure spinel phase** identical to undoped $MgAl_2O_4$ (*Figure 3.2.a*) is obtained for **higher temperature**. These results indicate that **Co^{2+} doping has no sensible effect on the reactivity** during synthesis (Co^{2+} substituting Mg^{2+} in LDH) and calcination. However, the photographs show that the **uncolored powder up to 700°C** gets a **blue tint typical of Co^{2+}:$MgAl_2O_4$** as soon as spinel is formed, evidencing the successful insertion of Co^{2+}; the tint becomes stronger with increasing temperature due to structural rearrangements. Similar results were obtained for the other doped materials, XRD revealing **pure spinel** after calcination at 900°C (*Figure 3.46.b*). The initially uncolored **Cr^{3+}-doped sample** becomes **yellow** after treatment at **900°C**, and **pink-light red** after treatment at **1500°C**, **typical of Cr^{3+}:$MgAl_2O_4$**. The other doped materials are uncolored, so they have been analyzed under 254 nm UV-light; the **successful doping**, **including 1 at%Fe^{2+}-1 at%Ti^{4+} co-doping**, is revealed by comparison with undoped $MgAl_2O_4$.

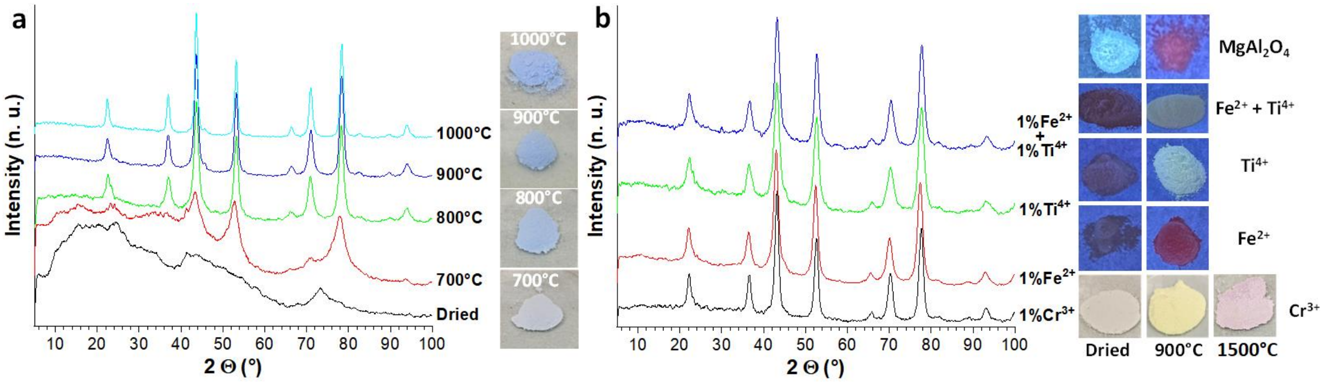

Figure 3.46: XRD of polyol synthesized 1 at% doped samples with a) Co^{2+} through calcination and b) Cr^{3+}, Fe^{2+}, Ti^{4+} and Fe^{2+}-Ti^{4+} calcined at 900°C. Photographs under normal light for Co^{2+} and Cr^{3+} doped samples and under 254 nm UV-light for others

The microstructures of the doped spinels are presented in *Figure 3.47*. The microstructure appears to be **identical with undoped $MgAl_2O_4$** material synthesized with reference conditions (*Figure 3.3*), since all samples are constituted by **irregular micronic agglomerates of ~10 nm spherical crystallites**, independently of the doping conditions.

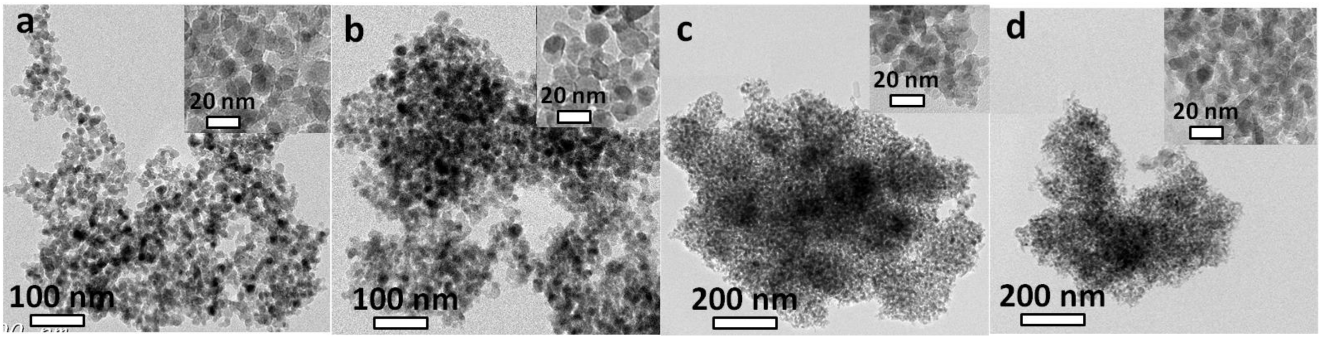

Figure 3.47: TEM micrographs of the spinel powders doped with a) 1 at%Co^{2+}, b) 1 at%Cr^{3+}, c) 1 at%Fe^{2+} and d) 1 at%Ti^{4+}

The evolution of the XRD through calcination and the thermal analysis of the **zinc aluminate material** are presented in *Figure 3.48.a* and *b*, respectively. The XRD pattern of the **as-synthesized material** is typical of **pure LDH-type1**, with d-spacings d_{003} = 7.56 Å and d_{110} = 1.52 Å indicating a **cationic composition of $ZnAl_2$**, by comparison with previous report [350]. It should be noted that the M^{2+}/M^{3+} range of existence of MgAl LDH-type1 is 2-4, while ZnAl LDH-type1 can be obtained in the range 0.5-2 [351]. Therefore, a pure LDH with cationic ratio corresponding to stoichiometric $ZnAl_2O_4$ spinel can be synthesized, constituting a precursor for the latter with the **highest possible chemical homogeneity** favoring the spinel formation during calcination. The DT-TG analysis shows several phenomena: *i)* two endothermic mass losses peaking at 90°C and 185°C from the removal of adsorbed H_2O and interlayered EG, respectively, *ii)* a small endothermic **mass loss at 285°C** from **decomposition of the the intercalates**, *iii)* a **wide endothermic mass loss** spread over **350°C-500°C** attributed to **progressive conversion of hydroxide into oxide**, and *iv)* an **exothermic peak at 575°C** due to **spinelization**. The formation of **$ZnAl_2O_4$ at 600°C** is confirmed by XRD, while 900°C treatment leads to coarsening of the crystallites. The lattice constant was calculated as a = 8.0839 Å, which is consistent with values previously reported for $ZnAl_2O_4$ spinel [352], and the crystallites sizes were calculated as **11.9 nm** at 600°C and **31.9 nm** at 900°C. The thermal analysis of $ZnAl_2$-LDH is in agreement with the analysis carried out in [350]; however, the authors observed spinel crystallization at 700°C-800°C, indicating that the material synthesized *via* polyol route is more reactive.

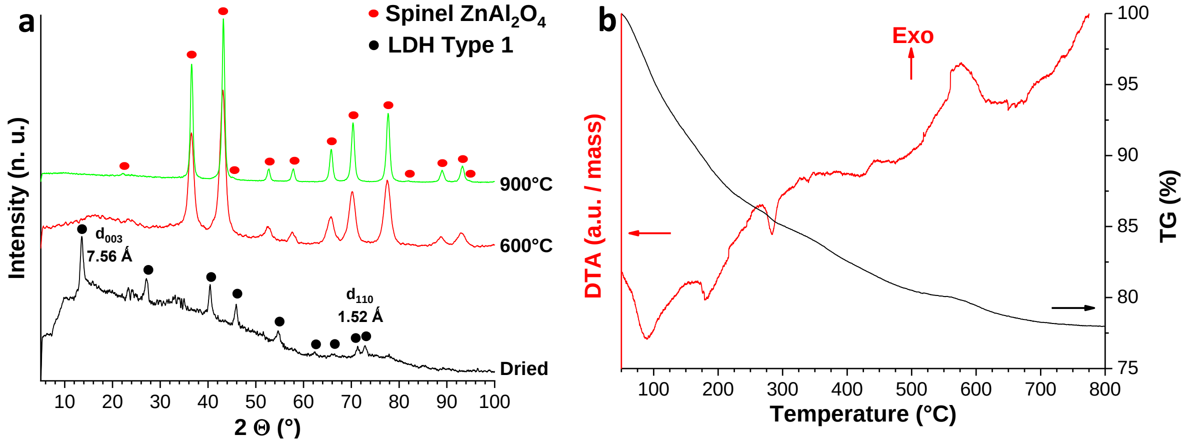

Figure 3.48: a) Evolution of the XRD pattern of $ZnAl_2$ material synthesized in polyol and b) DT-TG analysis

The microstructures of the $ZnAl_2$-LDH-type1 and $ZnAl_2O_4$ calcined at 600°C are presented in *Figure 3.49*. The **as-synthesized hydroxide** has a **characteristic LDH platelet morphology**, with **~100-200 nm large particles** (*Figure 3.49.a*). After calcination at 600°C, the $ZnAl_2O_4$ spinel consists in **~10 nm nanospheres** assembled in **~100-200 nm** microspheres. This regular morphology is due to the single-phased intermediate hydroxide material, and should induce great sinterability.

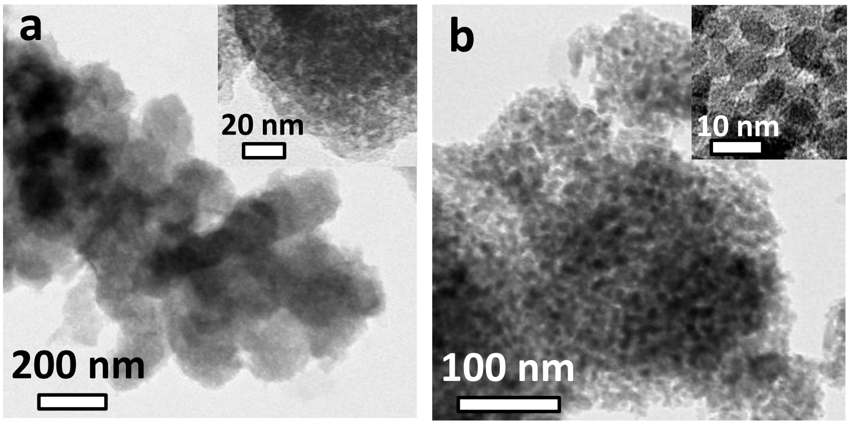

Figure 3.49: TEM micrographs of polyol synthesized a) $ZnAl_2$-LDH-type1 and b) $ZnAl_2O_4$ calcined at 600°C

In conclusion, the **polyol route is well adapted for the synthesis of doped spinel nanopowders**, with various possible doping elements, without any effect of the doping on the synthesis reaction, phase formation or microstructure. However, the elemental compositions of the doped materials have not been measured, and the light colorations of the Co^{2+}:$MgAl_2O_4$ and Cr^{3+}:$MgAl_2O_4$ samples after thermal decomposition compared to literature hint for a low doping rate < 1 at%. This issue will be addressed in future work. In addition, **other aluminate spinel can be prepared through the very same synthesis mechanism**. In the case of $ZnAl_2O_4$, a single-phase intermediate hydroxide with cationic ratio corresponding to spinel stoichiometry is obtained, and converted to nanocrystalline spinel phase at temperature as low as 600°C.

12. Conclusion

The synthesis *via* polyol route has been investigated for the synthesis of nanocrystalline $MgAl_2O_4$ particles. The reaction mechanism, while not fully understood at the moment, includes interactions of the dissolved cations with acetate ions and the polyol medium, and leads to the formation of **intimately mixed gibbsite α-$Al(OH)_3$ and brucite-based layered double hydroxide** intercalated with acetate and/or glycol species. Through thermal decomposition, the phases are progressively converted to **well-crystallized stoichiometric $MgAl_2O_4$**, with a mean size of coherently scattering domains of **~7 nm** at 800°C.

The optimized synthesis conditions have been determined as a **synthesis temperature ≥ ~180°C** with **hydrolysis ratio $h \leq 6$**, **acetate ratio $r = 2.67$**, and a **concentration $[Mg^{2+} + Al^{3+}] \approx 0.100$ M** to maximize the mass of spinel product per synthesis, while a **12 h synthesis** improves the **mass yield to 80%**.

The composition and microstructure of the as-synthesized hydroxides mixture has been found to depend on the temperatures of synthesis and of addition of the precursor salts to the medium, the nature and concentration of additives and the polyol solvent serving as medium. In particular, it was observed that **hot-injection** leads to the **simultaneous** formation of brucite-based **LDH-type1** and boehmite-based **LDH-type2**. The utilization of **long alkane-1,m-diol** such as butane-1,4-diol and pentane-1,5-diol as polyol medium modifies the microstructure of the synthesized spinel to **sheet-like particles**, which may have great potential for catalytic applications due to increased specific surface area. In addition, **high concentration of acetate** such as $[CH_3COO^-]/[Mg^{2+}+Al^{3+}] = 5.34$ favors the formation of spinel **rod-like particles**.

The cationic stoichiometry was investigated, and **nanocrystalline $MgO{\cdot}nAl_2O_3$ spinel** materials were successfully synthesized in the range **$1 \leq n \leq 5$** for the first time, allowing thorough study of the Al_2O_3-rich spinel in the future. The synthesis of **Co^{2+}, Cr^{3+}, Fe^{2+} and Ti^{4+} doped $MgAl_2O_4$** and **zinc aluminate spinel** $ZnAl_2O_4$ *via* the same synthesis protocol was carried out as well, extending the great potential of the developed method for the fabrication of aluminate spinel with functionalized properties.

II. Synthesis *via* the liquid impregnation of nanofibrous alumina

In this sub-chapter, we report on the controlled synthesis of nanocrystalline spinel particles *via* **the impregnation of nanofibrous ultraporous alumina** (UPA) prepared by the amorphous UPA monoliths growth technique developed and patented by members of our laboratory [146]. Previous attempts for the synthesis of alumina based nanocompounds have been reported since the early 2000's [146, 149–151], however no thorough study of the synthesis process has been carried out. The interest of this method lies in the high variety of compounds that can be easily obtained. The aim of the present work is to investigate the liquid impregnation route for the synthesis of alumina based material and evaluate its potentiality for the fabrication of fine nanopowders. The liquid impregnation protocol is detailed in *Chapter 2.II.1.ii*.

In a first part, attention is paid to the liquid impregnation of Mg^{2+} cations into the nanofibrous UPA and $MgAl_2O_4$ formation *via* heat treatment. We assess the influence of **Al_2O_3 crystalline form** (amorphous, γ, α) and **surface modification** with trimethylethoxysilane (TMES) as a **diffusion inhibitor**. To our best knowledge, the impact of alumina polymorphism on $MgAl_2O_4$ formation and microstructure has only be reported in [87, 353] for solid state reaction. In a second part, in a desire to extend the potentiality of the new synthesis route and demonstrate its versatility, we **generalize** it for a **series of compounds** with **composition MAl_2O_4 (M: Co, Ni, Zn, Ba)**. Besides others, these compounds have already deserved much interest in numerous fields of applications including insulators, catalysts, pigments and optical materials and their preparation in the nanocrystalline state has been reported *via* different methods, such as sol-gel [111, 354–357], coprecipitation [93, 97, 355, 358], combustion route [359–361] and modified Pechini process [352].

1. Preparation of the alumina precursors

The protocol for the synthesis of UPA monoliths has been has been inspired from previous works in our team [17, 148], and is presented in *Chapter 1.III.4.i*. The present section focuses on the **conditions of treatment of the monoliths** for the preparation of the different alumina precursors.

The **raw UPA monolith** is a hydrated, amorphous, very light and fragile material due to its **high porosity of ~99%**. **Various crystalline structures** can be obtained through **heat treatment**, while the microstructural and mechanical stability of the monolith are increased with an increase of the calcination temperature. Another way to **stabilize the structure** while inhibiting the coarsening and **retaining phase transition** consists in a **TMES vapor impregnation** of the raw monolith [147, 150]. The silica monolayer after heat treatment covers the structural fibrils hindering the surface mass transport.

The different alumina precursors synthesized are referenced in *Table 3.7*, along with their conditions of preparation and their structural and microstructural properties. The precursors are *i)* **UPA300**: UPA calcined at 300°C for 4 h, *ii)* **UPA1050**: UPA calcined at 1050°C for 4 h, *iii)* **UPA1250**: UPA calcined at 1250°C for 4 h and *iv)* **UPA-TMES**: UPA treated with TMES prior to calcination at 1250°C for 4 h. After the calcination, UPA-TMES shows a mass gain of ~7 wt% due to the surface silica added.

Table 3.7: The alumina precursors prepared from UPA with preparation conditions, structural and microstructural properties

Precursor	Calcination conditions	Crystal structure	Morphology[b]
UPA300	300°C, 4 h	Amorphous	Fibers, d = 5 nm, a ~150 nm
UPA1050	1050°C, 4 h	γ-Al_2O_3	Fibrils with spheroid crystallites d = 5 nm, a ~50 nm
UPA1250	1250°C, 4 h	α-Al_2O_3	Ellipsoidal crystallites, d = 115 nm
UPA-TMES	1250°C, 4 h	γ-Al_2O_3 [a]	Almost spherical crystallites, d ~7 nm

[a] with addition of TMES forming surface silica layer
[b] TEM data, with d the fibers/grains diameter and a the fibers length

The XRD patterns of the UPA precursors are presented in *Figure 3.50.a*. In agreement with the model predictions [148], **raw UPA treated at 300°C** remained **amorphous**, **UPA1050** converted to the metastable cubic **γ-Al_2O_3** and **UPA1250** crystallized into the stable **α-Al_2O_3** (corundum). Furthermore, **UPA-TMES** calcined at 1250°C showed an expected pattern of **γ-Al_2O_3, with no crystallized SiO_2**.

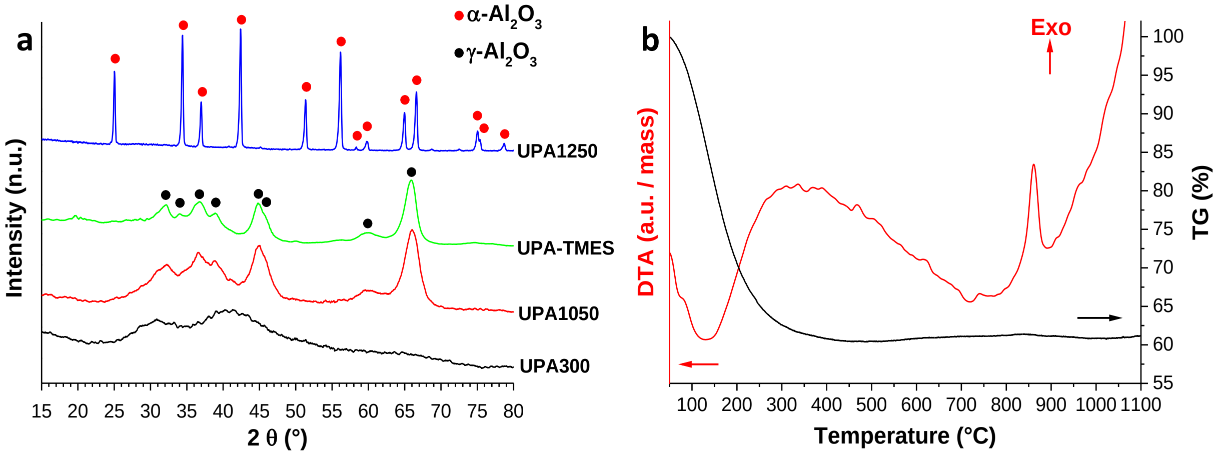

Figure 3.50: a) XRD patterns of the different UPA precursors and b) DT-TG analysis of raw UPA

The DT-TG analysis of raw UPA is shown in *Figure 3.50.b*. A single step endothermic **mass loss of 35-40 wt%** occurs **below 350°C** with maximum rate at 130°C, and was assigned to the **dehydration process** connected to elimination of the physisorbed and chemisorbed water from the material [148]. No further mass loss is observed indicating that raw UPA consists of hydrated aluminum (oxohydr)oxide, and treatment at ~300°C allows to obtain almost **dry amorphous Al_2O_3**. In addition, a sharp **exothermic peak** is observed **at 860°C**, which indicates the **γ-Al_2O_3 crystallization** in agreement with [148]. For **$T \geq 1100$°C**, **the shrinking** of the powder takes place corresponding to the **phase transition to θ and α-Al_2O_3**. The temperature of 1250°C has been experimentally identified as the threshold for the formation of pure α-Al_2O_3 from raw UPA.

Figure 3.51 shows the microstructures of the precursors. UPA300 kept the **fibrous structure** inherent to raw UPA with **fibers of ~5 nm diameter** and **~100 nm length**, while SAED pattern (inset in *Figure 3.51.a*) confirms their amorphous nature. The microstructure of UPA1050 is similar to UPA300 (*Figure 3.51.b*), except for the formation of **spheroidal crystallites** within the fibers. UPA-TMES (*Figure 3.51.c*) is also composed of **rounded grains** of **~7 nm diameter** and **~50 nm length**. This slight increase of diameter is in agreement with an enhanced surface mass transport at a higher temperature and thin silica layer. UPA1250 (*Figure 3.51.d*) underwent coalescence of its fibrils to **large ellipsoidal particles of 115 nm average size**.

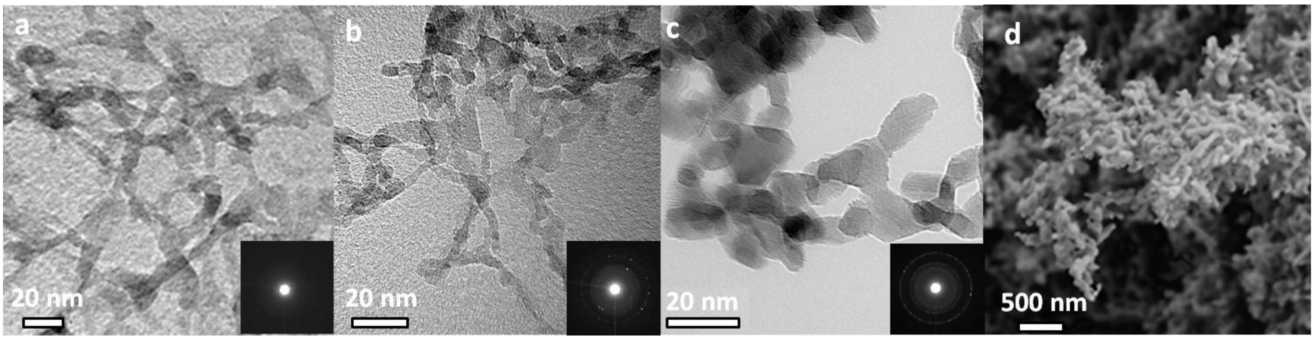

Figure 3.51: TEM images of a) UPA300, b) UPA1050, c) UPA-TMES with SAED patterns in insets and d) SEM of UPA1250

2. Synthesis of $MgAl_2O_4$ from UPA: influence of alumina precursors

Table 3.8: Structural and microstructural properties of the Mg-UPAX materials synthesized from the different UPA precursors

Precursor	Calcination T (°C)	Phases	Lattice constant [a] (Å)	Crystallite size [a] (nm)	Mean size [b] (nm)
UPA300	500	Spinel	8.031(1)	4.7(1)	-
	600	Spinel	8.035(1)	5.3(1)	4.9
	700	Spinel	8.0661(7)	5.7(1)	-
	800	Spinel MgO 21%	8.098(3)	6.1(1)	-
	900	Spinel MgO 2%	8.0752(3)	9.0(1)	-
	1000	Spinel	8.0736(3)	16.8(1)	16.0
UPA1050	1000	Spinel	8.0683(2)	15.1(2)	13.5
UPA-TMES	1000	Spinel	8.0465(4)	8.8(1)	7.9
UPA1250	1300	Spinel ~90% α-Al_2O_3 ~6% MgO ~4%	-	~100	~140

[a] Obtained from XRD refinement, given only for the spinel phase
[b] Obtained from TEM analysis

The UPA materials described in *Chapter 4.II.1* have been used to investigate the **influence of the crystallographic form of Al_2O_3** (amorphous, γ, α) and **the surface modification with TMES** on **the synthesis of $MgAl_2O_4$ nanopowders** by liquid impregnation with Mg^{2+}. The impregnated powders dried at 100°C overnight were composed of $Mg(NO_3)_2{\cdot}6H_2O$ and initial Al_2O_3 polymorph (XRD not shown). The structural and microstructural properties of the synthesized compounds after heat treatment, referred to as Mg-UPAX with UPAX designating UPA materials from *Table 3.7*, are summarized in *Table 3.8*.

The XRD patterns of the Mg-UPAX materials post-treated for 1 h at different temperatures are shown in *Figure 3.52*. For **Mg-UPA300** starting from **amorphous alumina** (*Figure 3.52.a*), the **single phase spinel** structure is obtained after treatment at **temperature as low as 500°C**, with very broad reflections indicating small **crystallites of ~5 nm** composing the nanopowder. Compared to normal (uninversed) stoichiometric $MgAl_2O_4$ spinel with a_0 = 8.0826 Å [32], the Bragg reflections are shifted to higher angles, which evidences a substantial decrease of the cell parameter to a = 8.031 Å (*Table 3.8*). The shift in spinel lattice constant is well-known, and has been attributed to two main causes that are compositional shift from stoichiometry [29] and antisite defects involving Mg^{2+} cations localized in Al^{3+} normal interstices and/or inversely [46]. Furthermore, **no free MgO** crystallization is observed, contrarily to its previously reported crystallization at 400-450°C from decomposition of $Mg(NO_3)_2{\cdot}6H_2O$ [362], hinting for a **full reaction of UPA and Mg^{2+} to form stoichiometric MAS**. Therefore, we assume the **formation of an inverse stoichiometric material** in these conditions. For a higher calcination temperature of **700°C**, the cell parameter begins to strongly increase toward that of normal spinel, due to the effective **annealing of the structural defects**. For a treatment at **800°C**, the diffraction peaks are shifted to low angles, while **MgO is crystallized**. The cell parameter a = 8.098 Å is larger than that of normal spinel, which could indicate MgO-rich compositions [36]. For higher temperatures of calcination, the intensity of MgO peaks decreases (900°C) and then **single spinel phase is retrieved at 1000°C**, with the lattice constant a reaching a *plateau* corresponding to ***I* ~0.3**. The nature of the synthesized compounds and the reaction mechanism with temperature of treatment will be discussed at the end of this section, with the other characterizations helping in the assessment.

The pre-crystallized defective spinel **γ-Al_2O_3, UPA1050** (*Figure 3.52.b*) and **UPA-TMES** (*Figure 3.52.c*), resulted in the **formation of MgO at 500°C** and onset of the **reaction with γ-Al_2O_3 at 800°C**. The formation of the **spinel phase $MgAl_2O_4$** is then **completed at 1000°C** with no residual magnesia. The cell parameter of Mg-UPA1050 and crystalline size appear quite similar to that of Mg-UPA300, after the heat treatment at 1000°C. In contrast, significantly broader and shifted XRD peaks of **Mg-UPA-TMES** indicate smaller crystallite size and cell constant compared to Mg-UPA1050. The small lattice constant a = 8.0465 Å in Mg-UPA-TMES exposed to T = 1000°C can be explained by a **small incorporation of Si^{4+}**, which 1 wt% decreases the lattice constant to ~8.025 Å [295]. We notice that neither SiO_2 nor mullite crystalline phases are observed in Mg-UPA-TMES. The pre-crystallized **α-Al_2O_3**, **UPA1250** (*Figure 3.52.d*) did not react with MgO at **T < 1000°C**, showing biphasic XRD patterns. At higher temperatures, spinel phase $MgAl_2O_4$ appears; however, **non-reacting MgO and α-Al_2O_3 phases remain appreciable**, as **spinel content** goes from 36 at% at 1000°C to **83 at% at 1300°C**, with crystallite size of **~100 nm**.

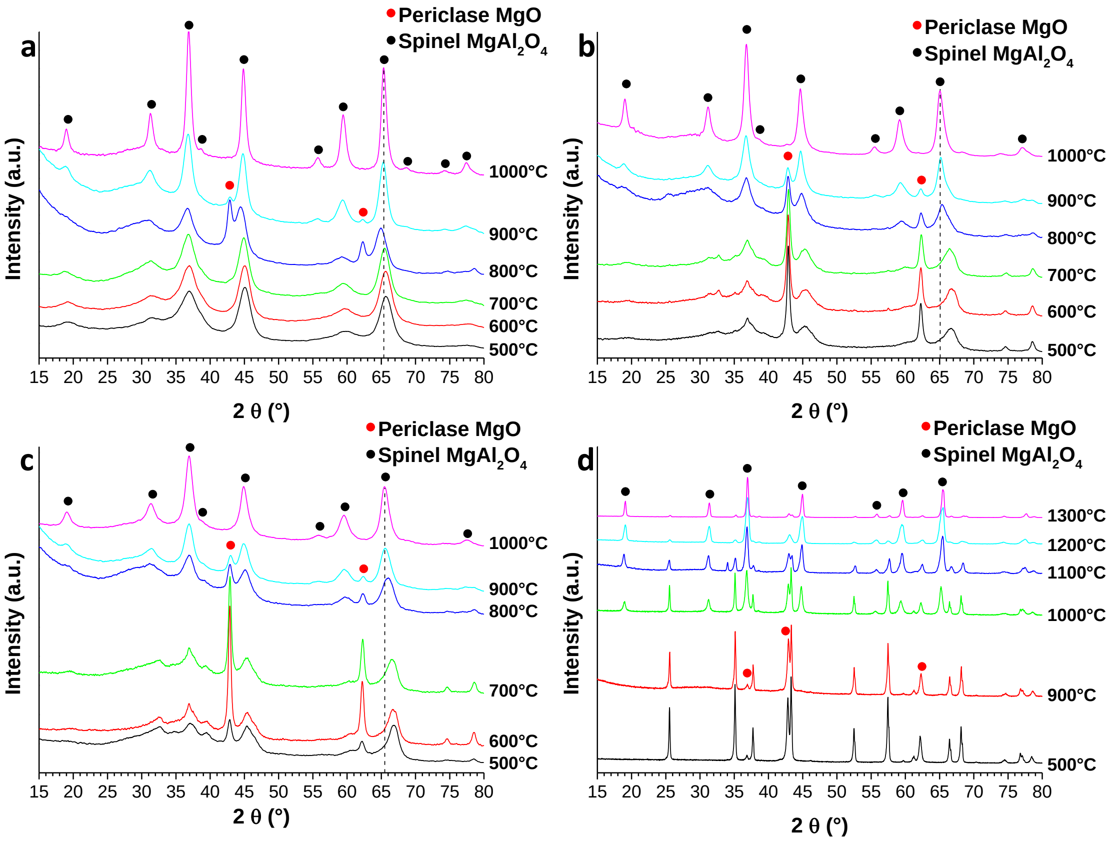

Figure 3.52: Evolution of the XRD pattern with the calcination temperature for a) Mg-UPA300, b) Mg-UPA1050, c) Mg-UPA-TMES and d) Mg-UPA1250. The vertical lines are guides for the eye to emphasize peak shift

The comparison of the synthesis routes employing the different UPA precursors permits to conclude that the **amorphous precursor is more suitable for the spinel phase formation**. In contrast, γ-phase alumina begin to react with MgO at 800°C, *i.e.* onset temperature of the bulk mass transport, completing pure spinel formation at 1000°C, and α-phase precursor leads to the spinel phase at T ≥ 1000°C, always accompanied by remaining MgO and α-Al_2O_3 precursor phases. The difference between γ- and α-Al_2O_3 can be related to the size of elementary fibrils, since Mg insertion into 100 nm α-Al_2O_3 domains requires longer time compared to that smaller 10 nm of γ-Al_2O_3. In addition, corundum is the most stable phase of alumina, often used as an inert material for application at high temperature, hence its reaction requires high energetic conditions. On the other hand, sizes of the elementary fibrils of amorphous and γ-Al_2O_3 are quite similar (~5 nm). The difference between the last two reaction routes is then attributed to **free energy** and will be discussed below.

DT-DTG analysis of Mg-UPAX materials are shown in *Figure 3.53*. The thermal decomposition and subsequent oxidation is similar in these samples; however, some differences can be observed depending on UPAX. Several endothermic phenomena occur during the calcination. First, a sharp peak at **T < 100°C** without any mass loss is observed and attributed to **$Mg(NO_3)_2$ melting** [362]. Another broad band peaks at **125°C** accompanied by a **mass loss** is attributed to **desorption of the physisorbed water**. The shoulder at **~200°C** and the following sharper peak at **215°C** are attributed to the **partial dehydration of $Mg(NO_3)_2 \cdot 6H_2O$ to $Mg(NO_3)_2 \cdot 2H_2O$**. At higher temperatures, the further dehydration to **anhydrous $Mg(NO_3)_2$** and subsequent **denitration/oxidation** are observed at **365°C and 405°C**.

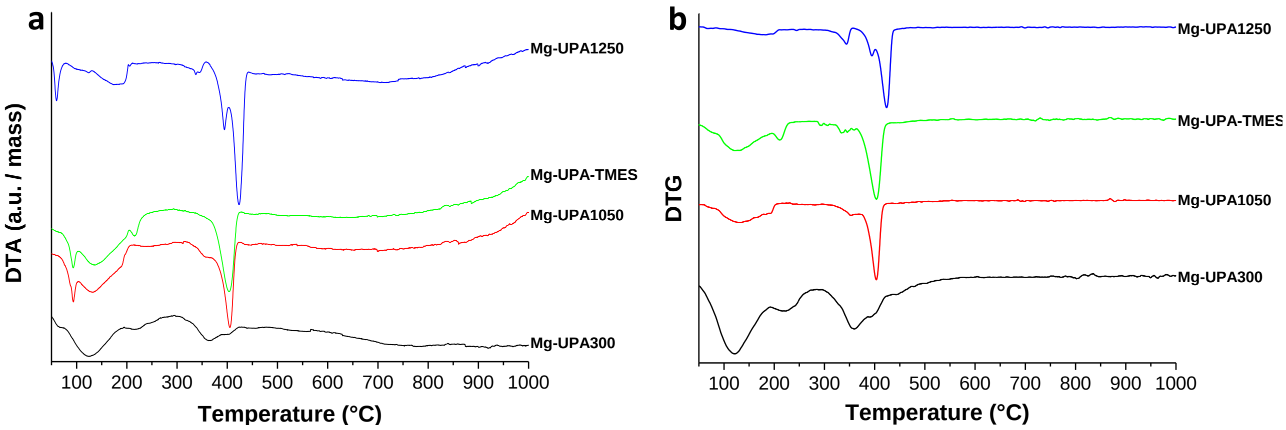

Figure 3.53: a) DT and b) DTG analysis of the Mg-UPAX materials

As stated above, differences can be observed depending on UPA material receiving Mg^{2+} cations; Mg-IMP1050 and Mg-IMP-TMES provide rather identical DT-DTG data. Starting from amorphous alumina (Mg-UPA300), the dehydration phenomena are the most intense, while the opposite trend is observed for γ-Al_2O_3 and α-Al_2O_3. Furthermore, a sharp intense peak appears at 405°C in Mg-IMP1050 material, while for Mg-UPA1250 material an additional sharp peak appears at 395°C while the peak at 405°C is shifted to 425°C. We suggest that these features are connected to the solute interaction with host matrix, which accounts for reaction kinetic of the spinel formation process. Indeed, in agreement with [148], UPA possesses stable compositions **Al_2O_3·1.5H_2O** and **Al_2O_3·0.9H_2O** respectively formed at **100°C** and **380°C**, the latter affecting the Mg-UPA300 material analysis through the massive endothermic mass loss around 360°C overlapping with the endothermic mass loss from deninitration. In Mg-UPA1050 and Mg-UPA1250 materials, the structural water content is very small and physisorbed water is removed below 300°C, which cannot account for the discussed DT-DTG peculiarities. On the other hand, the elementary structural unit of Mg-UPA1250 is more than 10 times larger to that of Mg-UPA1050. This morphology necessary affects the Mg^{2+} insertion kinetic, requiring higher temperatures and/or longer time to be completed, which is supported by experiment (peak shift 405→425°C). The complementary peak at 395°C may be explained by the very beginning of the **$MgAl_2O_4$ phase formation in a surface layer**, which spans afterwards into the α-Al_2O_3 grain volume. Because of the fine 10 nm structural fibril and similar spinel structures, the **surface and volumic processes run simultaneously** in Mg-UPA1050 and Mg-UPA-TMES materials and their respective DT/DTG peaks merge. In Mg-UPA300, the denitration seems to begin at 365°C during the final dehydration as both peaks are particularly convoluted, which explains a relatively small mass loss at 405°C. Then the otherwise highly endothermic denitration is attenuated by the exothermic spinel phase formation [110] occurring concomitantly, in agreement with XRD patterns in Fig. 3a. We notice that no exothermic signal of the $MgAl_2O_4$ spinel phase formation was observed, suggesting that this process progressively occurs via Mg^{2+} cations diffusion in the Al_2O_3-spinel solids.

The microstructures of nanopowders prepared from different UPA polymorphs after calcination at 600 and 1000°C (Mg-UPA300, Mg-UPA1050, Mg-UPA-TMES) and 1300°C (Mg-UPA1250) are shown in *Figure 3.54*.

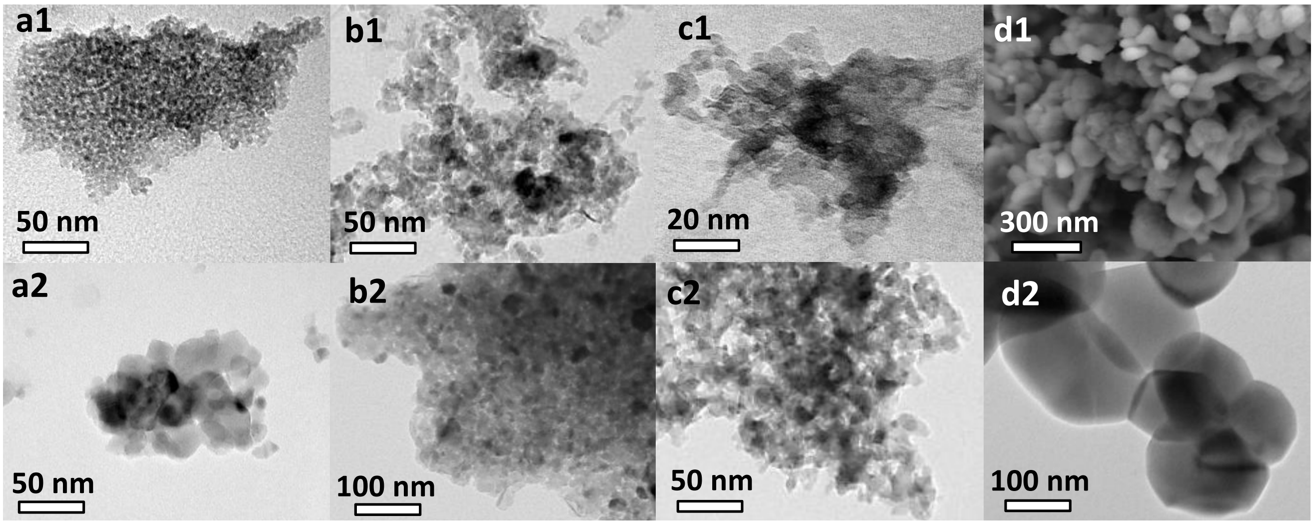

Figure 3.54: Micrographs of materials a) Mg-UPA300, b) Mg-UPA1050, c) Mg-UPA-TMES and d) Mg-UPA1250 calcined at a1,b1,c1,d1) 600°C and a2,b2,c2) 1000°C and d2) 1300°C

Mg-UPA300 treated at 600°C (*Figure 3.54.a1*) shows the metastable spinel structure composed of very fine **~5 nm spherical crystallites** agglomerated in **irregular particles**. The increase of temperature to 1000°C (*Figure 3.54.a2*) leads to an increase of the **crystallite size to ~16 nm** and of the polydispersity, while the agglomerates seem to shrink. Mg-UPA1050, Mg-UPA-TMES and Mg-UPA1250 materials treated at 600°C show large **shapeless agglomerates** of small crystallites of polyphasic nature. MgO and Al_2O_3 species are apparently well-mixed within these particles providing a **good macroscopic chemical homogeneity**, although microstructural features inherent to the original UPA fibrils materials can be seen in micrographs of Mg-UPA1050, Mg-UPA-TMES and Mg-UPA1250 in *Figure 3.54.b1*, *c1* and *d1*. After completion of the spinelization at 1000/1300°C, no remaining features from UPA are observed. The spinel particles of Mg-UPA1050 (*Figure 3.54.b2*) are **highly agglomerated** and present a mean crystallite size comparable to Mg-UPA300 in the same conditions of treatment. In Mg-UPA-TMES material, the particle size is about **8 nm** (*Figure 3.54.c2*), in good agreement with the crystallite size of 8.8 nm obtained from XRD analysis. The small crystalline size close to that of the original UPA permits to conclude about **effective coalescence inhibition by using TMES**. The almost spherical shape of Mg-UPA1250 particles calcined at 1300°C compared to elongated shape of UPA1250 particles, with a **contrast neck** between them (*Figure 3.54.d2*), support the volumic mass transport characteristic of **sintering stage**.

In order to investigate the nature of synthesized compounds and the reaction mechanism specific to UPA300, *Figure 3.55* presents additional analyses for Mg-UPA300. The **evolution of the mean crystallite size and already discussed lattice constant** of MAS phase with temperature are shown in *Figure 3.55.a*. The particles coarsening followed an **exponential law** with increasing temperature, which reflects classical behavior. However, **two ranges with different coarsening mechanisms** can be distinguished, evidenced by different slopes of experimental data with **crossover at $T^* \approx 850$°C**. In **range 1** ($T < T^*$) the **crystallite size increases** slowly from 4.7 nm at 500°C to 6.1 nm at 800°C, while in **range 2** ($T^* \leq T$) it **increases rapidly** to 16.8 nm at 1000°C. Indeed, the crossover point separates two mass transport mechanisms in the fibrous UPA structure [148] and corresponds to the γ-Al_2O_3 spinel crystallization temperature of 870°C [17]: **1- surface and 2- bulk mass transports**. These data can be set in connection with Raman analysis of the samples.

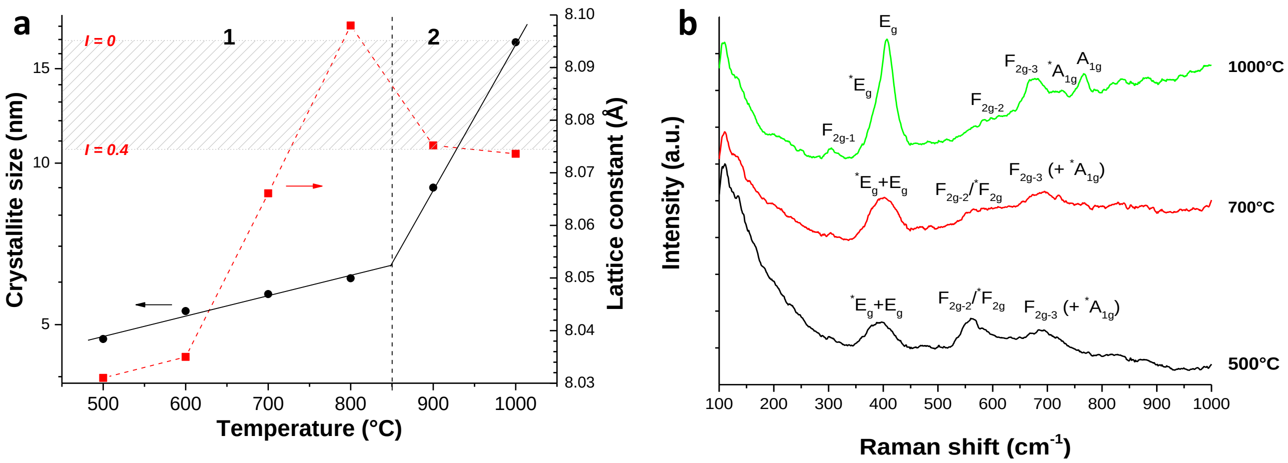

Figure 3.55: a) Crystallite size and lattice constant of spinel phase vs calcination temperature for Mg-UPA300 and b) Raman spectra of Mg-UPA300 calcined at 500, 700 and 1000°C. Range of lattice constant corresponding to inversion $0 \leq I \leq 0.4$ (according to [36]) is shown by hatched area in a). Raman modes assigned with (*) in b) are provoked by inversion.

The Raman spectra of Mg-UPA300 calcined at 500, 700 and 1000°C are shown in *Figure 3.55.b*. There are **five Raman active fundamental modes** A_{1g} (1), E_g (1) and F_{2g} (3), and **several additional due to cation disorder** and marked by (*) [52, 54, 310, 363]. **A_{1g}** and **E_g** have been ascribed to respectively symmetric Mg-O stretching and asymmetric O-Mg-O bending vibrations in MgO_4 tetrahedron; **$F_{2g\text{-}1}$** to translation vibrations in MgO_4, while replacement of Mg^{2+} by Al^{3+} induces a slight shift to lower frequencies, and **$F_{2g\text{-}3}$** to bending vibrations in AlO_6 octahedron, while replacement of Al^{3+} by Mg^{2+} induces a shift to higher frequencies [310]. The **$F_{2g\text{-}2}$** mode has been less discussed in literature due to its weak intensity, however it is suggested to originate from Mg-O antisymmetric stretching vibrations in MgO_4. Depending on calculation method, its position was found at 553 cm^{-1} [363] and 597 cm^{-1} [364], while it has been experimentally observed at 492 cm^{-1} [365], 520 cm^{-1} [310], 570 cm^{-1} [276] and even split in two peaks at 493 and 562 cm^{-1} [52]. In view of these significant discrepancies, one could suggest the existence of several modes in this frequency range, including $F_{2g\text{-}2}$ and another **$^*F_{2g}$** related to cation disorder [52, 310]. The literature is too scarce for a better assignment. Other modes apparently arising from antisite defects are **$^*E_g$** at 375 cm^{-1} appearing as a shoulder of E_g and **$^*A_{1g}$** at 727 cm^{-1}, generally attributed to Al-O bending and stretching in AlO_4 [52]. Alternatively, $^*A_{1g}$ has been calculated as a silent mode of MgO_4 activated by inversion [54].

The spectra of Mg-UPA300 calcined at 500 and 700°C show similar bands at 395 cm^{-1} ($^*E_g$+E_g), 562 cm^{-1} ($F_{2g\text{-}2}$/$^*F_{2g}$) and 690 cm^{-1} ($F_{2g\text{-}3}$+$^*A_{1g}$). However, E_g and $^*F_{2g}$ are respectively stronger (factor 1.7) and weaker (factor 1.4) at 500°C. In addition, a very weak $F_{2g\text{-}1}$ mode is seen at 300 and 303 cm^{-1} after treatment at 500 and 700°C. The spectrum of the powder treated at 1000°C shows the whole fingerprint of synthetic $MgAl_2O_4$ spinel: $F_{2g\text{-}1}$ (305 cm^{-1}), E_g (406 cm^{-1}) with shouldering $^*E_g$, $F_{2g\text{-}3}$ (675 cm^{-1}), $^*A_{1g}$ (727 cm^{-1}), A_{1g} (767 cm^{-1}) and very weak $F_{2g\text{-}2}$ (690 cm^{-1}). A comparison of Raman spectra makes it clear that the **normal spinel structure is not obtained below the critical temperature T' ≈ T^***. Indeed, at 500°C the modes of MgO_4 are either absent (A_{1g}, $^*A_{1g}$) or drastically weakened and negatively shifted (E_g and $F_{2g\text{-}1}$), while $^*E_g$ of AlO_4 appears. Furthermore, generally weak $F_{2g\text{-}2}$/$^*F_{2g}$ exhibits a high intensity and $F_{2g\text{-}3}$ intensity of AlO_6 is barely impacted, indicating the formation of MgO_6. These observations permits to conclude about **fully inverse structure of Mg-UPA300 material calcined at 500°C**, suggesting that strong band at ~560 cm^{-1} is due to cation inversion (most probably in AlO_4) with major contribution of $^*F_{2g}$. Upon calcination at 700°C, the material keeps its **highly disordered spinel structure**, however, an increase of E_g and decrease of $^*F_{2g}$ intensities together with a poor resolved $F_{2g\text{-}3}$, $^*A_{1g}$ and A_{1g} suggest an enhanced contribution from MgO_4. After calcination at 1000°C, the material loses signature of the strongly disordered structure, although $^*E_g$ and $^*A_{1g}$ bands indicate a remaining inversion characteristic of synthetic $MgAl_2O_4$ spinel. We notice that weak $F_{2g\text{-}2}$ mode observed in our spectra at 590 cm^{-1} is in agreement with theoretical calculation of [364]. These results provide **first tentative description of Raman spectra of the fully inverse $MgAl_2O_4$ spinel**.

The correlation between the $MgAl_2O_4$ spinel particles coarsening and the mass transport mechanisms of Al_2O_3 noted in *Figure 3.55.a* together with other characterizations allows assessing diffusion mechanisms involved in the process of phase formation. In **domain 1** ($T \leq T^* \approx 850°C$) where surface mass transport in UPA dominates, it can be deduced that **Mg^{2+} effectively diffuses into the host** nanofibril, which insertion is facilitated by $Mg(NO_3)_2$ decomposition and UPA transformation from $Al_2O_3{\cdot}1.5H_2O$ to $Al_2O_3{\cdot}0.9H_2O$ around 380°C. This hypothesis is supported by a prevented MgO crystallization which takes place by using crystalline Al_2O_3 polymorphs (*Figure 3.52.b-d*). Consequently, spinel structure is formed at the remarkably low temperature in a metastable 'inverse' phase characterized by the low lattice constant a = 8.031 Å (*Figure 3.55.a*), which most probably corresponds to a strong cation disorder. We reject an alternative hypothesis of formation of Mg-deficient material. Indeed, based on the Vegard's law, experimental lattice constant would indicate a substantial deviation from stoichiometry by lack of ~35 at% Mg [29]. Such composition might be explained by a poor insertion of MgO in Al_2O_3 host material. However, prior to heat treatment Mg nitrate was homogeneously distributed in the nanofibrous alumina network, thus forming a gangue surrounding elementary structural nanofibrils. Hence, as the reaction starts (T ~500°C) **Mg^{2+} progressively diffuse** into alumina fibrils with the material composition evolving in following stages: *i)* **surface Mg^{2+}**, *ii)* **Mg^{2+} concentration gradient** from exterior to interior of fibril, until attaining ultimate *iii)* **homogeneous spatial distribution of Mg**. A non-attained stage *iii)* after 1 hour of heat treatment fixes the material system in the compositional state of stages *i)-iii)*. However, since nitrate precursor is decomposed at ~450°C (*Figure 3.53*) and no free MgO crystallizes (*Figure 3.52.a*), it can be inferred that **all Mg^{2+} is successfully integrated** in UPA host after heat treatment. We notice that Mg-rich spinel has no large metastability domain [26] and an excess MgO would be readily excluded from the host material and crystallized, which was not observed. Furthermore, if gradient concentration of Mg^{2+} in Al_2O_3 fibril took place, the core fibril composition would have MgO deficit while shell would have MgO excess. The XRD pattern of such material is expected to possess the peaks widening because of Mg-rich (to lower angles) and Al-rich (to larger angles) spatial domains. Since none of these was observed, this hypothesis must be rejected, and it is to be assumed that the reaction kinetic at 500°C is quick enough to complete Mg insertion and attain homogeneity of the material composition. We notice that Mg diffusion in aluminate spinel is rather slow [366] that generally requires high temperatures and long time to achieve homogeneity of a bulk material. In contrast, Mg insertion in the ultraporous nanofibrous matrices was successful in moderate heat-treatment conditions. Thus, the proposed method appears to be effective in preparation of $MgAl_2O_4$ spinel nanoparticles.

Discarding the hypothesis of non-stoichiometry leaves the **cation disorder hypothesis**, quantified by the **inversion degree *I***: $(Mg_{1-I}Al_I)^T(Mg_IAl_{2-I})^OO_4$, where $(X)^T$ and $(X)^O$ refer respectively to tetrahedral and octahedral sites in spinel lattice. Several studies have addressed the relation between inversion of Mg^{2+} and Al^{3+} sites and lattice constant, however, these studies (both theoretical and experimental) were limited to $I \leq 0.4$, characteristic of most synthetic and natural $MgAl_2O_4$ spinel materials [46, 47]. No data concerning hypothetical higher-inversion materials are available. However, simple extrapolation of the available relationships beyond their confidence range permits concluding about **fully inverted spinel ($I \approx 1$)** obtained after the calcination of Mg-UPA300 at 500°C. Despite all such extrapolations have to be taken with caution, Raman spectroscopy (*Figure 3.55.b*) provides a strong support to this conclusion. It can be noticed in this connection that fully inverse magnetite $FeFe_2O_4$ shows similar Raman features to Mg-UPA300 treated at 500°C [52]. The analysis showed that the moderate heat processing of amorphous UPA300 results in **pure stoichiometric inverse spinel $(Al)^T(MgAl)^OO_4$**, which was not achieved by the similar processing of crystallized UPA. This result apparently follows **Ostwald's rule of phase nucleation**. In fact, an appearing phase is not necessary thermodynamically stable but that closest in energy to the initial one. Starting from amorphous compounds sets the **initial free energy at the highest possible level**, making fully inverse metastable state of spinel accessible. The energy cost of antisites formation is the smallest one between other elementary lattice defects [3, 367, 368], which makes inversion commonly appearing in the spinel structure. Meanwhile, formation energy of the inverted spinel is inherently higher than that of normal spinel, which orders a set of metastable material states depending on inversion parameter E(I). The energy increased with I toward the uppermost fully inversed phase E(I = 1). A possibility of synthesis of the inverted phase then depends on the free energy of MgO and Al_2O_3 precursors as shown in *Figure 3.56*. In agreement with results of this work, metastable state with full inversion ($I \approx 1$) can be accessed starting from amorphous precursors, MgO and *a*-Al_2O_3, and by applying moderate temperatures for a limited time (long treatment can promote relaxation of this phase). Its experimental observation is unprecedented to the best of our knowledge.

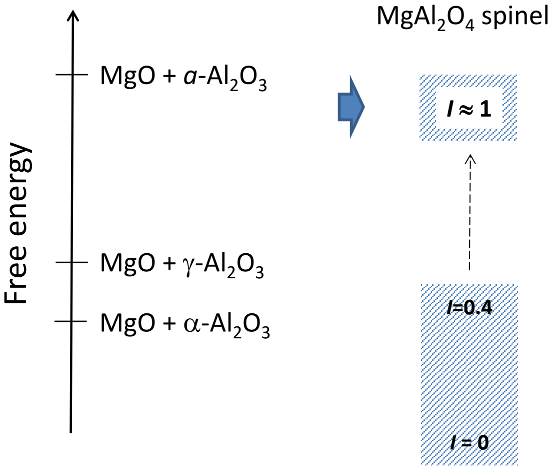

Figure 3.56: Tentative schema of inverse spinel formation ($I \approx 1$), following Ostwald's rule of phase nucleation

At 800°C ≤ T ≤ 900°C, *i.e.* around T^* where bulk mass transport in UPA begins, formation of normal spinel takes place, implying **great rearrangements of lattice**. At 800°C, lattice constant suddenly increased to a = 8.098 Å, which is significantly larger than a_0 in stoichiometric spinel, being characteristic of the Mg-rich compositions [36]. However, rejection of MgO from the spinel structure at this singular point (see *Figure 3.52*.a) ruled out the possibility of MgO-rich spinel formation, otherwise requiring the rejection of

Al_2O_3. Then at T ≥ 900°C, **bulk mass transport dominates** (domain 2 in *Figure 3.55.a*), enabling **effective diffusion of both Al^{3+} and Mg^{2+} cations**, leading in a phase pure stoichiometric spinel to be attained at 1000°C with a remaining inversion I ~0.3-0.4, which is common for synthetic spinel. Though precise formation mechanisms cannot be asserted at the moment, slightly inversed materials obtained at T ≥ 800°C most probably are formed by a recovery following formation of metastable state with $I \approx 1$. Indeed, during the heat up stage from 500 to 800°C, the metastable state is expected to be already formed before any structural rearrangement in a-Al_2O_3 toward γ-Al_2O_3 begins at the dwell temperature of 800°C. Furthermore, significant difference between lattice constants 8.098 Å in Mg-UPA300 and 8.0689 Å in Mg-UPA1050 at 800°C made strong doubts on their similar formation mechanisms. Because of this, we assign formation mechanism in Mg-UPA300 at temperatures in the vicinity of T^* to the **rearrangement of metastable lattice** ($I \approx 1$) toward its stable state *via* activation of Al^{3+} bulk diffusion. In support of this hypothesis, it has been calculated that the preferred migration path of Al^{3+} in spinel is through Mg^{2+} sublattice, as well as Mg^{2+} migration [369]. Hence, it could be supposed than at T ~T^*, **Mg^{2+} cations migrate to normal tetrahedral sites while Al^{3+} cations are still located on normally vacant tetrahedral sites** of spinel lattice, leading to a high concentration of **Frenkel defects** [45] with the **structure $(MgAl)^T(Al)^OO_4$**, not included in the inversed spinel range as defined above by the inversion degree I. This would provoke an increase of the lattice volume and explain abnormally large lattice constant. At this point, because of the stronger mobility of Mg^{2+} compared to Al^{3+} [369], **MgO rejection from the spinel structure might dominate Al^{3+} displacement to normal octahedral sites**. Then at T ≥ 900°C, effective bulk mass transport of $(Al^{3+})^T$ in domain 2 (*Figure 3.55.a*) enables **its migration in the octahedral sites permitting Mg^{2+} reintegration in the spinel lattice**.

3. Synthesis of other aluminate MAl_2O_4 compounds (M: Co^{2+}, Ni^{2+}, Zn^{2+}, Ba^{2+})

The following study is aimed to **extent applicability of UPA and impregnation method to the synthesis of a large variety of binary compounds with the composition MAl_2O_4** including cations M: Co, Ni, Zn, Ba. Functional properties of these compounds, having found numerous application fields (insulators [370, 371], catalysts [355, 359, 372], pigments [15, 181] and optical materials [356, 360, 371]), will not be considered. An advantage of the UPA impregnation route which we intent to demonstrate, is that it can be **easily adapted** to different compositions of the metal oxide nanomaterials. Based on results obtained with $MgAl_2O_4$ spinels by using different UPA hosts, UPA300 was applied in the synthesis with the goal to complete the reactions at lowest temperatures and compare the reaction mechanisms in the different MAl_2O_4 systems. The structural and microstructural properties of the synthesized compounds are summarized in *Table 3.9*. Since only the M^{2+} cation was changed between the synthesis series, these materials will be labeled as **M-UPA300 with M: Co, Ni, Zn, Ba** standing for inserted cation.

The XRD patterns of M-UPA300 nanopowders calcined at different temperatures are shown in *Figure 3.57*, together with photographic images of Co-UPA300, Ni-UPA300 and Zn-UPA300 having characteristic colorations.

Table 3.9: Structural and microstructural properties of the synthesized M-UPA300 materials (M: Co, Ni, Zn, Ba)

Calcination T (°C)		500	600	700	800	900	1000
Co-UPA300	Phases	$CoAl_2O_4$					
	a^{a} (Å)	8.0682(1)	8.0741(1)	8.0796(3)	8.0912(5)	8.0933(3)	8.0941(3)
	Crystallite size ^{a}, nm	26.4(4)	30.3(5)	35.9(8)	37.1(4)	42.4(6)	49.4(1)
Ni-UPA300	Phases	$NiAl_2O_4$					
	a^{a} (Å)	8.093(1)	8.080(1)	8.061(1)	8.038(1)	8.0323(7)	8.0235(3)
	Crystallite size ^{a}, nm	2.6(6)	2.5(3)	3.3(1)	4.9(1)	8.4(1)	16.9(1)
Zn-UPA300	Phases	$ZnAl_2O_4$ ZnO (10%)					
	a^{a} (Å)	8.0962(4)	8.0937(7)	8.0877(4)	8.0874(2)	8.0863(2)	8.0848(1)
	Crystallite size ^{a}, nm	9.5(1)	11.7(1)	14.1(1)	19.9(1)	32.0(2)	48.5(2)
Ba-UPA300	Phases	$Ba(NO_3)_2$	$BaAl_2O_4$ $Ba(NO_3)_2$	$BaAl_2O_4$ $BaCO_3$ (5%)			
	a^{a} (Å) c^{a} (Å)	-	-	10.4424(3) 8.8015(5)			
	Crystallite size ^{a}, nm	-	-	~60(5)			

^{a} Measured from XRD refinement, given only for the MAl_2O_4 phase

XRD of **Co-UPA300** (*Figure 3.57.a*) indicates that **pure well crystallized $CoAl_2O_4$ spinel** structure is obtained in the temperature range **$500 \leq T \leq 1000$°C**; one can expect the spinel formation even below 500°C. As temperature increases, the intensity of Bragg reflections is increased due to spinel mass involved, while the peaks are slightly shifted to low angles highlighting larger lattice constant a (see *Table 3.9*). They attained values reported for **non-defective $CoAl_2O_4$ spinel** [15, 373] after the heat treatment at **$T \geq 900$°C**. Accordingly, the **coloration of powders evolved from dark to deep blue** (famous cobalt blue, or Thenard's blue) with an increase of temperature, as the lattice constant increased toward 8.095 Å, which is common for $CoAl_2O_4$ (JCPDS card #70-0753) indicating structural rearrangement into the stable normal spinel structure. The smaller values of a in $CoAl_2O_4$ at lower temperatures correspond to the spinels with **inversion between Co^{2+} and Al^{3+}** positions [373]. This result confirms the previously discussed structural evolution of $MgAl_2O_4$ with temperature, from metastable inverse to stable normal spinel, in agreement with Ostwald's rule.

The XRD of **Ni-UPA300** nanopowders (*Figure 3.57.b*) show **pure $NiAl_2O_4$ spinel** structure after calcination at temperatures in the range **$500 \leq T \leq 1000$°C**. However, for temperatures < 800°C, the material shows very broad Bragg reflections, which may belong to an **intermediate defective spinel** structure similar to that of Mg-UPA300 (*Figure 3.52.a*). In this case, **no NiO exsolution** is observed in the vicinity of the mass transport mechanisms crossover of pure UPA, which can indicate a better Ni^{2+} cations dissolution into the host matrix. The lattice constant a decreases from 8.098 Å at 500°C to 8.0285 Å at 1000°C, which last is very close to the reported values of the stable state of the **naturally partially inverted** $NiAl_2O_4$ spinel (JCPDS card #10–0339) [147, 355, 374]. Accordingly, the **coloration evolved** with an increase of temperature through **dark green** at 500°C, **turquoise/cyan** at 700-800°C, **azure** at 900°C and **vivid blue** at 1000°C. These changes of coloration can be connected to the structural rearrangements, indicating transition from normal to inverse spinel. Unlike to $CoAl_2O_4$ and $MgAl_2O_4$ materials, **inversion in $NiAl_2O_4$ was promoted by increasing temperature**. This evolution results in the stable inverse spinel, suggesting formation of a metastable normal spinel at lower temperatures of 500°C, in agreement with Ostwald's rule.

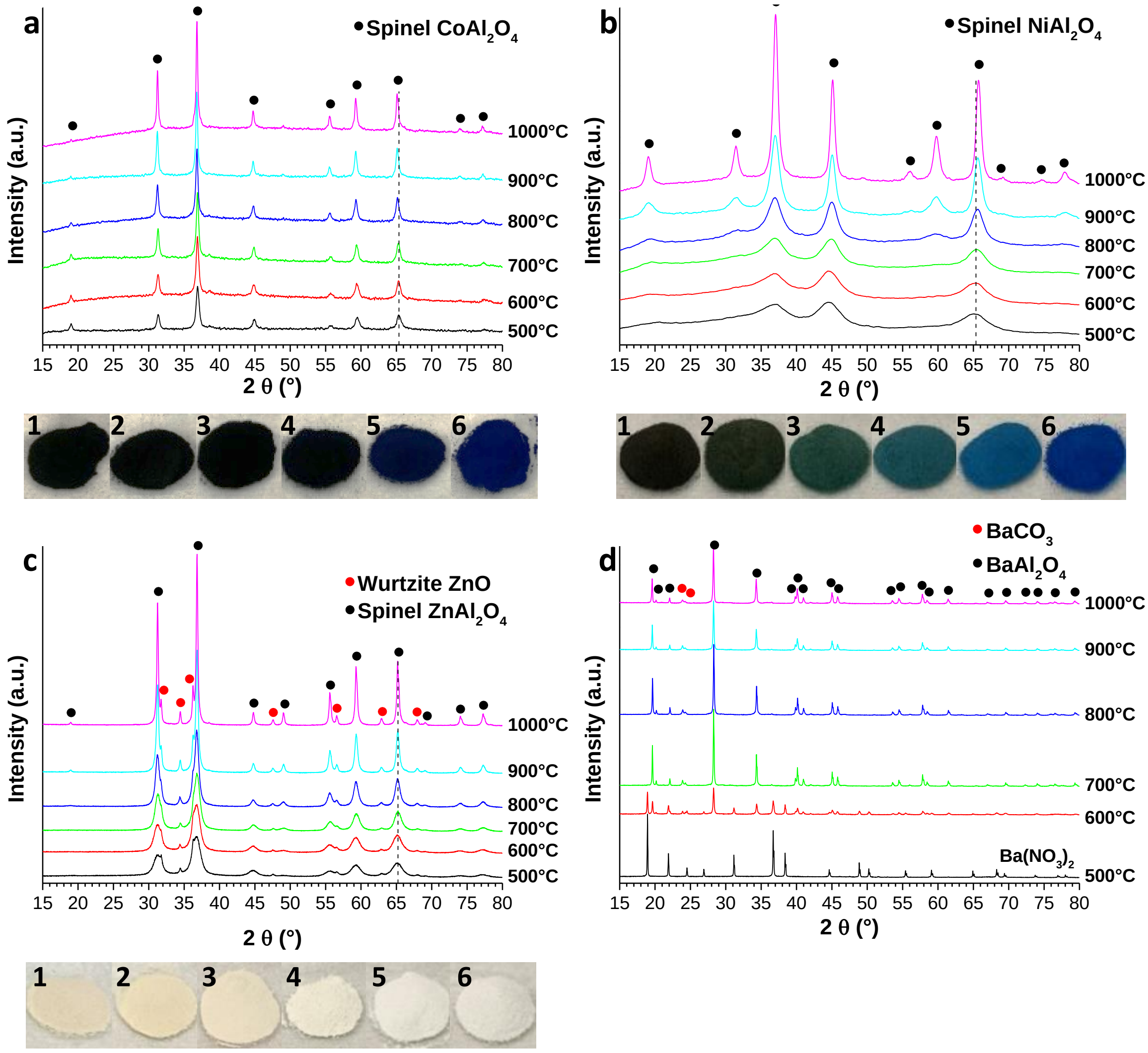

Figure 3.57: Evolution of the XRD patterns with the calcination temperature for a) Co-UPA300, b) Ni-UPA300, c) Zn-UPA300 and d) Ba-UPA300. Photographs are provided for a)-c) for the powders treated at 1) 500, 2) 600, 3) 700, 4) 800, 5) 900 and 6) 1000°C

The XRD patterns of **Zn-UPA300** (*Figure 3.57.c*) show **$ZnAl_2O_4$ spinel** structure with an admixture of **~10 wt% ZnO** phase at calcination temperatures in the range **$500 \leq T \leq 1000$°C**. The ZnO content does not undergo a significant variation with temperature; it is probably due to an overdosing by zinc nitrate during the impregnation process, since this spinel structure does not tolerate much variation of the Al/Zn ratio and inversion [52, 354]. A more careful components admixing during the synthesis will therefore provide phase pure $ZnAl_2O_4$ spinel nanopowders. Since it was not the first purpose of this work, the pure $ZnAl_2O_4$ compound was not further attempted to be synthesized in this work. The spinel structure shows a slight decrease of the lattice constant *a* with an increase of temperature toward the reported value in normal spinel (JCPDS card #73-1961), which corresponds to a **disorder-to-order structural transition** [375] accompanied by changes in coloration from **off-white in defective lattice** to **common white powder in normal spinel**. We notice that a small variation of the lattice constant in $ZnAl_2O_4$ upon calcination indicates negligible variation of inversion explained by a strong preference of Zn for tetrahedral coordination [52, 375].

The XRD patterns of **Ba-UPA300** nanopowders are shown in *Figure 3.57.d*. The heat treatment temperature of 500°C is not sufficient to decompose the impregnated solute since XRD pattern of $Ba(NO_3)_2$ was observed. The decomposition starts at ~600°C, where a mixture of $Ba(NO_3)_2$ and $BaAl_2O_4$ is identified. At **700°C**, the **complete decomposition to $BaAl_2O_4$** is observed and higher temperatures up to 1000°C do not led to further evolution. Two small peaks near 24° are identified as whiterite phase of $BaCO_3$, which was formed alongside $BaAl_2O_4$ by using carbonate groups probably coming from solute impurities in $Ba(NO_3)_2$ salt (95 wt% purity). We notice that $BaCO_3$ is a common impurity of $BaAl_2O_4$ synthesis, which can be eliminated at elevated temperatures of ~1200°C [360, 361]. Consequently, almost pure **$BaAl_2O_4$ stuffed tridymite** with crystallite size of **60 nm** was successfully synthesized by impregnation of UPA.

The DT-DTG analyses of the M-UPA300 materials are shown in *Figure 3.58*. The decomposition of $Co(NO_3)_2$ (*Figure 3.58.a*) at about **185°C** takes place in **Co-UPA300** leading to the formation of cobalt oxide mass from $Co(NO_3)_2{\cdot}4H_2O$ [376]. It is important to notice that cobalt is a divalent cation in $CoAl_2O_4$, while it is trivalent in Co_2O_3. This mixed valence Co^{2+}/Co^{3+} may promote a structural disorder in the material prepared at calcination temperature < 700°C. No thermal phenomenon is observed, which can probably be explained by a slow **continuous phase transformation** in the whole temperature range, seen as the intensification of XRD peaks in *Figure 3.57.a*. In **Ni-UPA300** (*Figure 3.58.b*), the endothermic decomposition of $Ni(NO_3)_2{\cdot}6H_2O$ into oxide form occurs via two overlapping steps between **300 and 400°C**: the sharp peak at 315°C is due to the dehydration to anhydrous $Ni(NO_3)_2$, followed by a shoulder at 340-400°C due to its decomposition into oxide. These findings are in a general agreement with previous studies [376]. No distinct thermal phenomena observed at higher temperatures suggest a **progressive formation of $NiAl_2O_4$** (supported by an increase of XRD peaks intensity in *Figure 3.57.b*) without prior crystallization of monocationic oxides, as is suggested above for $CoAl_2O_4$ spinel. In **Zn-UPA300** (*Figure 3.58.c*), the decomposition of $Zn(NO_3)_2{\cdot}6H_2O$ into oxide form occurred in steps evidenced by several endothermic peaks, which is in agreement with results of previous studies [377, 378]. The process begins at 115°C resulting in the formation of layered $Zn(NO_3)_2{\cdot}2Zn(OH)_2$ structure, with almost no loss of nitrates [377]. Then two overlapping features at 200 and 235°C appear due to the dehydroxylation of the former compound into $Zn(NO_3)_2{\cdot}2ZnO$. Finally, the denitration to ZnO mass takes place at temperatures between **290 and 350°C**. A small mass loss at constant rate was observed between 350 to 450°C, probably due to remaining nitric oxides departure. No distinct thermal features are observed and intensification of the XRD patterns of the spinel phase (*Figure 3.57.c*) was observed over the full thermal range. In agreement with our observations on Co and Ni aluminate spinels, this allows concluding that **$ZnAl_2O_4$ progressively forms directly from the UPA and $Zn(NO_3)_2{\cdot}6H_2O$** precursors in course of their thermal chemical modifications.

In contrast to the previous materials, Ba-UPA300 shows endothermic features at a higher temperature, preceding the formation of $BaAl_2O_4$ as XRD confirmed (*Figure 3.57.d*). A first endothermic mass loss is observed at 270°C probably due to the departure of surface hydroxyl groups or chemisorbed water. Then endothermal nitrates decomposition occurs in several steps. At 590°C, the sharp peak with low mass loss is due to $Ba(NO_3)_2$ melting with some nitrates departure [379]. At 610°C, further nitrate loss takes place, although not full decomposition. A sharp mass loss at 650°C is attributed to the decomposition of $Ba(NO_3)_x$ to BaO_2 mass ($1.5 \leq x < 2$), which fully turns to **BaO mass at 700°C**. Once again, **no intermediate oxide** compounds of $BaAl_2O_4$ are evidenced in this synthesis route, confirming our previous conclusion about the **direct formation of binary oxide compounds** in course of thermal modifications of the reacted components.

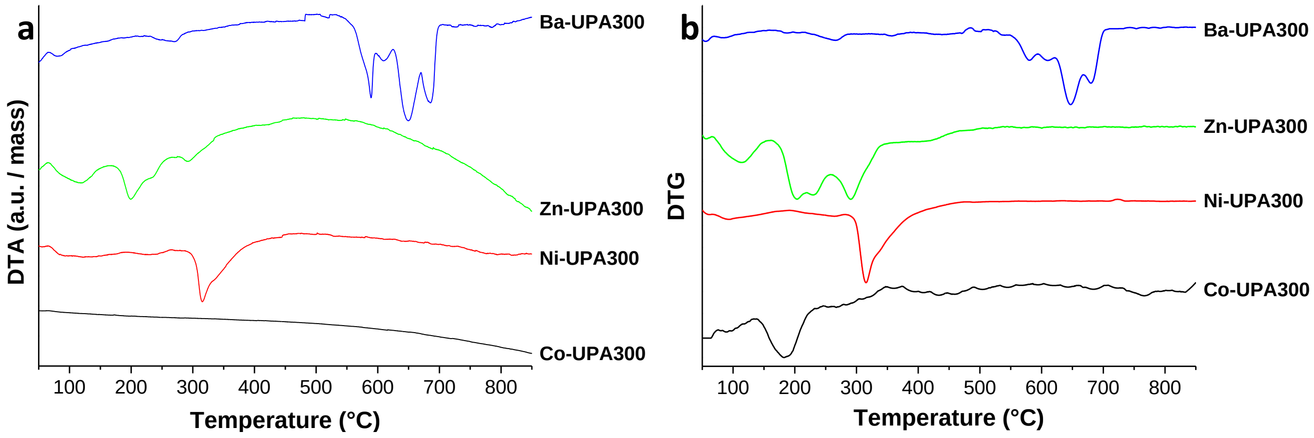

Figure 3.58: a) DT and b) DTG of the M-UPA300 materials (M: Co, Ni, Zn, Ba)

The microstructures of M-UPA300 materials calcined at 1000°C are shown in *Figure 3.59*. TEM of calcined Co-UPA300 (*Figure 3.59.a*) reveals particles with the mean size of **50 nm**, which is in agreement with that of crystallites from XRD. The large size distribution indicates **abnormal growth** at temperature well above the crystallization onset. Ni-UPA300 (*Figure 3.59.b*) shows **spherical particles** with a **narrow size distribution** around **12 nm**, which is smaller than 16.9 nm obtained from XRD refinement. Zn-UPA300 (*Figure 3.59.c*) shows the mean particle size of **48 nm**, in good agreement with crystallite size from XRD. Clusters of small crystallites of about 10 nm (not shown) were also noticed and assigned to second phase ZnO. Ba-UPA300 (*Figure 3.59.d*) shows **spherical crystallites** with the mean size of **31 nm**, associated into **large dense polycrystalline particles**; a similar morphology of this compound has been previously reported [361]. The crystallite size of $BaAl_2O_4$ obtained after XRD refinement was much larger at ~60 nm, which apparent discrepancy with TEM can be due to the crystallographic texture arising from material sintering. Nanowires can be also seen at the top left part of TEM image, and belong to impurity phase $BaCO_3$.

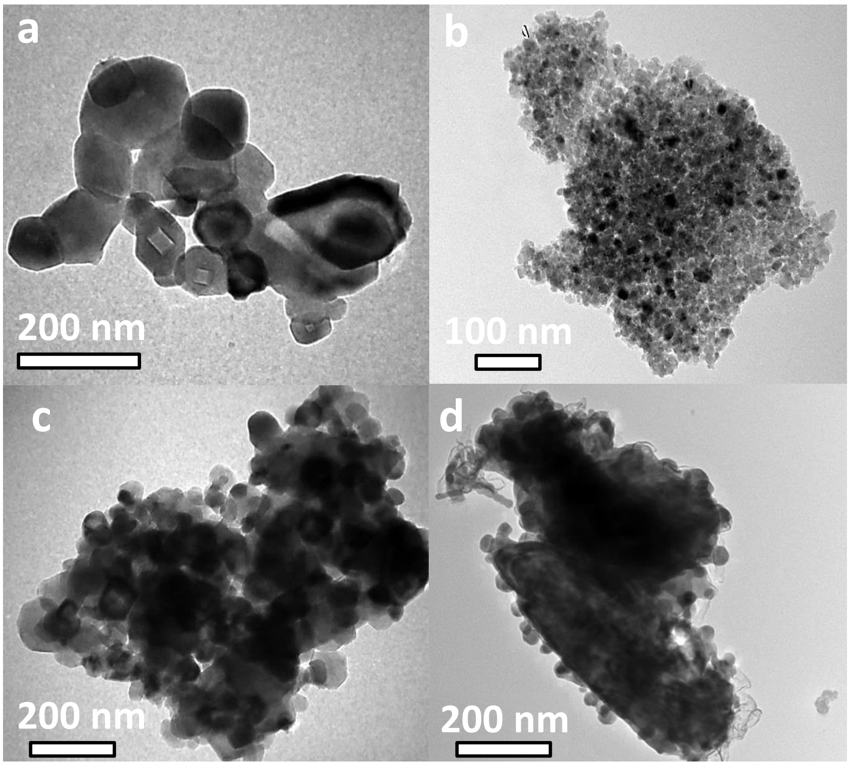

Figure 3.59: TEM of a) Co-UPA300, b) Ni-UPA300, c) Zn-UPA300 and d) Ba-UPA300 calcined at 1000°C during 1 hour

The mean crystallite size of MAl_2O_4 (M: Co, Ni, Zn) spinel nanopowders is plotted versus calcination temperature in *Figure 3.60*. The lattice constants are included for guidance of the structure evolution. While in Co-UPA300 (*Figure 3.60.a*) the crystallite size CS follows a single exponential law from 26 to 50 nm in the range $500 \leq T \leq 1000$°C, **two domains of size evolution** are observed in Ni-UPA300 (*Figure 3.60.b*) and Zn-UPA300 (*Figure 3.60.c*), similar to Mg-UPA300 (*Figure 3.55.a*). These domains apparently correspond to **different diffusion mechanisms** with the crossover point in the vicinity of $T^* \approx 800$°C. Differences of the crossover point for the different spinels can be connected to the inserted M cations (Mg, Ni, Zn) which affect diffusion in the host UPA. As followed from DT-DTG and XRD, the **spinel phase is formed** in $NiAl_2O_4$ and $ZnAl_2O_4$ after calcination in **domain 1 down to ≤ 500°C**, and smallest **CS < 10 nm** can be attained in this synthesis route. In contrast, the calcination in **domain 2** leads to **coarsening**. In $CoAl_2O_4$ nanopowder, spinel is formed at 500°C with small crystallites of ~26 nm. This temperature range may however already belong to domain 2 and T < 500°C may result in the decrease of $CoAl_2O_4$ crystallite size as well as apparition of a domain 1 of metastability. It is remarkable that starting from amorphous UPA300, **all spinel materials studied exhibited a metastable state of cationic disorder**, with peculiarities relative to each M^{2+} cations, while $BaAl_2O_4$ stuffed tridymite was directly formed in ordered state. This specificity of the spinel structure emphasizes **the great mobility of the cations within the lattice**, which provides its radiation tolerance [3].

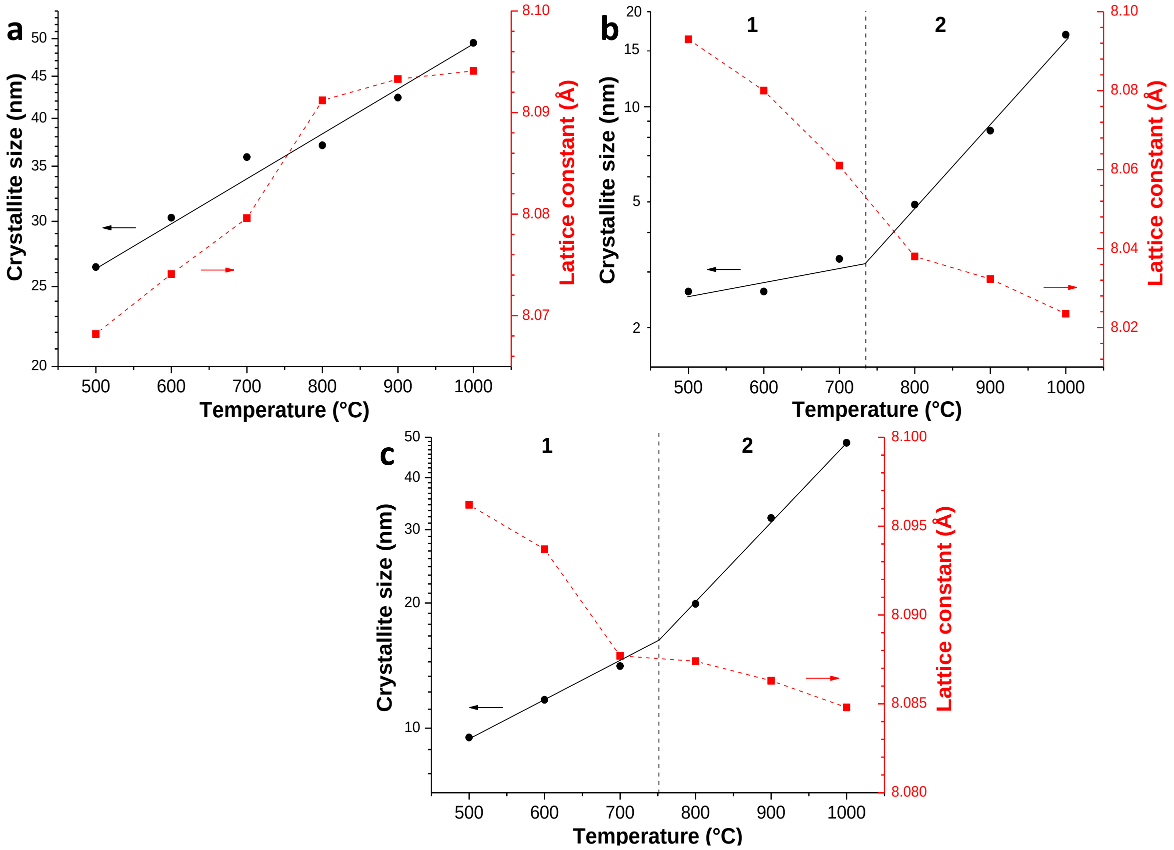

Figure 3.60: Crystallite size and lattice constant of a) Co-UPA300, b) Ni-UPA300 and c) Zn-UPA300 spinels vs temperature

4. Conclusion

The liquid impregnation of nanofibrous UPA materials has been proven efficient for the **synthesis of $MgAl_2O_4$ nanopowders with crystallite size < 20 nm**. The crystalline structure of UPA host material, heat treatment temperature and kinetic appeared to be important issues in achieving single-phase nanopowders.

We investigated the **influence of alumina polymorphism** on the formation of $MgAl_2O_4$ from the UPA. The reaction with crystallized UPA seems to follow **solid state reaction** kinetic as MgO crystallizes prior to reaction with the host. Stable α-Al_2O_3 appeared to be inappropriate for a facile restructuring into $MgAl_2O_4$ spinel, which was incomplete even at 1300°C. γ-Al_2O_3 permitted formation of MAS at 1000°C with **16 nm crystallites**, while lower temperatures resulted in biphasic MAS-MgO material. In addition, the **silica impregnation** into γ-Al_2O_3 UPA **inhibited coarsening** resulting in smaller spinel particles of **8 nm**.

In comparison, **amorphous dehydrated *a*-Al_2O_3 UPA** led to a **fully inverse (*I* ~1) spinel** material after treatment at moderate T ~500°C without prior MgO crystallization, indicating an effective Mg insertion into structural 5-7 nm fibrils. The **annealing of antisite defects** resulted in **normal spinel** (*I* ~0.3) after treatment at **~1000°C**. The crossover of particle coarsening kinetic at T^* = 850°C, which fits onset of the bulk mass transport [148], confirms this conclusion. The first observation of fully inverse MAS follows Ostwald's rule of phase nucleation, confirming that the highest free energy of amorphous precursors and limited time of treatment at moderate temperatures make this highest-energy metastable state accessible.

The **high versatility** of the proposed route was demonstrated through successful syntheses of **MAl_2O_4 (M: Co, Ni, Zn, Ba) nanopowders** from *a*-Al_2O_3. The analysis extended the conclusions of phase nucleation according to the Ostwald's rule for all aluminate spinel materials. The heat treatement at 500°C led to small **crystallites size < 10 nm** in **NiAl and ZnAl spinels** and larger crystallites of **26 nm for $CoAl_2O_4$**, which may be related to temperature of crossover point < 500°C in the latter. In contrast to Mg, Co, Ni and Zn cations, insertion of Ba cations resulted in the **stuffed tridymite $BaAl_2O_4$** phase, further expanding the range of alumina-based nanoparticle compounds that can be synthesized through the liquid impregnation of UPA.

III. Conclusion on the synthesis of nanocrystalline $MgAl_2O_4$ powders

In this chapter, we developed two different synthesis techniques for the preparation of $MgAl_2O_4$ nanoparticles, namely the polyol-mediated route and the UPA impregnation route.

The **synthesis *via* polyol route** consists on the preparation of a MgAl hydroxides mixture, which is **thermally decomposed to spinel at 800°C** with **crystallite size of 7 nm**. Several parameters have been found to influence the reaction mechanism and structural and microstructural properties (temperature, precursor salts, additives…) and could help in optimizing the sinterability of the powder in the future.

The **synthesis *via* liquid impregnation of nanofibrous alumina** followed by thermal treatment led to fine spinel crystallites as well. We investigated the influence of four UPA precursors on $MgAl_2O_4$ synthesis. The **amorphous *a*-Al_2O_3** (UPA300) allows formation of **fully inverse $MgAl_2O_4$** at 500°C with **~5 nm crystallites**, and **normal structure** at 1000°C with **16 nm crystallites**. The **metastable spinel γ-Al_2O_3** (UPA1050) leads to pure $MgAl_2O_4$ at 1000°C with **16 nm crystallites** too, while prior **silica impregnation** limits the size to **8 nm**. Finally, **stable corundum α-Al_2O_3** (UPA1250) does not allow complete reaction to $MgAl_2O_4$ even up to 1300°C (residual reactants ~10 wt%), with **crystallite size of ~115 nm**.

In order to investigate the influence of the powder's structure and microstructure, the sintering of the powders synthesized from reference polyol synthesis conditions and all four Mg-UPA precursors will be adressed in *Chapter 4.III*. The results will provide insights on the features of nanoprecursors to be adjusted.

This page intentionally left blank.

Chapter 4
Consolidation of $MgAl_2O_4$ ceramics

The goal of the second part of this PhD project is to fabricate highly transparent and fine-grained magnesium aluminate spinel ceramics *via* the spark plasma sintering process. For this purpose, we are using mostly two commercial $MgAl_2O_4$ precursor powders and comparing their sinterability and the ceramic properties they are leading to, in order to assess the influence of the precursor powder's features on the fabrication of dense ceramics. Afterward, the sinterability of the nanopowders synthesized in *Chapter 3* is assessed, in order to determine their suitability as a base material for the fabrication of transparent spinel ceramics with grain size at the nanoscale.

In this chapter, several axes of work have been investigated to both improve the ceramic properties and provide a better understanding on the sintering mechanisms during SPS of our powders. Firstly, the influence of mechanical pre-treatments of the commercial powders on their sinterability and subsequent ceramic's features is studied. Next, a parametric study of the sintering is carried out on both commercial powders, to identify the most influential SPS parameters and optimal conditions for transparent and fine-grained spinel ceramic fabrication. Then, the sintering of the nanopowders synthesized in *Chapter 3* through polyol and impregnation routes is carried out to assess their suitability for the fabrication of transparent spinel ceramics. Afterward, we investigate the effect of annealing and HIP post-sintering treatments of ceramics on their features, especially transparency and microstructure. Finally, we investigate the phenomenology during SPS of ionic conductors with the cases of Ta_2O_5 and Ta_2O_5 added $MgAl_2O_4$ powders.

I. Influence of mechanical pre-processing

As detailed in *Chapter 1.IV.3.v.b*, the processing of powders prior to their sintering can greatly improve their sinterability and the subsequent ceramic properties, as raw powders do not always have ideal microstructural features for good sinterability. In this section, we **investigate the influence of pre-sintering comminution** on the commercial powders' microstructures and sinterability. Two mechanical treatments have been used and compared: a **low-energy milling** carried out on a 3D-mixer with ZrO_2 grinding media and a **high-energy milling** carried out on a planetary ball mill with steel grinding media. The protocol and experimental set-up are detailed in *Chapter 2.II.2.iii*. The different conditions of preparation experimented are given in *Table 4.1*. The studied ranges for the different parameters have been set based on literature.

Table 4.1: The mechanical pre-processing conditions experimented on $MgAl_2O_4$ commercial powders

Name	Processing	Wetness state	BPR [a]	Speed (rpm)	Duration (h)
3MD	3D-mixing	Dry powder	3	32	24
3MS	3D-mixing	Slurry, ϕ ~35 vol%	3	32	24
PMD100-BPR10	Planetary milling	Dry powder	10	100	2
PMD200-BPR10	Planetary milling	Dry powder	10	200	2
PMD200-BPR20	Planetary milling	Dry powder	20	200	2
PMS100-BPR10	Planetary milling	Slurry, ϕ ~35 vol%	10	100	2
PMS200-BPR10	Planetary milling	Slurry, ϕ ~35 vol%	10	200	2

[a] BPR refers to milling ball to powder mass ratio

1. Pre-processing of the Sasol powder

i. Influence of the pre-processing on the powder features

The commercially available $MgAl_2O_4$ powder referred to as Sasol, *c.f. Chapter 2.II.2.i*, presents a **raw microstructure** consisting of **30 µm spherical aggregates of 2 µm platelets with pre-sintered ~140 nm crystallites** (SEM in *Figure 4.1.a*), which is non-ideal for the sinterability. Both low- and high-energy comminution have been used to improve this initial morphology, with all conditions presented in *Table 4.1*.

It is to be noted that the **most energetic PM processing conditions led to steel contamination** of the powder from the grinding media, as the retrieved material was light gray for PMD200-BPR20 and dark gray for PMS200-BPR10. After calcination at 900°C for 4 h in order to eliminate eventual volatile contamination, the powders coloration turned slightly pink due to oxidation of the steel impurities into **iron oxide**.

SEM of the Sasol powder as-received and after comminution are presented in *Figure 4.1*. Both **low-energy comminution** in dry state (3MD, *Figure 4.1.b*) and slurry state (3MS, *Figure 4.1.c*) greatly modified the raw Sasol microstructure: **3MD** led to the **breakage of most of the initial aggregates**, except for the smaller ones with size ≤ 10 µm, while **3MS resulted in their full breakage**, and both processing led to subsequent reaglomeration in **large weakly bonded and loose agglomerates** which should induce better sinterability than the initial hard and dense aggregates [80]. In addition, insets reveal the **platelets particles have been broken** as well, and the initial spherical crystallites stand as primary particles. The **planetary**

milling in dry state PMD provided varying results depending on the milling conditions. The **softest conditions** at 100 rpm with BPR 10 (PMD100-BPR10, *Figure 4.1.d*) resulted in **only slight effects**: the aggregates have been rounded, with altered surface platelets (see inset). The **higher speed of 200 rpm** (PMD200-BPR10, *Figure 4.1.e*) permitted to **fully break the aggregates and platelets**, with weak re-agglomeration as for 3MD. Stronger milling conditions (PMD200-BPR20, *Figure 4.1.f*) resulted in larger size distribution of the agglomerates with irregular shapes, including flattening due to the cold welding of the particles as a result of the higher milling energy. The **planetary milling in slurry state PMS provided similar results than PMD** in comparable milling conditions: PMS100-BPR10 did not greatly modify the raw Sasol microstructure (*Figure 4.1.g*), while PMS200-BPR10 resulted in the full breakage of the aggregates and platelets with severe re-agglomeration afterward (*Figure 4.1.h*).

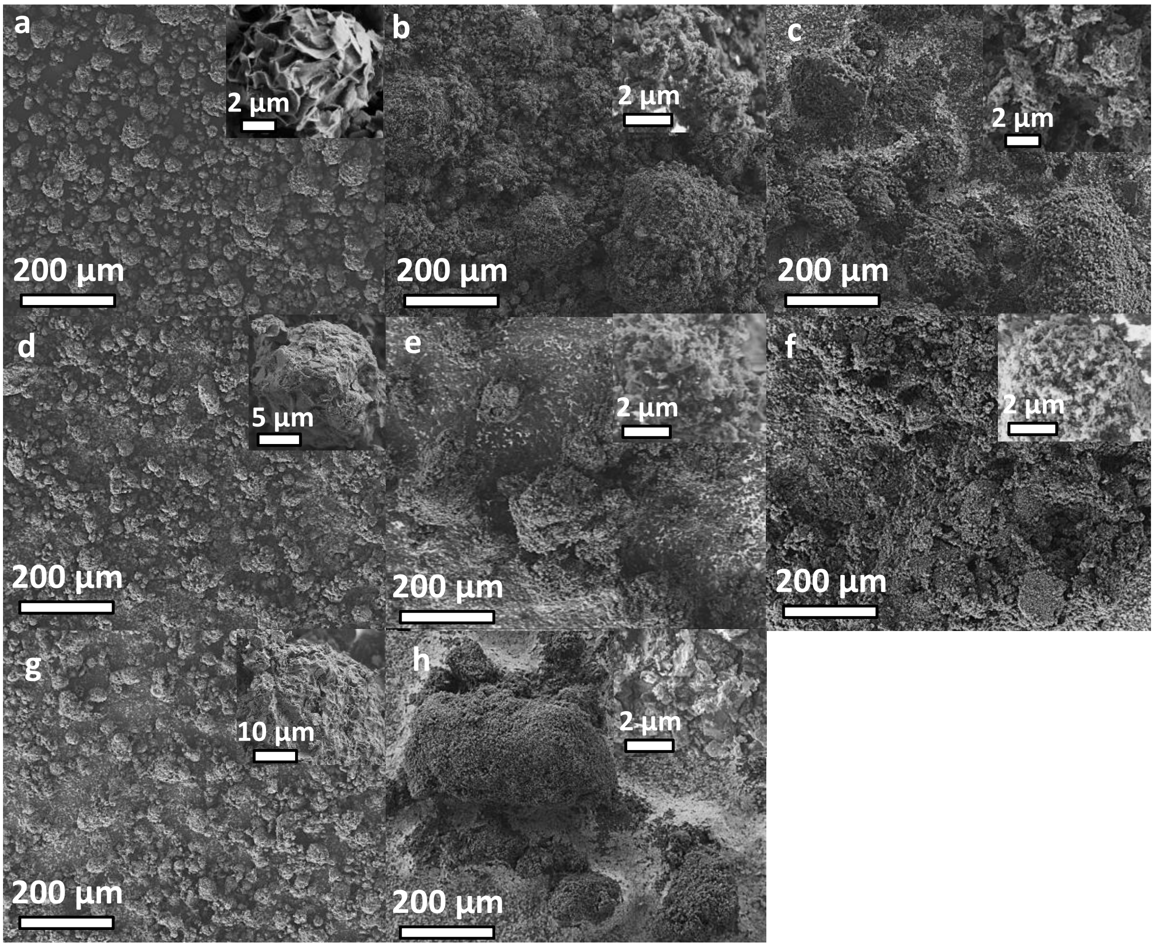

Figure 4.1: SEM micrographs of the Sasol powder a) as received and after mechanical processing b) 3MD, c) 3MS, d) PMD100-BPR10, e) PMD200-BPR10, f) PMD100-BPR20, g) PMS100-BPR10 h) and PMS200-BPR10; insets show high magnification

Based on the microstructures, the most interesting processing carried out appears to be 3MD, 3MS, PMD200-BPR10 and PMS200-BPR10, thus only these treatments were further analyzed. **Uncontrolled re-agglomeration** occurs systematically after milling, therefore a subsequent granulation step could be added in the process in order to obtain controlled agglomerates of regular shapes and size distribution.

The particle size distribution (PSD) of the Sasol powder as-received and after comminution has been investigated by DLS, after dilute suspension in deionized water, and the results are presented in *Figure 4.2*. These results are complementary to SEM analysis, as the latter gives informations on the large agglomerates while the former focuses on the particles of size < 6 µm more strongly bonded. It can be observed that the

raw Sasol powder, while presenting **large aggregates** of size **$PS_{1\text{-raw}}$ ~30 µm** (mode beginning at 4000 nm, black curve), also has a **lower particle size mode $PS_{2\text{-raw}}$ = 450 nm** with large PSD from 200 to 1000 nm, probably from non-aggregated platelet particles. For the processed powders with no more platelets and large aggregates, the PSD obtained by DLS can be assumed to better represent the real PSD. Both **processing in dry state** 3MD (red) and PMD200-BPR10 (blue) resulted in **identical bimodal PSD**, with **$PS_{1\text{-dry}}$ ~1500 nm** arising from the breakage of $PS_{1\text{-raw}}$ aggregates and **$PS_{2\text{-dry}}$ ~370 nm** residual from $PS_{2\text{-raw}}$. The **3MS processing** (green) results in a main mode **$PS_{1\text{-3MS}}$ = 900 nm** and a minor **$PS_{2\text{-3MS}}$ = 200 nm** remaining from $PS_{2\text{-raw}}$. Finally, PMS200-BPR10 (light blue) appears to be less efficient, as two highly populated modes of large particles **$PS_{1\text{-PMS}}$ = 3000 nm** and **$PS_{2\text{-PMS}}$ = 850 nm** are obtained. From these results, it appears that the smaller particles of **$PS_{2\text{-raw}}$ are less impacted by milling**, especially when performed in dry state. The **3MS processing** appears to be **more efficient to refine the microstructure**.

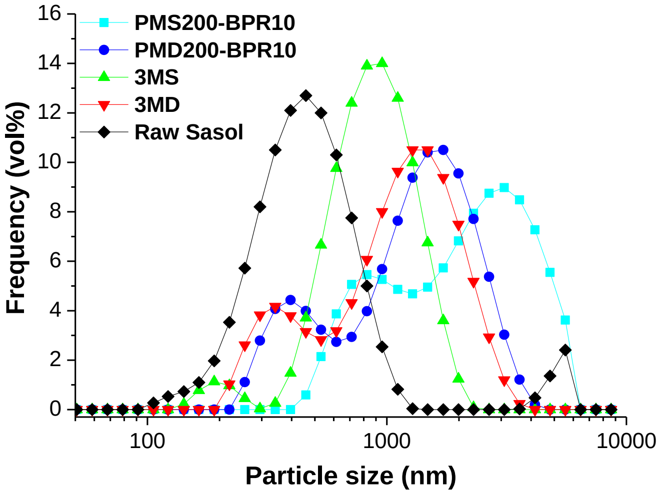

Figure 4.2: Particle size distribution of the Sasol powder in aqueous suspension after mechanical processing

The XRD patterns of the Sasol powder as-received and after comminution are presented in *Figure 4.3*. It appears clearly that the mechanical treatments had **no impact on the structural composition** of the powder, with no variation of cell parameter and crystallite size. Thus, in comparison with results obtained for high-energy ball milling in [276, 278], the processing conditions experimented in this work did not lead to mechanical activation of the MAS material.

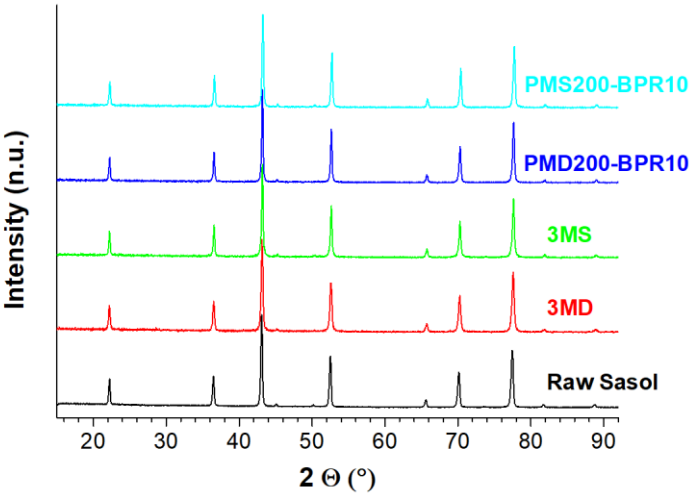

Figure 4.3: X-Ray diffractograms of the Sasol powder after mechanical processing

ii. Influence of the pre-processing on the sinterability and the ceramic properties

The Sasol powders processed with milling conditions 3MD, 3MS, PMD200-BPR10 (hereafter simply referred to as PMD) and PMS200-BPR10 (hereafter simply referred to as PMS) have been used to **investigate the impact of the milling on the sinterability and on the properties of the ceramic**.

In a first place, a short SPS cycle at 1450°C with a heating rate of 100°C/min and no temperature dwell was applied, providing an insight on the sinterability through the relative displacement of the pistons during SPS presented in *Figure 4.4* in function of the instant temperature. The negative displacement prior to densification is due to thermal expansion, and will not be considered here. The onset temperature for the **raw Sasol powder** densification (black curve) is ~1100°C, and a *plateau* is reached at **1400°C**. The **3MD** and **PMD** curves (in red and blue, resp.) indicate similar sinterability for both powders: densification takes place between **1050** and **1450°C**. The **3MS** powder (green) is densified in the range **1000-1450°C**. Finally, the **PMS** powder (light blue) is densified in the lowest temperature range **950-1385°C**. From these observations, it appears that pre-processing has **no great effect on the sinterability** of the Sasol powder, except for a diminution of the sintering onset temperature by ~100°C for milling in slurry state (3MS and PMS).

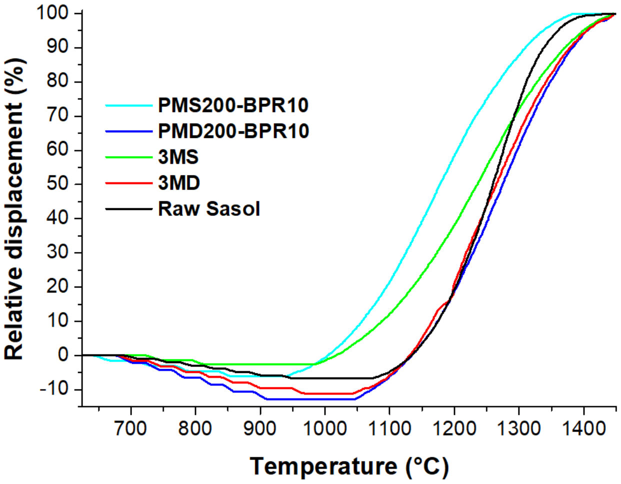

Figure 4.4: Relative displacement of the SPS pistons during sintering of the Sasol powder after the different mechanical processing

From the sinterability study of the different powders, we decided to apply a sintering cycle at 1450°C with a lower heating rate of 10°C/min and a 20 min temperature dwell in order to prepare and compare the fully dense ceramics. The properties of the materials obtained are summarized in *Table 4.2*.

Table 4.2: Properties of the ceramics SPSed at 1450°C, 20 min from Sasol powder precursors with different mechanical processing

Powder	Relative density (%)	Grain size (µm)	Transmittance at 600 nm (%)
Raw Sasol	99.8(1)	3.13	30.6
3MD	99.1(1)	2.16	44.7
3MS	99.2(1)	1.64	38.7
PMD200-BPR10	99.7(1)	1.72	45.8
PMS200-BPR10	100.4(2)	1.18	1.0

The XRD patterns of the ceramics obtained from SPS of the different Sasol precursors are presented in *Figure 4.5*. It appears clearly that the **patterns are identical** for all ceramics and exhibit no variation from the XRD patterns of their precursor powders (*Figure 4.3*), independently of the pre-processing carried out.

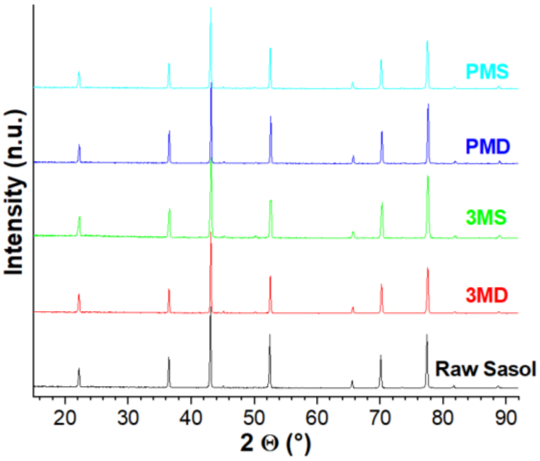

Figure 4.5: X-Ray diffractograms of the ceramics SPSed from the Sasol powder treated by different mechanical processing

SEM of the ceramics obtained from the different Sasol powders is presented in *Figure 4.6*. The ceramic prepared from **raw Sasol** exhibits the **highest grain size of 3.13 µm** with **full densification**, as no porosity is observable on *Figure 4.6.a*. The **3MD** and **3MS** processing (*Figure 4.6.b* and *c*, resp.) led to a **decrease of GS to 2.16 and 1.64 µm**, respectively, but density only reaches *d* ~99.1 % due to **large remaining pores**. The **PMD ceramic** (*Figure 4.6.d*) also contains a high content of pores with **GS ~1.72 µm**, while the **PMS ceramic** (*Figure 4.6.e*) has only small pores in low content with the **smallest GS of 1.18 µm**. It is interesting to notice that the pre-processing of the powder allows a **great diminution of grain size after sintering**, from a decrease factor of ~1.5 for 3MD, ~2 for 3MS/PMD, and ~2.7 for PMS. This influence of the mechanical treatment on the ceramic microstructure confirms its effect on the sinterability.

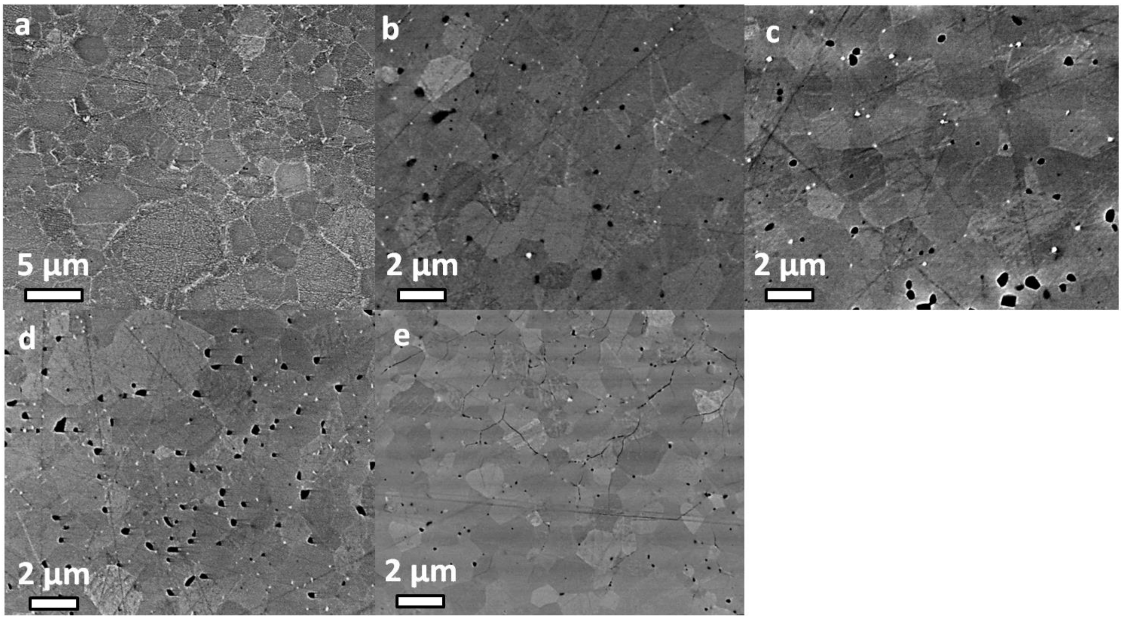

Figure 4.6: SEM of the ceramics SPSed at 1450°C from the Sasol powder a) as received, b) 3MD, c) 3MS, d) PMD200-BPR10 and e) PMS200-BPR10

The transmittance spectra of these ceramics are shown in *Figure 4.7*, together with photographs of the materials. All pre-processing except PMS **increased the transparency**, especially for λ < 500 nm. Both treatments in **dry state 3MD and PMD** resulted in almost identical transmittance, with the highest curves on the λ-range. Indeed, the photographs show that 3MD and PMD ceramics have close aspects, with **lighter darkening** than for raw Sasol. The **3MS ceramic** appears even less colored, but a close examination reveals small **black and opaque inclusions** distributed in the whole material, which we attribute to **carbon contamination** during SPS processing independently of the pre-processing, altering its normally high transparency. The **PMS ceramic** is **opaque and black**, due to the **steel contamination** from pre-processing.

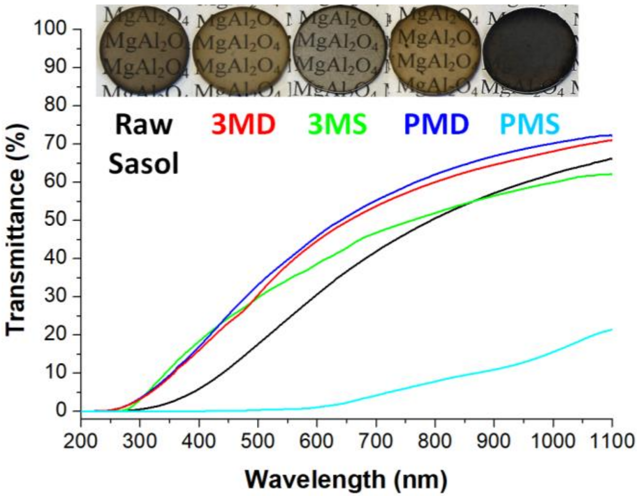

Figure 4.7: Transmittance spectra and photographs of the ceramics SPSed from the Sasol powder treated by different pre-processing

From these results, a significant influence of the powder mechanical pre-processing on the properties of the Sasol ceramics has been established. It should be noticed that as the particle size distributions of the 3MD and PMD powders were very close, their sinterability and ultimately their transparency were very close as well. However, the 3MD processing did not lead to full refinement of the Sasol morphology as the aggregates of size < 10 µm remained, which could have resulted in the bigger grain size after SPS. The **3MS processing** appears to present the **best compromise** between grain size refinement (GS/2) and transparency.

2. Pre-processing of the S25CR powder

i. Influence of the pre-processing on the powder features

The S25CR commercially available $MgAl_2O_4$ powder presents a better raw microstructure than the Sasol powder, with **soft agglomerates** of **~70 nm crystallites** (*Chapter 2.II.2.i*). Since the primary particles are not aggregated in raw S25CR, only **low-energy treatments 3MD and 3MS** has been investigated (*Table 4.1*).

The SEM of the S25CR powder before and after comminution is presented in *Figure 4.8*. **Little modifications** are noticeable, as the soft agglomerates and primary particles kept their initial shape and bonding nature. However, the raw S25CR powder presented a wide particle size distribution, with **larger agglomerates** of several hundred nm (*Figure 4.8.a*), which seem to be **refined in the processed powders**.

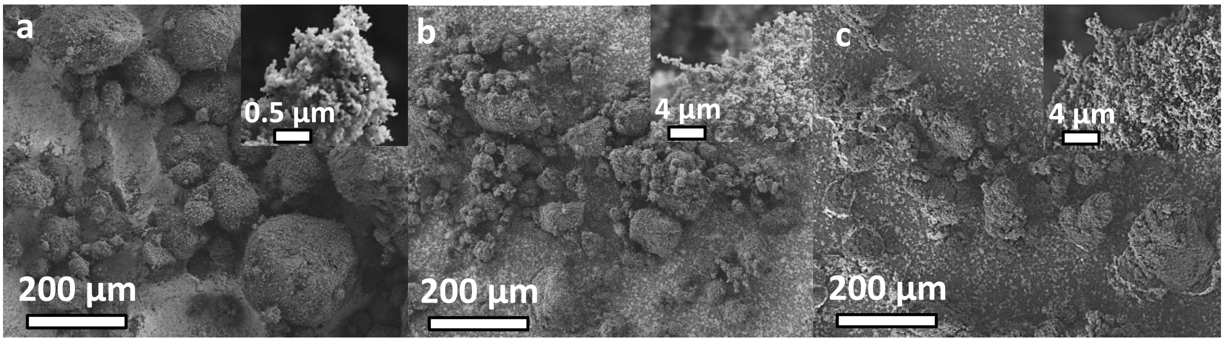

Figure 4.8: SEM of the S25CR powder a) as received and b) 3MD and c) 3MS processed; insets show high magnification

The DLS particle size distributions of the S25CR powder before and after treatment are presented in *Figure 4.9*. A single particle size mode is observed for **raw S25CR** (black curve) as **$PS_{2\text{-raw}}$ = 600 nm**; however, a **more populated mode $PS_{1\text{-raw}}$** >> **$PS_{2\text{-raw}}$** is inferred from SEM. The PSD after **3MD processing** (red) is bimodal as well, with **$PS_{1\text{-3MD}}$ ~700 nm** arising from $PS_{2\text{-raw}}$, and a minor **$PS_{2\text{-3MD}}$ ~5000 nm** most probably from de-agglomeration of $PS_{1\text{-raw}}$. The PSD after **3MS processing** (green) presents a mode **$PS_{1\text{-3MS}}$ ~500 nm** from $PS_{2\text{-raw}}$ and a minor **$PS_{2\text{-3Ms}}$ ~130 nm** from particles formed by 2-3 crystallites.

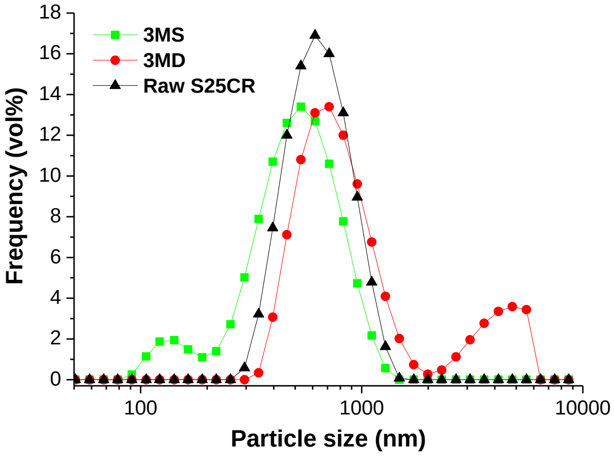

Figure 4.9: Particle size distribution of the S25CR powder in aqueous suspension after mechanical processing

The XRD patterns of the S25CR powder before and after processing are presented in *Figure 4.10*. As for the Sasol powder, the **mechanical treatments did not modify the cell constant or crystallite size of MAS**.

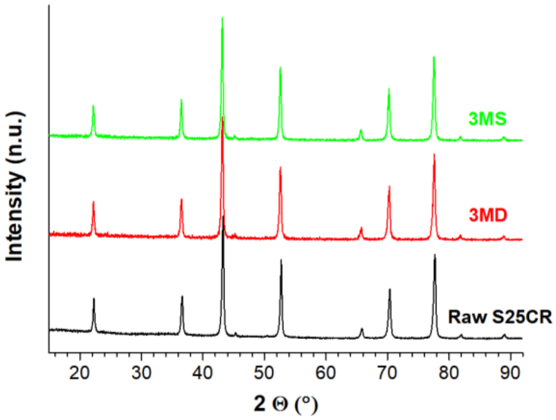

Figure 4.10: X-Ray diffractograms of the S25CR powder after mechanical processing

ii. Influence of the pre-processing on the sinterability and the ceramic properties

The different S25CR precursor powders have been used to **investigate the impact of the different pre-processing on the sinterability and on the properties of the ceramic**.

The sinterability was studied with the same SPS cycle than for the Sasol powders (1450°C, 100°C/min, no dwell), with the relative displacement of the pistons shown in *Figure 4.11*. The effect of the pre-processing on the sintering path is much less significant than for Sasol, due to the lesser refinement of the raw microstructure. The **onset temperature of densification** is **885°C for raw S25CR**, **910°C for 3MD** and **890°C for 3MS**; the **densification *plateau*** is reached at **1340°C for raw and 3MS S25CR**, and at **1360°C for 3MD**. These small variations are within the experimental uncertainty of the temperature measurement. Hence, it can be considered that **pre-processing has no sensible effect on the sinterability of S25CR**.

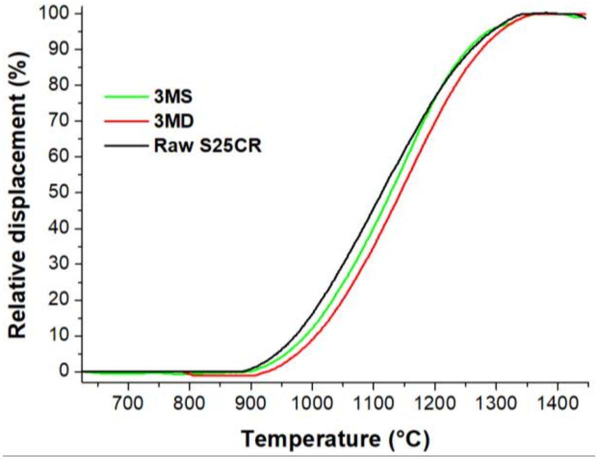

Figure 4.11: Relative displacement of the SPS pistons during sintering of the S25CR powder after different pre-processing

From this sinterability study, we decided to apply a **sintering cycle at 1375°C with heating rate of 10°C/min and a 20 min dwell** to prepare and compare the dense ceramics. The properties of the materials obtained are summarized in *Table 4.3*. Their XRD patterns (not shown) are identical.

Table 4.3: Properties of the ceramics SPSed at 1375°C, 20 min from S25CR powder precursors with different pre-processing

Powder	Relative density (%)	Grain size (µm)	Transmittance at 600 nm (%)
Raw S25CR	99.4(1)	0.63	70.5
3MD	99.4(1)	0.43	71.9
3MS	99.5(1)	0.45	79.7

The SEM of the ceramics prepared from SPS of the different S25CR powders are presented in *Figure 4.12*. All the ceramics have the same level of **density *d* ~99.4(1)% with no visible pores**. While the raw S25CR powder led to GS = 0.63 µm, both **milling** resulted in a **decrease by a factor 1.5 to GS ~0.45 µm**. Thus, low-energy pre-processing of S25CR powder allows the **refinement of the ceramic microstructure**, even if no influence was noted on the sintering path. However, it can be seen that the **3MS ceramic** microstructure (*Figure 4.12.c*) is **homogeneous** with regular grain shapes and narrow size distribution, while the **3MD ceramic** (*Figure 4.12.b*) is **non-homogeneous** with irregular grain shape (rounded, acicular…).

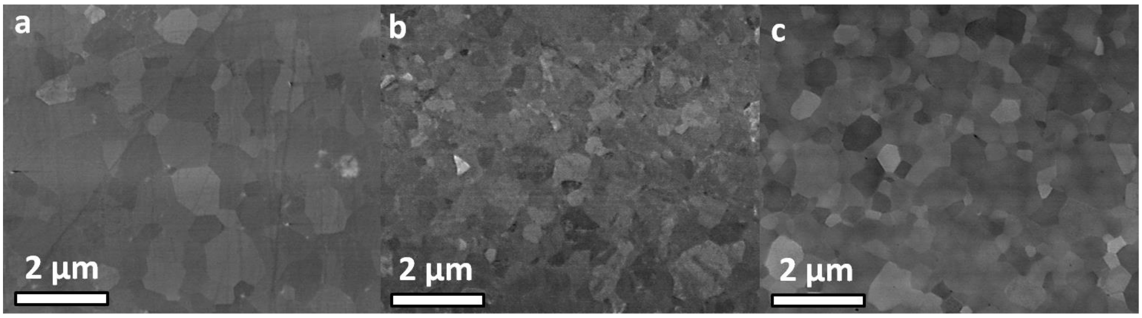

Figure 4.12: SEM of the ceramics SPSed at 1375°C from the S25CR precursor a) as received, b) 3MD and c) 3MS

The transmittance spectra of the ceramics are shown in *Figure 4.13*, together with photographs of the materials. It is interesting to observe that both **pre-processing** led to a **shift of the UV cut-off from 240 to 210 nm**. However, the **3MD** transmittance then reaches a ***plateau* at ~72%** comparable to the **70.5% of the raw S25CR ceramic**. The close visible transparency of these ceramics is confirmed by optical images. The **3MS ceramic** has a **higher *plateau* of transmittance at ~80%**.

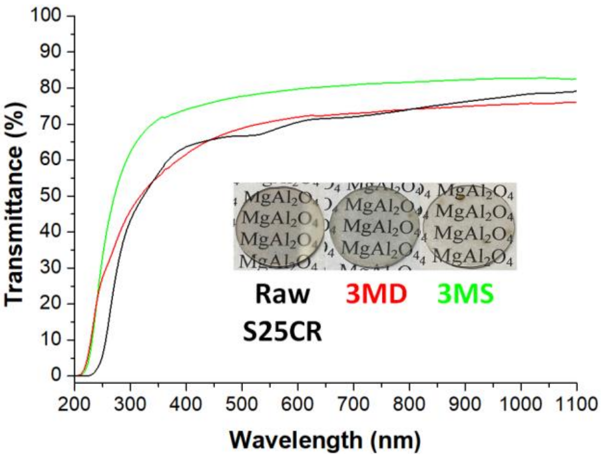

Figure 4.13: Transmittance spectra of the ceramics SPSed from the different S25CR precursor powders with optical images

From these results, it appears that the pre-processing of the S25CR powder has small effect on its microstructure and sinterability, as it is initially weakly agglomerated. However, the **comminution sensibly reduces the grain size of sintered ceramics**. In addition, the **most homogeneous microstructure and best transparency** is obtained after a **pre-processing in slurry state (3MS)**.

3. Conclusion

In this section, we investigated the **influence of mechanical pre-processing of the Sasol and S25CR commercially available powders on the sinterability and ceramic properties**. We experimented both low-energy 3D mixing and high-energy planetary milling, and the former provided **better compromise between grain size refinement and transparency improvement** of the ceramics. In both case, a **great decrease of the grain size up to a factor 2.5** was observed. The planetary milling induced **steel contamination** from the balls and vials, which could be avoided with ZrO_2 or Si_3N_4 grinding media.

In addition, **milling in slurry state** was found to **better de-agglomerate** the powder, and resulted in **more homogeneous microstructure** and **higher transparency** after sintering. However, re-agglomeration occurred during the un-optimized drying step, which could be controlled by addition of a granulation step.

Finally, the comparison between Sasol and S25CR ceramics evidences that the latter is more adapted for the desired application: **factor 3 in grain size** and higher **transparency**. Beyond the development of an adequate pre-processing treatment, the **most crucial parameter appears to be the raw powder**.

II. Spark Plasma Sintering of commercial $MgAl_2O_4$ powders

In this section, we study the Spark Plasma Sintering of both commercial $MgAl_2O_4$ powders. We assess the **influence of the most significant sintering parameters** on the properties of the consolidated ceramics, *i.e.* **the temperature T_d, the sintering dwell duration t_d, the heating rate α and the applied pressure P**, in order to optimize the sintering cycle for development of highly transparent materials with ultrafine grain size. A two-step SPS scheme has been used, with the general sintering schedule schematized in *Figure 2.9*.

Based on the results on the influence of powder pre-processing (*Chapter 4.I*), we decided to use **raw Sasol powder** as milling could not provide enough improvement to the ceramic properties to be interesting, and the **S25CR-3MS precursor** which led to the best results. Both powders were subjected to **calcination at 900°C** for 4 h prior to sintering to homogenize the particle size distributions and suppress volatile species.

1. Spark plasma sintering study of raw Sasol powder

i. *Effect of the sintering dwell temperature T_d*

The **sintering dwell temperature T_d effect** was investigated using so-called *long* (α = 10°C/min, t_d = 20 min) and *short* cycle (α = 100°C/min, t_d = 3 min) *SPS cycles* with P = 80 MPa, in order to reveal the **kinetic effect** as well. The results obtained with the **long cycle** in the temperature range **$900 \leq T_d \leq 1450$°C** and the **short cycle** in the range **$1400 \leq T_d \leq 1650$°C** are summarized in *Table 4.4* and *Table 4.5*, respectively.

Table 4.4: Influence of the sintering temperature on the properties of Sasol ceramics SPSed with 10°C/min, 20 min, 80 MPa

Temperature of sintering (°C)	**900**	**1000**	**1100**	**1200**	**1300**	**1400**	**1450**
Relative density (%)	100.0(1)	99.1(2)	94.7(1)	98.8(1)	99.8(2)	99.8(1)	99.8(1)
Grain size mode [a] (µm)	~0.28	0.46	0.54	0.73; 1.60	1.96	2.21	2.95
Transmittance at 600 nm (%)	0	0	0	20.9	42.6	38.1	30.6

[a] Two values of grain size mode indicate a bimodal distribution

Table 4.5: Influence of the sintering temperature on the properties of Sasol ceramics SPSed with 100°C/min, 3 min, 80 MPa

Temperature of sintering (°C)	**1400**	**1450**	**1500**	**1550**	**1650**
Relative density (%)	97.5(1)	98.4(1)	99.2(1)	99.1(1)	99.9(3)
Grain size mode (µm)	0.77	0.87	2.44	2.95	4.9
Transmittance at 600 nm (%)	6.1	12.6	34.1	31.6	18.5

The XRD patterns of the Sasol ceramics prepared with the long cycle are presented in *Figure 4.14*. **No sensible evolution** from the XRD of the Sasol powder is observed through SPS with increasing temperature. Furthermore, reflections from the **MgO periclase phase** are still observed with same intensities, indicating that the free MgO has not been integrated within MAS phase during sintering. Similar observations were made for the XRD evolution for all studied parameters, so they will not be presented in other sections to avoid redundancy. It indicates that the **Sasol phase composition is stable during sintering**.

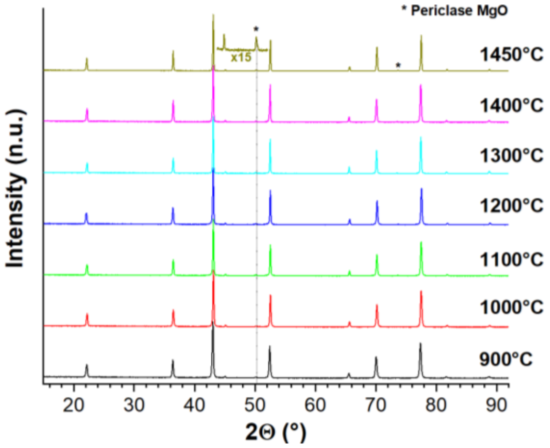

Figure 4.14: XRD patterns of Sasol MAS ceramics SPSed for 20 min at different temperatures between 900°C and 1450°C

The photographs of the ceramics prepared with the long cycle in the range $900 \leq T_d \leq 1450$°C are shown in *Figure 4.15*. The materials prepared with **T_d < 1200°C are opaque white**. The **1200°C sample** is **translucent gray**, while the ones with **T_d > 1200°C are transparent with a dark coloration**.

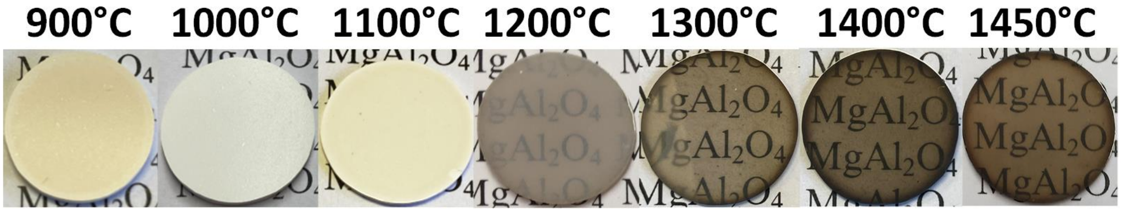

Figure 4.15: Photographs of Sasol MAS ceramics SPSed for 20 min at different temperatures between 900 and 1450°C

The SEM of these materials is presented in *Figure 4.16*. The microstructure of the **ceramic SPSed at 900°C** (*Figure 4.16.a*) consists of the **initial aggregates** of the raw Sasol powder **bounded by sinter necks** ensuring the mechanical strength of the material. **Two levels of porosity** are observed: *i)* **5-20 µm large inter-aggregates pores** and *ii)* **< ~1 µm small intra-aggregate pores** between the platelet primary particles. The microstructure is not homogeneous; some parts are not sintered and present crystallites unchanged from the powder (left inset), while sintered parts are denser with slightly coarser crystallites (right inset). The density has been measured to be *d* = 100%, which is due to the **fully open porosity** to which pycnometry is not sensible. For **increasing T_d < 1200°C**, the open porosity **progressively turned to close porosity** so the measured density decreased (see *Table 4.4*), and the sintering becomed more homogeneous. For the **ceramic sintered at 1200°C** (*Figure 4.16.d*), the microstructure is uniform with **fine grain size** and **small spherical pores of size < ~100 nm** evenly distributed, for a measured density of 98.8%. For **T_d > 1200°C**, the pores disappeared and the density increased to 99.8(1)%, while the **grains coarsened proportionally to T_d**.

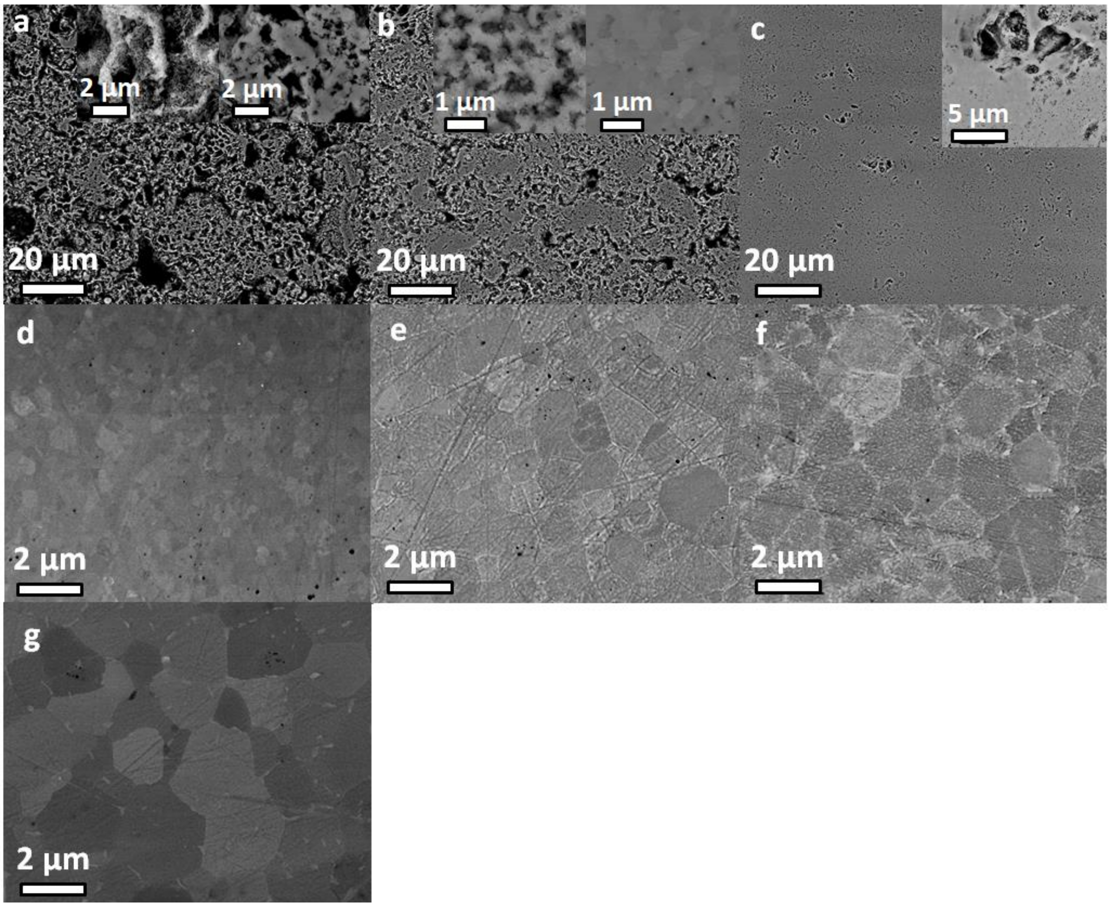

Figure 4.16: SEM of Sasol MAS ceramics SPSed for 20 min at a) 900, b) 1000, c) 1100, d) 1200, e) 1300, f) 1400 and g) 1450°C

The grain size distributions (GSD) of the ceramics prepared with the long cycle at different T_d are presented in *Figure 4.17.a*. The grain sizes follow **log-normal distributions** with modes GS increasing with

T_d. For T_d = 900°C, the GSD presents a somehow large standard deviation due to the non-homogeneous microstructure. The GSD are monomodal except for **T_d = 1200°C, where it is bimodal** with **GS_1 = 0.73 µm and GS_2 = 1.60 µm**. It is to be noted that the microstructure is homogeneous, and the two modes appear **well mixed together**. This seems to correspond to the **transition between open and close porosity** (final stage of sintering), with the sintering **transitioning from consolidation to densification mechanisms** (*cf. Chapter 1.IV.2*). For T_d > 1200°C, GS_1 disappears to the benefit of large grains.

The modes of GSD are plotted in function of T_d in *Figure 4.17.b*. It is clear that the **grain size increases exponentially with the temperature**, although the sintering behavior transition at 1200°C is observed here as well. In the **low-T_d range**, GS grows exponentially **up to GS_1 at 1200°C**, while in the **high-T_d range** it grows exponentially **from GS_2**. Both **growth laws have close slopes** such as **$\log(GS) \propto \sim 1 \times 10^{-3}\ T_d$**, with an offset at the pore closure stage appearing as a **GS jump $\Delta GS = GS_2 - GS_1$**. We also indicated the corresponding **grain growth factor GF** (grain size over the initial powder's crystallite size, right axis). It can be seen for **T_d < 1200°C** that GF evolves **from 2 to 5**, then **jumps to 10** and increases **up to 20** for **T_d > 1200°C**. Hence, the GS jump from the transition of sintering mechanisms induces the highest growth rate.

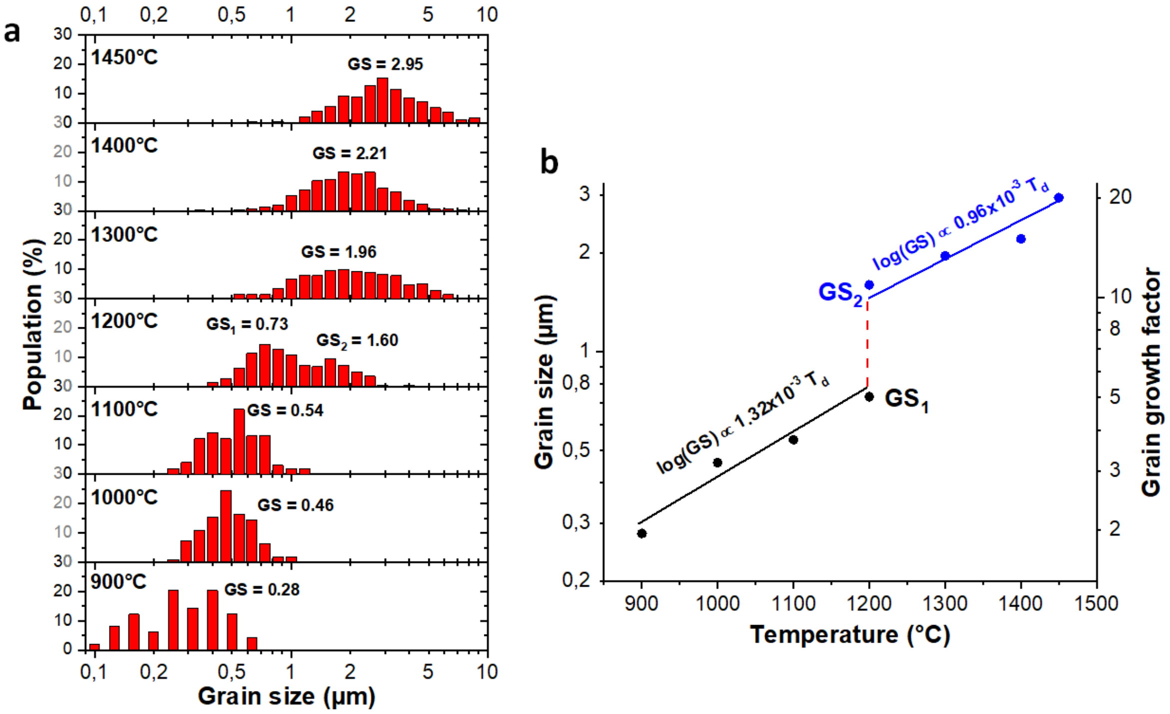

Figure 4.17: a) Histograms of grain size distribution (GSD) of Sasol MAS ceramics SPSed for 20 min at 900, 1000, 1100, 1200, 1300, 1400 and 1450°C and b) modes of GSD plotted as a function of the sintering temperature

The same grain size analysis has been carried out for the short cycle samples and is presented in *Figure 4.18*. **All the GSD are monomodal** (*Figure 4.18.a*) contrarily to what was obtained for the long cycle, while GS is **exponentially T_d-dependent** with this kinetic as well (*Figure 4.18.b*). Furthermore, a GS jump is observed as well for **1450 < T_d < 1500°C**, *i.e.* the temperature range of transition to the final sintering stage (see relative density in *Table 4.5*). Hence, three stages of growth are observed in *Figure 4.18.b*: *i)* a **slow growth** with **$\log(GS) \propto 1.06 \times 10^{-3}\ T_d$** for $T_d \leq$ 1450°C, *ii)* an **abrupt growth** with **$\log(GS) \propto 8.96 \times 10^{-3}\ T_d$** for 1450 $\leq T_d \leq$ 1500°C and finally *iii)* a **second slow growth stage** with **$\log(GS) \propto 2.05 \times 10^{-3}\ T_d$** for $T_d \geq$ 1500°C. The ΔGS jump is even more important in these conditions, as GF passes from 6 to 17.

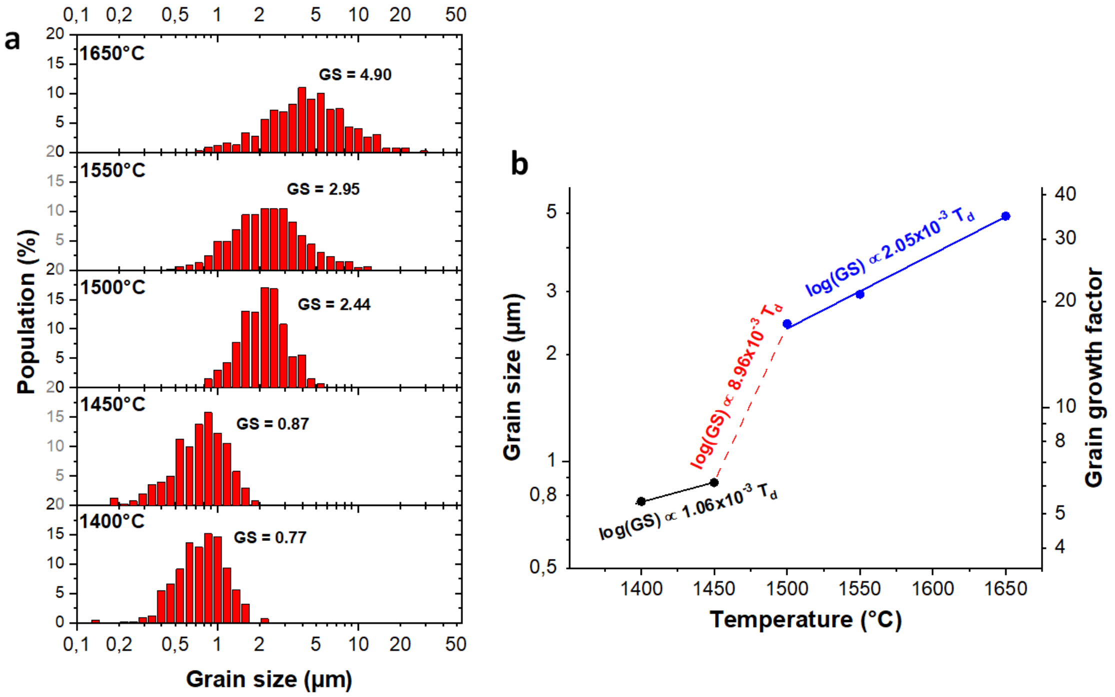

Figure 4.18: a) Histograms of grain size distribution (GSD) of Sasol MAS ceramics SPSed for 3 min at different temperatures between 1400°C and 1650°C and b) modes of GSD plotted as a function of the sintering temperature

Comparing the results obtained for both cycles, it can be seen that **for a same T_d**, the **grain size is sensibly lower for the short cycle** (GS/~3) while **full densification is delayed** to T_d = 1500°C. For both cycles, **three stages of grain growth** are observed; the first and third stages have low growth rates, while the second one near full densification is abrupt. Simpson *et al.* also observed such grain growth behavior in 4 stages with T_d for Cd and Pb [380], the second stage resulting in substantial grain growth. Recently, this sudden coarsening has been reattributed to **abnormal grain growth** leading to bimodal GSD *via* preferential growth of some grains consuming the smaller ones [185]. The fourth growth stage occurs at T_d above our sintering conditions, but the other observations in these studies are in very good agreement with our results.

The transmittance spectra of the ceramics obtained with the long cycle are presented in *Figure 4.19.a*, and $T_{il\text{-}600\ nm}$ is indicated in *Table 4.4*. The **translucent 1200°C sample** has the lowest T_{il} curve, and the **highest transparency** is obtained for **T_d = 1300°C**, *i.e.* the **lowest temperature to reach full densification**. With further increase of T_d, T_{il} decreases due to a **stronger darkening effect** favored by high temperature.

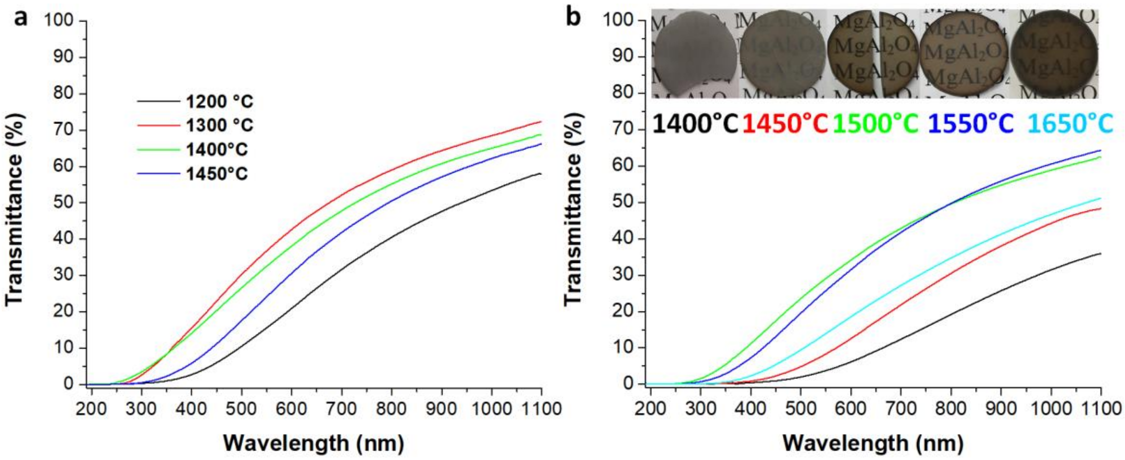

Figure 4.19: Transmittance spectra of Sasol MAS ceramics SPSed a) for 20 min at 1200, 1300, 1400 and 1450°C and b) for 3 min at 1400, 1450, 1500, 1550 and 1650°C; photographs of the materials are provided for b)

The photographs and transmittance spectra of the short cycle ceramics are presented in *Figure 4.19.b*, and $T_{il\text{-}600\ nm}$ is indicated in *Table 4.5*. The observations are similar thet for the long cycle: the **transmittance increases with T_d until full densification** is reached at 1500°C, then decreases back with further increase of T_d. At 1650°C, the stronger darkening effect evidences the thermal activation of its causes.

From the results presented in this section, it appears the **grain size of MAS ceramics increases exponentially with the sintering temperature**; however the **most important grain growth** is observed during an **abnormal grain growth stage** occurring in T_d-range of full densification, independently of the sintering kinetic. Since full densification is required for transparency, T_d should be superior to the temperature of GS jump anyway. Furthermore, ΔGS is proportional to the temperature of its occurence, depending on the kinetic conditions, as the long cycle led to smaller ΔGS and better transparency at 1200°C than the short cycle at 1500°C. Hence, for the **fabrication of transparent fine-grained MAS ceramics**, the kinetic of the sintering cycle should allow **minimizing the sintering temperature**.

ii. Effect of the sintering dwell duration t_d

The **sintering dwell duration t_d effect** was investigated in the range **0-20 min** at 1450°C with α = 100°C/min and P = 80 MPa. The results are summarized in *Table 4.6*.

Table 4.6: Influence of the sintering dwell duration on the properties of Sasol ceramics SPSed at 1450°C, 100°C/min, 80 MPa

Sintering dwell duration (min)	**0**	**3**	**10**	**20**
Relative density (%)	97.5(1)	98.4(1)	99.2(1)	99.1(1)
Grain size mode (µm)	0.67	0.87	1.61	1.85
Transmittance at 600 nm (%)	2.5	12.6	25.5	26.6

The SEM of these materials is presented in *Figure 4.20*. The ceramic prepared **with t_d =0 min** (*Figure 4.20.a*) **did not reach full densification** and many pores of various size and shape are observed. The **3 min dwell** (*Figure 4.20.b*) reduced the porosity to **small spherical pores** with slight increase of the grain size. The **maximum density** is reached for **$t_d \geq$ 10 min**, longer dwells only resulting in further grain coarsening.

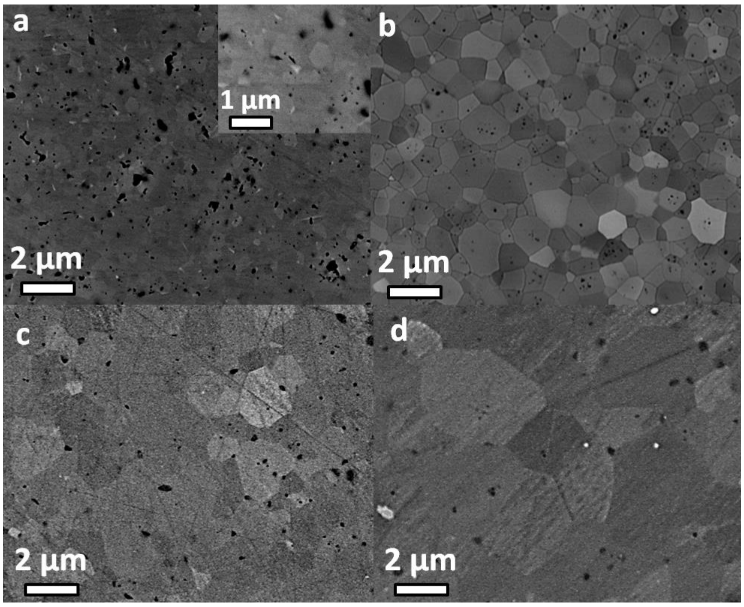

Figure 4.20: SEM micrographs of Sasol MAS ceramics SPSed at 1450°C with soaking time of a) 0, b) 3, c) 10 and d) 20 min

The grain size distributions (GSD) of the ceramics and their analysis are presented in *Figure 4.21*. In the whole range of studied soaking times, the **GSD are monomodal** with similar widths and GS increases exponentially with t_d (*Figure 4.21.a*) with **two stages of growth**: *i)* before full densification for **t_d < 10 min**, a **fast growth** with **$\log(GS) \propto 38.1\text{x}10^{-3}\ t_d$** and *ii)* once d_{max} is reached the **growth rate decreases** to **$\log(GS) \propto 6.04\text{x}10^{-3}\ t_d$**. As for the grain growth behavior with T_d (*Figure 4.17* and *Figure 4*.18), the **growth mode changes in the final sintering stage**, passing from consolidating to densification mechanisms. However, in this case the **second stage of growth has only limited effect**: GS goes from 1.61 to 1.85 µm with a doubled soaking time from 10 to 20 min. It is to believe that for **t_d > critical t_d, no further grain growth** will occur.

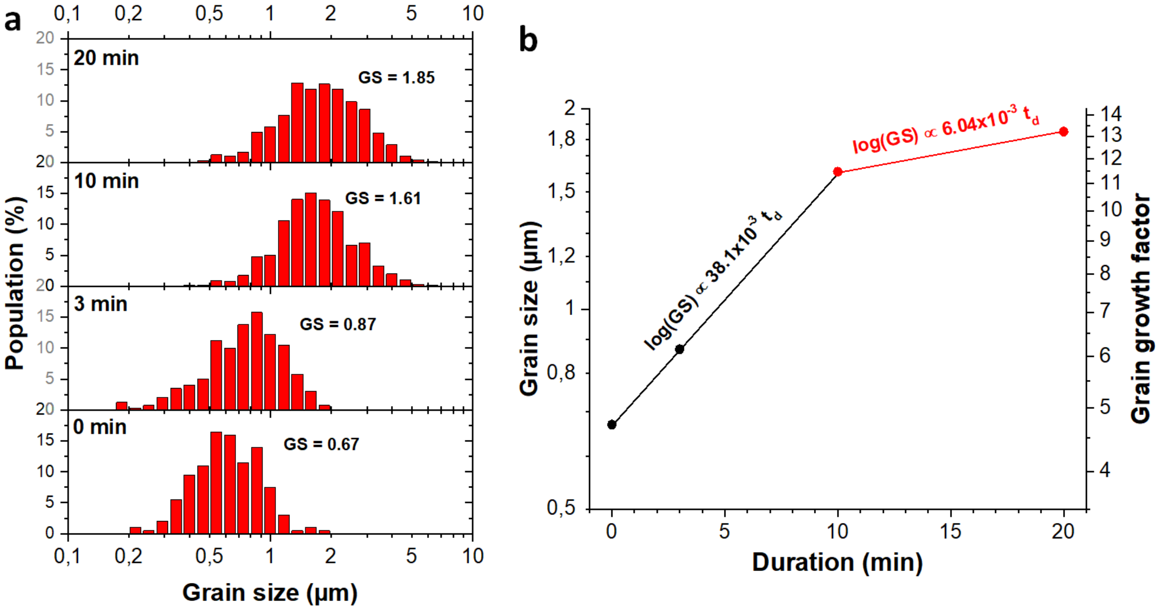

Figure 4.21: a) Histograms of grain size distribution (GSD) of Sasol MAS ceramics SPSed at 1450°C with soaking time of 0, 3, 10 and 20 min and b) modes of GSD plotted as a function of the sintering dwell duration

The photographs and transmittance spectra of the ceramics are presented in *Figure 4.22* and $T_{il\text{-}600\ nm}$ is indicated in *Table 4.6*. In correlation with the materials' density, the **transparency increases greatly until d_{max} is reached** for t_d = 10 min, and only **slightly increases for longer duration**. It is noticed that with T_d = 1450°C, even a 20 min dwell could not provide the transparency level obtained with T_d = 1500°C and t_d = 3 min (*Figure 4.19*), revealing that **temperature is much more impactful than duration** in SPS. In addition, it is remarkable that the darkening is similar for all soaking times, thus it is **not dependent on the duration**.

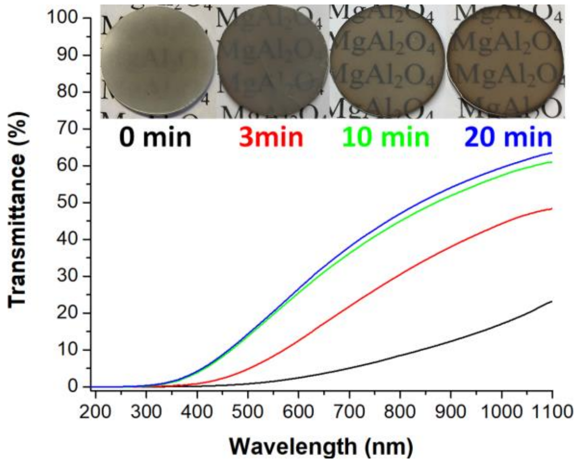

Figure 4.22: Photographs and transmittance spectra of Sasol MAS ceramics SPSed at 1450°C for 0, 3, 10 and 20 min

iii. Effect of the heating rate α

The **effect of the heating rate α** was investigated in the range **10-100°C/min at 1450°C, with both t_d = 3 and 20 min**, and applied pressure of 80 MPa. The results obtained are summarized in *Table 4.7*.

Table 4.7: Influence of the heating rate on properties of ceramics SPSed at 1450°C for 3 and 20 minutes, 80 MPa from raw Sasol

Sintering dwell duration (min)	**3**			**20**	
Heating rate (°C/min)	**100**	**20**	**10**	**100**	**10**
Relative density (%)	98.4(1)	98.8(1)	99.2(1)	99.1(1)	99.8(1)
Grain size mode (µm)	0.87	1.17	1.21	1.85	2.95
Transmittance at 600 nm (%)	12.6	20.9	24.8	26.6	30.6

In a first place, the influence of the heating rate on the densification was evaluated by comparison of the relative displacement of the pistons during SPS (*Figure 4.23*). It can be observed that the **temperature of densification *plateau* is inversely proportional to α**: 1450°C for α = 100°C/min and ~1370°C for α = 20 and 10°C/min. The difference is very important from high to medium heating rate, then negligeable up to low rates, and thus **medium/low α** allows **reducing T_d required for full densification by almost 100°C**.

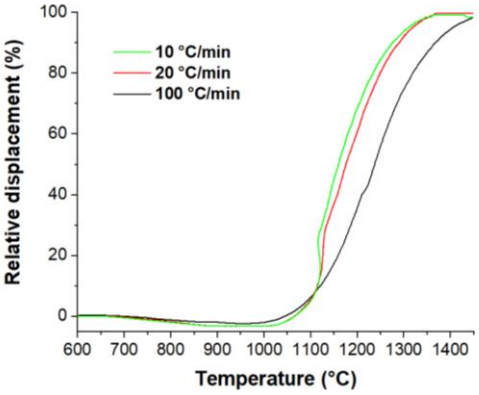

Figure 4.23: Relative displacement of the SPS pistons during sintering of Sasol powder with heating rate of 100, 20 and 10°C/min

The SEM of the **t_d = 3 min** samples is presented in *Figure 4.24*. It is observed that **decreasing α reduces the porosity** and **increase the grain size.** This is because lower heating rates induce longer heating times (*e.g.* the heat up from 1150 to 1450°C with α = 100, 20 and 10°C/min is carried out in 3, 15 and 30 min, resp.), so the **sintering kinetics is impacted**. Similar results were obtained for the t_d = 20 min samples.

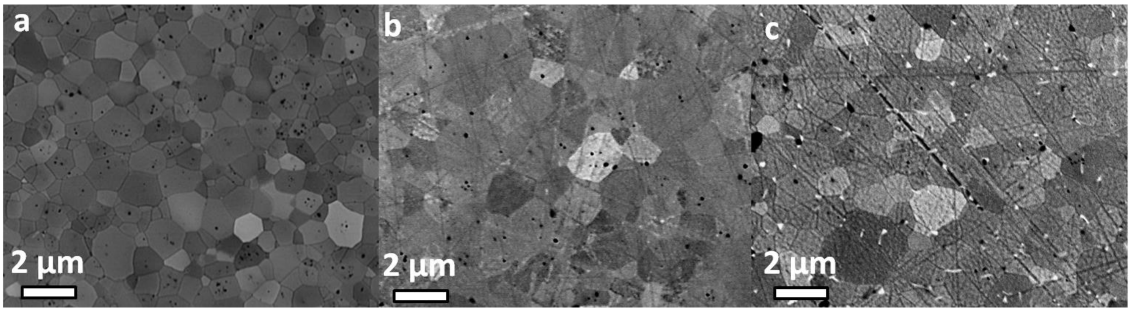

Figure 4.24: SEM of Sasol MAS ceramics SPSed at 1450°C for 3 min with heating rate of a) 100, b) 20 and c) 10°C/min

The grain size evolution with the heating rate is presented in *Figure 4.25*. **GS decreases exponentially with α**, with **log(GS) ∝ 1.60x10^{-3} α** for t_d = 3 min and **log(GS) ∝ 2.25x10^{-3} α** for t_d = 20 min. The growth rate seems greater for longer sintering, but the lack of experimental points prevents certainty. In comparison, Morita *et al.* found the same effect of α on the porosity but no effect on GS, for SPS of MAS at 1300°C for 20 min, 80 MPa [219]. This discrepancy can be due to the different sintering temperatures in the two studies, which could induce differing sintering mechanisms and kinetics. In the other hand, it is known that high heating rates hinder grain growth and favor porosity for short dwell durations [216].

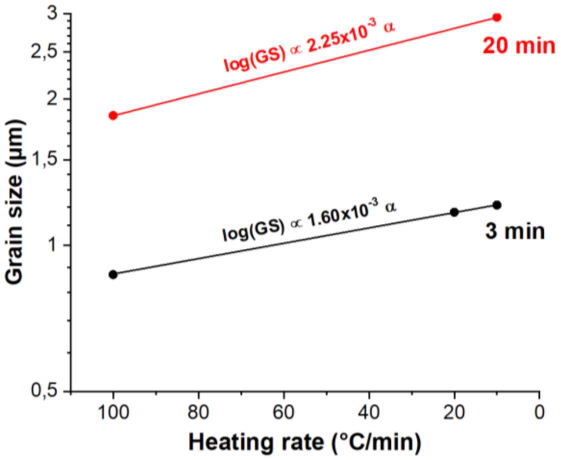

Figure 4.25: GSD modes of Sasol MAS ceramics SPSed at 1450°C for 3 and 20 min plotted as a function of the heating rate

The photographs and transmittance spectra of these ceramics are presented in *Figure 4.26* and $T_{il\text{-}600\ nm}$ is indicated in *Table 4.7*. The **transparency improves with decreasing heating rate**, especially when a short dwell is applied. Indeed, as observed in SEM, higher heating rates induces more remaining porosity, leading to translucency for the 3 min dwell. The effect is less pronounced with a 20 min dwell because it favors the densification. It can be seen that the transmittance curves obtained for the materials sintered with α = 100°C/min and t_d = 20 min and α = 10°C/min and t_d = 3 min are almost identical, as the same level of density *d* ~99.1(1)% is reached. However, the latter sintering conditions allow a substantial diminution of the grain size from 1.85 to 1.21 µm. In addition, it appears from these results that **the heating rate has no effect on the darkening effect**, while Morita *et al.* reported an increase of discoloration with high heating rate [50].

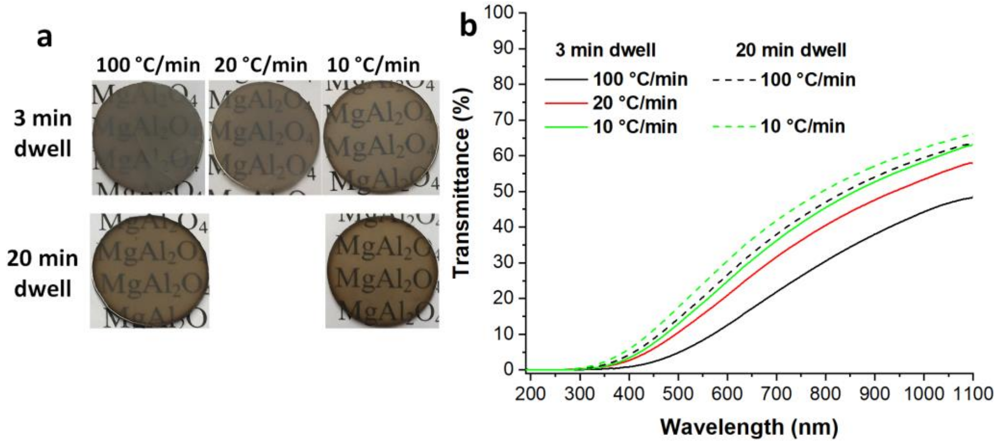

Figure 4.26: a) Photographs and b) transmittance spectra of Sasol MAS ceramics SPSed at 1450°C for 3 and 20 min with heating rate of 100, 20 and 10°C/min

iv. Effect of the applied pressure P

We investigated the effect of the applied pressure on the sintering of the Sasol powder and the properties of the resulting ceramics in the range of low to medium pressure 80 MPa ≤ P ≤ 230 MPa at 1450°C and 1350°C for 280 MPa, with t_d = 3 min and α = 100°C/min. The results obtained are summarized in *Table 4.8*.

Table 4.8: Influence of the applied pressure on properties of Sasol ceramics SPSed at 1450°C for 3 min, 100°C/min

Sintering temperature (°C)	**1450**				**1350**
Applied pressure (MPa)	**80**	**130**	**180**	**230**	**280**
Relative density (%)	98.4(1)	99.92(4)	99.85(5)	100.0(1)	99.9(1)
Grain size mode (µm)	0.87	1.70	0.90	0.84	0.46
Transmittance at 600 nm (%)	12.6	47.9	50.6	53.7	38.5

The influence of the applied pressure on the densification is evaluated by the displacement of the pistons during SPS in *Figure 4.27*. The compaction stage at 600°C (increase of the pressure up to P) is not shown, as we focus on the effect of P on the thermal densification. It is observed that **higher pressures decrease the temperature of densification *plateau*** from 1450°C for 80 MPa to 1350°C for 230 MPa. Therefore, for the higher P = 280 MPa, SPS was carried out at 1350°C, as the graphite composite die could not hold 1450°C.

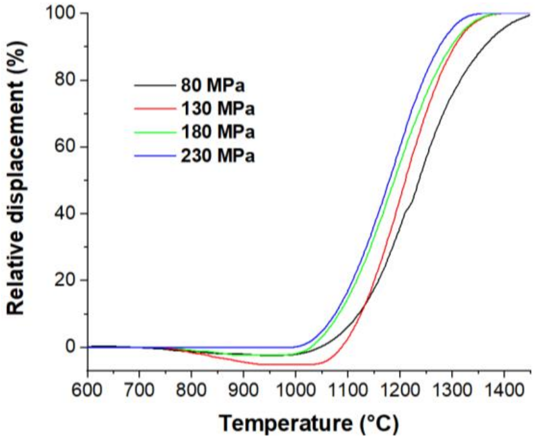

Figure 4.27: Relative displacement of the SPS pistons during sintering of Sasol with applied pressure of 80, 130, 180 and 230 MPa

The SEM of the ceramics prepared with different P is presented in *Figure 4.28*. It can be observed that the **pore concentration is greatly reduced** for P ≥ 130 MPa. For the same T_d = 1450°C, the **grain size seems unaffected by P**, except for the 130 MPa sample which exhibits coarser grain size. For P = 280 MPa and T_d = 1350°C (*Figure 4.28.e*), **the grain size is much finer**, with a somehow higher pore concentration.

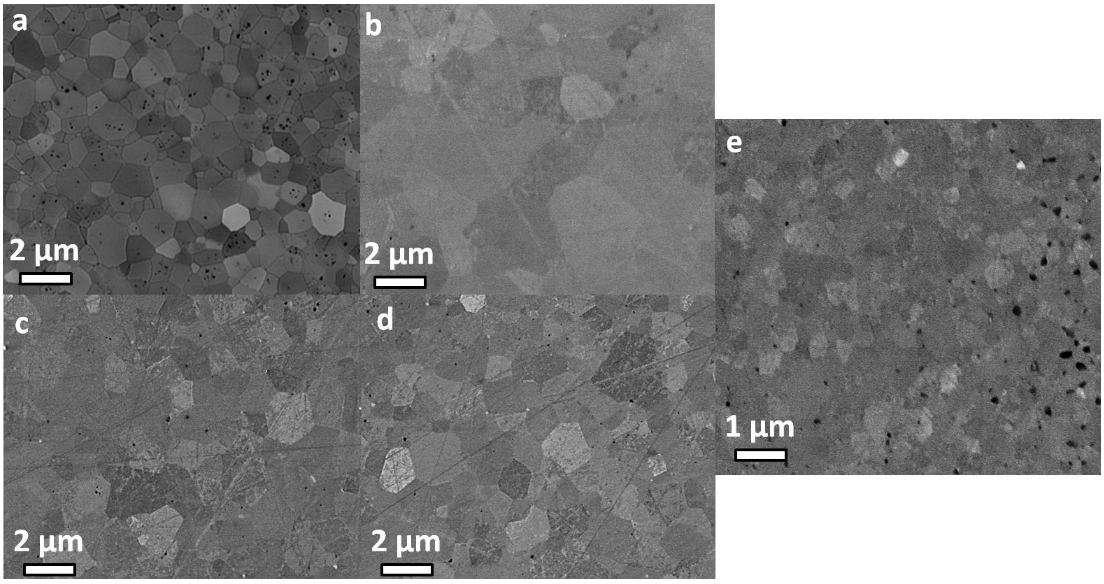

Figure 4.28: SEM of Sasol MAS ceramics SPSed at 1450°C with applied pressure of a) 80, b) 130, c) 180 and d) 230 MPa, and e) at 1350°C with applied pressure of 280 MPa

The grain size distributions of the materials are presented in *Figure 4.29*. The **monomodal GSD** for 80, 180 and 230 MPa are **very close**. However, the 130 MPa sample presents higher GS, which we attribute to an unidentified failure during SPS; for this reason, it will not be considered for the discussion on pressure effect. The **P = 280 MPa and T_d = 1350°C** sample has the **finest GSD**, with a **mode two times smaller at GS = 0.46 µm**. Therefore, it is clear that the **grain size is dependent on T_d** rather than on P. Since the T_d required for full densification depends on P (*Figure 4.27*), the microstructure depends on the couple P-T_d.

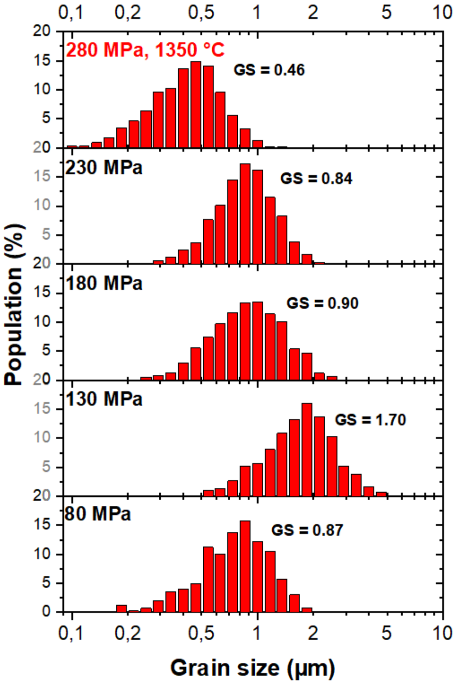

Figure 4.29: Histograms of grain size distribution (GSD) of Sasol MAS ceramics SPSed at 1450°C with applied pressure of 80, 130, 180 and 230 MPa and at 1350°C with applied pressure of 280 MPa

The photographs and transmittance spectra of the ceramics are presented in *Figure 4.30* with $T_{il\text{-}600\ nm}$ in *Table 4.8*. For the samples SPSed at T_d = 1450°C, the **transparency is greatly improved** for P ≥ 130 MPa, *i.e.* for fully dense ceramics, while no sensible effect is noted once full densify is reached. The transparency of the sample SPSed with **P = 280 MPa at T_d = 1350°C** is **reduced** due to the remaining porosity. However, a longer soaking time t_d should greatly improve the transparency in these P-T_d conditions.

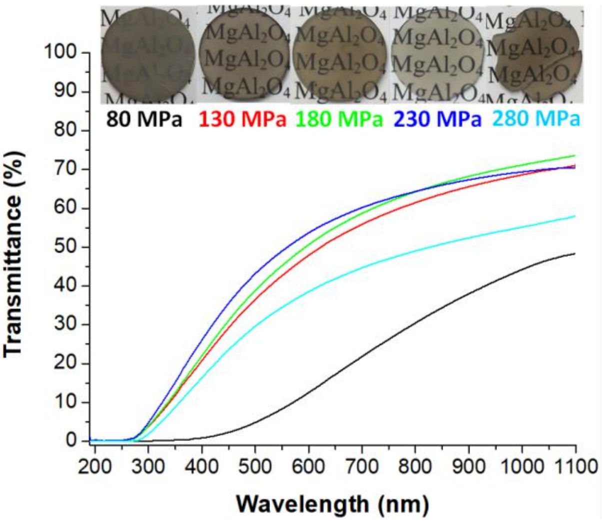

Figure 4.30: Photographs and transmittance spectra of Sasol MAS ceramics SPSed at 1450°C with applied pressure of 80, 130, 180 and 230 MPa and at 1350°C with applied pressure of 280 MPa

v. Investigation of the microstructural defects specific to Sasol ceramics

Despite the parametric study performed above and optimization of the sintering conditions, the optical transparency reached for ceramics prepared from the raw Sasol powder **could not meet the state of the art**. For example, the widely used S30CR nanopowder SPSed at T_d = 1300°C and P = 100 MPa results in high transparency with $T_{il\text{-}600\ nm}$ = ~70% after thickness correction [224], while we reached $T_{il\text{-}600\ nm}$ = ~53.7% for T_d = 1450°C and P = 230 MPa. We assume that this **limited transparency is specific to the Sasol powder**. For this reason, this section is dedicated to the investigation of the **microstructural defects found in Sasol ceramics.** The structural defects (vacancies, impurities…) will be investigated in *Chapter 5*.

Figure 4.31 presents the EBSD study carried out on a large area of a Sasol ceramic SPSed at 1450°C for 3 min with α = 100°C/min and P = 80 MPa. The image quality (IQ) map (*Figure 4.31.a*) reveals a **homogeneous level of crystallinity**, as the only dark parts are the pores. The inverse pole figure (IPF) map (*Figure 4.31.b*) shows **no preferential crystal orientation**, as the orientations are randomly distributed.

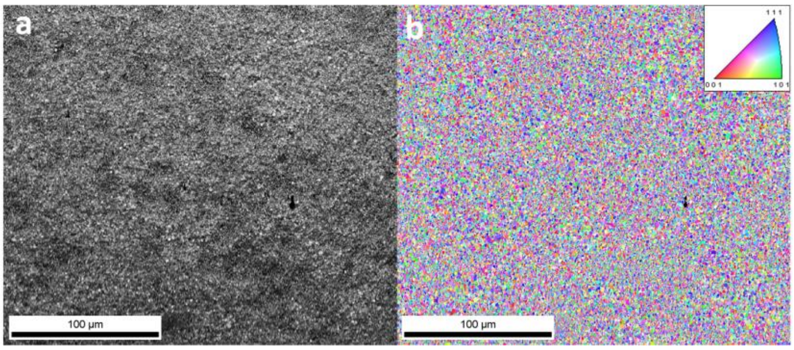

Figure 4.31: EBSD a) image quality (IQ) and b) inverse pole figure (IPF) maps of Sasol MAS ceramic SPSed at 1450°C, 3 min with α = 100°C/min and P = 80 MPa

We investigated the microstructure radial homogeneity for several sintering conditions. The SEM of ceramics SPSed with T_d = 1500°C, t_d = 3 min, α = 100°C, P = 80 MPa and T_d = 1450°C, t_d = 3 min, α = 100°C, P = 230 MPa is presented in *Figure 4.32*. Regardless of the sintering conditions, the **microstructure seems equivalent from the edge to the center positions**, and the deviation of GS observed (GSD not presented) between the regions is attributed to statistical deviation.

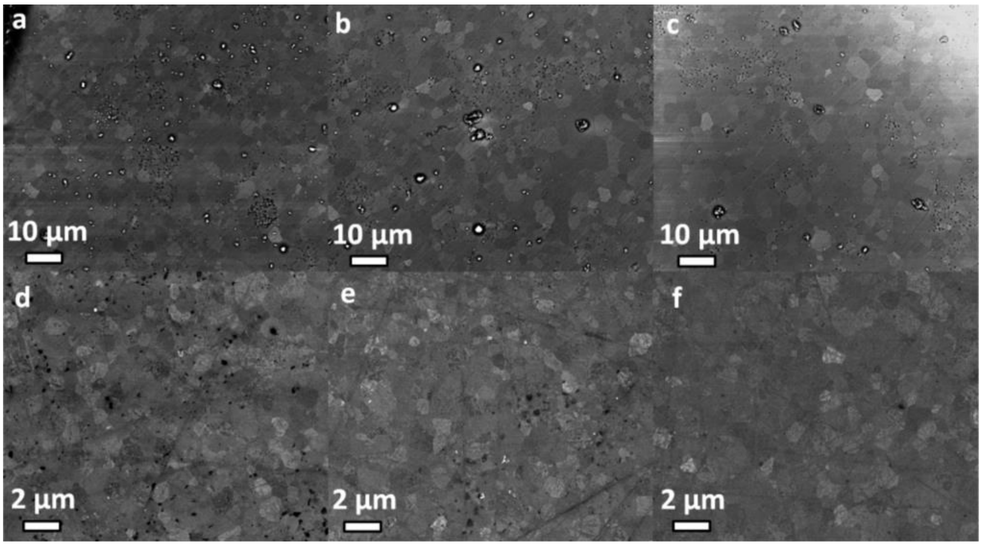

Figure 4.32: SEM of Sasol MAS ceramics SPSed with a-c) T_d = 1500°C, t_d = 3 min, α = 100°C, P = 80 MPa and d-f) T_d = 1450°C, t_d = 3 min, α = 100°C, P = 230 MPa from a,d) edge, b,e) midpoint and c,f) center regions of the samples

The SEM analyses carried out on Sasol ceramics revealed **several types of microstructural defects**. The **most typical one** (in all Sasol samples) is presented in *Figure 4.33* and *Figure 4*.34. It appears on SEM in BSE mode as **submicronic dark grains** both in clusters of size up to ~100 nm and dispersed within the MAS grains matrix (*Figure 4.33.a* and *b*, resp.). The topographic contrast in SE mode (*Figure 4.33.c2*) rules out the presence of pores and indicates **a second phase**, identified by EDX elemental mapping (*Figure 4.34*) as the **~3 wt% free MgO periclase** observed by XRD in the Sasol powder (*Figure 2.2*) and after SPS (*Figure 4.14*). It is a **defect in high concentration**, degrading the transparency due to the difference of refractive index between MAS and MgO. In addition, the difference of thermal expansion coefficients induces **cracks** during SPS cooling stage (*Figure 4.33.a*, *c1* and *c2*), further degrading the materials.

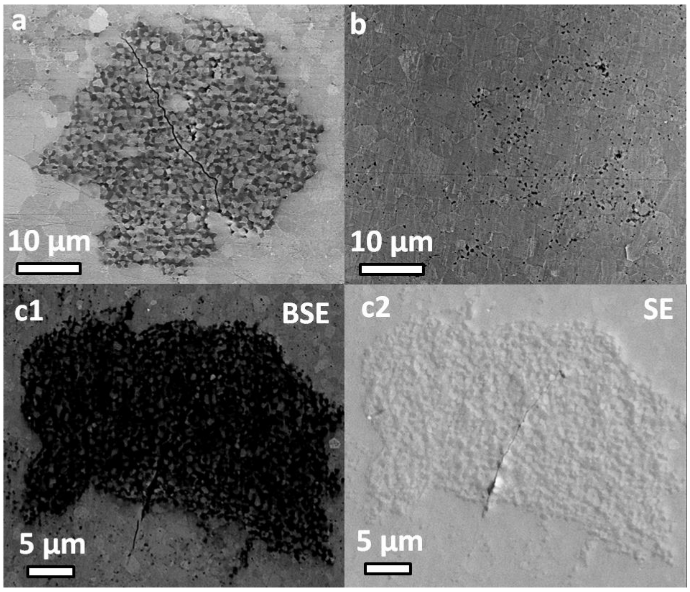

Figure 4.33: SEM of the most typical microstructural defect observed in Sasol MAS ceramics appearing a) in cluster and b) dispersed within the MAS grains matrix; c1) chemical (BSE) and c2) topographic (SE) contrasts of a cluster

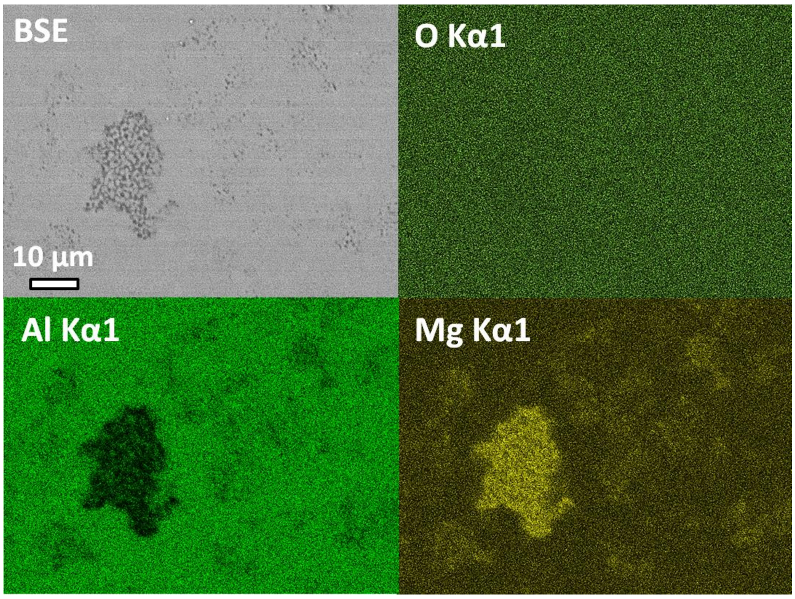

Figure 4.34: SEM and EDX elemental mapping of the most typical microstructural defect observed in Sasol MAS ceramics

Another type of defect detrimental to transparency was observed occasionally and is presented in *Figure 4.35*. These **large defects** with diameter up to over 200 µm were detected by naked eye, as they induce **opaque spots** in the transparent MAS matrix. SEM reveals a **three-dimensional interpenetrating network**

microstructure organized in cells of 5-10 µm in diameter (*Figure 4.35.a*). Their core consist in **mixed nanometric white and black grains** of different compositions (chemical contrast) and the shell is a ~0.5-1 µm thick **layer of "white phase"** (see inset). The topographic contrast (*Figure 4.35.b1* and *b2*) excludes the involving of pores. This microstructure is **typical of binary eutectics**, and was notably observed for $MgAl_2O_4$-MgO eutectic crystals [28, 381]. However, in our case, the EDX elemental mapping in *Figure 4.35.c1-c3* reveals an **Al_2O_3-rich composition**, assumed to be **Al_2O_3-$MgAl_2O_4$ eutectic**.

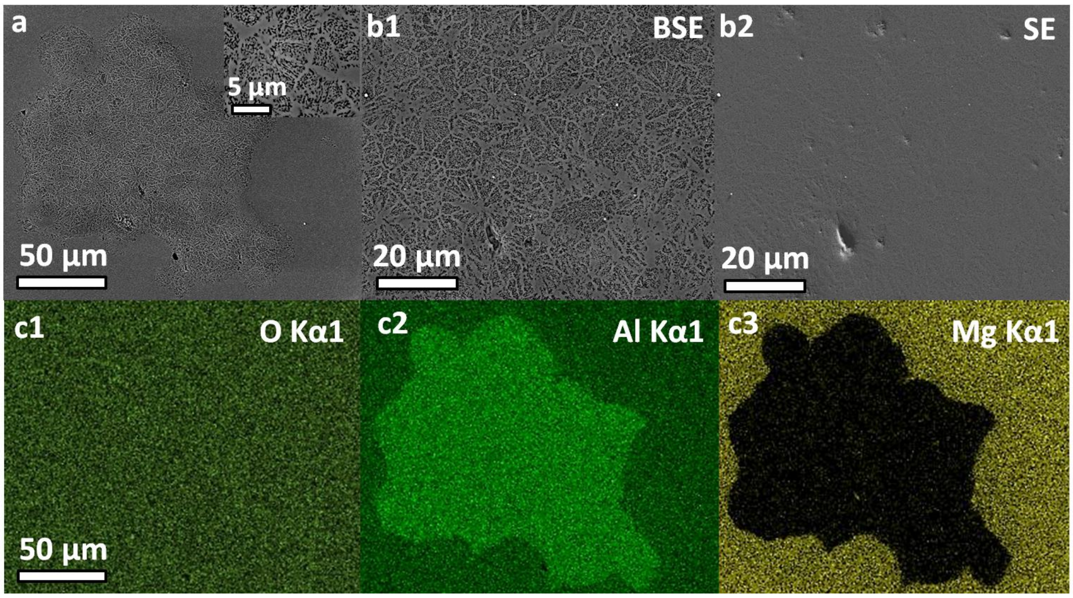

Figure 4.35: a) SEM of an opacifying defect observed in Sasol ceramics, with b1) chemical (BSE) and b2) topographic (SE) contrasts and c1-c3) EDX elemental mapping

Figure 4.36 presents **less recurring defects** in Sasol ceramics, which do not induce local opacification as Al_2O_3-$MgAl_2O_4$ clusters and are less evidently linked to the degradation of transparency than the highly concentrated MgO-type defects. *Figure 4.36.a* and *b* show respectively a **cluster of very big 10-50 µm MAS grains** and a **cluster of very small 0.3-1 µm MAS grains** within a matrix of ~3 µm grains.

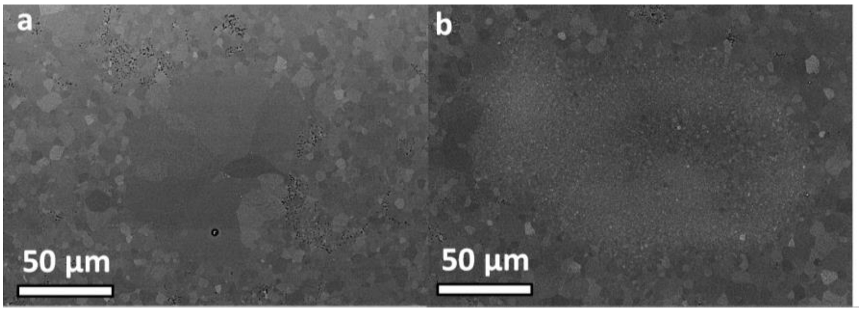

Figure 4.36: SEM of typical local inhomogeneity of grain size observed in Sasol MAS ceramics with a) cluster of very big grains and b) cluster of very small grains in normally-sized grain matrix

Therefore, it appears that both **free MgO and Al_2O_3 phases** are present in the raw Sasol powder, in respectively high and low contents. As both phases appear in large clusters after SPS, it is assumed that they already form **agglomerates** in the powder; MgO is also observed as dispersed grains, thus it is also in part **mixed within the MAS aggregates**. Thus, these defects highly detrimental to transparency **arise directly from the Sasol powder**. On the other hand, the clusters of abnormally-sized MAS grains observed in *Figure 4.36* do not arise with certainty from the powder, as they could arise from the sintering process as well.

Finally, we investigated **the effect of pressing** on the microstructure. The *Figure 4.37* shows a typical micrograph of the cross section (parallel to pressing direction) of a Sasol ceramic SPSed with P = 80 MPa. No effect of pressing is noted on the grains, as they appear isotropic in size and shape as for the radial section (perpendicular to pressing direction). However, a **strong effect is observed on the defects**, evidenced on dispersed (area A) and clustered (areas B, C and D) MgO grains. The grains are **organized perpendicularly to the pressing direction**, forming parallel lines with length up to 50 µm. The clusters are **flattened in the pressing direction** with a ratio length/thickness of ~3. This anisotropy can be extended to all defects **including porosity**, and is clearly **due to the uniaxial pressing** during SPS processing.

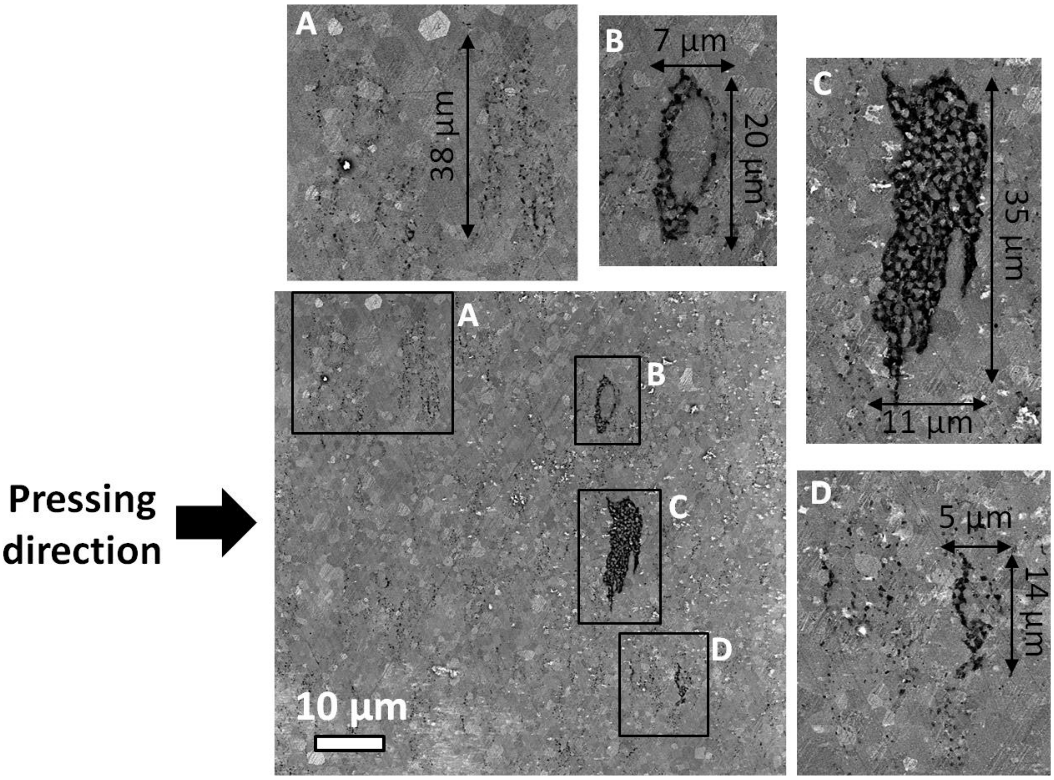

Figure 4.37: Typical SEM micrograph of the cross section of a Sasol MAS ceramic sintered with P = 80 MPa evidencing the effect of pressing with magnification on areas of most prominent defects

2. Spark plasma sintering study of S25CR-3MS powder

Based on the previous section on SPS of raw Sasol powder, we opted for a **limited parametric study of S25CR-3MS precursor**, in the range close to **full densification**. Hence, very high relative densities are reached and their values will not be presented as the uncertainty is higher than the noted differences. **The reference sintering conditions** have been set as **T_d = 1375°C, α = 10°C/min, t_d = 20 min and P = 80 MPa**.

i. Effect of the sintering dwell temperature T_d

The **effect of the sintering temperature T_d** was investigated in the range **$1225 \leq T_d \leq 1375$°C**. The results are summarized in *Table 4.9*.

Table 4.9: Influence of the sintering temperature on properties of S25CR-3MS ceramics SPSed with 10°C/min, 20 min, 80 MPa

Sintering temperature (°C)	**1225**	**1275**	**1325**	**1375**
Grain size mode (nm)	210	310	480	870
Transmittance at 600 nm (%)	62.6	78.8	73.9	69.0

The XRD patterns of the prepared S25CR ceramics are presented in *Figure 4.38*. As for ceramics fabricated from Sasol powder, n**o sensible evolution** from the initial pattern of S25CR-3MS powder is observed through SPS with increasing temperature. Similar observations were made for the XRD evolution for all studied parameters, so they will not be presented in other sections to avoid redundancy.

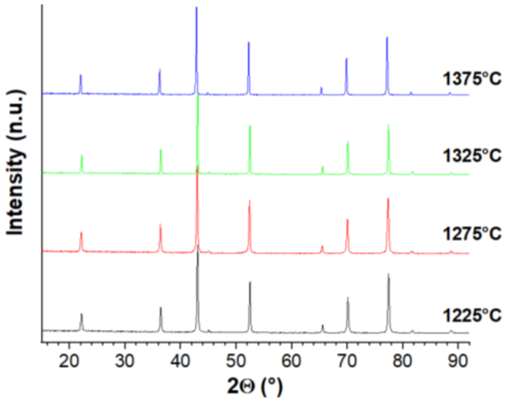

Figure 4.38: XRD patterns of S25CR-3MS MAS ceramics SPSed at 1225, 1275, 1325 and 1375°C for 20 min

The SEM of these materials is presented in *Figure 4.39*. It is observed that the increase of temperature T_d results in a **substantial increase of the grain size**, while the low porosity for T_d = 1225°C **further decreases** until no pores are detected for T_d = 1375°C (*Figure 4.39.d*). For **T_d = 1225°C** (*Figure 4.39.a*), the inset shows the **highly porous edge** of the material. This heterogeneous densification is mainly attributed to **radial gradients of temperature** as it has been shown that the temperature can be inferior by ~60°C in the periphery of the material [382, 383]. In addition, **gradients of stress** are also noted locally at the powder/die interface due to frictions [384]. For T_d > 1225°C, the edge and center microstructure are homogeneous.

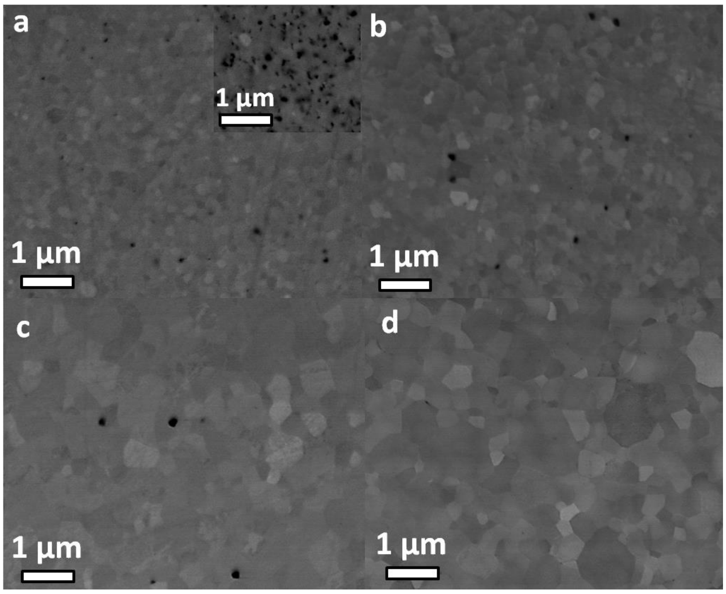

Figure 4.39: SEM of S25CR-3MS ceramics SPSed at a) 1225, b) 1275, c) 1325 and d) 1375°C; inset shows the ceramic's periphery

The grain size distributions (GSD) of the ceramics are presented in *Figure 4.40.a*. They are **monomodal log-normal distributions**. The mode GS is plotted vs T_d in *Figure 4.40.b*. As for Sasol, **GS increases exponentially** from 210 to 870 nm from 1225 to 1375°C with **growth law log(GS) ∝ ~4.16×10^{-3} T_d**. We notice that the grain growth factor is GF = 4.4 for $T_{d.min}$ = 1275°C, *i.e.* the lowest T_d for homogeneous sintering, which is **significantly lower than GF = 14 observed for Sasol** SPSed at $T_{d.min}$ = 1300°C.

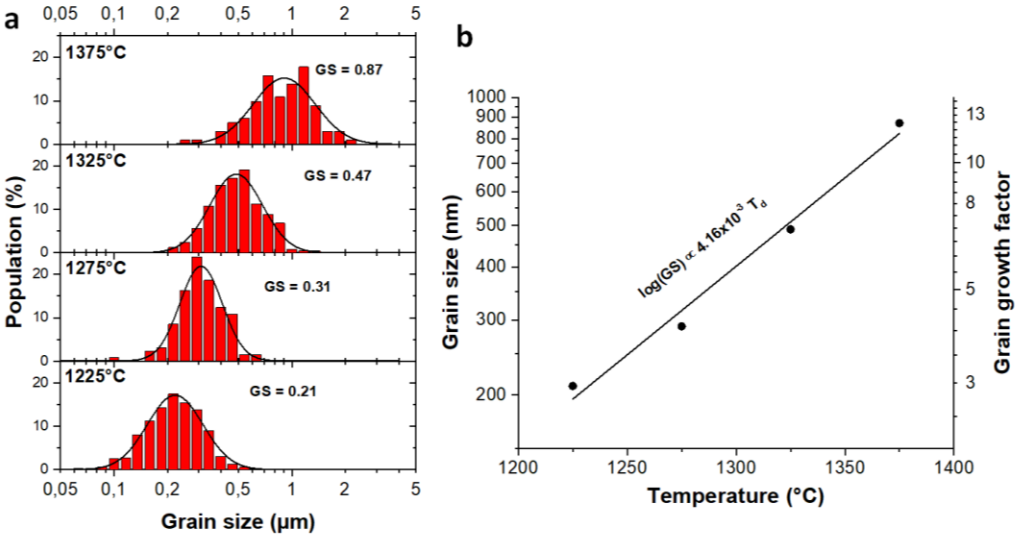

Figure 4.40: a) Histograms of grain size distribution (GSD) of S25CR-3MS MAS ceramics SPSed at 1225, 1275, 1325 and 1375°C and b) modes of GSD plotted as a function of the sintering temperature

The photographs and transmittance spectra of the ceramics are presented in *Figure 4.41* with $T_{il\text{-}600\ nm}$ in *Table 4.9*. We note that the materials are **less colored than Sasol ceramics**. The **1225°C** sample **is opaque in its periphery** due to the high local porosity. The **highest transparency of ~80%** is obtained for **the minimal T_d for full densification** $T_{d.min}$ = 1275°C, while the **transparency decreases back for $T_d \geq T_{d.min}$.**

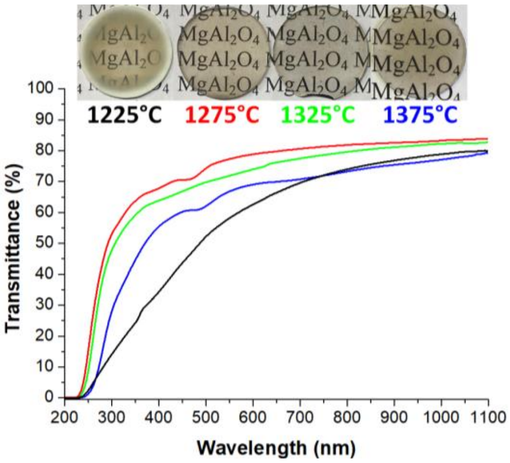

Figure 4.41: Photographs and transmittance spectra of S25CR-3MS MAS ceramics SPSed at 1225, 1275, 1325 and 1375°C

ii. Effect of the sintering dwell duration t_d

The **effect of the sintering dwell duration t_d** was investigated in the range **3-20 min** at both 1275 and 1375°C, in order to reveal the temperature-duration dependence. The results are summarized in *Table 4.10*.

Table 4.10: Influence of the dwell duration on properties of S25CR-3MS ceramics SPSed at 1275 and 1375°C, 10°C/min, 80 MPa

Sintering temperature (°C)	**1275**			**1375**		
Sintering dwell duration (min)	**3**	**10**	**20**	**3**	**10**	**20**
Grain size mode (µm)	0.22	0.28	0.31	0.52	0.79	0.87
Transmittance at 600 nm (%)	76.1	78.1	78.8	73.3	75.2	69.0

The SEM of these materials is presented in *Figure 4.42*. For both T_d = 1275°C (*Figure 4.42.a-c*) and 1375°C (*Figure 4.42.d-f*), it can clearly be seen that **the grain size slightly increases with longer sintering duration**, while the porosity does not seem to be greatly affected.

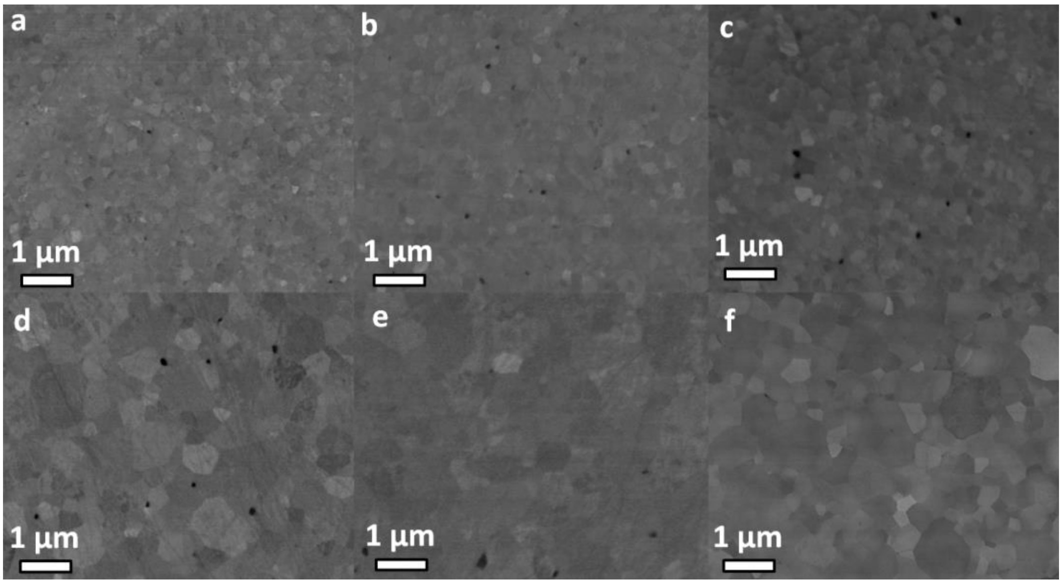

Figure 4.42: SEM of S25CR-3MS MAS ceramics SPSed at a-c) 1275 and d-f) 1375°C for a,d) 3, b,e) 10 and c,f) 20 min

The analysis of the grain size distributions of the ceramics is presented in *Figure 4.43*. All the GSD are **monomodal** and the **GSD mode increases with t_d**. A similar growth behavior is observed for both T_d (*Figure 4.43.c*); GS increases exponentially with **two stages of growth**, with a **turning point at t_d = 10 min**. For **$t_d \leq$ 10 min**, the growth is fast with **log(GS) $\propto$ 15.0x10^{-3} t_d** and **25.9x10^{-3} t_d** for T_d = 1275 and 1375°C, respectively. For **$t_d \geq$ 10 min**, the growth rate decreases to **log(GS) $\propto$ ~4.30x10^{-3} t_d** for both T_d. However, these growth laws should be considered with cautiousness due to lack of experimental points.

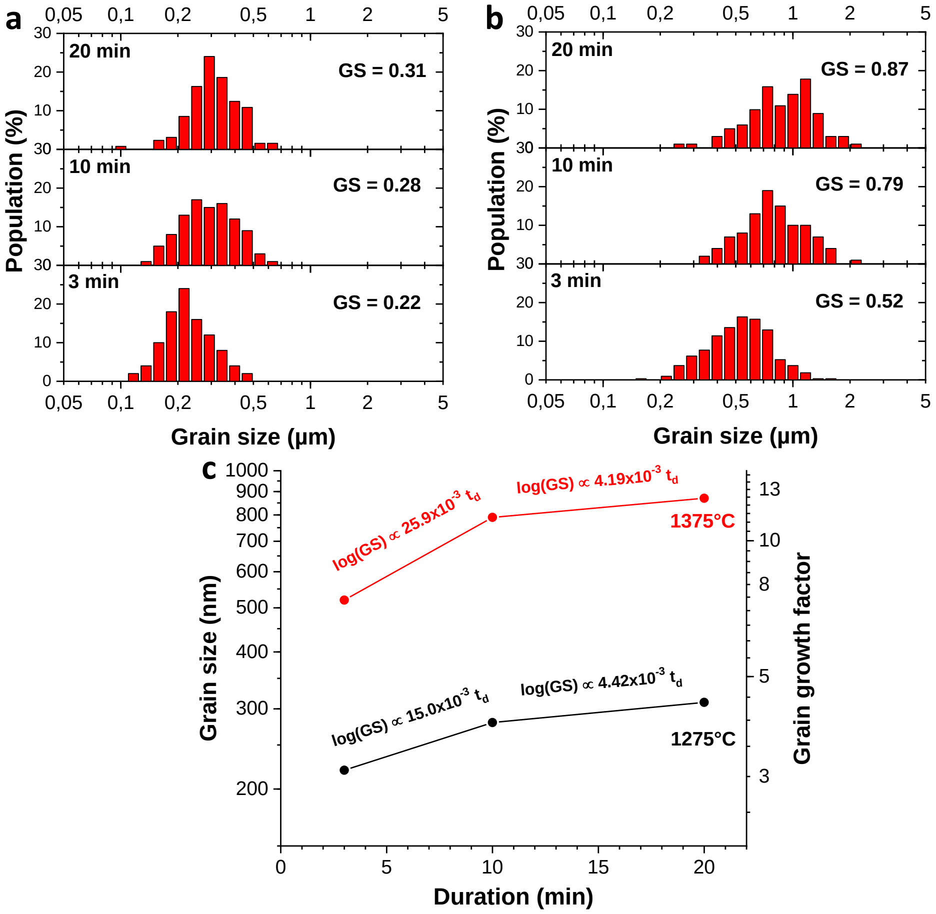

Figure 4.43: Histograms of grain size distribution of S25CR-3MS MAS ceramics SPSed at a) 1275 and b) 1375°C for 3, 10 and 20 min, and c) modes of GSD plotted as a function of the sintering dwell duration

The photographs and transmittance spectra of the ceramics are presented in *Figure 4.44* with $T_{il\text{-}600\ nm}$ in *Table 4.10*. The photographs of the materials SPSed at 1225°C (*Figure 4.44.a*, 1st row) evidences that the **sintering begins in the center** of the sample then **propagates toward the edges**, as the opaque ring width decreases with longer processing. For **T_d = 1275°C** (2nd row), a 3 min dwell is not enough for the material's edge to be densified, but $t_d \geq$ **10 min** leads to homogeneous ceramics, while **T_d = 1375°C** provides dense and transparent samples for **$t_d \geq$ 3 min**. The evolution of the transmittance curves is different depending on T_d (*Figure 4.44.b*). For T_d = 1275°C, **T_{il} slightly increases in the low λ-range < 500 nm** up to t_d = 10 min, then no more significant effect is noted. For T_d = 1375°C, the transparency decreases for t_d > 10 min.

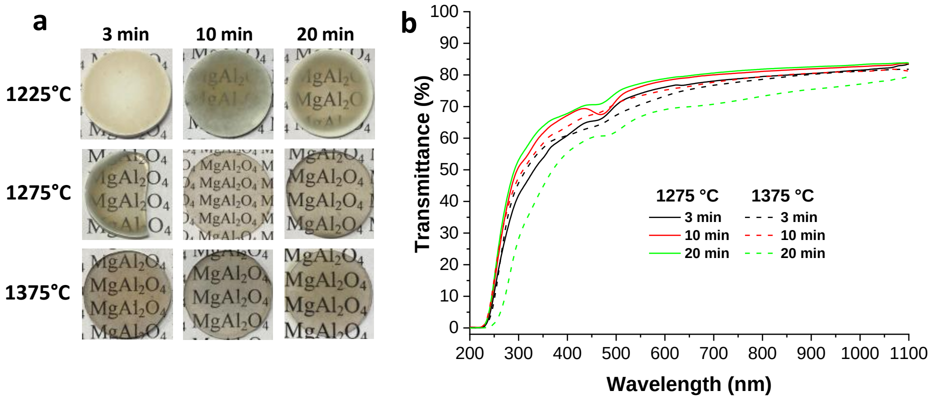

Figure 4.44: a) Photographs and b) transmittance spectra of S25CR-3MS ceramics SPSed at 1225 ≤ T_d ≤ 1375°C for 3 to 20 min

These results show that **the temperature effect is much more important than duration in SPS**, and particularly for the microstructure. Hence, finer microstructures and better transparencies are obtained for **sintering at lower temperatures with long dwells** (GS = 310 nm and T_{il} = 78.8% for 1275°C, 20 min) than at higher temperature with short dwells (GS = 520 nm and T_{il} = 73.3% for 1375°C, 3 min).

iii. Effect of the heating rate α

The **effect of the heating rate α** was investigated in the range **10-100°C/min** for **T_d = 1225 and 1375°C** with a **duration of 20 min**. In addition, some experiments were carried out with a sintering dwell of 3 min, in order to investigate further the mechanisms by which occurs the darkening phenomenon.

The photographs of the ceramics are shown in *Figure 4.45*. In *Figure 4.45.a*, for **α ≥ 50°C/min**, a **slight darkening** is noted for the **1225°C samples** (1st row), while the **1375°C samples** (2nd row) exhibit **very dark centers with transparent edges**. The **3 min-samples** have **less marked crowning effects** (*Figure 4.45.b*, 1st row). At **1450°C** (2nd row), the ceramic is **fully opaque**. Therefore, it appears the **darkening phenomenon** is directly related to the **sintering temperature**, while it is **promoted by high heating rates**.

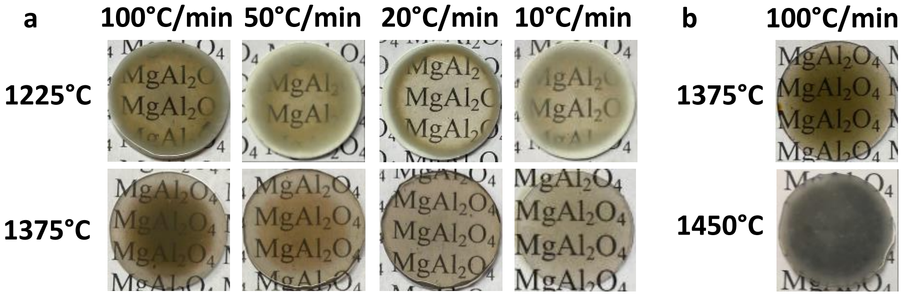

Figure 4.45: Photographs of S25CR-3MS ceramics SPSed a) at 1225 and 1375°C for 20 min with 10 ≤ α ≤ 100°C/min, and b) at 1375 and 1450°C for 3 min with heating rate of 100°C/min

The darkening has been investigated for the samples SPSed at 1375°C, 20 min by Raman spectroscopy (*Figure 4.46*). From comparison with the spectrum of the insulating graphite paper (Papyex®) used in SPS, it is clear that the **darkening arises from carbon contamination**. If it is unclear if the 10°C/min sample exhibits the graphite signature, for **α ≥ 20°C/min** the D- and G-bands at 1360 and 1580 cm^{-1} are increasingly strong up to 100°C/min. The **very low C contamination in the edges** is also confirmed. Similar results were obtained by Talimian *et al.* [222], who attributed the distribution of carbon content to the formation of **hot zones in the center** of the sintered compacts inducing reactions between graphite and spinel. **Carbonaceous volatile gasses** produced by the reactions are then **entrapped within closing pores** in the final sintering stage, to finally **precipitate** as disordered carbon due to the increase of pressure during the pores shrinkage. In addition, Raman modes of **inverted spinel** appear **together with C contamination**, the latter favoring the formation of defects through the reactions with graphite. Two unassigned modes at 460 and 913 cm^{-1} also appear in highly contaminated area, and are assumed to arise from defects in the altered MAS as well.

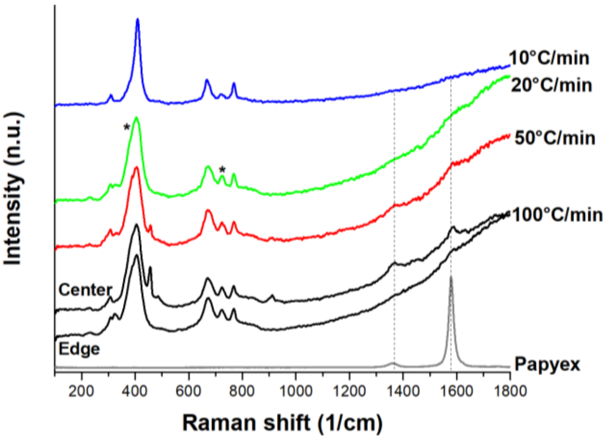

*Figure 4.46: Raman spectra of S25CR-3MS ceramics SPSed at 1375°C for 20 min with heating rates of 10, 20, 50 and 100°C/min, and spectrum of the insulating graphite paper Papyex. The spinel modes marked by * arise from antisite defects*

The transmittance spectra of these samples are presented in *Figure 4.47*. Indeed, the **transparency increases with lower heating rates**, $T_{il\text{-}600\ nm}$ being 14.5%, 50.0%, 62.5% and 69.0% for respectively 100, 50, 20 and 10°C/min. The sensible improvement from 20 to 10°C/min confirms slight contamination in the former case. Hence, to avoid transparency degradation, the **heating rate should not exceed 10°C/min**.

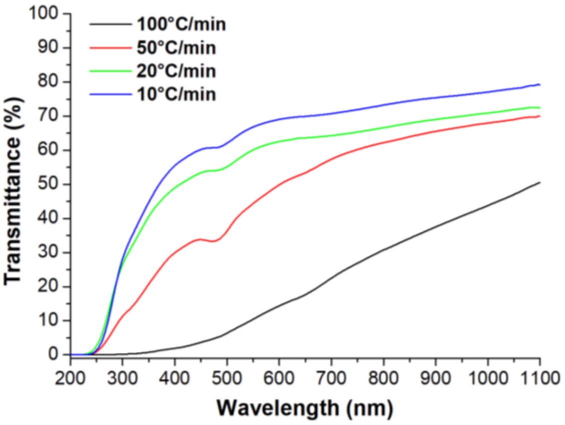

Figure 4.47: Transmittance spectra of S25CR-3MS ceramics SPSed at 1375°C for 20 min with heating rates of 10 to 100°C/min

We studied the microstructure of the ceramic SPSed at 1450°C, 3 min with α = 100°C/min at different positions from edge to center in *Figure 4.48*. Within **0.125 mm from the edge** (*Figure 4.48.a* and *b*), some

abnormally big grains with size up to 20 µm are observed, while uniform grain sizes are observed further toward the center. An **increasing concentration of pores** is observed from **0.250 to 2.0 mm from the edge** (*Figure 4.48.c* to *f*), then remains stable up to the center. This porosity arises from the **entrapped carbon**.

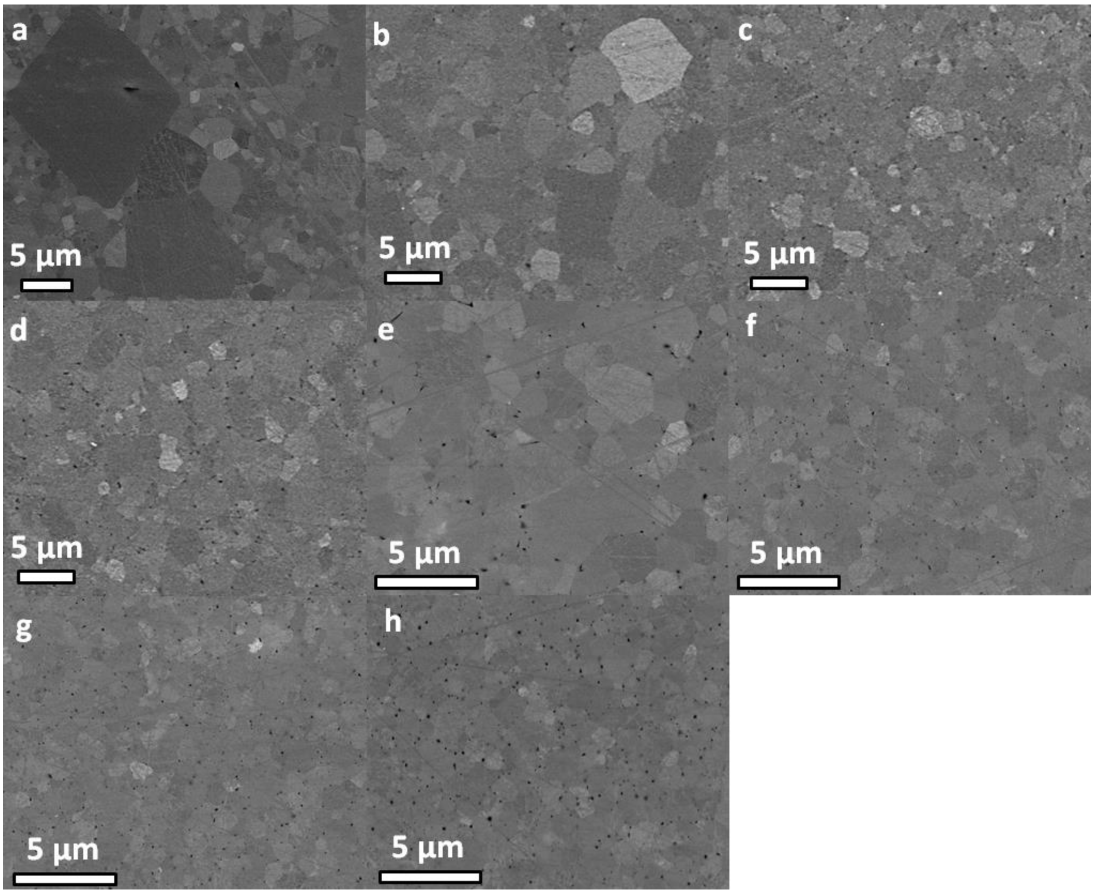

Figure 4.48: SEM of S25CR-3MS ceramics SPSed at 1450°C for 3 min with 100°C/min, at a) the edge and at distance from the edge of b) 0.125, c) 0.250, d) 0.500, e) 1.00, f) 2.00, g) 3.75 and h) 7.50 mm (center)

The grain size distributions at the different radial positions are presented together with a plot of the evolution of the grain size mode with the distance from the edge in *Figure 4.49.a* and *b*, respectively. The GSD are **wide** with **modes at ~2 µm within 1.00 mm** from the edge, while they are **narrow** around **~1 µm** further toward the center. The frontier corresponds to the **visual crown effect** (*Figure 4.45.b*, 2nd row). The smaller GS in the carbon-contaminated area is due to the **pores/precipitates hindering grain coalescence**. It should be mentioned that Talimian *et al.* [222] observed bigger grains in the center of the ceramics instead.

It is interesting to note that the influence of the heating rate depends on the sintered powder. Indeed, the darkening of raw Sasol ceramics was only affected by the sintering temperature. In the case of S25CR-3MS precursor, it is assumable that the **discoloration is also caused by temperature** (see photographs in *Figure 4.45*), but **only high heating rates allow its occurrence**. This contrast of behavior can be explained by the difference of sintering kinetic between both powders. The Sasol powder is constituted by large aggregates hard to sinter, and **open porosity remains until at least ~1200°C** depending on conditions (*Section II.1.i*), while the **critical temperature for carbon contamination through graphite sublimation is 1150°C** [222]. Hence, the contamination cannot be prevented in this case. For the S25CR-3MS powder, the **stage of pore closure is reached for T < 1150°C** if the heating rate is low enough, **thus no contamination occurs**.

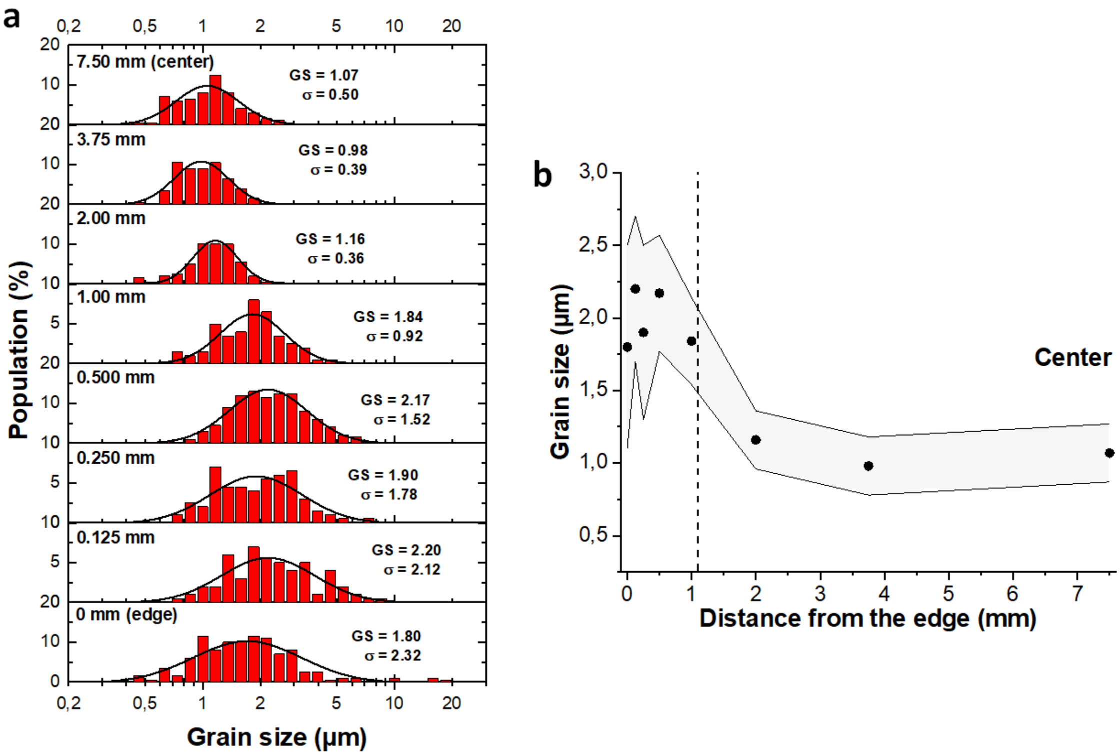

Figure 4.49: a) Histograms of grain size distribution of S25CR-3MS ceramics SPSed at 1450°C for 3 min with 100°C/min at different radial positions, and b) modes of GSD plotted as a function of the distance from the edge

iv. Effect of the applied pressure P: high pressure spark plasma sintering HPSPS

In this section we investigate **the effect of pressure** during SPS, and specifically **high pressure up to 1 GPa** using a non-conventional **high pressure SPS device** (HPSPS, *Chapter 2.II.3.i*). More accurately, we study the **influence of the coupled P-T_d conditions** in order to optimize the material properties, and especially to obtain finer microstructures, as hinted by our work on Sasol powder (*Section II.1.iv*).

The P-T_d sintering conditions and the properties of resulting materials are presented in *Table 4.11*. The dwell duration is t_d = 20 min and the heating rate is α = 10°C/min for all ceramics in this paragraph.

Table 4.11: Influence of the P-T_d conditions on the properties of S25CR-3MS ceramics SPSed for 20 min with 10°C/min

Sintering temperature (°C)	**1400**	**1275**	**1200**	**1150**	**1100**	**1050**	**1035**	**1015**	**~1000[a]**
Applied pressure (MPa)	**20**	**80**	**150**	**200**	**300**	**400**	**500**	**700**	**1000**
Grain size mode (nm)	1100	310	235	226	168	158	135	126	98
Transmittance at 600 nm (%)	44.8	75.2	74.0	74.3	84.8	84.7	86.3	84.37	83.0
UV cut-off (nm)	268	235	230	229	228	225	224	228	221

[a] The sintering temperature of 1000 MPa sample is in the range 1000-1100°C, due to incertainty in the measurement. However, we estimate $T_d \approx$ 1000°C based on literature and developed models (*Equation 4.1* to *Equation 4.6*).

The influence of the applied pressure on the densification of the powder is evaluated by comparison of the relative displacement of the pistons during SPS in *Figure 4.50*. As for the Sasol precursor, it is observed that **the raise of applied pressure decreases the minimal temperature for full densification** $T_{d.min}$: ~1400°C is required when P = 20 MPa, while it is dramatically reduced to **1000°C** when pressing at **1000 MPa**. For all densification curves in this figure, a small "bump" is observed, which is only due to the change of heating rate from 100°C/min to 10°C/min at critical temperature $T_c = T_d - 150$°C (max 1150°C).

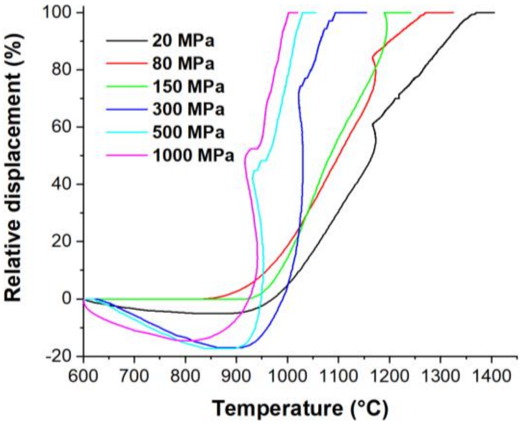

Figure 4.50: Relative displacement of the SPS pistons during sintering of S25CR-3MS with applied pressure of 20 to 1000 MPa

From the analysis of these densification curves, we plotted the minimal full densification temperature as a function of the applied pressure in *Figure 4.51*. This ***d* ~100% isodensification curve** shows the decrease of $T_{d.min}$ with P is much more important in the low pressure range; for **P > 400 MPa, very small reduction** is implied. It can be pointed out that conventional pressureless sintering of MAS requires $T_d \geq$ ~1650°C for full densification [254], while **even small applied pressure < 100 MPa** allows **great reduction** by ~400°C down to 1275°C. It demonstrates the high interest of sintering under pressure allowed in SPS processing.

An empirical relation can be written between the coupled conditions P-T_d for full densification state:

$$\boldsymbol{T_d = 1862 * P^{-0.094}}$$ *Equation 4.1*

This relation allows estimating the sintering temperature required for full densification at a particular applied pressure (or inversely), which is especially useful if one considers its validity beyond studied range of P-T_d. In [19], Sokol *et al.* carried out a similar study while sintering the raw commercial S30CR MAS powder from Baikowski, with an average crystallite size of ~50 nm. They obtained a close relationship between P and T_d, although the required temperature at specific P is generally found to be lower in our case.

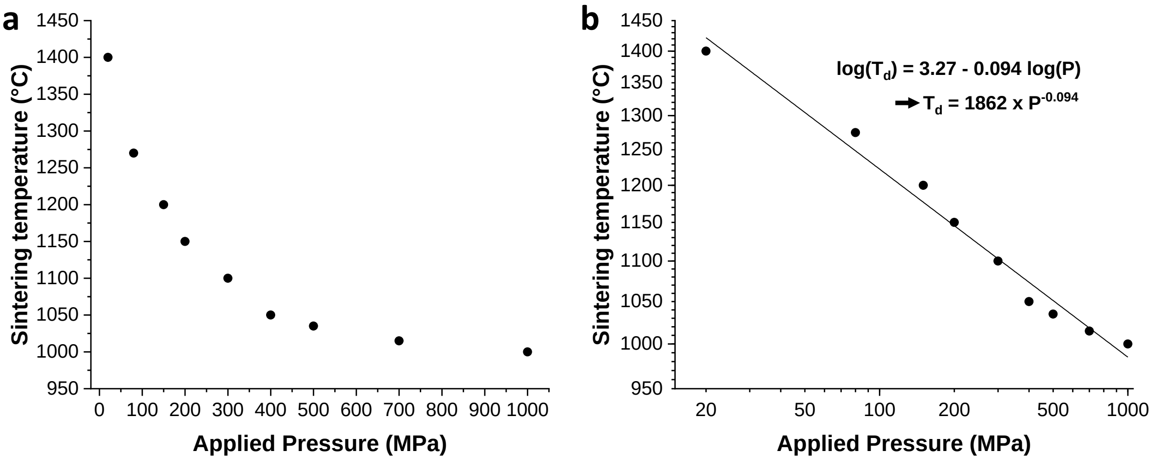

Figure 4.51: Isodensification curve of the coupled P-T_d conditions for full densification of S25CR-3MS SPSed for 20 min with heating rate of 10°C/min, with a) linear and b) logarithmic axes scales

Considering the **creep densification model** which relies on the assumption that mass transport during sintering under pressure is similar to that of high temperature creep, the **densification rate $\dot{\rho}$** is expressed as:

$$\boldsymbol{\dot{\rho} = A * GS^{-n} * \sigma_{eff}{}^{s} * exp\left(-\frac{Q}{RT}\right)}$$ *Equation 4.2*

where A is a constant, σ_{eff} is the effective stress, *n* and *s* are respectively the grain size and stress exponents, *Q* is the activation energy, R is the gas constant and T is the absolute temperature. σ_{eff} decreases together with the porosity and can be assimilated as the applied stress P for the final stage of sintering, while *s* varies from 1 to 5 depending on the densification mechanism [19].

Following the reasoning in [19], it can be assumed that the **relatively low sintering temperatures do not induce significant changes of grain growth and densification rate** during the final stage of sintering (especially true for $T_d \leq 1225°C$, see *Figure 4.43*), the equation (*Equation 4.2*) can be simplified as:

$$\dot{\rho} = A' * P^{s} * exp\left(-\frac{Q}{RT}\right)$$ *Equation 4.3*

with A' a constant. Finally, *Equation 4.3* can be rearranged in:

$$ln(P) = K + \frac{Q}{s.RT}$$ *Equation 4.4*

with $K = \frac{ln(\dot{\rho}) - ln(A')}{n}$ constant during the final stage of sintering.

Thus, considering the average activation energy of polycrystalline MAS densification being ~475 kJ/mol based on the literature listed in [19], the **stress exponent can be estimated as *s* = ~3.1(5)**. This value is close to *s* = 3.7(4) calculated for similar sintering conditions in [19], hence we conclud that the **densification of MAS in the final stage of SPS** in range $20 \leq P \leq 1000$ MPa is **controlled by deformation of the grains *via* grain boundary sliding accommodated by dislocation motion**, rather than by O^{2-} diffusion *s* = ~1 [385].

The photographs of the ceramics prepared with different P-T_d conditions are shown in *Figure 4.52*. It is clear that the **transparency dramatically increases until T_d decreases to 1100°C for P = 300 MPa**. From this P-T_d couple, **no darkening phenomenon** can be observed by naked eye. However, a **slight yellow tint** is present in these ceramics due to **colored centers**, except for the one fabricated at 1000 MPa and ~1000°C.

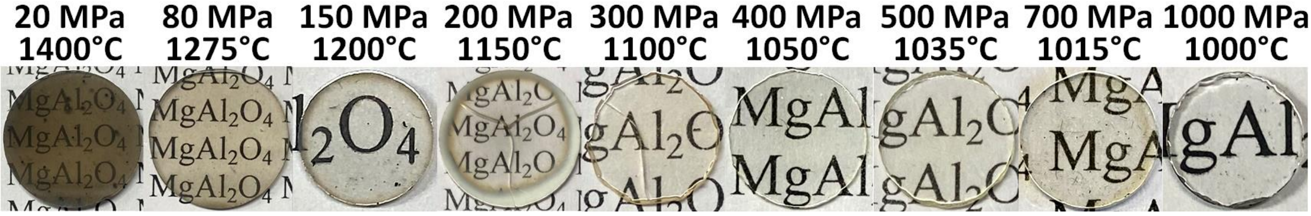

Figure 4.52: Photographs of S25CR-3MS ceramics SPSed for 20 min with different P-T_d conditions

The transmittance spectra of these ceramics are presented in *Figure 4.53* with their $T_{il\text{-}600\ nm}$ and UV cut-off indicated in *Table 4.11*. The **transmittance increases significantly for P ≥ 300 MPa**, as we reach a T_{il} ***plateau* at ~85% for λ = 500 nm**, very close to the theoretical limit of 87% calculated from the Sellmeier equation (*Equation 1.9*) [73]. This **level of transparency** in the visible wavelengths is **comparable to the best results** reported in literature [19, 199, 228]. The T_{il} *plateaus* discrepancies observed for the P ≥ 300 MPa materials do not arise from a trend with P-T_d conditions, but rather from the **imperfect reproducibility of the processing** with our SPS apparatus. It should be noted that the 200 MPa sample was not obtained with the HPSPS device but with a graphite composite mold for P ≤ 300 MPa (quality CX31V Toyo Tenso), which we assume to be the cause for its limited transparency (comparable to the 80 MPa).

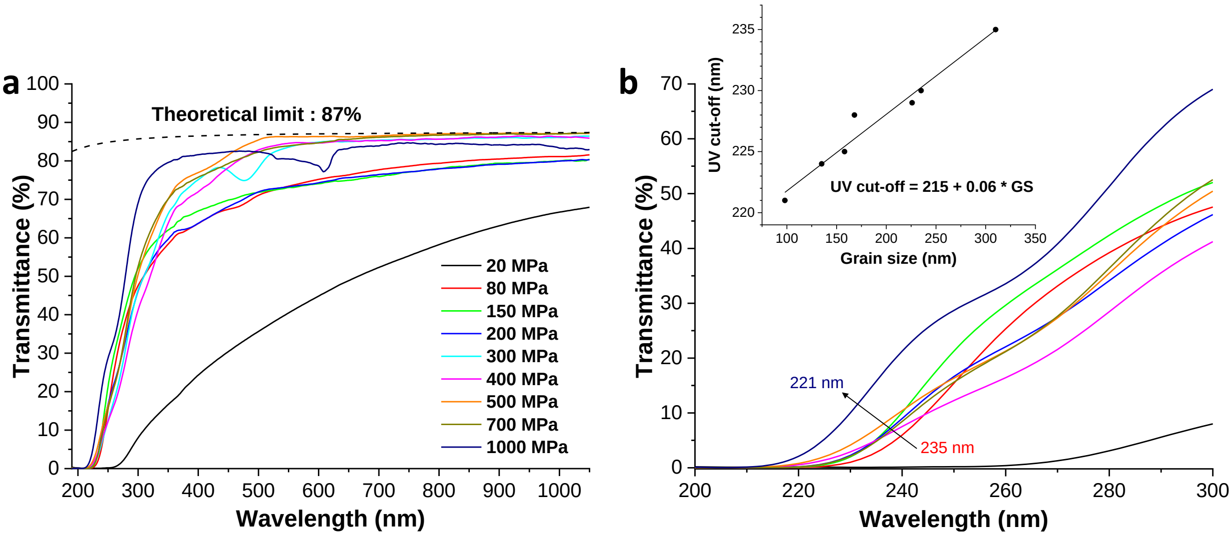

Figure 4.53: a) Transmittance spectra of S25CR-3MS ceramics SPSed with different P-T_d conditions and b) detail of the UV region with the UV cut-off plotted in function of the average grain size in inset

Some **absorption centers** are observed: **two bands at 410 and 480 nm** with intensities varying without obvious trend in all spectra except for 1000 MPa, which presents absorption **bands at 530 and 610 nm**. The first two centers are assumed to cause the **yellow tint** observed (*Figure 4.52*). A magnification in the UV region (*Figure 4.53.b*) reveals a **color center at 250-280 nm** for P > 150 MPa ceramics, which is believed to be caused by the **high applied stress** during sintering. These centers are assessed to be of **V-type (400-600 nm)** and **F-type (230-270 nm)** nature, based on calculations and experiments [45, 55, 56].

It is remarkable in *Figure 4.53.b* that the **UV cut-off is shifted toward low wavelength** with increasing applied pressure/decreasing temperature, down to **221 nm for the 1000°C-1000 MPa sample**. The inset shows a **linear relationship between the UV cut-off and grain size** as **UV cut-off = 215 + 0.06 GS**. This shift toward the theoretical UV cut-off E_g = 160 nm indicating a **better crystalline state** [11] is of high interest for applications requiring the largest possible transparency window in the UV-Vis-NIR range.

The SEM of the ceramics fabricated with P up to 700 MPa are presented in *Figure 4.54*. As expected, when P increases and, most of all, T_d decreases, the **refinement of the microstructure** occurs, while almost no pores are observed for all P-T_d conditions and especially for P ≥ 150 MPa. However, differences are hardly distinguishable for P ≥ 300 MPa, as T_d decreases only by 100°C in this whole range.

The TEM analysis of the 1000°C-1000 MPa ceramic is presented in *Figure 4.55*. The very fine grain size follows a **log-normal monomodal distribution** (fitted in dashed line, *Figure 4.55.b*), with a mode **GS = 98 nm** and a **standard deviation σ = 44.4 nm** (relative deviation σ_r = 2.22). This GSD is narrow, with the **median grain size GS_{50} = 91 nm** close to GS (highly symmetrical distribution) and the **100% percentile GS_{100} = 250 nm**. The image in **atomic resolution** (4096 x 4096 pixels^2, *Figure 4.55.c1*) reveals the **monocrystalline quality of the grains**, with **low content of apparent microstructural defects**. The FFT in inset and the surimposed $MgAl_2O_4$ 2*2*2 cell (ICSD 31373) indicate a [110] orientation of the grain. The images after **Wiener filtering** and simulated on Dr Probe software are shown in *Figure 4.55.c2*. It is interesting to notice (see arrows in inset) that the intensities are not corresponding for some atomic positions. This is due to **partial inversion of position** between ions; in particular, it is observed that **cations Al^{3+}/Mg^{2+} may occupy anionic O^{2-} interstices**. A thorough investigation is currently under way.

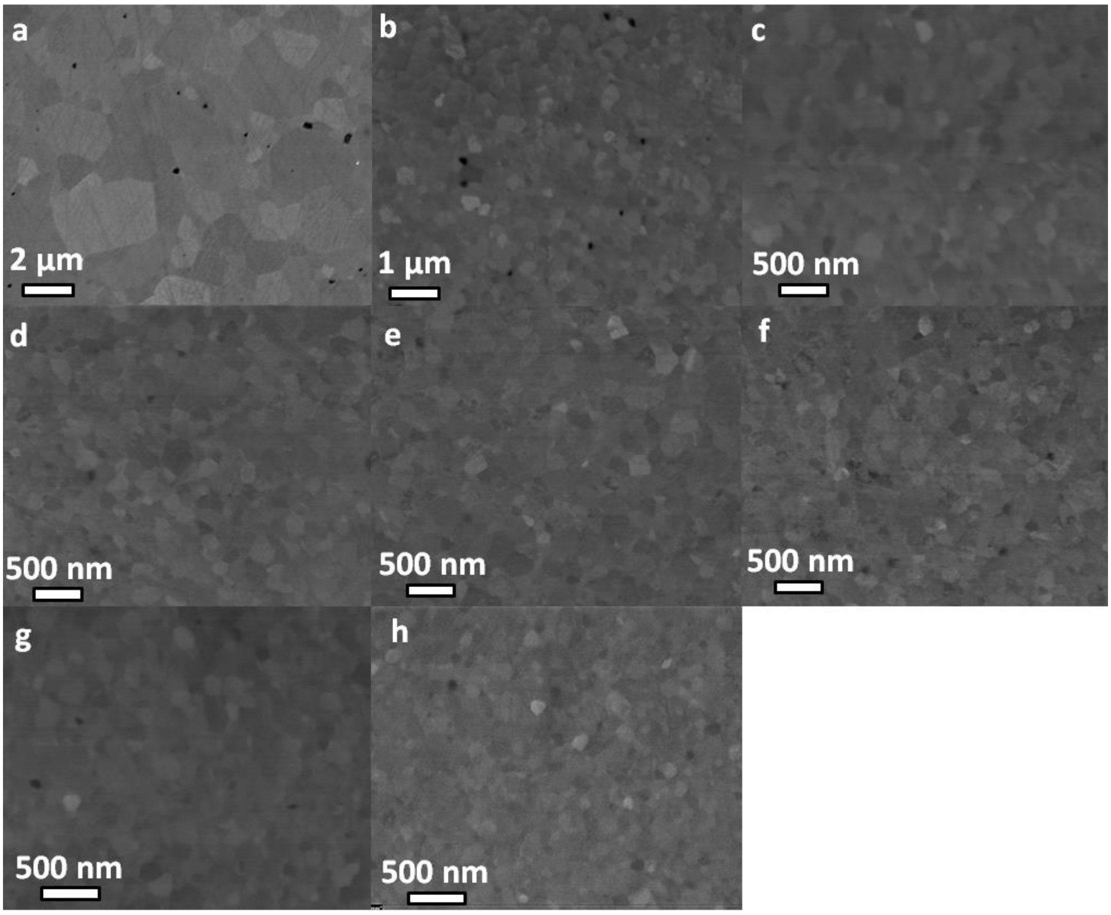

Figure 4.54: SEM of S25CR-3MS ceramics SPSed at a) 1400°C-20 MPa, b) 1275°C-80 MPa, c) 1200°C-150 MPa, d) 1150°C-200 MPa, e) 1100°C-300 MPa, f) 1050°C-400 MPa, g) 1035°C-500 MPa and h) 1015°C-700 MPa

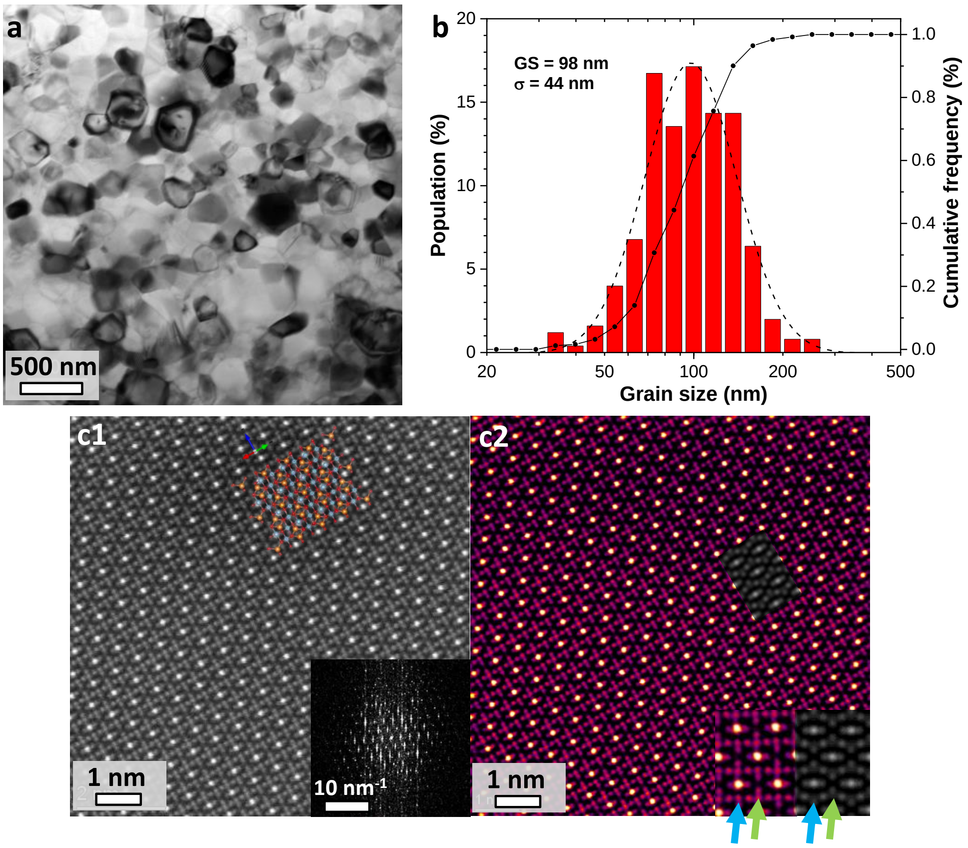

*Figure 4.55: a) Bright field TEM and b) grain size distribution of the S25CR-3MS ceramic SPSed at 1000°C-1000 MPa; c1) HAADF atomic resolution (78 pA, α = 22.1 mrad,β = 65-200 mrad) with surimposition of 2*2*2 MAS cell (Mg: orange, Al: blue, O: red) and FFT in inset, c2) same image with Wiener filter (highest frequency = 40) and simulated image (Dr Probe software) in gray*

The grain size modes obtained from the GSD presented in *Table 4.11* are plotted in function of the applied pressure and the sintering temperature in *Figure 4.56*. The **grain size decreases with $\propto (1/P)^{0.6}$** (*Equation 4.5*), and **increases exponentially with $T_d/500$** (*Equation 4.6*). It can be noted that for 500 MPa-1035°C, 700 MPa-1015°C and 1000 MPa-1000°C the **grain growth factor is inferior to 2**, due to **almost non-occurring coarsening** of the grains during sintering. In particular, **GF = 1.4** for the latter P-T_d couple.

The formulated equations of dependence toward P and T_d are of high interest for our study, because they allow us to **estimate the P-T_d conditions for any desired grain size**. By extrapolation of the curves, and assuming their validity in the range of higher P-lower T_d, it is possible to estimate the **conditions P_{max}-$T_{d.min}$ for which the sintering occurs with negligible grain growth**, hence a grain size very close to the crystallite size of the powder ($GS_0 \approx CS$). These parameters are the constants of *Equation 4.5* and *Equation 4.6*, determined as **$P_{max} \approx 1500$ MPa, $T_{d.min} \approx 950$°C and $GS_0 = 70$ nm**.

$$GS = GS_0 * \left(\frac{P_{max}}{P}\right)^{0.6} \qquad \textit{Equation 4.5}$$

$$GS = GS_0 * 10^{\frac{T_d - T_{d.min}}{500}} \qquad \textit{Equation 4.6}$$

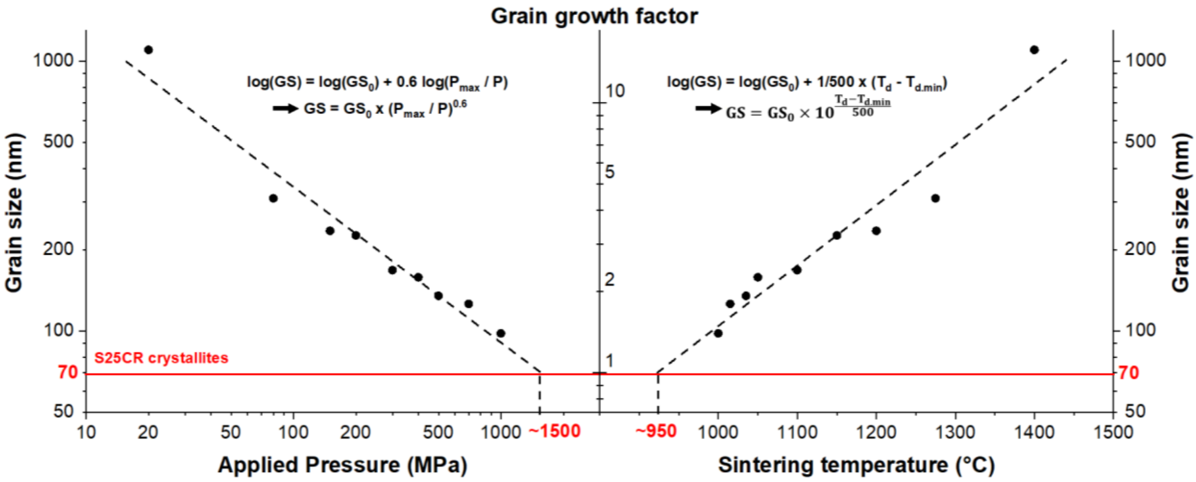

Figure 4.56: Modes of grain size distribution plotted as a function of the applied pressure (left) and the sintering temperature (right)

These results emphasize the importance of the **coupled P-T_d conditions**, which are the **most important parameters of leverage to optimize both the microstructure to the nanoscale and the transparency**. The materials SPSed with P ≥ 500 MPa almost **reach the theoretical transmittance in the visible with ultrafine microstructures**. However, it is clear that for further improving even slightly the features of our ceramics, a great increase of the applied pressure is required. Furthermore, we are ultimately limited in the refinement of the microstructure by the initial crystallite size of the powder.

v. Investigation of the defects of the S25CR-3MS ceramics and scale-up

Based on the results obtained for the ceramics prepared from the S25CR-3MS precursor, some general remarks can be made in order to consider a few paths for the improvement and optimization of the materials.

We **investigated the defects** of these ceramics. As pointed out when discussing *Figure 4.53*, several color centers are present in the materials and are assumed to arise from structural defects of F-center and V-center types. In particular, the absorption center at 480 nm is observed for all samples, with a relatively strong absorption band. However, these defects may be beneficial for applications in extreme environments, as they have been found to lead to **enhanced tolerance toward radiation damage** through self-healing mechanisms [2, 386]. The structural defects in S25CR-3MS ceramics will be further studied in *Chapter 5*.

No particular microstructural defects were observed in S25CR-3MS materials, which emphasizes the **good quality of the powder** (homogeneity, purity…). However, as pointed out in *Figure 4.46*, carbon contamination occurs during SPS processing from the die apparatus, and especially from the insulating graphite paper. It may be limited with appropriate sintering conditions ($\alpha \leq 10$°C/min, $T_d \leq 1150$°C), but even for HPSPSed samples at low T_d, **some small graphite particles** may be entrapped in the powder during preparation of the mold: such inclusions are highlighted in the photograph *Figure 4.57.a*. This contamination is hard to avoid even by careful manipulation due to the brittle character of graphite paper. It can be prevented by **replacing the graphite paper by a foil of another material**; promising results have been obtained using Mo [264], Pt [263] and Ta [197] foils, although these alternatives may be expensive.

For sintering at standard applied pressure of P = 80 MPa, the **optimal SPS conditions** for the fabrication of a fine-grained transparent MAS ceramic consist in **T_d = 1275°C** with a duration **t_d = 10 min** ensuring homogeneous densification and a low heating rate **α = 10°C/min** to avoid carbon contamination.

With these conditions, we fabricated a **20 mm diameter sample** instead of 15 mm (surface ratio ~2). The photograph and SEM are presented in *Figure 4.57*. Its **transmittance at 600 nm is 78.1%**, and its **microstructure is homogeneous** between edge and center with **GS = 280 nm**. **No differences** are noted with the 15 mm sample, which is promising for considering the scale-up of the process.

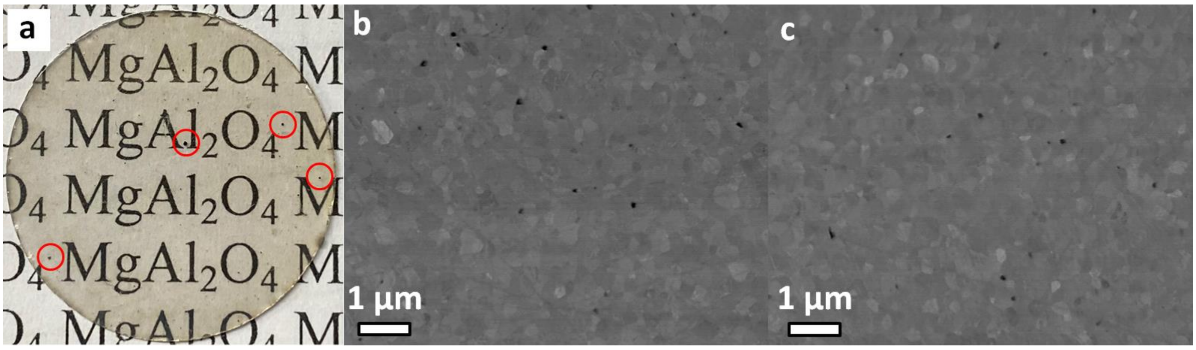

Figure 4.57: a) Photograph and SEM micrographs b) in the periphery and c) in the center of the 20 mm diameter MAS ceramic SPSed with optimized sintering conditions for an applied pressure P = 80 MPa: T_d = 1275°C, t_d = 10 min and α = 10°C/min

3. Conclusion

In this sub-chapter, we studied the **effect of the different sintering parameters** for the fabrication of fine-grained transparent $MgAl_2O_4$ ceramics from the raw Sasol and S25CR-3MS commercial powders.

It is remarkable that the sinterability of both precursor powders highly differs, as well as the properties of the fabricated ceramics. The **Sasol powder is sintered homogeneously** through the radial and axial sections, while the **S25CR-3MS is sintered from the center toward the edges of the compacts**, requiring specific settings for homogeneous ceramics. The **S25CR-3MS precursor appears much more adapted for obtaining the desired ceramic features** (high transparency and fine grain size at the nanoscale).

The parametric study showed that the **most impactful SPS conditions are the sintering temperature and the applied pressure**, as the **grain growth is mostly driven by thermal effect** while the **densification**

depends on the coupled applied pressure-temperature conditions. The sintering dwell duration acts as an **optimization parameter** for reaching full densification (and therefore transparency).

The influence of the heating rate on the **darkening phenomenon** depends on the powder and sintering kinetic, but it was found best in general to use **low heating rate ≤ 10°C/min** to limit carbon contamination.

The ceramic with best features has been obtained for **HPSPS of S25CR-3MS powder at 1000°C and 1000 MPa**. The **transmittance *plateau* reaches ~85% at 400 nm**, **with a grain size of 98 nm**. This quality of $MgAl_2O_4$ polycrystalline material is comparable with the best results reported in literature.

For further improving the properties of our ceramics, especially for the decrease of the grain size, two main ways exist. First, we could use **more severe sintering conditions**, *i.e.* applied pressure up to 1.5 GPa with temperature down to 950°C. However, we are **limited by technical feasibility**, as our HPSPS mold can hold up to 1 GPa, and ultimately we cannot go lower than the crystallite size of S25CR powder (70 nm). Another way is to use a **finer $MgAl_2O_4$ precursor powder**. Since no such powder is commercially available yet, the sintering of the nanocrystalline precursor powders synthesized *via* polyol and impregnation routes (*Chapter 3*) appears as the most pertinent path to improvement. This study is carried out in the next section.

III. Spark Plasma Sintering of synthesized nanocrystalline $MgAl_2O_4$ powders

In this sub-chapter, we **investigate the sintering of the nanocrystalline powders synthesized *via* polyol and impregnation routes** presented in *Chapter 3*. Note that this work is only a preliminary study meant for assessing the sinterability of these precursors in general, and determining the major defects in sintered samples in order to implement required modifications to the synthesis processes. All sintering experiments have been carried out with **$P = 80$ MPa, $\alpha = 100$°C/min, $t_d = 20$ min, at different T_d**.

1. Precursors synthesized *via* the polyol route

For this preliminary study on the sinterability of polyol synthesized MAS precursors, only **powders synthesized with reference conditions** (see *Table 3.1* and *Chapter 3.I.1*) and **calcined at 900°C** for 1 h were investigated. **Monophasic $MgO{\cdot}nAl_2O_3$** powders with **~10 nm crystallites** have been synthesized with ***n* = 0.716** (MgO-rich MAS), ***n* = 1** (stoichiometric MAS) and ***n* = 5** (Al_2O_3-rich MAS), in order to assess the influence of the stoichiometry on the sinterability and properties of resulting ceramics.

The influence of the stoichiometry on the densification of the polyol precursor is evaluated by relative displacement of the pistons during SPS in *Figure 4.58*. The **sintering path** for **$MgO{\cdot}0.716Al_2O_3$** and **$MgO{\cdot}1Al_2O_3$ is classical**, with a single-step densification and **full densification *plateaus* reached at 1235 and 1350°C**, respectively. In comparison, the densification of **$MgO{\cdot}5Al_2O_3$** powder goes through **several stages**: *i)* the **onset of densification** at **700°C**; *ii)* a decrease of **densification rate** in the range **800-950°C**; *iii)* an **intermediary densification *plateau*** for **1100-1400°C**; i*v)* **a high densification rate after 1400°C**. We limited our experiment to 1450°C, which was below the full densification temperature. The behavior observed in stage *ii)* is typical of phase transition, reaction or demixtion phenomena. In our case, since we have a metastable Al_2O_3-rich spinel, we assume that it corresponds to **phase demixtion** into several phases, part of which is fully densified below stage *iv) plateau* and others above stage *v)* range.

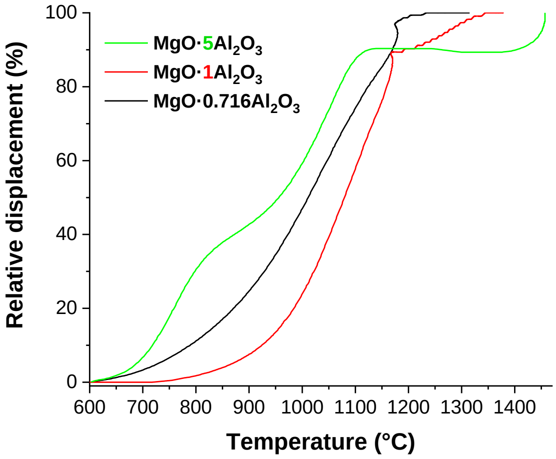

Figure 4.58: Relative displacement of the SPS pistons during sintering of the polyol precursor with different stoichiometry

The XRD patterns of the ceramics prepared from the polyol precursors are presented in *Figure 4.59*. Independently of the initial composition of the monophasic spinel powder, **all the obtained ceramics are biphasic**. The structural characterizations are summarized in *Table 4.12*.

Table 4.12: Structural characterizations of the ceramics prepared from polyol precursors with different MgO·nAl$_2$O$_3$ compositions

Powder composition	Sintering T (°C)	Composition	spinel cell constant *a* (Å)	*n* [a]	x_t [b]
MgO·0.716Al$_2$O$_3$	1450	spinel 94 at% MgO 6 at%	8.1204(2)	0.776	0.422
MgO·1Al$_2$O$_3$	1375	spinel 44 at% α-Al$_2$O$_3$ 56 at%	8.1028(2)	0.878	0.681
	1450	spinel 35 at% α-Al$_2$O$_3$ 65 at%	8.1106(4)	0.830	0.729
MgO·5Al$_2$O$_3$	1450	spinel 4 at% α-Al$_2$O$_3$ 96 at%	8.0518(5)	1.31	0.953

[a] *n* is defined as the atomic ratio Al:Mg within spinel phase
[b] x_t is defined as the total Al$_2$O$_3$ atomic fraction taking into consideration all observed phases

In *Figure 4.59.a*, **traces of MgO** can be seen for **MgO·0.716Al$_2$O$_3$** SPSed at 1450°C. XRD refinement indicates a composition of **94 at% MAS** with cell constant *a* = 8.1204(2) Å **and 6 at% MgO**. In comparison with the initial powder constant *a* = 8.1326 Å, a decrease of MgO content within MAS phase is deduced, and following Viertel and Seifert's law (*Equation 1.1*) the spinel composition is estimated as ***n* = 0.776**. Considering the ceramic being polyphasic, the **total Al$_2$O$_3$ mole fraction** is calculated to be **x_t = 0.422**, slightly higher than the powder's *x* = 0.412. Starting from **stoichiometric MgAl$_2$O$_4$** (*Figure 4.59.b*), the ceramics obtained are constituted of **MAS and corundum α-Al$_2$O$_3$**. The cell parameter of the spinel phase and the **Al$_2$O$_3$ phase content** increased during SPS, together with the sintering temperature. In comparison with the powder (*a* = 8.082 Å, *x* = 0.5), the ceramics compositions are: **44 at% MAS with *n* = 0.878** and **x_t = 0.681** at 1375°C, and **35 at% MAS with *n* = 0.830** and **x_t = 0.729** at 1450°C. Hence, the MgO content within MAS increases with T$_d$ due to **Al$_2$O$_3$ exsolution out of the spinel phase**, while the **total MgO content decreases**, even so no phase demixtion was evidenced in *Figure 4.58*. Finally, SPS of the **Al$_2$O$_3$-rich MAS** at 1450°C (*Figure 4.59.c*) results in a composition of **96 at% corundum**, with **4 at% MAS** with ***n* = 1.31** remaining for a total Al$_2$O$_3$ content **x_t = 0.953**. Since the powder composition is *n* = 5 with *x* = 0.833, it appears that **Al$_2$O$_3$ has been massively exsoluted** from MAS during SPS, which is consistent with the densification curve observed in *Figure 4.58*, while the total MgO content has decreased concurrently.

From these results, it is clear that SPS of polyol synthesized MAS precursors leads to **depletion of MgO** in consideration of the initial composition, while the **spinel phase undergoes demixtion** to reach an **equilibrium that does not correspond to stoichiometric $MgAl_2O_4$** and depends on the initial composition. Indeed, it is known that the vapor pressure of MgO is up to 1000 that of Al_2O_3 in MAS, which may result in **MgO evaporation and loss** during SPS [42]. However, such MgO loss is generally observed at high temperature and low vacuum pressure, *e.g.* 1900°C under 10^{-3} Pa [32]. It is to be noted that we did not observed such phenomena for SPS of commercial powders, nor for heat treatment of the polyol precursors in air up to 1600°C (*Figure 3.2.a*). We attribute this peculiar sintering behavior to the particularly **high reactivity of the polyol precursors**, while it may be activated by current path through the compacted powder during SPS, as it was already observed for flash sintering of $MgAl_2O_4$ [254].

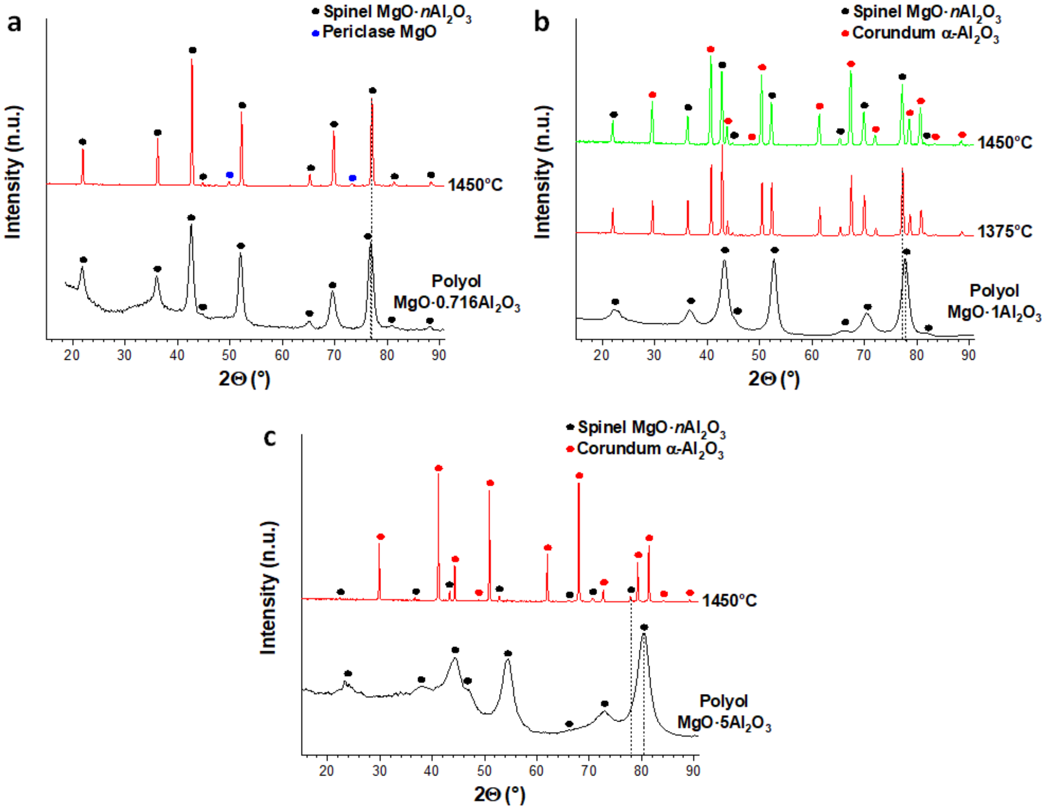

Figure 4.59: XRD patterns of the ceramics SPSed from the polyol $MgO{\cdot}nAl_2O_3$ precursors with a) n = 0.716, b) n = 1 and c) n = 5

The photographs of the ceramics SPSed at 1450°C are presented in *Figure 4.60*. All the samples are **fully opaque**, with **black coloration for *n* = 0.716 and 1** materials and a **white ceramic** for *n* = 5. The latter white appearance is due to the incomplete densification of the material (*Figure 4.58*). The black coloration of the other samples is less expected. It is not due to carbon contamination as observed for commercial powders under specific SPS conditions, since it is a drastically different darkening even from naked eye observation. Instead, we suspect the coloration to be linked to **very high content of structural defects**, and especially **oxygen vacancies**, which are believed to arise from the strong and rapid phase demixtion/MgO loss. Indeed, oxygen vacancies have been often reported to induce a strong black coloration of ceramic materials including MAS [254, 387, 388]. Many **white spots** can be seen on the black samples, which are believed to be due to a **locally non-densified microstructure** induced by the aggregation state of the powder. The same observations were made for the *n* = 1 material SPSed at 1375°C.

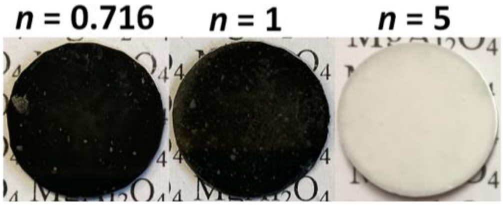

Figure 4.60: Photographs of the ceramics SPSed at 1450°C from the polyol MgO·nAl$_2$O$_3$ precursors with n = 0.716, 1 and 5

The SEM of these ceramics is presented in *Figure 4.61*. The *n* = 0.716 ceramic (*Figure 4.61.a*) presents a **classic MAS microstructure**, with **low remaining porosity** and a **grain size of 250 ± 70 nm**. The microstructure of the *n* = 1 samples (*Figure 4.61.b1* and *b2*) is quite different due to their polyphasic nature. We observe a **chemical contrast**, with a **dark continuous phase and bright embedded clusters within**. Indeed, such microstructure is **typical of eutectic compositions** that could result from the demixtion/MgO loss during SPS. Thus, the dark matrix and the bright embedded phases should be **MgAl$_2$O$_4$ and α-Al$_2$O$_3$**, respectively, based on XRD (*Figure 4.59.b*). The **Al$_2$O$_3$ clusters** have a size of **~2 µm**, separated by the **~1 µm thick matrix**. While the spinel matrix is highly dense even at 1375°C, the clusters present pores with concentration and size decreasing with increasing temperature: numerous pores with size ranging from 100-500 nm at 1375°C, and few pores with size diminished to 30-350 nm at 1450°C. We believe the Al$_2$O$_3$ particles are porous due to MgO exsolution, and progressively densify up to over 1450°C. The *n* = 5 ceramic (*Figure 4.61.c*) presents a **complex microstructure** analyzed separately in *Figure 4.62*. However, it can already be observed that the material is highly porous, as full densification has not been reached.

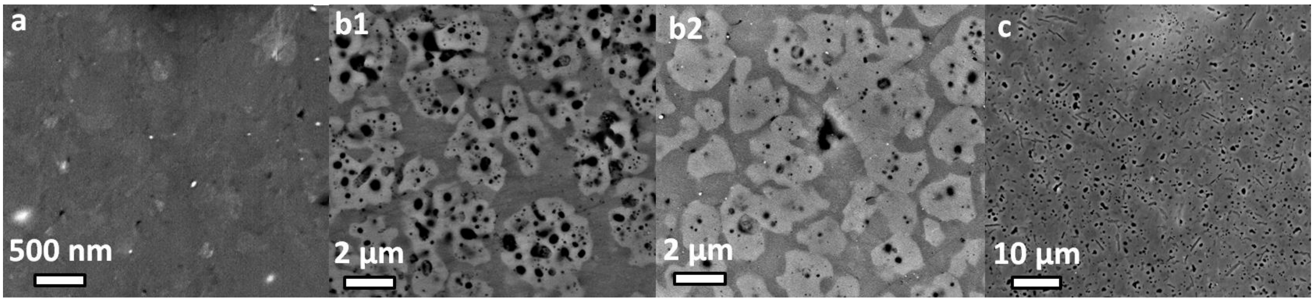

Figure 4.61: SEM of the ceramics from polyol MgO·nAl$_2$O$_3$ powders with n = a) 0.716, b) 1 and c) 5, at a,b2,c) 1450 and b1) 1375°C

The microstructure of the *n* = 5 ceramic is investigated in *Figure 4.62*. It is not homogeneous, and several distinctive features are observed. In *Figure 4.62.a* and *b,* a **three-dimensional interpenetrating network** organized in **cells of ~2 µm** diameter is shown: contrarily to the *n* = 1 ceramics (*Figure 4.61.b1* and *b2*), this is not particles embedded within a matrix, but rather particles with inhomogeneous composition. Their **cores** consist of **mixed nanometric white and black phases**, while **shells form a 400 ± 100 nm thick layer** of the white phase. This microstructure can somehow be compared with that of the defect found in Sasol ceramics and presented in *Figure 4.35*, which we tentatively ascribed to an **Al$_2$O$_3$-MgAl$_2$O$_4$ eutectic** based on EDX analysis, in good agreement with the composition estimated as 96 at% Al$_2$O$_3$-4 at% MAS.

Topographic contrast by SE imaging (*Figure 4.62.c1* and *c2*) reveals that black areas with diameter over 200 nm may be pores, while smaller ones within cells are grains, confirming the formation of a eutectic. *Figure 4.62.d* shows a **divorced eutectic microstructure** with phases in massive form, with **dendritic Al$_2$O$_3$ matrix** (bright) and **small MAS grains** (dark) precipitated within. Such a microstructure was reported in [27] through peritectic reaction of alumina and MAS for a composition x_t = 0.95, close to our conditions.

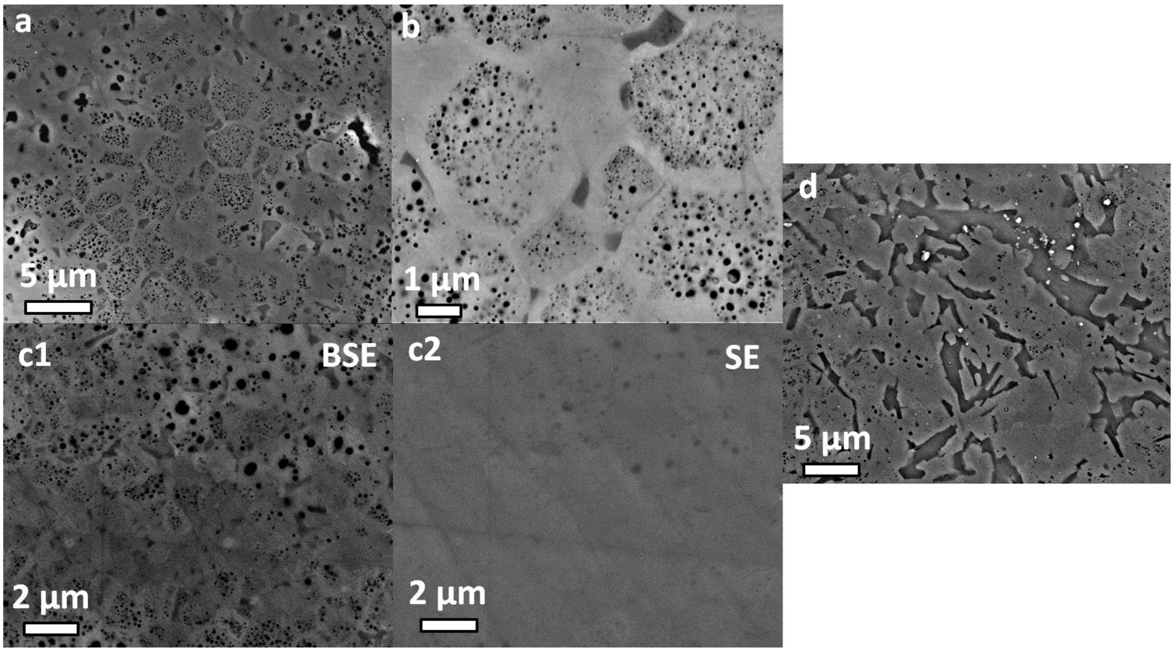

Figure 4.62: SEM of the $MgO{\cdot}5Al_2O_3$ ceramic SPSed at 1450°C, with a,b) three-dimensional interpenetrating network organized in cells, with c1) chemical (BSE) and c2) topographic (SE) contrasts, and d) divorced Al_2O_3-$MgAl_2O_4$ eutectic microstructure

Further experiments are required to better understand the phenomenology behind the high reactivity of the polyol precursors leading to demixtion and MgO loss during SPS. Afterward, avoiding the demixtion could allow fabricating transparent MAS ceramics with tunable composition. In the mean time, the ceramics obtained here may have interesting properties for other applications due to their peculiar compositions/microstructures, and deserve proper characterization to assess their applicability.

2. Precursors synthesized *via* the impregnation route

This paragraph is dedicated to the **sintering study of the $MgAl_2O_4$ precursor powders synthesized through the impregnation process** (*Chapter 3.II*). In order to investigate the influence of the powder's structure and microstructure, the spinel powders prepared from the **four UPA hosts** will be compared: Mg-UPA300 (*a*-Al_2O_3), Mg-UPA1050 (θ-Al_2O_3), Mg-UPA-TMES (θ-Al_2O_3 covered by SiO monolayer) and Mg-UPA1250 (α-Al_2O_3). In addition, to **investigate the influence of the spinel conversion rate**, three calcination temperatures have been used for the Mg-UPA1250 precursor, *i)* 600°C for **0 at% spinel**), *ii)* 1000°C for **36 at% spinel**) and *iii)* 1300°C for **83 at% spinel**, while the other precursors were pre-treated at 1000°C for 1 h (minimum temperature for single phased MAS from Mg-UPA1050 and Mg-UPA-TMES).

The densification behavior is evaluated by the displacement of the pistons during SPS in *Figure 4.63*. In *Figure 4.63.a*, the Mg-UPA300, Mg-UPA1050 and Mg-UPA-TMES precursors are **fully densified** at **1285, 1230 and 1270°C**, respectively. The delay observed for Mg-UPA-TMES compared to Mg-UPA1050, both formed from γ-Al_2O_3, is believed to be due to the **SiO monolayer acting as a sintering inhibitor**. In *Figure 4.63.b*, all three Mg-UPA1250 precursors are **densified in a single step**, with no indication of further spinelization occurring. However, the 0% MAS powder reaches the full densification *plateau* at 1300°C, while the 36% and 83% MAS powders are fully densified at ~1370°C. The inferior temperature required for the unreacted powder can be explained by the **concomitant MAS formation and densification**, the energy released by the reaction favoring the sintering.

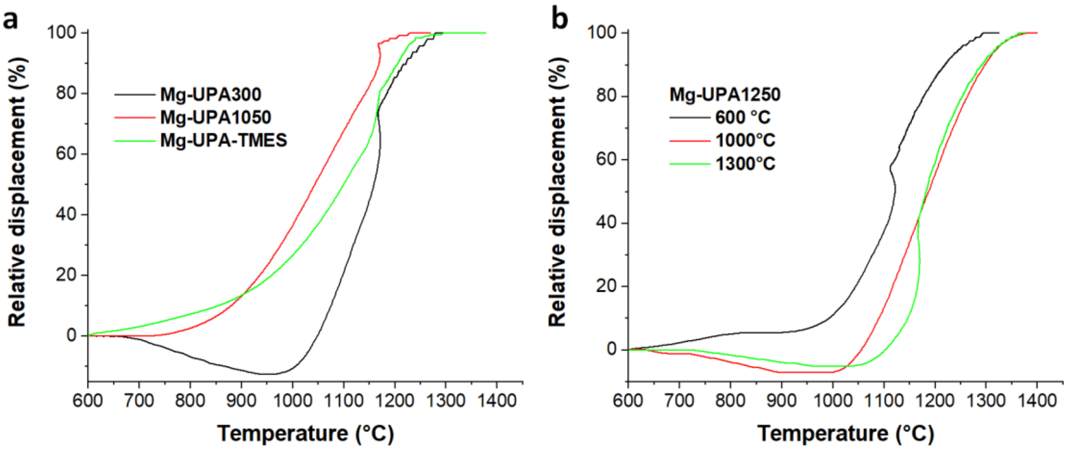

Figure 4.63: Relative displacement of the SPS pistons during sintering of the impregnation MAS precursors a) Mg-UPA300, Mg-UPA1050 and Mg-UPA-TMES calcined at 1000°C for 1 h and b) Mg-UPA1250 calcined at 600, 1000 and 1300°C for 1 h

The XRD patterns of these ceramics are presented in *Figure 4.64*. It should be noted that all the powders used here presented an excess of MgO, which leads to systematic **5-7 wt% free periclase** in all precursors. This problem, already observed for the Zn-UPA300 synthesis (*Chapter 3.III.3*) is due to the rehydration of the UPA from atmospheric humidity between its heat treatment and its impregnation, leading to an incorrect amount of Al_2O_3 calculated from UPA mass. Particular attention should be given to this issue in future experimentations; however, for this preliminary study, the excess MgO is considered a minor inconvenience.

Figure 4.64.a, *b* and *c* present the XRD evolution through sintering of Mg-UPA300, Mg-UPA1050 and Mg-UPA-TMES, respectively. Independently of the precursor and sintering temperature, the cell parameter of the spinel phase remains unchanged. However, the evolution of the excess MgO phase depends on the precursor: the **free MgO content is unchanged** through SPS at 1325-1375°C for **Mg-UPA300**, it **decreases** until not observed anymore at 1375°C for **Mg-UPA1050**, and **no free MgO** is noted for **Mg-UPA-TMES** at 1375-1450°C but traces of **forsterite Mg_2SiO_4** are observed instead. In the case of Mg-UPA1050, the excess MgO may have been accommodated within the MAS phase, most probably at the grain boundaries which explains the absence of increase of cell parameter. In comparison to what was observed for the sintering of the polyol precursors, no phase demixtion or MgO loss is noted in this case.

Figure 4.64.d1, *d2* and *d3* present the XRD evolution through SPS of Mg-UPA1250 pre-treated at 600, 1000 and 1300°C, respectively. When the unreacted powder (600°C) is SPSed at 1375-1450°C, both residual Al_2O_3 and MgO remain, for an **extent of reaction of over 95%**. For sintering at **1650°C**, only the excess MgO is observed, as the **reaction is completed**. It can be noted that the abnormally high relative intensity of the (311) spinel reflection at 43°2θ, as well as the abnormally low relative intensity of the (404) reflection at 77°2θ, seems to indicate a **texture of the material**, that we attribute to the **highly energetic reactive sintering conditions**. It would be interesting to sinter this powder at its minimum temperature for full densification of 1300°C (*Figure 4.63.b*), in order to see the extent of reaction in these conditions. The 36at% (1000°C) and 83at% MAS (1300°C) ceramics have also reached an **extent of reaction of 100% after SPS** at **1375°C**, as only excess MgO remains along the MAS phase. However, the powder treated at 1300°C leads to a ceramic with wider MAS reflections, which indicates a finer microstructure close to the nanometric state. Here also, we can attribute this difference of crystalline state to the higher energy released by the reaction starting from the lowest extent of reaction, resulting in greater coarsening.

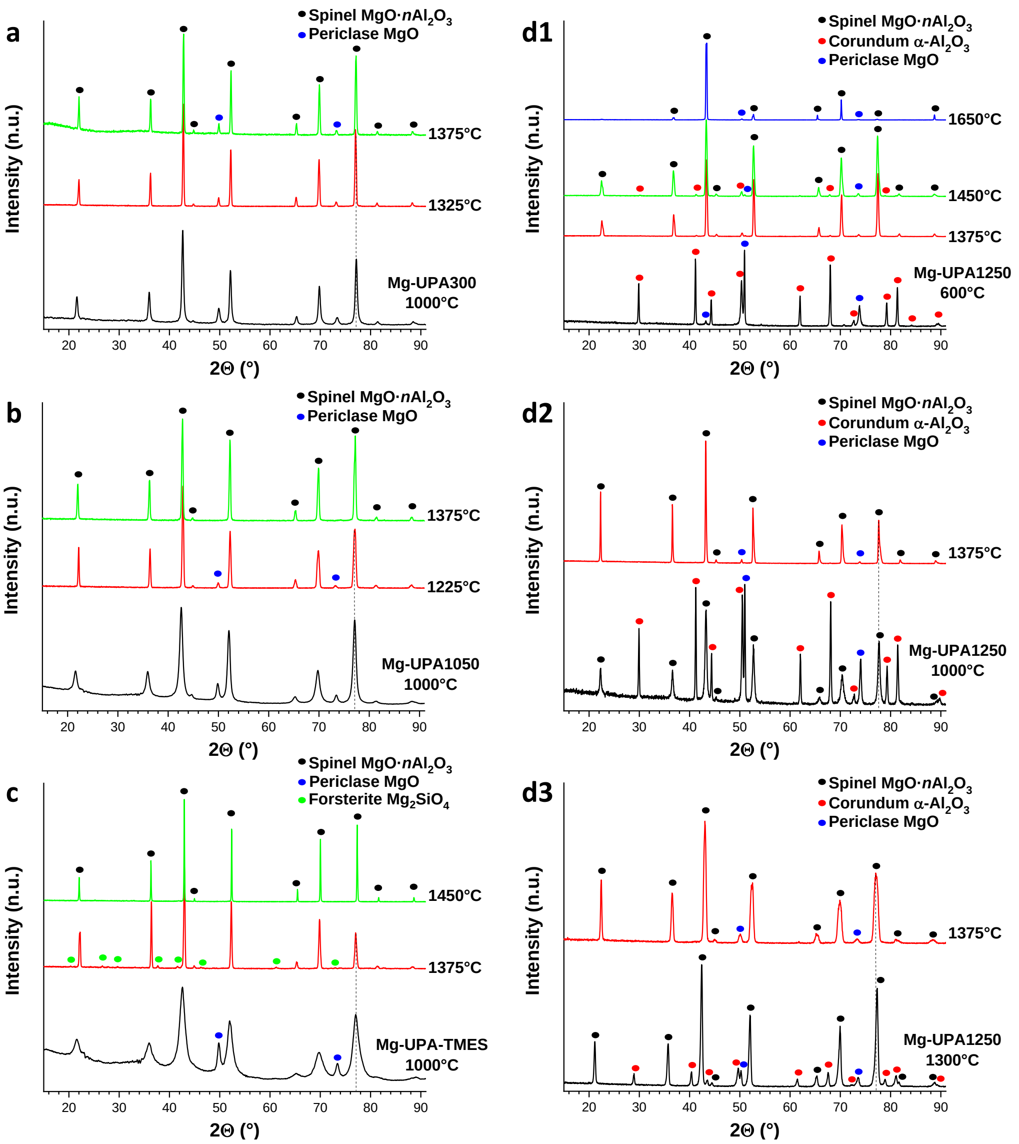

Figure 4.64: XRD patterns of the ceramics SPSed from the impregnation MAS precursors a)Mg-UPA300, b) Mg-UPA1050 and c) Mg-UPA-TMES calcined at 1000°C for 1 h, and d1-d3) Mg-UPA1250 treated at d1) 600, d2) 1000 and d3) 1300°C

Figure 4.65 presents the photographs of the ceramics SPSed at 1375°C. The materials made from a same Mg-UPAX powder at various T_d are identical by naked eye, hinting that **the visual aspect depends mostly on the precursor powder**. Only the **Mg-UPA300 samples** are partly **transparent** with a **brown/yellow tint**, while others are gray opaque materials. Dark spots can be seen on the ceramics with excess MgO remaining. The **reactive SPS** of Mg-UPA1250 treated at 600 and 1000°C resulted in samples with white spots, arising from inhomogeneous densification. The **Mg-UPA-TMES** samples have a **uniform aspect**.

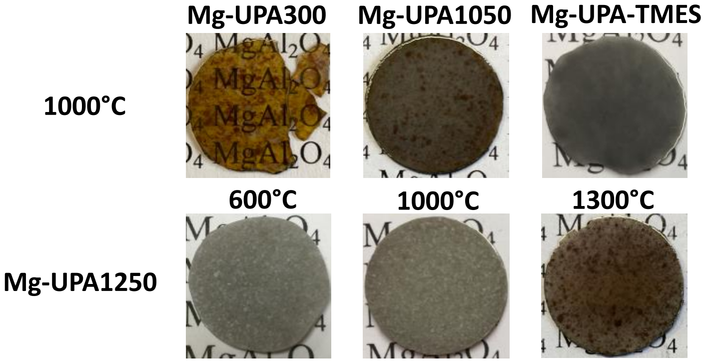

Figure 4.65: Photographs of the ceramics SPSed at 1375°C from the different impregnation precursors

The transmittance and absorbance spectra of the Mg-UPA300 ceramic SPSed at 1325°C are presented in *Figure 4.66*. The transmittance increases for **λ ≥ 500 nm**, with **$T_{il\text{-}600\ nm}$ = 21%** << 85% of HPSPSed S25CR powder. Indeed, the transparency is partly degraded by the dark spots, and a single phase precursor will lead to higher transmittance. In addition, the optical density curve reveals a **strong color center absorbing in the range 2-3.5 eV/350-620 nm**, close to the one observed for HPSPS ceramics (*Figure 4.53*), with an induced optical density **ΔOD = 0.88 at 2.74 eV** responsible for the low transparency in UV-low visible and the tint of the material. Such absorptions in $MgAl_2O_4$ ceramics are reported for **V-type centers** [38, 56] or **Mn impurity** localized in octahedral sites [59, 389]. The latter case seems less probable in this case.

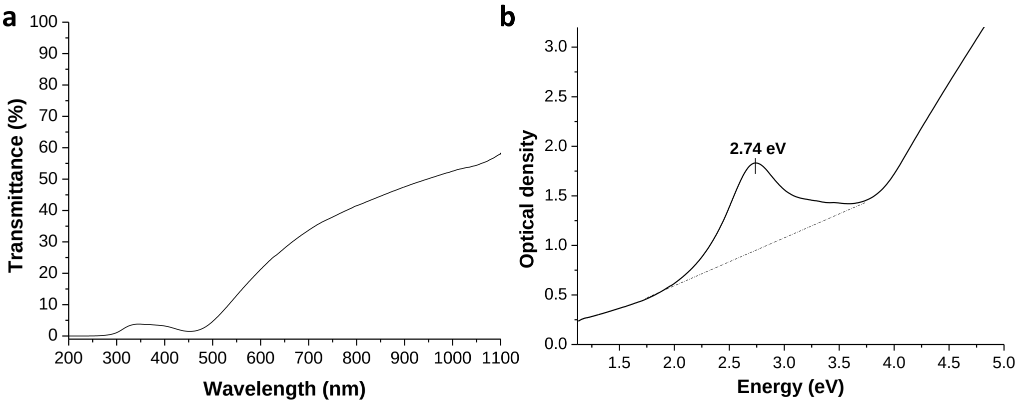

Figure 4.66: a) Transmittance and b) absorbance spectra of the ceramic SPSed at 1325°C from Mg-UPA300

The SEM of the Mg-UPA300, Mg-UPA1050 and Mg-UPA1250 ceramics are presented in *Figure 4.67*. The microstructure of the Mg-UPA300 ceramics (*Figure 4.67.a1* and *a2*) consists of mixed **grains of MAS** (bright) and **another phase** (dark). The density of dark grains varies locally, and highly concentrated areas are associated with microcracks. The MAS grain size is **0.75 and 1.0 µm** at 1325 and 1375°C. For Mg-UPA1050 and Mg-UPA1250 (*Figure 4.67.b* and *c1-c3*), the microstructure is classical except for the defects (see *Figure 4.68*), with GS = **0.50 µm** for Mg-UPA1050 at 1225°C, and **GS = 1.0, 1.5 and 0.2 µm** for SPS at 1375°C of Mg-UPA1250 treated at 600, 1000 and 1300°C. We note that the **reactive sintering favors the grain growth** due to the exothermic reaction providing energy to activate the coarsening mechanisms.

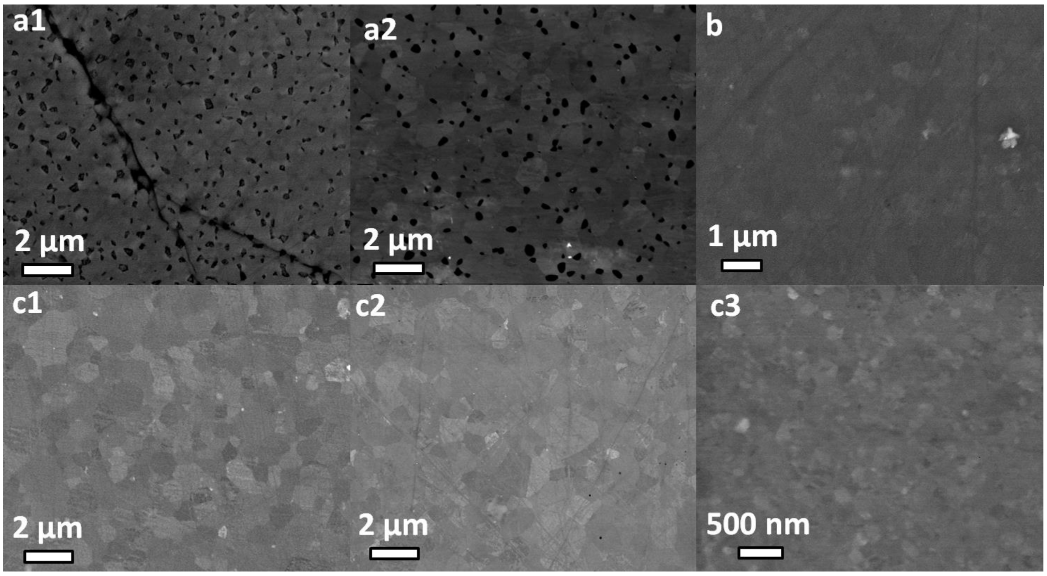

Figure 4.67: SEM of the ceramics SPSed from a1,a2) Mg-UPA300 at a1) 1325 and a2) 1375°C, b) Mg-UPA1050 at 1225°C and c1-c3) Mg-UPA1250 pre-treated at c1) 600, c2) 1000 and c3) 1300°C and SPSed at 1375°C

We investigated the microstructural defects in these ceramics by SEM (*Figure 4.68*) and EDX elemental mapping (*Figure 4.69* to *Figure 4.*71) to elucidate the causes for our materials opacity. The low magnification SEM reveals inhomogeneous microstructures. The materials densified through **non-reactive SPS** (*Figure 4.68.a1*) present **large darker areas** (200-500 µm) with mixed grains of MAS and another phase, while **reactive SPS** produces ceramics with **high local porosity**. These large defects are assessed to be responsible for the **dark and white**, respectively, **opaque spots** observed by naked eye. Some typical but less systematic defects are presented in *Figure 4.68.b-d*: **filament-like clusters** of 150-500 nm dark-phase grains (*Figure 4.68.b*), **rod-like clusters** of 1-5 µm dark-phase grains, up to 150 x 20 µm in dimensions (*Figure 4.68.c*) and **in-relief islands-like** of small brighter-phase grains (*Figure 4.68.d*).

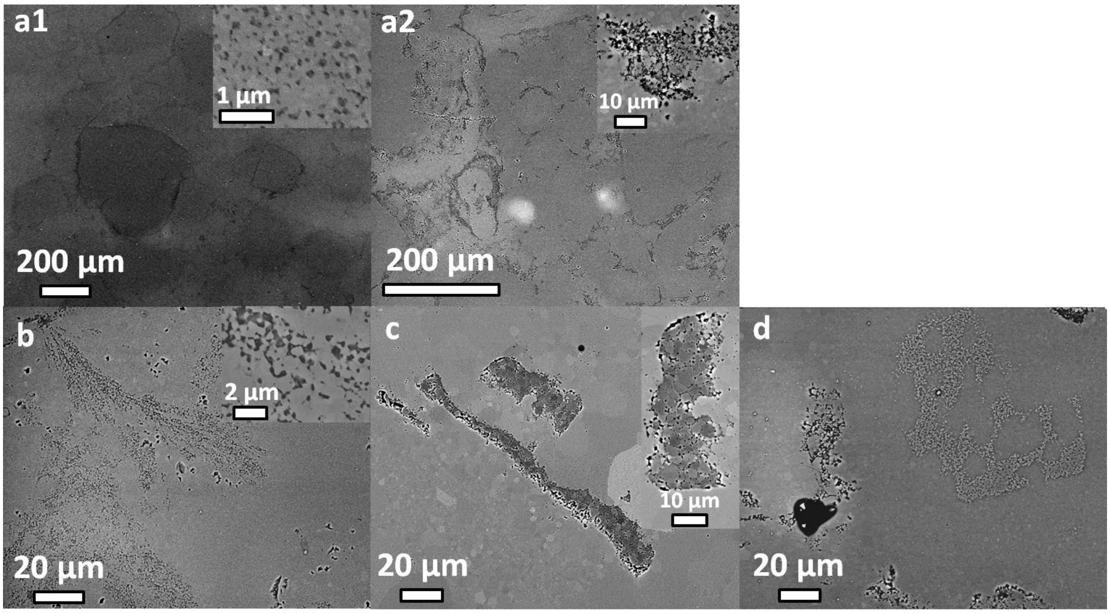

Figure 4.68: SEM of Mg-UPA ceramics: a1,a2)general view (magnification in inset) of samples obtained through a1) non-reactive and a2) reactive SPS, and b-d) typical microstructural defects encountered

The EDX elemental mapping of the defects presented in (*Figure 4.68*) are shown hereafter. The **dark phase** observed in 200-500 µm large areas and in filament-like clusters are **MgO grains mixed together with MAS grains** (*Figure 4.69*). The large concentration of these defects is due to the excess MgO in the precursors, thus should be easily reduced/suppressed by adjustment of the composition.

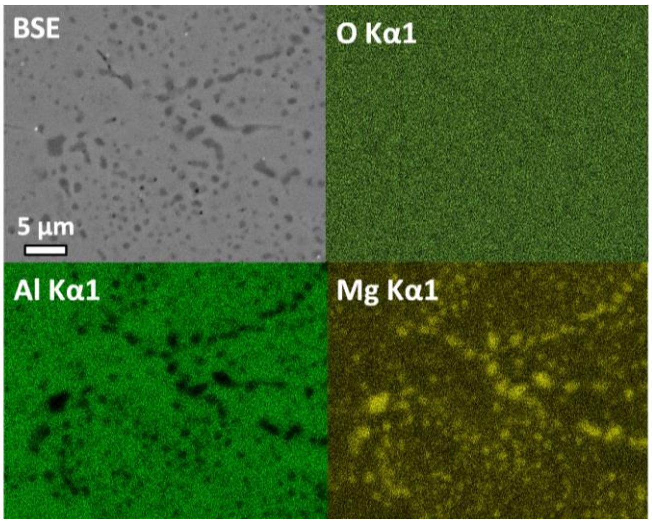

Figure 4.69: SEM and EDX elemental mapping of mixed bright and dark grains, observed in Mg-UPA ceramics

The **rod-like inclusions** of dark phase are also identified as **MgO dense clusters** (*Figure 4.70*), while the **in-relief island-like inclusions** are identified as **Al_2O_3 clusters** (*Figure 4.71*). These cluster defects are assumed not to arise from excess MgO or Al_2O_3, but from **incomplete mixing** of the precursor oxides.

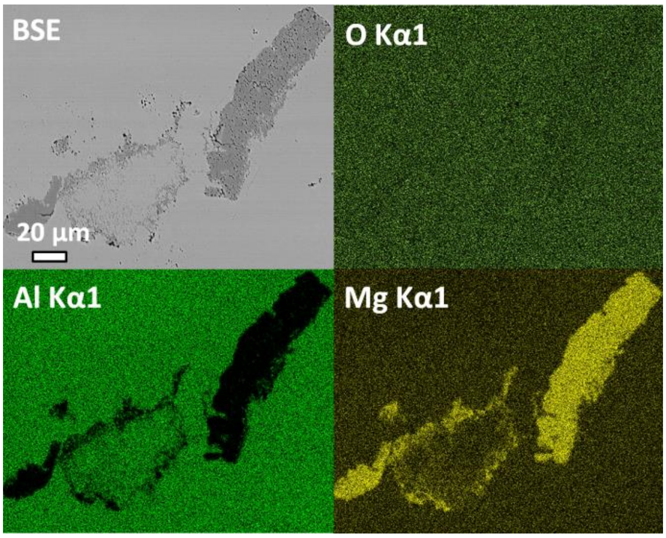

Figure 4.70: SEM and EDX elemental mapping of a rod-like inclusion of dark phase, observed in Mg-UPA ceramics

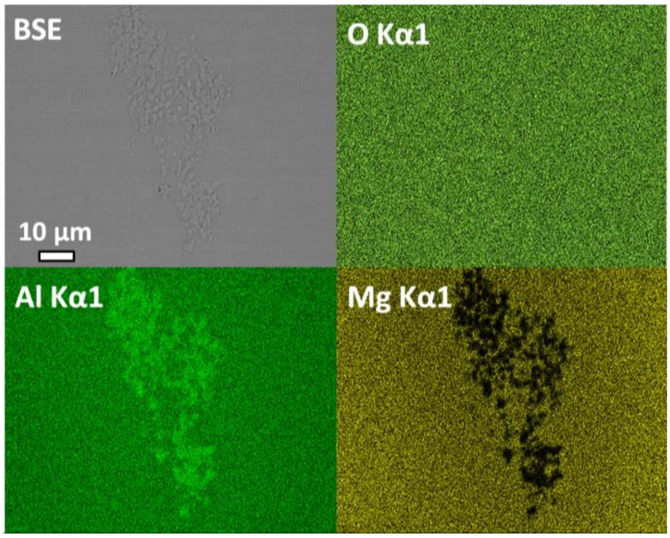

Figure 4.71: SEM and EDX elemental mapping of an in-relief island-like inclusion of brighter phase, observed in Mg-UPA ceramics

The microstructure of the **Mg-UPA-TMES ceramic**s is presented in *Figure 4.72*, with EDX elemental mapping in *Figure 4.73*. **No large defects** are observed for materials prepared from this precursor powder, in comparison with the other Mg-UPA precursors. However, **~300 nm precipitates** are observed **at the boundaries** of the ~4 µm MAS grains, which EDX reveals to be **Mg_2SiO_4 forsterite precipitates**.

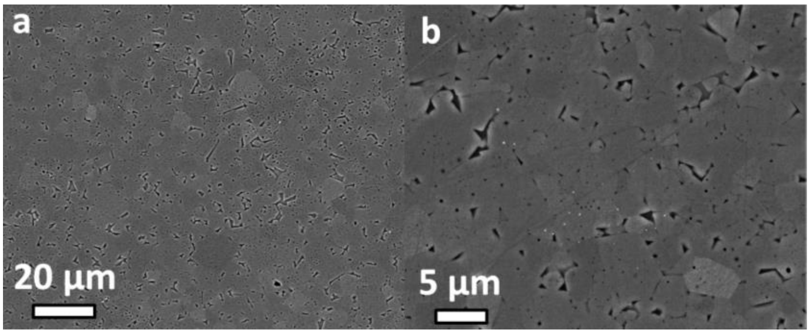

Figure 4.72: SEM of the Mg-UPA-TMES ceramic SPSed at 1450°C: a) low magnification and b) high magnification

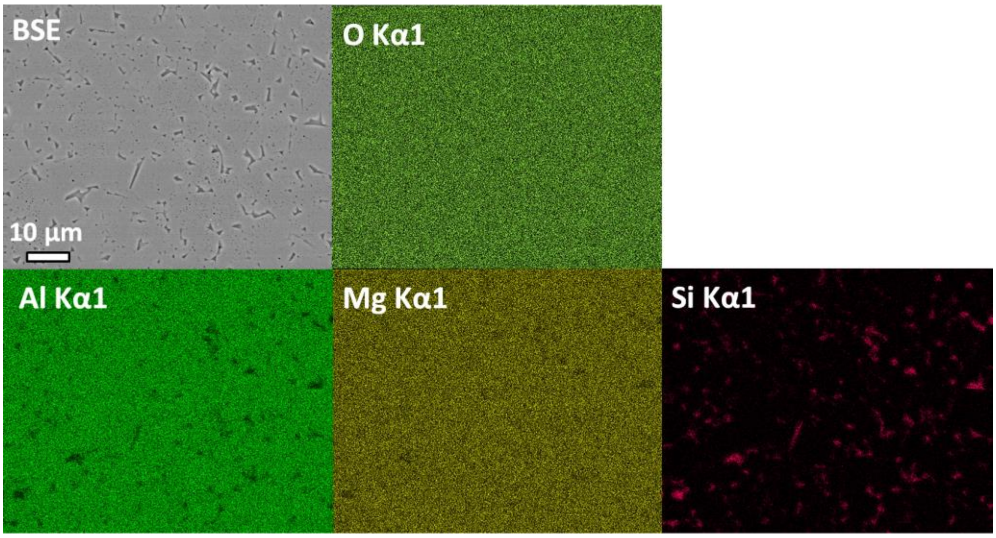

Figure 4.73: SEM and EDX elemental mapping of the Mg-UPA-TMES ceramic sintered at 1450°C

Finally, we investigated the **effect of pressing** on the microstructure. *Figure 4.74* shows micrographs of the cross section (parallel to pressing direction) of the ceramic sintered at 1450°C from the Mg-UPA300 precursor calcined at 600°C. As for what was found for the pressure effect on Sasol ceramics (*Figure 4.37*), a **strong anisotropy of the defects** is observed. For example, as the most concentrated defect, the **MgO grains are organized perpendicularly to the pressing direction** in filament-like clusters of grains with length up to 200 µm with a **ratio length/thickness of ~7**. However, it can be seen in high magnification in *Figure 4.74.b* that the grains of both MAS and MgO phases appear to be isotropic in size and shape. Hence, the grains themselves are not impacted by the pressing effect.

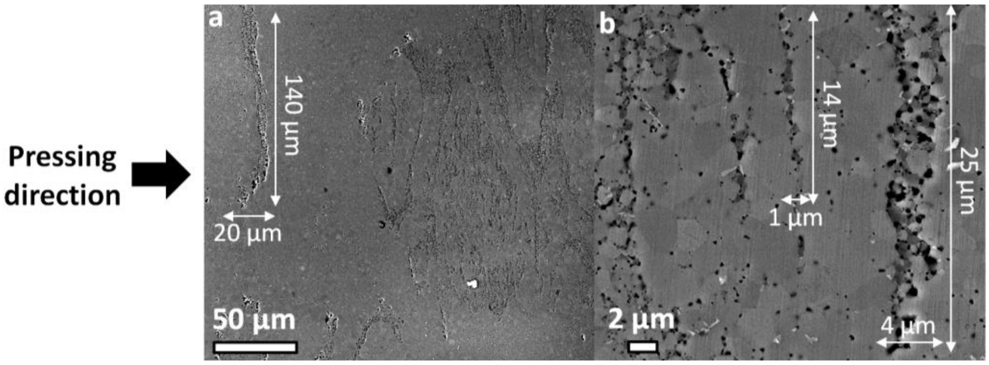

Figure 4.74: SEM of the cross section of Mg-UPA1250 ceramic SPSed at 1450°C, with a) low and b) high magnification

3. Conclusion

In this sub-chapter, we carried out a **preliminary study on the SPS of the MAS precursors synthesized *via* polyol and impregnation routes** (*Chapter 3*) in order to assess their sinterability.

For the polyol precursors, we sintered **single-phased spinel $MgO{\cdot}nAl_2O_3$ with $n = 0.716$, 1 and 5**. In every case, **MAS phase demixtion and MgO loss** was observed during SPS, which we attributed to a **particularly high reactivity**. All the polyol materials are **fully opaque**, and **eutectic microstructures** are obtained for $n \geq 1$. Further experiments are required to better understand the phenomenology behind MAS demixtion/MgO loss, and assess the possibility to fabricate transparent MAS ceramics with polyol powders.

We compared the sinterability of several precursors synthesized from impregnation of different UPA hosts. All the sintered impregnation powders presented a 5-7 wt% excess of MgO due to improper synthesis preparation, which was considered a minor inconvenience for this preliminary study. In comparison with SPS of polyol synthesized powders, **no phase demixtion or MgO loss** was observed during SPS of the impregnation precursors. However, only the ceramics fabricated from **MAS synthesized from amorphous UPA host presented a certain transparency** with $T_{il\text{-}600\ nm}$ = 21%. The **finest microstructure with grain size of 200 nm** was obtained for the ceramics prepared from the **α-Al_2O_3 impregnated precursor**. The **reactive SPS favors the densification**, but leads to **heterogeneous microstructure** with larger grain size. Several types of microstructural defects detrimental to the transparency have been observed, related to the excess MgO in the powder or to an **incomplete mixing of the reacting precursor** prior to calcination.

IV. Post-densification treatments: air annealing and hot isostatic pressing

This sub-chapter is dedicated to the **investigation of post-densification treatments** on the ceramics features. The studied treatments are the **thermal annealing in air** and **successive hot isostatic pressing** of the densified materials. This study is aimed to assess the potentiality of such treatments to improve the properties, in particular the transparency of magnesium aluminate spinel ceramics densified by SPS.

The **post-densification air annealing** has been reported in many occurrences to have a great impact on the properties of $MgAl_2O_4$ ceramics sintered by HP, HIP and SPS [266, 285, 286]. In particular, all the cited references claim that **treatments at T ≥ 1000°C for typically 1 h** allow improving the transparency mostly due to suppression of carbon contamination. For this reason, we attempted air annealing on our ceramics.

Based on literature, we first performed successive 1 h annealing at increasing temperature to determine the lowest effective temperature. Such treatments had no effect on transparent samples, but a **strong apparent impact on opaque blackened ceramics** which were **whitened**. However, a slight repolishing revealed that the annealing was only **effective within the very surface**, as illustrated in *Figure 4.75.*

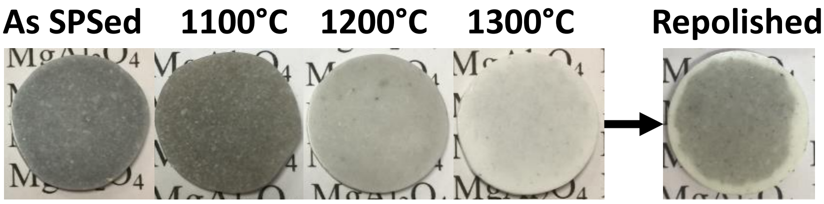

Figure 4.75: Photographs of a MgUPA1250 ceramic successively annealed for 1 h at 1100, 1200 and 1300°C, then repolished

Therefore, we **investigated the annealing duration** for temperatures of 900-1250°C (not shown), which revealed that **long heat treatments of 100 to 200 h**, depending on the sample thickness (from 0.5 to 1 mm), are required to treat the materials through their whole thickness due to the slow oxygen diffusion, regardless of the temperature of annealing. It was also noted that once reached the duration for homogeneous annealing at a given temperature, longer treatments have no further effect as a metastable state is attained.

1. Effect of the air annealing on the optical properties

The optical analysis of the **influence of the air annealing** on ceramics SPSed from Sasol, S25CR-3MS and polyol/impregnation precursors are presented in *Figure 4.76, Figure 4.77* and *Figure 4.78*, respectively.

Figure 4.76 shows the effect of annealing on a Sasol ceramic SPSed at 1450°C for 10 min with a heating rate of 100°C/min and applied pressure of 80 MPa. The photographs show the progressive **dissipation** of the black coloration with annealing temperature up to **1150°C for 200 h**; we note that a 100 h treatment at 1150°C was insufficient for full whitening of the ~1 mm-thick sample. Meanwhile, the material is gradually **opacified**. Indeed, the 1100°C annealing slightly improved the transmittance in the IR, but degraded it in the visible. The effect is even stronger after the 1150°C treatment. The relative density of the material decreased from 99.3% after SPS to 98.5% after annealing at 1150°C, hinting for the formation of porosity. Similar annealing effects were observed for Sasol ceramics consolidated with other SPS conditions.

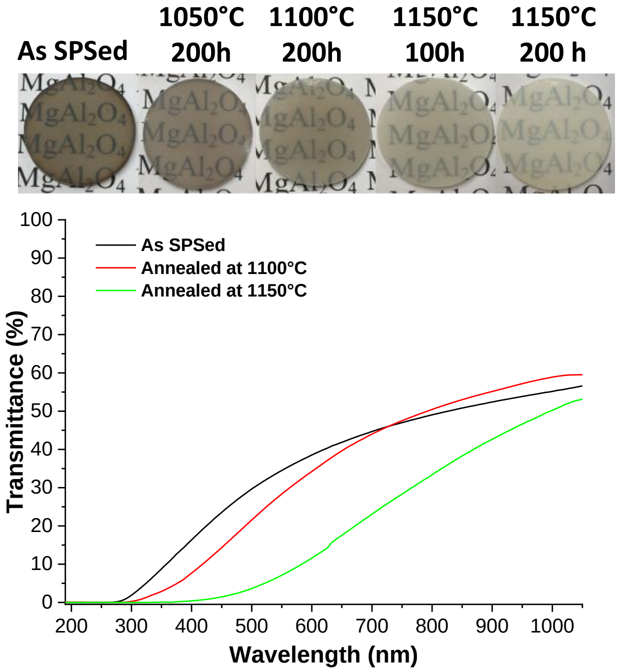

Figure 4.76: Photographs and transmittance spectra of a Sasol ceramic successively annealed for 200 h at 1050, 1100 and 1150°C

Figure 4.77.a shows the effect of 200 h annealing on a S25CR-3MS ceramic SPSed at 1275°C for 20 min with 10°C/min heating rate and applied pressure of 80 MPa. The light darkening seems to be suppressed for **annealing at 1100°C**, lower temperatures having arguable effect on the coloration. However, **cloudiness** of the sample is progressively induced (emphasized by photographs on black background), such as after treatment at 1100°C, the material is only slightly **translucent**. *Figure 4.77.b* shows that for a same annealing treatment, a **similar effect** on optical properties is induced **independently of the P-T$_d$ sintering conditions**. It should be highlighted that the ceramic SPSed at 1035°C-500 MPa shows the same slight cloudiness as the other samples when treated at 1000°C, *i.e.* **just below its sintering temperature**.

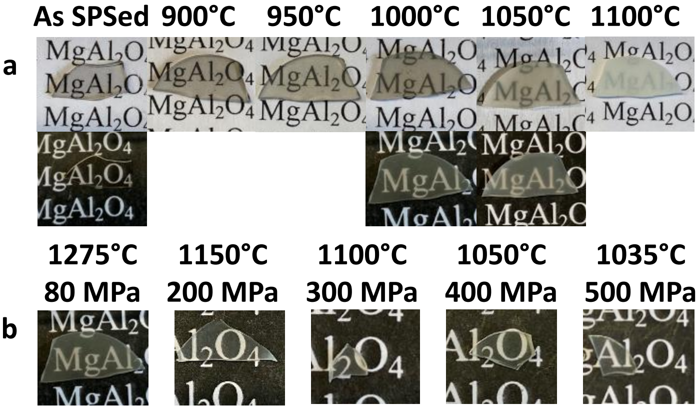

Figure 4.77: Photographs of S25CR-3MS ceramics a) SPSed at 1275°C and 80 MPa successively treated for 200 h at 900-1100°C and b) SPSed at different P-T$_d$ conditions treated at 1000°C for 200 h; black background is aimed to emphasize cloudiness

The effect of the annealing on the ceramics prepared from the impregnation and polyol precursors are presented in *Figure 4.78*. A detailed presentation is showned for the transparent Mg-UPA300 ceramic. We observe that the **initial coloration progressively disappeared** with annealing in the range **900-1100°C**, temperature at which the material became **opaque**. The treatments performed on the ceramics fabricated from the other precursors **systematically led to whitening** with a **progressive translucency** developed for **the Mg-UPA1250 and Mg-UPA-TMES materials**. Interestingly, the temperature of treatment required for full whitening depends on the precursor, with notably the **$MgO\cdot0.716Al_2O_3$ polyol ceramic remaining dark up to 1150°C**. Since these colorations were assigned to structural defects, these results indicate that different defects are formed during SPS depending on the sintered precursor.

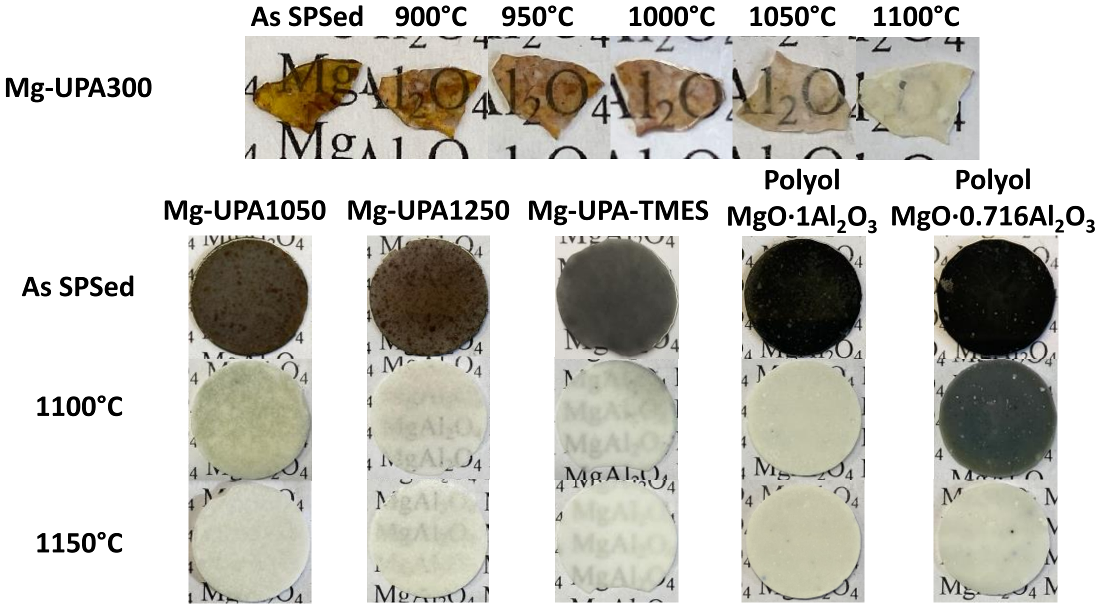

Figure 4.78: Photographs illustrating the annealing effect on ceramics prepared from impregnation and polyol precursors

2. Effect of the air annealing on the structural properties

The evolution of the structural properties through annealing has been investigated by XRD and Raman spectroscopy, in order to assess the influence of the treatments on phase composition and structural defects.

For the examples of Sasol and Mg-UPA300 ceramics presenting a minor MgO phase, XRD revealed **no noticeable effect** after 200 h treatments up to 1150°C, as the cell constants and phase composition remained unchanged. In particular, the **excess MgO has not been incorporated into MAS** through the annealing.

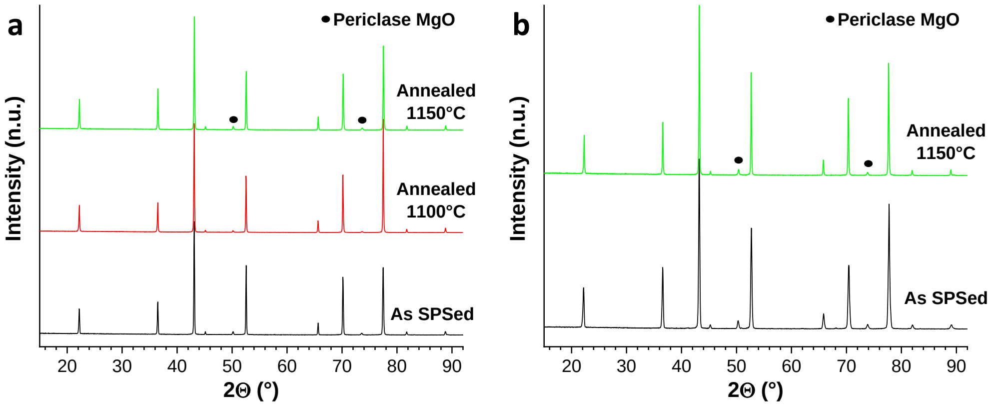

Figure 4.79: XRD patterns evolution with annealing of ceramics SPSed from a) Sasol at 1450°C and b) Mg-UPA300 at 1325°C

Raman analyses were performed to investigate the evolution of the spinel signature through annealing for ceramics SPSed from Sasol and S25CR-3MS precursors (*Figure 4.80*). In both cases, the Raman spectra remained unchanged after treatment up to 1250°C. In particular, the modes arising from antisite defects (375 cm^{-1}, 727 cm^{-1}) kept the same intensities, hinting that **the inversion degree is conserved** upon annealing.

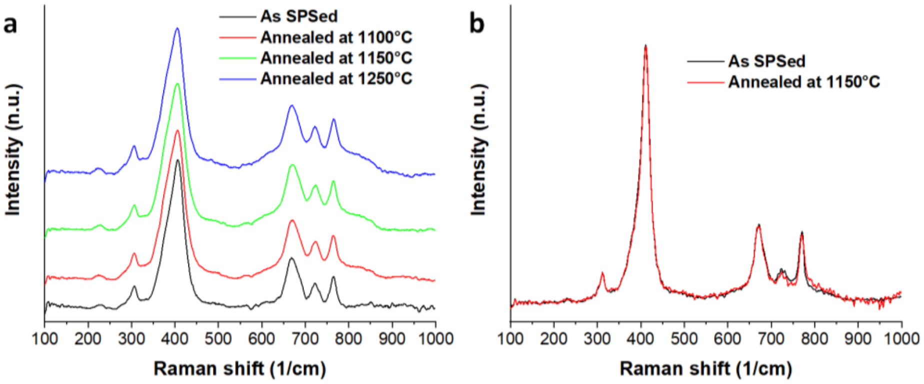

Figure 4.80: Raman spectra of $MgAl_2O_4$ signature through annealing for ceramics prepared from a) Sasol at 1500°C, 3 min with 100°C/min heating rate and 80 MPa and b) S25CR-3MS at 1300°C, 20 min with 10°C/min heating rate and 80 MPa

3. Effect of the air annealing on the microstructural properties

The evolution of the microstructure through thermal treatment is evaluated for Sasol, S25CR-3MS and Mg-UPA300 ceramics in *Figure 4.81.a*, *b* and *c*, respectively. It is remarkable that **the microstructure appears almost unchanged** after the annealing, and in particular **no grain growth** can be observed.

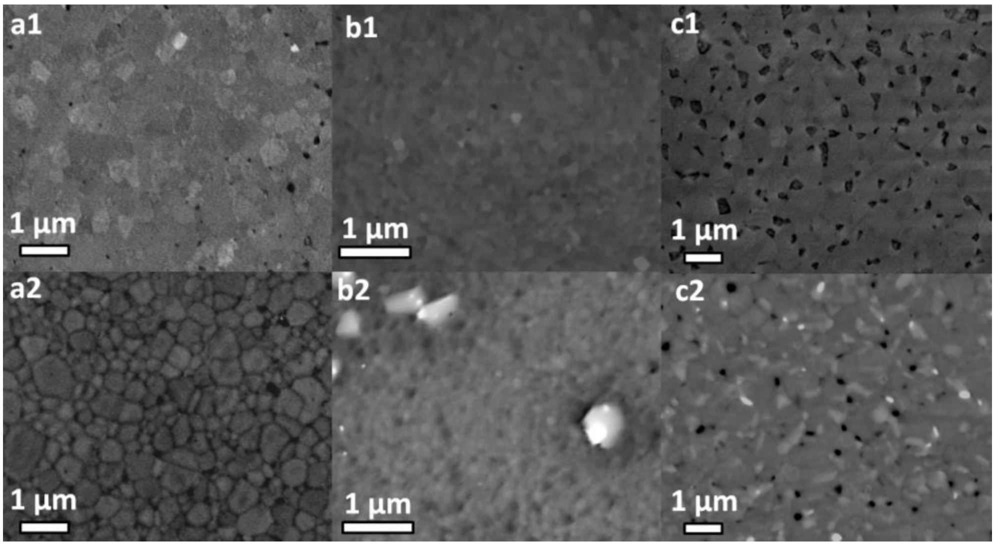

Figure 4.81: SEM micrographs of ceramics SPSed from a1,a2) Sasol at 1350°C, 280 MPa, b1,b2) S25CR-3MS at 1035°C, 500 MPa and c1,c2) Mg-UPA300 at 1325°C, 80 MPa, a1,b1,c1) as SPSed and annealed for 200 h at a2) 1150, b2) 1000 and c2) 1050°C

The grain size distributions (GSD) of these Sasol and S25CR-3MS ceramics in *Figure 4.82.a* and *b*, respectively, confirm that virtually **no coarsening** occurred during the post-densification treatment. It is very interesting to note that the grain size remains unchanged for the S25CR ceramic SPSed at 1035°C for 20 min and annealed at 1000°C for 200 h. In constrast, the GSD evolution through annealing of a Sasol ceramic SPSed at 1500°C for 3 min, with much bigger initial grain size, shows **a great coarsening effect at 1250°C far below its T_d** (*Figure 4.82.c*). Hence, it can be deduced that the annealing effect on microstructure is not dependent on the difference between sintering and annealing temperatures, but rather on the **sole annealing temperature**, allowing or not the activation of the coarsening mechanisms at a given grain size.

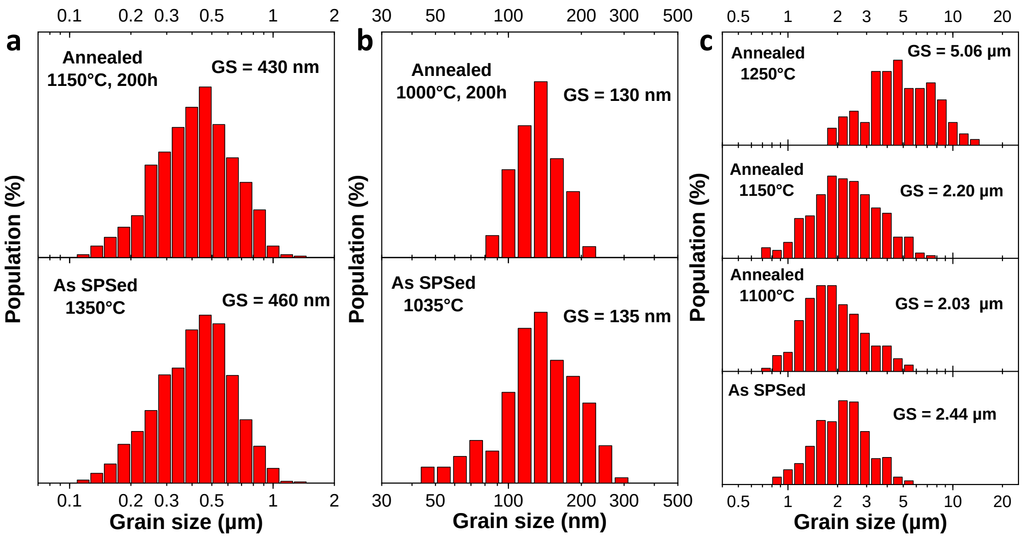

Figure 4.82: Grain size distribution (GSD) evolution through annealing of MAS ceramics prepared from a) Sasol SPSed at 1350°C and 280 MPa, b) S25CR-3MS SPSed at 1035°C and 500 MPa and c) Sasol SPSed at 1500°C and 80 MPa

Figure 4.83 shows the defects induced by annealing for the ceramics analyzed in *Figure 4.81*, and most likely responsible for the loss of transparency. After annealing at ≥ ~1150°C, Sasol ceramics' surfaces present **15-100 µm circular and in-relief blisters** with ~10-15 blisters/mm^2 (*Figure 4.83.a1*), surrounded by a **crown of disrupted microstructure** (*Figure 4.83.a2*). BSE (*Figure 4.83.a3*) reveals the microstructure to be locally fractured, with a high density of pores. These blisters seem to arise from the **microstructure bursting out** from the inside of the ceramic, which we believe has been caused by the **oxidation of the carbon phases entrapped during SPS**, forming CO_2 gas in the ceramics. The solid-to-gas transition leads to high local pressure exceeding the stress bearable by the microstructure, which eventually bursts to release the gas. Morita *et al.* [53] also observed the conversion of $C_{(s)}$ to $CO_{2(g)}$ through annealing, leading to the formation of pores and opacification, but it was assumed that the gas remained entrapped in the materials.

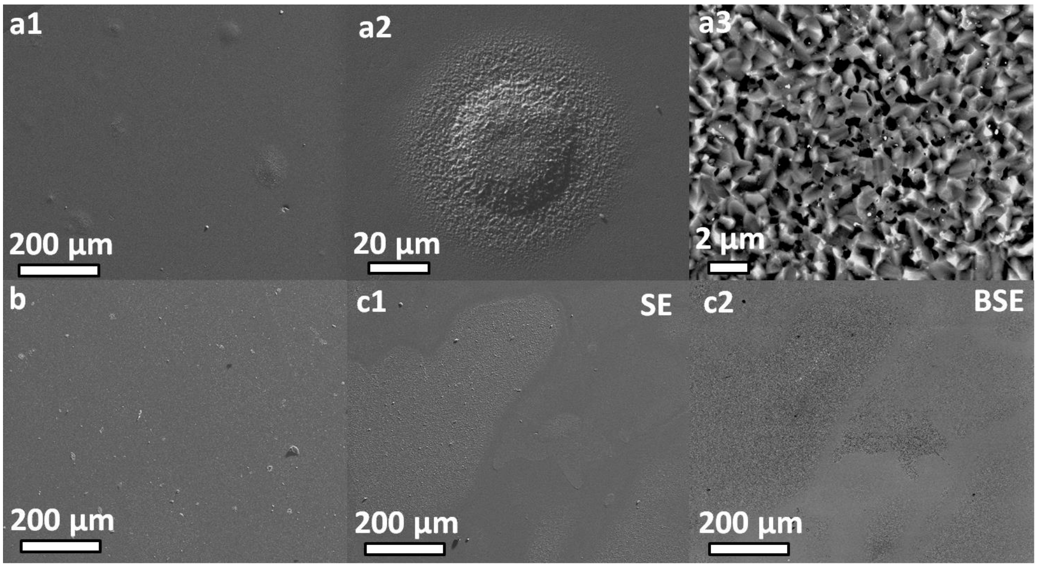

Figure 4.83: SEM micrographs of the microstructural defects induced by annealing in ceramics SPSed from a1-a3) Sasol at 1350°C, 280 MPa, b) S25CR-3MS at 1035°C, 500 MPa and c1,c2) Mg-UPA300 at 1325°C, 80 MPa

No blistering occured in materials prepared from other precursors allowing lesser carbon contamination. However, other defects were observed. Heat treatments of S25CR-3MS ceramics do not induce major or large defects (*Figure 4.83.b*); the opacification is attributed to the formation of **small pores at grain**

junction due to the different thermal dilatation of the grains depending on crystal orientation. The annealed Mg-UPA300 ceramic (*Figure 4.83.c1* and *c2*) presents very large **in-relief areas** (SE), which appear to be **porous** (BSE), probably due to the difference of thermal dilatation between MgO and MAS grains.

4. Effect of the air annealing on the ordering of the carbon contamination

The suppression of the carbon contamination through annealing is not investigated in this work, as the matter has been focused on in many studies [53, 285, 286, 301]. However, some aspects of the effect of heat treatment on the carbon contamination were not discussed elsewhere, and therefore will be addressed here.

As mentioned above, in highly contaminated samples showing strong dark coloration, long annealing (≥ 100 h) at high enough temperature allows suppression of the carbon phases. This process is very long due to the low kinetic of oxygen diffusion through the MAS material, required for carbon oxidation. However, other **annealing effects on carbon could arise from thermal effect**, and thus be independent of the oxygen diffusion: in that case, the influence of the annealing should be observed for much shorter treatments.

In order to better illustrate such effect, we used samples SPSed with conditions leading to a **peculiar carbon impurity**. In several instances, a short processing at 1450°C for 0-3 min with 100°C/min heating and cooling rates resulted in **white and cloudy** samples, **strongly darkened by short annealing at 1000°C** (*Figure 4.84.a*). The same SPS conditions often resulted in **dark samples**, used as reference for comparison.

Such samples were analyzed by Raman spectroscopy to follow **the evolution of the nature of carbon contamination with annealing** (*Figure 4.84.b*). The white, darkened and dark specimens exhibit the carbon signature: the **D-, G- and D'-bands at ~1360, ~1590** and **~1620 cm^{-1}**, respectively. The G-band is the primary mode of graphitic carbon arising from sp^2 C-C bond, while D- and D'-bands are related to **disorder in the sp^2 network** [92, 390]. The Raman spectra of the darkened and dark samples are close, while for the white material the G-band is broaden due to disorder. The intensity ratio I_D/I_G used to estimate **the degree of disorder** in the carbon phases is **~28, 1.44 and 1** for the white, darkened and dark samples, respectively. We assume that **the highly disordered carbon** for the white sample is responsible for the absence of darkening. We believe the fast sintering and cooling did not let time for carbon, vaporized from the graphite die/paper and condensed within the pores, to be organized in graphitic phase, which was allowed by the annealing and induced the darkening of the sample. It should be noted that the Raman modes of $CO_{2(g)}$ at 1285 and 1388 cm^{-1} [391] are absent, confirming that the carbon has not been oxidized during the air annealing.

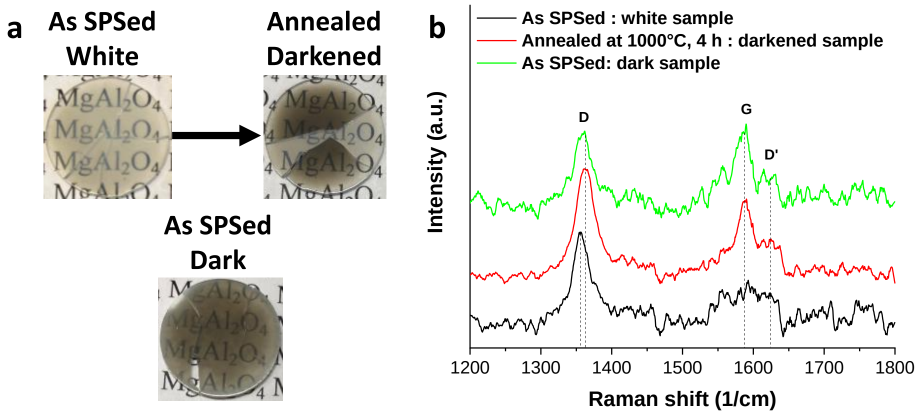

Figure 4.84: a) Photographs and b) Raman spectra of S25CR-3MS ceramics (1450°C with 100°C/min, no dwell) white after SPS and darkened through quick annealing at 1000°C for 4 h, and comparison with a dark ceramic sintered in the same conditions

The important information provided by this analysis is that the **annealing provokes the organization of the carbon contamination** occurring during SPS, and induces a stronger darkening of the materials. Longer treatments allow oxidation and vaporization of the carbon, forming large pores resulting in opacification. Thus, it can be concluded that annealing of SPSed MAS samples is not efficient to improve their properties.

5. Influence of hot isostatic pressing (HIP) on the ceramics

In the last decade, several studies have investigated the improvement of the transparency of SPSed $MgAl_2O_4$ and Al_2O_3 materials through application of a following HIP treatment [201, 226, 347]. In particular, it was shown in [201] that the sample should be free of carbon contamination, which otherwise remained within the spinel ceramics after HIP treatment, limiting the benefits on optical properties.

The **post-densification HIP treatment** was experimented on a Sasol ceramic SPSed at 1450°C for 20 min with applied pressure of 80 MPa and a 10°C/min heating rate. In order to have the lowest possible carbon content prior to HIP, a **100 µm Ta foil was used to separate the powder** from the graphite paper to avoid direct contact between MAS and carbon parts during SPS, as Pt and Mo foils have been successfully used to suppress contamination [263, 264]. The as-SPSed sample presented a black tint anyway, which was suppressed with **limited opacification after annealing at 1100°C** (*Figure 4.85.a*). Then, a HIP treatment was applied with an **isostatic pressure of 350 MPa at 1400°C for 4 h**, resulting in an **uncolored ceramic**.

The transmittance analysis confirmed the sensible improvement of the transparency through the process (*Figure 4.85.b*). In particular, the combined air annealing and HIP treatment improved the **overall UV-visible transparency by 20-30 %** (see inset).

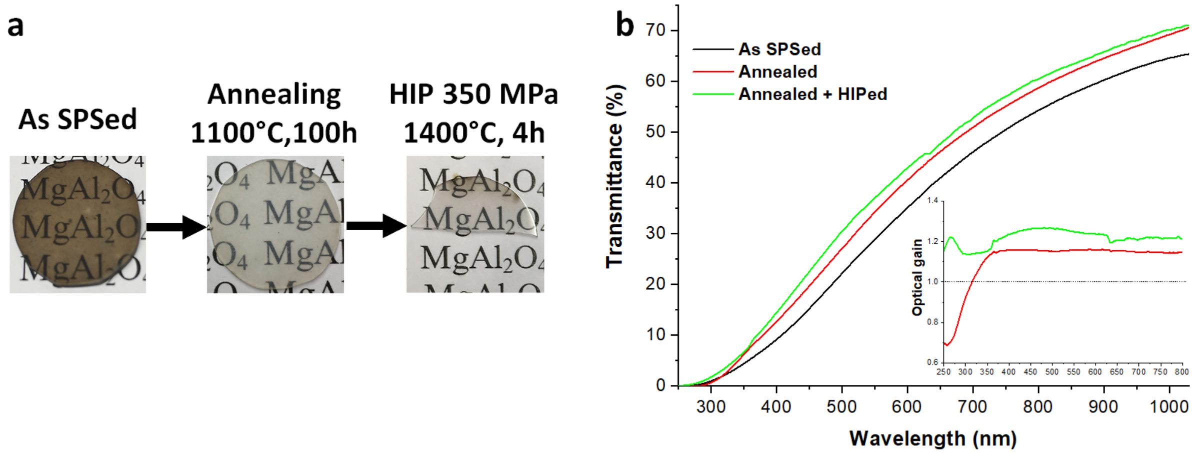

Figure 4.85: Evolution of the a) photographs and b) transmittance spectra of a Sasol ceramic SPSed at 1450°C for 20 min successively annealed at1100°C for 100 h and HIPed at 1400°C and 350 MPa for 4 h

The evolution of the microstructure and grain size distributions through the process is presented in *Figure 4.86*. It is remarkable that the **grain size appears virtually unchanged** through the whole process, and particularly during HIP at relatively high temperature. However, such observation was made for post-SPS HIP of alumina in [226], where grain growth only occurred above a **critical temperature of treatment**. It is believed that the thermal annealing in air improved transparency at high wavelength due to suppression of the limited carbon contamination, while the decrease in low wavelength is due to the formation of porosity, as it can be seen in *Figure 4.86.b*. The HIP treatment then allowed increasing further the transparency in the whole UV-visible range by **collapsing the newly formed pores** (*Figure 4.86.c*).

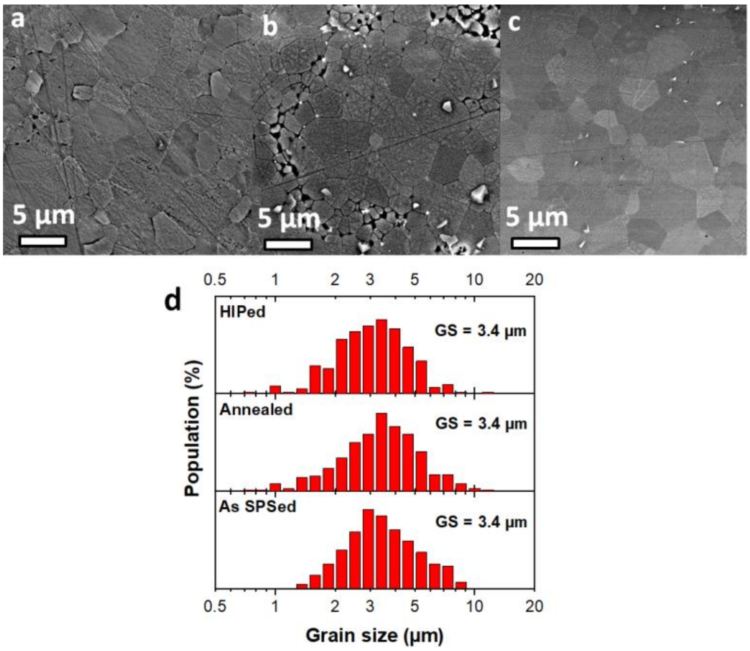

Figure 4.86: SEM micrographs of the Sasol ceramic a) as SPSed at 1450°C for 20 min, b) after annealing in air at 1100°C for 100 h and c) after HIP at 1400°C and 350 MPa for 4 h, with d) the evolution of the grain size distribution

6. Conclusion

In this sub-chapter, we investigated the influence of **post-densification thermal annealing in air and successive hot isostatic pressing treatments** on the ceramics features.

It was found that **short annealing** treatments (few hours) were insufficient to suppress the carbon contamination from SPS, but instead could lead to an increased degree of order in the carbon phases, resulting in **stronger darkening**.

Long annealing of ≥ 100 h are required for treatment through the whole thickness of the samples, due to limited oxygen diffusion kinetic in MAS. Then, **suppression of carbon occurs at ~1100-1150°C**, accompanied by formation of **channels of pores and blistering** during evacuation of the highly pressurized CO_2 gas formed. It was found that **no coarsening** of the grains occurred during annealing, even at temperature very close to the sintering one, and only temperature of treatment ≥ 1250°C activated the grain growth mechanisms.

An **additional HIP treatment** allows **increasing the transparency** by collapsing the pores induced by annealing, with **no grain growth** occurring for a 4 h treatment at 1400°C. However, limited improvement of the optical properties was noted, and further experiments are required to assess the potential of the treatment.

Finally, annealing on ceramics prepared from the sintering of polyol and impregnation precursors resulted in a whitening of the materials, due to the **healing of the highly concentrated structural defects**. In particular, annealing at ≥ 1100°C of the Mg-UPA1250 and Mg-UPA-TMES ceramics resulted in their **translucency**, which is a very encouraging result to pursue on their fabrication.

V. Investigation of Ta_2O_5 addition effect on the sintering of $MgAl_2O_4$

In this section, we investigate **the effect of Ta_2O_5 addition on the sintering of $MgAl_2O_4$**, with a particular focus on the sintering path and mechanisms and the interactions between the MAS host and the Ta-based particles.

The addition of compounds to the material precursor prior to sintering is indeed a very effective way to modify and/or control its properties and microstructure. The different types of additives, their effect and their acting mechanisms have been presented in *Chapter 1.IV.3.v.c*. In addition to traditional effects of additives, if **ionic/mixed conductors** are used with sintering processes involving electrical current like SPS, electrical effects can be observed and greatly modify the sintering mechanisms (ionic current, hot spots…) [80].

We choose to investigate Ta_2O_5 as an additive for $MgAl_2O_4$ sintering due to its interesting properties that could help better understand the phenomenology during spark plasma sintering. Ta_2O_5 properties include a wide band gap of ~3.9-4 eV, thus transparency in the NUV-Vis range [315, 316, 392], a high dielectric constant $\varepsilon = 25\text{-}100$ [314] and good thermal stability up to its melting point about 1900°C [392–394]. In particular, tantalum pentoxide materials have been shown to **easily form oxygen vacancies**, then taking a **characteristic black coloration** [388, 395]. This feature could allow evidencing electrical effects during SPS, due to the migration of oxygen vacancies from the anode to the cathode [255]. Ta_2O_5 has been used as an additive in multiple occasions, with different effect observed depending on the host material: grain growth hindering for SnO_2 [396] and KNN [397], abnormal grain growth for $BaTiO_3$ [398, 399] or reaction with the host promoting densification and coarsening for Al_2O_3 [400]. In our case, **reaction with $MgAl_2O_4$** can be expected considering the $MgO\text{-}Ta_2O_5$ and $Al_2O_3\text{-}Ta_2O_5$ binary systems.

The phase diagram of $MgO\text{-}Ta_2O_5$ presents the 3 distinct phases **$Mg_4Ta_2O_9$**, $Mg_3Ta_2O_8$ and **$MgTa_2O_6$** [393, 401–403] ; $Mg_3Ta_2O_8$ has been reported to be stable only between 1475 and 1675°C, $Mg_4Ta_2O_9$ and $MgTa_2O_6$ are stable up to their melting points at 1830°C and 1770°C, respectively [393]. The two stable phases $Mg_4Ta_2O_9$ and $MgTa_2O_6$ are optically transparent [401, 402, 404] and present excellent microwave dielectric properties (high quality factor and low dielectric loss) as well as heavy and fast scintillation properties [401, 402, 404]. These materials are also known to easily form oxygen vacancies as Ta_2O_5 [387, 404]. As for the $Al_2O_3\text{-}Ta_2O_5$ phase diagram, $AlTaO_4$ is the only known phase [405], forming at about 1050°C [406] and stable at least up to 1500°C [407]. So far, the information about this phase is restricted.

In this study, we first assess the **sinterability of pure Ta_2O_5** by SPS, after what we investigate its **effect as an additive on $MgAl_2O_4$ sintering**, with focus on the influence of the addition rate, the sintering temperature and applied pressure during SPS.

1. Sintering of pure Ta_2O_5

Due to its properties, Ta_2O_5 is considered as one of the best candidates for applications as a dielectric in microelectronics as well as for low loss anti-reflective layer for optical waveguides and electroluminescent displays [314]. It is generally used in form of powder, thin film or single crystal, while there are very few reports on the sintering of pure Ta_2O_5. The highest densification is reached through conventional sintering at 1300°C held for several hours, but the sintering kinetic is too slow to allow total suppression of the porosity, hence the material remains opaque [408]. So far, only the very fast laser sintering technique resulted in translucent Ta_2O_5 ceramics [392, 409], and in this optic SPS could also be an appropriate sintering process.

Ta_2O_5 exists in different crystalline forms: the **amorphous *a*-Ta_2O_5**, the orthorhombic **low temperature phase L-Ta_2O_5** and the tetragonal **high temperature H-Ta_2O_5**. The **reversible transition** from L- to H-Ta_2O_5 occurs **around 1350°C** with a large increase of volumic mass (from 8.18 to 8.47 $g.cm^{-3}$).

In this paragraph, we study the **influence of the SPS conditions on the Ta_2O_5 ceramics** fabricated from the sintering of L-Ta_2O_5 and *a*-Ta_2O_5 powders (characterized in *Chapter 2.II.2.ii*), and their **stability when subjected to post-SPS air annealing**. This preliminary study on pure Ta_2O_5 is considered important in order to fully understand its possible effects on $MgAl_2O_4$ sintering.

i. Influence of the sintering conditions

A preliminary study revealed that only the temperature T_d has a sensible effect on the sinterability of the Ta_2O_5 powders. The other conditions were set as P = 80 MPa, t_d = 20 min and α = 10°C/min.

The sinterability of both Ta_2O_5 powders has been evaluated by the relative displacement of the pistons during SPS in *Figure 4.87*. The **L-Ta_2O_5** is densified in a **single step** between **800 and 1170°C**, then a **decrease of the density** is observed for **T ≥ 1210°C**. The ***a*-Ta_2O_5** is densified in **several steps**. The densification begins at 600°C, **stops in the range 740-815°C**, before resuming. In the range **1090-1170°C**, the **densification rate drops**. A decrease of density is observed for this powder as well, for **T ≥ 1190°C**. It is worth noting that the densification *plateau* is reached at the same temperature in both cases, suggesting that the first *plateau* observed for *a*-Ta_2O_5 may correspond to the **crystallization to L-Ta_2O_5**.

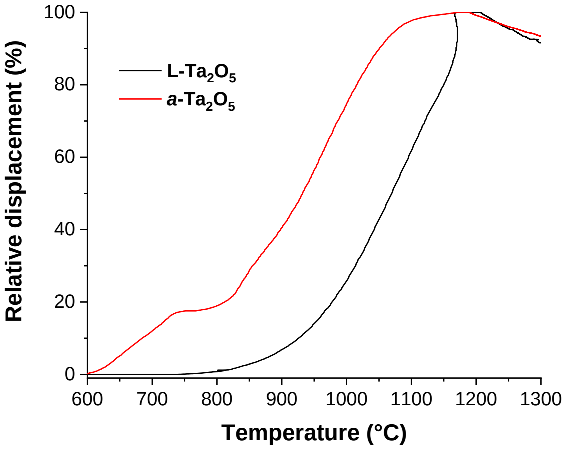

Figure 4.87: Relative displacement of the SPS pistons during sintering of L-Ta_2O_5 and a-Ta_2O_5 powders

The properties of the Ta_2O_5 ceramics SPSed from both powders are presented in *Table 4.13*.

Table 4.13: Influence of the sintering temperature on the properties of Ta_2O_5 ceramics SPSed with 10°C/min, 20 min, 80 MPa

Powder	**L-Ta_2O_5**							***a*-Ta_2O_5**		
T_d (°C)	**1000**	**1100**	**1200**	**1300**	**1350**	**1400**	**1450**	**1100**	**1200**	**1400**
Aspect	White, gray spots	Gray, black spots	Gray, black spots + black on: 28% thickness	54% thickness	Shiny black with thin bronze surfaces, large cavities			Shiny black		
Density (g.cm^{-3})	8.25(1)	8.43(2)	8.46(1)	8.45(1)	8.30(2)	8.34(2)	8.28(1)	8.40(1)	8.41(1)	8.50(2)
Grain size (µm)	0.54	-	0.95	1.26	-	160	160	0.56	1.00	2.82

The photographs, XRD patterns and Raman spectra of the ceramics prepared from the L- and *a*-Ta_2O_5 powders are presented in *Figure 4.88.a1-a3* and *b1-b3*, respectively. The L-Ta_2O_5 ceramics are **darkened with increasing sintering temperature** (*Figure 4.88.a1*). Below 1200°C, the materials are **white/gray with darker spots**. For T_d = 1200 and 1300°C, the samples are **black on 28% and 54% of their thickness**, respectively, **on the cathode side**. For T_d ≥ 1350°C, the ceramics are **fully black**, except for a thin bronze layer, with **large cavities**. The XRD (*Figure 4.88.a2*) shows that the **L-Ta_2O_5 phase is converted to the H-phase for $T_d \geq$ 1350°C**. The Raman analysis (*Figure 4.88.a3*) confirms these results; however, the spectra collected on the **black surfaces** of the 1200 and 1300°C samples (dashed curves) reveal the **conversion to H-Ta_2O_5 on the cathode side**, although far below the normal temperature of transition 1350°C. In addition, we attribute the spectrum of the bronze surface of samples SPSed at $T_d \geq$ 1350°C (dotted curve) to **tantalum carbide TaC_x** formed by reduction of the Ta_2O_5 layer in contact with the graphite insulating foil.

The *a*-Ta_2O_5 ceramics are **black and shiny** regardless of the sintering temperature (*Figure 4.88.b1*). The XRD (*Figure 4.88.b2*) show that the amorphous powder is **crystallized to the L-Ta_2O_5 phase** during sintering; it can be noted that the transition to the H- phase does not occur even at T_d = 1400°C, which could be due to the presence of Nb^{5+} impurity in the powder (common contamination in Ta_2O_5) [410]. Indeed, the Raman analysis (*Figure 4.88.b3*) confirms the conversion to L-Ta_2O_5. However, the Raman mode marked by an asterisk (*) at 150 nm, which appears only after sintering, does not belong to the normal L- phase signature and remains unidentified so far. It will be further discussed in the next paragraph.

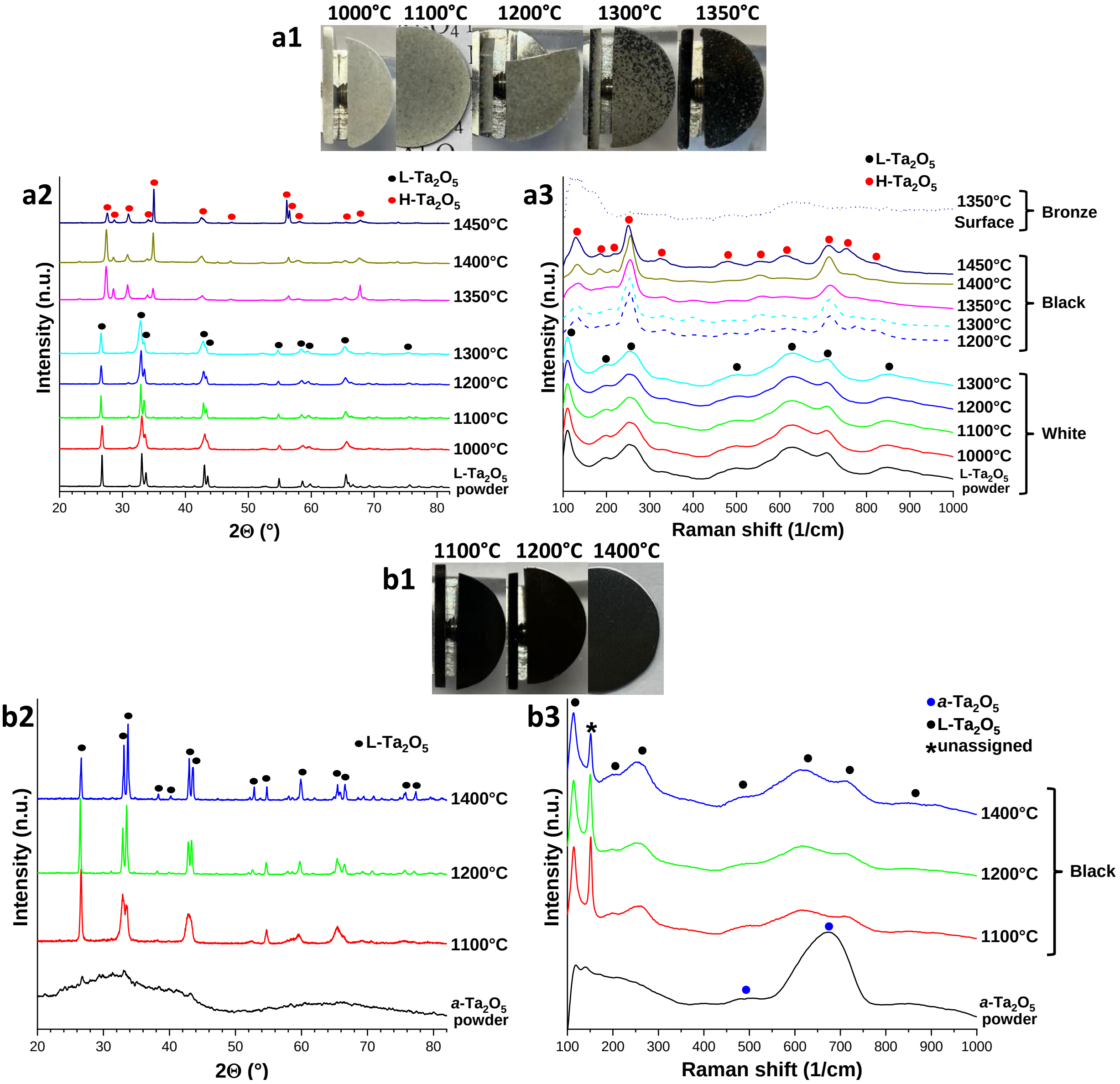

Figure 4.88: a1,b1) Photographs, a2,b2) XRD patterns and a3,b3) Raman spectra of the Ta_2O_5 ceramics SPSed at different temperatures from a1-a3) L-Ta_2O_5 and b1-b3) a-Ta_2O_5 powders

The **strong darkening** observed is of high interest for our study, as it unequivocally arises from **oxygen vacancies V_O^{2+} formed** during SPS. It should be noticed that it is not directly caused by temperature or a particular phase, but rather to **phase transition** independently of the initial and final phases. In addition, the phase transition and darkening **start from the cathode side and propagate toward the anode**. Darkening was reported for sintering of ionic/mixed conductors under electric field, *e.g.* flash sintering of CeO_2 [255] and $SrTiO_3$ [210] or SPS of CeO_2 [411], and attributed **to partial reduction** of oxides **at the positive anode** and **migration of V_O^{2+} toward the negative cathode**. It was shown to be caused by **nonthermal but electrochemical effects**, that can also lead to phase transformation [210]. However, **axial gradients of temperature** were shown to exist in SPS, with higher temperature at the cathode [411, 412]. Hence, both ionic migrations and temperature gradients could be responsible for the preferential reduction at the cathode.

SEM of the Ta_2O_5 ceramics is presented in *Figure 4.89.* Starting from L-Ta_2O_5, the grain size increases from 1000 to 1300°C, while the porosity decreases up to 1200°C (*Figure 4.89.a-c1*). In the cross section of the 1300°C sample's black side (*Figure 4.89.c2*), **GS is ~2 times bigger** with high density of **microcracks**; **abnormal grain growth** occurs locally, with **GS_{abn} > 10 µm**. At 1400°C and conversion to H-Ta_2O_5 (*Figure 4.89.d*), **rapid coarsening** occurs to **GS = 160 µm**. The **shrinkage** associated with phase transition results in a **network of cracks**, **disrupting the grain boundaries** and leading to embrittlement of the ceramics, with grains pulled out (large cavities observed by naked eye). The pores present at 1300°C became intragranular pores. For the *a*-Ta_2O_5 ceramics (*Figure 4.89.e-g*), GS increases monotonously with temperature, and low porosity remains even at 1100°C. No abnormal coarsening is observed at 1400°C, even so microcracks are formed. It is important to notice that the density of the ceramics is more important than the theoretical L-phase density (8.17 g.cm^{-3} [314]), then decreases after conversion to H- phase due to the numerous cracks.

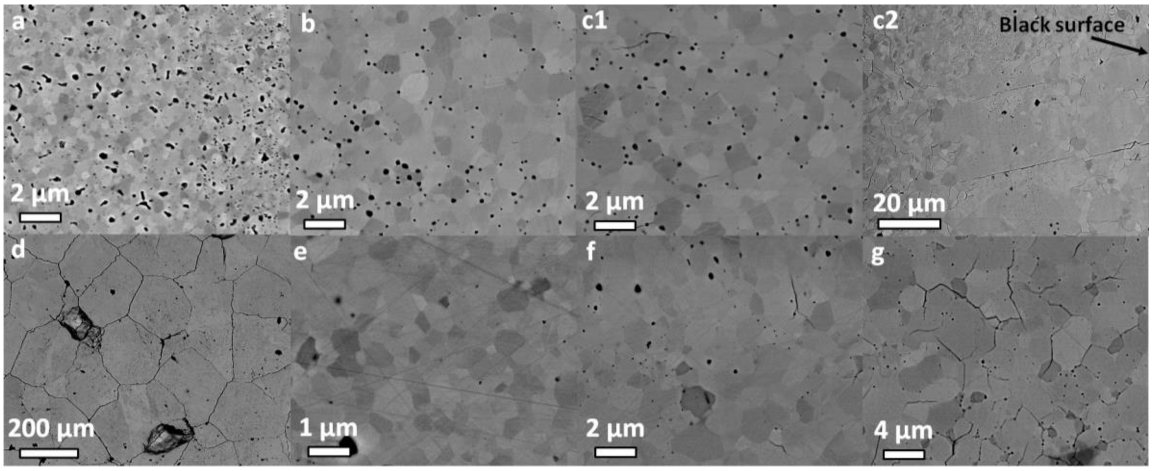

Figure 4.89: SEM of the Ta_2O_5 ceramics SPSed from a-d) L-Ta_2O_5 at a) 1000, b) 1200, c1,c2) 1300°C, with c2) showing the black surface of the sample in cross section, and d) 1400°C, and from e-g) a-Ta_2O_5 at e) 1100, f) 1200 and g) 1400°C

Some important remarks can be made from these results. *i)* SPS processing could not allow fabricating transparent Ta_2O_5 ceramics due to remaining porosity, thus the technique is not fast enough compared to laser sintering [392]. *ii)* The darkening effect evidences the **formation of oxygen vacancies** progressively spreading from the negative to the positive electrodes, accompanied by **phase transition** much below the normal temperature of transition; so far, it is uncertain which one leads to the other. This last point is of high interest, and could help to better understand the phenomenology during SPS of ionic/mixed conductors.

ii. Study of the effect of air annealing on the SPSed Ta_2O_5 materials

In this section, we investigate **the air annealing of the Ta_2O_5 ceramics**, in order to assess the stability of the oxygen vacancies formed during SPS as well as the different phases, in particular H-Ta_2O_5.

Figure 4.90 present the XRD and Raman spectra evolution through annealing for the L-Ta_2O_5 samples SPSed at 1200 (1st row) and 1400°C (2nd row), the *a*-Ta_2O_5 ceramic SPSed at 1200°C (3rd row) and the *a*-Ta_2O_5 powder (4th row). For L-Ta_2O_5 SPSed at 1200°C, XRD shows that the **L- phase is kept up to 1400°C** in the bulk, while Raman shows that its black H-Ta_2O_5 surface **converts back to L- phase at 900°C**, and back to H-Ta_2O_5 at 1400°C (only on surface considering XRD). Meanwhile, the sample **gradually whitens** from 300 to 800°C, due to the **annealing of the oxygen vacancies** (see photographs). For L-Ta_2O_5 SPSed at 1400°C, XRD shows **partial transition from H- to L- phases** at 900°C, completed at higher temperature. Raman reveals a **higher temperature of conversion** to L-Ta_2O_5 than for the 1200°C sample: 1000 and 1100°C at the anode (dashed curve) and cathode side, respectively. The photographs show that the annealing of the oxygen vacancies started **from the anode side at 300°C up to the cathode at 600°C**, the sample being fully white at 800°C. We assume these discrepancies are related to the phenomenology during SPS.

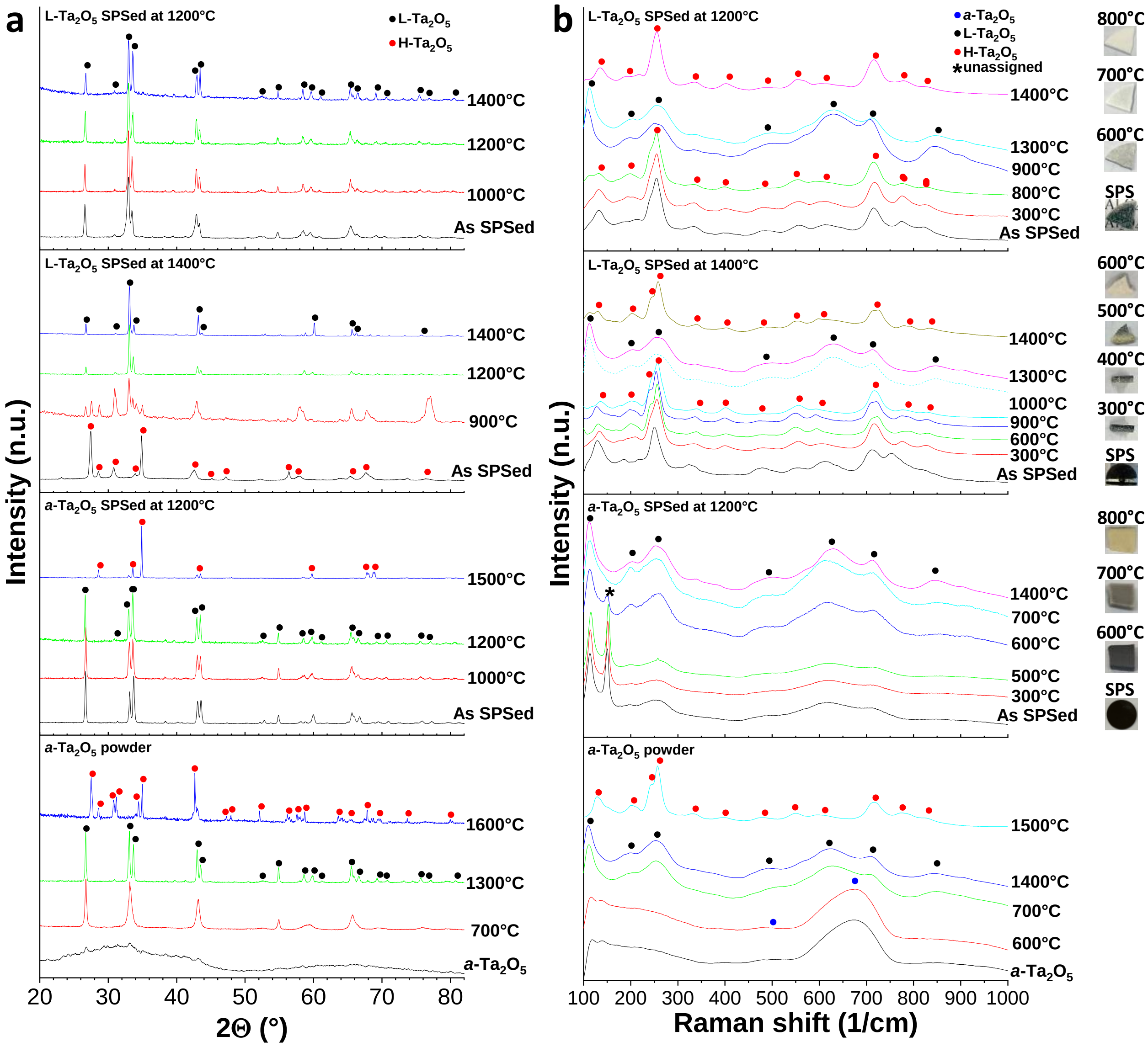

Figure 4.90: a) XRD and b) Raman spectra (cathode side) through 30 min annealing of ceramics SPSed from L-Ta_2O_5 at 1200 (1st row) and 1400°C (2nd row), a-Ta_2O_5 at 1200°C (3rd row) and of the a-Ta_2O_5 powder (4th row); photographs are provided on the right

For the sample SPSed at 1200°C from *a*-Ta_2O_5, XRD and Raman analyses show that the **L- phase is conserved up to 1500°C**, where it converts to H-Ta_2O_5. Interestingly, the unattributed peak at 150 cm^{-1} (marked by *) is progressively suppressed between **600 and 800°C**, which corresponds to **the annealing of the oxygen vacancies** (see photographs), and the sample becomes yellow (Nb^{5+} impurity [410]).

The comparative study of the annealing of the *a*-Ta_2O_5 powder shows that the **amorphous material crystallizes to L-Ta_2O_5 at 700°C**, confirming our observation on the densification curve (*Figure 4.87*), with transition to H-Ta_2O_5 at 1500°C explaining that L-phase was kept for SPS at 1400°C. It is interesting to note that the Raman spectrum of L-Ta_2O_5 crystallized in air annealing does not present the peak at 150 cm^{-1}. Hence, we can affirm with confidence that this mode **arises from oxygen vacancies within the L-phase**.

2. Spark plasma sintering of $MgAl_2O_4$ with Ta_2O_5 addition

Following the study of SPS of pure Ta_2O_5, which evidenced phenomena specific to sintering under reductive atmosphere *via* electrical current, we investigate the **effect of Ta_2O_5 addition to $MgAl_2O_4$** on SPS.

We used different sintering schemes depending on the parameter investigated. The Ta_2O_5 addition rate effect was studied with a sintering temperature T_d = 1650°C, a holding time t_d = 3 min, a heating rate α = 50°C/min and an applied pressure P = 80 MPa. The influence of T_d was studied with t_d = 20 min, α = 10°C/min and P = 80 MPa. The influence of P was studied with T_d = 1450°C, t_d = 20 min and α = 10°C/min.

It should be noted that in this paragraph, the normalized intensity of the XRD is presented in logarithm scale in order to better reveal the formation of minor phases.

i. Powder processing

For this study, we mostly used the **Sasol $MgAl_2O_4$ powder and the L-Ta_2O_5 powder** as raw material. The S25CR, Mg-UPA1250 and *a*-Ta_2O_5 powders were briefly used to investigate the influence of the precursor powders on the phenomenology, in *section v*. Unless indicated otherwise, the raw powders were mixed with agate mortar and pestle by small batches of 0.250 g to ensure best possible homogeneity.

SEM of the 1 wt% L-Ta_2O_5:Sasol powder is presented in *Figure 4.91*. The chemical contrast and EDX (*Figure 4.91.a* and *d*) show **large bright Ta_2O_5 agglomerates** up to ~50 µm which did not break during grinding. High magnification reveals that most of the Ta_2O_5 is **dispersed onto MAS aggregates** (*Figure 4.91.b*), with each ~30 µm Sasol particles covered by several 1-3 µm Ta_2O_5 particles (*Figure 4.91.c*).

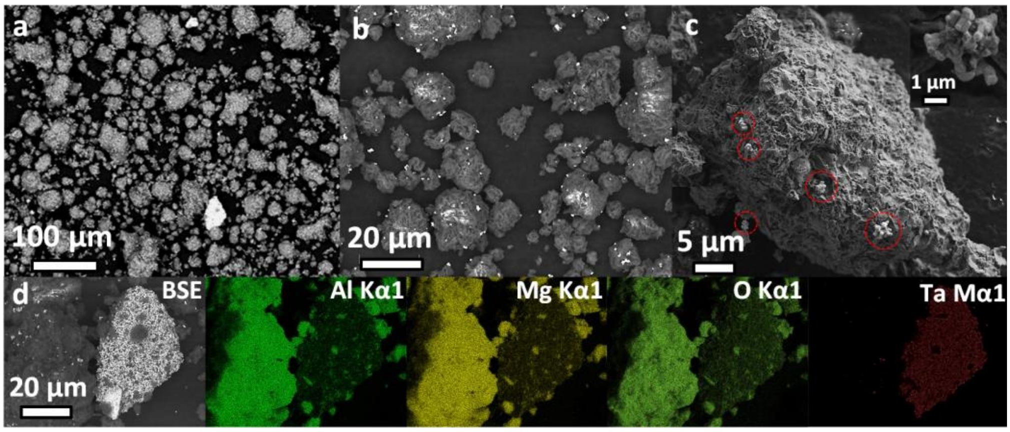

Figure 4.91: SEM of the 1 wt% Ta_2O_5 added Sasol powder mixed in a mortar: a-b) BSE and c) SE imaging, with Ta_2O_5 particles evidenced by red circles; inset shows a high magnification on a single Ta_2O_5 particle. d) EDX elemental mapping

SEM of the 1 wt% Ta_2O_5:S25CR powder reveals a similar distribution of Ta_2O_5, with **some MAS agglomerates more heavily covered by Ta_2O_5** (*Figure 4.92.a1-a3*). However, the S25CR particles are **much smaller** than the Ta_2O_5 ones (*Figure 4.92.b*), contrarily to what was observed for the Sasol powder.

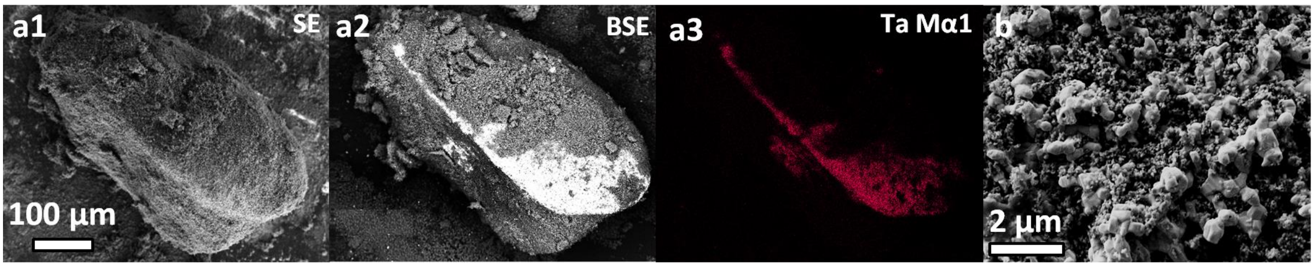

Figure 4.92: SEM micrographs of the 1 wt% Ta_2O_5 added S25CR powder mixed in a mortar: a1) topographic (SE) and a2) chemical contrast (BSE) of a large MAS agglomerate, with a3) EDX mapping of Ta; b) high SE magnification on the Ta_2O_5 particles

We performed the thermal analysis of the 10 wt% L-Ta_2O_5:$MgAl_2O_4$ powders by DSC (*Figure 4.93.a*). The analyses of the pure Sasol and S25CR powders show **no thermal events**, except for a progressive decrease of DSC signal at T > 1200°C due to sintering. The pure L-Ta_2O_5 analysis shows one endothermic pic at **1450°C**, which is attributed to the **reversible transition to H-Ta_2O_5**. The Ta_2O_5 added MAS powders show several phenomena; no transition to H-Ta_2O_5, but an exothermic peak is noted at **1560°C** for both Sasol and S25CR precursors. In addition, an endothermic peak is observed at 1593°C for Sasol and 1638°C for S25CR, evidencing **reactions** between Ta_2O_5 and MAS **influenced by the spinel precursor**. XRD (*Figure 4.93.b*) confirms that different reactions occur for both powders. While the pure Sasol contains ~3 wt% MgO as a minor second phase, it is **not observed anymore** with Ta_2O_5 addition, instead **$Mg_4Ta_2O_9$** is formed. For the S25CR powder which does not contain sensible free MgO, the reaction with Ta_2O_5 results on the formation of **$MgTa_2O_6$**. Thus, **depending on the accessible MgO for reaction**, the phase formed from the MgO – Ta_2O_5 diagram is either **MgO-rich ($Mg_4Ta_2O_9$) or MgO-poor ($MgTa_2O_6$)**.

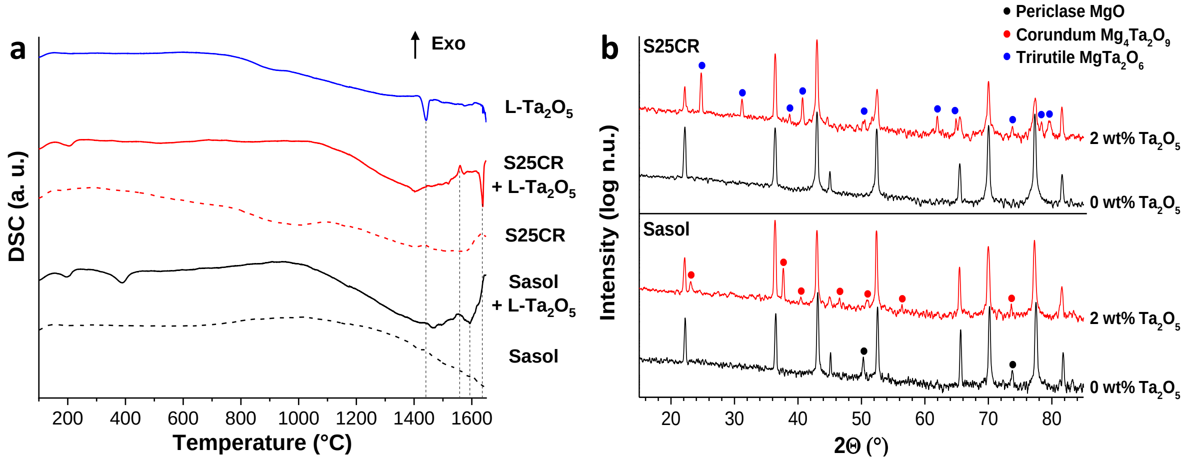

Figure 4.93: a) DSC of the pure and 10 wt% L-Ta_2O_5 added Sasol and S25CR powders, and b) XRD of the pure and 2 wt% Ta_2O_5 added powders after calcination at 1600°C for 10 h

ii. Influence of the Ta_2O_5 addition rate

We studied the **influence of the Ta_2O_5 content** added to the Sasol powder in the range **0.1-10 wt%**.

Figure 4.94.a presents the XRD patterns of the ceramics prepared with different Ta_2O_5 addition rate. **Above 0.5 wt% Ta_2O_5**, new phases are detected while the initial free MgO in pure Sasol **progressively disappears** up to 4 wt%. All new reflections for ≤ 4 wt% are indexed from **$Mg_4Ta_2O_9$ (M_4T_2)** pattern [401].

For 4 wt%, an additional reflection at 31.2° from **$MgTa_2O_6$ (MT_2)** is observed [404], and when **10 wt% Ta_2O_5** are added, all the reflections from this phase are detected and M_4T_2 becomes a very minor phase, due to **insufficient free MgO** for its formation. **No unreacted Ta_2O_5** is detected. No change of the spinel lattice is induced by the reaction, so **no sensible insertion of Ta^{5+}** within the MAS lattice is provoked and **no MgO is "extracted" from the spinel phase** to react with Ta_2O_5, which instead reacts with the free available MgO.

The Raman analysis (*Figure 4.94.b*) confirms and completes these results. No modification of the MAS signature is induced, in particular of the modes arising from antisites. New modes assigned to **M_4T_2** [401] appear with relative intensity proportional to wt% Ta_2O_5. The most intense mode at 830 cm^{-1} is detected even for 0.5 wt% Ta_2O_5, revealing M_4T_2 formation below the XRD detection threshold.

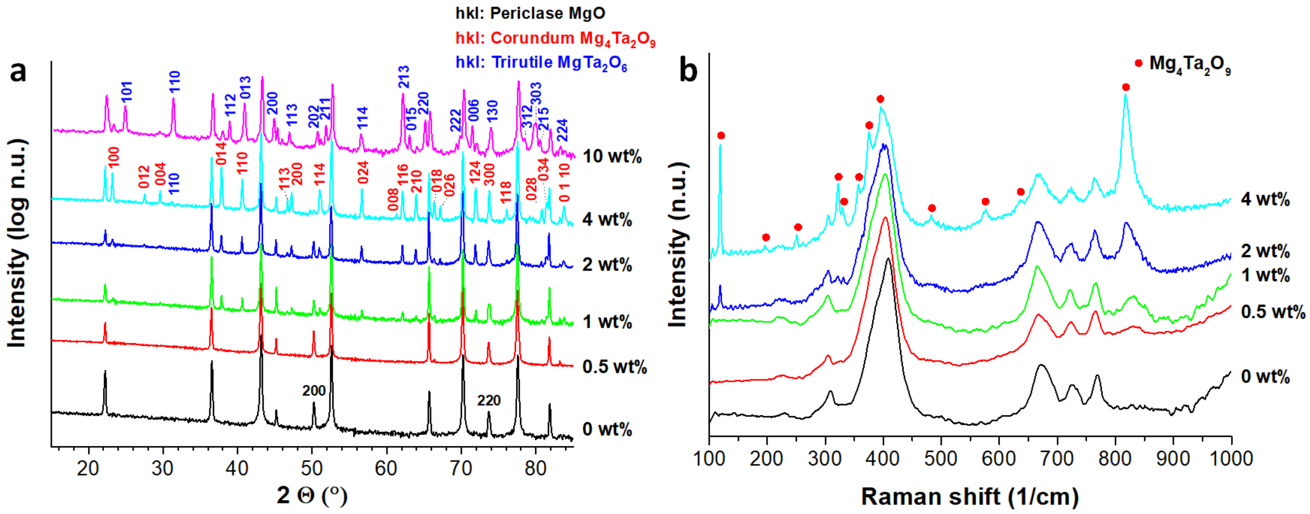

Figure 4.94: Evolution of the a) XRD patterns and b) Raman spectra of Sasol ceramics with increasing Ta_2O_5 addition rates

The Ta_2O_5 addition has a **strong effect on the transparency** of the MAS ceramics, even at the lowest amount of 0.1 wt%. The photographs and transmittance spectra of the materials are presented in *Figure 4.95*. **For 0.1 wt% Ta_2O_5**, the ceramics appears **homogeneous** by naked eye inspection, but the transmittance is **greatly decreased from 33 to 15%** at 600 nm. For higher addition rates, the transmittance decreases further, with **opaque spots** formed for **0.5-2 wt% Ta_2O_5** inducing translucency. Above this concentration, the **ceramics are fully opaque**.

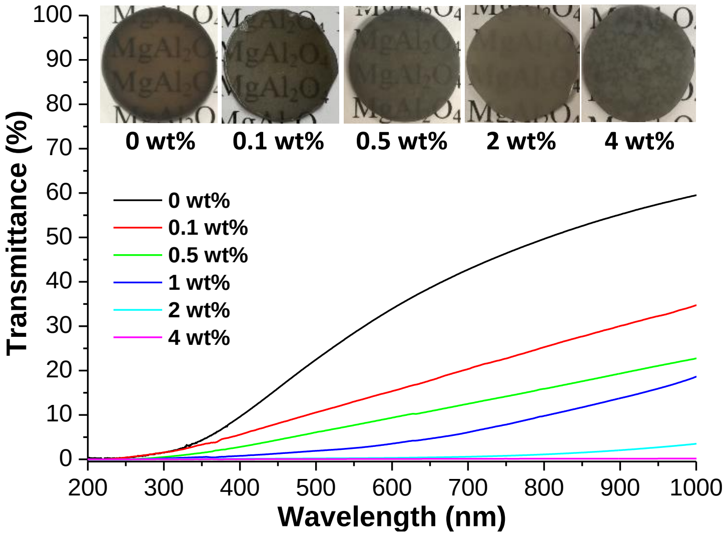

Figure 4.95: Photographs and transmittance spectra of the MAS ceramics SPSed at 1650°C with Ta_2O_5 addition rate of 0-4 wt%

The evolution of the microstructure and MAS grain size distributions with Ta_2O_5 addition rate is presented in *Figure 4.96*. Different effects are observed depending on the Ta_2O_5 concentration. While the pure MAS ceramic presents a monomodal grain size distribution (GSD) with GS = 4.6 µm, **0.1 wt% Ta_2O_5** addition results in a **dramatic coarsening** of the grains with **GS = 45 µm**, *i.e.* 10 times bigger. For **0.5 wt% or above**, the **GSDs become bimodal**, with a **normal grain size mode GS_1 close to the one of pure MAS** and an **abnormal mode GS_2 close to the one obtained with 0.1 wt% Ta_2O_5**, which population increases with the addition rate. In the range 0.5-4 wt%, this second mode is characterized by **clusters of big MAS grains** distributed within a matrix of normal MAS grains (*Figure 4.96.c-e*). The $Mg_4Ta_2O_9$ phase appearing bright is located in the matrix, more or less dispersed depending on concentration, and also forming a **continuous layer at the grain boundaries** of the clustering big grains. For 10 wt% addition, the big grains of MAS are not clustering anymore, and Ta-based large particles are dispersed in the matrix. The inhomogeneous microstructures observed for Ta_2O_5 addition rates above 0.1 wt% are **clearly responsible for the inhomogeneous optical aspect** of these materials.

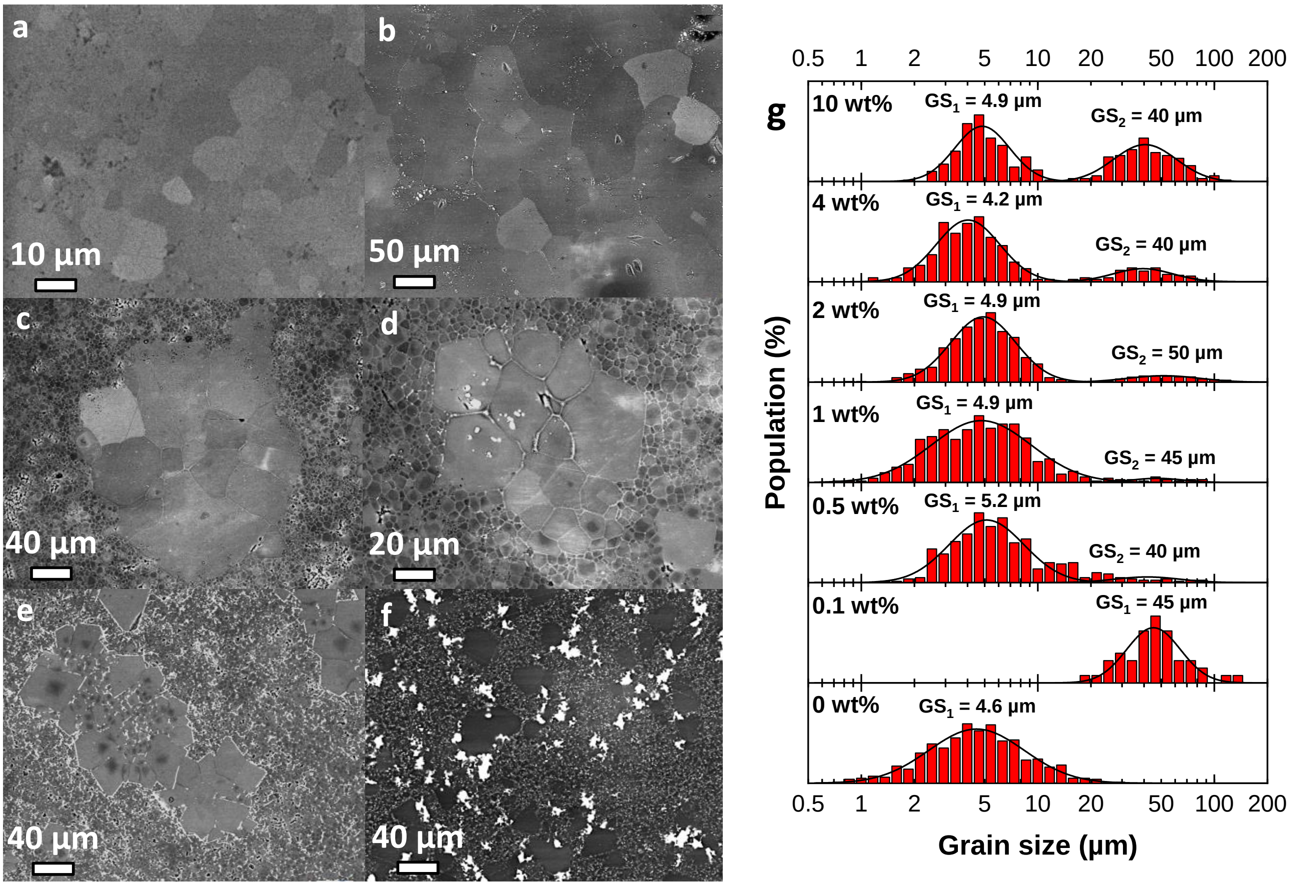

Figure 4.96: SEM micrographs of the MAS ceramics SPSed at 1650°C with Ta_2O_5 addition rate of a) 0 wt% (pure MAS), b) 0.1 wt%, c) 0.5 wt%, d) 1 wt%, e) 4 wt% and f) 10 wt%, and g) the evolution of the grain size distribution with the Ta_2O_5 addition rate

The influence of the Ta_2O_5 addition rate was also investigated on ceramics sintered at 1450°C with applied pressure of 230 MPa, which conditions provided better transparency and finer microstructure for pure Sasol powder, and similar observations were made on the influence of Ta_2O_5 impact. The addition of 0.1 wt% resulted in homogeneous microstructure and aspect, with the transmittance decreased by 7% in the visible range, while higher concentrations led to opaque spots. However, only small effect was observed on the MAS grains distribution in these conditions.

iii. Effect of the sintering temperature

We followed **the evolution of the structure and microstructure of the ceramics with the sintering temperature**. For this investigation, we used a Ta_2O_5 addition rate of 1 wt%. The difference of electronic density in Ta-based and MAS phases results in the impossibility to analyze the microstructure of both types of phase with the same SEM settings due to high chemical contrast in BSE imaging. Therefore, SEM was performed with either normal settings for characterizable MAS and very bright Ta-based particles, or with high contrast and low luminosity for characterizable Ta-based particles and very dark MAS phase.

Figure 4.97 presents the evolution of the ceramics external observation (photographs), microstructure (SEM) and composition (Raman spectra of the zones marked by red squares) SPSed in the range of sintering temperature 850°C (1^{st} row) to 1650°C (last row). These different characterizations are discussed together to better evidence the relation between the changes induced by increase of temperature. The evolution of the aspect, composition and microstructure with T_d is summarized in *Table 4.14.*

With a **sintering temperature of 850°C**, the ceramic is white and very porous as the **sintering barely began**. The low magnification SEM imaging reveals the presence of up to **50 µm large Ta-based inclusions** distributed in the MAS matrix, which can be attributed to the Ta_2O_5 agglomerates that resisted breaking during the grinding process (*Figure 4.91.a* and *d*). In addition, the major part of Ta_2O_5 dispersed during grinding appears as **small Ta_2O_5 particles well distributed**. Focus on the Ta-based inclusions shows that they are already **fairly densified** and sintered, and the Raman analysis indicates that they are composed by **L-Ta_2O_5** which did not react with surrounding MAS yet, even at the contact interface (zone B).

For **T_d = 1000°C**, sintering of the MAS host started, but the ceramic is still **white and porous**. The Ta-based inclusions appear globally **larger** (up to > 100 µm) and **fully sintered**, and developed a **core-shell structure** with ~20% shell; the core (zone A) is characterized by **unreacted L-Ta_2O_5 (T_2)** large grains, and the shell (zone B) is composed by small **$MgTa_2O_6$ (MT_2) grains** formed by reaction of L-Ta_2O_5 with the surrounding MAS host and identified by Raman [404]. The core-shell interface is disrupted, indicating the **propagation of the reaction front**. Such **composite microstructures** with partially reacted Ta-based inclusions were already observed for SPS of Ta_2O_5 added mullite [413]. Raman of zone C shows that the **dispersed Ta-based particles** (*i.e.* not aggregates) reacted to form the **MgO-rich phase $Mg_4Ta_2O_9$ (M_4T_2)** [401]; the difference of reactivity in both types of Ta_2O_5 particles (inclusions and dispersed) is related to their respective size: smaller ones have a higher relative availability of MgO from the surrounding MAS.

Table 4.14: Influence of the sintering temperature on the properties of Ta_2O_5 ceramics SPSed with 10°C/min, 20 min, 80 MPa

T_d (°C)	**850**	**1000**	**1100**	**1200**	**1275**	**1350**	**1400**	**1450**	**1550**	**1650**
Naked eye observation	Opaque/white		Opaque, black spots	Translucent, black spots	Transparent, black spots	Transparent, opaque uncolored spots becoming larger with increased T_d				
Evolution of the Ta-based inclusions	Sintered unreacted Ta_2O_5	Development of a core-shell structure Ta_2O_5-$MgTa_2O_6$		Low remaining Ta_2O_5, conversion of $MgTa_2O_6$ to $Mg_4Ta_2O_9$ in the surrounding host	Diffusion of $Mg_4Ta_2O_9$ in the MAS matrix *via* possible melting, propagation front forms a crown	No more Ta-based inclusions, progressive coarsening of MAS grains within the $Mg_4Ta_2O_9$ crowns			Dissipation of the crowns, clusters of big MAS grains remaining	

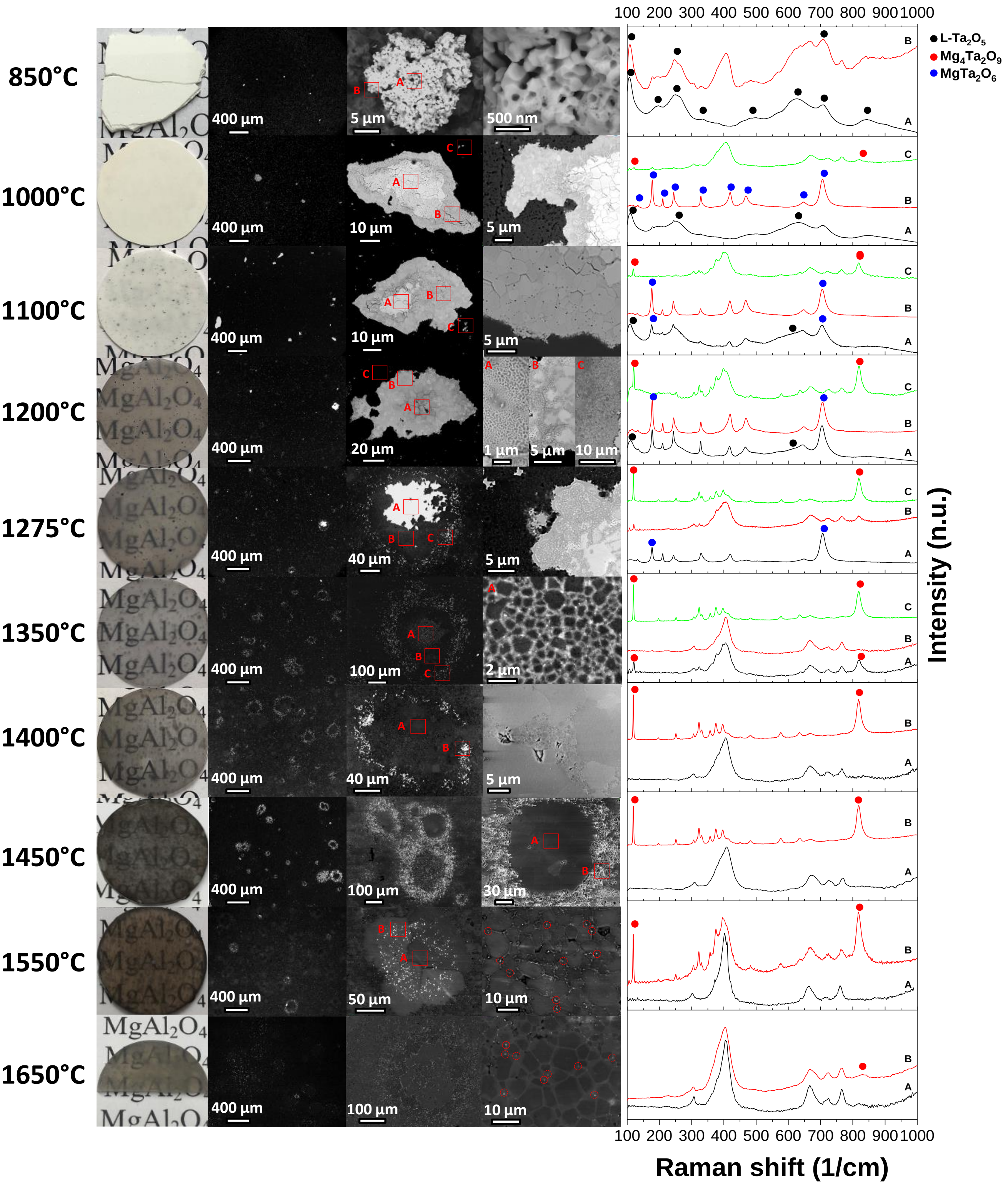

Figure 4.97: Evolution of the Ta_2O_5 added MAS ceramics with the sintering temperature from 850°C (1st row) to 1650°C (last row): photographs (1st col.), SEM with low magnification (2nd col.), focus on a Ta-based inclusion (3rd col.) and details of such inclusions and/or in their vicinity (4th col.), with local Raman analysis of areas indicated by red squares (5th col.)

At **1100°C**, the ceramic is still **opaque and white** but **black spots** are observed and identified as the Ta-based inclusions. The reaction front progressed toward the T_2 core (A) constituting ~¼ of the inclusions. The MT_2 shell (B) presents pores at the interface with MAS. The **blackening** is attributed to **oxygen vacancies** [404] formed during reaction, as for phase transition of pure T_2 (*section 1.i*). For **1200°C**, the reaction front reached the inclusions centers (A), which present a **T_2-MT_2 eutectic-like microstructure**. The MT_2 large grains in the shell (B) **fragmented into nanograins** while further reacting with MAS, and **diffused into the**

matrix (C) along grain boundaries to form **M_4T_2**. At **1275°C**, the conversion to M_4T_2 progressed and a **thin continuous layer** formed on the inclusions surface, possibly from **local melting** given its unstructured nature (see 4th col.). M_4T_2 diffused within the matrix from this liquid layer, and solidified in a **crown-like structure surrounding the inclusion**. Raman confirms that the remaining inclusion (A) consists of MT_2 while the crown (C) and in-between region (B) are composed by **mixed MAS and M_4T_2**. The hypothesis of local melting relies on the **formation of hot spots in the inclusions** during SPS, and explains both M_4T_2 melting in the hot inclusions (normally at ~1825°C [401]) and its solidification in the cold matrix resulting in crowns.

Above 1275°C, the **black spots turned to opaque uncolored spots related to porous areas** resulting from the melting and diffusion of the inclusions. **At 1350°C**, the areas within crowns consist in **small MAS grains coated by M_4T_2 layers** (zone A). An **abnormal coarsening** of these grains occurs while T_d increases **up to 1450°C**, resulting in **clusters of ~50-100 µm large MAS grains** (zone A), while their prior M_4T_2 coating diffused to the crowns. This abnormal growth may happen due to the hot spots mentioned before.

For $T_d \geq$ 1450°C, the crowns **gradually dissipates** by dispersion in the MAS matrix, forming **small M_4T_2 precipitates at triple junctions** (evidenced by red dotted circles). This can be explained by the increased temperature in the matrix allowing M_4T_2 diffusing farther before solidifying.

The evolution of the XRD with T_d is presented in *Figure 4.98*. While it is confirmed that at **850°C**, **unreacted T_2** remains in the material, **reaction to MT_2** is already well advanced. Since the T_2 inclusions were shown not to have reacted yet, it means that the much smaller **dispersed T_2 particles reacted**. For **$T_d \geq$ 1000°C**, the only secondary phase detected by XRD is **M_4T_2**, and no sensible evolution of the pattern occurs for further increase of T_d up to 1650°C. As T_2 and MT_2 were shown to be present in Ta-based inclusions up to 1200 and 1275°C, resp., we assume that the inclusions are a minority fraction of the total T_2 content.

XRD shows that MT_2 and M_4T_2 formations are **thermodynamically stable** at least at respectively **850 and 1000°C**, so the reactions were not completed within Ta-based agglomerates even at higher T_d because of **longer required duration for Mg^{2+} to diffuse through the large particles**. It can be noted that **no Al_2O_3, Al-rich MAS or $AlTaO_4$ formation** has been observed globally (XRD) or locally (Raman), even so the reaction of T_2 with MgO from $MgAl_2O_4$ (since it cannot solely react with free MgO locally) should also result in an Al-rich phase. However, it has been reported that the system $MgTa_2O_6$-$AlTaO_4$ presents an extensive domain of crystalline solution with maximum solubility of ~50 mol% $AlTaO_4$ in MT_2 at 1450°C [414]. Thus, it can be assumed that **excess Al^{3+} is solubilized within $MgTa_2O_6$** during its formation.

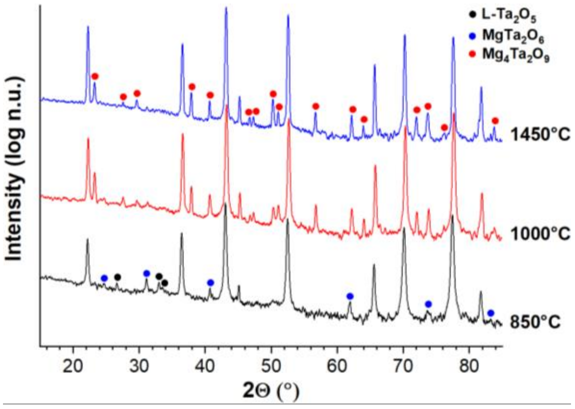

Figure 4.98: Evolution of the XRD patterns of 1 wt% Ta_2O_5 added Sasol ceramics with increasing SPS temperature

To confirm and complete these results, additional microstructural analyses have been carried out. *Figure 4.99* presents the EDX elemental mapping and in-line quantification on a Ta-based inclusion with core-shell structure on the ceramic SPSed at 1100°C. The analysis confirms that the agglomerates are constituted by a **core containing solely Ta and O elements**, thus corresponding to **Ta_2O_5**, and the **shell contains Ta, Mg and O elements**. The quantification reveals that the shell phase is **MT_2** according to Mg and Ta content. Interestingly, **strictly no variation of the O-density** is observed between T_2 and MT_2, while the latter should exhibit a slightly higher one; this could be due to the **oxygen vacancies**, which may have form due to the limited O diffusion in comparison to Mg diffusion (factor 10^4 in MAS [415]). In addition, Raman of the T_2 cores in *Figure 4.97* do not exhibit the sharp peak at 150 cm^{-1} attributed to O vacancies in L-Ta_2O_5 for SPS of pure T_2 (*Figure 4.88.b3* and *Figure 4.90.b*); this leaves only the **MT_2 phase to exhibit O deficiency**.

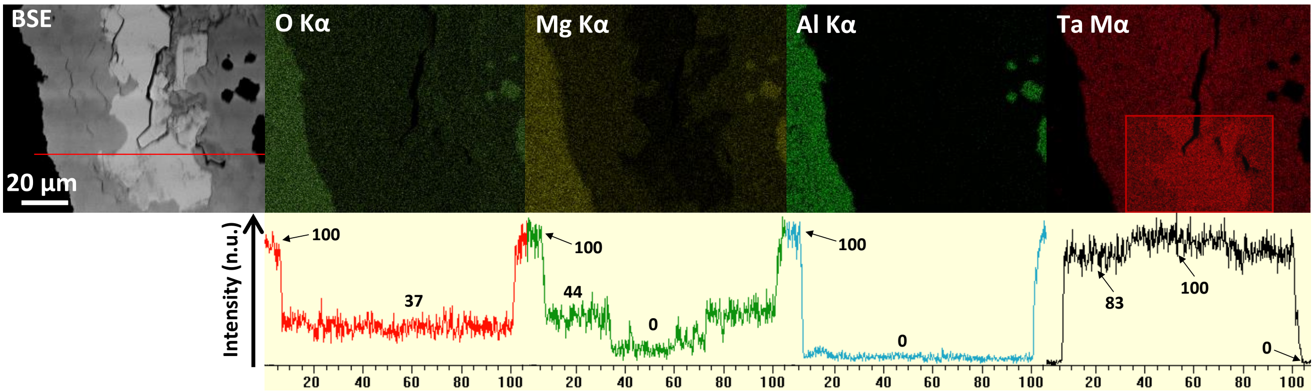

Figure 4.99: EDX elemental mapping and in-line quantification (red line in BSE) on a core-shell Ta-based inclusion at 1100°C

Figure 4.100 presents the analysis of the MAS matrix in the vicinity of a Ta-based inclusion in a ceramic SPSed at 1200°C. As shown in *Figure 4.97*, for T_d in the range 1200-1350°C, the MT_2 outer-shell of the inclusions progressively diffuses in the surrounding host and form M_4T_2 nanograins, moving through the MAS grain boundaries. *Figure 4.100.a* shows that at **1200°C**, these **M_4T_2 particles remain within ~10 µm** of the inclusions; the MAS grains in this layer appear to be **much smaller** than the grains in the next ~10 µm layer. The EBSD analysis of the MAS matrix surrounding the inclusion has been performed. The GS map (*Figure 4.100.b*) reveals that the inclusion (in white, not indexed) is surrounded by a **first crown of small MAS grains** with size in the range **0-0.8 µm**, and a **second crown of much larger MAS grains** of **1.5-4 µm**. The farther MAS matrix is composed by grains of various sizes in the range 0-4 µm. The inverse pole figure map (*Figure 4.100.c*) indicates that this local coarsening is not associated with texturation.

We ascribe this **differential coarsening in the MAS material** to the formation of **hot spots in the Ta-based inclusions**, as mentioned above. We believe that the hot spots are localized in the whole regions delimited by outer big-grains MAS crowns, inducing the observed coarsening. The inner fine-grains MAS crowns are not subjected to rapid grain growth due to an **efficient pining effect of the M_4T_2 particles** at grain boundaries. Based on GS in the outer crown, and considering the GS dependency on T_d during SPS of pure Sasol (*Figure 4.17*), we estimate **the temperature on the edge of hot spots to be ~1450°C**, *i.e.* 250°C above T_d. At higher temperature, M_4T_2 diffuses to the edges of hot spots, as the **temperature farther in the MAS matrix is too low** for effective diffusion, and the outer MAS crown turns into M_4T_2 crowns.

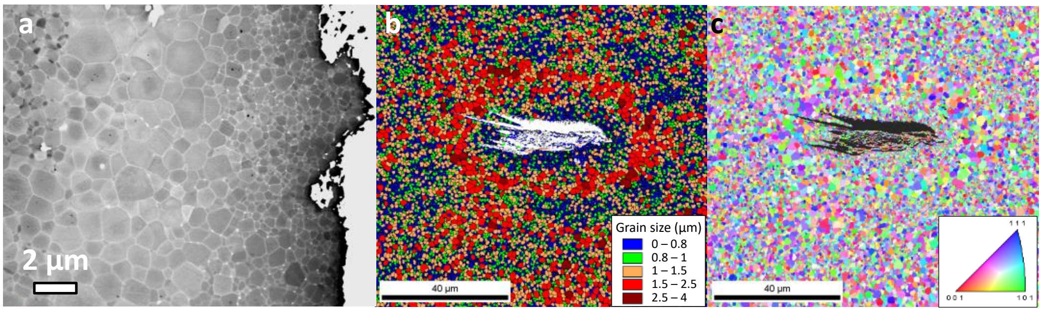

Figure 4.100: a) SEM of the vicinity of a Ta-based inclusion at 1200°C, and EBSD b) grain size and c) inverse pole figure maps

Figure 4.101 presents a SEM investigation of the Ta-based particles. *Figure 4.101.a* shows the MAS matrix in early sintering stages (1000°C) and evidences that the dispersed Ta-based particles coat the initial Sasol aggregates. Focus on an opaque uncolored spot (*Figure 4.101.b*) reveals that it is a Ta-based inclusion with M_4T_2 crown, and opacity induced by the **highly porous in-between area** (*Figure 4.101.b1*). The remaining inclusion exhibits **partially disrupted grain interfaces** due to high stress (*Figure 4.101.b2*). The the remaining T_2 core in core-shell inclusions also presents high internal stress resulting in **microcracks** and **severe relief** (SE, *Figure 4.101.c2*). At higher temperature, the microstructure is even more disorganized with **large cavities in the core of inclusions**, possibly arising from local melting (*Figure 4.101.d* and *e*).

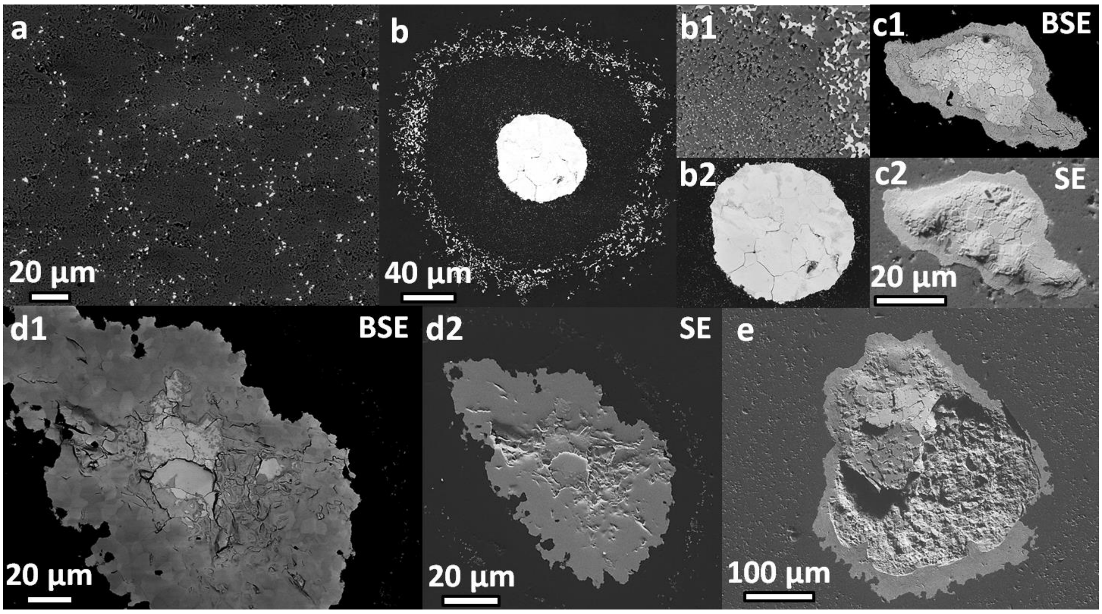

Figure 4.101: SEM micrographs of the Ta-based particles: a) dispersed particles in early stages of sintering, b) inclusion surrounded by a crown of Ta-based particles with details of b1) the area between the inclusion and the crown and b2) the inclusion, c1) chemical (BSE) and c2) topographic (SE) contrasts of a core-shell inclusion and d1,d2) of an inclusion with disorganized core microstructure, and e) topographic contrast of an inclusion with large cavity in its center.

The results presented in this paragraph seem to indicate the **formation of hot spots localized on the Ta-based inclusions**, which can be explained by two hypotheses: *i)* $MgTa_2O_6$ and $Mg_4Ta_2O_9$ formations from Ta_2O_5 and MgO are reported to be **exothermic** [416, 417], and may **release heat locally**; *ii)* **electrical effects during SPS** may have occurred (percolation paths…) due to the **predominantly ionic conductive nature** of Ta-based phases, particularly at low O_2 pressure and high temperature ($10^{-4}\ \Omega^{-1}cm^{-1}$ at 1000°C to $10^{-1}\ \Omega^{-1}cm^{-1}$ at 1200°C) [418]. However, the DSC analysis (*Figure 4.93*) did not reveal strong thermal effects, which favors hypothesis *ii)*. This study fuels the long and wide debate on the exact nature of SPS mechanisms. Further experiments are required to undoubtfully identify the origin of the hot spots formation.

iv. *Influence of the applied pressure on the microstructure*

The materials obtained can be considered as **ceramic-ceramic composites** with a MAS matrix and Ta-based inclusions reinforcements. Therefore, it was considered interesting to **investigate the influence of the applied pressure on the microstructure of the composite ceramics**. The Ta_2O_5 addition rate is 1 wt%.

Figure 4.102 presents the evolution of the microstructure with the applied pressure. SEM of the radial sections (1st row) shows that P has a **great effect on the development of the inclusions**. At 80 MPa (*Figure 4.102.a1*), **100-300 µm circular M_4T_2 crowns** are observed, while their size decreases to **50-250 µm** at 130 MPa (*Figure 4.102.b1*) with remaining inclusions within the larger crowns. The effect is greater at 230 MPa (*Figure 4.102.d1*): **no crowns** are observed, as the Ta-based phases **entirely remained in inclusion form**.

SEM of the cross-sections (2nd row) shows that the Ta-based crowns/inclusions are **flattened be the pressing**: they are **oval at 80-130 MPa** (*Figure 4.102.a2* and *b2*), and develop a **thin lenticular shape** above. In comparison, no preferential orientation is observed on radial section.

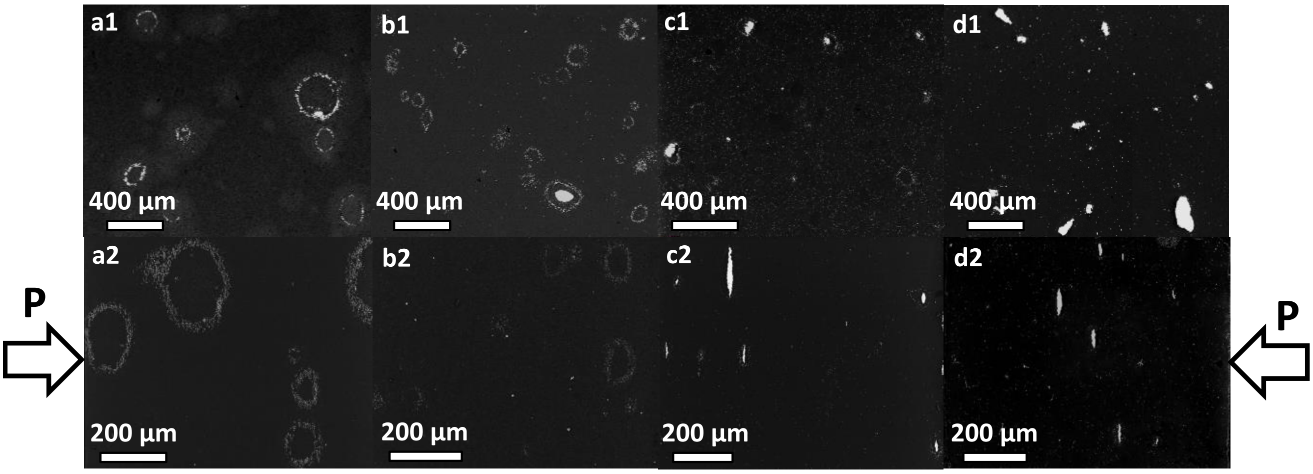

Figure 4.102: SEM micrographs of 1 wt% Ta_2O_5 added Sasol ceramics SPSed at 1450°C with an applied pressure of a1,a2) 80 MPa, b1,b2) 130 MPa, c1,c2) 180 MPa and d1,d2) 230 MPa, on a1-d1) the radial and a2-d2) the cross sections

This orientation of the Ta-based reinforcements in the matrix induces an **anisotropy**. We quantified this effect of the pressure by the determination of an **anisotropy factor**, defined as the **ratio length/width of the inclusions** in the *Figure 4.103*; the distances were measured from the outer of the structures, *i.e.* outer shell of the inclusions when no crowns are observed and outer diameter of the crowns otherwise. It is remarkable that this factor is greater with increasing P, from **~1.5 at 80-130 MPa to ~2 at 180 MPa** and almost **4 at 230 MPa**. However, it is clear that this flattening effect is limited, thus the factor cannot increase much further.

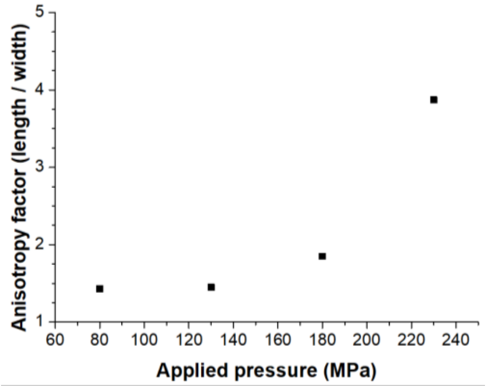

Figure 4.103: Anisotropy factor in the cross section defined as the ratio length/width of the inclusions vs the applied pressure

We remark that *i)* the flattening of the Ta_2O_5 agglomerates dispersed in the powder occurs **during the compaction stage**, and *ii)* the increase of P **inhibits the diffusion of the inclusions** into crowns. Raman of the P = 230 MPa ceramic (*Figure 4.104*) reveals that **MT_2 inclusions did not convert to M_4T_2**, which is only observed in the surrounding matrix. We assume that this is due to an **effective inhibition of Ta^{5+} diffusion within MAS**, while Mg^{2+} diffusion in T_2 does not seem to be hindered since MT_2 has been formed.

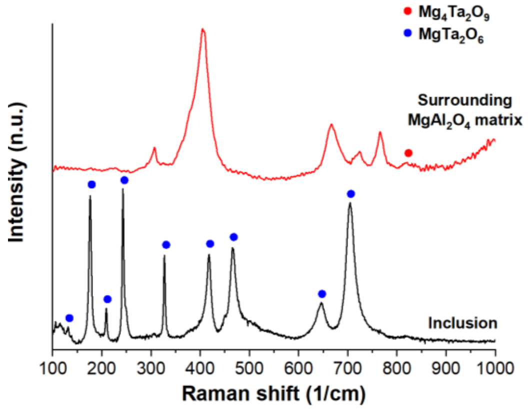

Figure 4.104: Raman spectra of a Ta-based inclusion and its surrounding $MgAl_2O_4$ matrix in a ceramic SPSed at 1450°C, 230 MPa

It should be noted that this effect of the applied pressure on the organization of composite microstructures has never been reported before, to the best of our knowledge. Its application to the fabrication of materials with desired anisotropy could be interesting for numerous applications.

v. *Influence of the precursors*

We investigated the effect of the $MgAl_2O_4$ and Ta_2O_5 precursors as well as the mixing method on the ceramics fabricated, with 1 wt% Ta_2O_5 addition rate. This effect is presented on the *Figure 4.105*.

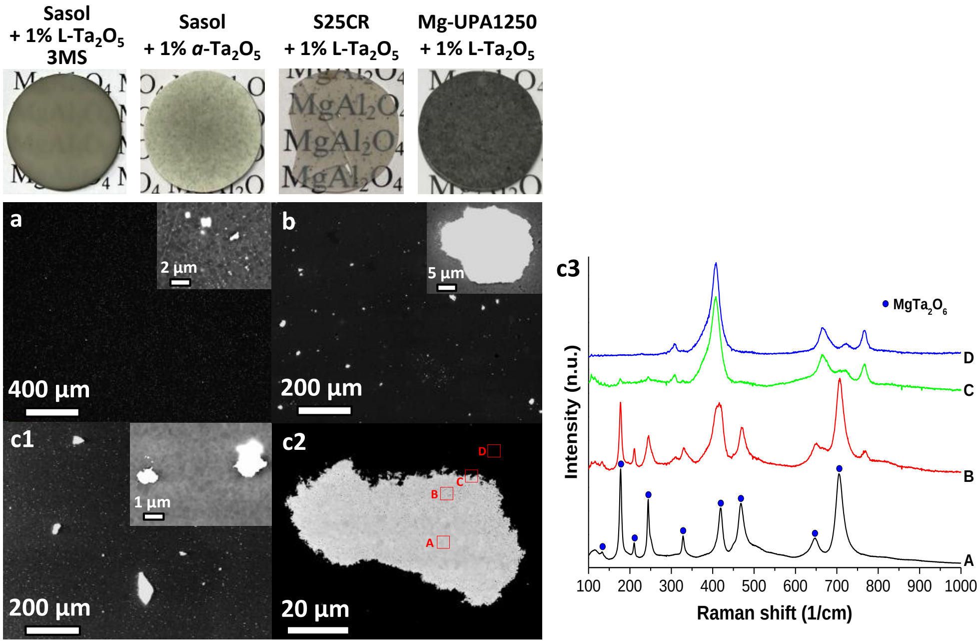

Figure 4.105: Photographs of the ceramics prepared from the different precursors (1st row), and SEM micrographs of the ceramics SPSed a) at 1300°C from Sasol + 1 wt% of L-Ta_2O_5 mixed by 3MS protocol, b) at 1300°C from Sasol + 1 wt% of a-Ta_2O_5, c1) at 1200°C from S25CR + 1 wt% of L-Ta_2O_5 with c2) focus on a Ta-based inclusion and c3) Raman analysis of the areas indicated

The **3MS mixing** method, presented in *section I.1* and consisting in de-agglomeration in slurry state with ZrO_2 balls, resulted in a better chemical homogeneity with **breakage of the Sasol aggregates and L-**

Ta_2O_5 agglomerates. After sintering at 1300°C (20 min dwell), the ceramic obtained is **homogeneous in appearance with no black or opaque** spots, and is **slightly translucent**. The SEM analysis (*Figure 4.105.a*) reveals **no large Ta-based inclusions**, but well-dispersed Ta_2O_5 particles in the MAS matrix.

After sintering at 1300°C for 20 min of the **mixed *a*-Ta_2O_5 with Sasol powder**, the ceramic obtained is **opaque white** (not dense), with **black spots** from Ta-based inclusions (*Figure 4.105.b*). No crown effect is observed, in contrast with the SPS of L-Ta_2O_5 added Sasol in the same conditions.

For the SPS of **L-Ta_2O_5 added S25CR** at 1200°C (20 min), we also obtain a **transparent ceramic** with **black spots** linked to the presence of Ta-based inclusions (*Figure 4.105.c1*). However, the Raman analysis reveals that the **$Mg_4Ta_2O_9$ phase is not formed** neither in the core, the shell nor the surrounding matrix, and **only $MgTa_2O_6$** is observed (*Figure 4.105.c2* and *c3*). This is confirmed by XRD analysis (*Figure 4.106*, bottom row) where only the latter phase is observed, due to the lower free MgO content in S25CR precursor.

Finally, we investigated the effect of Ta_2O_5 addition on the **reactive sintering of mixed MgO/α-Al_2O_3 synthesized *via* impregnation route** (Mg-UPA1250 calcined at 600°C). The ceramic obtained after SPS at 1300°C for 20 min is opaque as for pure Mg-UPA1250, but presents **black spots** from Ta-based inclusions (see photograph in *Figure 4.105*). The microstructure of the latter (not shown) is very similar to the one obtained for Ta_2O_5 added Sasol powder. The XRD analysis reveals that the reaction between Ta_2O_5 and MgO **occured to form both $MgTa_2O_6$ and $Mg_4Ta_2O_9$**, which did not prevent the formation of the spinel phase.

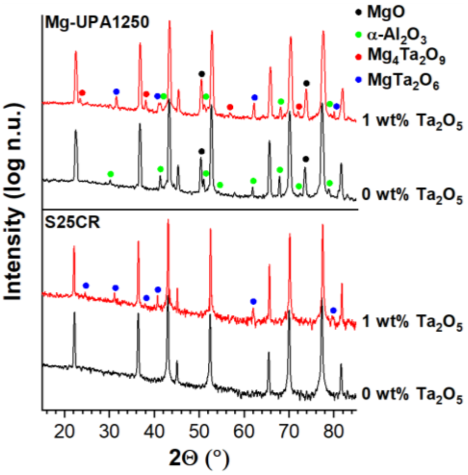

Figure 4.106: XRD patterns of the ceramics prepared from pure and 1 wt% Ta_2O_5 added Mg-UPA1250 SPSed at 1370°C (top row) and S25CR (bottom row) powders

3. Conclusion

In this section, we investigate the **sintering phenomenology of pure Ta_2O_5 and Ta_2O_5 added $MgAl_2O_4$**. Ta_2O_5 was chosen because of its **high ionic conduction** and its ability to **easily form oxygen vacancies**, which features can help evidencing the sintering mechanisms of such materials.

The SPS processing of pure Ta_2O_5 could not allow fabricating transparent Ta_2O_5 ceramics in the applied conditions. A **strong darkening effect occurs during the phase transitions** from *a*-Ta_2O_5 to L-Ta_2O_5 and L-TaO_5 to H-Ta_2O_5 (at temperature much lower than normally required for such transitions), which evidences the **formation of oxygen vacancies progressively spreading from the cathode to the anode**. This phenomenon was attributed to either an **inhomogeneous axial temperature or to an ionic current percolating through the ceramic** to counter balance the electronic current during SPS.

The addition of Ta_2O_5 to $MgAl_2O_4$ leads to the degradation of the transparency of the ceramics, in particular for addition rate superior to 0.1 wt% with the formation of opaque spots. These spots are related to **Ta-based inclusions** from agglomerates in the powder, and their microstructure depends on the sintering temperature and applied pressure. The initial L-Ta_2O_5 inclusions form **core-shell structures** in the range 1000-1200°C, due to the **diffusion of Mg^{2+} from the surrounding $MgAl_2O_4$ matrix** within the Ta-based particles. For higher temperatures, the inclusions progressively diffuse in the matrix resulting in **Ta-based crowns** and **abnormal coarsening** of the MAS grains contained within. We attributed this phenomenon to the **formation of hot spots localized in the inclusions**, which may be due to **electrical effects during SPS**.

It was shown that the applied pressure results in a **preferential orientation of the inclusions perpendicular to the pressing direction**. The factor of anisotropy is proportional to the loading force.

VI. Conclusion on the consolidation of $MgAl_2O_4$ ceramics

This chapter was dedicated to the **consolidation of $MgAl_2O_4$ ceramics by spark plasma sintering**.

In the first part, we investigated the influence of the mechanical pre-processing of the powder on its sinterability. It was found that high-energy comminution leads to a contamination of the material from the grinding media, which is highly detrimental for the transparency. The **low-energy processing in slurry state** was found efficient for the **de-agglomeration/de-aggregation** of the initial particles, providing better ceramic properties after sintering, in particular **finer microstructure and better transparency**.

Afterward, we carried out a parametric study of the sintering. This investigation revealed that **the most impactful SPS conditions** for the fabrication of transparent ceramics with fine grains are the **sintering temperature and the applied pressure**. In particular, the **grain growth is mostly driven by thermal effect**, while the **densification depends on the couple applied pressure-sintering temperature**. The sintering dwell duration can be used as an optimization parameter for the improvement of the densification and transparency, while the heating rate should not exceed 10°C/min to avoid any carbon contamination. The produced ceramic presenting the **best properties** was obtained for **HPSPS of S25CR-3MS powder at 1000°C and 1000 MPa**, with a 20 min dwell. Its **transmittance *plateau* reaches ~85% at 400 nm**, and its **grain size is 98 nm**, which is comparable with the best results reported in the literature.

In order to further improve our materials, and especially to decrease the grain size, we performed a preliminary study on the sintering of the precursor powders synthesized by polyol and impregnation routes in *Chapter 3*. The **polyol precursors** were systematically subjected to **phase demixtion and MgO loss**, which we attributed to a **particularly high reactivity**. The only ceramic which presented a **certain transparency with $T_{il\text{-}600\ nm} = 21\%$** was fabricated from the **Mg-UPA300 (*a*-Al_2O_3 initial reactant) precursor**.

The post-densification air annealing and HIP treatments were investigated, but resulted in only **moderated improvement of the transparency**, while no further coarsening was noted.

Finally, we investigated the phenomenology during SPS of ionic conductors with the case of Ta_2O_5 and Ta_2O_5 added $MgAl_2O_4$. We observed the **formation of oxygen vacancies** in the materials at the negative electrode and propagating to the positive one. We also evidenced the **formation of hot spots** during the sintering. We attributed these phenomena to **electric effects specific to SPS of ionic/mixed conductors**.

Chapter 5

Physical investigation of the defects in $MgAl_2O_4$ and irradiation behavior

In this last chapter, we investigate the intrinsic and extrinsic defects in $MgAl_2O_4$ ceramics and the irradiation behavior of our materials *via* physical characterizations, namely cathodoluminescence (CL), photoluminescence (PL) and electron paramagnetic resonance (EPR) spectroscopies. These methods are not widely used in the field of ceramic fabrication, however they have been used for decades by physicists in order to understand the defects environment and stability, mostly on highly pure monocrystals to facilitate the analysis of specific defects. We believe these techniques could help understand further the formation of defects and their evolution through the processing.

First, we studied the evolution of the defects in $MgAl_2O_4$ ceramics fabricated from commercial powders through the processing, focusing on the influence of the SPS processing and subsequent annealing and of the sintering conditions. We also investigated the effect of Ta_2O_5 addition on the structural defects. Afterward, we assessed the He^+ irradiation behavior of chosen samples. Finally, we evaluated the influence of the synthesis route (polyol and impregnation, see *Chapter 3*) on the $MgAl_2O_4$ nanopowders' defects.

I. Evolution of the defects in $MgAl_2O_4$ materials through processing

1. Influence of SPS processing and subsequent annealing

In order to investigate the **evolution of the defects in $MgAl_2O_4$ ceramics through SPS processing and subsequent air annealing**, we choose a sample prepared from the sintering of the Sasol commercial powder with a sintering temperature of 1500°C, a duration dwell of 3 min, a heating rate of 100°C/min and an applied pressure of 80 MPa. This specimen was chosen because of its reasonable transparency and its strong dark discoloration which can be attributed to both carbon contamination and partial reduction of $MgAl_2O_4$ during sintering process [49, 50, 218]. Several air annealing treatments were applied on the material, at 1100, 1150 and 1250°C for 200 h in order to assess this discoloration phenomenon.

Figure 5.1 presents some of the "classical" characterizations of this ceramic before and after annealing. The photographs (*Figure 5.1.a*) show that the as-SPSed sample was transparent with strong dark discoloration. After heat treatment at 1100°C, only a **slight lightening** is observed, indicating an **insufficient annealing temperature** for the diffusion of oxygen throughout the thickness of the pellet. With a treatment at 1150°C, **no darkening** remained, but a yellow tint appeared, and the material transparency decreased to translucency. Finally at 1250°C, the ceramic was **white and totally opaque**. The decrease of transparency observed in our study has been previously reported in Ref. [302], where the recombination of vacancies leading to a new porosity has been invoked. By microscopic analysis we can also observe **blistering** at the surface after annealing (see *Figure 4.83.a1-a3*) that seemingly comes from the **oxidation of carbon into CO_2** gas causing high strain and local porosity after the gas evacuation from solids. The XRD patterns of the ceramic (*Figure 5.1.b*) reveal that no sensible modification of the spinel lattice is induced by thermal treatment, and the grain size distributions measured from SEM analysis (*Figure 5.1.c*) indicate that **no coarsening occurs until a treatment at 1250°C**, which led to a grain size doubled from ~2.2 to ~5 µm.

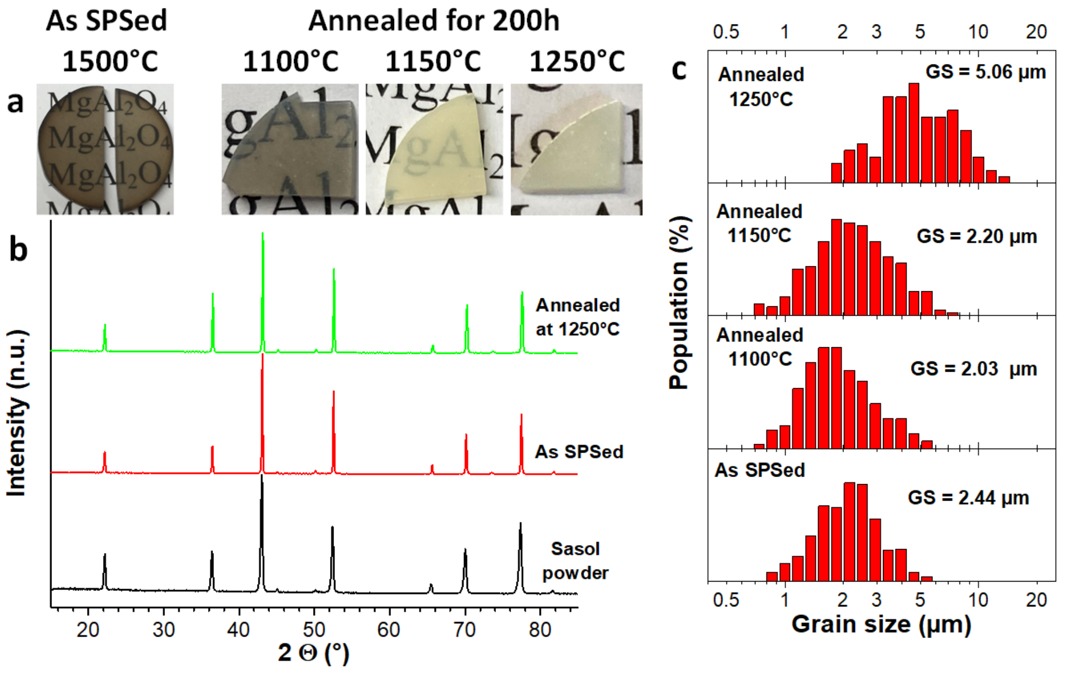

Figure 5.1: Sasol ceramic SPSed at 1500°C (3 min, 80 MPa) and subsequently annealed at 1100, 1150 and 1250°C for 200 h: a) photographs, b) XRD patterns and c) grain size distributions

i. Characterizations of the optical and magnetic centers

In this section, we study the evolution of the defects in the materials presented in *Figure 5.1* through the processing by **cathodoluminescence CL and electron paramagnetic resonance EPR spectroscopies**.

The CL spectra measured at 5K are presented in *Figure 5.2.a*, and the results are summarized in *Table 5.1*. These spectra exhibit **four main bands**: one at **1.8 eV due to Cr^{3+} cation impurities** substituting Al^{3+} in octahedral sites [64, 221, 389, 419, 420], one at **2.4 eV due to Mn^{2+} cations impurities** substituting Mg^{2+} in tetrahedral sites [221, 389, 419, 420], and two broad bands at **~3.4 eV and ~5.2 eV attributed mainly respectively to F-type centers** [32, 300, 419, 421] and **cationic disorder including inversion defects and V-type centers** [45, 419, 420]. Note that the latter two broad peaks are the convolution of several bands, as it has been previously reported [32, 300, 419, 421] and as evidenced in the case of the CL of the sample annealed at 1250°C (*Figure 5.2.a*, blue line). In this case, the overall 3.4 eV band intensity is highly reduced while a 3.3 eV narrower peak linked to a “harder to anneal” F-type center clearly remains. In addition, a minor peak is observable at **2.55 eV** after annealing at T ≥ 1150°C. This peak is slightly below the one of F^+ center (2.7 eV [32]) and can be attributed to the luminescence band of the **agglomerate F_2 center** (*i.e.* the combination of two F centers) [66, 300], and could be hidden in the overall 3.4 eV band in the as-SPSed sample. However, it may have appeared due to the formation of F_2 centers by coalescence of simple F/F^+ centers during the annealing, which would be in good agreement with the mechanism proposed in [302], contributing to the newly formed porosity and explaining the dramatic loss of transparency (*Figure 5.1.a*). It can be noticed from *Table 5.1* observation that the **half-width ΔE of the Mn^{2+} and V-type centers signals is not sensibly varying** through the processing, while **ΔE of F-type centers is somehow decreased after annealing**, which we attribute to the suppression of some simple and more easily annealed F-type centers.

Table 5.1: Main CL bands (E: mean energy, ΔE: half-width, I: intensity) at 5K for the Sasol powder and ceramic SPSed at 1500°C and annealed at 1150 and 1250°C for 200 h

CL signal	Mn^{2+}			F-type centers			V-type centers		
	E (eV)	ΔE (eV)	I (a.u.)	E (eV)	ΔE (eV)	I (a.u.)	E (eV)	ΔE (eV)	I (a.u.)
Sasol powder	2.40	0.15	3.65	3.43	1.25	22.55	5.17	1.07	18.61
As SPSed	2.39	0.12	22.3	3.41	1.25	22.72	5.27	1.01	17.68
Annealed at 1150°C	2.40	0.15	4.42	3.37	0.97	14.40	5.21	1.05	5.46
Annealed at 1250°C	2.39	0.13	5.05	3.23	1.02	4.63	5.17	1.07	0.76

The Cr and Mn impurities come from the powder, and cannot be suppressed during our fabrication process, hence should remain in **constant elemental concentration** independently of the applied treatment. In addition, Cr can only be in the Cr^{3+} valence state in the MAS material, thus the intensity of its signal should roughly be constant, which condition is respected in regard to the focused analysis using cut-off filter OG550, in order to prevent stray light interfering with luminescence from the samples, presented in *Figure 5.2.b*. In comparison, the intensity of the **tetrahedral Mn^{2+}** signal peaking at 2.4 eV **evolves significantly through the SPS and annealing treatments** (*Table 5.1*), indicating a **modification of the oxidation state of Mn**. More specifically, the intensity of this peak is **multiplied by a factor 6** from the powder to the as-SPSed ceramic. This can be explained by the reductive atmosphere during the sintering, thus favouring the conversion of predominant Mn^{III}_{Al}/$Mn^{IV}_{Al}{}^{+}$ ions in the powder into Mn^{II}_{Mg} during SPS. After air annealing (oxidizing atmosphere), the 2.4 eV peak intensity decreases back to the same level as the powder's one, indicating the **re-oxidation of Mn^{2+}** in higher valence ions. Such conversion of Mn oxidation state has already been reported in several oxides, during both sintering [422] and post-sintering annealing [423, 424]. *Figure 5.2.b* reveals the presence of a small signal at **~1.9 eV after annealing**. This band has been often reported and attributed to **Mn^{4+} red luminescence** in numerous phosphors including $MgAl_2O_4$ [70, 425, 426], confirming the conversion of oxidation states through the processing. Although, $Mn^{IV}_{Al}{}^{+}$ center requires charge compensation, thus it could be inferred that Mn^{III}_{Al} defects are more likely to be formed. Only limited information exists on the luminescence of Mn^{3+}, which is generally quenched due to large Jahn-Teller splitting of its energy levels [426]. Nonetheless, a far-red luminescence band at ~1.8 eV (~700 nm) in Mn:$MgAl_2O_4$ has been tentatively ascribed to the Mn^{3+} spin-forbidden $^1T_2 \rightarrow {}^5E$ transition [426]. This band being very close to Cr_{Al} and $Mn^{IV}_{Al}{}^{+}$ ones, the presence of Mn^{3+} cannot be deduced from *Figure 5.2.b*. In addition, it should be noted that the CL set-up used to collect these spectra, and in particular the detector (H8259, Hamamatsu photon counting head) is not ideal for measurement of the emission in NIR range. Thus, no qualitative analysis of the Cr_{Al} and $Mn^{IV}_{Al}{}^{+}$/Mn^{III}_{Al} signals can be carried out.

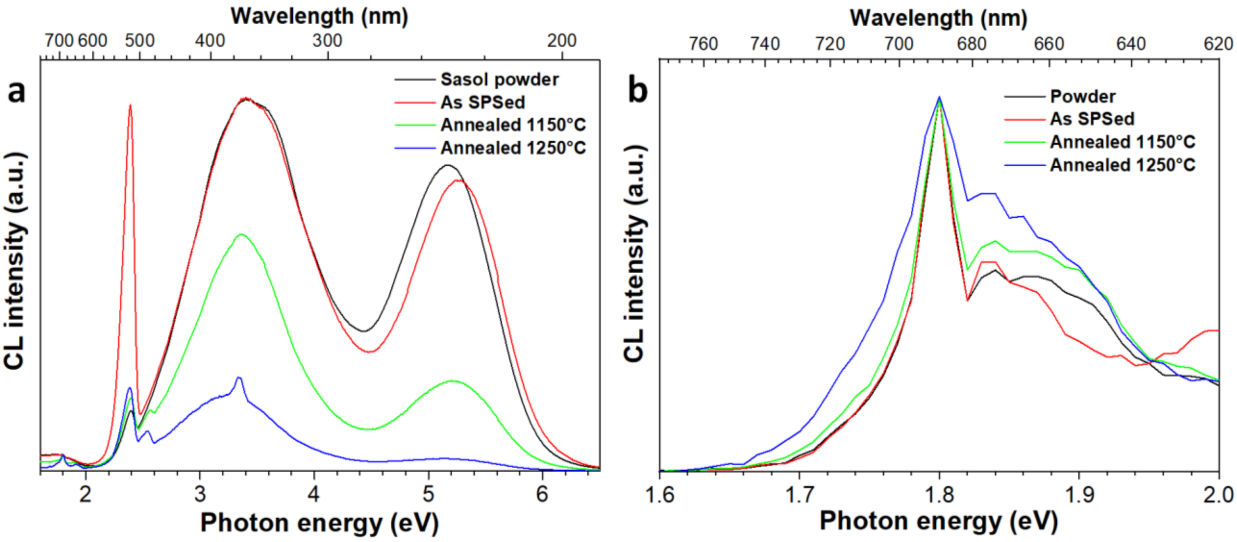

Figure 5.2: a) Cathodoluminescence spectra at 5K of the Sasol powder and ceramic SPSed at 1500°C (3 min, 80 MPa) and subsequently annealed at 1150 and 1250°C for 200 h; b) focused analysis with OG550 filter on the 1.6-2.0 eV region

The CL spectra in *Figure 5.2.a* evidence **strong modifications on the intrinsic defects** as well. The SPS processing did not modify the initial F-type centers luminescence of Sasol powder (3.4 eV band), although it was expected to have the greatest influence on this band due to partial reduction of MAS and formation of oxygen vacancies. The already high concentration of F-centers in the raw powder may explain the absence of further spinel reduction; since the O^{2-} vacancies density did not evolve after SPS, the dark discoloration of the material afterward (*Figure 5.1.a*) is most likely not arising from these defects. However, the **V-type centers** luminescence (5.2 eV) **undergoes a blue shift** from 5.17 to 5.27 eV, revealing a **change in the cationic defects nature/environment** (possibly *via* inversion) and emphasizing the complex nature of this band. After annealing, the luminescence of F and V centers are **greatly decreased and shifted to lower energy** (*Table 5.1*), which can be ascribed to the healing of the structural defects, and which is corroborated by a progressive change of the coloration from black to white (observed in *Figure 5.1.a*). After treatment at

1250°C, **almost no V-type centers remain** in the material and the sample is fully opaque white. Thus, these last defects may be **responsible for the yellow tint** remaining after heat treatment at 1150°C.

The conventional X-band (9.47 GHz) EPR spectra collected at room temperature are presented in *Figure 5.3*. In this paragraph, the spectra of ceramics were collected in the direction of their cross sections (perpendicular to pressing direction during SPS); the angular dependency is discussed in the next section. Strong modifications of the magnetic defects occur through the processing. The general view in *Figure 5.3.a* reveals the presence of **three main signals** which were then individually analyzed: *i)* a **hyperfine structure (HFS) sextet** in the range 3000-3800 G (*Figure 5.3.c*), *ii)* a **broad signal BS1** superimposed with the HFS (*Figure 5.3.d*) and *iii)* a **broad signal with weak intensity BS2** in the range 1000-2000 G (*Figure 5.3.b*).

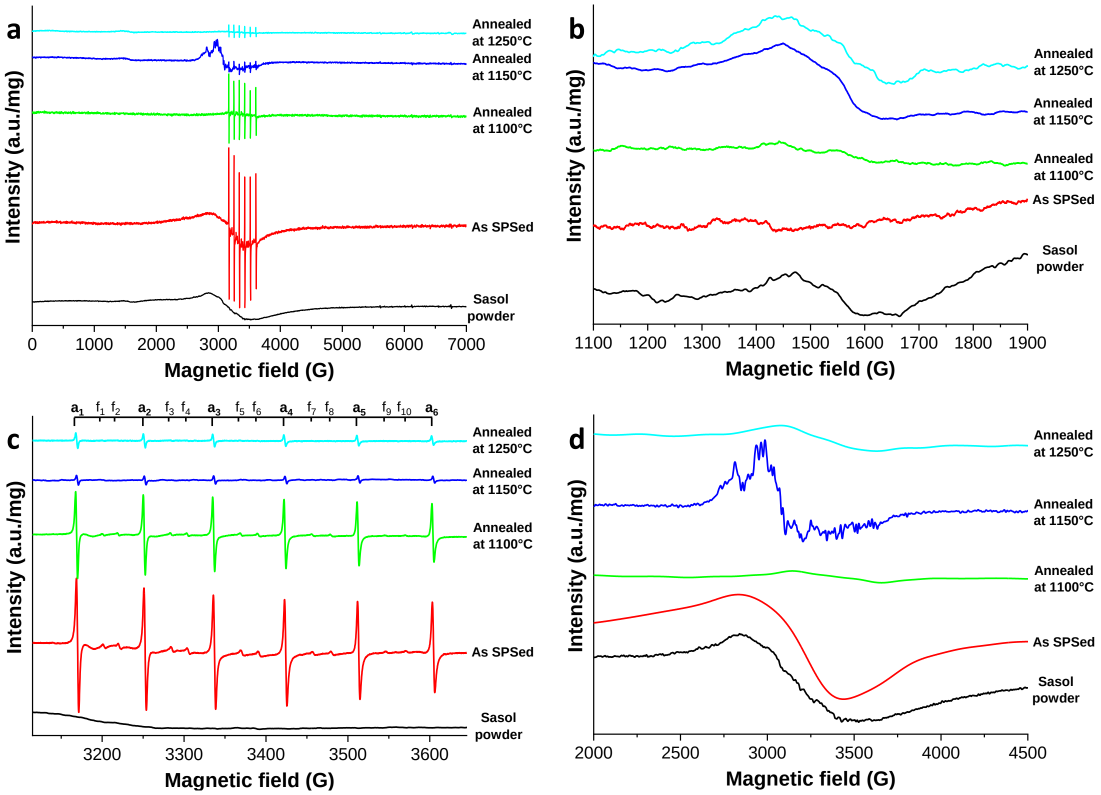

Figure 5.3: EPR spectra (300K) of the Sasol powder and ceramic SPSed at 1500°C (3 min, 80 MPa) and subsequently annealed at 1100, 1150 and 1250°C: a) general view and focus on the signals b) BS2, c) HFS and d) BS1 after numerical subtraction of HFS

The **HFS signal** (*Figure 5.3.c*) is well known and arise from **Mn^{II}_{Mg} center** [58, 70, 427], in agreement with the CL results. It is composed by **six intense lines** respecting the selection rules $\Delta m_S = 1$ (electronic spin transition) and $\Delta m_I = 0$ (no nuclear spin transition) [308], thus referred to as the “authorized” bands a_1 to a_6 with a **hyperfine splitting constant A_0 = 87(3) G**. In addition, **five pairs of weak lines** with 4(1)% intensity of the a-lines are observed between the latter, and are “forbidden” lines ($\Delta m_S = 1$ and $\Delta m_I = 1$) named f_1 to f_{10}, **arising from distortion of the spinel lattice** causing 2nd order perturbations involving zero field splitting (ZFS) and quadruple interactions [59, 308]. The mean resonance fields (H_0) and the linewidth (ΔH) of each lines are indicated in *Table 5.2* and the average mean resonance field is **H_0 = 3384(2) G**, *i.e.* the independent resonance field **g = 2.000(1)**. The value of the splitting constant is known to depend on the electronegativity of the atoms surrounding Mn^{2+}, thus provides a qualitative measure of covalency of the bonding with O^{2-} [58]. The measured A_0 = 87(3) G is superior to the common ~82 G yielding a covalent parameter *CP* ≈13% [51, 58, 60, 428], indicating a more ionic bonding in our case **CP ≈8%**. This was previously observed and ascribed to the increase of O^{2-} ligands surrounding Mn^{2+} from 4 in single crystals to ~6 in fine grained MAS ceramics, compensating the local positive shift charge arising from antisite defects Al_{Mg}^{+} and F^{+} centers [51].

It is interesting to note that the **HFS is absent from the powder spectrum** and only appears after SPS processing (*Figure 5.3.c*). After annealing, the mean resonance fields and linewidth of HFS do not present sensible variation. However, the intensities of the lines decrease progressively with temperature of the treatment up to 1150°C where they become **very weak**; higher temperature of treatment at 1250°C do not lead to further decrease of the intensity of the signal. This trend of evolution of the HFS intensity is in good agreement with the evolution of Mn^{2+} luminescence band in CL analysis (*Figure 5.2.a*).

Table 5.2: Mean resonance fields (H_0) and linewidth (ΔH) of the lines of Mn^{2+} hyperfine structure (HFS)

	a_1 [a]	f_1 [b]	f_2 [b]	a_2 [a]	f_3 [b]	f_4 [b]	a_3 [a]	f_5 [b]	f_6 [b]	a_4 [a]	f_7 [b]	f_8 [b]	a_5 [a]	f_9 [b]	f_{10} [b]	a_6 [a]
H_0 (G)	3170.1	3202.6	3221.5	3252.5	3285.6	3305.4	3337.2	3371.5	3392.4	3424.2	3458.7	3481.3	3513.3	3547.9	3572.7	3604.6
ΔH (G)	2.9	3.5	3.8	3.0	3.4	3.5	2.9	4.5	4.1	2.9	3.9	4.2	3.0	4.4	4.8	3.0

[a] a_i refers to the i^{th} allowed line of the HFS, in blue background
[b] f_i refers to the i^{th} forbidden line of the HFS, in white background

The **BS1 signal** (*Figure 5.3.d*, presented after numerical subtraction of the HFS signal) is observed around the **mean resonance field H_0 ≈ 3200 G** and has a **very broad linewidth ΔH ≈ 600 G**. This signal is already present in the powder spectrum, and is not strongly altered after SPS processing. After annealing at 1100°C, this signal has **almost completely disappeared**. However, further annealing at 1150°C results in its reappearance, and **numerous constituent fine lines** can be observed forming the large BS1 envelope. The heat treatment at 1250°C leads again to its disappearance. This broad magnetic signal is indeed the superimposition of numerous magnetic centers, which makes its proper analysis difficult. It has been reported in several occasions in $MgAl_2O_4$ ceramics, and can be related to mainly three causes:

i) **Mn^{2+} dipolar and cluster interactions**, as well as numerous forbidden transitions of the HFS, which are orientation dependent and therefore unresolved in powdered samples (polycrystalline with aleatory orientation of the crystallites) [58, 429, 430], resulting in a broad background for the HFS signal.

ii) **Cr^{3+} exchange-coupled interactions** (clusters of pairs), observed at g = 1.98 [61, 431, 432], as expected from CL spectra (*Figure 5.2.b*); however, this line is reported to be much sharper (ΔH ≈ 100 G).

iii) Finally, **the superimposition of numerous lines**, evidenced after annealing at 1150°C, may include **all the intrinsic paramagnetic defects** (V-type centers, F-type centers, complex combination *e.g.* F_2…) which are indeed expected in large density from the CL spectra (*Figure 5.2.a*). It has been reported that sintering in reducing atmosphere (HIP, SPS) [12, 49] and with carbon contamination [102] provokes the formation of a broad signal at g = 1.8-2.0 with ΔH ≈ 300-500 G, which was tentatively attributed to absorptive clusters of interacting F^{+}- and F-centers (the former normally exhibiting a sharp intense line and the latter not being paramagnetic). In addition, numerous elementary and combined V-centers have been reported and characterized, all in the resonance field around g = 2.0 [8, 10, 38, 44, 45]. These defects are **highly**

anisotropic and dependent on their crystal environment, thus a broad unresolved envelope centered at g ≈ 2.0 would indeed be expected in powdered samples.

Finally, the **BS2 signal** (*Figure 5.3.b*) is observed at the much lower resonance field **H_0 ≈ 1550 G** and is **very weak** compared to BS1. Interestingly, it is present in the raw Sasol powder and disappears after SPS, then reappears during annealing at T ≥ 1150°C. It should be noted that BS2 seems to be the **superimposition of 2 signals** (better observable on the spectrum of the sample annealed at 1150°C). EPR lines in this range of resonance field have been reported several times, with various causes: *i)* Fe^{III}_{Al} centers [12], *ii)* two distinctive but close Cr^{III}_{Al} centers, due to isolated Cr^{3+} in axial and rhombic symmetries [432] and *iii)* Mn^{2+}/Mn^{4+} in rhombic symmetry, reported in numerous oxide and glass systems [422, 424, 433–436].

The first derivative EPR spectra presented in *Figure 5.3*, convenient to accentuate features of the absorption signals, have been integrated in order to better compare the spectral weight W of the different paramagnetic centers in *Figure 5.4*. The results of the analysis of each signal in the different samples are provided in *Table 5.3*. The **principal absorption is from BS1** for all the samples. It is important to notice that the HFS signal is clearly very weak in comparison to both BS1 and BS2 (factor 100 to 1000). In addition, BS2 is much more intense after annealing at 1150 and 1250°C than in the raw Sasol powder. The most important informations from this figure concern the BS1 absorption. It can be noticed that its mean resonance field varies significantly in the range 3066-3426 G, in particular for the samples annealed at 1100 and 1250°C for which **BS1 weight is greatly decreased and H_0 is shifted toward higher fields**. We can also notice that in the sample annealed at 1150°C, BS1 is quite asymmetrical.

Table 5.3: EPR signals (RT) for the Sasol powder and ceramic SPSed at 1500°C and annealed at 1100, 1150 and 1250°C for 200 h

EPR signal	HFS [a]				BS2				BS1			
	Average H_0		ΔH (G)	W (10^7 a.u./g)	H_0		ΔH (G)	W (10^7 a.u./g)	H_0		ΔH (G)	W (10^{10} a.u./g)
	G	g			G	g			G	g		
Sasol powder	-	-	-	~0	1542(1)	4.38(4)	164(2)	100(2)	3165(1)	2.14(2)	666(2)	31(3)
As SPSed	3384(2)	2.000(1)	4.7(1)	42(1)	-	-	-	~0	3253(1)	2.08(2)	630(5)	25(2)
Annealed 1100°C				27(1)	-	-	-	~0	3426(1)	1.98(2)	574(2)	2.5(2)
Annealed 1150°C				3.0(1)	1564(1)	4.33(3)	289(3)	399(3)	3066(3)	2.21(8)	559(2)	18(1)
Annealed 1250°C				4.9(1)	1564(1)	4.33(3)	281(2)	390(3)	3338(2)	2.03(2)	596(2)	1.7(1)

[a] Average resonance (H_0), linewidth (ΔH) and spectral weight (W) from allowed bands only, due to negligible forbidden ones

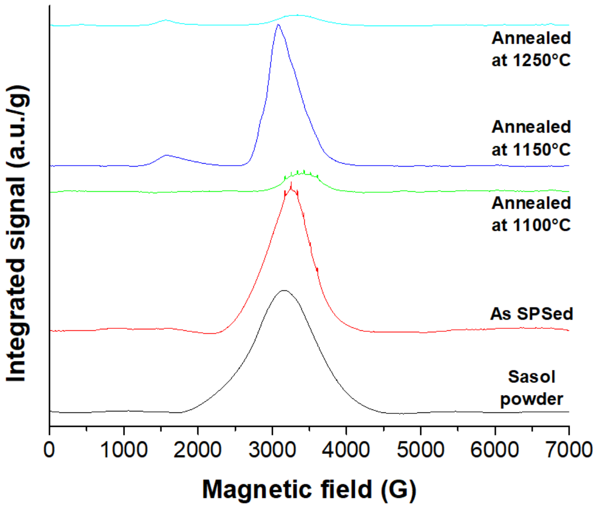

Figure 5.4: Integrated signal of the EPR spectra used for the estimation of the spectral weight of each paramagnetic centers

The absorption bands' spectral weights W are somehow indicative of the **concentration in paramagnetic centers**. The HFS weight goes from ~0 in the powder to 42(1) 10^7 u.a./g after SPS, then decrease to 3-5 10^7 u.a./g after annealing up to 1150-1250°C, which can be considered constant and indicates that we reached a **stable conversion rate of Mn^{2+} into Mn^{3+}/Mn^{4+} states**. An inverse trend is observed for the spectral weight W(BS2), which decreases from 100(2) 10^7 a.u./g for the powder to ~0 after SPS and annealing at 1100°C, before increasing back to almost 400 10^7 a.u./g during heat treatment at 1150 and 1250°C. Therefore, it appears clearly that the **HFS and BS2 signals are linked**, with their **spectral weight inversely proportional** (up to a multiplicative constant), so the concentration of the paramagnetic centers they respectively arise from should also be correlated and inversely proportional. The BS1 evolution does not seem to be strongly related to the previous ones: W(BS1) = 25-31 10^{10} a.u./g up to after the SPS processing, than decreases by a factor 10 after annealing at 1100°C. Further heat treatment at 1150°C provokes its increase back to 18 10^{10} a.u./g, to finally decrease to 1.7 10^{10} a.u./g after treatment at 1250°C.

Taking into consideration all the characterizations of these samples (visual aspect, SEM, CL and EPR), the attribution of the different EPR signals and their evolution through processing can be discussed. Some points are well-known and therefore can be considered as indisputable:

i) The **HFS signal arises from Mn^{2+} in tetrahedral sites (Mn_{Mg})**, and the evolution of its spectral weight is in very good agreement with CL spectra. However, no HFS is observed for the Sasol powder, even if CL reveals the presence of Mn_{Mg} in close concentration than after annealing at 1150°C, for which HFS is observed. This indicates that at least part of the Mn_{Mg} centers interact together through **broad dipolar interaction and exchange-coupled clusters**, resulting in a **broad unresolved absorption** centered on the HFS resonance field and potentially hidden the latter [58, 429, 430, 437]. That broad unresolved absorption must be a contribution to BS1 signal.

ii) **Cr^{3+} is known to be contained** in the samples from CL. Its EPR signal can be in the range of BS2 (isolated Cr^{3+}) or BS1 (Cr^{3+} pairs). Since its concentration is constant (no possible change of oxidation state in MAS host) and its interactions with surrounding Cr^{3+} are unlikely to strongly evolve, **we discard the possibility of its contribution to BS2**. Indeed, BS2 is observed in the powder, but not in SPSed sample, then again after annealing at 1150°C, which is not concordant with isolated Cr^{3+} pairing during SPS, then separating during annealing. Hence, **Cr^{3+} rather contributes to BS1**.

iii) The CL spectra clearly indicate **large density of intrinsic defects of F- and V- type nature**. These absorption centers are all located around the resonance field of the free electron $g_e = 2.0023$, thus are indubitably a **large contribution to BS1 resonance**. Unfortunately, their very large concentration and interactions result in a broadband absorption which cannot be deconvoluted.

iv) **BS2 is clearly linked to the HFS**, and in particular its spectral weight is inversely proportional to the concentration of Mn^{II}_{Mg}. In addition, it is well known that Mn^{2+} can be converted to higher oxidation states Mn^{3+}/Mn^{4+} through oxidizing annealing, and reversely under reducing treatment [422–424, 438]. However, Mn^{3+} ions are diamagnetic [69, 439], so only Mn^{4+} can be detected in EPR with a somehow weak absorption in the range of BS2. *Ergo*, we ascribe **BS2 absorption to Mn^{4+} substituting Al^{3+} in octahedral sites**. However, Mn^{III}_{Al} may still be formed as well, CL and EPR giving no information on this point.

Therefore, to summarize the above reflections: HFS is due to Mn^{II}_{Mg} centers, BS2 most likely arise from $Mn^{IV}_{Al}{}^{+}$ centers, and BS1 if formed by superimposed contributions of Mn^{2+} broad background, Cr^{3+} pairs and mostly intrinsic complex F- and V-type centers.

We notice that the BS1 signal is greatly decreased after annealing at 1100°C, which we attribute to the **annealing of most of the intrinsic defects** as elementary F^{+} centers and V centers have been reported to be almost completely healed at 700°C [8] and 600°C [10, 38, 45], respectively. Therefore, the remaining BS1 signal after treatment at 1100°C is mostly due to the HFS broad background and Cr^{3+} pairs, and the **dark discoloration** which appeared during sintering and remained after heat treatment at 1100°C (*Figure 5.1.a*) cannot be attributed to the intrinsic defects, and is **solely due to carbon contamination from SPS processing**. This discoloration disappears after treatment at 1150°C, resulting from the **oxidation of the carbon in the ceramic**, which is accompanied by the reappearance of a strong BS1 absorption. We assume the carbon oxidation has occurred through the **partial reduction of $MgAl_2O_4$**, then when the highly pressurized CO_2 gas evacuated from the ceramic, it caused **great internal stresses and intrinsic defects** (see blistering phenomenon in *Figure 4.83.a1-a3*). This would explain the highly different BS1 signal after heat treatment at 1150°C. After further annealing at 1250°C, BS1 decreases back in a comparable way as after treatment at 1100°C, indicating that the **prior formed defects have been healed**, and only the HFS broad background and Cr^{3+} pairs contributions remain. In addition, the CL spectrum (*Figure 5.2.a*) reveals that the V-type centers concentration is greatly reduced, while the density of F-type centers remains appreciable. Since the **yellow tint** appearing after treatment at 1150°C is not observed anymore at 1250°C, we must assume this **coloration is arising mostly from the V-centers**. It should be mentioned that the HFS and BS2 spectral weight seems to be correlated in samples annealed at 1150 and 1250°C, while it is not the case for the raw powder, for which the Mn^{2+} content is low (see CL spectra *Figure 5.2.a*) and yet W(BS2) is only ¼ of what it is in the annealed samples. Therefore, we conclude that part of the Mn content must be in the

oxidation state Mn^{3+} at least in the powder. Photoluminescence measurements should allow proper distinction of Mn^{III} and Mn^{IV} centers.

It is interesting to underline that the intrinsic defects undergo little change during SPS. Hence, the **applied sintering does not have a strong effect on structural defects in $MgAl_2O_4$ spinel**, in spite of what is commonly accepted.

ii. Investigation of the angular dependency of the paramagnetic centers

We carried out the analysis of **EPR spectra angular dependency** in this paragraph. It is not a common investigation for polycrystalline materials with randomly oriented crystallites, since the defects are generally also randomly oriented and therefore their resulting EPR signal is averaged. Indeed, the analysis of the Sasol powder (not shown) revealed no angular dependency, but it was thought interesting to study this dependency on the SPSed and annealed samples in order to evidence eventual anisotropy due to the fabrication process.

The angular dependency was investigated through two measurement configurations, resulting in the definition of two rotating angles (*Figure 5.5*): the magnetic field is either directed toward *i)* the **cross section of the sample** (perpendicular to SPS pressing direction) which rotates with a **radial angle θ** (left, θ = 0° defined arbitrarily), or *ii)* its **radial section** (perpendicular to the radial direction) which rotates with an **axial angle φ** (right, φ = 0° corresponds to the magnetic field perpendicular to the SPS pressing direction).

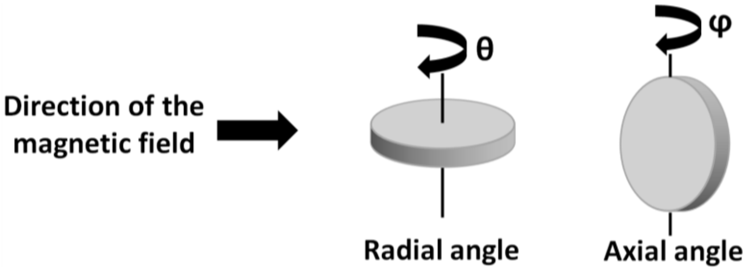

Figure 5.5: Principle of the EPR angular dependency analyses, rotating with a radial angle θ (left) and an axial angle φ (right)

A preliminary study of the angular dependency of the paramagnetic centers' features, with only few θ and φ angles studied, is presented for all samples in *Figure 5.6*. It can be seen that **only the sample annealed at 1150°C for 200 h exhibits an anisotropy of EPR signals**, while the sample as SPSed, annealed at 1100 and 1250°C show no sensible dependency on either θ and φ angles. The angular dependency of the sample annealed at 1150°C is somehow **weak with rotation along the radial angle** (*Figure 5.6.a*, 2nd row), the mean resonance field remaining unchanged but the **elementary signals convoluted within BS1 clearly varying**. In the other hand, its dependency with **rotation along the axial angle** (*Figure 5.6.b*, 2nd row) is **very strong both on the mean resonance field and on the elementary lines of BS1**. While a more thorough investigation of the radial angular dependency may be helpful for the elucidation of the elementary lines and the constituent paramagnetic centers, the high concentration and variety of centers contributing to BS1 signal render this analysis difficult. Therefore, solely the axial angular dependency has been further studied, with consideration only for the envelopes of the defects.

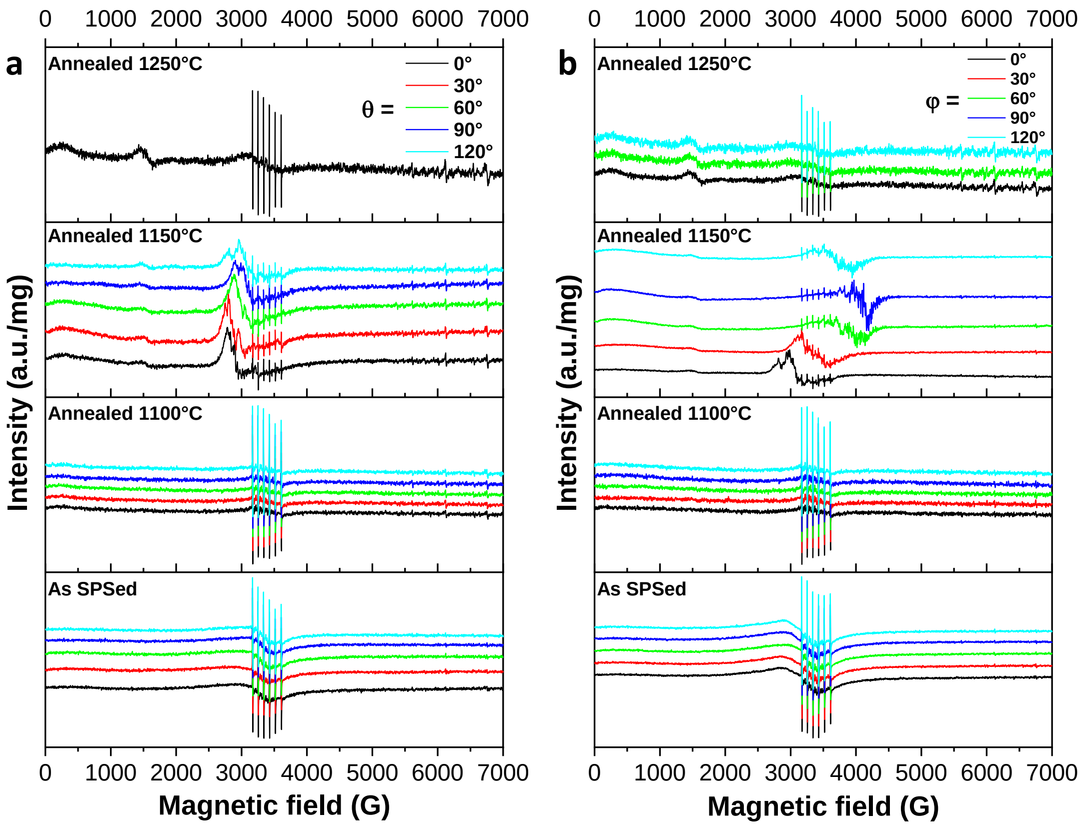

Figure 5.6: Angular dependency of the EPR spectra (300K) of the Sasol ceramic SPSed at 1500°C (3 min, 80 MPa) and subsequently annealed at 1100, 1150 and 1250°C: a) along the radial angle θ and b) the axial angle φ

Figure 5.7.a, *b* and *c* present a more thorough angular dependency analysis along the axial angle (φ = 0-210°, Δφ = 10°) of the sample annealed at 1150°C in the range H_0 = 0-7000 G (general view), then with focuses on the absorption range of BS2 and BS1 + HFS, respectively. The general view indicates that no new signal appears with φ-rotation, and the BS2, BS1 and HFS are observed for all angles. The focus on **BS2** (*Figure 5.7.b*) shows that **this center is not angular dependent**, as its position and linewidth remain constant. The focus on the range H_0 = 2500-4500 G (*Figure 5.7.c*) reveals that the **HFS is isotropic** as well, but the BS1 is strongly affected by the rotation along the axial angle φ. It is important to notice that BS1 exhibits a **minimum resonance field for φ = 0°**, *i.e.* in the **direction perpendicular to SPS pressing direction**, and a **maximum resonance field for φ = 90°**, *i.e.* in the **direction parallel to pressing direction**. In addition, it can be noticed that the signal, and in particular the elementary lines, is sensibly equivalent for $\varphi_2 = \varphi_1 + 180°$, *e.g.* φ = 0/180°, 10/190° and 20/200°, indicating the existence of a **plan of symmetry coplanar with the radial section** while the averaged BS1 center is oriented in the SPS pressing direction with no apparent preferential sense.

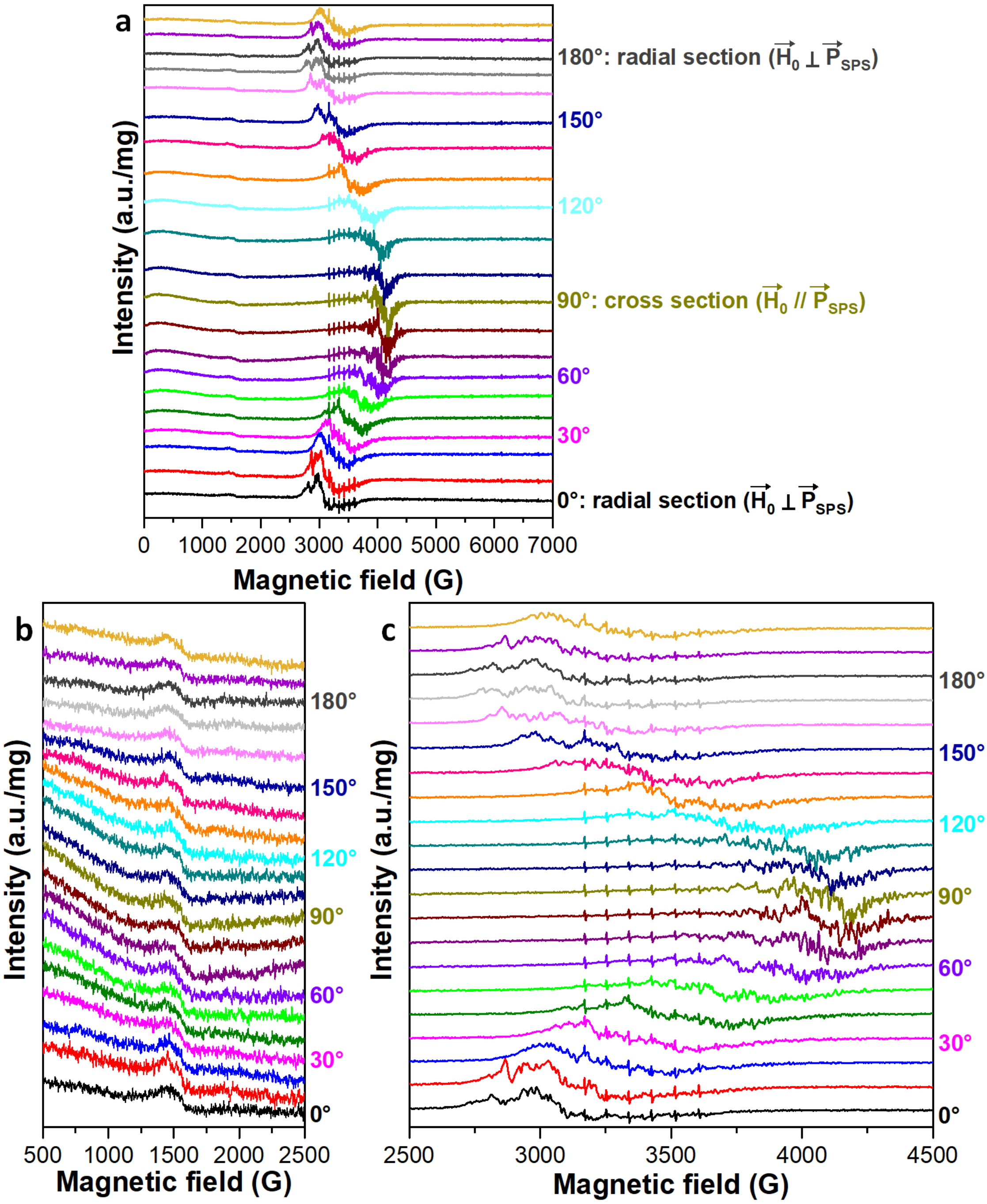

Figure 5.7: Angular dependency of the EPR spectra (300K) of the Sasol ceramic annealed at 1150 along the angle φ in the range 0-210°, with Δφ = 10°: a) general view and focus on the range of absorption of b) BS2 and c) BS1 and HFS signals

The features of the BS1 center are further analyzed in *Figure 5.8*. It was collected more carefully for φ = 85, 90 and 95° in the range H = 3600-4700 G *Figure 5.8.a*, in order to prevent any contribution from the HFS by full separation of the signals. Numerous elementary lines can be observed, which are attributed to **several hyperfine structures arising from different complex intrinsic centers**, since the different signals from simple V-type centers are all much narrower (Δ ≤ 150 G) and far less impacted by orientation [38, 45]. Unfortunately, the identification of the different hyperfine structures could not be achieved, as no regular splitting of the lines could be observed for establishing the splitting constants. In addition, the **strong modification of the elementary lines** with small rotation of Δφ = 5° was not helpful to better determine the different set of lines. It should be mentioned that the measurement of the BS1 signals has been repeated several times to ensure the reproducibility of the observed elementary lines and exclude from consideration the possibility of strong noise contribution; indeed, it was verified that all the observed lines are purely arising from intrinsic defects.

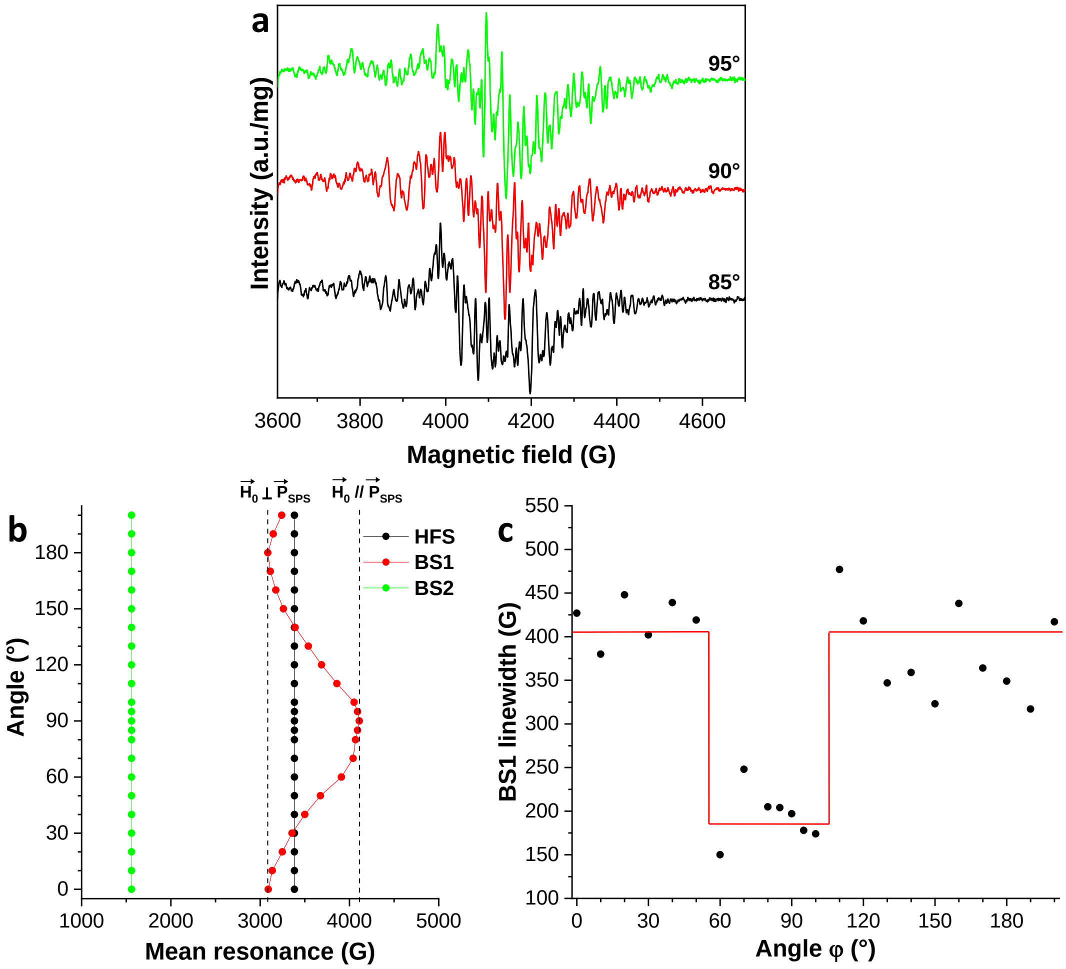

Figure 5.8: a) EPR of BS1 at φ= 85-95° and angular diagrams of b) the mean resonance of the centers and c) BS1 linewidth

The *Figure 5.8.b* and *c* present respectively the angular diagrams of the mean resonance of the different centers and of BS1 linewidth. The former shows that **the mean resonance of BS1 greatly shifts from H_0 (φ = 0/180°) = 3085 G, *i.e.* g = 2.19, to H_0 (φ = 90°) = 4110 G, *i.e.* g = 1.65**. It is the first report of such a strong anisotropy of intrinsic defects in $MgAl_2O_4$ to the best of our knowledge. It is interesting to note that the evolution of the position with the axial angle is somehow sinusoidal, and in particular the extrema are not “sharp”: in the range φ = ~70-~100°, the resonance is almost unchanged at H_0 = 4040-4110 G (g = 1.67-1.65). In the same time, the **linewidth** of **BS1** (*Figure 5.8.c*) **is greatly decreased** in approximately the same angular range, as it goes **from ~400 G for φ = 0-50° and 120-180° to ~185 G in the range φ = 60-110°**. However, the transition between the two linewidth angular ranges is **very abrupt**, and its trend somehow appears as **a well**. Therefore, it can be inferred that **all the intrinsic defects forming the BS1 envelope are oriented together in the direction of the cross section** of the sample (φ = 90°, SPS pressing direction), with a distribution of their orientation in the range φ = ~65-~115°, taking into consideration the experimental uncertainty of the angle (*e.g.* initial position of the sample, modification of the planarity during polishing…). In addition, since the linewidth decreases, we assume the resonance fields of the individual defects are closer in this φ-range.

Some points should be highlighted for a proper understanding of the cause of this preferential orientation of the intrinsic defects. The strong anisotropy is only observed after annealing at 1150°C and not immediately after SPS processing, therefore it must be deduced that it is not directly related to the sintering technique, and in particular to an orientation of the intrinsic defects through electrical effects (percolation paths, ionic current…), but rather to the **formation of defects during the oxidation of the carbon contamination**. Hence, it appears that the pressurized carbon oxide gas is then **evacuated in the axial direction** corresponding to the SPS pressing direction, while the **intrinsic defects resulting from the internal stress provoked are oriented along the evacuation path**. We infer this preferential orientation of the evacuation path and internal defects is related to the uniaxial pressing during SPS, which may result in a remaining strain in this direction in the sintered ceramic favoring the oxidation/evacuation mechanisms in the same direction with activation by thermal annealing. Further experiments are required to better elucidate this phenomenon.

2. Influence of the sintering conditions

In this section, we studied the **influence of the sintering conditions on the defects** contained in the ceramics. We first carried out a brief comparison between conventional sintering and SPS processing, then we investigated the effects of the $MgAl_2O_4$ precursor powder and the sintering temperature, as well as the applied pressure.

i. Comparison between SPS and pressureless conventional sintering

In order to **highlight the effect of the SPS processing on the defects in MAS ceramics**, we compared CL et EPR spectra of the samples as SPSed at 1500°C (3 min, 80 MPa) analyzed in the previous section and conventionally sintered in a muffle furnace at 1500°C for 200 h, both from Sasol powder. The latter specimen was not dense enough to be even translucent, but was however appreciably consolidated.

The CL and EPR spectra are compared in *Figure 5.9.a* and *b*, respectively. The former indicates that while the SPS processing maintained the density of intrinsic defects initially contained in the powder, the pressureless conventional sintering (PCS) resulted in a great annealing of the intrinsic defects. In addition, **part of the Mn^{3+}/Mn^{4+} in the powder has been converted to Mn^{2+} during the thermal treatment** under air atmosphere, while the reducing environment of SPS resulted in a full conversion. The **F-type centers** located at 2.42 eV in the powder and SPSed sample are **shifted to the lower energy** 3.25 eV after PCS while the **V-type centers** located at 5.17 eV in the powder and PCS sample are **shifted to the higher energy** 5.27 eV after SPS; The values obtained for PCS are comparable to what was observed after annealing at 1250°C (*Table 5.1*). These results clearly indicate that the **energy of the oxygen vacancies (F-centers) luminescence is decreased through oxidizing treatments**, while the **luminescence energy of the cationic vacancies/inversion (V-centers) increases during SPS**. The latter point seems particularly interesting and requires further investigation.

The EPR spectra (*Figure 5.9.b*) confirm that part of the Mn^{3+}/Mn^{4+} has been converted to Mn^{2+} (apparition of the HFS sextet), while Mn^{4+} signal remains predominant (BS2). The BS1 signal is particularly affected by the PCS processing, as **most of the constituent signals have disappeared** and only 2 remaining bands can be identified at **H_0 = 2922 G (g = 2.32) and H_0 = 3391 G (g = 2.00)**. The latter may correspond to the F^+ centers, as the oxygen vacancy with one electron trapped within normally resonates at the free electron resonance g_e = 2.0023 [8, 440]. The former has not been identified yet to the best of our knowledge, and may arise from remaining V-centers already present in the powder.

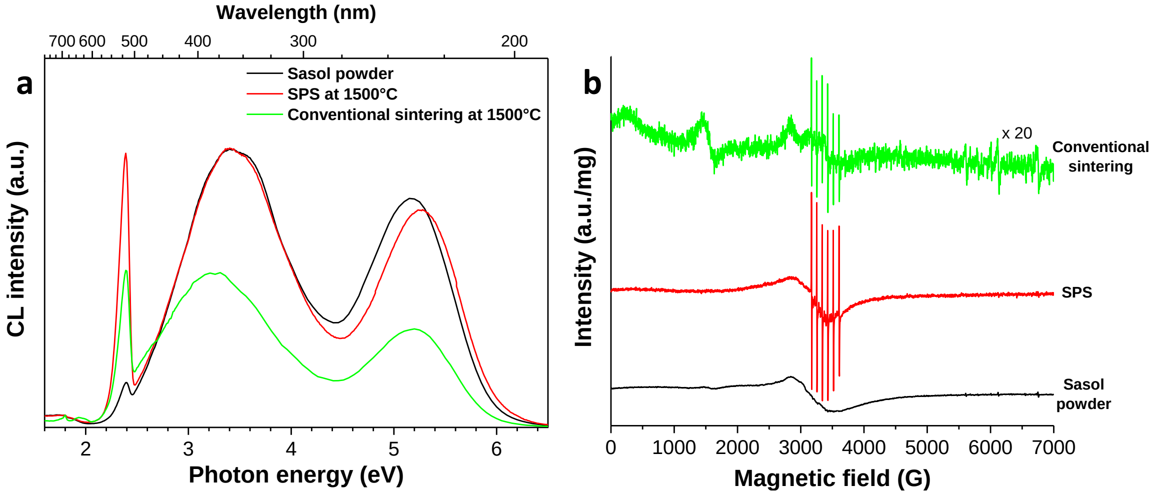

Figure 5.9: a) CL (5K) and b) EPR (RT) spectra of the Sasol powder and ceramics SPSed at 1500°C (3 min, 80 MPa) and conventionally sintered at 1500°C for 200 h

ii. *Influence of the $MgAl_2O_4$ powder precursor*

We compared the **cathodoluminescence of ceramics prepared with the same SPS conditions** (1375°C, 20 min, 10°C/min, 80 MPa) **from Sasol and S25CR-3MS powders**. Except for the precursor powder, the main differences in the properties of the samples are their mean grain size and transparency, which are respectively of 1.75 µm and 42.6% for the Sasol specimen and 870 nm and 69.0% for the S25CR-3MS one. In addition, the Sasol one has a black coloration due to carbon contamination.

The spectra are presented in *Figure 5.10*. It should be noted that a different CL set-up has been used than the one used for collecting the spectra of *Figure 5.2* and *Figure 5.9.a*, allowing proper characterization in the NIR range. Therefore, the **characteristic R-lines from Cr^{3+} luminescence** are well observed at R_1 = 1.80 eV and R_2 = 1.75 eV [441, 442]. It is clear that **the S25CR powder is by far less contaminated by Cr^{3+} and Mn^{2+}** (2.38 eV band) impurities, which may partly explain the better transparency obtained in comparison with Sasol ceramics.

In addition, what were observed as envelopes of luminescence bands of F-type (low visible, 2.5-4.5 eV) and V-type (UV, 4.6-6 eV) centers in *Figure 5.2* are better resolved with this CL set-up, and the different bands convoluted can be distinguished. **Twelve bands** (centered at 2.60, 2.81, 3.04, 3.27, 3.60, 3.68, 4.01, 4.48, 4.67, 5.01, 5.24 and 5.63 eV) assumed to arise **from intrinsic defects** are observed in the ceramics prepared from both commercial powders, with very small differences of intensity of these bands depending on the precursor that has been used. The shouldering band at ~2.60 eV (476 nm) may correspond to the remaining band at 2.55 eV observed after annealing at 1150°C or above in *Figure 5.2.a*, which was attributed to **clustering oxygen vacancies giving rise to F_2 defects** [8, 66, 300]. The band at **2.81 eV** (441 nm) has been reliably interpreted as **F^+-center emission** [32], while Savita *et al.* attributed the emission at **3.04 eV** (408 nm) to **charge compensated cluster F^+-Mg_{Al}^- complex center** [421]. The 3.27 eV (379 nm) and 4.01

eV (309 nm) emission bands has been calculated to arise from the **F-center** (oxygen vacancy with two trapped electrons) [55] and **V_{Al}^{2-}** (Al^{3+} vacancy with a single hole trapped at a nearby O^{2-}) [56]. The bands at 3.60 and 3.68 eV (344 and 337 nm, resp.) as well as the bands at higher energy in the range 4.5-6.0 eV have been tentatively related, at least partly, to **antisite defects Al_{Mg}^{+} and Mg_{Al}^{-} and intrinsic luminescence of $MgAl_2O_4$ spinel crystals** [38, 45, 420], while their proper attribution remains an ongoing matter of investigation.

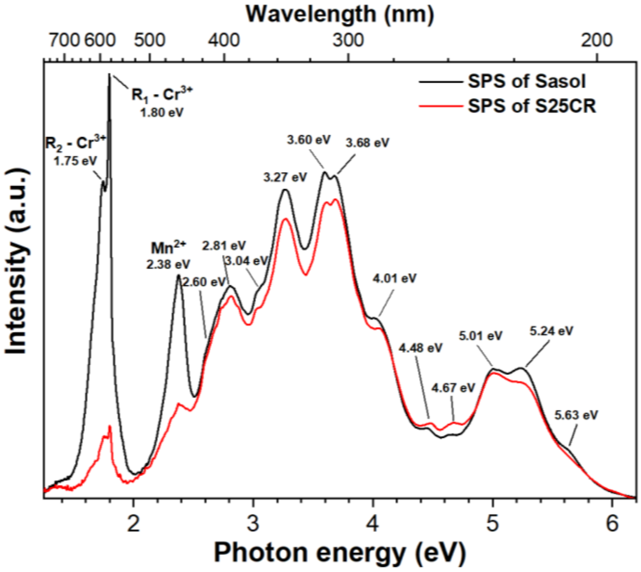

Figure 5.10: CL (RT) spectra of the ceramics SPSed at 1375°C (20 min, 80 MPa) from raw Sasol and S25CR-3MS powders

It is interesting to notice that the **MAS precursor powder**, as well as the grain size (at least in this range) and carbon contamination, **have marginal influence on the intrinsic defects**. Therefore, these defects may be formed during SPS processing, with an equilibrium state of their nature and concentration depending on sintering conditions, given the very close intensity of the different CL bands, and regardless of the initial defects in the precursor.

iii. Influence of the sintering temperature

We investigated **the effect of the sintering temperature on the concentration and nature of defects** in S25CR-3MS ceramics by cathodoluminescence. Two ceramics were analyzed, SPSed at 1275 and 1375°C, other sintering parameter being unchanged (1375°C, 20 min, 10°C/min, 80 MPa). Their most relevant properties are their mean grain size and transmittance at 600 nm, which are respectively 310 nm and 78.8% for the 1275°C- sample and 870 nm and 69.0% for the 1375°C-sample (complete analysis in *Chapter 4.II.2.i*).

The CL spectra (RT) are presented in *Figure 5.11*. The very same emission bands are observed for both samples, confirming **the same nature of defects**. However, except for the Cr^{3+} and Mn^{2+} luminescence at 1.8 and 2.38 eV, respectively, **almost all bands are more intense for sintering at 1275°C**. In particular, the bands related to **F^{+} centers at 2.81 and 3.04 eV** and even more importantly the bands in the range **4.6-6 eV ascribed to antisite defects** are highly increased at lower temperature. This may be due to a **partial annealing of the defects during the sintering**, in particular the cationic inversion, with higher temperature of sintering. However, this point must be further investigated to better understand the causes and mechanisms of the formation and healing of the defects during SPS processing.

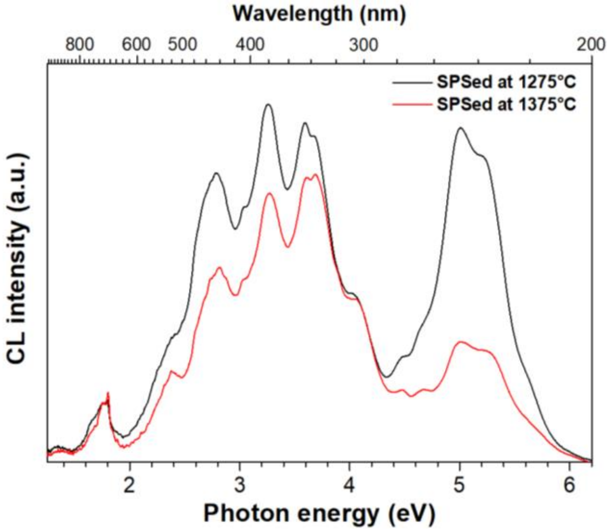

Figure 5.11: CL (RT) spectra of the S25CR-3MS ceramics SPSed at 1275 and 1375°C (20 min, 80 MPa)

We also investigated **the effect of sintering temperature at higher applied pressure of 400 MPa**. Two samples SPSed at 1050°C (minimimal temperature for full densification at 400 MPa) and at higher temperature of 1100°C have been analyzed by optical UV-vis transparency and EPR spectroscopies. It must be noted that both ceramics had very similar mean grain size of ~185 nm, and therefore the differences observed in the following analysis cannot arise from the difference of size of the crystalline domains. The transmittance spectra with optical photographs are presented in *Figure 5.12.a*. The comparative observation of the photographs clearly evidences a **yellow tint of the material SPSed at 1100°C**, with a **transmittance sensibly decreased for λ < 500 nm**.

The optical density OD of the samples (*Figure 5.12.b*) show some **absorption bands at ~2.95, 3.95 and 4.65 eV**, which are not well defined due to their small intensities and positions in the UV cut-off region of the samples (200-400 nm). According to literature, these bands can be ascribed to **hole-type V-centers** [45, 56]; based on calculations using the density functional theory, the 2.95 eV band arises from $\mathbf{V_{Al}^{-}}$/ $\mathbf{V_{Al}^{3-}}$ color centers, the 3.95 eV band from $\mathbf{V_{Mg}^{2-}}$ and the 4.65 eV one from $\mathbf{V_{Al}^{2-}}$ centers [56]. The difference of optical density between the two samples is plotted in inset, and permits evidencing **stronger absorption bands in the 1100°C sample**. At least three bands are more intense in this material: the previously described 2.95 and 3.95 eV ones from V-centers, and a **higher energy band at 5.65 eV**, which was hidden in the cut-off region in the optical density spectra. The latter band is in the range of absorption of **F-centers**, *i.e.* oxygen vacancies with two trapped free electrons for charge compensation (~5.3 eV) [45, 55]. These results indicate that the higher temperature used with high applied pressure provoked **the formation of additional intrinsic defects**, thus reducing the optical transparency and giving a yellow tint to the material.

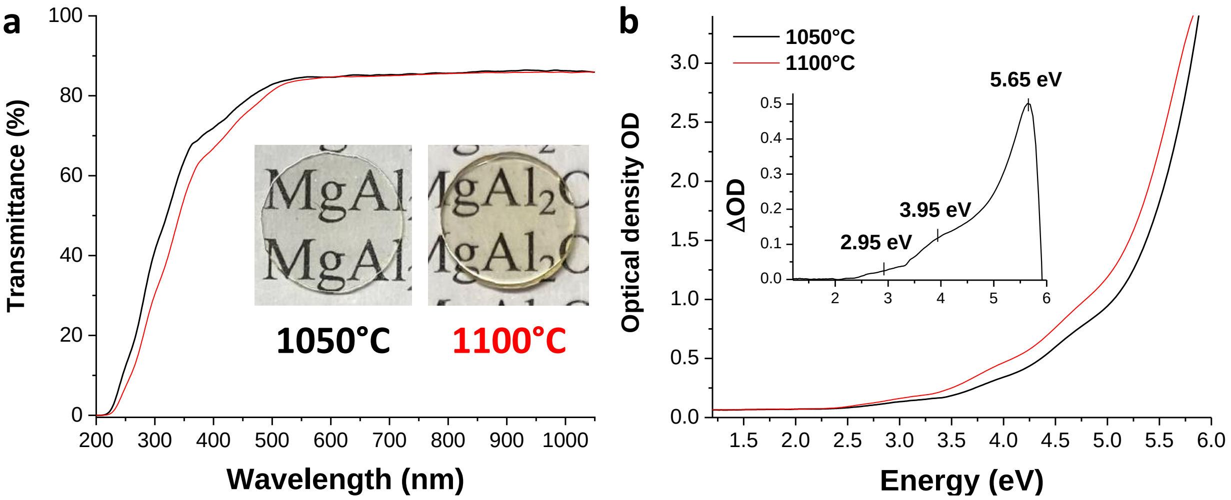

Figure 5.12: a) Transmittance spectra and photographs and b) absorption spectra of the S25CR-3MS ceramics SPSed at 1050 and 1110°C with 400 MPa applied pressure; inset in b) shows the difference of optical density between the 1100 and 1050°C samples

A complementary preliminary electron paramagnetic resonance (EPR) spectroscopic analysis has been carried out on the samples, and is presented in *Figure 5.13*. It appears clearly that the **BS1 paramagnetic center** with mean resonance field H_0 = 3300 G ascribed mostly to intrinsic defects is **much stronger in the sample processed with higher temperature**, confirming the **higher density of intrinsic defect centers**.

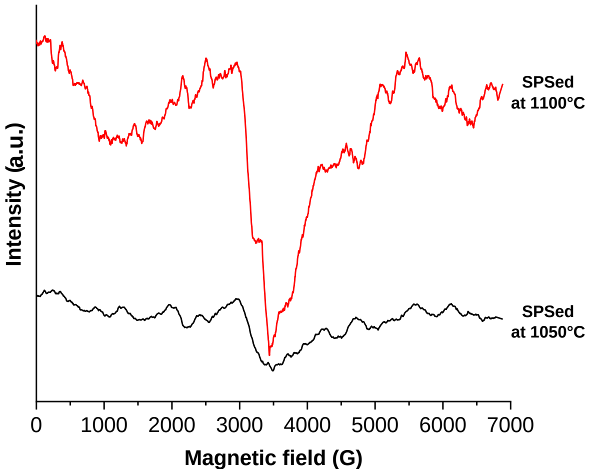

Figure 5.13: EPR (RT) spectra of the S25CR-3MS ceramics SPSed at 1050 and 1110°C with 400 MPa applied pressure

iv. Influence of the applied pressure

Finally, we investigated **the influence of the applied pressure during SPS on the evolution of the defects** in $MgAl_2O_4$ ceramics prepared from S25CR-3MS precursor powder, presented and discussed in *Chapter 4.II.2.iv*. The samples sintered with applied pressure from 80 to 500 MPa and sintering temperature from 1275 to 1050°C were characterized by electron paramagnetic resonance (EPR) and photoluminescence (PL) spectroscopies to analyze their defects. The relevant characteristics of the prepared ceramics as well as their preparation conditions are summarized in *Table 5.4*. The samples will be referred to only by the applied pressure during their sintering in the following for simplicity.

Table 5.4: Preparation conditions and properties of ceramics SPSed with different applied pressure-sintering temperature conditions

Applied pressure (MPa)	Sintering temperature (°C)	Mean grain size (nm)	Transmittance at 600 nm (%)	Inversion parameter [(b)] (%)
80	1275	310	75.2	41
150	1200	235	74.0	48
200	1150	226	74.3	50
300	1100	168	84.8	42
400	1050	158	84.7	41
500	1035	135	86.3	45
700	1015	126	84.7	46
1000	1000	116 [(a)]	83.0	45

(a) Estimated from *Equation 4.6*
(b) Evaluated from combined energy minimization – Monte Carlo predictions in [46] based on the lattice constant

The XRD patterns of the ceramics are presented in *Figure 5.14*. The diffractograms evidence **pure spinel phase**, with no appreciable variation of the lattice cell constant when the grain size diminishes. The fine analysis of the XRD patterns by Rietveld refinement reveals a **significant cationic inversion** in the prepared ceramics about **40-50%** (evaluated from the combined energy minimization – Monte Carlo predictions by Ball *et al.* in [46]), which was not specific to the preparation conditions of temperature and pressure.

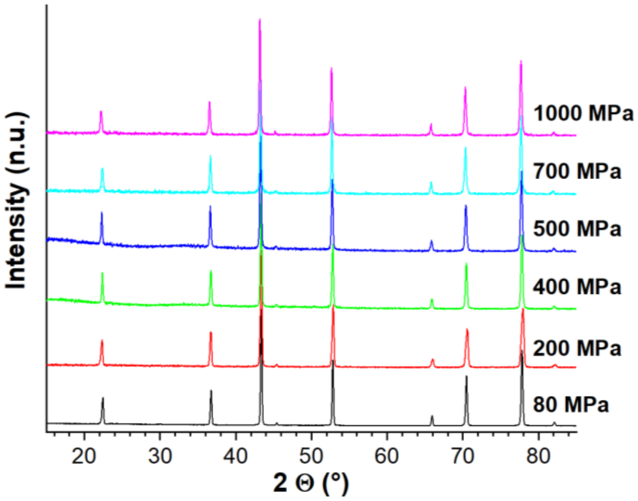

Figure 5.14: XRD patterns of the S25CR-3MS $MgAl_2O_4$ ceramics prepared by SPS at 80-1000 MPa

The HAAD-STEM imaging and 4D-STEM of the ceramic prepared with P = 500 MPa were performed in order to clarify the nature of grain boundaries, and are shown in *Figure 4.13*. The low magnification micrograph in *Figure 5.15.a* permits distinguishing **fine grains of size ~100-150 nm**, in agreement with SEM results, and **grain boundary (GB) regions of thickness $w \leq 5$ nm**. This value of *w* may seem high, but it is mostly an artefact of characterization due to the fact that depending on the angle between the electron beam and the interface between two grains, the GB appears larger than it is really. At higher magnification, **no amorphous interface** is evidenced even on GB that does not seem to be abrupt (irregular and curved GB).

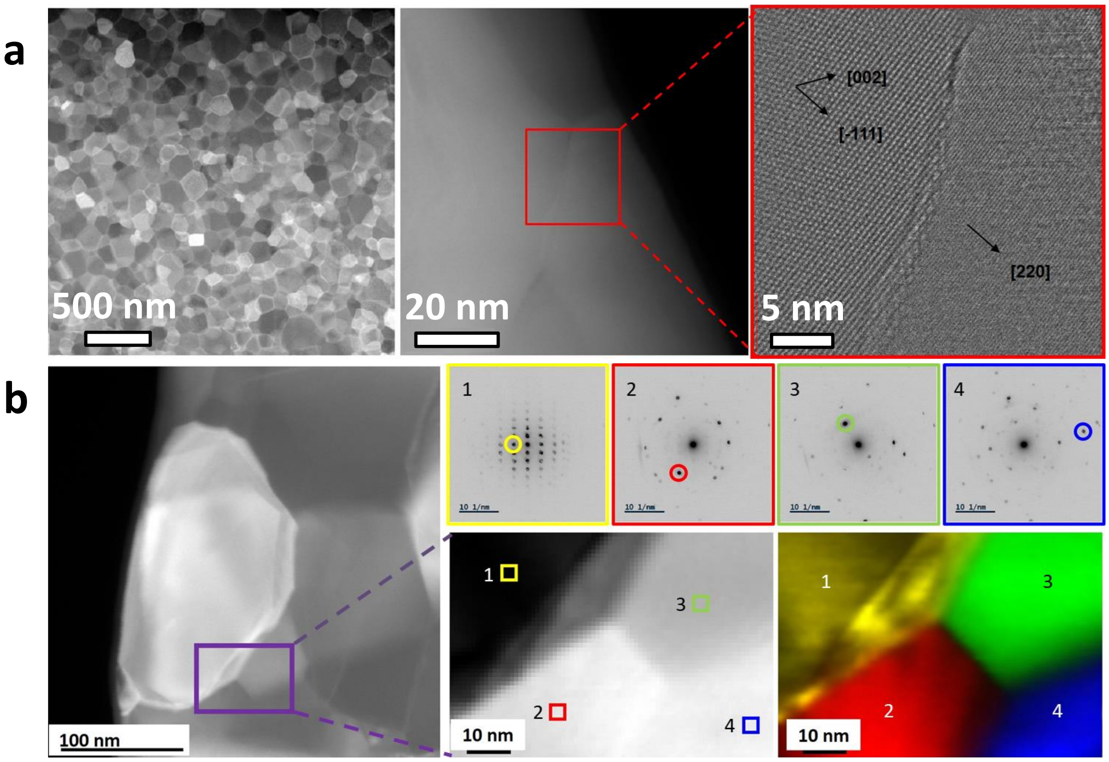

Figure 5.15: a) HAADF-STEM micrographs of the ceramic SPSed at 500 MPa with low (left), medium (middle) and high (right) magnification and b) 4D-STEM analysis of grain boundaries area (marked by square) on HAADF STEM image (left); electron diffraction patterns (ED) in selected pixels 1, 2, 3 and 4 are shown (upper raw) as well as virtual dark field image (right, down) obtained by selecting signals defined by colored circles in ED patterns with a numerical mask

In *Figure 5.15.b*, several GB are characterized with the help of 4D-STEM technique, in which each pixel of the map contains 2D electron diffraction (ED) pattern. One must notice that the TEM lamella was oriented to align a low index zone axis of the brighter grain with the optical axis of the TEM (*Figure 5.15.b*, left image). 4D-STEM allows to reconstruct virtual dark field (VDF) images extracting signal from diffracted spots characteristic of each grain. On superimposed VDF images (*Figure 5.15.b*, bottom, right), **no amorphous area is present in grain boundaries** as stated by STEM imaging. Moreover, the composition of the ceramics over the grain bulk and boundary regions is **homogenous** (EDX, not shown).

In disagreement with previous conclusions based on the crystalline field weakening in $MgAl_2O_4$ nanoceramics sintered with high applied pressures [443], we reject the appearance of amorphous phase at GB. Our observations are in agreement with results of Sokol *et al.* [19], who have found that SPSed MAS ceramics with P up to 1 GPa and T down to 1000°C, *i.e.* similar conditions than in this work, present clean GB with no evidence of any amorphous layer, but are thought to accommodate dislocations due to a final stage densification mechanism involving GB sliding. This point is investigated in *Figure 5.16*, where a grain boundary between two grains oriented in [110] direction with parallel plans is analyzed by inversed fast Fourier transform (IFFT) constructed from (220) planes. **Numerous crystalline defects** are observed, in particular **dislocations and stacking faults**, evidencing **the high microstrain** in the ceramics. However, the **defects are not especially located on the GB area** highlighted by the orange lines, which appears to be **quite well crystallized instead**, and therefore the mechanism proposed in [19] cannot be verified.

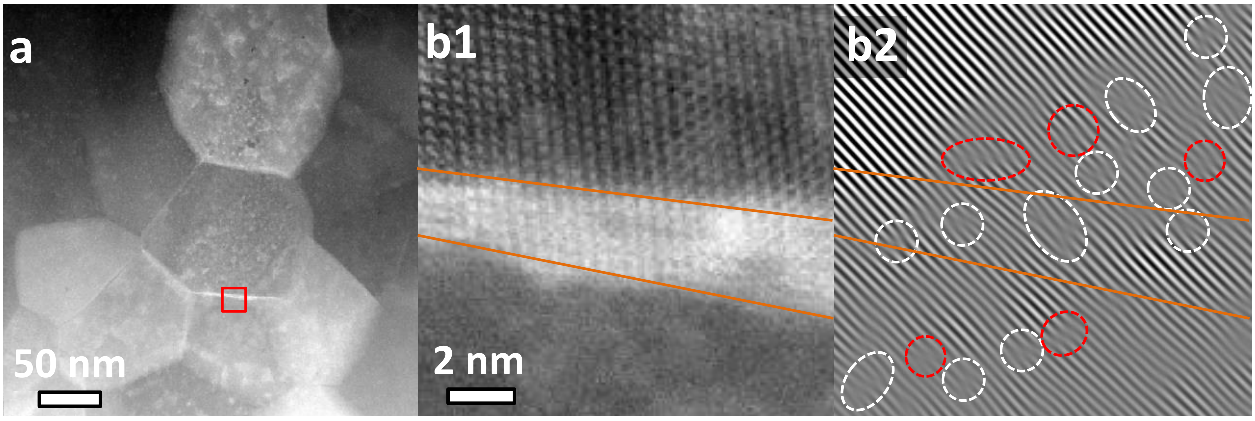

Figure 5.16: a) HAADF-STEM micrograph of the ceramic SPSed at 500 MPa; b1) high magnification on the garain boundary interface in red square area in a), and b2) the corresponding inversed fast Fourier transform (IFFT) constructed from (220) planes, with most of the edge dislocations and stacking fault circled in white and red, respectively; the grain boundary is highlited in b1) and b2) by orange lines

It should be noted that it has been reported that **GB readily accumulate V_{Mg}^{2-} vacancies compensated via Al_{Mg}^{+} antisite defects** [444]. Inversion due to the antisite formation at grain boundaries can therefore be a reason of the crystalline field reduction reported in [443]. According to our measurements, the **inversion did not show a dependence on the grain size** of the prepared ceramics (see *Table 5.4*), as this could be expected based on the above-mentioned accumulation of antisite defect at GB. However, in view of the thin boundary layer $w \leq 5$ nm, the variation of the boundaries area in the prepared ceramics constitutes only about 5% of the ceramics volume, which is within the confidence range of these measurements.

A preliminary study by EPR spectroscopy of the ceramics densified with applied pressure of 80 to 500 MPa has been performed to investigate the evolution of the paramagnetic centers with an increase of loading force. The spectra are presented in *Figure 5.17*. It is remarkable that **only the BS1 defect** already mentioned and ascribed **mostly to intrinsic defects** is detected, with **no particular influence of the sintering conditions** on the mean resonance field at $H_0 \approx 3300$ G and on the linewidth $\Delta H \approx 650$ G. In particular, no HFS sextet (Mn^{2+}) or BS_2 (ascribed to Mn^{4+}) signals are observed, due to the higher purity of S25CR powder in comparison with Sasol. These results seem to indicate that **in this low temperature range** (minimum temperature required for full densification with the specific applied pressure), the **pressing with high load during HPSPS does not imply further intrinsic defects**. Forthcoming complementary measurements in order to deconvolute the contribution of the different intrinsic defects should allow better analysis of the BS1 defects in these materials.

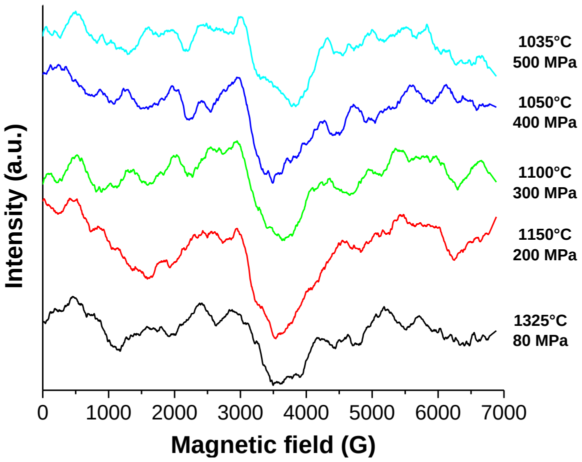

Figure 5.17: EPR spectra of the S25CR-3MS ceramics SPSed with applied pressure between 80 and 500 MPa

The characteristic PL spectra of the prepared ceramics with smallest and largest grain sizes (SPSed at 500 and 80 MPa, resp.) in the UV-visible-NIR range (300-900 nm) are shown in *Figure 5.18*. The most intense PL band of $MgAl_2O_4$ spinels, with spectral maximum in the range of 230-250 nm (5.0-5.4 eV) and intensity commonly depending on the sample origin and processing, is out of our interest in this work. Although this band has been earlier assigned to the recombination of conduction-band electrons with holes captured at the oxygen ions nearby cation vacancy or antisites [445], its nature remains an issue. Our attention is focused on *i)* the **broadband emission of F-type centers spanning over the UV-visible range** and *ii)* the **structured and non-structured broadband emissions of Cr^{3+} in the NIR range**. The PL was excited on the excitonic transitions (160 nm, 7.8 eV) [446] and in the range of the F-centers absorption (245 nm, 5.1 eV). The structured component of the NIR PL is broadened: this is a **signature of inverse spinel phase** [447], in agreement with data of *Table 5.4*. We also notice the **heterogeneous nature of the F-centers** PL, which spectral position changes depending on the excitation energy, in agreement with earlier studies [10, 32].

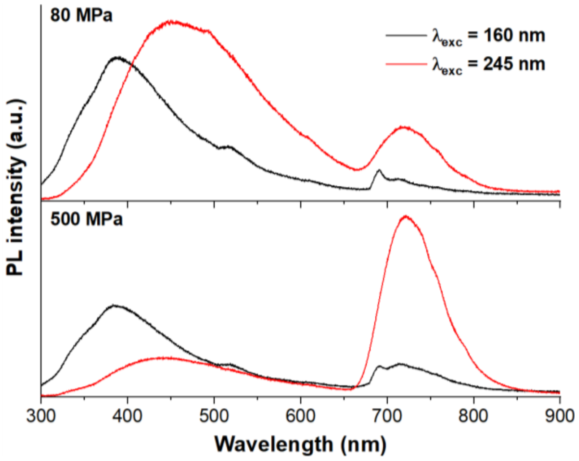

Figure 5.18: Low temperature (12K) PL spectrum of the ceramics SPSed with P = 80 MPa (top) and 500 MPa (bottom) with excitation at 160 and 245 nm; the spectral resolution is $\Delta\lambda_{PL}$ = 3 nm

It is well know that PL of Cr^{3+} ions in $MgAl_2O_4$ spinel depend on the ligand field, exhibiting **narrow structured (R lines) emission on $^2E_g \rightarrow {}^4A_{2g}$ electronic transitions in the strong field** and **broadband unstructured emission on $^4T_{2g} \rightarrow {}^4A_{2g}$ transitions in the weak field** [448, 449], which has been explained by the electron-lattice and spin-orbit coupling of the excited states [450, 451]. Complementary, so-called N lines related to the lattice imperfections (and more particularly to perturbed short-range order by neighbour substitutional impurity atoms and/or defects) can appear in $MgAl_2O_4$ spinels, the most intense of which N_i (i = 1, 2, 3,…) are situated close to the R lines at ~690 nm [452]. The appearance of N-line and broadband emissions has been connected to Cr^{3+} sites with respectively strong and weak ligand characters [453]. In our PL spectra taken with a low resolution of 3 nm, the R and N lines and their sidebands were not resolved. However, PL spectra with a higher resolution of 0.3 nm showed several very weak peaks (*e.g.* at 709 and 717 nm) superimposed on the broad band, which supports a **negligible contribution of the structured transitions to the broadband intensity**. We notice that the N_4 line at 700.4 nm did not show up in our spectra indicating a negligible amount of Cr^{3+}-Cr^{3+} pairs, in accordance with previous studies [454].

The photoluminescence excitation (PLE) spectra of Cr^{3+} ions in a reference $MgAl_2O_4$ spinel single crystal (ALINEASON GmBH) and in the 500 MPa ceramic are presented in *Figure 5.19*. The **PLE spectrum of Cr^{3+} in single crystal** (top, λ_{em} = 685 nm) consists of the **main band at 185 nm** (6.8 eV), which results in the $^2E_g \rightarrow {}^4A_{2g}$ electronic transitions in the strong ligand field. Although the bandgap energy of MAS is still an issue, a value of **E_g = 8.3 ± 0.1 eV** has been reported following low-temperature CL and PL measurements [419, 420, 446]. The contribution to the Cr^{3+} emission of free charges (after E_g excitation > 8.3 eV), excitons (7.8 eV) and F-centers (5.3 eV) seems to be insignificant. In contrast, the **PLE spectrum of F-centers** (top, λ_{em} = 420 nm) evidences **two major contributions from mainly excitons (7.8 eV) and F-centers (5.3 eV)**. Because of the net separation of Cr^{3+}, F-centers and excitons PLE bands, we assume no coupling between the respective excited states and intrinsic relaxation channels, which allows assigning the **6.8 eV band to the electronic transition of Cr^{3+} substituting Al^{3+} in MAS**. In contrast to the single crystal, **PLE spectra of the prepared ceramic are strongly modified** (bottom), as both excitons and F-centers contribute to the NIR luminescence of Cr^{3+}. This result evidences an **effective energy transfer from excitons and F-centers to ^2E_g and $^4T_{2g}$ excited states of Cr^{3+}**. Comparison between PLE at λ_{em} = 685 and 725 nm permits distinguishing proper electronic transitions in Cr^{3+} ions resulting in the structured $^2E_g \rightarrow {}^4A_{2g}$ emission, which appears at 6.8 eV similarly to single crystal.

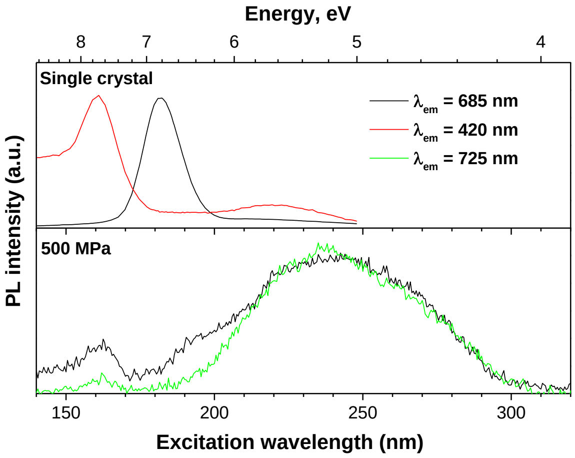

Figure 5.19: Excitation spectra of NIR (685 nm) and UV-Vis (420 nm) PL in reference $MgAl_2O_4$ single crystal (ALINEASON GmBH) and structured (685 nm) and non-structured (725 nm) PL components in the 500 MPa ceramic; spectral resolution $\Delta\lambda_{PL}$ = 0.33 nm

Furthermore, scanning the excitation wavelength across this band induces strong modifications of the PL lineshape, which was different in single crystal and nanophase ceramics, as shown in *Figure 5.20*. Indeed, while **structured PL peaks at λ_{exc} = 185 nm** in both materials, the **broadband PL remains almost constant in the single crystal and progressively intensifies in the ceramics** with an increase of $\lambda_{exc} > 185$ nm. This corresponds to a weak tail of the Cr^{3+} excitation spectrum in the UV spectral range (top, λ_{em} = 685 nm in *Figure 5.19*). We notice that **no signature of the structured Cr^{3+} emission is observed after excitation at $\lambda_{exc} > 200$ nm**. This observation supports the conclusion about low Cr^{3+} ions concentration (< 0.1 at%) in the material, in accordance with NIR PL measurements by Izumi *et al.* [455]. This spectral range corresponds to the **excitation of F-centers**, which are involved in the energy transfer to Cr^{3+} ions coordinated in the weak ligand field. In the same time, the energy transfer from F-type centers to Cr^{3+} ions coordinated in the strong ligand field seems to be prohibited. Furthermore, analysis of the PL spectra shows that the **unstructured NIR emission on the $^4T_{2g} \rightarrow {}^4A_{2g}$ transition intensifies** (λ_{exc} = 160 nm, *Figure 5.18*) and the **intensity ratio between F-centers and Cr^{3+} ions luminescence weakens** (λ_{exc} = 245 nm, *Figure 5.18*) **with decrease of crystalline size order**. Based on these observations, we postulate that **the energy transfer from excitons and F-centers in $MgAl_2O_4$ ceramics is grain size-dependent**.

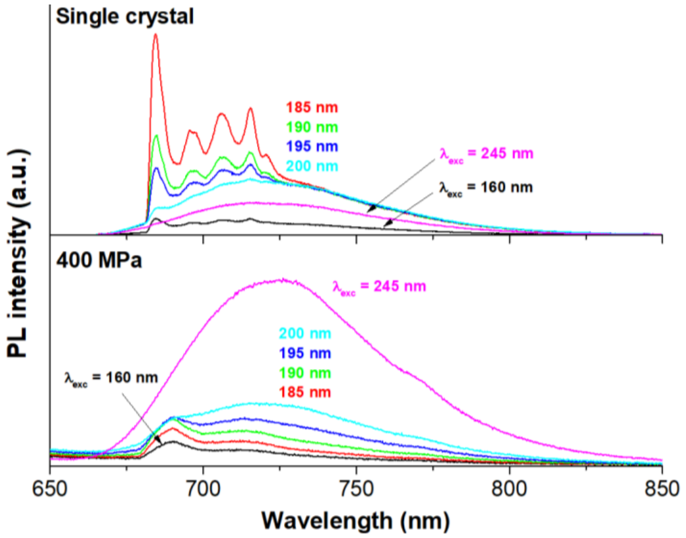

Figure 5.20: PL spectra (12K) of ALINEASON single crystal and 400 MPa ceramic at different excitation wavelengths; $\Delta\lambda_{PL}$ = 3 nm

The PL intensity ratio of Cr^{3+} ions on the $^2E_g \rightarrow {}^4A_{2g}$ and $^4T_{2g} \rightarrow {}^4A_{2g}$ electronic transitions, *i.e.* the structured and non-structured emission respectively, after light absorption by excitons (λ_{exc} = 160 nm, $h\nu_{exc}$ = 7.8 eV) is shown in *Figure 5.21*, as a function of the mean crystalline grain size (GS) of the $MgAl_2O_4$ ceramics. The experimental points fit **linear dependence on size**:

$$\frac{I_{685\,nm}}{I_{725\,nm}} \propto GS \qquad \textit{Equation 5.1}$$

which is a **clear signature of the size effect** expressed *via* **volume-to-surface ratio V/S = αGS** [11], where α is a coefficient dependent on the grain geometry.

We attribute this phenomenon to **the energy transfer from an exciton X^*, taking place in the crystalline volume** (*Equation 5.2*) and **at the grain boundaries** (*Equation 5.3*):

$X^* \rightarrow Cr^{3+}\ (^2E_g)$ *Equation 5.2*

$X^* \rightarrow Cr^{3+}\ (^4T_{2g})$ *Equation 5.3*

Assuming the homogeneous spatial distribution of Cr^{3+} in the ceramics, PL intensity coming from $Cr^*(^2E_g)$ and $Cr^*(^4T_{2g})$ would be **proportional to respectively bulk crystalline (V) and interface (V_w) volumes**, where *w* is the interface thickness. This explanation is supported by the conclusions about a weak ligand field of grain boundary regions in $MgAl_2O_4$ ceramics due to the antisites formation.

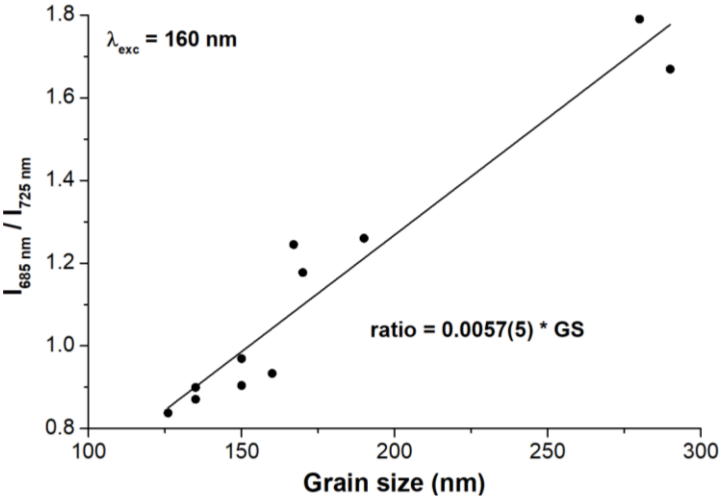

Figure 5.21: Intensity ratio between structured (λ_{em} = 685 nm) and non-structured (λ_{em} = 725 nm) PL of Cr^{3+} impurity in $MgAl_2O_4$ ceramics spinel versus crystalline grain size for λ_{exc} = 160 nm; linear least-squares fit of experimental data is shown by solid line

Another confirmation of the grain size effect was obtained from PL analysis after F-type centers excitation at λ_{exc} = 245 nm ($h\nu_{exc}$ = 5.1 eV) and λ_{exc} = 210 nm ($h\nu_{exc}$ = 5.9 eV). As it was stated above, this spectral range ($\lambda_{exc} \geq$ 210 nm) results in: *i)* UV-Vis luminescence of F-centers and *ii)* unstructured NIR emission of Cr^{3+} ions on $^4T_{2g} \rightarrow {}^4A_{2g}$ transitions. The **luminescence intensity ratio $I_{UV\text{-}Vis}/I_{NIR}$ of F-centers and Cr^{3+} ions as a function of the mean crystalline grain size of $MgAl_2O_4$ ceramics** is shown in *Figure 5.22*. Both experimental series fit **linear dependence on grain size**:

$\frac{I_{UV-VIS}}{I_{NIR}} \propto GS$ *Equation 5.4*

We attribute this phenomenon to the **energy transfer from F-centers taking place at the grain boundaries**:

$F^* \rightarrow Cr^{3+}\ (^4T_{2g})$ *Equation 5.5*

We notice that **PL bands of F-type centers are red-shifted after excitation at 5.1 eV** with respect to that at 5.9 eV (*Figure 5.18*), suggesting their different environments. By consequence, **the energy transfer process from F-centers to Cr^{3+} ions has also different efficiencies**, which are expressed by the lines slopes in *Figure 5.22*. This additionally supports the conclusion about **heterogeneous nature of these defects**. Moreover, the energy transfer from higher lying F-centers (excited at 5.9 eV, 210 nm) appears to be significantly stronger, which reflects a **longer interaction distance** and, consequently **larger material volume concerned by the process**.

In agreement with PL spectra in *Figure 5.20*, F-centers do not transfer energy to the ^2E_g state of chromium. Furthermore, a comparison between two excitation wavelengths in *Figure 5.22* shows that the energy transfer from the more energetic type of F-centers has stronger rate (slopes of straight lines), which confirms strong heterogeneity of these centres in the material. One more interesting feature of this phenomenon is **the apparent critical grain size GS ≈ 120 nm of the crystalline grains**, obtained by the intensity ratios extrapolation to zero in *Figure 5.22*. This size could be interpreted as that of **the dominant electronic coupling of different electronic states in the spinel matrix**, resulting in the efficient energy transfer.

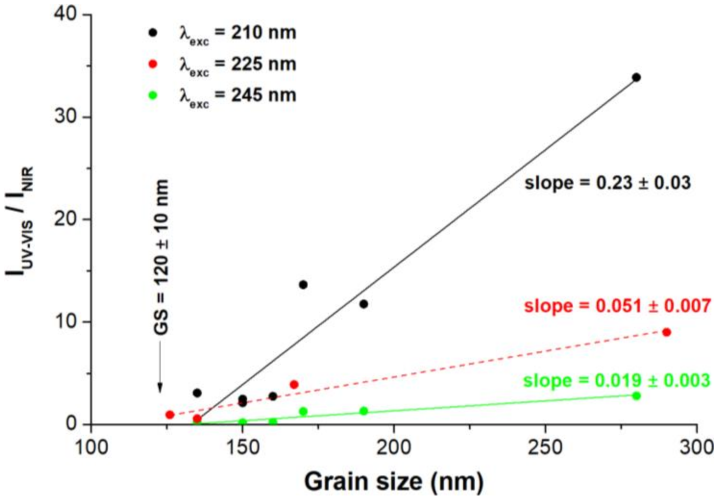

Figure 5.22: Intensity ratio between UV-Vis (F-centers) and non-structured NIR (Cr^{3+}) PL of $MgAl_2O_4$ ceramics spinel versus crystalline grain size with λ_{exc} = 210, 225 and 245 nm; linear least-squares fits of experimental data are shown by solid lines

We notice that the decrease of crystalline field strength with an increase of sintering pressure and consequent decrease of the crystalline size has been suggested by Gluchowski and Strek [443]. In connection with results of Sokol *et al.* [19] and Nuns *et al.* [444], **our results clarify the mechanism of the energy transfer over the crystalline core to grain boundaries in the nanophase spinel ceramics**. Some spread of the experimental data in *Figure 5.21* and *Figure 5.22* can reflect the spread of shapes of the crystalline domains, which control the electron transport and excitation transfer in the material. Furthermore, localization of antisites at the $MgAl_2O_4$ spinel grain boundaries is expected to be a feature of the SPS process. Future studies will provide more precision to the grain size effect in nanophase spinel ceramics.

3. Conclusion

In this sub-chapter, we studied the evolution of defects in $MgAl_2O_4$ ceramics through their processing, including the influences of SPS processing and subsequent annealing and sintering conditions.

We found that **SPS processing do not introduce dramatic content of intrinsic defects in MAS ceramics**, although comparison with conventional sintering evidenced higher concentration of defects, the cation-related defects (antisite, vacancies…) being the most impacted. The common Mn impurity in MAS is greatly affected by SPS, as the reducing atmosphere converts all possible oxidation states to Mn^{2+} form. **Subsequent annealing at moderate temperature ~1100°C allows important healing of the intrinsic defects**. Higher temperature of treatment at 1150°C results in the oxidation of entrapped carbon contamination, provoking **high internal stress in the material**. Therefore, **new intrinsic defects are**

formed with a preferential orientation along the evacuation path of the CO_2 gas, resulting in a **strong anisotropy of the paramagnetic resonance field** from g = 2.19 in the radial section $\left(\vec{H}_0 \perp \vec{P}_{SPS}\right)$ to g = 1.65 in the cross section $\left(\vec{H}_0 \parallel \vec{P}_{SPS}\right)$. Such anisotropy of intrinsic defects in $MgAl_2O_4$ ceramic is reported here for the first time, to the best of our knowledge. Further annealing at 1250°C suppresses these newly formed defects, while Mn^{2+} is progressively converted to Mn^{4+}.

It was found that the precursor powder has little effect on the intrinsic defects found in ceramics, for same sintering conditions. In contrast, the temperature of SPS processing was shown to have a great impact on these defects: for low applied pressure (80 MPa), lower temperatures result in higher content of F^+ centers and antisite defects, while **for higher pressure** (400 MPa), **the formation of defects is favored by higher temperature** instead, resulting in yellow tint of the materials. This may be due to the fact that higher applied pressures induce the final stage of densification to be controlled by deformation of the grains *via* grain boundary sliding accommodated by dislocation motion, rather than by oxygen ions diffusion (see *Chapter 4.II.2.iv*). Finally, the effect of increasing the applied pressure, and most of all decreasing the grain size by lowering the temperature, was investigated. The PL and PLE spectra were strongly affected by the crystalline grain size varied between 100 and 300 nm, which was explained by **optical transitions of Cr^{3+} in ordered (grains bulk) and perturbed (grains boundary) regions of samples**. It was found that the structured PL component of Cr^{3+} ions on the $^2E_g \rightarrow {}^4A_{2g}$ electronic transition weakened and the broadband one on the $^4T_{2g} \rightarrow {}^4A_{2g}$ electronic transition intensified with the decrease of grain size after energy transfer from the exciton. The PL intensity ratio of $Cr^*(^2E_g)/Cr^*(^4T_{2g})$ linearly increased with the grain size. A careful analysis of the grain boundaries evidenced **no amorphous material**, and therefore **high local inversion** was assumed. It was observed that F-centers transfer energy to Cr^{3+} at the grain boundaries and the **PL intensity ratio of F-center/Cr^{3+} linearly increased with the grain size**.

II. Influence of Ta_2O_5 addition on the defects

In this section, we study **the effect of Ta_2O_5 addition on the structural defects in MAS ceramics** by luminescence spectroscopies. The ceramics studied have been prepared from Sasol and L-Ta_2O_5 precursor powders. We choose to investigate the influence of Ta_2O_5 solely with a nominal addition rate of 1 wt%.

The cathodoluminescence spectra recorded at 5K of ceramics SPSed at 1450°C for 3 min, without and with TaO_5 addition, are presented in *Figure 5.23*. It should be noted that the Ta_2O_5-added ceramic presented black spots observable by naked eyes, which we interpreted as **highly oxygen deficient area within Ta-based inclusions**; in addition, Ta-based phases in the materials are trirutile $MgTa_2O_6$ and mostly corundum-like $Mg_4Ta_2O_9$ (see *Chapter 4.V.2.iii*). It appears clearly that Ta_2O_5 addition has **a great effect on the luminescence emission** of MAS material. The band at 2.4 eV arising from **Mn^{2+} cations impurity in tetrahedral position** [221, 389, 419, 420] is **greatly decreased in intensity**. We suggest this is due to the **$Mg_4Ta_2O_9$ phase acting as a sink for Mn^{2+}**, as it was prior reported that such phase accepts a high rate of Mg^{2+} substitution by Mn^{2+} [456]; it could also be the case for the $MgTa_2O_6$ phase, but no literature on the matter exists to corroborate this. Indeed, in both Ta-based phases the divalent cations Mg^{2+}/Mn^{2+} occupy octahedral sites [457, 458], and therefore **no 2.4 eV-emission should arise from them**.

In addition, **great modifications of the CL ascribed to intrinsic defects** are noted with Ta_2O_5-MAS. The broad band attributed mainly to **multiple F-type centers** in the range ~2.5-4.5 eV [32, 300, 419, 421] is **more intense**, with its center **shifted from 3.41 to 3.32 eV**. Moreover, some of the convoluted peaks experience a greater increase of their intensities, and can clearly be distinguished: a **2.56 eV-emission** prior attributed to the luminescence band of the **agglomerate F_2-center** [66, 300], and a **3.35 eV band** which has been calculated to arise from **the F-center** [55]. Therefore, it appears that **Ta_2O_5 addition provokes a higher content of oxygen vacancies**, in agreement with our prior hypothesis. Finally, the broad band attributed mainly to **cationic disorder including inversion defects and V-type centers** [45, 419, 420] is **slightly shifted from ~5.26 to 5.22 eV**, and **greatly decreased in intensity with Ta_2O_5 addition**. This could be due to Ta-based inclusions draining Mg^{2+}, initially in slight excess in Sasol powder, to form MgO-Ta_2O_5 phases. In that way, spinel phase would be closer to stoichiometry, and the concentration of antisite/V-centers defects will decrease in consequence.

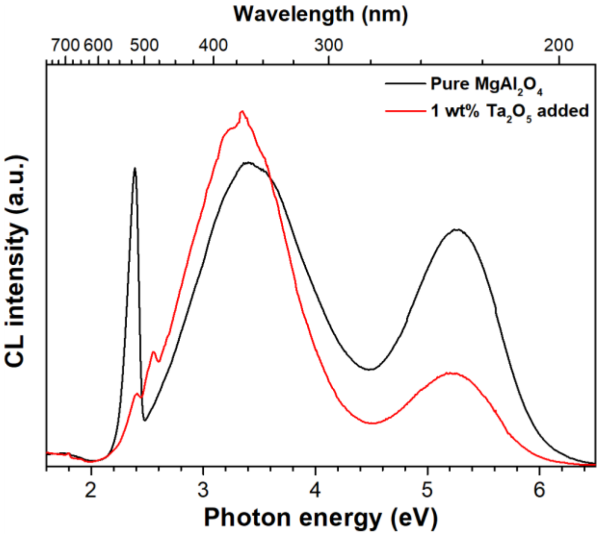

Figure 5.23: CL (5K) spectra of Sasol ceramics SPSed at 1450°C, 3 min, 80 MPa without and with 1 wt% Ta_2O_5 addition

In order to complete CL study, we carried out photoluminescence measurements (9K, λ_{exc} = 157 nm) of ceramics SPSed at 1650°C for 3 min (*Figure 5.24*). It should be noted that in the Ta-added material, Ta was solely observed as $Mg_4Ta_2O_9$ phase, dispersed in the MAS matrix at grain boundaries and triple junctions (see *Chapter 4.V.2.iii*). The spectra include **five principal bands labeled UV1, UV2, V1, V2 and NIR**, which have been previously discussed in literature. The **UV1 band at 228 nm** (5.44 eV) has been assigned to the **recombination of conduction-band electrons with holes captured at nearby oxygen ions** [445]. The broad PL band situated between 2.5 and 4.5 eV can be decomposed in two well resolved sub-bands: **V1 with maximum at 410 nm** (3.0 eV) and **UV2 at 320 nm** (3.9 eV), which can be respectively assigned to **F^+ centers** (one electron trapped at oxygen vacancy) [32] and **F centers** (two electrons trapped at oxygen vacancy) [221]. The **V2 band at 520 nm** (2.4 eV) belongs to **tetrahedrally coordinated Mn^{2+} cations** [445] and the most long-wavelength **near-infrared (NIR) band at ~700 nm** (1.8 eV) is due to **well-known R-lines of Cr^{3+} ions** [71, 454].

The presence of Ta in the spinel materials affects intensities of the PL bands. While intensities of NIR and UV2 bands do not change with Ta addition, the intensity of V1 band significantly increases, hinting for

higher density of F^+-centers, and that of V2 band decreases dramatically. The latter point confirms that the $Mg_4Ta_2O_9$ phase acts as a **sink for Mn^{2+} ions**. Moreover, intensities of UV1 and V2 bands are strongly correlated and the addition of Ta suppresses them by the same factor 10. Our microstructural analysis (see *Chapter 4.V.2.iii*) showed a **net correlation between spatial zones enriched with Ta and O depletion**. This apparently affects the population of F^+ centers formed of O vacancies, which can be promoted in the material by the removal of O^{2-} from the spinel structure, resulting in V1 band enhancement. Since band gap energy of solid Ta_2O_5 is 3.8-4.1 eV [315, 316, 459], the related interband absorption can appear at $\lambda \leq 320$ nm, which might explain the attenuation of UV1. However, we reject this hypothesis, since PL excited at 157 nm comes from a thin layer of 1/k ~100 nm thickness (k is the characteristic absorption coefficient at direct transitions in semiconductors) while penetration depth of UV1 photons (228 nm) in 1 wt% Ta_2O_5 solid is much longer about ~10 µm. Consequently, the interband Ta_2O_5 absorption cannot explain strong UV1 band attenuation observed in the experiment. We conclude that a **quenching phenomenon** is responsible for this effect.

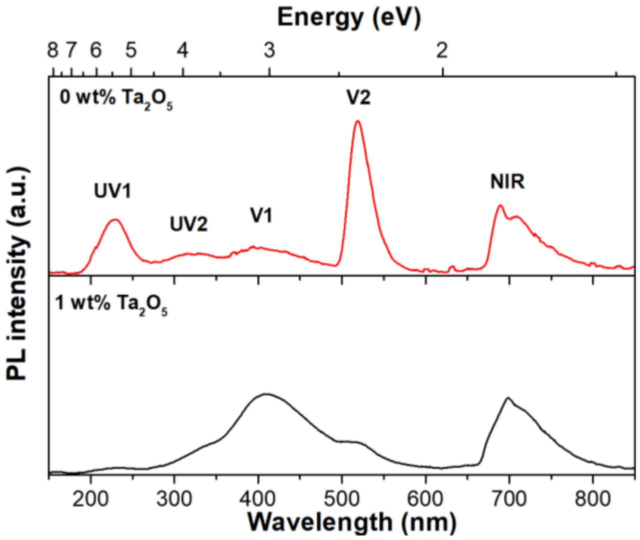

Figure 5.24: PL spectra (9K) of Sasol ceramics SPSed at 1650°C, 3 min, 80 MPa without and with 1 wt%Ta_2O_5, λ_{exc} = 157 nm

III. He^+ irradiation and tolerance of our ceramics

This section is dedicated to the investigation of **the effects of ionizing radiation on the fabricated $MgAl_2O_4$ ceramics**. Unfortunately, due to Corona pandemic, very few samples could be irradiated, in particular the highly transparent ceramics with fine microstructures obtained by HPSPS of S25CR-3MS powder have not been tested yet. Therefore, the results presented here should be considered as a preliminary study for the identification of some consequences of ionizing radiation on polycrystalline fine-grained $MgAl_2O_4$ ceramics.

In order to evaluate the structural damage induced by the ionized irradiation, PL and PL excitation (PLE) spectra of as-prepared and irradiated ceramics were compared. The irradiation was performed with 150 keV energy He^+ ions to total dose 10^{17} cm^{-2}. Pure $MgAl_2O_4$ and 1 wt% Ta_2O_5 added samples made from Sasol powder were tested. The different PL bands analyzed are attributed and discussed for *Figure 5.24*.

The PLE spectra of pristine and Ta-added ceramics SPSed at 1650°C, 3 min (*Figure 5.25.a* and *b*, resp.) before and after irradiation permit deep insight into structural modifications. The minimum of PLE spectrum at **E_g = 8.3 ± 0.1 eV** of the shorter wavelength PL band UV1 in *Figure 5.25.a* can be attributed to **the fundamental absorption onset and assigned to the band gap energy of $MgAl_2O_4$ spinel**. This value is somehow higher than those earlier obtained from optical reflection and transmission at 7.8 eV [460] and 8.0 eV [461] and theoretical predictions (*e.g.* 7.5 eV in [462]), which generally underestimate this energy. Meanwhile, it is close to the 8.2 eV suggested for spinel single crystals, based on the analysis of PL/PLE spectra [419, 420]. The interband electronic transitions $h\nu \geq 8.3$ eV can also be seen in PLE spectra of all PL of pristine $MgAl_2O_4$ (*Figure 5.25.a*), while they are less pronounced in PLE spectrum of Ta-added ceramics (*Figure 5.25.b*).

The PLE band in the range of $7.0 \text{ eV} \leq h\nu \leq E_g$ with **maximum at 7.8 eV** (*Figure 5.25.a*) can be attributed to **an exciton absorption**, and the correspondent **UV1 band at λ_{em} = 230 nm** (5.44 eV, see *Figure 4.16*) can be attributed to a **localized exciton**. The nature of the localization sites still remains an issue, while recent studies [419, 420] tentatively assigned them to antisite defects. The excitonic transitions at 7.8 eV are clearly observed in PLE spectra of UV2 and V2 bands, which indicates an **effective energy transfer from exciton to F-centers and Mg^{2+} sites**, respectively. In contrast, the **energy transfer from excitons to F^+-centers (V1 band) is found ineffective** since the respective PLE spectrum shows no signature of the excitonic transitions. This signifies rather complex energy transfer between the neutral (exciton) and charged (F^+) states. A **strong correlation between UV1 and V2** PL supports an assumption about its substitutional position at tetrahedral sites of the spinel structure Mn^{II}_{Mg}. Below the band gap energy, PLE spectrum of V2 consists of almost one Mg^{2+} band with the maximum at 6.35 eV (*Figure 5.25.a*); a weak broad contribution from 7.35 eV to ~4.6 eV common with V1 can be explained by a superposition of the PL bands (see *Figure 5.24*).

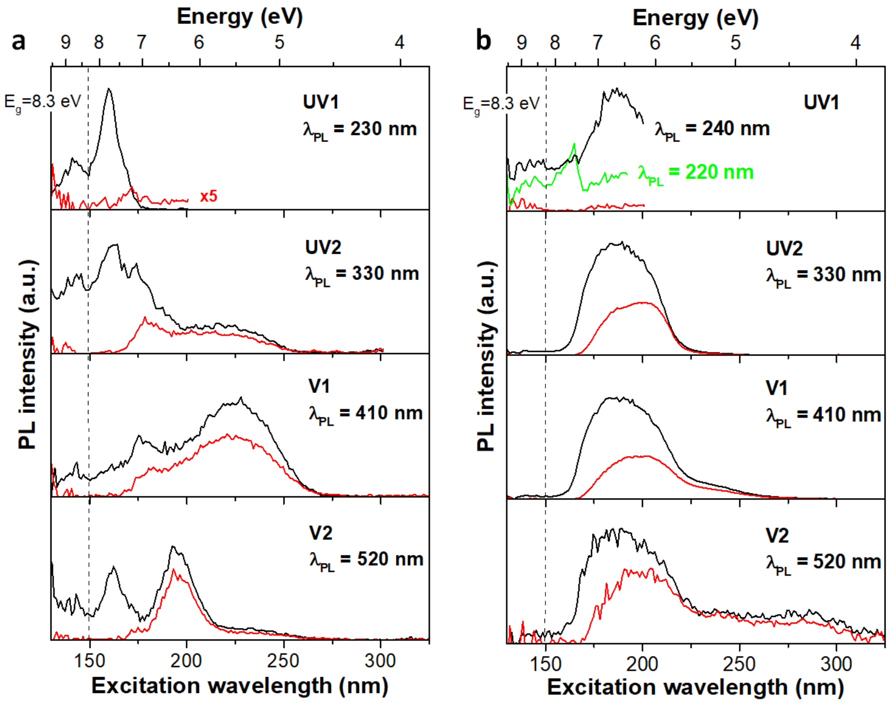

Figure 5.25: PLE spectra (9K) of a) pure and b) 1 wt% Ta_2O_5 added Sasol MAS ceramics before (black and green curves) and after He^+ irradiation (red curves) at the different indicated emission band and respective wavelengths of photoluminescence λ_{PL}

The irradiation of samples with He$^+$ ions weakenes PL and strongly modifies PLE spectra of all bands, except for that of Cr^{3+} impurity (not shown). In particular, UV1 band is strongly suppressed, which is in agreement with previous radioluminescence and cathodoluminescence observations of spinel crystals after protons and neutrons irradiation [280, 460, 463, 464]. This effect, not specific to the nature of ionized particles, has been tentatively ascribed to **partial inversion of normal spinel and formation of antisite defects**.

The most fundamental question from the point of view of radiation tolerance of spinel is **how much antisites concentration can be increased after the irradiation**. The damage profile in the irradiated layer of 0.5-0.6 µm thickness was simulated by SRIM software and indicated quite a high value of displacements per atom, up to 0.5 dpa at the maximum of distribution [304], which can be interpreted as a full amorphization. However, a significant part of this displacement is expected to recombine during the irradiation, which makes the real concentration of antisites smaller [465]. The detailed analysis of PL in He$^+$-irradiated samples is complicated because the penetration depth of photons does not always match the thickness of irradiated layer. Depending on the excitation wavelength (below the band gap, $\lambda > 150$ nm), a part of the pristine layer may be excited as well. Anyway, we have not observed any new PL band after the irradiation, which is expected to produce defects in the spinel structure; moreover the deep-ultraviolet PLE bands above 7.5 eV were lost. In overall, from spectroscopic point of view, a non-negligible density of antisites may be produced in the ceramics after irradiation. For example, the experimental uncertainty of the inversion $\Delta I = 0.01$ corresponds to a density of antisites ~10^{20} cm^{-3}, which can strongly affect PL spectra of non-irradiated ceramics. Because of the observed difference in PL/PLE spectra of the ceramics before and after irradiation, it was assumed that **the natures of as-grown and radiation-induced defects are different**. Our results confirm that possible effect of **the antisite creation may be an alternation of the energy relaxation channels leading to the exciton quenching**. On the other hand, **weak transitions at E' = 7.25 ± 0.25 eV** in UV1 PLE spectrum (*Figure 5.25.a*) may be connected to a **disorder in pristine spinels**, which is conserved after the irradiation.

The comparison of PLE spectra shows their significant modifications related to the intensity changes of several poor-resolved superposed bands of the sub-band gap electronic transitions in Ta-added ceramics (*Figure 5.25.b*). The most striking features concern a strong weakening of UV1 PLE at 7.8 eV and intensification of PLE between 6.0 and 7.5 eV common for all other PL emissions UV2, V1 and V2, except for UV1 one (the seeming presence of this PLE band in UV1 PL is explained by a contribution of the intense broad UV2 PL, as shows PLE spectrum at $\lambda_{em} = 240$ nm in *Figure 5.25.b*). We notice that PLE bands of pristine ceramics (*Figure 5.25.a*) are still visible in PLE of Ta-doped ceramics at low intensity, superposed by this new dominant PLE band, which apparently **originates from the grain boundary region enriched with Ta**. The modification of the force of electronic transitions by Ta may be the reason. The irradiation provokes similar consequences on the PLE spectra, as in pristine spinel ceramics: the high energy part above 7.5 eV vanishes and that between 7.5 and 6.0 eV weakens.

The irradiation with He$^+$ ions permits an additional bands selection, helpful for the understanding of the energy transfer process. The ratio of PLE spectra of F (UV2 PL band) and F$^+$ centers (V1 PL band) of samples before and after the ionized irradiation are shown in *Figure 5.26*. The **ratio in Ta-free ceramics** (top layer) **is close to 1** below energies of the excitonic transitions hν < 7.0 eV, which indicates a **negligible modification of the related intra-gap states**. In contrast, the PL ratio in the **Ta-added ceramics is close to 1 in the energy range below E* = 5.75 eV** (bottom layer) while it increases to 4 at 7.0 eV. Consequently, **two contributions** can be resolved in this PLE analysis: **5.75 eV ≤ E" < 7 eV** and **5 eV ≤ E"' < 5.75 eV**. We assign **E"' to the direct absorption of F/F+ centers** and **E" to a common intermediate excited state, which transfers energy to these centers**. We notice that a careful comparison of the PLE lineshapes shows an **extension of F$^+$ band to lower energies** compared with that of F band, which is in agreement with the energy shift of the respective absorptions at 5.3 and 4.75 eV [26]. The **E" transitions are most probably located at the grain boundaries**, since the energy transfer to the emitting F and F$^+$ states is strongly affected by Ta (UV2 and V1 in *Figure 5.25.a* and *b*). Our results show that F/F$^+$ PL spectra are similar after excitation in the spectral range of the excitonic transitions (7.8 eV) and direct complex excitation (E"), which indicates an **effective energy transfer exciton → complex → F/F$^+$**. Moreover, the stronger PL attenuation in the range of E" transitions (*Figure 5.26*, bottom layer) indicates that **Ta weakens the structure facilitating damage produced by He$^+$ ions**. Summing up the results from structural and microstructural analyses (see *Chapter 4.V.2.iii*) and PL measurements, the **hypothetic complex may be assigned with the nucleated $Mg_4Ta_2O_9$ phase at grain boundaries and triple junctions of spinel grains**.

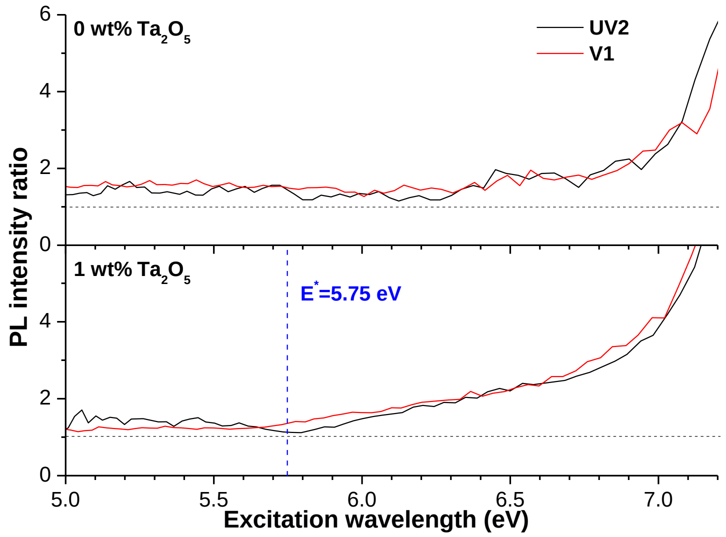

Figure 5.26: Intensity ratio of PLE spectra (9K) before and after irradiation of Sasol MAS ceramics without and with 1 wt% Ta_2O_5 addition for UV2 band (F-centers) and V1 band (F^+-centers)

PL intensities of both F and F$^+$ centers were strongly intensified in Ta-doped ceramics (*Figure 5.25.b*) indicating, in agreement with the microstructural analysis (see *Chapter 4.V.2.iii*), their preferential position at the grain boundaries. Consequently, **antisites situated at the grain boundaries enriched with Ta** can be proposed for the explanation of the E" band attenuation after He$^+$ irradiation. This alternation of the energy relaxation from interaction with bulk to interface states (after He$^+$ irradiation) may be a reason of the excitonic PL suppression. A stronger attenuation of the energy transfer from localized excitons E' (7.25 eV) can be also noticed, which according to *Figure 5.26* was not appreciably sensitive to Ta addition. This band may therefore belong to **exciton localized near bulk antisites**.

An additional support to the conclusion about preferential position of F and F^+ centers at the grain boundaries in the sintered ceramics comes from the fact that the related PLE spectra are **extremely weak in $MgAl_2O_4$ single crystals** [466]. Their PL intensities with excitation below the band gap are almost conserved after the irradiation with He^+ ions indicating a **small structural damage**, since F^+ center is expected to readily interact with defects derived from the cation disorder in the spinel structure, forming clusters of various defect centers [32] affecting PL bands.

The UV1 band intensity is also significantly lower in our small grain ceramics compared to $MgAl_2O_4$ single crystals [465]. Its intensity is lower in Ta-added ceramics as well (*Figure 5.24*) with no change of the lineshape. Moreover, our observations showed that the **excitonic PL suppression after He^+ irradiation is stronger in the ceramics than in single spinel crystals**. This supports our conclusion about **exciton quenching at the grain boundaries due to interactions with the Ta-spinel complex and radiation-induced antisites**.

IV. Influence of the synthesis route on the defects in $MgAl_2O_4$ nanopowders

This final section is dedicated to the preliminary **evaluation of the structural defects in the $MgAl_2O_4$ spinel nanocrystalline powders synthesized *via* polyol and impregnation synthesis routes** presented in *Chapter 3*, and sintered in *Chapter 4.III*. For this investigation, that will be further deepened in order to better understand the nature of defects in the synthesized powders and link them to the sinterability, only the powders exhibiting single phased stoichiometric and non-inversed spinel have been studied, *i.e.* the **polyol powder with MgO·*1*Al_2O_3 stoichiometry treated at 900°C** and the **impregnation powders Mg-UPA300, Mg-UPA1050 and Mg-UPA-TMES treated at 1000°C for 4 h**.

The EPR spectra of the powders, in comparison with the Sasol powder spectrum, are presented in *Figure 5.27*. It appears that the powders synthesized by impregnation route only present a **single paramagnetic signal BS1 at the mean resonance field $H_0 \approx 3250$ G** (g = 2.08) with a **linewidth of $\Delta H = 500$ G**, which is clearly **more intense than for the Sasol powder**. We assigned this signal to **several types of intrinsic defects**, and in particular **cationic defects such as V-centers**. The polyol MAS precursor also presents the **BS1 absorption**, **highly comparable to the BS1 signal observed in the spectrum of Sasol powder** in mean resonance field, linewidth and intensity. In addition, a **very strong signal** is observed at **$H_0 = 1555$ G (g = 4.37) with $\Delta = 80$ G**. This signal is close in spectral position from the BS2 signal that we tentatively attributed to Mn^{4+} cations in octahedral position. However, it is unlikely that the polyol precursor presents such a high quantity of Mn impurity, given that EDX measurements did not reveal any sensible contamination above detection range, and therefore we reject this hypothesis. This paramagnetic center may not be BS2 in this case, and be related to **another defect absorbing at the same field** (for instance, several impurities are known to absorb in this range, *e.g.* Fe^{3+} [12] and Cr^{3+} [432]).

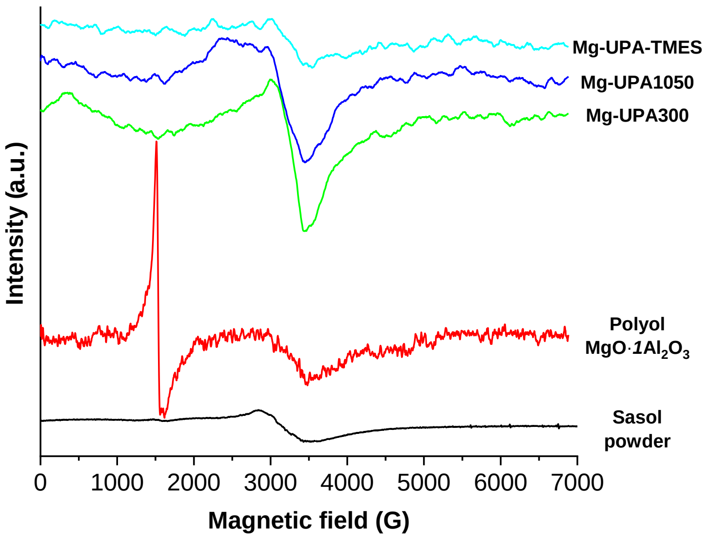

Figure 5.27: EPR (RT) spectra of the $MgAl_2O_4$ nanopowders synthesized via *polyol and impregnation routes*

It is remarkable that the impregnation precursors present greater intrinsic defects than the Sasol commercial powder, which may be explained by their smaller crystallite size (in the range of 10 nm, vs 140 nm for Sasol) inducing **more crystal surface expected to be less crystalline**. It is in agreement with the **strong absorption band** centered at 2.74 eV (450 nm) observed in the transparent ceramics SPSed from Mg-UPA300 precursor (*Chapter 4.III.2*, *Figure 4.66.b*), responsible for the **low transparency** in the UV-low visible range and **brown/yellow tint** of the materials. Such absorptions have been reported for $MgAl_2O_4$ ceramics containing either V-type centers [38, 56] or Mn impurity localized in octahedral sites [59, 389]. However, we discard this last possibility since no HFS or BS2 signals are observed in the EPR spectra, therefore we assume **no sensible Mn impurity content in impregnation precursors**. This seems to confirm the **high content in V-centers in the prepared nanopowders** and their predominant contribution to BS1 paramagnetic signal. In comparison, the polyol powder seems to have **less intrinsic defects** in regard to its BS1 signal's intensity comparable to Sasol's one. However, we suggest that the **strong absorption band at g = 4.37 may be related to complex intrinsic defects**, as we reject the possibility of a somehow strong contamination from extrinsic elements. This last signal could indeed explain the **peculiar mechanism of $MgAl_2O_4$ dissociation observed during SPS** (*Chapter 4.III.1*), which was never reported before to our best knowledge. We leave this discussion open until further characterizations allow elucidating these results.

V. Conclusion on the investigation of defects in $MgAl_2O_4$ materials

In this final chapter, we investigated **the intrinsic and extrinsic defects in $MgAl_2O_4$ ceramics and the irradiation behavior of these materials** *via* physical characterizations, namely cathodoluminescence (CL), photoluminescence (PL) and electron paramagnetic resonance (EPR) spectroscopies, which are not widely used in the field of ceramic fabrication.

In the first part, we studied the evolution of the defects in $MgAl_2O_4$ ceramics through their processing. SPS processing was found **not to introduce high content of intrinsic defects** in MAS ceramics, the cation-related defects (antisite, vacancies…) being the most impacted. **Subsequent annealing** provokes an evolution of these defects in several steps: *i)* an **important healing** is observed **at moderate temperature ~1100°C**, *ii)* the **oxidation of entrapped carbon contamination** during treatment at **1150°C results in high**

internal stress in the material leading to **formation of new intrinsic defects with preferential orientation along the cross section** (paramagnetic resonance field g = 2.19 for $\vec{H}_0 \perp \vec{P}_{SPS}$ and g = 1.65 for $\vec{H}_0 \parallel \vec{P}_{SPS}$). Such anisotropy of intrinsic defects in $MgAl_2O_4$ ceramic is reported here for the first time, to the best of our knowledge. Finally, *iii)* **further annealing at 1250°C suppresses these newly formed intrinsic defects and the yellow coloration associated to them**. In addition, it was found that the common Mn elemental impurity is greatly affected by SPS, the **reducing atmosphere converting all possible oxidation states to Mn^{2+} form**, while subsequent annealing allows a **controlled conversion to Mn^{4+} state**. It was found that the **precursor powder has little effect on the intrinsic defects** in ceramics, while the **SPS processing temperature have a great impact**: *i)* at low applied pressure (80 MPa), lower temperatures result in higher content of F^+ centers and antisite defects, and *ii)* for higher pressure (400 MPa), the formation of defects is favored by temperature exceeding minimum temperature for full densification. Finally, the effect of the applied pressure and decreasing grain size was investigated. The PL and PLE spectra were strongly affected by the crystalline grain size, which was explained by **optical transitions of Cr^{3+} in ordered (grains bulk) and perturbed (grains boundary) regions** of samples. In particular, the structured PL component of Cr^{3+} ions on the $^2E_g \rightarrow {}^4A_{2g}$ electronic transition weakened and the broadband one on the $^4T_{2g} \rightarrow {}^4A_{2g}$ electronic transition intensified with the decrease of grain size. It was observed that **F-centers transfer energy to Cr^{3+} at the grain boundaries** and the PL intensity ratio of F-center/Cr^{3+} linearly increased with the grain size.

Afterward, we investigated the effect of Ta_2O_5 addition on the structural defects and luminescence properties of spinel ceramics. The results indicate strong influence of the grain boundaries on PL and PLE spectra, as **Ta_2O_5 addition promotes deficiency in O element at the grain interfaces leading to the formation of a high density of F^+ centers**, which provokes an inhibition of the excitonic PL and enhancement of that of F and F^+ centers. We explained this by an **intermediate state** (with electronic transitions in the spectral range between 5.75 and 7.0 eV) **situated at the grain boundaries**, which was tentatively assigned to the **nucleated $Mg_4Ta_2O_9$ phase interacting with excitons** and effectively transferring energy to F and F^+ centers.

We also assessed the He^+ irradiation behavior of chosen samples. The disorder of the spinel structure induced by He^+ ions irradiation results in the suppression of the excitonic PL and exciton energy transfer. This effect was attributed to an interaction of excitons with radiation-induced antisites situated at the grain boundaries. Consequently, the **irradiation-induced displacements**, effectively recombining in bulk spinel crystals, **accumulate at the grain boundaries of the spinel ceramics**. A weak residual PL excitation band at 7.25 eV may belong to excitons localized near bulk antisites.

Finally, we evaluated the influence of the synthesis route (polyol and impregnation, see *Chapter 3*) on the $MgAl_2O_4$ nanopowders' defects. It was found that the synthesized powders were **not containing elemental impurities** detectable by EPR spectroscopy, but exhibited **high density of intrinsic defects** in comparison to commercial powders, which we attributed to their smaller crystallite size (decreased by a factor of 10). In addition, the polyol powder exhibited a **strong paramagnetic absorption at g = 4.37**, which we tentatively related to **complex intrinsic defects**, and could explain the peculiar mechanism of $MgAl_2O_4$ dissociation observed during SPS (*Chapter 4.III.1*).

This page intentionally left blank.

Conclusions and perspectives

This PhD thesis is dedicated to the **development of a bottom-up methodology for the fabrication of optically transparent $MgAl_2O_4$ spinel ceramics with ultrafine microstructure**. It has been carried out within the framework of the EUROfusion Consortium, and is aimed for the development of reproducible radiation resistant polycrystalline optical materials. Indeed, their application as **optical windows in extreme environments** including future nuclear fusion facilities is foreseen in the field of radiation tolerant detectors.

This work is divided in three experimental parts: *Chapter 3* focuses on the **development of two synthesis routes for $MgAl_2O_4$ nanopowders**, *Chapter 4* is dedicated to the **consolidation of $MgAl_2O_4$ nanopowders into dense ceramics** by spark plasma sintering (SPS) technique and *Chapter 5* is aimed to **investigate the structural defects and He^+ irradiation** by physical characterization methods.

In *Chapter 3*, we developed two different synthesis techniques for the preparation of $MgAl_2O_4$ nanoparticles, namely the polyol-mediated route and the UPA impregnation route.

The **synthesis *via* polyol route** consists on the preparation of a **MgAl hydroxides mixture**, with composition and morphology highly dependent on the synthesis conditions. Afterward, the as-synthesized product is **thermally decomposed to form well crystallized spinel at 800°C with crystallite size of 7 nm**. Of the most important results obtained, the polyol synthesis permits the preparation of **non-stoichiometric spinel nanoparticles** in a wide range of composition **$MgO \cdot nAl_2O_3$ with $1 \leq n \leq 5$**, which has never been reported before to our best knowledge.

The **synthesis route *via* liquid impregnation of nanofibrous alumina** followed by thermal treatment led to very fine spinel crystallites as well. The crystalline structure of the Al_2O_3 host, heat treatment temperature and kinetic appeared as critical issues for producing single-phase nano-spinel. In particular, the influence of the polymorphism of nanofibrous alumina (UPA) precursors on the spinelization was investigated. It was shown that crystallized UPA resulted in $MgAl_2O_4$ formation by solid state reaction mechanism with prior MgO crystallization, **γ-Al_2O_3 phase** permitting total reaction with **spinel crystallites of 16 nm** at 1000°C. The **vapor impregnation with silica precursor** before spinelization allowed **reducing the crystallite size to 8 nm**. In comparison, **amorphous dehydrated *a*-Al_2O_3 UPA** led to a **fully inverse ($I \approx 1$) pure spinel** material after treatment at **moderate temperatures of ~500°C**, due to the effective Mg^{2+} insertion into UPA fibrils of 5 nm diameter. The **conversion to normal spinel** structure took place at higher temperature of **~850°C**, resulting in **crystallite size of 16 nm** after treatment at 1000°C.

The *Chapter 4* was dedicated to the consolidation of $MgAl_2O_4$ nanopowders into dense ceramics by spark plasma sintering, with focuses on the influence of the precursor powder and mechanical pre-processing treatments, the parametric study of the SPS conditions and the influence of thermal post-densification treatments. In addition, we investigated the phenomenology during SPS of the ionic conductor Ta_2O_5 and Ta_2O_5 added $MgAl_2O_4$.

The **mechanical pre-processing** of the powder was found to have a **great impact on the properties of the sintered ceramics**. We showed that **low-energy processing in slurry state** resulted in efficient **de-agglomeration/de-aggregation** of the initial particles, providing more homogeneous microstructure with **grain size decreased by a factor 1.5-2.5 and better transparency** of the ceramics. However, it was found that **the quality of the raw powder is the most crucial parameter**.

The parametric study revealed that the **most impactful SPS conditions** for the fabrication of transparent ceramics with fine microstructure are the **sintering temperature and the applied pressure**. In particular, the **grain growth is mostly driven by thermal effect**, while **the densification depends on the couple applied pressure-sintering temperature**. The soaking time at sintering temperature was found useful as an optimization parameter for the improvement of densification and transparency, while low heating rate ≤ 10°C/min are required to avoid any carbon contamination. Using the commercial powder S25CR (Baikowski) with low-energy pre-processing, **high pressure SPS with applied pressure up to 1 GPa and reduced temperature down to 1000°C permitted to obtain ceramics of high quality**, with a **transmittance *plateau* of ~85% reached at 400 nm and a grain size of 98 nm**. This high quality of $MgAl_2O_4$ polycrystalline material is comparable with the best results reported in literature.

The preliminary sintering study of the precursor powders synthesized by polyol and impregnation routes showed that **polyol precursors are systematically subjected to phase demixtion and MgO loss**, which we attributed to a **particularly high reactivity**, while no such phenomenon is observed for the impregnation precursors. The only **ceramics presenting a certain transparency with $T_{il\text{-}600\ nm}$ = 21%** was prepared from the sintering of the **Mg-UPA300 (*a*-Al2O3 initial reactant) precursor**.

The **post-densification air annealing and HIP treatments** resulted in **only moderated improvement of the transparency**, with only long annealing of ≥ 100 h being able to treat the ceramics through their whole thickness. In particular, air annealing led to an **encouraging gain of transparency for the materials prepared from the densification of the impregnation precursors**.

The SPS processing of Ta_2O_5 and Ta_2O_5 added $MgAl_2O_4$ allowed us to evidence **peculiar phenomena specific to SPS**. In particular, the **formation of oxygen vacancies at the negative electrode** and **their propagation to the positive one** was observed, as well as the **formation of hot spots during the sintering**. We attributed these phenomena to **electric effects specific to SPS of ionic/mixed conductors**.

In *Chapter 5*, we investigated the intrinsic and extrinsic defects in $MgAl_2O_4$ ceramics and the irradiation behavior of our materials *via* spectroscopic methods of characterizations not widely used in the field of ceramic fabrication.

The evolution of the defects in $MgAl_2O_4$ ceramics through their processing showed that **SPS processing do not introduce high content of intrinsic defects** in MAS ceramics. **Subsequent annealing** provokes the **healing of these defects** at moderate temperature ~1100°C, while the **oxidation of entrapped carbon contamination at 1150°C results in high internal stress** in the material leading to **formation of new intrinsic defects oriented along the cross section**, inducing a **strong paramagnetic anisotropy** reported for the first time in this work. It was also found that the precursor powder has little effect on the intrinsic defects content in ceramics, which is rather governed by the **sintering conditions and in particular the temperature**. The increase of applied pressure did not result in modification of the defects in itself, but the associated decrease of grain size **strongly affected the luminescence optical transitions**. This was attributed to the **increase relative volume of grain boundaries** with the reduction of crystalline grain size.

Finally, we assessed the material damage provoked by He^+ irradiation on $MgAl_2O_4$ ceramics. The disorder of the spinel structure induced by the ionizing radiation results in the suppression of the excitonic photoluminescence and exciton energy transfer, due to an interaction of excitons with radiation-induced antisites situated at the grain boundaries. Consequently, the **irradiation-induced displacements**, effectively recombining in bulk spinel crystals, **accumulate at the grain boundaries** of the spinel ceramics.

The results obtained in this thesis are interesting in many ways. However, several perspectives can be proposed for future works:

- The testing of our $MgAl_2O_4$ ceramics **tolerance toward ionizing radiation** should be thoroughly investigated, in particular for polycrystalline materials highly transparent with fine grain size close to 100 nm.
- In order to assess the suitability of the SPS processing for producing transparent ceramics with dimensions required for applications, it is important to investigate the **scaling-up of the HPSPS technique**, *e.g.* the technical feasibility, homogeneity of the material…
- It is expected that the finest grain size ≤ 20 nm would provide increased tolerance of the materials toward ionizing radiation. We demonstrated in this work that the only realistic way to achieve such microstructure is to use nanoprecursors not commercially available. Therefore, it is amongst the **highest priority to pursue the study started here on the synthesis and subsequent sintering of nanospinel powders**.
- The spinel structure was chosen due to the high flexibility for the atoms to move within the lattice without great damaging. We focused in this thesis on the most common magnesium aluminate $MgAl_2O_4$ spinel; however, **other compositions could be good candidates** as well, such as $ZnAl_2O_4$ and $ZnGa_2O_4$ spinel ceramics. We already demonstrated the possibility to easily synthesize nanocrystallites of the former compound with both polyol and impregnation routes, and $ZnGa_2O_4$ could be synthesized *via* the polyol technique as well. The **sintering of these compounds and comparison of their ceramic properties** should be investigated.
- Both synthesis routes developed in this work have been shown to be highly versatile, and could be very **easily adapted for the synthesis of doped/different materials** following the same synthesis protocols. We think it is important to **extend the great potential of these methods for other applications**, *e.g.* phosphors, catalysis, jewelry…
- Finally, **the mechanical properties** have not been investigated here, although they are highly important for many applications of $MgAl_2O_4$ polycrystalline materials (*e.g.* transparent armors, windows for watches…). These properties should be characterized in order to extend the applicability of our materials to eventual applications other than in the nuclear field.

This page intentionally left blank.

Contributions and scientific productions of the PhD candidate

In the framework of this thesis, the PhD candidate, I - I will allow myself to use "I" and not "we" in this section - have participated to several tasks in addition to my experiments and research activities. I effectuated a complementary teaching activity during four years, which includes:

- practical courses on
    - computational fluids dynamics simulations on Ansyns Fluent (1st year engineer's degree)
    - methods of experimental chemistry (1st year bachelor's degree)
    - process engineering (1st year master's degree)
- tutorial classes on
    - chemistry (1st year bachelor's degree)
- lecture classes on
    - atomistic (1st year bachelor's degree).

I co-supervised four students in their end-of-cycle internships, and the results of their works are included in this thesis:

- Luiza Dorca (DUT, USPN) on the polyol synthesis
- Mohamed-Amine Belaabd (bachelor, USPN) on the impregnation synthesis
- Maria Dioupro (engineer, INP-HB) on the SPS parametric study
- Ameni Hawel (master, USPN), on the preparation of few SPSed ceramics.

I presented my results in four meetings of our EUROfusion consortium, and wrote the drafts for the annual final reports of activity in two occasions. I attended two international and five national conferences, where I gave oral presentations:

- Poudres2019, Grenoble, France – "*Effect of Ta_2O_5 addition on microstructure and optical properties of $MgAl_2O_4$ ceramics*" 15 min
- ECers2019, Turin, Italy – "*Effect of Ta_2O_5 addition on microstructure and optical properties of $MgAl_2O_4$ ceramics*" 10 min
- SPS2019, Limoges, France – "*Elaboration de céramiques $MgAl_2O_4$ nanostructurées et optiquement transparentes par Spark Plasma Sintering*" 15 min
- STPMF2021, Saint-Etienne, France – "*Elaboration of optically transparent $MgAl_2O_4$ ceramics with fine microstructures by Spark Plasma Sintering: influence of the precursor powder*" 15 min
- ICFRM2021, Granada, Spain – "*Development of $MgAl_2O_4$ transparent ceramics with fine microstructures for radiation resistant optical materials: effects of irradiation with He^+ ions*" 5 min
- JMC17 in 2021, France – "*Structural defects in fine-grained $MgAl_2O_4$ sintered ceramics through the elaboration process: from the powder to the post-densification treatment*" 10 min

I also attended one summer school, during which I presented my work in a poster:

- Summer school Erin2 C'NANO in 2021, on the interdisciplinarity of nanosciences and nanotechnologies

Finally, the work of this thesis has resulted in five articles - so far - accepted for publication in peer-reviewed journals:

- A. Pille, H. Spiridigliozzi *et al.*, Morphology and luminescence of $MgAl_2O_4$ ceramics obtained via spark plasma sintering. *Ceramics International*, **45** (2019), https://doi.org/10.1016/j.ceramint.2019.01.137
- H. Spiridigliozzi *et al.*, Effects of Ta doping and irradiation with He^+ ions on photoluminescence of $MgAl_2O_4$ spinel ceramics. *Journal of the European Ceramic Society* **40** (2020), https://doi.org/10.1016/j.jeurceramsoc.2020.02.032
- H. Spiridigliozzi *et al.*, Structural defects effect in fine-grained $MgAl_2O_4$ sintered ceramics: optical and RPE properties as function of microstructure. *The European Physical Journal Special Topics* **123** (2022), https://doi.org/10.1140/epjs/s11734-022-00574-x
- H. Spiridigliozzi *et al.*, Synthesis of MAl_2O_4 (M = Mg, Co, Ni, Zn, Ba) nanopowders by liquid impregnation of nanofibrous alumina. *Industrial & Engineering Chemistry Research* **62** (2023) https://doi.org/10.1021/acs.iecr.3c00301 + Front cover (see below)
- H. Spiridigliozzi *et al.*, Grain-size dependence of Cr^{3+} and F-centres photoluminescence in nanophase $MgAl_2O_4$ ceramics. *Journal of the European Ceramic Society* **43** (2023), https://doi.org/10.1016/j.jeurceramsoc.2023.06.005

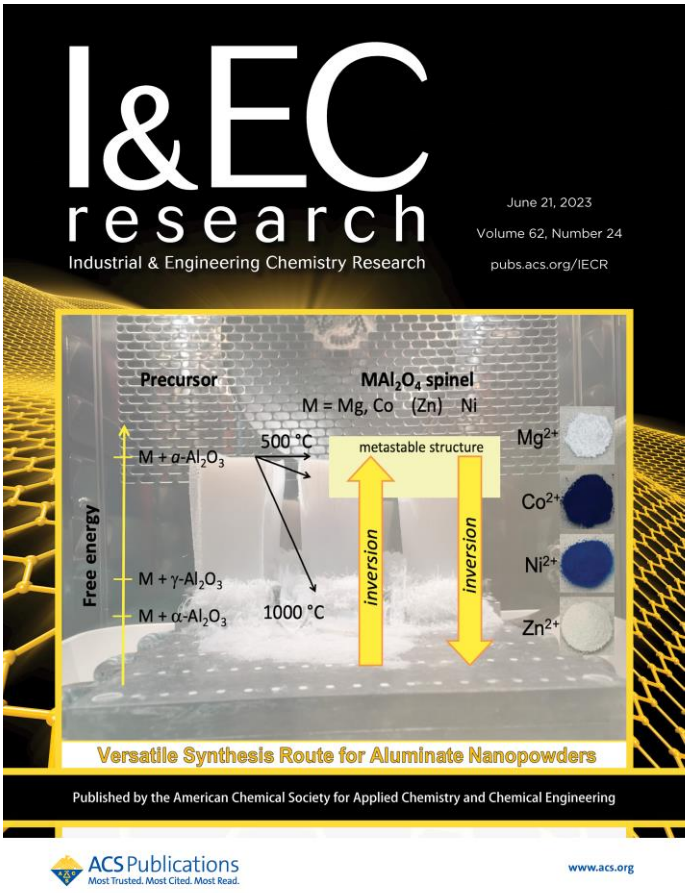

Front cover of Industrial & Engineering Chemistry Research ***62****, illustrated by the article on the synthesis by impregnation of UPA*

References

[1] G. Ackland, “Controlling Radiation Damage,” *Science (80-.).*, vol. 327, no. 5973, pp. 1587–1588, **2010**, doi: 10.1126/science.1188088.

[2] X. M. Bai, A. F. Voter, R. G. Hoagland, M. Nastasi, and B. P. Uberuaga, “Efficient annealing of radiation damage near grain boundaries via interstitial emission,” *Science (80-.).*, vol. 327, no. 5973, pp. 1631–1634, **2010**, doi: 10.1126/science.1183723.

[3] K. E. Sickafus, L. Minervini, R. W. Grimes, J. A. Valdez, M. Ishimaru, F. Li, K. J. McClellan, and T. Hartmann, “Radiation tolerance of complex oxides,” *Science (80-.).*, vol. 289, no. 5480, pp. 748–751, **2000**, doi: 10.1126/science.289.5480.748.

[4] K. E. Sickafus, N. Yu, R. Devanathan, and M. Nastasi, “The irradiation damage response of MgO · 3Al2O3 spinel single crystal under high-fluence ion-irradiation,” *Nucl. Instruments Methods Phys. Res. Sect. B Beam Interact. with Mater. Atoms*, vol. 106, no. 1–4, pp. 573–578, **1995**, doi: 10.1016/0168-583X(95)00772-5.

[5] K. E. Sickafus, “Radiation-induced effects on material properties of ceramics (mechanical and dimensional),” in *Comprehensive Nuclear Materials*, 2012. doi: 10.1016/B978-0-08-056033-5.00005-7.

[6] E. Feldbach, L. Museur, V. Krasnenko, A. Zerr, M. Kitaura, and A. Kanaev, “Defects induced by He+ irradiation in γ-Si3N4,” *J. Lumin.*, vol. 237, no. April, p. 118132, **2021**, doi: 10.1016/j.jlumin.2021.118132.

[7] A. J. Samin, D. A. Andersson, E. F. Holby, and B. P. Uberuaga, “On the role of electro-migration in the evolution of radiation damage in nanostructured ionic materials,” *Electrochem. commun.*, vol. 96, no. August, pp. 47–52, **2018**, doi: 10.1016/j.elecom.2018.09.010.

[8] A. Ibarra, D. Bravo, F. J. Lopez, and F. A. Garner, “High-dose neutron irradiation of MgAl2O4 spinel: effects of post-irradiation thermal annealing on EPR and optical absorption,” *J. Nucl. Mater.*, vol. 336, no. 2–3, pp. 156–162, **2005**, doi: 10.1016/j.jnucmat.2004.09.003.

[9] N. Mironova-Ulmane, V. Skvortsova, A. Pavlenko, E. Feldbach, A. Lushchik, C. Lushchik, V. Churmanov, D. Ivanov, V. Ivanov, and E. Aleksanyan, “Luminescence and EPR spectroscopy of neutron-irradiated single crystals of magnesium aluminium spinel,” *Radiat. Meas.*, vol. 90, pp. 122–126, **2016**, doi: 10.1016/j.radmeas.2015.12.020.

[10] A. Lushchik, E. Feldbach, E. A. Kotomin, I. Kudryavtseva, V. N. Kuzovkov, A. I. Popov, V. Seeman, and E. Shablonin, “Distinctive features of diffusion-controlled radiation defect recombination in stoichiometric magnesium aluminate spinel single crystals and transparent polycrystalline ceramics,” *Sci. Rep.*, vol. 10, no. 1, p. 7810, **2020**, doi: 10.1038/s41598-020-64778-8.

[11] M. Rubat du Merac, H.-J. Kleebe, M. M. Müller, and I. E. Reimanis, “Fifty Years of Research and Development Coming to Fruition; Unraveling the Complex Interactions during Processing of Transparent Magnesium Aluminate (MgAl 2 O 4) Spinel,” *J. Am. Ceram. Soc.*, vol. 96, no. 11, pp. 3341–3365, **2013**, doi: 10.1111/jace.12637.

[12] A. Goldstein, “Correlation between MgAl2O4-spinel structure, processing factors and functional properties of transparent parts (progress review),” *J. Eur. Ceram. Soc.*, vol. 32, no. 11, pp. 2869–2886, **2012**, doi: 10.1016/j.jeurceramsoc.2012.02.051.

[13] I. Ganesh, “A review on magnesium aluminate (MgAl2O4) spinel: Synthesis, processing and applications,” *Int. Mater. Rev.*, vol. 58, no. 2, pp. 63–112, **2013**, doi: 10.1179/1743280412Y.0000000001.

[14] D. N. F. Muche, J. W. Drazin, J. Mardinly, S. Dey, and R. H. R. Castro, “Colossal grain boundary strengthening in ultrafine nanocrystalline oxides,” *Mater. Lett.*, vol. 186, no. June 2016, pp. 298–300, **2017**, doi: 10.1016/j.matlet.2016.10.035.

[15] M. Khajeh Aminian, T. Azizi, R. Dehghan, and M. Hakimi, “Synthesis and Characterization of CoAl2O4 Nano Pigments by Polyol Method,” *Prog. Color. Color. Coatings*, vol. 10, no. 4, pp. 231–238, **2017**, doi: 10.30509/pccc.2017.75730.

[16] L. Poul, S. Ammar, N. Jouini, F. Fievet, and F. Villain, “Synthesis of inorganic compounds (metal, oxide and hydroxide) in polyol medium: A versatile route related to the sol-gel process,” *J. Sol-Gel Sci. Technol.*, vol. 26, no. 1–3, pp. 261–265, **2003**, doi: 10.1023/A:1020763402390.

[17] J.-L. Vignes, C. Frappart, T. Di Costanzo, J.-C. Rouchaud, L. Mazerolles, and D. Michel, “Ultraporous monoliths of alumina prepared at room temperature by aluminium oxidation,” *J. Mater. Sci.*, vol. 43, no. 4, pp. 1234–1240, **2008**, doi: 10.1007/s10853-007-2260-z.

[18] M. Eriksson, Y. Liu, J. Hu, L. Gao, M. Nygren, and Z. Shen, “Transparent hydroxyapatite ceramics with nanograin structure prepared by high pressure spark plasma sintering at the minimized sintering temperature,” *J. Eur. Ceram. Soc.*, vol. 31, no. 9, pp. 1533–1540, **2011**, doi: 10.1016/j.jeurceramsoc.2011.03.021.

[19] M. Sokol, M. Halabi, S. Kalabukhov, and N. Frage, “Nano-structured MgAl2O4 spinel consolidated by high pressure spark plasma sintering (HPSPS),” *J. Eur. Ceram. Soc.*, vol. 37, no. 2, pp. 755–762, **2017**, doi: 10.1016/j.jeurceramsoc.2016.09.037.

[20] J. R. Smyth, S. D. Jacobsen, and R. M. Hazen, “Comparative crystal chemistry of dense oxide minerals,” *Rev. Mineral. Geochemistry*, vol. 41, no. 1, pp. 157–186, **2000**, doi: 10.2138/rmg.2000.41.6.

[21] G. Busca, *Structural, Surface, and Catalytic Properties of Aluminas*, 1st ed., vol. 57. Elsevier Inc., 2014. doi: 10.1016/B978-0-12-800127-1.00003-5.

[22] I. Levin and D. Brandon, “Metastable alumina polymorphs: Crystal structures and transition sequences,” *J. Am. Ceram. Soc.*, vol. 81, no. 8, pp. 1995–2012, **1998**, doi: 10.1111/j.1151-2916.1998.tb02581.x.

[23] M. G. Baronskiy, S. V. Tsybulya, A. I. Kostyukov, A. V. Zhuzhgov, and V. N. Snytnikov, “Structural properties investigation of different alumina polymorphs (η-, γ-, χ-, θ-, α-Al2O3) using Cr3+ as a luminescent probe,” *J. Lumin.*, vol. 242, no. October 2021, p. 118554, **2022**, doi: 10.1016/j.jlumin.2021.118554.

[24] G. A. Rankin and H. E. Merwin, “THE TERNARY SYSTEM CaO-Al 2 O 3 -MgO.,” *J. Am. Chem. Soc.*, vol. 38, no. 3, pp. 568–588, **1916**, doi: 10.1021/ja02260a006.

[25] A. M. ALPER, R. N. McNALLY, P. H. RIBBE, and R. C. DOMAN, “The System MgO-MgAl2O4,” *J. Am. Ceram. Soc.*, vol. 45, no. 6, pp. 263–268, **1962**, doi: 10.1111/j.1151-2916.1962.tb11141.x.

[26] B. Hallstedt, “Thermodynamic Assessment of the System MgO–Al2O3,” *J. Am. Ceram. Soc.*, vol. 75, no. 6, pp. 1497–1507, **1992**, doi: 10.1111/j.1151-2916.1992.tb04216.x.

[27] T. Zienert and O. Fabrichnaya, "Thermodynamic assessment and experiments in the system MgO-Al 2O3," *Calphad Comput. Coupling Phase Diagrams Thermochem.*, vol. 40, pp. 1–9, **2013**, doi: 10.1016/j.calphad.2012.10.001.

[28] B. M. Moshtaghioun, J. I. Peña, and R. I. Merino, "Medium infrared transparency of MgO-MgAl2O4 directionally solidified eutectics," *J. Eur. Ceram. Soc.*, vol. 40, no. 4, pp. 1703–1708, **2020**, doi: 10.1016/j.jeurceramsoc.2019.10.053.

[29] B. Tu, H. Wang, X. Liu, W. Wang, and Z. Fu, "Theoretical predictions of composition-dependent structure and properties of alumina-rich spinel," *J. Eur. Ceram. Soc.*, vol. 36, no. 4, pp. 1073–1079, **2016**, doi: 10.1016/j.jeurceramsoc.2015.11.043.

[30] Z. Shi, Q. Zhao, B. Guo, T. Ji, and H. Wang, "A review on processing polycrystalline magnesium aluminate spinel (MgAl2O4): Sintering techniques, material properties and machinability," *Mater. Des.*, vol. 193, p. 108858, **2020**, doi: 10.1016/j.matdes.2020.108858.

[31] S. T. Murphy, C. A. Gilbert, R. Smith, T. E. Mitchell, and R. W. Grimes, "Non-stoichiometry in MgAl2O4 spinel," *Philos. Mag.*, vol. 90, no. 10, pp. 1297–1305, **2010**, doi: 10.1080/14786430903341402.

[32] S. Sawai and T. Uchino, "Visible photoluminescence from MgAl 2 O 4 spinel with cation disorder and oxygen vacancy," *J. Appl. Phys.*, vol. 112, no. 10, p. 103523, **2012**, doi: 10.1063/1.4767228.

[33] K. SHIRASUKA and G. YAMAGUCHI, "Precise measurement of the crystal data and the solid solution range of the defective spinel, MgO nAl2O3.," *J. Ceram. Assoc. Japan*, vol. 82, no. 952, pp. 650–653, **1974**, doi: 10.2109/jcersj1950.82.952_650.

[34] R. Sarkar, A. Ghosh, and S. K. Das, "Reaction sintered magnesia rich magnesium aluminate spinel: Effect of alumina reactivity," *Ceram. Int.*, vol. 29, no. 4, pp. 407–411, **2003**, doi: 10.1016/S0272-8842(02)00152-9.

[35] Y. -M Chiang and W. D. Kingery, "Grain-Boundary Migration in Nonstoichiometric Solid Solutions of Magnesium Aluminate Spinel: I, Grain growth study," *J. Am. Ceram. Soc.*, vol. 73, no. 5, pp. 1153–1158, **1990**, doi: 10.1111/j.1151-2916.1990.tb05172.x.

[36] Y. Li, D. Yang, C. Liu, P. Yang, P. Mu, J. Wen, S. Chen, and Y. Li, "Preparation and characterization of novel nonstoichiometric magnesium aluminate spinels," *Ceram. Int.*, vol. 44, no. 13, pp. 15104–15109, **2018**, doi: 10.1016/j.ceramint.2018.05.145.

[37] A. NAVROTSKY, B. A. WECHSLER, K. GEISINGER, and F. SEIFERT, "Thermochemistry of MgAl2O4-Al8/3O4 Defect Spinels," *J. Am. Ceram. Soc.*, vol. 69, no. 5, pp. 418–422, **1986**, doi: 10.1111/j.1151-2916.1986.tb04772.x.

[38] V. Seeman, E. Feldbach, T. Kärner, A. Maaroos, N. Mironova-Ulmane, A. I. Popov, E. Shablonin, E. Vasil'chenko, and A. Lushchik, "Fast-neutron-induced and as-grown structural defects in magnesium aluminate spinel crystals with different stoichiometry," *Opt. Mater. (Amst).*, vol. 91, pp. 42–49, **2019**, doi: 10.1016/j.optmat.2019.03.008.

[39] A. Krell, K. Waetzig, and J. Klimke, "Influence of the structure of MgO·nAl 2O 3 spinel lattices on transparent ceramics processing and properties," *J. Eur. Ceram. Soc.*, vol. 32, no. 11, pp. 2887–2898, **2012**, doi: 10.1016/j.jeurceramsoc.2012.02.054.

[40] D. Han, J. Zhang, P. Liu, G. Li, L. An, and S. Wang, "Preparation of high-quality transparent Al-rich spinel ceramics by reactive sintering," *Ceram. Int.*, vol. 44, no. 3, pp. 3189–3194, **2018**, doi: 10.1016/j.ceramint.2017.11.089.

[41] J. W. Kim, J. W. Ko, Y. J. Park, J. Do Yun, D. H. Choi, and H. N. Kim, "Microstructural evolution and relevant mechanical properties of Al-rich transparent magnesium aluminate ceramics," *J. Eur. Ceram. Soc.*, vol. 40, no. 8, pp. 3222–3234, **2020**, doi: 10.1016/j.jeurceramsoc.2020.02.046.

[42] M. A. Sainz, A. D. Mazzoni, E. F. Aglietti, and A. Caballero, "Thermochemical stability of spinel (MgO·Al2O3) under strong reducing conditions," *Mater. Chem. Phys.*, vol. 86, no. 2–3, pp. 399–408, **2004**, doi: 10.1016/j.matchemphys.2004.04.007.

[43] D. Dwibedi, "From cation flexibility to multifaceted industrial adoptability: a voyage to the resourceful spinel*," *Adv. Appl. Ceram.*, vol. 117, no. 2, pp. 85–99, **2018**, doi: 10.1080/17436753.2017.1371946.

[44] A. Ibarra, F. J. López, and M. Jiménez de Castro, "V centers in MgAl 2 O 4 spinels," *Phys. Rev. B*, vol. 44, no. 14, pp. 7256–7262, **1991**, doi: 10.1103/PhysRevB.44.7256.

[45] A. Lushchik, S. Dolgov, E. Feldbach, R. Pareja, A. I. Popov, E. Shablonin, and V. Seeman, "Creation and thermal annealing of structural defects in neutron-irradiated MgAl2O4 single crystals," *Nucl. Instruments Methods Phys. Res. Sect. B Beam Interact. with Mater. Atoms*, vol. 435, pp. 31–37, **2018**, doi: 10.1016/j.nimb.2017.10.018.

[46] J. A. Ball, M. Pirzada, R. W. Grimes, M. O. Zacate, D. W. Price, and B. P. Uberuaga, "Predicting lattice parameter as a function of cation disorder in MgAl 2O4 spinel," *J. Phys. Condens. Matter*, vol. 17, no. 48, pp. 7621–7631, **2005**, doi: 10.1088/0953-8984/17/48/014.

[47] Y. Ma, X. Bao, Z. Sui, X. Zhao, and X. Liu, "Quantifying Mg–Al cation distribution in MgAl2O4-spinel using Raman spectroscopy: An experimental calibration," *Solid Earth Sci.*, vol. 7, no. 1, pp. 60–71, **2022**, doi: 10.1016/j.sesci.2021.09.002.

[48] A. Krell and A. Bales, "Grain size-Dependent hardness of transparent magnesium aluminate spinel," *Int. J. Appl. Ceram. Technol.*, vol. 8, no. 5, pp. 1108–1114, **2011**, doi: 10.1111/j.1744-7402.2010.02583.x.

[49] K. Morita, B. N. Kim, H. Yoshida, K. Hiraga, and Y. Sakka, "Spectroscopic study of the discoloration of transparent MgAl2O4 spinel fabricated by spark-plasma-sintering (SPS) processing," *Acta Mater.*, vol. 84, pp. 9–19, **2015**, doi: 10.1016/j.actamat.2014.10.030.

[50] K. MORITA, B.-N. KIM, H. YOSHIDA, K. HIRAGA, and Y. SAKKA, "Assessment of carbon contamination in $MgAl_2O_4$ spinel during spark-plasma-sintering (SPS) processing," *J. Ceram. Soc. Japan*, vol. 123, no. 1442, pp. 983–988, **2015**, doi: 10.2109/jcersj2.123.983.

[51] A. F. Zatsepin, A. N. Kiryakov, D. R. Baytimirov, T. V. Dyachkova, A. P. Tyutyunnik, and Y. G. Zainulin, "Paramagnetic Mn Antisite Defects in Nanoceramics of Aluminum–Magnesium Spinel," *Phys. Solid State*, vol. 62, no. 1, pp. 137–143, **2020**, doi: 10.1134/S1063783420010370.

[52] V. D'Ippolito, G. B. Andreozzi, D. Bersani, and P. P. Lottici, "Raman fingerprint of chromate, aluminate and ferrite spinels," *J. Raman Spectrosc.*, vol. 46, no. 12, pp. 1255–1264, **2015**, doi: 10.1002/jrs.4764.

[53] K. Morita, B. N. Kim, H. Yoshida, K. Hiraga, and Y. Sakka, "Distribution of carbon contamination in MgAl2O4 spinel occurring during spark-plasma-sintering (SPS) processing: I – Effect of heating rate and post-annealing," *J. Eur. Ceram. Soc.*, vol. 38, no. 6, pp. 2588–2595, **2018**, doi: 10.1016/j.jeurceramsoc.2017.09.038.

[54] M. Lazzeri and P. Thibaudeau, "Ab initio Raman spectrum of the normal and disordered Mg Al2 O4 spinel," *Phys. Rev. B - Condens. Matter Mater. Phys.*, vol. 74, no. 14, **2006**, doi: 10.1103/PhysRevB.74.140301.

[55] Q. Li, T. Liu, X. Xu, X. Wang, R. Guo, X. Jiao, and Y. Lu, "Study on the optical spectra of MgAl2O4 with oxygen vacancies,"

Mater. Technol., vol. 36, no. 5, pp. 279–285, **2021**, doi: 10.1080/10667857.2020.1750163.

[56] Q. Li, T. Liu, X. Xu, R. Guo, X. Jiao, X. Wang, and Y. Lu, “Study of cation vacancies with localized hole states in MgAl2O4 crystals,” *J. Phys. Chem. Solids*, vol. 145, no. February, p. 109542, **2020**, doi: 10.1016/j.jpcs.2020.109542.

[57] B. Sieber, “Cathodoluminescence - Principes physiques et systèmes de détection,” *Tech. l’Ingénieur*, vol. P3792, no. 0, pp. 1--16, **2012**.

[58] J. S. Shaffer, H. A. Farach, and C. P. Poole, “Electron-spin-resonance study of manganese-doped spinel,” *Phys. Rev. B*, vol. 13, no. 5, pp. 1869–1875, **1976**, doi: 10.1103/PhysRevB.13.1869.

[59] A. Tomita, T. Sato, K. Tanaka, Y. Kawabe, M. Shirai, K. Tanaka, and E. Hanamura, “Luminescence channels of manganese-doped spinel,” *J. Lumin.*, vol. 109, no. 1, pp. 19–24, **2004**, doi: 10.1016/j.jlumin.2003.12.049.

[60] V. Singh, R. P. S. Chakradhar, J. L. Rao, and D. K. Kim, “Synthesis, characterization, photoluminescence and EPR investigations of Mn doped MgAl2O4 phosphors,” *J. Solid State Chem.*, vol. 180, no. 7, pp. 2067–2074, **2007**, doi: 10.1016/j.jssc.2007.04.030.

[61] H. Van den Boom and J. C. M. Henning, “An orthorhombic chromium-center in the spinel MgAl2O4,” *J. Phys. Chem. Solids*, vol. 34, no. 7, pp. 1211–1216, **1973**, doi: 10.1016/S0022-3697(73)80211-2.

[62] T. Sakuma, S. Minowa, T. Katsumata, S. Komuro, and H. Aizawa, “Compositional variation of photoluminescence from Mn doped MgAl2O4 spinel,” *Opt. Mater. (Amst).*, vol. 37, no. C, pp. 302–305, **2014**, doi: 10.1016/j.optmat.2014.06.014.

[63] Y. Hao, Y. Zhang, and S. Wang, “Synthesis, structure and photoluminescence of sheet-like MgAl2O4: Cr3+,” *Inorg. Chem. Commun.*, vol. 132, no. August, p. 108853, **2021**, doi: 10.1016/j.inoche.2021.108853.

[64] M. G. Brik, J. Papan, D. J. Jovanović, and M. D. Dramićanin, “Luminescence of Cr3+ ions in ZnAl2O4 and MgAl2O4 spinels: Correlation between experimental spectroscopic studies and crystal field calculations,” *J. Lumin.*, vol. 177, pp. 145–151, **2016**, doi: 10.1016/j.jlumin.2016.04.043.

[65] E. Alagu Raja, S. Menon, B. Dhabekar, N. S. Rawat, and T. K. Gundu Rao, “Investigation of defect centres responsible for TL/OSL in MgAl2O4:Tb3+,” *J. Lumin.*, vol. 129, no. 8, pp. 829–835, **2009**, doi: 10.1016/j.jlumin.2009.03.001.

[66] D. Valiev, O. Khasanov, E. Dvilis, S. Stepanov, E. Polisadova, and V. Paygin, “Luminescent properties of MgAl2O4 ceramics doped with rare earth ions fabricated by spark plasma sintering technique,” *Ceram. Int.*, vol. 44, no. 17, pp. 20768–20773, **2018**, doi: 10.1016/j.ceramint.2018.08.076.

[67] E. F. Polisadova, V. A. Vaganov, D. T. Valiev, S. A. Stepanov, V. D. Paygin, E. S. Dvilis, and O. L. Khasanov, “Influence of Temperature on the Luminescence Properties of MgAl2O4:Dy3+ Ceramics Synthesized by Spark Plasma Sintering,” *Phys. Solid State*, vol. 61, no. 10, pp. 1829–1834, **2019**, doi: 10.1134/S1063783419100299.

[68] T. Sato, M. Shirai, K. Tanaka, Y. Kawabe, and E. Hanamura, “Strong blue emission from Ti-doped MgAl2O4 crystals,” *J. Lumin.*, vol. 114, no. 2, pp. 155–161, **2005**, doi: 10.1016/j.jlumin.2004.12.016.

[69] P. Lombard, B. Boizot, N. Ollier, A. Jouini, and A. Yoshikawa, “Spectroscopic studies of Ti3+ ions speciation inside MgAl2O4 spinels,” *J. Cryst. Growth*, vol. 311, no. 3, pp. 899–903, **2009**, doi: 10.1016/j.jcrysgro.2008.09.131.

[70] Y. Wakui, Y. J. Shan, K. Tezuka, H. Imoto, and M. Ando, “Crystal-site engineering approach for preparation of Mg B2O4:Mn2+, Mn4+ (B = Al, Ga) phosphors: Control of green/red luminescence properties,” *Mater. Res. Bull.*, vol. 90, pp. 51–58, **2017**, doi: 10.1016/j.materresbull.2017.02.001.

[71] N. M. Khaidukov, M. N. Brekhovskikh, N. Y. Kirikova, V. A. Kondratyuk, and V. N. Makhov, “Luminescence of MgAl2O4 and ZnAl2O4 spinel ceramics containing some 3d ions,” *Ceram. Int.*, vol. 46, no. 13, pp. 21351–21359, **2020**, doi: 10.1016/j.ceramint.2020.05.231.

[72] R. Apetz and M. P. B. Van Bruggen, “Transparent alumina: A light-scattering model,” *J. Am. Ceram. Soc.*, vol. 86, no. 3, pp. 480–486, **2003**, doi: 10.1111/j.1151-2916.2003.tb03325.x.

[73] M. Bass, C. DeCusatis, J. Enoch, V. Lakshminarayanan, G. Li, C. MacDonald, V. Mahajan, and E. Van Stryland, *Handbook of Optics*, 3rd editio. McGraw-Hill Education, 2010. [Online]. Available: https://emc2physics.com/wp-content/uploads/2021/03/Michael-Bass-Virendra-N.-Mahajan-Handbook-of-Optics.-vol-II-MGH-2010.pdf

[74] G. Bonnefont, G. Fantozzi, S. Trombert, and L. Bonneau, “Fine-grained transparent MgAl2O4 spinel obtained by spark plasma sintering of commercially available nanopowders,” *Ceram. Int.*, vol. 38, no. 1, pp. 131–140, **2012**, doi: 10.1016/j.ceramint.2011.06.045.

[75] B. N. Kim, K. Hiraga, K. Morita, and H. Yoshida, “Spark plasma sintering of transparent alumina,” *Scr. Mater.*, vol. 57, no. 7, pp. 607–610, **2007**, doi: 10.1016/j.scriptamat.2007.06.009.

[76] A. Krell, T. Hutzler, and J. Klimke, “Defect strategies for an improved optical quality of transparent ceramics,” *Opt. Mater. (Amst).*, vol. 38, pp. 61–74, **2014**, doi: 10.1016/j.optmat.2014.09.030.

[77] A. Goldstein, P. Loiko, Z. Burshtein, N. Skoptsov, I. Glazunov, E. Galun, N. Kuleshov, and K. Yumashev, “Development of Saturable Absorbers for Laser Passive Q-Switching near 1.5 μm Based on Transparent Ceramic Co2+:MgAl2O4,” *J. Am. Ceram. Soc.*, vol. 99, no. 4, pp. 1324–1331, **2016**, doi: 10.1111/jace.14102.

[78] A. F. Dericioglu and Y. Kagawa, “Effects of grain boundary microcracking on the light transmittance of sintered transparent MgAl2O4,” *J. Eur. Ceram. Soc.*, vol. 23, no. 6, pp. 951–959, **2003**, doi: 10.1016/S0955-2219(02)00205-4.

[79] E. Tõldsepp, F. Schoenstein, M. Amamra, R. Saar, E. Feldbach, A. Kanaev, and M. Kirm, “Spark plasma sintering of ultra-porous γ-Al2O3,” *Ceram. Int.*, vol. 42, no. 10, pp. 11709–11715, **2016**, doi: 10.1016/j.ceramint.2016.04.089.

[80] Ricardo H. R. Castro • Klaus van Benthem, *Sintering - Mechanisms of Convention Nanodensification and Field Assisted Processes*, vol. 35. 2013.

[81] G. Mattoeno, G. Righini, G. Montesperelli, and E. Traversa, “X-ray photoelectron spectroscopy investigation of MgAl204 thin films for humidity sensors,” *J. Mater. Res.*, vol. 9, no. 6, pp. 1426–1433, **1994**, doi: 10.1557/JMR.1994.1426.

[82] R. H. ARLETT and M. ROBBINS, “Growth of Stoichiometric MgAl2O4 Single Crystals,” *J. Am. Ceram. Soc.*, vol. 50, no. 5, pp. 273–274, **1967**, doi: 10.1111/j.1151-2916.1967.tb15106.x.

[83] G. H. Sun, Q. L. Zhang, J. Q. Luo, W. P. Liu, X. F. Wang, S. Han, L. L. Zheng, W. M. Li, and D. L. Sun, “Bulk Crystal Growth of Cr-doped MgAl2O4 spinel by Czochralski method and properties characterization,” *Mater. Chem. Phys.*, vol. 204, pp. 277–281, **2018**, doi: 10.1016/j.matchemphys.2017.10.049.

[84] D. Bootkul, T. Tengchaisri, U. Tippawan, and S. Intarasiri, “Analysis and modification of natural red spinel by ion beam techniques for jewelry applications,” *Surf. Coatings Technol.*, vol. 306, pp. 211–217, **2016**, doi: 10.1016/j.surfcoat.2016.05.084.

[85] S. Su, Q. Liu, Z. Hu, X. Chen, H. Pan, X. Liu, L. Wu, and J. Li, "A simple way to prepare Co:MgAl2O4 transparent ceramics for saturable absorber," *J. Alloys Compd.*, vol. 797, pp. 1288–1294, **2019**, doi: 10.1016/j.jallcom.2019.04.322.

[86] C. Wagner, "Über den Mechanismus der Bildung von Ionenverbindungen höherer Ordnung (Doppelsalze, Spinelle, Silikate)," *Zeitschrift für Phys. Chemie*, vol. 34B, no. 1, pp. 309–316, **1936**, doi: 10.1515/zpch-1936-3422.

[87] Z. Zhang and N. Li, "Effect of polymorphism of Al2O3 on the synthesis of magnesium aluminate spinel," *Ceram. Int.*, vol. 31, no. 4, pp. 583–589, **2005**, doi: 10.1016/j.ceramint.2004.06.025.

[88] R. Sarkar and G. Banerjee, "Effect of compositional variation and fineness on the densification of MgO-Al2O3 compacts," *J. Eur. Ceram. Soc.*, vol. 19, no. 16, pp. 2893–2899, **1999**, doi: 10.1016/S0955-2219(99)00078-3.

[89] R. Sarkar and S. Sahoo, "Effect of raw materials on formation and densification of magnesium aluminate spinel," *Ceram. Int.*, vol. 40, no. PB, pp. 16719–16725, **2014**, doi: 10.1016/j.ceramint.2014.08.037.

[90] L. B. Kong, J. Ma, and H. Huang, "MgAl2O4 spinel phase derived from oxide mixture activated by a high-energy ball milling process," *Mater. Lett.*, vol. 56, no. 3, pp. 238–243, **2002**, doi: 10.1016/S0167-577X(02)00447-0.

[91] I. Ganesh, B. Srinivas, R. Johnson, B. P. Saha, and Y. R. Mahajan, "Microwave assisted solid state reaction synthesis of MgAl2O4 spinel powders," *J. Eur. Ceram. Soc.*, vol. 24, no. 2, pp. 201–207, **2004**, doi: 10.1016/S0955-2219(03)00602-2.

[92] L. Yang, Q. Meng, N. Lu, G. He, and J. Li, "Combustion synthesis and spark plasma sintering of MgAl2O4-graphene composites," *Ceram. Int.*, vol. 45, no. 6, pp. 7635–7640, **2019**, doi: 10.1016/j.ceramint.2019.01.060.

[93] G. Gusmano, P. Nunziante, E. Traversa, and G. Chiozzini, "The mechanism of MgAl2O4 spinel formation from the thermal decomposition of coprecipitated hydroxides," *J. Eur. Ceram. Soc.*, vol. 7, no. 1, pp. 31–39, **1991**, doi: 10.1016/0955-2219(91)90051-Z.

[94] M. F. Zawrah, H. Hamaad, and S. Meky, "Synthesis and characterization of nano MgAl2O4 spinel by the co-precipitated method," *Ceram. Int.*, vol. 33, no. 6, pp. 969–978, **2007**, doi: 10.1016/j.ceramint.2006.02.015.

[95] M. J. Iqbal and B. Ismail, "Electric, dielectric and magnetic characteristics of Cr3+, Mn3+ and Fe3+ substituted MgAl2O4: Effect of pH and annealing temperature," *J. Alloys Compd.*, vol. 472, no. 1–2, pp. 434–440, **2009**, doi: 10.1016/j.jallcom.2008.04.079.

[96] J. Rufner, D. Anderson, K. Van Benthem, and R. H. R. Castro, "Synthesis and sintering behavior of ultrafine (<10 nm) magnesium aluminate spinel nanoparticles," *J. Am. Ceram. Soc.*, vol. 96, no. 7, pp. 2077–2085, **2013**, doi: 10.1111/jace.12342.

[97] D. Li, M. Lu, Y. Cai, Y. Cao, Y. Zhan, and L. Jiang, "Synthesis of high surface area MgAl2O4 spinel as catalyst support via layered double hydroxides-containing precursor," *Appl. Clay Sci.*, vol. 132–133, pp. 243–250, **2016**, doi: 10.1016/j.clay.2016.06.010.

[98] S. Nam, M. Lee, B. N. Kim, Y. Lee, and S. Kang, "Morphology controlled Co-precipitation method for nano structured transparent MgAl2O4," *Ceram. Int.*, vol. 43, no. 17, pp. 15352–15359, **2017**, doi: 10.1016/j.ceramint.2017.08.075.

[99] C. Păcurariu, I. Lazău, Z. Ecsedi, R. Lazău, P. Barvinschi, and G. Mărginean, "New synthesis methods of MgAl2O4 spinel," *J. Eur. Ceram. Soc.*, vol. 27, no. 2–3, pp. 707–710, **2007**, doi: 10.1016/j.jeurceramsoc.2006.04.050.

[100] S. Tripathy and D. Bhattacharya, "Rapid synthesis and characterization of mesoporous nanocrystalline MgAl2O4 via flash pyrolysis route," *J. Asian Ceram. Soc.*, vol. 1, no. 4, pp. 328–332, **2013**, doi: 10.1016/j.jascer.2013.08.006.

[101] W. A. I. Tabaza, H. C. Swart, and R. E. Kroon, "Luminescence of Ce doped MgAl2O4 prepared by the combustion method," *Phys. B Condens. Matter*, vol. 439, pp. 109–114, **2014**, doi: 10.1016/j.physb.2013.10.060.

[102] S. S. Raj, S. K. Gupta, V. Grover, K. P. Muthe, V. Natarajan, and A. K. Tyagi, "MgAl2O4 spinel: Synthesis, carbon incorporation and defect-induced luminescence," *J. Mol. Struct.*, vol. 1089, pp. 81–85, **2015**, doi: 10.1016/j.molstruc.2015.02.002.

[103] M. S. Abdi, T. Ebadzadeh, A. Ghaffari, and M. Feli, "Synthesis of nano-sized spinel (MgAl2O4) from short mechanochemically activated chloride precursors and its sintering behavior," *Adv. Powder Technol.*, vol. 26, no. 1, pp. 175–179, **2015**, doi: 10.1016/j.apt.2014.09.011.

[104] Y. S. Naeini and F. Golestani-Fard, "Low temperature molten salt synthesis of nano crystalline MgAl 2O4," *Key Eng. Mater.*, vol. 512–515, pp. 77–81, **2012**, doi: 10.4028/www.scientific.net/KEM.512-515.77.

[105] Z. Z. Chen, E. W. Shi, H. W. Zhang, Y. Zhang, X. B. Li, X. C. Liu, and B. Xiao, "Hydrothermal synthesis of magnesium aluminate platelets," *J. Am. Ceram. Soc.*, vol. 89, no. 12, pp. 3635–3637, **2006**, doi: 10.1111/j.1551-2916.2006.01289.x.

[106] R. Li, J. Liu, L. Xu, and J. Zhou, "Microwave idrothermal synthesis of magnesium-aluminium spinel," *Ceram. Int.*, vol. 46, no. 18, pp. 29207–29211, **2020**, doi: 10.1016/j.ceramint.2020.08.094.

[107] R. Li and J. Liu, "Effect of Reaction Time on the Synthesis and Sintering of Magnesium-Aluminium Spinel by Microwave Hydrothermal Synthesis," *Trans. - Indian Ceram. Soc.*, vol. 80, no. 4, pp. 265–269, **2021**, doi: https://doi.org/10.1080/0371750X.2021.2014637.

[108] P. V. M. Kutty and S. Dasgupta, "Low temperature synthesis of nanocrystalline magnesium aluminate spinel by a soft chemical method," *Ceram. Int.*, vol. 39, no. 7, pp. 7891–7894, **2013**, doi: 10.1016/j.ceramint.2013.03.050.

[109] M. Borlaf and R. Moreno, "Colloidal sol-gel: A powerful low-temperature aqueous synthesis route of nanosized powders and suspensions," *Open Ceram.*, vol. 8, no. October, p. 100200, **2021**, doi: 10.1016/j.oceram.2021.100200.

[110] S. S. Milani, M. G. Kakroudi, N. P. Vafa, S. Rahro, and F. Behboudi, "Synthesis and characterization of MgAl2O4 spinel precursor sol prepared by inorganic salts," *Ceram. Int.*, vol. 47, no. 4, pp. 4813–4819, **2021**, doi: 10.1016/j.ceramint.2020.10.051.

[111] S. Sanjabi and A. Obeydavi, "Synthesis and characterization of nanocrystalline MgAl2O4 spinel via modified sol-gel method," *J. Alloys Compd.*, vol. 645, pp. 535–540, **2015**, doi: 10.1016/j.jallcom.2015.05.107.

[112] N. Habibi, Y. Wang, H. Arandiyan, and M. Rezaei, "Low-temperature synthesis of mesoporous nanocrystalline magnesium aluminate (MgAl2O4) spinel with high surface area using a novel modified sol-gel method," *Adv. Powder Technol.*, vol. 28, no. 4, pp. 1249–1257, **2017**, doi: 10.1016/j.apt.2017.02.012.

[113] H. Li, H. Y. Wei, Y. Cui, R. L. Sang, J. L. Bu, Y. N. Wei, J. Lin, and J. H. Zhao, "Synthesis and characterisation of MgAl2O4 spinel nanopowders via nonhydrolytic sol-gel route," *J. Ceram. Soc. Japan*, vol. 125, no. 3, pp. 100–104, **2017**, doi: 10.2109/jcersj2.16297.

[114] Q. Xu, D. P. Huang, W. Chen, J. H. Lee, H. Wang, and R. Z. Yuan, "Citrate method synthesis, characterization and mixed electronic-ionic conduction properties of La0.6Sr0.4Co0.8Fe 0.2O3 perovskite-type complex oxides," *Scr. Mater.*, vol. 50,

no. 1, pp. 165–170, **2004**, doi: 10.1016/j.scriptamat.2003.09.008.

[115]P. Y. Lee, H. Suematsu, T. Yano, and K. Yatsui, “Synthesis and characterization of nanocrystalline MgAl2O 4 spinel by polymerized complex method,” *J. Nanoparticle Res.*, vol. 8, no. 6, pp. 911–917, **2006**, doi: 10.1007/s11051-005-9055-4.

[116]C. Feldmann, “Polyol mediated synthesis of oxide particle suspensions and their application,” *Scr. Mater.*, vol. 44, no. 8–9, pp. 2193–2196, **2001**, doi: 10.1016/S1359-6462(01)00902-2.

[117]C. Feldmann and H. O. Jungk, “Polyol-mediated preparation of nanoscale oxide particles,” *Angew. Chemie - Int. Ed.*, vol. 40, no. 2, pp. 359–362, **2001**, doi: 10.1002/1521-3773(20010119)40:2<359::AID-ANIE359>3.0.CO;2-B.

[118]V. Rives, *Layered Double Hydroxides*, vol. 119. Berlin/Heidelberg: Springer-Verlag, 2006. doi: 10.1007/b100426.

[119]D. Kim, J. H. Jung, and J. Ihm, “Theoretical study of aluminum hydroxide as a hydrogen-bonded layered material,” *Nanomaterials*, vol. 8, no. 6, pp. 1–12, **2018**, doi: 10.3390/nano8060375.

[120]D. Jin, X. Gu, X. Yu, G. Ding, H. Zhu, and K. Yao, “Hydrothermal synthesis and characterization of hexagonal Mg(OH)2 nano-flake as a flame retardant,” *Mater. Chem. Phys.*, vol. 112, no. 3, pp. 962–965, **2008**, doi: 10.1016/j.matchemphys.2008.07.058.

[121]T. Sun, Q. Zhuo, Y. Chen, and Z. Wu, “Synthesis of boehmite and its effect on flame retardancy of epoxy resin,” *High Perform. Polym.*, vol. 27, no. 1, pp. 100–104, **2015**, doi: 10.1177/0954008314540312.

[122]A. D. V. Souza, C. C. Arruda, L. Fernandes, M. L. P. Antunes, P. K. Kiyohara, and R. Salomão, “Characterization of aluminum hydroxide (Al(OH)3) for use as a porogenic agent in castable ceramics,” *J. Eur. Ceram. Soc.*, vol. 35, no. 2, pp. 803–812, **2015**, doi: 10.1016/j.jeurceramsoc.2014.09.010.

[123]N. Chubar, R. Gilmour, V. Gerda, M. Mičušík, M. Omastova, K. Heister, P. Man, J. Fraissard, and V. Zaitsev, “Layered double hydroxides as the next generation inorganic anion exchangers: Synthetic methods versus applicability,” *Adv. Colloid Interface Sci.*, vol. 245, no. April, pp. 62–80, **2017**, doi: 10.1016/j.cis.2017.04.013.

[124]N. Kurnia Julianti, T. Kusuma Wardani, I. Gunardi, and A. Roesyadi, “Effect of Calcination at Synthesis of Mg-Al Hydrotalcite Using co-Precipitation Method,” *J. Pure Appl. Chem. Res.*, vol. 6, no. 1, pp. 7–13, **2017**, doi: 10.21776/ub.jpacr.2017.006.01.280.

[125]J. S. Valente, H. Pfeiffer, E. Lima, J. Prince, and J. Flores, “Cyanoethylation of alcohols by activated Mg-Al layered double hydroxides: Influence of rehydration conditions and Mg/Al molar ratio on Brönsted basicity,” *J. Catal.*, vol. 279, no. 1, pp. 196–204, **2011**, doi: 10.1016/j.jcat.2011.01.018.

[126]J. Y. Lee, G. H. Gwak, H. M. Kim, T. Il Kim, G. J. Lee, and J. M. Oh, “Synthesis of hydrotalcite type layered double hydroxide with various Mg/Al ratio and surface charge under controlled reaction condition,” *Appl. Clay Sci.*, vol. 134, pp. 44–49, **2016**, doi: 10.1016/j.clay.2016.03.029.

[127]A. V. Besserguenev, A. M. Fogg, R. J. Francis, S. J. Price, D. O’Hare, V. P. Isupov, and B. P. Tolochko, “Synthesis and Structure of the Gibbsite Intercalation Compounds [LiAl2(OH)6]X {X = Cl, Br, NO3} and [LiAl2(OH)6]Cl·H2O Using Synchrotron X-ray and Neutron Powder Diffraction,” *Chem. Mater.*, vol. 9, no. 1, pp. 241–247, **1997**, doi: 10.1021/cm960316z.

[128]A. M. Fogg, G. R. Williams, R. Chester, and D. O’Hare, “A novel family of layered double hydroxides - [MAl4(OH) 12](NO3)2·xH2O (M = Co, Ni, Cu, Zn),” *J. Mater. Chem.*, vol. 14, no. 15, pp. 2369–2371, **2004**, doi: 10.1039/b409027f.

[129]R. Chitrakar, Y. Makita, A. Sonoda, and T. Hirotsu, “Synthesis of a novel layered double hydroxides [MgAl4(OH)12](Cl)2·2.4H2O and its anion-exchange properties,” *J. Hazard. Mater.*, vol. 185, no. 2–3, pp. 1435–1439, **2011**, doi: 10.1016/j.jhazmat.2010.10.066.

[130]S. Britto and P. V. Kamath, “Synthesis, structure refinement and chromate sorption characteristics of an Al-rich bayerite-based layered double hydroxide,” *J. Solid State Chem.*, vol. 215, pp. 206–210, **2014**, doi: 10.1016/j.jssc.2014.02.031.

[131]S. Miyata, “Anion-exchange properties of hydrotalcite-like compounds.,” *Clays Clay Miner.*, vol. 31, no. 4, pp. 305–311, **1983**, doi: 10.1346/CCMN.1983.0310409.

[132]M. Zubair, M. Daud, G. McKay, F. Shehzad, and M. A. Al-Harthi, “Recent progress in layered double hydroxides (LDH)-containing hybrids as adsorbents for water remediation,” *Appl. Clay Sci.*, vol. 143, no. April, pp. 279–292, **2017**, doi: 10.1016/j.clay.2017.04.002.

[133]D. Cosano, D. Esquivel, F. J. Romero-Salguero, C. Jiménez-Sanchidrián, and J. R. Ruiz, “Use of Raman spectroscopy to assess nitrate uptake by calcined LDH phases,” *Colloids Surfaces A Physicochem. Eng. Asp.*, vol. 602, no. April, p. 125066, **2020**, doi: 10.1016/j.colsurfa.2020.125066.

[134]M. A. Iqbal, M. Secchi, M. A. Iqbal, M. Montagna, C. Zanella, and M. Fedel, “MgAl-LDH/graphene protective film: Insight into LDH-graphene interaction,” *Surf. Coatings Technol.*, vol. 401, no. March, p. 126253, **2020**, doi: 10.1016/j.surfcoat.2020.126253.

[135]Y. Su, S. Qiu, D. Yang, S. Liu, H. Zhao, L. Wang, and Q. Xue, “Active anti-corrosion of epoxy coating by nitrite ions intercalated MgAl LDH,” *J. Hazard. Mater.*, vol. 391, no. October 2019, p. 122215, **2020**, doi: 10.1016/j.jhazmat.2020.122215.

[136]H. Wang, W. Duan, Y. Wu, Y. Tang, and L. Li, “Synthesis of magnesium-aluminum layered double hydroxide intercalated with ethylene glycol by the aid of alkoxides,” *Inorganica Chim. Acta*, vol. 418, no. 3, pp. 163–170, **2014**, doi: 10.1016/j.ica.2014.04.031.

[137]G. A. Borges, G. M. D. Ferreira, K. P. F. Siqueira, A. Dias, K. O. N. Navarro, S. J. B. e. Silva, G. D. Rodrigues, and A. B. Mageste, “Adsorption of organic and inorganic arsenic from aqueous solutions using MgAl-LDH with incorporated nitroprusside,” *J. Colloid Interface Sci.*, vol. 575, pp. 194–205, **2020**, doi: 10.1016/j.jcis.2020.04.078.

[138]S. Tanasoi, G. Mitran, N. Tanchoux, T. Cacciaguerra, F. Fajula, I. Sndulescu, D. Tichit, and I. C. Marcu, “Transition metal-containing mixed oxides catalysts derived from LDH precursors for short-chain hydrocarbons oxidation,” *Appl. Catal. A Gen.*, vol. 395, no. 1–2, pp. 78–86, **2011**, doi: 10.1016/j.apcata.2011.01.028.

[139]J. Kuljiraseth, A. Wangriya, J. M. C. Malones, W. Klysubun, and S. Jitkarnka, “Synthesis and characterization of AMO LDH-derived mixed oxides with various Mg/Al ratios as acid–basic catalysts for esterification of benzoic acid with 2-ethylhexanol,” *Appl. Catal. B Environ.*, vol. 243, no. June 2018, pp. 415–427, **2019**, doi: 10.1016/j.apcatb.2018.10.073.

[140]T. N. Ramesh, M. Rajamathi, and P. V. Kamath, “Ammonia induced precipitation of cobalt hydroxide: observation of turbostratic disorder,” *Solid State Sci.*, vol. 5, no. 5, pp. 751–756, **2003**, doi: 10.1016/S1293-2558(03)00086-4.

[141]N. Chakroune, G. Viau, C. Ricolleau, F. Fiévet-Vincent, and F. Fiévet, “Cobalt-based anisotropic particles prepared by the

polyol process," *J. Mater. Chem.*, vol. 13, no. 2, pp. 312–318, **2003**, doi: 10.1039/b209383a.

[142]T. Zhu, J. S. Chen, and X. W. (David) Lou, "Highly Efficient Removal of Organic Dyes from Waste Water Using Hierarchical NiO Spheres with High Surface Area," *J. Phys. Chem. C*, vol. 116, no. 12, pp. 6873–6878, **2012**, doi: 10.1021/jp300224s.

[143]L. Poul, N. Jouini, and F. Fievet, "Layered hydroxide metal acetates (metal = zinc, cobalt, and nickel): Elaboration via hydrolysis in polyol medium and comparative study," *Chem. Mater.*, vol. 12, no. 10, pp. 3123–3132, **2000**, doi: 10.1021/cm991179j.

[144]D. Redaoui, F. Sahnoune, M. Heraiz, and A. Raghdi, "Mechanism and kinetic parameters of the thermal decomposition of gibbsite Al(OH)3 by thermogravimetric analysis," *Acta Phys. Pol. A*, vol. 131, no. 3, pp. 562–565, **2017**, doi: 10.12693/APhysPolA.131.562.

[145]F. M. Labajos, V. Rives, and M. A. Ulibarri, "Effect of hydrothermal and thermal treatments on the physicochemical properties of Mg-Al hydrotalcite-like materials," *J. Mater. Sci.*, vol. 27, no. 6, pp. 1546–1552, **1992**, doi: 10.1007/BF00542916.

[146]M. Beauvy, J.-L. Vignes, D. Michel, L. Mazerolles, C. Frappart, and T. Di Costanzo, "Method of preparation of monolithic hydrated aluminas, amorphous or crystalline aluminas, aluminates and composite materials by oxidation of aluminum or of an aluminum alloy," US7799385B2, 2010 [Online]. Available: https://patentimages.storage.googleapis.com/dc/7a/1b/8da837d02b50ab/US7799385.pdf

[147]J. L. Vignes, L. Mazerolles, and D. Michel, "A novel method for preparing porous alumina objects," *Key Eng. Mater.*, vol. 132–136, pp. 432–435, **1997**, doi: 10.4028/www.scientific.net/kem.132-136.432.

[148]A. Khodan, T. H. N. Nguyen, M. Esaulkov, M. R. Kiselev, M. Amamra, J. L. Vignes, and A. Kanaev, "Porous monoliths consisting of aluminum oxyhydroxide nanofibrils: 3D structure, chemical composition, and phase transformations in the temperature range 25–1700 °C," *J. Nanoparticle Res.*, vol. 20, no. 7, **2018**, doi: 10.1007/s11051-018-4285-4.

[149]L. Mazerolles, D. Michel, T. di Costanzo, and J. L. Vignes, "New Developments in Nanometric Porous Mullite, Spinel, and Aluminas," in *Innovative Processing and Synthesis of Ceramics, Glasses, and Composites VI*, 2012, pp. 225–235. doi: 10.1002/9781118380826.ch20.

[150]L. Mazerolles, D. Michel, T. Di Costanzo, J.-L. L. Vignes, Z. Huang, and D. Jiang, "Nanostructured Materials Based on Alumina," in *27th Annual Cocoa Beach Conference on Advanced Ceramics and Composites: A: Ceramic Engineering and Science Proceedings, Volume 24, Issue 3*, vol. 24, W. M. Kriven and H.-T. Lin, Eds. Hoboken, NJ, USA: John Wiley & Sons, Inc., 2003, pp. 105–110. doi: 10.1002/9780470294802.ch16.

[151]T. di Costanzo, A. A. Fomkin, C. Frappart, A. N. Khodan, D. G. Kuznetsov, L. Mazerolles, D. Michel, A. A. Minaev, V. A. Sinitsin, and J. L. Vignes, "New Method of Porous Oxide Synthesis: Alumina and Alumina Based Compounds," *Mater. Sci. Forum*, vol. 453–454, pp. 315–322, **2004**, doi: 10.4028/www.scientific.net/MSF.453-454.315.

[152]O. Khatim, T. H. N. Nguyen, M. Amamra, L. Museur, A. Khodan, and A. Kanaev, "Synthesis and photoluminescence properties of nanostructured mullite/α-Al2O3," *Acta Mater.*, vol. 71, pp. 108–116, **2014**, doi: 10.1016/j.actamat.2014.03.006.

[153]T. Di Costanzo, C. Frappart, L. Mazerolles, J. C. Rouchaud, M. Fédoroff, D. Michel, M. Beauvy, and J. L. Vignes, "Fixation de divers polluants dans des alumines monolithiques poreuses," *Ann. Chim. Sci. des Mater.*, vol. 26, no. 2, pp. 67–78, **2001**, doi: 10.1016/S0151-9107(01)80047-7.

[154]H. Xu, G. Boeuf, Z. Jia, A. Kanaev, R. Azouani, M. Amamra, A. Elm'selmi, and M. Traore, "Novel synthesis of oxidoreductase immobilized biocatalyst for effective anthraquinone dye treatment in bioreactor," *Chem. Eng. Trans.*, vol. 84, no. November 2020, pp. 157–162, **2021**, doi: 10.3303/CET2184027.

[155]H. Xu, G. Boeuf, Z. Jia, K. Zhu, M. Nikravech, A. Kanaev, R. Azouani, M. Traore, and A. Elm'selmi, "Solvent-free synthesized monolithic ultraporous aluminas for highly efficient removal of remazol brilliant blue R: Equilibrium, kinetic, and thermodynamic studies," *Materials (Basel).*, vol. 14, no. 11, pp. 1–19, **2021**, doi: 10.3390/ma14113054.

[156]K. E. Yorov, A. N. Khodan, A. E. Baranchikov, V. V. Utochnikova, N. P. Simonenko, A. N. Beltiukov, D. I. Petukhov, A. Kanaev, and V. K. Ivanov, "Superhydrophobic and luminescent highly porous nanostructured alumina monoliths modified with tris(8-hydroxyquinolinato)aluminium," *Microporous Mesoporous Mater.*, vol. 293, no. September 2019, p. 109804, **2020**, doi: 10.1016/j.micromeso.2019.109804.

[157]H. Dong, Y.-C. Chen, and C. Feldmann, "Polyol synthesis of nanoparticles: status and options regarding metals, oxides, chalcogenides, and non-metal elements," *Green Chem.*, vol. 17, no. 8, pp. 4107–4132, **2015**, doi: 10.1039/C5GC00943J.

[158]F. Fievet, S. Ammar-Merah, R. Brayner, F. Chau, M. Giraud, F. Mammeri, J. Peron, J. Y. Piquemal, L. Sicard, and G. Viau, "The polyol process: a unique method for easy access to metal nanoparticles with tailored sizes, shapes and compositions," *Chem. Soc. Rev.*, vol. 47, no. 14, pp. 5187–5233, **2018**, doi: 10.1039/c7cs00777a.

[159]S. Murali, P. K. Dammala, B. Rani, R. Santhosh, C. Jadhao, and N. K. Sahu, "Polyol mediated synthesis of anisotropic ZnO nanomaterials and composite with rGO: Application towards hybrid supercapacitor," *J. Alloys Compd.*, vol. 844, p. 156149, **2020**, doi: 10.1016/j.jallcom.2020.156149.

[160]A. J. Biacchi and R. E. Schaak, "The Solvent Matters: Kinetic versus Thermodynamic Shape Control in the Polyol Synthesis of Rhodium Nanoparticles," *ACS Nano*, vol. 5, no. 10, pp. 8089–8099, **2011**, doi: 10.1021/nn2026758.

[161]V. K. LaMer and R. H. Dinegar, "Theory, Production and Mechanism of Formation of Monodispersed Hydrosols," *J. Am. Chem. Soc.*, vol. 72, no. 11, pp. 4847–4854, **1950**, doi: 10.1021/ja01167a001.

[162]A. D. Omrani, M. A. Bousnina, L. S. Smiri, M. Taibi, P. Leone, F. Schoenstein, and N. Jouini, "Elaboration of nickel nanoparticles by modified polyol process and their spark plasma sintering, characterization and magnetic properties of the nanoparticles and the dense nano-structured material," *Mater. Chem. Phys.*, vol. 123, no. 2–3, pp. 821–828, **2010**, doi: 10.1016/j.matchemphys.2010.05.068.

[163]P. Canaud, R. Mahayri, F. Schoenstein, E. Gautron, K. L. Tan, T. Chauveau, J. M. Morelle, F. Maroteaux, and N. Jouini, "Synthesis of Ag3Sn Submicrometer Particles via an Adapted Polyol Process in View of Their Use As Die-Attach Material in Power Modules," *J. Electron. Mater.*, vol. 48, no. 7, pp. 4637–4646, **2019**, doi: 10.1007/s11664-019-07238-y.

[164]M. Taibi, S. Ammar, F. Schoenstein, N. Jouini, F. Fiévet, T. Chauveau, and J. M. Greneche, "Powder and film of nickel and iron-layered double hydroxide: Elaboration in polyol medium and characterization," *J. Phys. Chem. Solids*, vol. 69, no. 5–6, pp. 1052–1055, **2008**, doi: 10.1016/j.jpcs.2007.10.115.

[165]S. Chkoundali, S. Ammar, N. Jouini, F. Fiévet, P. Molinié, M. Danot, F. Villain, and J. M. Grenèche, "Nickel ferrite nanoparticles: Elaboration in polyol medium via hydrolysis, and magnetic properties," *J. Phys. Condens. Matter*, vol. 16, no.

24, pp. 4357–4372, **2004**, doi: 10.1088/0953-8984/16/24/017.

[166]S. Imine, F. Schoenstein, S. Mercone, M. Zaghrioui, N. Bettahar, and N. Jouini, “Bottom-up and new compaction processes: A way to tunable properties of nanostructured cobalt ferrite ceramics,” *J. Eur. Ceram. Soc.*, vol. 31, no. 15, pp. 2943–2955, **2011**, doi: 10.1016/j.jeurceramsoc.2011.06.004.

[167]V. Prevot, C. Forano, and J. P. Besse, “Hydrolysis in Polyol: New Route for Hybrid-Layered Double Hydroxides Preparation,” *Chem. Mater.*, vol. 17, no. 26, pp. 6695–6701, **2005**, doi: 10.1021/cm050581x.

[168]T. Itoh, T. Uchida, I. Matsubara, N. Izu, W. Shin, H. Miyazaki, H. Tanjo, and K. Kanda, “Preparation of γ-alumina large grain particles with large specific surface area via polyol synthesis,” *Ceram. Int.*, vol. 41, no. 3, pp. 3631–3638, **2015**, doi: 10.1016/j.ceramint.2014.11.028.

[169]C. Feldmann, S. Matschulo, and S. Ahlert, “Polyol-mediated synthesis of nanoscale Mg(OH)2 and MgO,” *J. Mater. Sci.*, vol. 42, no. 17, pp. 7076–7080, **2007**, doi: 10.1007/s10853-007-1547-4.

[170]A. J. Biacchi and R. E. Schaak, “Ligand-Induced Fate of Embryonic Species in the Shape-Controlled Synthesis of Rhodium Nanoparticles,” *ACS Nano*, vol. 9, no. 2, pp. 1707–1720, **2015**, doi: 10.1021/nn506517e.

[171]J. I. Tracey, S. Aziz, and D. M. O’Carroll, “Investigation of the role of polyol molecular weight in the polyol synthesis of silver nanoparticles,” *Mater. Res. Express*, vol. 6, no. 11, **2019**, doi: 10.1088/2053-1591/ab494c.

[172]Y. Zheng, J. Zeng, A. Ruditskiy, M. Liu, and Y. Xia, “Oxidative etching and its role in manipulating the nucleation and growth of noble-metal nanocrystals,” *Chem. Mater.*, vol. 26, no. 1, pp. 22–33, **2014**, doi: 10.1021/cm402023g.

[173]A. Subramania, G. Vijaya Kumar, A. R. Sathiya Priya, and T. Vasudevan, “Polyol-mediated thermolysis process for the synthesis of MgO nanoparticles and nanowires,” *Nanotechnology*, vol. 18, no. 22, **2007**, doi: 10.1088/0957-4484/18/22/225601.

[174]C. Hai, S. Li, Y. Zhou, J. Zeng, X. Ren, and X. Li, “Roles of ethylene glycol solvent and polymers in preparing uniformly distributed MgO nanoparticles,” *J. Asian Ceram. Soc.*, vol. 5, no. 2, pp. 176–182, **2017**, doi: 10.1016/j.jascer.2017.04.004.

[175]N. Chakroune, G. Viau, S. Ammar, N. Jouini, P. Gredin, M. J. Vaulay, and F. Fiévet, “Synthesis, characterization and magnetic properties of disk-shaped particles of a cobalt alkoxide: Co ii (C 2 H 4 O 2),” *New J. Chem.*, vol. 29, no. 2, pp. 355–361, **2005**, doi: 10.1039/B411117F.

[176]V. Prevot, V. Briois, J. Cellier, C. Forano, and F. Leroux, “An in-situ investigation of LDH-acetate prepared in polyol, under moderate thermal treatment,” *J. Phys. Chem. Solids*, vol. 69, no. 5–6, pp. 1091–1094, **2008**, doi: 10.1016/j.jpcs.2007.10.051.

[177]K. Ramachandra Rao, D. Vijay, K. Sujatha, C. Satya Kamal, T. Samuel, and S. E. Basha, “Structural and Photoluminescence Studies of Europium Doped Mgo Nanoparticles Synthesized by Polyol Technique,” *Mater. Today Proc.*, vol. 3, no. 10, pp. 4249–4253, **2016**, doi: 10.1016/j.matpr.2016.11.105.

[178]Z. Beji, L. S. Smiri, N. Yaacoub, J. M. Grenechè, N. Menguy, S. Ammar, and F. Fiévet, “Annealing effect on the magnetic properties of polyol-made Ni-Zn ferrite nanoparticles,” *Chem. Mater.*, vol. 22, no. 4, pp. 1350–1366, **2010**, doi: 10.1021/cm901969c.

[179]K. Vamvakidis, M. Katsikini, G. Vourlias, M. Angelakeris, E. C. Paloura, and C. Dendrinou-Samara, “Composition and hydrophilicity control of Mn-doped ferrite (MnxFe3-xO4) nanoparticles induced by polyol differentiation,” *Dalt. Trans.*, vol. 44, no. 12, pp. 5396–5406, **2015**, doi: 10.1039/c5dt00212e.

[180]J. Merikhi, H. O. Jungk, and C. Feldmann, “Sub-micrometer CoAl2O4 pigment particles - Synthesis and preparation of coatings,” *J. Mater. Chem.*, vol. 10, no. 6, pp. 1311–1314, **2000**, doi: 10.1039/a910201i.

[181]C. Feldmann, “Preparation of nanoscale pigment particles,” *Adv. Mater.*, vol. 13, no. 17, pp. 1301–1303, **2001**, doi: 10.1002/1521-4095(200109)13:17<1301::AID-ADMA1301>3.0.CO;2-6.

[182]U. Olevsky, Eugene A (San Diego State University, California, “Sintering theory: a Brief Introduction,” *Present. Tech. Univ. Darmstadt*, **2011**, [Online]. Available: https://fdocuments.net/document/olevsky-theory-of-sintering.html

[183]M. Kamyabi, R. Sotudeh-Gharebagh, R. Zarghami, and K. Saleh, “Principles of viscous sintering in amorphous powders: A critical review,” *Chem. Eng. Res. Des.*, vol. 125, pp. 328–347, **2017**, doi: 10.1016/j.cherd.2017.06.009.

[184]S.-J. L. Kang, *Sintering*, vol. 1999, no. December. Elsevier, 2005. doi: 10.1016/B978-0-7506-6385-4.X5000-6.

[185]F. Najafkhani, S. Kheiri, B. Pourbahari, and H. Mirzadeh, “Recent advances in the kinetics of normal/abnormal grain growth: a review,” *Arch. Civ. Mech. Eng.*, vol. 21, no. 1, pp. 1–20, **2021**, doi: 10.1007/s43452-021-00185-8.

[186]W. Zhang, L. Chen, C. Xu, X. Lv, Y. Wang, J. Ouyang, and Y. Zhou, “Grain growth kinetics and densification mechanism of (TiZrHfVNbTa)C high-entropy ceramic under pressureless sintering,” *J. Mater. Sci. Technol.*, vol. 110, pp. 57–64, **2022**, doi: 10.1016/j.jmst.2021.08.070.

[187]R. German, *Sintering: from Empirical Observations to Scientific Principles*. Elsevier, 2014. doi: 10.1016/C2012-0-00717-X.

[188]B. Castel, “Mise en forme des solides. 1. Aspects théoriques,” *Tech. l’ingénieur.Génie des procédés*, vol. 3, no. J3380, p. J3380. 1-J3380. 26, **1995**.

[189]R. Andrievski and A. Khatchoyan, *Nanomaterials in Extreme Environments*, vol. 230. Cham: Springer International Publishing, 2016. doi: 10.1007/978-3-319-25331-2.

[190]B. Ratzker, A. Wagner, M. Sokol, S. Kalabukhov, and N. Frage, “Stress-enhanced dynamic grain growth during high-pressure spark plasma sintering of alumina,” *Acta Mater.*, vol. 164, pp. 390–399, **2019**, doi: 10.1016/j.actamat.2018.11.001.

[191]C. Herring, “Effect of Change of Scale on Sintering Phenomena,” *J. Appl. Phys.*, vol. 21, no. 4, pp. 301–303, **1950**, doi: 10.1063/1.1699658.

[192]R. A. ANDRIEVSKI, “Compaction and sintering of ultrafine powders,” *Int. J. powder Metall.*, vol. 30, no. 1, pp. 59–66, **1994**.

[193]H. Song, R. L. Coble, and R. J. Brook, “The Applicability of Herring’s Scaling Law to the Sintering of Powders,” in *Materials Science Research*, vol. 16, G. C. Kuczynski, A. E. Miller, and G. A. Sargent, Eds. Boston, MA: Springer US, 1984, pp. 63–79. doi: 10.1007/978-1-4613-2761-5_5.

[194]Z. Xiao, S. Yu, Y. Li, S. Ruan, L. B. Kong, Q. Huang, Z. Huang, K. Zhou, H. Su, Z. Yao, W. Que, Y. Liu, T. Zhang, J. Wang, P. Liu, D. Shen, M. Allix, J. Zhang, and D. Tang, “Materials development and potential applications of transparent ceramics: A review,” *Mater. Sci. Eng. R Reports*, vol. 139, no. August 2019, p. 100518, **2020**, doi: 10.1016/j.mser.2019.100518.

[195]R. Macaigne, S. Marinel, D. Goeuriot, and S. Saunier, “Sintering paths and mechanisms of pure MgAl2O4 conventionally and microwave sintered,” *Ceram. Int.*, vol. 44, no. 17, pp. 21107–21113, **2018**, doi: 10.1016/j.ceramint.2018.08.149.

[196]K. HAMANO and S. KANZAKI, “Fabrication of Transparent Spinel Ceramics by Reactive Hot-pressing,” *J. Ceram. Assoc.*

Japan, vol. 85, no. 981, pp. 225–230, **1977**, doi: 10.2109/jcersj1950.85.981_225.

[197]L. L. Zhu, Y. J. Park, L. Gan, S. Il Go, H. N. Kim, J. M. Kim, and J. W. Ko, "Fabrication of transparent MgAl2O4 from commercial nanopowders by hot-pressing without sintering additive," *Mater. Lett.*, vol. 219, pp. 8–11, **2018**, doi: 10.1016/j.matlet.2018.02.010.

[198]Q. Liu, Y. Jing, S. Su, X. Li, X. Liu, Y. Feng, X. Chen, and J. Li, "Microstructure and properties of MgAl2O4 transparent ceramics fabricated by hot isostatic pressing," *Opt. Mater. (Amst).*, vol. 104, no. January, p. 109938, **2020**, doi: 10.1016/j.optmat.2020.109938.

[199]C. Gajdowski, J. Böhmler, Y. Lorgouilloux, S. Lemonnier, S. d'Astorg, E. Barraud, and A. Leriche, "Influence of post-HIP temperature on microstructural and optical properties of pure MgAl2O4 spinel: From opaque to transparent ceramics," *J. Eur. Ceram. Soc.*, vol. 37, no. 16, pp. 5347–5351, **2017**, doi: 10.1016/j.jeurceramsoc.2017.07.031.

[200]Y. Liu, J. Zhu, and B. Dai, "Transparent MgAl2O4 ceramics prepared by microwave sintering and hot isostatic pressing," *Ceram. Int.*, vol. 46, no. 16, pp. 25738–25740, **2020**, doi: 10.1016/j.ceramint.2020.07.051.

[201]S. Cohen, B. Ratzker, M. Sokol, S. Kalabukhov, and N. Frage, "Polycrystalline transparent magnesium aluminate spinel processed by a combination of spark plasma sintering (SPS) and hot isostatic pressing (HIP)," *J. Eur. Ceram. Soc.*, vol. 38, no. 15, pp. 5153–5159, **2018**, doi: 10.1016/j.jeurceramsoc.2018.07.024.

[202]G. Kerbart, C. Harnois, C. Bilot, and S. Marinel, "Pressure-assisted microwave sintering: A rapid process to sinter submicron sized grained MgAl 2 O 4 transparent ceramics," *J. Eur. Ceram. Soc.*, vol. 39, no. 9, pp. 2946–2951, **2019**, doi: 10.1016/j.jeurceramsoc.2019.03.046.

[203]S. H. Bang, K. Tsuji, A. Ndayishimiye, S. Dursun, J. H. Seo, S. Otieno, and C. A. Randall, "Toward a size scale-up cold sintering process at reduced uniaxial pressure," *J. Am. Ceram. Soc.*, vol. 103, no. 4, pp. 2322–2327, **2020**, doi: 10.1111/jace.16976.

[204]S. Funahashi, E. Kobayashi, M. Kimura, K. Shiratsuyu, and C. A. Randall, "Chelate complex assisted cold sintering for spinel ceramics," *J. Ceram. Soc. Japan*, vol. 127, no. 12, pp. 899–904, **2019**, doi: 10.2109/jcersj2.19140.

[205]T. Hérisson de Beauvoir and C. Estournès, "Translucent γ-AlOOH and γ-Al2O3 glass-ceramics using the cold sintering process," *Scr. Mater.*, vol. 194, p. 113650, **2021**, doi: 10.1016/j.scriptamat.2020.113650.

[206]W. R. Matizamhuka, "Spark plasma sintering (SPS) - An advanced sintering technique for structural nanocomposite materials," *J. South. African Inst. Min. Metall.*, vol. 116, no. 12, pp. 1171–1180, **2016**, doi: 10.17159/2411-9717/2016/v116n12a12.

[207]U. Anselmi-Tamburini, S. Gennari, J. E. Garay, and Z. A. Munir, "Fundamental investigations on the spark plasma sintering/synthesis process: II. Modeling of current and temperature distributions," *Mater. Sci. Eng. A*, vol. 394, no. 1–2, pp. 139–148, **2005**, doi: 10.1016/j.msea.2004.11.019.

[208]C. Manière, A. Pavia, L. Durand, G. Chevallier, K. Afanga, and C. Estournès, "Finite-element modeling of the electro-thermal contacts in the spark plasma sintering process," *J. Eur. Ceram. Soc.*, vol. 36, no. 3, pp. 741–748, **2016**, doi: 10.1016/j.jeurceramsoc.2015.10.033.

[209]O. Guillon, J. Gonzalez-Julian, B. Dargatz, T. Kessel, G. Schierning, J. Räthel, and M. Herrmann, "Field-assisted sintering technology/spark plasma sintering: Mechanisms, materials, and technology developments," *Adv. Eng. Mater.*, vol. 16, no. 7, pp. 830–849, **2014**, doi: 10.1002/adem.201300409.

[210]O. Guillon, R. A. De Souza, T. P. Mishra, and W. Rheinheimer, "Electric-field-assisted processing of ceramics: Nonthermal effects and related mechanisms," *MRS Bull.*, vol. 46, no. January, pp. 52–58, **2021**, doi: 10.1557/s43577-020-00008-w.

[211]C. Estournès, "Mise en forme de matériaux par frittage flash," *Tech. l'ingénieur*, vol. 33, no. 0, p. IN 56, **2006**.

[212]T. Voisin, L. Durand, N. Karnatak, S. Le Gallet, M. Thomas, Y. Le Berre, J. F. Castagné, and A. Couret, "Temperature control during Spark Plasma Sintering and application to up-scaling and complex shaping," *J. Mater. Process. Technol.*, vol. 213, no. 2, pp. 269–278, **2013**, doi: 10.1016/j.jmatprotec.2012.09.023.

[213]K. Morita, B. N. Kim, H. Yoshida, and K. Hiraga, "Spark-plasma-sintering condition optimization for producing transparent MgAl2O4 spinel polycrystal," *J. Am. Ceram. Soc.*, vol. 92, no. 6, pp. 1208–1216, **2009**, doi: 10.1111/j.1551-2916.2009.03074.x.

[214]S. Benaissa, M. Hamidouche, M. Kolli, G. Bonnefont, and G. Fantozzi, "Characterization of nanostructured MgAl2O4 ceramics fabricated by spark plasma sintering," *Ceram. Int.*, vol. 42, no. 7, pp. 8839–8846, **2016**, doi: 10.1016/j.ceramint.2016.02.130.

[215]P. Fu, W. Lu, W. Lei, Y. Xu, X. Wang, and J. Wu, "Transparent polycrystalline MgAl2O4 ceramic fabricated by spark plasma sintering: Microwave dielectric and optical properties," *Ceram. Int.*, vol. 39, no. 3, pp. 2481–2487, **2013**, doi: 10.1016/j.ceramint.2012.09.006.

[216]B. N. Kim, K. Hiraga, K. Morita, and H. Yoshida, "Effects of heating rate on microstructure and transparency of spark-plasma-sintered alumina," *J. Eur. Ceram. Soc.*, vol. 29, no. 2, pp. 323–327, **2009**, doi: 10.1016/j.jeurceramsoc.2008.03.015.

[217]V. Nečina and W. Pabst, "Influence of the heating rate on grain size of alumina ceramics prepared via spark plasma sintering (SPS)," *J. Eur. Ceram. Soc.*, vol. 40, no. 10, pp. 3656–3662, **2020**, doi: 10.1016/j.jeurceramsoc.2020.03.057.

[218]H. Hammoud, V. Garnier, G. Fantozzi, E. Lachaud, and S. Tadier, "Mechanism of Carbon Contamination in Transparent MgAl2O4 and Y3Al5O12 Ceramics Sintered by Spark Plasma Sintering," *Ceramics*, vol. 2, no. 4, pp. 612–619, **2019**, doi: 10.3390/ceramics2040048.

[219]K. Morita, B. N. Kim, K. Hiraga, and H. Yoshida, "Fabrication of transparent MgAl2O4 spinel polycrystal by spark plasma sintering processing," *Scr. Mater.*, vol. 58, no. 12, pp. 1114–1117, **2008**, doi: 10.1016/j.scriptamat.2008.02.008.

[220]K. Madhav Reddy, N. Kumar, and B. Basu, "Inhibition of grain growth during the final stage of multi-stage spark plasma sintering of oxide ceramics," *Scr. Mater.*, vol. 63, no. 6, pp. 585–588, **2010**, doi: 10.1016/j.scriptamat.2010.06.004.

[221]A. Pille, H. Spiridigliozzi, M. Amamra, T. Billeton, M. Zaghrioui, E. Feldbach, A. Kanaev, and F. Schoenstein, "Morphology and luminescence of MgAl2O4 ceramics obtained via spark plasma sintering," *Ceram. Int.*, vol. 45, no. 7, **2019**, doi: 10.1016/j.ceramint.2019.01.137.

[222]A. Talimian, V. Pouchly, H. F. El-Maghraby, K. Maca, and D. Galusek, "Transparent magnesium aluminate spinel: Effect of critical temperature in two-stage spark plasma sintering," *J. Eur. Ceram. Soc.*, vol. 40, no. 6, pp. 2417–2425, **2020**, doi: 10.1016/j.jeurceramsoc.2020.02.012.

[223]K. Morita, B. N. Kim, H. Yoshida, H. Zhang, K. Hiraga, and Y. Sakka, "Effect of loading schedule on densification of MgAl 2O 4 spinel during spark plasma sintering (SPS) processing," *J. Eur. Ceram. Soc.*, vol. 32, no. 10, pp. 2303–2309, **2012**, doi:

10.1016/j.jeurceramsoc.2012.02.016.
[224]C. Wang and Z. Zhao, "Transparent MgAl2O4 ceramic produced by spark plasma sintering," *Scr. Mater.*, vol. 61, no. 2, pp. 193–196, **2009**, doi: 10.1016/j.scriptamat.2009.03.039.
[225]Z. Shen, M. Johnsson, Z. Zhao, and M. Nygren, "Spark plasma sintering of alumina," *J. Am. Ceram. Soc.*, vol. 85, no. 8, pp. 1921–1927, **2002**, doi: 10.1111/j.1151-2916.2002.tb00381.x.
[226]D. Galusek, J. Sedláček, J. Chovanec, and M. Michálková, "The influence of MgO, Y2O3 and ZrO2 additions on densification and grain growth of submicrometre alumina sintered by SPS and HIP," *Ceram. Int.*, vol. 41, no. 8, pp. 9692–9700, **2015**, doi: 10.1016/j.ceramint.2015.04.038.
[227]B. Ratzker, A. Wagner, S. Kalabukhov, S. Samuha, and N. Frage, "Non-uniform microstructure evolution in transparent alumina during dwell stage of high-pressure spark plasma sintering," *Acta Mater.*, vol. 199, pp. 469–479, **2020**, doi: 10.1016/j.actamat.2020.08.036.
[228]M. Sokol, S. Kalabukhov, M. P. Dariel, and N. Frage, "High-pressure spark plasma sintering (SPS) of transparent polycrystalline magnesium aluminate spinel (PMAS)," *J. Eur. Ceram. Soc.*, vol. 34, no. 16, pp. 4305–4310, **2014**, doi: 10.1016/j.jeurceramsoc.2014.07.022.
[229]M. Sokol, S. Kalabukhov, R. Shneck, E. Zaretsky, and N. Frage, "Effect of grain size on the static and dynamic mechanical properties of magnesium aluminate spinel (MgAl2O4)," *J. Eur. Ceram. Soc.*, vol. 37, no. 10, pp. 3417–3424, **2017**, doi: 10.1016/j.jeurceramsoc.2017.04.025.
[230]R. Chaim, G. Chevallier, A. Weibel, and C. Estournès, "Grain growth during spark plasma and flash sintering of ceramic nanoparticles: A review," *J. Mater. Sci.*, vol. 53, no. 5, pp. 3087–3105, **2018**, doi: 10.1007/s10853-017-1761-7.
[231]J. G. Santanach, A. Weibel, C. Estourns, Q. Yang, C. Laurent, and A. Peigney, "Spark plasma sintering of alumina: Study of parameters, formal sintering analysis and hypotheses on the mechanism(s) involved in densification and grain growth," *Acta Mater.*, vol. 59, no. 4, pp. 1400–1408, **2011**, doi: 10.1016/j.actamat.2010.11.002.
[232]M. Ehsani, M. Zakeri, and M. Razavi, "The effect of temperature on the physical and mechanical properties of nanostructured boron nitride by spark plasma sintering," *J. Alloys Compd.*, vol. 835, p. 155317, **2020**, doi: 10.1016/j.jallcom.2020.155317.
[233]N. Firshtman, S. Kalabukhov, and N. Frage, "Effect of boron carbide composition on its densification behavior during spark plasma sintering (SPS)," *Ceram. Int.*, vol. 44, no. 17, pp. 21842–21847, **2018**, doi: 10.1016/j.ceramint.2018.08.291.
[234]D. Terentyev, M. Vilémová, C. Yin, J. Veverka, A. Dubinko, and J. Matějíček, "Assessment of mechanical properties of SPS-produced tungsten including effect of neutron irradiation," *Int. J. Refract. Met. Hard Mater.*, vol. 89, no. January, **2020**, doi: 10.1016/j.ijrmhm.2020.105207.
[235]B. Ratzker, A. Wagner, M. Sokol, S. Kalabukhov, M. P. Dariel, and N. Frage, "Optical and mechanical properties of transparent alumina fabricated by high-pressure spark plasma sintering," *J. Eur. Ceram. Soc.*, vol. 39, no. 8, pp. 2712–2719, **2019**, doi: 10.1016/j.jeurceramsoc.2019.03.025.
[236]A. Wagner, B. Ratzker, S. Kalabukhov, S. Kolusheva, M. Sokol, and N. Frage, "Highly-doped Nd:YAG ceramics fabricated by conventional and high pressure SPS," *Ceram. Int.*, vol. 45, no. 9, pp. 12279–12284, **2019**, doi: 10.1016/j.ceramint.2019.03.141.
[237]S. Ghanizadeh, S. Grasso, P. Ramanujam, B. Vaidhyanathan, J. Binner, P. Brown, and J. Goldwasser, "Improved transparency and hardness in α-alumina ceramics fabricated by high-pressure SPS of nanopowders," *Ceram. Int.*, vol. 43, no. 1, pp. 275–281, **2017**, doi: 10.1016/j.ceramint.2016.09.150.
[238]J. D. Kuntz, O. G. Cervantes, A. E. Gash, and Z. A. Munir, "Tantalum-tungsten oxide thermite composites prepared by sol-gel synthesis and spark plasma sintering," *Combust. Flame*, vol. 157, no. 8, pp. 1566–1571, **2010**, doi: 10.1016/j.combustflame.2010.01.005.
[239]R. T. Li, Z. L. Dong, and K. A. Khor, "Al-Cr-Fe quasicrystals as novel reinforcements in Ti based composites consolidated using high pressure spark plasma sintering," *Mater. Des.*, vol. 102, pp. 255–263, **2016**, doi: 10.1016/j.matdes.2016.04.040.
[240]B. N. Kim, E. Prajatelistia, Y. H. Han, H. W. Son, Y. Sakka, and S. Kim, "Transparent hydroxyapatite ceramics consolidated by spark plasma sintering," *Scr. Mater.*, vol. 69, no. 5, pp. 366–369, **2013**, doi: 10.1016/j.scriptamat.2013.05.011.
[241]B. Ratzker, M. Sokol, S. Kalabukhov, and N. Frage, "High-pressure spark plasma sintering of silicon nitride with LiF additive," *J. Eur. Ceram. Soc.*, vol. 38, no. 4, pp. 1271–1277, **2018**, doi: 10.1016/j.jeurceramsoc.2017.10.034.
[242]J. Chávez, L. Olmos, O. Jimenez, F. Alvarádo-Hernandez, H. Flores-Zñiga, J. P. Camarillo-Garcia, and S. J. Guevara-Martínez, "Investigation of a Ti.30Zr binary alloy fabricated through spark plasma sintering," *J. Mater. Res. Technol.*, vol. 9, no. 4, pp. 9328–9340, **2020**, doi: 10.1016/j.jmrt.2020.03.110.
[243]A. Sahu, R. S. Maurya, and T. Laha, "Effect of sintering temperature on phase evolution of Al86Ni6Y4.5Co2La1.5 bulk amorphous composites synthesized via mechanical alloying and spark plasma sintering," *Prog. Nat. Sci. Mater. Int.*, vol. 29, no. 1, pp. 32–40, **2019**, doi: 10.1016/j.pnsc.2019.01.009.
[244]M. Radune, M. Zinigrad, S. Kalabukhov, M. Sokol, V. I. Chumanov, and N. Frage, "Spark plasma sintering of Ti1-xAlxN nano-powders synthesized by high-energy ball milling," *Ceram. Int.*, vol. 42, no. 9, pp. 11077–11084, **2016**, doi: 10.1016/j.ceramint.2016.04.006.
[245]M. Biesuz, S. Grasso, and V. M. Sglavo, "What's new in ceramics sintering? A short report on the latest trends and future prospects," *Curr. Opin. Solid State Mater. Sci.*, vol. 24, no. 5, p. 100868, **2020**, doi: 10.1016/j.cossms.2020.100868.
[246]U. Anselmi-Tamburini, J. E. Garay, and Z. A. Munir, "Fast low-temperature consolidation of bulk nanometric ceramic materials," *Scr. Mater.*, vol. 54, pp. 823–828, **2006**, doi: 10.1016/j.scriptamat.2005.11.015.
[247]S. Grasso, B. N. Kim, C. Hu, G. Maizza, and Y. Sakka, "Highly transparent pure alumina fabricated by high-pressure spark plasma sintering," *J. Am. Ceram. Soc.*, vol. 93, no. 9, pp. 2460–2462, **2010**, doi: 10.1111/j.1551-2916.2010.03811.x.
[248]S. Grasso, H. Yoshida, H. Porwal, Y. Sakka, and M. Reece, "Highly transparent α-alumina obtained by low cost high pressure SPS," *Ceram. Int.*, vol. 39, no. 3, pp. 3243–3248, **2013**, doi: 10.1016/j.ceramint.2012.10.012.
[249]D. N. F. Muche, M. A. T. Marple, S. Sen, and R. H. R. Castro, "Grain boundary energy, disordering energy and grain growth kinetics in nanocrystalline MgAl2O4 spinel," *Acta Mater.*, vol. 149, pp. 302–311, **2018**, doi: 10.1016/j.actamat.2018.02.052.
[250]M. Sokol, M. Halabi, Y. Mordekovitz, S. Kalabukhov, S. Hayun, and N. Frage, "An inverse Hall-Petch relation in nanocrystalline MgAl2O4 spinel consolidated by high pressure spark plasma sintering (HPSPS)," *Scr. Mater.*, vol. 139, pp. 159–161, **2017**, doi: 10.1016/j.scriptamat.2017.06.049.
[251]B. Ratzker, A. Wagner, S. Kalabukhov, and N. Frage, "Improved alumina transparency achieved by high-pressure spark plasma

sintering of commercial powder," *Ceram. Int.*, vol. 46, no. 13, pp. 21794–21799, **2020**, doi: 10.1016/j.ceramint.2020.05.198.

[252]P. M. Radingoana, S. Guillemet-Fritsch, P. A. Olubambi, G. Chevallier, and C. Estournès, "Influence of processing parameters on the densification and the microstructure of pure zinc oxide ceramics prepared by spark plasma sintering," *Ceram. Int.*, vol. 45, no. 8, pp. 10035–10043, **2019**, doi: 10.1016/j.ceramint.2019.02.048.

[253]J. L. Bates and J. E. Gamier, "Electrical Conductivity of MgAl2O4 and Y3A15O12," *J. Am. Ceram. Soc.*, vol. 64, no. 10, pp. C-138-C–141, **1981**, doi: 10.1111/j.1151-2916.1981.tb10237.x.

[254]H. Yoshida, P. Biswas, R. Johnson, and M. K. Mohan, "Flash-sintering of magnesium aluminate spinel (MgAl 2 O 4) ceramics," *J. Am. Ceram. Soc.*, vol. 100, no. 2, pp. 554–562, **2017**, doi: 10.1111/jace.14616.

[255]S. K. Jha, H. Charalambous, H. Wang, X. L. Phuah, C. Mead, J. Okasinski, H. Wang, and T. Tsakalakos, "In-situ observation of oxygen mobility and abnormal lattice expansion in ceria during flash sintering," *Ceram. Int.*, vol. 44, no. 13, pp. 15362–15369, **2018**, doi: 10.1016/j.ceramint.2018.05.186.

[256]S. Bhandari, T. P. Mishra, M. Bram, O. Guillon, and D. Yadav, "Flash sintering behaviour of 8YSZ-NiO composites," *Ceram. Int.*, vol. 1446, no. 89, p. 2669, **2022**, doi: 10.1016/j.ceramint.2022.07.266.

[257]M. Biesuz and V. M. Sglavo, "Flash sintering of ceramics," *J. Eur. Ceram. Soc.*, vol. 39, no. 2–3, pp. 115–143, **2019**, doi: 10.1016/j.jeurceramsoc.2018.08.048.

[258]R. Marder, C. Estournès, G. Chevallier, and R. Chaim, "Numerical model for sparking and plasma formation during spark plasma sintering of ceramic compacts," *J. Mater. Sci.*, vol. 50, no. 13, pp. 4636–4645, **2015**, doi: 10.1007/s10853-015-9015-z.

[259]R. Marder, C. Estournès, G. Chevallier, and R. Chaim, "Plasma in spark plasma sintering of ceramic particle compacts," *Scr. Mater.*, vol. 82, pp. 57–60, **2014**, doi: 10.1016/j.scriptamat.2014.03.023.

[260]R. Marder, C. Estournès, G. Chevallier, and R. Chaim, "Spark and plasma in spark plasma sintering of rigid ceramic nanoparticles: A model system of YAG," *J. Eur. Ceram. Soc.*, vol. 35, no. 1, pp. 211–218, **2015**, doi: 10.1016/j.jeurceramsoc.2014.08.001.

[261]Z. H. Zhang, Z. F. Liu, J. F. Lu, X. B. Shen, F. C. Wang, and Y. D. Wang, "The sintering mechanism in spark plasma sintering - Proof of the occurrence of spark discharge," *Scr. Mater.*, vol. 81, pp. 56–59, **2014**, doi: 10.1016/j.scriptamat.2014.03.011.

[262]T. Saunders, S. Grasso, and M. J. Reece, "Plasma formation during electric discharge (50V) through conductive powder compacts," *J. Eur. Ceram. Soc.*, vol. 35, no. 3, pp. 871–877, **2014**, doi: 10.1016/j.jeurceramsoc.2014.09.022.

[263]P. Biswas, D. Chakravarty, M. B. Suresh, R. Johnson, and M. K. Mohan, "Fabrication of graphite contamination free polycrystalline transparent MgAl2O4 spinel by spark plasma sintering using platinum foil," *Ceram. Int.*, vol. 42, no. 15, pp. 17920–17923, **2016**, doi: 10.1016/j.ceramint.2016.07.214.

[264]P. Wang, M. Yang, S. Zhang, R. Tu, T. Goto, and L. Zhang, "Suppression of carbon contamination in SPSed CaF2 transparent ceramics by Mo foil," *J. Eur. Ceram. Soc.*, vol. 37, no. 13, pp. 4103–4107, **2017**, doi: 10.1016/j.jeurceramsoc.2017.04.070.

[265]R. Valenzuela, T. Gaudisson, and S. Ammar, "Severe reduction of Ni-Zn ferrites during consolidation by Spark Plasma Sintering (SPS)," *J. Magn. Magn. Mater.*, vol. 400, pp. 311–314, **2016**, doi: 10.1016/j.jmmm.2015.07.044.

[266]A. Zegadi, M. Kolli, M. Hamidouche, and G. Fantozzi, "Transparent MgAl2O4 spinel fabricated by spark plasma sintering from commercial powders," *Ceram. Int.*, vol. 44, no. 15, pp. 18828–18835, **2018**, doi: 10.1016/j.ceramint.2018.07.117.

[267]L. Liu and K. Morita, "Fabrication of MgAl2O4/Al2O3 laminated transparent composite by spark-plasma-sintering (SPS) processing," *Scr. Mater.*, vol. 205, p. 114205, **2021**, doi: 10.1016/j.scriptamat.2021.114205.

[268]P. Zhang, P. Liu, Y. Sun, X. Peng, Z. Wang, S. Wang, and J. Zhang, "Microstructure and properties of transparent MgAl2O4 ceramic fabricated by aqueous gelcasting," *J. Alloys Compd.*, vol. 657, pp. 246–249, **2016**, doi: 10.1016/j.jallcom.2015.10.113.

[269]Ł. Zych, R. Lach, and A. Wajler, "The influence of the agglomeration state of nanometric MgAl 2O4 powders on their consolidation and sintering," *Ceram. Int.*, vol. 40, no. 7 PART A, pp. 9783–9790, **2014**, doi: 10.1016/j.ceramint.2014.02.066.

[270]D. Han, J. Zhang, P. Liu, G. Li, and S. Wang, "Densification and microstructure evolution of reactively sintered transparent spinel ceramics," *Ceram. Int.*, vol. 44, no. 10, pp. 11101–11108, **2018**, doi: 10.1016/j.ceramint.2018.03.109.

[271]S. Meir, S. Kalabukhov, N. Froumin, M. P. Dariel, and N. Frage, "Synthesis and densification of transparent magnesium aluminate spinel by SPS processing," *J. Am. Ceram. Soc.*, vol. 92, no. 2, pp. 358–364, **2009**, doi: 10.1111/j.1551-2916.2008.02893.x.

[272]L. Zarazúa-Villalobos, G. Fantozzi, G. Bonnefont, L. Téllez-Jurado, and H. Balmori-Ramírez, "Transparent magnesium aluminate spinel ceramics obtained by one-step spark plasma reaction sintering of a sol-gel precursor powder," *Ceram. Int.*, no. December 2021, **2022**, doi: 10.1016/j.ceramint.2022.06.031.

[273]A. Talimian and D. Galusek, "Aqueous slip casting of translucent magnesium aluminate spinel: Effects of dispersant concentration and solid loading," *Ceram. Int.*, vol. 45, no. 8, pp. 10646–10653, **2019**, doi: 10.1016/j.ceramint.2019.02.134.

[274]G. Yang, H. Lai, W. Lin, J. Tong, Z. Peng, J. Cao, J. Luo, Y. Zhang, and C. Cui, "Approaching the structure-property relationship of sintered metal nano/microparticles from the perspective of the agglomerate size effect," *Powder Technol.*, vol. 399, p. 117254, **2022**, doi: 10.1016/j.powtec.2022.117254.

[275]H. M. Oh, Y. J. Park, H. N. Kim, J. W. Ko, and H. K. Lee, "Effect of milling ball size on the densification and optical properties of transparent Y2O3 ceramics," *Ceram. Int.*, vol. 47, no. 4, pp. 4681–4687, **2021**, doi: 10.1016/j.ceramint.2020.10.035.

[276]A. Talimian, V. Pouchly, H. F. El-Maghraby, K. Maca, and D. Galusek, "Impact of high energy ball milling on densification behaviour of magnesium aluminate spinel evaluated by master sintering curve and constant rate of heating approach," *Ceram. Int.*, vol. 45, no. 17, pp. 23467–23474, **2019**, doi: 10.1016/j.ceramint.2019.08.051.

[277]K. Vanmeensel, S. G. Huang, A. Laptev, S. A. Salehi, A. K. Swarnakar, O. Van Der Biest, and J. Vleugels, "Pulsed electric current sintering of electrically conductive ceramics," *J. Mater. Sci.*, vol. 43, no. 19, pp. 6435–6440, **2008**, doi: 10.1007/s10853-008-2631-0.

[278]N. Obradović, W. G. Fahrenholtz, S. Filipović, D. Kosanović, A. Dapčević, A. Đorđević, I. Balać, and V. B. Pavlović, "The effect of mechanical activation on synthesis and properties of MgAl 2 O 4 ceramics," *Ceram. Int.*, vol. 45, no. 9, pp. 12015–12021, **2019**, doi: 10.1016/j.ceramint.2019.03.095.

[279]H. M. Oh, Y. J. Park, H. N. Kim, J. W. Ko, and H. K. Lee, "Effect of powder milling routes on the sinterability and optical

properties of transparent Y2O3 ceramics," *J. Eur. Ceram. Soc.*, vol. 41, no. 1, pp. 775–780, **2021**, doi: 10.1016/j.jeurceramsoc.2020.08.006.

[280] J. M. Kim, H. N. Kim, Y. J. Park, J. W. Ko, J. W. Lee, and H. D. Kim, "Fabrication of transparent MgAl2O4 spinel through homogenous green compaction by microfluidization and slip casting," *Ceram. Int.*, vol. 41, no. 10, pp. 13354–13360, **2015**, doi: 10.1016/j.ceramint.2015.07.121.

[281] A. Rothman, S. Kalabukhov, N. Sverdlov, M. P. Dariel, and N. Frage, "The effect of grain size on the mechanical and optical properties of spark plasma sintering-processed magnesium aluminate spinel MgAl2O 4," *Int. J. Appl. Ceram. Technol.*, vol. 11, no. 1, pp. 146–153, **2014**, doi: 10.1111/j.1744-7402.2012.02849.x.

[282] A. Alhaji, M. H. Taherian, S. Ghorbani, and S. A. Sharifnia, "Development of synthesis and granulation process of MgAl2O4 powder for the fabrication of transparent ceramic," *Opt. Mater. (Amst).*, vol. 98, no. May, p. 109440, **2019**, doi: 10.1016/j.optmat.2019.109440.

[283] H. Shahbazi, H. Shokrollahi, and M. Tataei, "Gel-casting of transparent magnesium aluminate spinel ceramics fabricated by spark plasma sintering (SPS)," *Ceram. Int.*, vol. 44, no. 5, pp. 4955–4960, **2018**, doi: 10.1016/j.ceramint.2017.12.088.

[284] D. S. Kim, J. H. Lee, R. J. Sung, S. W. Kim, H. S. Kim, and J. S. Park, "Improvement of translucency in Al2O3 ceramics by two-step sintering technique," *J. Eur. Ceram. Soc.*, vol. 27, no. 13–15, pp. 3629–3632, **2007**, doi: 10.1016/j.jeurceramsoc.2007.02.002.

[285] K. Morita, B. N. Kim, H. Yoshida, K. Hiraga, and Y. Sakka, "Influence of pre- and post-annealing on discoloration of MgAl2O4 spinel fabricated by spark-plasma-sintering (SPS)," *J. Eur. Ceram. Soc.*, vol. 36, no. 12, pp. 2961–2968, **2016**, doi: 10.1016/j.jeurceramsoc.2015.11.010.

[286] A. Pourshamsi, A. Alhaji, and R. Emadi, "The effect of pre-annealing and post-annealing on the transparency of MgAl 2 O 4 , prepared by slip casting and spark plasma sintering (SPS)," *Ceram. Int.*, vol. 45, no. 6, pp. 7151–7156, **2019**, doi: 10.1016/j.ceramint.2018.12.221.

[287] L. Lallemant, N. Roussel, G. Fantozzi, V. Garnier, G. Bonnefont, T. Douillard, B. Durand, S. Guillemet-Fritsch, J. Y. Chane-Ching, D. Garcia-Gutierez, and J. Aguilar-Garib, "Effect of amount of doping agent on sintering, microstructure and optical properties of Zr- and La-doped alumina sintered by SPS," *J. Eur. Ceram. Soc.*, vol. 34, no. 5, pp. 1279–1288, **2014**, doi: 10.1016/j.jeurceramsoc.2013.11.015.

[288] M. M. Hasan, P. P. Dholabhai, S. Dey, B. P. Uberuaga, and R. H. R. Castro, "Reduced grain boundary energies in rare-earth doped MgAl2O4 spinel and consequent grain growth inhibition," *J. Eur. Ceram. Soc.*, vol. 37, no. 13, pp. 4043–4050, **2017**, doi: 10.1016/j.jeurceramsoc.2017.04.073.

[289] F. F. LANGE and M. M. HIRLINGER, "Hindrance of Grain Growth in Al2O3 by ZrO2 Inclusions.," *J. Am. Ceram. Soc.*, vol. 67, no. 3, pp. 164–168, **1984**, doi: 10.1111/j.1151-2916.1984.tb19734.x.

[290] M. Trunec, K. Maca, and R. Chmelik, "Polycrystalline alumina ceramics doped with nanoparticles for increased transparency," *J. Eur. Ceram. Soc.*, vol. 35, no. 3, pp. 1001–1009, **2015**, doi: 10.1016/j.jeurceramsoc.2014.09.041.

[291] K. Bodišová, R. Klement, D. Galusek, V. Pouchlý, D. Drdlík, and K. Maca, "Luminescent rare-earth-doped transparent alumina ceramics," *J. Eur. Ceram. Soc.*, vol. 36, no. 12, pp. 2975–2980, **2016**, doi: 10.1016/j.jeurceramsoc.2015.12.032.

[292] A. Goldstein, J. Raethel, M. Katz, M. Berlin, and E. Galun, "Transparent MgAl2O4/LiF ceramics by hot-pressing: Host-additive interaction mechanisms issue revisited," *J. Eur. Ceram. Soc.*, vol. 36, no. 7, pp. 1731–1742, **2016**, doi: 10.1016/j.jeurceramsoc.2016.02.001.

[293] G. R. Villalobos, J. S. Sanghera, and I. D. Aggarwal, "Degradation of magnesium aluminum spinel by lithium fluoride sintering aid," *J. Am. Ceram. Soc.*, vol. 88, no. 5, pp. 1321–1322, **2005**, doi: 10.1111/j.1551-2916.2005.00209.x.

[294] K. Rozenburg, I. E. Reimanis, H. J. Kleebe, and R. L. Cook, "Sintering kinetics of a MgAl2O4 spinel doped with LiF," *J. Am. Ceram. Soc.*, vol. 91, no. 2, pp. 444–450, **2008**, doi: 10.1111/j.1551-2916.2007.02185.x.

[295] T. Kim, D. Kim, and S. Kang, "Effect of additives on the sintering of MgAl2O4," *J. Alloys Compd.*, vol. 587, pp. 594–599, **2014**, doi: 10.1016/j.jallcom.2013.10.250.

[296] D. Drdlik, K. Drdlikova, H. Hadraba, and K. Maca, "Optical, mechanical and fractographic response of transparent alumina ceramics on erbium doping," *J. Eur. Ceram. Soc.*, vol. 37, no. 14, pp. 4265–4270, **2017**, doi: 10.1016/j.jeurceramsoc.2017.02.043.

[297] R. Boulesteix, A. Maître, K. Lemański, and P. J. Dereń, "Structural and spectroscopic properties of MgAl2O4:Nd3+ transparent ceramics fabricated by using two-step Spark Plasma Sintering," *J. Alloys Compd.*, vol. 722, pp. 358–364, **2017**, doi: 10.1016/j.jallcom.2017.06.101.

[298] B. Yoon, V. Avila, R. Kathiria, and L. M. Jesus, "Effects of powder dispersion on reactive flash sintering of 8 mol% yttria-stabilized zirconia and MgAl2O4 composites," *Scr. Mater.*, vol. 189, pp. 117–121, **2020**, doi: 10.1016/j.scriptamat.2020.08.009.

[299] M. Söderberg, "Resistive breakdown of inhomogeneous media," *Phys. Rev. B*, vol. 35, no. 1, pp. 352–357, **1987**, doi: 10.1103/PhysRevB.35.352.

[300] D. Valiev, S. Stepanov, O. Khasanov, E. Dvilis, E. Polisadova, and V. Paygin, "Synthesis and optical properties of Tb3+ or Dy3+-doped MgAl2O4 transparent ceramics," *Opt. Mater. (Amst).*, vol. 91, pp. 396–400, **2019**, doi: 10.1016/j.optmat.2019.03.049.

[301] S. M. Yong, D. H. Choi, K. Lee, S. Y. Ko, D. I. Cheong, Y. J. Park, and S. Il Go, "Study on carbon contamination and carboxylate group formation in Y2O3-MgO nanocomposites fabricated by spark plasma sintering," *J. Eur. Ceram. Soc.*, vol. 40, no. 3, pp. 847–851, **2020**, doi: 10.1016/j.jeurceramsoc.2019.10.035.

[302] P. Fu, Y. Xu, H. Shi, B. Zhang, X. Ruan, and W. Lu, "The effect of annealing process on the optical and microwave dielectric properties of transparent MgAl2O4 ceramics by spark plasma sintering," *Opt. Mater. (Amst).*, vol. 36, no. 7, pp. 1232–1237, **2014**, doi: 10.1016/j.optmat.2014.02.035.

[303] L. Lutterotti, D. Chateigner, S. Ferrari, and J. Ricote, "Texture, residual stress and structural analysis of thin films using a combined X-ray analysis," in *Thin Solid Films*, 2004. doi: 10.1016/j.tsf.2003.10.150.

[304] E. Feldbach, E. Tõldsepp, M. Kirm, A. Lushchik, K. Mizohata, and J. Räisänen, "Radiation resistance diagnostics of wide-gap optical materials," *Opt. Mater. (Amst).*, vol. 55, pp. 164–167, **2016**, doi: 10.1016/j.optmat.2016.03.008.

[305] M. Naamoun, A. Tallaire, P. Doppelt, A. Gicquel, M. Legros, J. Barjon, and J. Achard, "Reduction of dislocation densities in single crystal CVD diamond by using self-assembled metallic masks," *Diam. Relat. Mater.*, vol. 58, pp. 62–68, **2015**, doi:

10.1016/j.diamond.2015.06.012.

[306]M. Kitaura, S. Tanaka, M. Itoh, A. Ohnishi, H. Kominami, and K. Hara, “Excitation process of Ce 3+ and Eu 2+ ions doped in SrGa 2 S 4 crystals under the condition of multiplication of electronic excitations,” *J. Lumin.*, vol. 172, pp. 243–248, **2016**, doi: 10.1016/j.jlumin.2015.12.007.

[307]H. Wilcke, W. Böhmer, and N. Schwentner, “High flux and high resolution VUV beam line for synchrotron radiation,” *Nucl. Instruments Methods Phys. Res.*, vol. 204, no. 2–3, pp. 533–542, **1983**, doi: 10.1016/0167-5087(83)90083-2.

[308]J. A. Weil and J. R. Bolton, *Electron Paramagnetic Resonance*. Hoboken, NJ, USA: John Wiley & Sons, Inc., 2006. doi: 10.1002/0470084987.

[309]S. I. Omonmhenle and I. J. Shannon, “Synthesis and characterisation of surfactant enhanced Mg-Al hydrotalcite-like compounds as potential 2-chlorophenol scavengers,” *Appl. Clay Sci.*, vol. 127–128, pp. 88–94, **2016**, doi: 10.1016/j.clay.2016.03.033.

[310]S. P. Slotznick and S.-H. Shim, “In situ Raman spectroscopy measurements of MgAl2O4 spinel up to 1400 C,” *Am. Mineral.*, vol. 93, no. 2–3, pp. 470–476, **2008**, doi: 10.2138/am.2008.2687.

[311]B. R. Strohmeier, “ Magnesium Aluminate (MgAl 2 O 4) by XPS ,” *Surf. Sci. Spectra*, vol. 3, no. 2, pp. 121–127, **1994**, doi: 10.1116/1.1247772.

[312]J. T. Kloprogge, C. P. Ponce, and D. O. Ortillo, “X-ray Photoelectron Spectroscopic Study of Some Organic and Inorganic Modified Clay Minerals,” *Materials (Basel).*, vol. 14, no. 23, p. 7115, **2021**, doi: 10.3390/ma14237115.

[313]H. Wu, Y. Zhang, S. Long, L. Zhang, and X. Jie, “Tribological behavior of graphene anchored Mg-Al layered double hydroxide film on Mg alloy pre-sprayed Al coating,” *Appl. Surf. Sci.*, vol. 530, no. February, p. 146536, **2020**, doi: 10.1016/j.apsusc.2020.146536.

[314]A. B. Cusick, M. Lang, F. Zhang, K. Sun, W. Li, P. Kluth, C. Trautmann, and R. C. Ewing, “Amorphization of Ta2O5 under swift heavy ion irradiation,” *Nucl. Instruments Methods Phys. Res. Sect. B Beam Interact. with Mater. Atoms*, vol. 407, pp. 25–33, **2017**, doi: 10.1016/j.nimb.2017.05.036.

[315]K. N. Manukumar, B. Kishore, K. Manjunath, and G. Nagaraju, “Mesoporous Ta2O5 nanoparticles as an anode material for lithium ion battery and an efficient photocatalyst for hydrogen evolution,” *Int. J. Hydrogen Energy*, vol. 43, no. 39, pp. 18125–18135, **2018**, doi: 10.1016/j.ijhydene.2018.08.075.

[316]W. S. Liu, S. H. Huang, C. F. Liu, C. W. Hu, T. Y. Chen, and T. P. Perng, “Nitrogen doping in Ta 2 O 5 and its implication for photocatalytic H 2 production,” *Appl. Surf. Sci.*, vol. 459, no. July, pp. 477–482, **2018**, doi: 10.1016/j.apsusc.2018.07.185.

[317]C. Joseph, P. Bourson, and M. D. Fontana, “Amorphous to crystalline transformation in Ta 2O 5 studied by Raman spectroscopy,” *J. Raman Spectrosc.*, vol. 43, no. 8, pp. 1146–1150, **2012**, doi: 10.1002/jrs.3142.

[318]A. Pille, M. Amamra, A. Kanaev, and F. Schoenstein, “Microstructure and optical properties of alumina sintered from various phases,” *Ceram. Int.*, vol. 45, no. 7, pp. 9625–9630, **2019**, doi: 10.1016/j.ceramint.2018.10.209.

[319]Y. Wang, Y. Zhou, T. Zhang, M. He, X. Bu, and X. Yang, “Acetate-intercalated Ni-In layered double hydroxides with low infrared emissivity: Synthesis, delamination and restacked to form the multilayer films,” *Appl. Surf. Sci.*, vol. 288, pp. 710–717, **2014**, doi: 10.1016/j.apsusc.2013.10.109.

[320]P. Meenakshi, U. Sitharaman, and N. Rajamani, “Facile synthesis and characterization of acetate intercalated Co-La layered double hydroxide,” *J. Rare Earths*, vol. 35, no. 5, pp. 474–479, **2017**, doi: 10.1016/S1002-0721(17)60936-0.

[321]Q. Wang, Z. Wu, H. H. Tay, L. Chen, Y. Liu, J. Chang, Z. Zhong, J. Luo, and A. Borgna, “High temperature adsorption of CO2 on Mg-Al hydrotalcite: Effect of the charge compensating anions and the synthesis pH,” *Catal. Today*, vol. 164, no. 1, pp. 198–203, **2011**, doi: 10.1016/j.cattod.2010.10.042.

[322]N. Chubar, “New inorganic (an)ion exchangers based on Mg-Al hydrous oxides: (Alkoxide-free) sol-gel synthesis and characterisation,” *J. Colloid Interface Sci.*, vol. 357, no. 1, pp. 198–209, **2011**, doi: 10.1016/j.jcis.2011.01.098.

[323]K. Nakamoto, *Infrared and Raman Spectra of Inorganic and Coordination Compounds Part A*. Hoboken, NJ, USA: John Wiley & Sons, Inc., 2008. doi: 10.1002/9780470405840.

[324]M. L. Ramírez-Cedeño, N. Gaensbauer, H. Félix-Rivera, W. Ortiz-Rivera, L. Pacheco-Londoño, and S. P. Hernández-Rivera, “Fiber Optic Coupled Raman Based Detection of Hazardous Liquids Concealed in Commercial Products,” *Int. J. Spectrosc.*, vol. 2012, pp. 1–7, **2012**, doi: 10.1155/2012/463731.

[325]L. Gontrani, P. Tagliatesta, A. Agresti, S. Pescetelli, and M. Carbone, “New insights into the structure of glycols and derivatives: A comparative x-ray diffraction, raman and molecular dynamics study of ethane-1,2-diol, 2-methoxyethan-1-ol and 1,2-dimethoxy ethane,” *Crystals*, vol. 10, no. 11, pp. 1–15, **2020**, doi: 10.3390/cryst10111011.

[326]S. J. Palmer, T. Nguyen, and R. L. Frost, “Synthesis and Raman spectroscopic characterisation of hydrotalcite with CO32− and VO3− anions in the interlayer,” *J. Raman Spectrosc.*, vol. 38, no. 12, pp. 1602–1608, **2007**, doi: 10.1002/jrs.1820.

[327]K. El Hassani, H. Jabkhiro, D. Kalnina, B. H. Beakou, and A. Anouar, “Effect of drying step on layered double hydroxides properties: Application in reactive dye intercalation,” *Appl. Clay Sci.*, vol. 182, p. 105246, **2019**, doi: 10.1016/j.clay.2019.105246.

[328]G. Huang, Y. Sun, C. Zhao, Y. Zhao, Z. Song, J. Chen, S. Ma, J. Du, and Z. Yin, “Water–n-BuOH solvothermal synthesis of ZnAl–LDHs with different morphologies and its calcined product in efficient dyes removal,” *J. Colloid Interface Sci.*, vol. 494, pp. 215–222, **2017**, doi: 10.1016/j.jcis.2017.01.079.

[329]N. Drici-Setti, P. Lelli, and N. Jouini, “LDH-Co-Fe-Acetate: A New Efficient Sorbent for Azoic Dye Removal and Elaboration by Hydrolysis in Polyol, Characterization, Adsorption, and Anionic Exchange of Direct Red 2 as a Model Anionic Dye,” *Materials (Basel).*, vol. 13, no. 14, p. 3183, **2020**, doi: 10.3390/ma13143183.

[330]A. M. Baccarella, R. Garrard, M. L. Beauvais, U. Bednarksi, S. Fischer, A. M. M. Abeykoon, K. W. Chapman, B. L. Phillips, J. B. Parise, and J. W. Simonson, “Cluster mediated conversion of amorphous Al(OH)3 to γ-AlOOH,” *J. Solid State Chem.*, vol. 301, no. June, p. 122340, **2021**, doi: 10.1016/j.jssc.2021.122340.

[331]P. K. KIYOHARA, H. S. SANTOS, A. C. V. COELHO, and P. D. S. SANTOS, “Structure, surface area and morphology of aluminas from thermal decomposition of Al(OH)(CH3COO)2 crystals,” *An. Acad. Bras. Cienc.*, vol. 72, no. 4, pp. 471–495, **2000**, doi: 10.1590/S0001-37652000000400003.

[332]D. L. Perry, *Handbook of Inorganic Compounds*. CRC Press, 2016. doi: 10.1201/b10908.

[333]T. Sato, S. Ikoma, and F. Ozawa, “Thermal decomposition of organic basic aluminium salts-formate and acetate,” *Thermochim. Acta*, vol. 75, no. 1–2, pp. 129–137, **1984**, doi: 10.1016/0040-6031(84)85013-3.

[334]A. Jouini, H. Sato, A. Yoshikawa, T. Fukuda, G. Boulon, G. Panczer, K. Kato, and E. Hanamura, “Ti-doped MgAl2O4 spinel single crystals grown by the micro-pulling-down method for laser application: Growth and strong visible blue emission,” *J. Mater. Res.*, vol. 21, no. 09, pp. 2337–2344, **2006**, doi: 10.1557/jmr.2006.0280.

[335]B. Gu, C. Sun, J. C. Fettinger, W. H. Casey, A. Dikhtiarenko, J. Gascon, K. Koichumanova, K. Babu Sai Sankar Gupta, H. Jan Heeres, and S. He, “Synthesis, characterization and properties of a glycol-coordinated ε-Keggin-type Al 13 chloride,” *Chem. Commun.*, vol. 54, no. 33, pp. 4148–4151, **2018**, doi: 10.1039/C8CC01363B.

[336]G. V. Manohara, P. Vishnu Kamath, and W. Milius, “Reversible hydration and aqueous exfoliation of the acetate-intercalated layered double hydroxide of Ni and Al: Observation of an ordered interstratified phase,” *J. Solid State Chem.*, vol. 196, pp. 356–361, **2012**, doi: 10.1016/j.jssc.2012.06.017.

[337]R. Sousa, J. Jouin, O. Masson, F. Remondiere, A. Lemarchand, M. Colas, P. Thomas, J. Lameira, G. N. T. Bastos, A. B. Lima, J. L. M. Nascimento, M. Anicete-Santos, W. R. Monteiro, and C. N. Alves, “Structure and analgesic properties of layered double hydroxides intercalated with low amounts of ibuprofen,” *J. Am. Ceram. Soc.*, vol. 100, no. 6, pp. 2712–2721, **2017**, doi: 10.1111/jace.14763.

[338]W. Gong, D. Wu, Z. Cheng, H. Pang, Y. Lin, and G. Ning, “Direct synthesis of porous Mg(OH)2 nanoplates from natural brucite,” *Mater. Res. Bull.*, vol. 48, no. 3, pp. 1333–1337, **2013**, doi: 10.1016/j.materresbull.2012.12.033.

[339]M. Rajamathi, P. V. Kamath, and R. Seshadri, “Chemical synthesis of α-cobalt hydroxide,” *Mater. Res. Bull.*, vol. 35, no. 2, pp. 271–278, **2000**, doi: 10.1016/S0025-5408(00)00199-9.

[340]Z. . Xu and H. . Zeng, “A new approach for design and synthesis of CoII and CoII,III hydroxide materials,” *Int. J. Inorg. Mater.*, vol. 2, no. 2–3, pp. 187–196, **2000**, doi: 10.1016/S1466-6049(00)00020-9.

[341]P. Oliva, J. Leonardi, J. F. Laurent, C. Delmas, J. J. Braconnier, M. Figlarz, F. Fievet, and A. de Guibert, “Review of the structure and the electrochemistry of nickel hydroxides and oxy-hydroxides,” *J. Power Sources*, vol. 8, no. 2, pp. 229–255, **1982**, doi: 10.1016/0378-7753(82)80057-8.

[342]R. Prins, “On the structure of γ-Al2O3,” *J. Catal.*, vol. 392, pp. 336–346, **2020**, doi: 10.1016/j.jcat.2020.10.010.

[343]L. Jiang, J. Liu, K. Zuo, L. Zou, Y. Y. Li, G. Qian, and Z. P. Xu, “Performance of layered double hydroxides intercalated with acetate as biodenitrification carbon source: The effects of metal ions and particle size,” *Bioresour. Technol.*, vol. 259, no. March, pp. 99–103, **2018**, doi: 10.1016/j.biortech.2018.03.032.

[344]F. Cavani, F. Trifirò, and A. Vaccari, “Hydrotalcite-type anionic clays: Preparation, properties and applications.,” *Catal. Today*, vol. 11, no. 2, pp. 173–301, **1991**, doi: 10.1016/0920-5861(91)80068-K.

[345]Y. -M Chiang and W. D. Kingery, “Grain-Boundary Migration in Nonstoichiometric Solid Solutions of Magnesium Aluminate Spinel: II, Effects of Grain-Boundary Nonstoichiometry,” *J. Am. Ceram. Soc.*, vol. 73, no. 5, pp. 1153–1158, **1990**, doi: 10.1111/j.1151-2916.1990.tb05172.x.

[346]H. Sieber, D. Hesse, X. Pan, S. Senz, and J. Heydenreich, “TEM investigations of spinel-forming solid state reactions: Reaction mechanism, film orientation, and interface structure during MgAl2O4 formation on MgO (001) and Al2O3 (11.2) single crystal substrates,” *Zeitschrift fur Anorg. und Allg. Chemie*, vol. 622, no. 10, pp. 1658–1666, **1996**, doi: 10.1002/zaac.19966221007.

[347]M. Sokol, S. Kalabukhov, and N. Frage, “Fabrication of Polycrystalline Transparent Co+2: MgAl2O4 by a Combination of Spark Plasma Sintering (SPS) and Hot Isostatic Pressing (HIP) Processes,” *MATEC Web Conf.*, vol. 109, pp. 2–7, **2017**, doi: 10.1051/matecconf/201710903002.

[348]L. Basyrova, S. Balabanov, A. Belyaev, V. Drobotenko, A. Volokitina, V. Vitkin, O. Dymshits, and P. Loiko, “Synthesis, structure and spectroscopy of Fe2+:MgAl2O4 transparent ceramics,” *J. Phys. Conf. Ser.*, vol. 1410, no. 1, pp. 2–6, **2019**, doi: 10.1088/1742-6596/1410/1/012123.

[349]A. V. Belyaev, I. I. Evdokimov, V. V. Drobotenko, and A. A. Sorokin, “A new approach to producing transparent ZnAl2O4 ceramics,” *J. Eur. Ceram. Soc.*, vol. 37, no. 7, pp. 2747–2751, **2017**, doi: 10.1016/j.jeurceramsoc.2017.02.041.

[350]J. Song, M. Leng, X. Fu, and J. Liu, “Synthesis and characterization of nanosized zinc aluminate spinel from a novel Zn–Al layered double hydroxide precursor,” *J. Alloys Compd.*, vol. 543, pp. 142–146, **2012**, doi: 10.1016/j.jallcom.2012.07.111.

[351]J. Liu, J. Song, H. Xiao, L. Zhang, Y. Qin, D. Liu, W. Hou, and N. Du, “Synthesis and thermal properties of ZnAl layered double hydroxide by urea hydrolysis,” *Powder Technol.*, vol. 253, pp. 41–45, **2014**, doi: 10.1016/j.powtec.2013.11.007.

[352]L. Gama, M. A. Ribeiro, B. S. Barros, R. H. A. Kiminami, I. T. Weber, and A. C. F. M. Costa, “Synthesis and characterization of the NiAl2O4, CoAl2O4 and ZnAl2O4 spinels by the polymeric precursors method,” *J. Alloys Compd.*, vol. 483, no. 1–2, pp. 453–455, **2009**, doi: 10.1016/j.jallcom.2008.08.111.

[353]D. Han, J. Zhang, P. Liu, and S. Wang, “Effect of polymorphism of Al2O3 on the sintering and microstructure of transparent MgAl2O4 ceramics,” *Opt. Mater. (Amst).*, vol. 71, pp. 62–65, **2017**, doi: 10.1016/j.optmat.2016.06.016.

[354]L. K. Kurihara and S. L. Suib, “Sol-Gel Synthesis of Ternary Metal Oxides. 1. Synthesis and Characterization of MAl2O4 (M = Mg, Ni, Co, Cu, Fe, Zn, Mn, Cd, Ca, Hg, Sr, and Ba) and Pb2Al2O5,” *Chem. Mater.*, vol. 5, no. 5, pp. 609–613, **1993**, doi: 10.1021/cm00029a006.

[355]R. Chellammal Gayathri, V. Elakkiya, and S. Sumathi, “Effect of method of preparation on the photocatalytic activity of NiAl2O4,” *Inorg. Chem. Commun.*, vol. 129, no. April, p. 108634, **2021**, doi: 10.1016/j.inoche.2021.108634.

[356]A. V. Belyaev, M. I. Lelet, N. I. Kirillova, N. M. Khamaletdinova, M. S. Boldin, A. A. Murashov, and S. S. Balabanov, “Sol-gel synthesis and characterization of ZnAl2O4 powders for transparent ceramics,” *Ceram. Int.*, vol. 45, no. 4, pp. 4835–4839, **2019**, doi: 10.1016/j.ceramint.2018.11.179.

[357]P. Mohanty, S. Mohapatro, R. Mahapatra, and D. K. Mishra, “Low cost synthesis route of spinel ZnAl2O4,” *Mater. Today Proc.*, vol. 35, no. 3, pp. 130–132, **2021**, doi: 10.1016/j.matpr.2020.03.508.

[358]S. Boudiaf, N. Nasrallah, M. Mellal, C. Belabed, B. Belhamdi, D. Meziani, B. Mehdi, and M. Trari, “Synthesis and characterization of semiconductor CoAl2O4 for optical and dielectric studies: Application to photodegradation of organic pollutants under visible light,” *Optik (Stuttg).*, vol. 219, no. March, p. 165038, **2020**, doi: 10.1016/j.ijleo.2020.165038.

[359]S. Guo, H. Tang, L. You, H. Zhang, J. Li, and K. Zhou, “Combustion synthesis of mesoporous CoAl2O4 for peroxymonosulfate activation to degrade organic pollutants,” *Chinese Chem. Lett.*, no. xxxx, pp. 2–6, **2021**, doi: 10.1016/j.cclet.2021.01.019.

[360]K. A. Gedekar, S. P. Wankhede, S V Moharil, and R. M. Belekar, “d–f luminescence of Ce3+ and Eu2+ ions in BaAl2O4, SrAl2O4 and CaAl2O4 phosphors,” *J. Adv. Ceram.*, vol. 6, no. 4, pp. 341–350, **2017**, doi: 10.1007/s40145-017-0246-0.

[361]A. Salehabadi, M. Salavati-Niasari, F. Sarrami, and A. Karton, “Sol-Gel auto-combustion synthesis and physicochemical properties of BaAl2O4 nanoparticles; electrochemical hydrogen storage performance and density functional theory,” *Renew. Energy*, vol. 114, no. 2, pp. 1419–1426, **2017**, doi: 10.1016/j.renene.2017.07.119.

[362]D. Zhao, B. Ma, C. Wang, Y. Zhang, S. Shi, and Y. Chen, “Investigation of the thermal behavior of Mg(NO3)2·6H2O and its application for the regeneration of HNO3 and MgO,” *Chem. Eng. J.*, vol. 433, no. P3, p. 133804, **2022**, doi: 10.1016/j.cej.2021.133804.

[363]P. Thibaudeau and F. Gervais, “Ab initio investigation of phonon modes in the MgAl2O4 spinel,” *J. Phys. Condens. Matter*, vol. 14, no. 13, pp. 3543–3552, **2002**, doi: 10.1088/0953-8984/14/13/312.

[364]H. A. Lauwers and M. A. Herman, “Force field of some AB2C4 spinel compounds,” *J. Phys. Chem. Solids*, vol. 41, no. 3, pp. 223–230, **1980**, doi: 10.1016/0022-3697(80)90189-4.

[365]M. P. O’Horo, A. L. Frisillo, and W. B. White, “Lattice vibrations of MgAl2O4 spinel,” *J. Phys. Chem. Solids*, vol. 34, no. 1, pp. 23–28, **1973**, doi: 10.1016/0022-3697(73)90058-9.

[366]H. P. Liermann and J. Ganguly, “Diffusion kinetics of Fe2+ and Mg in aluminous spinel: Experimental determination and applications,” *Geochim. Cosmochim. Acta*, vol. 66, no. 16, pp. 2903–2913, **2002**, doi: 10.1016/S0016-7037(02)00875-X.

[367]C. A. Gilbert, R. Smith, S. D. Kenny, S. T. Murphy, R. W. Grimes, and J. A. Ball, “A theoretical study of intrinsic point defects and defect clusters in magnesium aluminate spinel,” *J. Phys. Condens. Matter*, vol. 21, no. 27, **2009**, doi: 10.1088/0953-8984/21/27/275406.

[368]R. Smith, D. Bacorisen, B. P. Uberuaga, K. E. Sickafus, J. A. Ball, and R. W. Grimes, “Dynamical simulations of radiation damage in magnesium aluminate spinel, MgAl2O4,” *J. Phys. Condens. Matter*, vol. 17, no. 6, pp. 875–891, **2005**, doi: 10.1088/0953-8984/17/6/008.

[369]S. T. Murphy, B. P. Uberuaga, J. B. Ball, A. R. Cleave, K. E. Sickafus, R. Smith, and R. W. Grimes, “Cation diffusion in magnesium aluminate spinel,” *Solid State Ionics*, vol. 180, no. 1, pp. 1–8, **2009**, doi: 10.1016/j.ssi.2008.10.013.

[370]M. Han, Z. Wang, Y. Xu, R. Wu, S. Jiao, Y. Chen, and S. Feng, “Physical properties of MgAl2O4, CoAl2O4, NiAl2O4, CuAl2O4, and ZnAl2O4 spinels synthesized by a solution combustion method,” *Mater. Chem. Phys.*, vol. 215, no. October 2017, pp. 251–258, **2018**, doi: 10.1016/j.matchemphys.2018.05.029.

[371]S. M. Rafiaei, G. Dini, and A. Bahrami, “Synthesis, crystal structure, optical and adsorption properties of BaAl2O4: Eu2+, Eu2+/ L3+ (L = Dy, Er, Sm, Gd, Nd, and Pr) phosphors,” *Ceram. Int.*, vol. 46, no. 12, pp. 20243–20250, **2020**, doi: 10.1016/j.ceramint.2020.05.106.

[372]A. J. Pamphile-Adrian, F. B. Passos, and P. P. Florez-Rodriguez, “Systematic study on the properties of nickel aluminate (NiAl2O4) as a catalytic precursor for aqueous phase hydrogenolysis of glycerol,” *Catal. Today*, no. July, **2021**, doi: 10.1016/j.cattod.2021.07.002.

[373]F. Tielens, M. Calatayud, R. Franco, J. M. Recio, Pérez-Ramírez, and C. Minot, “Periodic DFT study of the structural and electronic properties of bulk CoAl2O4 spinel,” *J. Phys. Chem. B*, vol. 110, no. 2, pp. 988–995, **2006**, doi: 10.1021/jp053375l.

[374]I. Halevy, D. Dragoi, E. Üstündag, A. F. Yue, E. H. Arredondo, J. Hu, and M. S. Somayazulu, “The effect of pressure on the structure of NiAl2O4,” *J. Phys. Condens. Matter*, vol. 14, no. 44 SPEC ISS., pp. 10511–10516, **2002**, doi: 10.1088/0953-8984/14/44/324.

[375]D. Dwibedi, C. Murugesan, M. Leskes, and P. Barpanda, “Role of annealing temperature on cation ordering in hydrothermally prepared zinc aluminate (ZnAl2O4) spinel,” *Mater. Res. Bull.*, vol. 98, no. October 2017, pp. 219–224, **2018**, doi: 10.1016/j.materresbull.2017.10.010.

[376]W. Brockner, C. Ehrhardt, and M. Gjikaj, “Thermal decomposition of nickel nitrate hexahydrate, Ni(NO3)2·6H2O, in comparison to Co(NO3)2·6H2O and Ca(NO3)2·4H2O,” *Thermochim. Acta*, vol. 456, no. 1, pp. 64–68, **2007**, doi: 10.1016/j.tca.2007.01.031.

[377]B. Małecka, R. Gajerski, A. Małecki, M. Wierzbicka, and P. Olszewski, “Mass spectral studies on the mechanism of thermal decomposition of Zn(NO3)2·nH2O,” *Thermochim. Acta*, vol. 404, no. 1–2, pp. 125–132, **2003**, doi: 10.1016/S0040-6031(03)00101-1.

[378]A. Moezzi, P. S. Lee, A. M. McDonagh, and M. B. Cortie, “On the thermal decomposition of zinc hydroxide nitrate, Zn5(OH)8(NO3)2·2H2O,” *J. Solid State Chem.*, vol. 286, no. 3, p. 121311, **2020**, doi: 10.1016/j.jssc.2020.121311.

[379]S. M. Pourmortazavi, S. G. Hosseini, S. S. Hajimirsadeghi, and R. F. Alamdari, “Investigation on thermal analysis of binary zirconium/oxidant pyrotechnic systems,” *Combust. Sci. Technol.*, vol. 180, no. 12, pp. 2093–2102, **2008**, doi: 10.1080/00102200802466014.

[380]C. J. Simpson, K. T. Aust, and W. C. Winegard, “The four stages of grain growth,” *Metall. Trans.*, vol. 2, no. 4, pp. 987–991, **1971**, doi: 10.1007/BF02664229.

[381]B. M. Moshtaghioun and J. I. Peña, “Non-Hall-Petch hardness dependence in ultrafine fibrous MgAl 2 O 4 -MgO eutectic ceramics fabricated by the laser-heated floating zone (LFZ) method,” *J. Eur. Ceram. Soc.*, vol. 39, no. 10, pp. 3208–3212, **2019**, doi: 10.1016/j.jeurceramsoc.2019.04.015.

[382]C. Wang, L. Cheng, and Z. Zhao, “FEM analysis of the temperature and stress distribution in spark plasma sintering: Modelling and experimental validation,” *Comput. Mater. Sci.*, vol. 49, no. 2, pp. 351–362, **2010**, doi: 10.1016/j.commatsci.2010.05.021.

[383]J. Diatta, G. Antou, N. Pradeilles, and A. Maître, “Numerical modeling of spark plasma sintering—Discussion on densification mechanism identification and generated porosity gradients,” *J. Eur. Ceram. Soc.*, vol. 37, no. 15, pp. 4849–4860, **2017**, doi: 10.1016/j.jeurceramsoc.2017.06.052.

[384]C. Manière, L. Durand, and C. Estournès, “Powder/die friction in the spark plasma sintering process: Modelling and experimental identification,” *Scr. Mater.*, vol. 116, pp. 139–142, **2016**, doi: 10.1016/j.scriptamat.2016.01.040.

[385]C. J. Ting and H. Y. Lu, “Hot-pressing of magnesium aluminate spinel - I. Kinetics and densification mechanism,” *Acta Mater.*, vol. 47, no. 3, pp. 817–830, **1999**, doi: 10.1016/S1359-6454(98)00400-5.

[386]K. E. Sickafus, R. W. Grimes, J. A. Valdez, A. Cleave, M. Tang, M. Ishimaru, S. M. Corish, C. R. Stanek, and B. P. Uberuaga, “Radiation-induced amorphization resistance and radiation tolerance in structurally related oxides,” *Nat. Mater.*, vol. 6, no. 3, pp. 217–223, **2007**, doi: 10.1038/nmat1842.

[387]E. Cui, Q. Meng, C. Ge, G. Yu, G. Hou, N. Xu, F. Zhang, and Y. Wu, “The roles of surface oxygen vacancy over Mg4Ta2O9-x

photocatalyst in enhancing visible-light photocatalytic hydrogen evolution performance," *Catal. Commun.*, vol. 103, no. September 2017, pp. 29–33, **2018**, doi: 10.1016/j.catcom.2017.09.018.

[388]W.-S. Liu, M.-W. Liao, S.-H. Huang, Y. I. A. Reyes, H.-Y. Tiffany Chen, and T.-P. Perng, "Formation and characterization of gray Ta2O5 and its enhanced photocatalytic hydrogen generation activity," *Int. J. Hydrogen Energy*, vol. 45, no. 33, pp. 16560–16568, **2020**, doi: 10.1016/j.ijhydene.2020.04.154.

[389]A. N. Kiryakov, A. F. Zatsepin, T. V. Dyachkova, and A. P. Tyutyunnik, "Residual strain and effects of lattice compression in thermobaric-synthesized optical nanoceramics MgAl2O4:Mn," *J. Eur. Ceram. Soc.*, vol. 43, no. 4, pp. 1671–1682, **2023**, doi: 10.1016/j.jeurceramsoc.2022.11.043.

[390]M. Couzi, J. L. Bruneel, D. Talaga, and L. Bokobza, "A multi wavelength Raman scattering study of defective graphitic carbon materials: The first order Raman spectra revisited," *Carbon N. Y.*, vol. 107, no. July, pp. 388–394, **2016**, doi: 10.1016/j.carbon.2016.06.017.

[391]D. V. Petrov, I. I. Matrosov, and A. R. Zaripov, "Determination of atmospheric carbon dioxide concentration using Raman spectroscopy," *J. Mol. Spectrosc.*, vol. 348, pp. 137–141, **2018**, doi: 10.1016/j.jms.2018.01.001.

[392]L. Ji and Y. Jiang, "Laser sintering of transparent Ta2O5 dielectric ceramics," *Mater. Lett.*, vol. 60, no. 12, pp. 1502–1504, **2006**, doi: 10.1016/j.matlet.2005.11.060.

[393]Y. BASKIN and D. C. SCHELL, "Phase Studies in the Binary System MgO–Ta2O5," *J. Am. Ceram. Soc.*, vol. 46, no. 4, pp. 174–177, **1963**, doi: 10.1111/j.1151-2916.1963.tb11709.x.

[394]J. L. Waring and R. S. Roth, "Effect of oxide additions on polymorphism of tantalum pentoxide (system Ta2O5-TiO2)," *J. Res. Natl. Bur. Stand. Sect. A Phys. Chem.*, vol. 72A, no. 2, p. 175, **1968**, doi: 10.6028/jres.072a.018.

[395]R. S. Devan, S. Y. Gao, W. Der Ho, J. H. Lin, Y. R. Ma, P. S. Patil, and Y. Liou, "Electrochromic properties of large-area and high-density arrays of transparent one-dimensional β-Ta2 O5 nanorods on indium-tin-oxide thin-films," *Appl. Phys. Lett.*, vol. 98, no. 13, pp. 3–5, **2011**, doi: 10.1063/1.3568896.

[396]C. Wang, J.-F. Wang, H. Chen, W. Wang, W.-B. Su, G. Zang, and P. Qi, "Effects of Ta2O5 on the grain size and electrical properties of SnO2-based varistors," *J. Phys. D. Appl. Phys.*, vol. 36, no. 23, pp. 3069–3072, **2003**, doi: 10.1088/0022-3727/36/23/031.

[397]F. Jean, F. Schoenstein, M. Zaghrioui, M. Bah, P. Marchet, J. Bustillo, F. Giovannelli, and I. Monot-Laffez, "Composite microstructures and piezoelectric properties in tantalum substituted lead-free K0.5Na0.5Nb1-xTaxO3 ceramics," *Ceram. Int.*, vol. 44, no. 8, pp. 9463–9471, **2018**, doi: 10.1016/j.ceramint.2018.02.163.

[398]M. F. Islam, R. Mahbub, and A. Mousharraf, "Effect of Sintering Parameters and Ta_2O_5 Doping on the Microstructure and Dielectric Properties of $BaTiO_3$ Based Ceramics," *Key Eng. Mater.*, vol. 608, pp. 247–252, **2014**, doi: 10.4028/www.scientific.net/KEM.608.247.

[399]T. M. HARKULICH, J. MAGDER, M. S. VUKASOVICH, and R. J. LOCKHART, "Ferroelectrics of Ultrafine Particle Size: II, Grain Growth Inhibition Studies," *J. Am. Ceram. Soc.*, vol. 49, no. 6, pp. 295–299, **1966**, doi: 10.1111/j.1151-2916.1966.tb13266.x.

[400]C. Wanqiu, Z. Yujuan, and Z. Yun, "Effects of Ta2O5 and MgO Additives on Microstructure and Mechanical Properties of Ultra-Pure Alumina Ceramics," **1988**.

[401]L. Li, W. Liu, B. Han, X. Jin, F. Li, W. Wang, Q. Zhou, D. Xu, and T. Cui, "Floating zone growth and optical phonon behavior of corundum Mg4Ta2O9 single crystals," *RSC Adv.*, vol. 5, no. 82, pp. 66988–66993, **2015**, doi: 10.1039/c5ra12071c.

[402]E. D. Bourret, D. M. Smiadak, R. B. Borade, Y. Ma, G. Bizarri, M. J. Weber, and S. E. Derenzo, "Scintillation of tantalate compounds," *J. Lumin.*, vol. 202, pp. 332–338, **2018**, doi: 10.1016/j.jlumin.2018.05.044.

[403]P. Mohanty, "Study of structural and conduction properties of Co3O4-doped corundum-type Mg4Ta2O9 ceramics," *RSC Adv.*, vol. 6, no. 77, pp. 73748–73759, **2016**, doi: 10.1039/c6ra09942d.

[404]D. Xu, S. Gao, W. Liu, Y. Liu, Q. Zhou, L. Li, T. Cui, and H. Yuan, "The Raman scattering of trirutile structure MgTa 2 O 6 single crystals grown by the optical floating zone method," *RSC Adv.*, vol. 9, no. 2, pp. 839–843, **2019**, doi: 10.1039/c8ra06113k.

[405]M. Sales, G. Eguia, P. Quintana, L. M. Torres-Martinez, and A. R. West, "The Phase Diagram CaO–Al2O3–Ta2O5and the Crystal Structures of Ca2AlTaO6and CaAlTaO5," *J. Solid State Chem.*, vol. 143, no. 1, pp. 62–68, **1999**, doi: 10.1006/jssc.1998.8079.

[406]T. Kitano, S. Okazaki, T. Shishido, K. Teramura, and T. Tanaka, "Generation of Brønsted acid sites on Al2O3-supported Ta2O5 calcined at high temperatures," *Catal. Today*, vol. 192, no. 1, pp. 189–196, **2012**, doi: 10.1016/j.cattod.2012.02.035.

[407]L. Chen, M. Hu, and J. Feng, "Mechanical properties, thermal expansion performance and intrinsic lattice thermal conductivity of AlMO 4 (M=Ta, Nb) ceramics for high-temperature applications," *Ceram. Int.*, vol. 45, no. 6, pp. 6616–6623, **2019**, doi: 10.1016/j.ceramint.2018.12.135.

[408]J. M. Heintz, J. J. M. Besson, L. Rabardel, and J. P. Bonnet, "Grain Growth and Densification Study of B-Ta2O5," **1992**.

[409]L. Ji and Y. Jiang, "Dielectric and microstructure modification of Ta2O5 ceramics by laser sintering," *Mater. Lett.*, vol. 60, no. 1, pp. 86–89, **2006**, doi: 10.1016/j.matlet.2005.07.077.

[410]Y. Zhang, Q. Zhang, X. He, H. Liang, T. Liu, and A. Lu, "Effect of partial substitution of Ta2O5 by Nb2O5 on the glass formation, structure and electrical properties of Li2O-Ta2O5-ZrO2-SiO2 glasses," *J. Non. Cryst. Solids*, vol. 571, no. May, pp. 1–13, **2021**, doi: 10.1016/j.jnoncrysol.2021.121054.

[411]S. K. Sistla, T. P. Mishra, Y. Deng, A. Kaletsch, M. Bram, and C. Broeckmann, "Polarity Induced Grain Growth of Gadolinium doped Ceria under Field- Assisted Sintering Technology / Spark Plasma Sintering (FAST/SPS) conditions," *J. Am. Ceram. Soc.*, vol. In Press, **2020**, doi: 10.1111/jace.17614.

[412]Y. Achenani, M. Saâdaoui, A. Cheddadi, G. Bonnefont, and G. Fantozzi, "Finite element modeling of spark plasma sintering: Application to the reduction of temperature inhomogeneities, case of alumina," *Mater. Des.*, vol. 116, pp. 504–514, **2017**, doi: 10.1016/j.matdes.2016.12.054.

[413]S. M. R. Derakhshandeh, M. S. Gohari, E. K. Saeidabadi, A. Jam, H. rajaei, A. Fazili, M. Alizadeh, E. Ghasali, A. H. Pakseresht, and T. Ebadzadeh, "Comparison of spark plasma and microwave sintering of mullite based composite: Mullite/Ta2O5 reaction," *Ceram. Int.*, vol. 44, no. 11, pp. 13176–13181, **2018**, doi: 10.1016/j.ceramint.2018.04.142.

[414]A. J. PERROTTA and J. E. YOUNG, "Rutile-Type Crystalline Solutions in the System MgTa2O6-AlTaO4," *J. Am. Ceram. Soc.*, vol. 56, no. 8, pp. 441–441, **1973**, doi: 10.1111/j.1151-2916.1973.tb12721.x.

[415]I. Reimanis and H. J. Kleebe, “A review on the sintering and microstructure development of transparent spinel (MgAl 2O 4),” *J. Am. Ceram. Soc.*, vol. 92, no. 7, pp. 1472–1480, **2009**, doi: 10.1111/j.1551-2916.2009.03108.x.

[416]M. Dang, H. Lin, X. Yao, H. Ren, T. Xie, H. Peng, and Z. Tan, “Effects of B2O3 and MgO on the microwave dielectric properties of MgTa2O6 ceramics,” *Ceram. Int.*, vol. 45, no. 18, pp. 24244–24247, **2019**, doi: 10.1016/j.ceramint.2019.08.135.

[417]H. T. Wu, C. H. Yang, W. B. Wu, and Y. L. Yue, “Study on synthesis and evolution of nanocrystalline Mg4Ta2O9 by aqueous so-gel process,” *Surf. Rev. Lett.*, vol. 19, no. 3, **2012**, doi: 10.1142/S0218625X12500242.

[418]Ø. Johannesen and P. Kofstad, “Electrical conductivity of stabilized low and high temperature modifications of tantalum pentoxide (L-Ta2O5 and H-Ta2O5) II: Electrical conductivity of H-Ta2O5 with additions of TiO2, HfO2 and Cr2O3,” *J. Less Common Met.*, vol. 98, no. 2, pp. 187–204, **1984**, doi: 10.1016/0022-5088(84)90216-9.

[419]E. Feldbach, I. Kudryavtseva, K. Mizohata, G. Prieditis, J. Räisänen, E. Shablonin, and A. Lushchik, “Optical characteristics of virgin and proton-irradiated ceramics of magnesium aluminate spinel,” *Opt. Mater. (Amst).*, vol. 96, no. August, p. 109308, **2019**, doi: 10.1016/j.optmat.2019.109308.

[420]G. Prieditis, E. Feldbach, I. Kudryavtseva, A. I. Popov, E. Shablonin, and A. Lushchik, “Luminescence characteristics of magnesium aluminate spinel crystals of different stoichiometry,” *IOP Conf. Ser. Mater. Sci. Eng.*, vol. 503, no. 1, **2019**, doi: 10.1088/1757-899X/503/1/012021.

[421]Savita, M. Jain, Manju, A. Kumar Sinha, F. Singh, A. Vij, and A. Thakur, “Modulation of radiative defects in MgAl 2 O 4 nanocrystals probed using NMR, ESR, and PL spectroscopies,” *J. Appl. Phys.*, vol. 129, no. 12, p. 125111, **2021**, doi: 10.1063/5.0045385.

[422]D. Ramírez-Rosales, R. Zamorano-Ulloa, and O. Pérez-Martínez, “Electron spin resonance study of the conversion of Mn4+ to Mn2+ in the Pb1−xEuxTi1−yMnyO3 ceramic system,” *Solid State Commun.*, vol. 118, no. 7, pp. 371–376, **2001**, doi: 10.1016/S0038-1098(01)00072-2.

[423]V. Amir-Ebrahimi and J. J. Rooney, “A novel ESR method based on dilute solid solutions of Mn3+/Mn2+ ions in MgO for detecting spillover of hydrogen from noble metals,” *J. Mol. Catal. A Chem.*, vol. 159, no. 2, pp. 429–432, **2000**, doi: 10.1016/S1381-1169(00)00208-9.

[424]Y. Zhang, S. Hu, Y. Liu, L. Chen, Z. Wang, G. Zhou, and S. Wang, “Influences of thermal post-treatment on the Mn valence states and luminescence properties of red-emitting Lu3Al5O12: Mn4+ transparent ceramic phosphors,” *Opt. Mater. (Amst).*, vol. 101, p. 109705, **2020**, doi: 10.1016/j.optmat.2020.109705.

[425]H. Ji, X. Hou, M. S. Molokeev, J. Ueda, S. Tanabe, M. G. Brik, Z. Zhang, Y. Wang, and D. Chen, “Ultrabroadband red luminescence of Mn 4+ in MgAl 2 O 4 peaking at 651 nm,” *Dalt. Trans.*, vol. 49, no. 17, pp. 5711–5721, **2020**, doi: 10.1039/D0DT00931H.

[426]N. Khaidukov, A. Pirri, M. Brekhovskikh, G. Toci, M. Vannini, B. Patrizi, and V. Makhov, “Time- and Temperature-Dependent Luminescence of Manganese Ions in Ceramic Magnesium Aluminum Spinels,” *Materials (Basel).*, vol. 14, no. 2, p. 420, **2021**, doi: 10.3390/ma14020420.

[427]A. F. Zatsepin, A. N. Kiryakov, D. A. Zatsepin, Y. V. Shchapova, and N. V. Gavrilov, “Structural and electron-optical properties of transparent nanocrystalline MgAl2O4 spinel implanted with copper ions,” *J. Alloys Compd.*, vol. 834, p. 154993, **2020**, doi: 10.1016/j.jallcom.2020.154993.

[428]E. Simanek and K. A. Mueller, “EPR parameters and ionic-covalent transition in solids,” *Chem. Phys. Lett.*, vol. 4, no. 8, pp. 482–484, **1970**, doi: 10.1016/0009-2614(70)85021-7.

[429]P. H. Borse, D. Srinivas, R. F. Shinde, S. K. Date, W. Vogel, and S. K. Kulkarni, “Effect of Mn 2 concentration in ZnS nanoparticles on photoluminescence and electron-spin-resonance spectra.”

[430]V. A. Dutov, A. N. Kiryakov, A. F. Zatsepin, D. R. Bajtimirov, T. V. Dyachkova, A. P. Tytunnyuk, and Y. G. Zainulin, “Low temperature ESR of MgAl2O4 nanoceramics,” in *AIP Conference Proceedings*, Dec. 2019, vol. 2174, p. 020097. doi: 10.1063/1.5134248.

[431]A. R. Molla, C. R. Kesavulu, R. P. S. Chakradhar, A. Tarafder, S. K. Mohanty, J. L. Rao, B. Karmakar, and S. K. Biswas, “Microstructure, mechanical, thermal, EPR, and optical properties of MgAl2O4:Cr3+ spinel glass-ceramic nanocomposites,” *J. Alloys Compd.*, vol. 583, pp. 498–509, **2014**, doi: 10.1016/j.jallcom.2013.08.122.

[432]V. Singh, R. P. S. Chakradhar, J. L. Rao, and D. K. Kim, “Combustion synthesized MgAl2O4:Cr phosphors-An EPR and optical study,” *J. Lumin.*, vol. 129, no. 2, pp. 130–134, **2009**, doi: 10.1016/j.jlumin.2008.08.011.

[433]M. R. Ahmed, B. Ashok, S. K. Ahmmad, A. Hameed, M. N. Chary, and M. Shareefuddin, “Infrared and Raman spectroscopic studies of Mn2+ ions doped in strontium alumino borate glasses: Describes the role of Al2O3,” *Spectrochim. Acta - Part A Mol. Biomol. Spectrosc.*, vol. 210, pp. 308–314, **2019**, doi: 10.1016/j.saa.2018.11.053.

[434]M. Aoyama, Y. Amano, K. Inoue, S. Honda, S. Hashimoto, and Y. Iwamoto, “Synthesis and characterization of Mn-activated lithium aluminate red phosphors,” *J. Lumin.*, vol. 136, pp. 411–414, **2013**, doi: 10.1016/j.jlumin.2012.12.012.

[435]Y. Zhang, S. Hu, Y. Liu, Z. Wang, W. Ying, G. Zhou, and S. Wang, “Preparation, crystal structure and luminescence properties of red-emitting Lu3Al5O12: Mn4+ ceramic phosphor,” *J. Eur. Ceram. Soc.*, vol. 39, no. 2–3, pp. 584–591, **2019**, doi: 10.1016/j.jeurceramsoc.2018.08.031.

[436]N. A. Zhuk, V. A. Belyy, V. P. Lutoev, B. A. Makeev, S. V. Nekipelov, M. V. Yermolina, and L. S. Feltsinger, “Mn doped BiNbO4 ceramics: Thermal stability, phase transitions, magnetic properties, NEXAFS and ESR spectroscopy,” *J. Alloys Compd.*, vol. 778, pp. 418–426, **2019**, doi: 10.1016/j.jallcom.2018.11.177.

[437]B. T. Allen, “Zero-field splitting parameter of the Mn++ ion in glassy and in polycrystalline media,” *J. Chem. Phys.*, vol. 43, no. 11, pp. 3820–3826, **1965**, doi: 10.1063/1.1696569.

[438]D. Zhang, C. Wang, Y. Liu, Q. Shi, W. Wang, and Y. Zhai, “Green and red photoluminescence from ZnAl 2O 4:Mn phosphors prepared by solgel method,” *J. Lumin.*, vol. 132, no. 6, pp. 1529–1531, **2012**, doi: 10.1016/j.jlumin.2012.01.025.

[439]M. Ozawa, K. Hashimoto, and S. Suzuki, “Structural and ESR characterization of heat-stable manganese-alumina lean NO removal catalyst,” *Appl. Surf. Sci.*, vol. 121–122, pp. 437–440, **1997**, doi: 10.1016/S0169-4332(97)00319-X.

[440]A. N. Kiryakov, A. F. Zatsepin, T. V. Dyachkova, A. P. Tytunyunnik, Y. G. Zainulin, G. Yakovlev, V. A. Pustovarov, and D. R. Bautimirov, “Microstructure of luminescent MgAl 2 O 4 nanoceramics,” *IOP Conf. Ser. Mater. Sci. Eng.*, vol. 443, no. 1, p. 012014, **2018**, doi: 10.1088/1757-899X/443/1/012014.

[441]N. Mironova-Ulmane, M. G. Brik, J. Grube, G. Krieke, A. Antuzevics, V. Skvortsova, M. Kemere, E. Elsts, A. Sarakovskis, M.

Piasecki, and A. I. Popov, “Spectroscopic studies of Cr3+ ions in natural single crystal of magnesium aluminate spinel MgAl2O4,” *Opt. Mater. (Amst).*, vol. 121, no. 1, p. 111496, **2021**, doi: 10.1016/j.optmat.2021.111496.

[442]C. Wang, A. H. Shen, and Y. Liu, “Characterization of order-disorder transition in MgAl2O4:Cr3+ spinel using photoluminescence,” *J. Lumin.*, vol. 227, no. December 2019, p. 117552, **2020**, doi: 10.1016/j.jlumin.2020.117552.

[443]P. Gluchowski and W. Strek, “Luminescence and excitation spectra of Cr3+:MgAl2O4 nanoceramics,” *Mater. Chem. Phys.*, vol. 140, no. 1, pp. 222–227, **2013**, doi: 10.1016/j.matchemphys.2013.03.025.

[444]N. Nuns, F. Béclin, and J. Crampon, “Grain-Boundary Characterization in a Nonstoichiometric Fine-Grained Magnesium Aluminate Spinel: Effects of Defect Segregation at the Space-Charge Layers,” *J. Am. Ceram. Soc.*, vol. 92, no. 4, pp. 870–875, **2009**, doi: 10.1111/j.1551-2916.2008.02901.x.

[445]V. T. Gritsyna, I. V. Afanasyev-Charkin, V. A. Kobyakov, and K. E. Sickafus, “Structure and electronic states of defects in spinel of different compositions MgO·nAl2O3:Me,” *J. Am. Ceram. Soc.*, vol. 82, no. 12, pp. 3365–3373, **1999**, doi: 10.1111/j.1151-2916.1999.tb02252.x.

[446]H. Spiridigliozzi, A. Pille, F. Schoenstein, L. Museur, E. Feldbach, H. Mändar, M. Kitaura, and A. Kanaev, “Effects of Ta doping and irradiation with He+ ions on photoluminescence of MgAl2O4 spinel ceramics,” *J. Eur. Ceram. Soc.*, vol. 40, no. 8, pp. 3215–3221, **2020**, doi: 10.1016/j.jeurceramsoc.2020.02.032.

[447]S. P. Feofilov, A. B. Kulinkin, and N. M. Khaidukov, “Inversion in synthetic spinel: Fluorescence of Cr3+ ions in MgAl2O4 spinel ceramics,” *J. Lumin.*, vol. 217, p. 116824, **2020**, doi: 10.1016/j.jlumin.2019.116824.

[448]P. J. Dereń, M. Malinowski, and W. Stręk, “Site selection spectroscopy of Cr3+ in MgAl2O4 green spinel,” *J. Lumin.*, vol. 68, no. 2–4, pp. 91–103, **1996**, doi: 10.1016/0022-2313(96)00020-8.

[449]C. Garapon, H. Manaa, and R. Moncorgé, “Absorption and fluorescence properties of Cr 3+ doped nonstoichiometric green spinel,” *J. Chem. Phys.*, vol. 95, no. 8, pp. 5501–5512, **1991**, doi: 10.1063/1.461623.

[450]A. J. Wojtowicz, M. Grinberg, and A. Lempicki, “The coupling of 4T2 and 2E states of the Cr3+ ion in solid state materials,” *J. Lumin.*, vol. 50, no. 4, pp. 231–242, **1991**, doi: 10.1016/0022-2313(91)90047-Y.

[451]E. O’Bannon and Q. Williams, “A Cr 3+ luminescence study of spodumene at high pressures: Effects of site geometry, a phase transition, and a level-crossing,” *Am. Mineral.*, vol. 101, no. 6, pp. 1406–1413, **2016**, doi: 10.2138/am-2016-5567.

[452]W. Mikenda and A. Preisinger, “N-lines in the luminescence spectra of Cr3+ -doped spinels (I) identification of N-lines,” *J. Lumin.*, vol. 26, no. 1–2, pp. 53–66, **1981**, doi: 10.1016/0022-2313(81)90169-1.

[453]W. Stręk, P. Dereń, and B. Jeżowska-Trzebiatowska, “Optical properties of Cr3+ in MgAl2O4 spinel,” *Phys. B Condens. Matter*, vol. 152, no. 3, pp. 379–384, **1988**, doi: 10.1016/0921-4526(88)90006-3.

[454]T. Phan, S. Yu, and T. P. J. Han, “Photoluminescence Properties of Cr 3 + -Doped MgAl 2 O 4 Natural Spinel,” *J. Korean Phys. Soc.*, vol. 45, no. 1, pp. 63–69, **2004**.

[455]K. Izumi, S. Miyazaki, S. Yoshida, T. Mizokawa, and E. Hanamura, “Optical properties of 3d transition-metal-doped MgAl2O4 spinels,” *Phys. Rev. B*, vol. 76, no. 7, p. 075111, **2007**, doi: 10.1103/PhysRevB.76.075111.

[456]U. Rohweder and H. Muller-Buschbaum, “Uber ein Oxotantalat mit teilgeordneter Korundstruktur: Mn0,6Mg3,4Ta2O9,” *Zeitschrift fur Anorg. und Allg. Chemiei*, vol. 573, no. 1, pp. 19–23, **1989**, doi: 10.1002/zaac.19895730104.

[457]Q. J. Mei, C. Y. Li, J. D. Guo, S. X. Huang, X. H. Zhang, and H. T. Wu, “Influence of sintering temperature on dielectric properties and crystal structure of corundum-structured Mg4Ta2O9 ceramics at microwave frequencies,” *Ceram. Int.*, vol. 39, no. 8, pp. 9145–9149, **2013**, doi: 10.1016/j.ceramint.2013.05.012.

[458]S. Chen, Y. Qi, G. Liu, J. Yang, F. Zhang, and C. Li, “A wide visible-light-responsive tunneled MgTa2O6−xNx photocatalyst for water oxidation and reduction,” *Chem. Commun.*, vol. 50, no. 92, pp. 14415–14417, **2014**, doi: 10.1039/c4cc06682k.

[459]B. Z. Saggioro, M. R. B. Andreeta, A. C. Hernandes, M. MacAtro, M. Peres, F. M. Costa, T. Monteiro, N. Franco, and E. Alves, “Effect of Eu2O3 doping on Ta2O5 crystal growth by the laser-heated pedestal technique,” *J. Cryst. Growth*, vol. 313, no. 1, pp. 62–67, **2010**, doi: 10.1016/j.jcrysgro.2010.09.083.

[460]M. L. Bortz, R. H. French, D. J. Jones, R V Kasowski, and F. S. Ohuchi, “Temperature dependence of the electronic structure of oxides: MgO, MgAl 2 O 4 and Al 2 O 3,” *Phys. Scr.*, vol. 41, no. 4, pp. 537–541, **1990**, doi: 10.1088/0031-8949/41/4/036.

[461]M. E. Thomas, W. J. Tropf, and S. L. Gilbert, “Vacuum-ultraviolet characterization of sapphire, ALON, and spinel near the band gap,” *Opt. Eng.*, vol. 32, no. 6, p. 1340, **1993**, doi: 10.1117/12.135837.

[462]S. M. Hosseini, “Structural, electronic and optical properties of spinel MgAl 2 O 4 oxide,” *Phys. status solidi*, vol. 245, no. 12, pp. 2800–2807, **2008**, doi: 10.1002/pssb.200844142.

[463]O. A. Plaksin and V. A. Stepanov, “Radiation-induced electrical and optical processes in materials based on Al2O3,” *Opt. Spectrosc.*, vol. 90, no. 4, pp. 542–551, **2001**, doi: 10.1134/1.1366748.

[464]W.-J. Chun, A. Ishikawa, H. Fujisawa, T. Takata, J. N. Kondo, M. Hara, M. Kawai, Y. Matsumoto, and K. Domen, “Conduction and Valence Band Positions of Ta 2 O 5 , TaON, and Ta 3 N 5 by UPS and Electrochemical Methods,” *J. Phys. Chem. B*, vol. 107, no. 8, pp. 1798–1803, **2003**, doi: 10.1021/jp027593f.

[465]K. E. Sickafus, A. C. Larson, N. Yu, M. Nastasi, G. W. Hollenberg, F. A. Garner, and R. C. Bradt, “Cation disorder in high dose, neutron-irradiated spinel,” *J. Nucl. Mater.*, vol. 219, pp. 128–134, **1995**, doi: 10.1016/0022-3115(94)00386-6.

[466]L. Museur, E. Feldbach, M. Kitaura, and A. Kanaev, “UV-visible spectroscopy of MgAl2O4 spinel single crystal,” in *UVSOR Annual report*, 2018.

This page intentionally left blank.

Abstract

This thesis concerns the fabrication of transparent $MgAl_2O_4$ ceramics with ultrafine microstructures, for applications in the field of ionizing radiation resistant materials. Such materials require simultaneously high relative density to be transparent, and small grain size at the nanoscale for radio-tolerance.

Different commercial magnesium aluminate spinel (MAS) powders were consolidated by spark plasma sintering (SPS). A parametric study revealed that the most determinant SPS conditions are the coupled applied pressure-sintering temperature. In particular, high pressure with reduced temperature (1 GPa, 1000°C) permitted to produce highly transparent ceramics up to the theoretical limit (87%), with limited grain growth (98 nm). In order to further reduce the grain size, we developed two synthesis routes for the preparation of $MgAl_2O_4$ nanopowders. The synthesis *via* polyol route led to MAS powders with crystallite size of 7 nm, with controllable $MgO{\cdot}nAl_2O_3$ composition (n = 0.716-5). The synthesis by liquid impregnation of nanofibrous alumina led to powders of 8-20 nm depending on the crystalline state of the initial Al_2O_3; in particular, amorphous alumina resulted in the formation of unique fully inverse MAS. The preliminary sintering study of these powders resulted in promising materials. We also investigated the phenomenology during SPS with the addition of the ionic conductor Ta_2O_5, which evidenced the formation of hot spots. Unusual characterization methods in the field of materials fabrication revealed defects arising specifically from the SPS technique. Finally, we assessed the irradiation behavior of our ceramics in order to estimate their tolerance toward ionizing radiations.

Keywords: *$MgAl_2O_4$ spinel, nanopowder synthesis, spark plasma sintering, transparent ceramics, ultrafine microstructure, structural defects*

Résumé

Cette thèse porte sur l'élaboration de céramiques de spinelle $MgAl_2O_4$ transparentes à microstructures ultrafines pour application dans le domaine des matériaux résistants aux rayonnements ionisants. Ces matériaux requièrent à la fois une haute densité relative pour une bonne transparence, et des grains nanométriques pour une tolérance accrue à l'irradiation.

Différentes poudres commerciales de spinelle ont été consolidées par spark plasma sintering (SPS). Nous avons montré que les paramètres déterminants de ce procédé sont le couple pression-température, l'utilisation de hautes pressions à basse température (1 GPa, 1000°C) ayant permis d'élaborer des céramiques de transparence proche de la limite théorique (87%), avec une croissance de grains limitée (98 nm). Afin de réduire davantage la taille des grains, deux voies de synthèse de nanopoudres $MgAl_2O_4$ ont été développées. La voie polyol a permis d'obtenir des particules de 7 nm avec une composition $MgO{\cdot}nAl_2O_3$ contrôlable (n = 0,716-5). L'imprégnation d'alumine nanofibreuse a conduit à des particules de 8 à 20 nm selon l'état cristallin initial de l'alumine ; en particulier, l'élaboration de spinelle $MgAl_2O_4$ inverse a été opérée pour la première fois. L'étude préliminaire du frittage de ces poudres a donné des résultats prometteurs. Nous avons aussi étudié la phénoménologie durant le SPS *via* l'ajout du conducteur ionique Ta_2O_5, mettant en évidence la formation de points chauds. L'utilisation de méthodes de caractérisation peu répandues dans notre domaine a révélé des défauts découlant directement de la technique SPS. Enfin, nous avons évalué le comportement à l'irradiation de nos matériaux afin d'estimer leur tolérance aux rayonnements ionisants.

Mots clés : *spinelle $MgAl_2O_4$, synthèse de poudres nanométriques, spark plasma sintering, céramiques transparentes, microstructure ultrafine, défauts structuraux*